Applied Bayesian Pre-Posterior and Life-Cycle Cost Analysis for Determining and Optimizing the Value of Structural Health Monitoring for Concrete Structures

Eline Vereecken

Supervisors

Prof. Robby Caspeele, PhD* – Prof. Geert Lombaert, PhD** – Wouter Botte, PhD*

*   Department of Structural Engineering and Building Materials
    Faculty of Engineering and Architecture, Ghent University

** Department of Civil Engineering
    Faculty of Engineering Science, KU Leuven

March 2022

GHENT
UNIVERSITY

KU LEUVEN

Applied Bayesian Pre-Posterior and Life-Cycle Cost Analysis for Determining and Optimizing the Value of Structural Health Monitoring for Concrete Structures

Eline Vereecken

Doctoral dissertation submitted to obtain the academic degrees of

Doctor of Civil Engineering (UGent) and Doctor of Engineering Science (PhD): Civil Engineering (KU Leuven)

Supervisors

Prof. Robby Caspeele, PhD* - Prof. Geert Lombaert, PhD** - Wouter Botte, PhD*

* Department of Structural Engineering and Building Materials
  Faculty of Engineering and Architecture, Ghent University

** Department of Civil Engineering
  Faculty of Engineering Science, KU Leuven

March 2022

GHENT UNIVERSITY

KU LEUVEN

Members of the Examination Board

Chair

Prof. Filip De Turck, PhD, Ghent University

Other members entitled to vote

Prof. Hans De Backer, PhD, Ghent University
Prof. Alan O'Connor, PhD, Trinity College Dublin, Ireland
Prof. Edwin Reynders, PhD, KU Leuven
Prof. Raphaël Steenbergen, PhD, TNO, the Netherlands
Prof. Ruben Van Coile, PhD, Ghent University
Prof. Els Verstrynge, PhD, KU Leuven

Supervisors

Prof. Robby Caspeele, PhD, Ghent University
Prof. Geert Lombaert, PhD, KU Leuven
Wouter Botte, PhD, Ghent University

For Tom…

Dankwoord

Ik heb zelf ondervonden dat bij het doorbladeren van een doctoraat, het oog meestal blijft hangen bij het dankwoord. Daarom wil ik van deze gelegenheid zeker gebruik maken om iedereen te bedanken die (on)rechtstreeks heeft bijgedragen aan het verwezenlijken van dit werk.

Eerst en vooral wil ik het woord richten aan mijn promotoren Robby, Geert en Wouter. Robby, bedankt om potentieel te zien in mij en mij de kans te geven om te doctoreren. Stiekem droomde ik er al sinds het begin van mijn studies van om een doctoraat te doen, dus ik was dan ook zeer enthousiast toen u mij deze mogelijkheid aanreikte. Gedurende mijn doctoraat kon ik steeds rekenen op uw ondersteunende feedback, maar ook op uw raad en advies als het even wat moeilijker ging. Ik wil u dan ook bedanken om steeds te blijven geloven in mij en om ervoor te zorgen dat ook ik het vertrouwen in mezelf vond. Geert, voor de aanvang van dit doctoraat was de onderzoeksgroep aan de KU Leuven mij geheel onbekend. Ik wil u dan ook bedanken om mij hier te introduceren en mij steeds te helpen als ik mijn weg niet vond in het papierwerk dat een gezamenlijk doctoraat met zich meebrengt. Daarnaast wil ik u ook bedanken voor de vele waardevolle en aangename feedbackmomenten, in Leuven of online. Wouter, bedankt om mijn eerstelijns contact te zijn, mij te helpen met de vele uitdagingen die ik onderweg tegenkwam en om op tijd op mijn rempedaal te gaan staan. Aan alle drie ook een heel groot woord van dank om, ondanks jullie drukke agenda's, telkens weer tijd vrij te maken om mijn (vele) teksten na te lezen, mij bij te staan met advies, dit doctoraat na te lezen… Robby, Geert en Wouter, ik heb genoten van de jaren onderzoek die ik heb mogen doen onder jullie supervisie.

Daarnaast wil ik ook de leden van mijn 'Supervisory Committee', Els Verstrynge en Hans De Backer, bedanken voor de nuttige feedback die zij geleverd hebben tijdens de formele evaluatiemomenten, maar ook daarnaast. *I would also like to thank the other members of the jury for their valuable comments and suggestions: prof. O'Connor, prof. Reynders, prof. Van Coile and prof. Steenbergen. Their feedback led to a great improvement of this work.*

Ook het technisch personeel van het labo heeft in een belangrijke mate bijgedragen aan het goede verloop van de voorbije jaren. Tommy, bedankt om mij te helpen met de puzzel die de planning van de corrosieproeven soms was en bedankt voor al het advies, zowel voor dienstverlening als voor mijn eigen experimenten. De corrosieproeven hebben heel wat voeten in de aarde gehad en daarom wil ik ook alle techniekers bedanken voor het harde werk tijdens deze proefcampagne: het herhaaldelijk vullen van het zoutbad (en het dichten van de vele lekken), het steeds

opnieuw manipuleren van de balken, de uitvoering van de proeven zelf, …. Zonder jullie technische expertise was dit allemaal niet gelukt. Ook Christel, Jens en Marijke verdienen een woord van dank voor alle administratieve hulp.

De voorbije jaren zijn voorbij gevlogen en daar heeft de aangename werksfeer in Gent en in Leuven zeker toe bijgedragen. Thomas en Evelien, bedankt voor de fijne momenten op onze bureau en de babbeltjes en mopjes die vaak een aangename onderbreking vormden tijdens de werkdag. Evelien, bedankt ook voor de vlotte samenwerking bij de oefenzittingen van draagsystemen en alle steun en berichtjes naast het werk. *Manu and Sharyar, thanks for the nice working environment in our office. Also a lot of thanks to the members of the Structural Reliability group under supervision of Robby for their valuable feedback during our team meetings and the nice atmosphere during our team activities.* Jolien, Kim, Lien, Bert en Jan, bedankt voor de aangename samenwerking tijdens het lesgeven. Om wegwijs te geraken in Leuven kon ik steeds rekenen op mijn bureaugenoten daar, Cédric en Pieter. Zij zorgden er samen met de andere collega's in Leuven voor dat ik mij ook daar welkom voelde. *Also special thanks to Dimi, for performing the dynamic tests on the beams here in Ghent and all the help with analysing the results.* Ook Eline wil ik bedanken voor het uitwisselen van haar kennis met betrekking tot de corrosieproeven.

Naast het werk dient er natuurlijk ook voldoende ontspanning te zijn. Daar zorgden onder andere mijn vrienden 'van de bouwkunde' voor met al onze gezellige samenkomsten (die vaak ontaarden in 'nerdy' discussies). Ook Maxime en Mathieu hebben hun bijdrage geleverd met onder andere coronawandelingen en 'dinner dates'. Tenslotte kon ik ook elke vrijdagavond mijn hoofd helemaal leegmaken dankzij mijn vriendinnen van de rope skipping.

Ook mijn familie wil ik zeker bedanken. Nena, bedankt voor je enthousiasme toen je hoorde dat ik een doctoraat wou gaan doen en om hier zo trots op te zijn. Wannes, bedankt voor alle hulp met mijn codes, elke keer dat ik mijn foutmeldingen weer niet opgelost kreeg. Mama en papa, jullie hebben mij de kans gegeven om te studeren, waardoor ik daarna dit doctoraat kon gaan doen. Jullie hebben mij steeds gesteund in mijn keuzes en stonden mij op tijd bij met raad en advies. Bedankt om steeds te geloven in mij! Zonder jullie had ik hier niet gestaan en was dit boek nooit tot stand gekomen. Kathy, bedankt voor de fijne babbeltjes, al je enthousiasme en je steun in alles wat ik onderneem. Filip, bedankt om altijd zo lekker te koken, voor de vele wandelingen en om altijd geïnteresseerd te blijven in mijn bezigheden. Simon, Sarah en Bert, bedankt voor de vele grappige momenten op familieaangelegenheden. Deze vormden een waardevolle bron van ontspanning.

Ik wil graag ook mijn schoonfamilie bedanken voor hun warme ontvangst en voor hun interesse in mijn onderzoek. Benny en Liliane, bedankt voor jullie steun bij

het lopen en het fietsen. Jullie zijn een grote bron van motivatie en inspiratie geweest voor mij. Liliane, ook bedankt voor al het lekkers dat we steeds krijgen en voor het delen van je recepten.

Mijn grootouders wil ik ook bedanken, ook al hebben ze dit helaas niet meer kunnen meemaken. Mémé, bedankt dat je elke keer bleef vragen hoe het nog was 'in Gent'. Ook al heb je het einde van mijn doctoraat net niet gehaald, ik weet zeker dat je trots zou geweest zijn op mij. Monique en Valeer, bedankt om steeds interesse te tonen in mijn doctoraat, om ervoor te zorgen dat we ons welkom voelden en voor alle lekkere taarten. Aan de bomma's van Tom ook een dankjewel om te weten dat ik 'iets met bruggen' deed, ook al was mijn naam moeilijker te onthouden.

Tenslotte rest er mij nog de belangrijkste persoon te bedanken. Tom, heel erg bedankt om mij bij te staan de afgelopen jaren. Jou leren kennen is het beste wat me is overkomen en heeft mij er op veel vlakken terug bovenop gebracht. Je hebt veel afgezien met mij en we hebben samen naar een goed evenwicht moeten zoeken. Ook jij bent veelvuldig op mijn rempedaal moeten gaan staan en je hebt veel van mijn stressmomenten meegemaakt, maar toch was je er altijd voor mij. Zonder jou was dit mij nooit gelukt, bedankt voor al je steun! Op naar het volgende hoofdstuk in ons leven samen. Ik zie je graag!

Eline Vereecken

Maart 2022, Gent

Table of contents

GENERAL CONCLUSIONS AND FURTHER RESEARCH

APPENDICES

List of symbols

Roman symbols

a	- Ageing exponent in the time-dependent model of the diffusion coefficient of concrete (Chapter II)
	- Factor for the relationship between the dynamic and static Young's modulus (Chapter VI)
	- Pit depth (Chapter II)
	- Action (Chapters V & XI)
	- Rate of reduction of the prestressing steel section (Chapter VIII)
A	- Observation (Chapter IV)
	- Girder cross-section area (Chapter IX)
A_p	Area of prestressing steel (Chapter VIII)
A_{p0}	Initial area of the prestressing steel (Chapter VIII)
a_j	Action (Chapters V & IX)
A_s	Steel section (Chapters II, VI, X & XI)
A_{s0}	Initial steel section (Chapters II, IV & VI)
$A_{s,insp}$	Measured reinforcement section (Chapter IV)
A_{sw}	Shear reinforcement section (Chapter XII)
b	Beam width (Chapter IX)
$\boldsymbol{B}$	Matrix representing the relationship between strains and displacements (Chapter X)
b_0	Initial concrete section width before degradation (Chapter II)
b_c	Exponent of regression in the calculation of the initiation period for carbonation-induced corrosion (Chapters II & XII)
b_d	Deck width (Chapter IX)
b_e	Regression variable in the time-dependent model for the diffusion coefficient of concrete (Chapters II & XII)
b_f	Flange width (Chapter XI)

b_w	Exponent of regression in the calculation of the initiation period for carbonation-induced corrosion (Chapters II & XII)
c	- Concrete cover (Chapters II, VII, IX, XI & XII)
	- Constant to normalize the PDF (Chapter IV)
C	- Torsion constant (Chapter XII)
	- Costs (Chapter XI)
C_0	- Initial chloride content of concrete (Chapter II)
	- Structural/construction costs (Chapter XI)
C_a	Cost of a (repair) action (Chapter IX)
C_A	Cost accounting for all actions (Chapter IX)
C_{BV}	Total bridge value (Chapter XI)
C_{cr}	Critical chloride concentration (Chapters II, VI, IX & XII)
C_F	Failure cost (Chapters V, IX & XI)
C_{F0}	Initial failure cost (Chapter IX)
C_I	Inspection cost (Chapters V, IX & XI)
C_{insp}	Cost of an individual inspection or measurement (Chapter IX)
C_{prior}	Prior cost (Chapters V, IX & XI)
$C_{post}/C_{posterior}$	Posterior cost (Chapters V, IX & XI)
C_R	Repair cost (Chapters V & XI)
c_{rj}	Homogeneous solution of the equation of Nelson (Chapter X)
C_s	- Surface chloride concentration (Chapters II, VI, IX, X & XI)
	- CO_2-concentration (Chapters II & XII)
C_S	Covariance function (Chapter III)
C_{SL}	Service life cost (Chapter V)
C_T	Total cost (Chapters V, IX & XI)
$\boldsymbol{d}$	True system output (Chapter IV)
d	- Effective depth of tendons (Chapter IX)
	- Effective depth of reinforcement (Chapter XII)
$\overline{\boldsymbol{d}}$	Data vector (Chapters IV, X & XI)
D	- Diffusion coefficient of concrete (Chapters II, VI, IX, X, XI & XII)
	- Diameter of steel reinforcing bar (Chapter II)
	- Diameter of prestressing wire (Chapter VIII)
D_0	Initial diameter of steel bar or wire (Chapters II & VIII)

$\bar{d}_j$	Data point (Chapter VI)
D_{max}	Maximum aggregate size (Chapter VII)
d_R	Repair criterion (Chapter V)
D_{RCM}	Chloride migration coefficient (Chapters II, VII & XII)
E	- Expected value (Chapters V & X)
	- Young's modulus (Chapter XI)
EA	Axial stiffness (Chapter X)
E_c	Young's modulus of concrete (Chapters II, VII & VIII)
E_{cd}	Dynamic Young's modulus (Chapter VI)
E_{cs}	Static Young's modulus (Chapter VI)
E_d	Reduced Young's modulus due to cracking (Chapter X)
E_{ef}	Effective elastic modulus of concrete (Chapter II)
E_i	Event (Chapter IV)
EI	Bending stiffness (Chapter X)
E_p	Young's modulus of prestressing steel (Chapter VIII)
E_s	Elastic modulus of steel (Chapter II)
E_s^*	Reduced elastic modulus of steel (Chapter II)
F	Constant of Faraday (Chapter VII)
$\boldsymbol{F}$	Force vector (Chapter X)
f'	Prior distribution (Chapters IV & XI)
f''	Posterior distribution (Chapters IV & XI)
f_B	Factor for multiplication of the bridge value due to its importance in the network (Chapter XI)
f_c	Concrete compressive strength (Chapters II, VI, VIII, IX & XI)
f_c^*	Reduced concrete compressive strength due to cracking (Chapter II)
$f_{c,cube}$	Concrete compressive strength tested on cubes (Chapter VII)
$f_{c,cyl}$	Concrete compressive strength tested on cylinders (Chapters VII & VIII)
f_{cm}	Mean concrete compressive strength (Chapter VIII)
f_{ct}	Axial concrete tensile strength (Chapters VI & VII)
$f_{ct,fl}$	Flexural tensile strength of concrete (Chapter VII)
f_{ctm}	Average tensile strength of concrete (Chapter VIII)
$f_{ct,sp}$	Splitting tensile strength of concrete (Chapters VII & VIII)

f_e	Exponent in the calculation of the environmental function k_e (Chapters II & XII)
F_m	Tensile strength of prestressing steel (Chapter VIII)
F_{MAP}	MAP objective function (Chapter XI)
F_{MAPr}	Regularization term based on available prior information (Chapter XI)
F_{ML}	Maximum likelihood function (Chapters IV & XI)
$F_{p0.2}$	0.2% strain limit of prestressing steel (Chapter VIII)
f_{rep}	Ratio of repair cost to total bridge value (Chapter XI)
f_u	Ultimate strength of steel (Chapter II)
$f_u{}^*$	Reduced ultimate strength of steel (Chapter II)
F_X	Cumulative distribution function of the variable X (Chapter VIII)
f_y	Yield strength of steel (Chapters II, IX & XI)
f_Y	Probability density function of Y (Chapter IX)
f_{y0}	Initial yield stress of steel (Chapter II)
f_{ypk}	Tensile strength of prestressing steel (Chapter IX)
g	Limit state function (Chapters IX & XI)
$\boldsymbol{G}$	Model to simulate the measured quantity (Chapters IV, VI, IX & XII)
G	- Permanent load effect (Chapters IX & XI)
	- Shear modulus (Chapter XI)
G_{AADT}	Factor to account for average annual daily traffic (Chapter XI)
G_{DD}	Factor to account for detour distance (Chapter XI)
g_e	Exponent in the calculation of the environmental function k_e (Chapters II & XII)
G_f	Fracture energy of concrete in tension (Chapter VII)
G_{LS}	Factor to account for largest span (Chapter XI)
G_{RC}	Factor to account for road category (Chapter XI)
G_{TL}	Factor to account for total length of the bridge (Chapter XI)
h	- Beam height (Chapters IX & XI)
	- Information entropy (Chapter X)
H	Approximation of the information entropy (Chapter X)
h_b	Beam depth (Chapter VII)
h_d	Deck height (Chapter IX)
h_f	Flange height (Chapter XI)

I	- Second moment of inertia (Chapter XII)
	- Current (Chapter VII)
	- Number of parts or number of samples (Chapter VII)
i_{corr}	Corrosion current density (Chapters II & VII)
J	Number of operators or number of strain gauges (Chapter VII)
$\boldsymbol{K}$	Stiffness matrix (Chapter X)
K_{As}	Stiffness matrix of the finite elements modelling the reinforcement (Chapter X)
k_c	Execution transfer parameter (Chapters II & XII)
K_d	Stiffness matrix in the finite elements of the damaged concrete (Chapter X)
k_e	Environmental function (Chapters II & XII)
K_E	Load model uncertainty (Chapters IX & XI)
K_R	Resistance model uncertainty (Chapters IX & XI)
k_t	Transfer parameter in the time-dependent model of the diffusion coefficient of concrete (Chapters II & XII)
l	Length of a beam element (Chapter X)
L	- Wire length (Chapter II)
	- Likelihood function (Chapter IV)
	- Beam length (Chapter IX)
	- Sensor configuration (Chapter X)
	- Span length of the bridge (Chapter XII)
$\boldsymbol{L}$	Relationship between static strains and displacements (Chapter X)
L_0	Standard length of a reinforcement bar (Chapter II)
l_c	Correlation length (Chapters III, IX & X)
L_u	Reinforcement length (Chapter II)
L_w	Number of elements in a post-tensioned girder (Chapter III)
Δm	Mass loss per unit surface (Chapter VII)
M	Atomic weight of iron atoms (Chapter VII)
n	- Number of elements in the random field (Chapter III)
	- Hyperparameter for the sample size (Chapter VIII)
	- Number of measurement results (Chapter VIII)
N	Number of measurements (Chapters VI, XI & XII)
n_{bars}	Number of reinforcement bars in the compression zone of concrete (Chapter II)

n_d	- Number of modes considered in the decomposition of the random field (Chapter III)
	- Number of damaged elements (Chapter XI)
N_d	Degrees of freedom (Chapter X)
$n_{decisions}$	Number of decisions (Chapter IX)
n_{el}	Total number of elements in which the structure is discretized (Chapter XI)
$n_{el,insp}$	Number of inspected/measured elements (Chapter IX)
n_g	Number of tendons (Chapter IX)
n_l	Initial number of inspection locations (Chapter V)
n_M	Number of elements in a post-tensioned girder (Chapter III)
N_m	Number of modes considered (Chapter VI)
n_p	Number of pits in an element (Chapter III)
N_p	Measureable degrees of freedom (Chapter X)
n_r	Number of reinforcement bars (Chapter II)
N_θ	Number of variables (Chapter X)
m	- Number of model evaluations (Chapter VI)
	- Number of measurements (Chapter VII)
	- Distributed moment (Chapter XII)
M	- Mean of a distribution represented as a random variable (Chapter VIII)
	- Bending moment (Chapters VII & XII)
$\boldsymbol{M}$	Mass matrix (Chapter X)
M_{cr}	Cracking moment (Chapter VII)
M_G	Bending moment due to permanent loads (Chapters IX & XII)
M_Q	Bending moment due to variable loads (Chapters IX & XII)
M_{Rd}	Bending moment resistance (Chapter IX)
p	- Pit depth (Chapter II)
	- Load per m² or load per m (Chapter XII)
P	- Probability (Chapters IV & XII)
	- Load (Chapter VIII)
P'	Prior probability (Chapter V)
P''	Posterior probability (Chapter V)
P_0	Load corresponding to decompression of the bottom fibre (Chapter VIII)

P_{cr}	Cracking load (Chapter VIII)
P_{crit}	Critical probability (Chapter XII)
P_{δ}	Load corresponding to a fixed displacement (Chapter VIII)
P_f	Probability of failure (Chapters IX & XI)
p_F	Cumulative probability of failure (Chapters IX & XI)
$P_{f,s}$	Probability of failure of a series system (Chapter IX)
p_{SR}	Probability of driving rain (Chapters II & XII)
p_{th}	Reliability threshold (Chapter V)
q	Transition distribution (Chapter IV)
Q	- Variable load effect (Chapters IX & XI)
	- Fisher information matrix (Chapter X)
Q_k	Characteristic value of the load (Chapter XI)
r	Discount factor (Chapter IX)
R	- Penetration ratio between maximum and average penetration (Chapter II)
	- Average pit depth (Chapter III)
	- Correlation function (Chapter X)
R^2	Coefficient of determination (Chapters VI & XII)
r_0	Initial radius of reinforcement bar (Chapter II)
R_{ACC}^{-1}	The inverse effective carbonation resistance of concrete (Chapters II & XII)
$\boldsymbol{R_G}$	Matrix representing a linear model relationship (Chapter IV)
RH_{real}	Relative humidity of the carbonated layer (Chapter II)
RH_{ref}	Reference relative humidity (Chapters II & XII)
s	Spacing between stirrups (Chapter XII)
S	Random field (Chapter III)
$\boldsymbol{S}$	Random vector representing a random field (Chapter III)
$\mathcal{S}$	Inspection strategy (Chapter V)
$\mathcal{S}^*$	Optimal inspection strategy (Chapter V)
s'_{lnX}	Hyperparameter of the standard deviation (lognormal) (Chapter VIII)
t	Time (Chapters II, VI, VII, IX & XI)
t_0	- A reference point of time (Chapters II & XII)
	- Current time (Chapter XI)
t_a	Time of performing an action (Chapters IX & XI)
t_c	Period of curing (Chapters II & XII)

T_{cr}	Time between initiation of corrosion and the onset of cover cracking (Chapters II & VI)
T_i	Initiation period of corrosion (Chapters II, IV, VI & VIII)
t_{insp}	Time of inspection or measurement (Chapters IV, V, IX & XI)
$\boldsymbol{T_{insp}}$	List with inspection times (Chapter IX)
ToW	Time of Wetness (Chapters II, VI, VIII, IX & XII)
T_r	Trace (Chapter III)
T_{real}	Temperature of the structural element or ambient air in the time-dependent model for the diffusion coefficient of concrete (Chapters II & XII)
t_{ref}	Reference period (Chapter XII)
T_{ref}	Standard test temperature in the time-dependent model for the diffusion coefficient of concrete (Chapters II & XII)
t_{rust}	First point in time at which rust stains are observed (Chapter VI)
T_{ser}	Time between first cracking and severe cracking (Chapter VI)
$t_{ser,observed}$	Time of observing severe cracking (Chapter VI)
t_{SL}	Anticipated service life (Chapters IX & XI)
$T_{\nu'}$	Student's t-distribution (Chapter VIII)
u	- Utility (Chapter V)
	- Gumbel parameter (Chapter VIII)
	- Displacement (Chapter X)
U	Displacement vector (Chapter X)
u_L	Random sample from a uniform distribution between 0 and 1 to be accepted according to likelihood function (Chapter IV)
u_P	Random sample from a uniform distribution between 0 and 1 to be accepted according to prior distribution (Chapter IV)
V_{corr}	Corrosion rate (Chapters II, IV, VI, VIII, X & XI)
$V_{corr,a}$	Mean corrosion rate when corrosion is active (Chapters II, VI, IX & XII)
V_G	Shear load effect due to permanent loads (Chapter XII)
V_Q	Shear load effect due to variable loads (Chapter XII)
w/c	Water-to-cement ratio of concrete (Chapter VI)
w_{cr}	Crack width (Chapters II & VII)

$W(t)$	Function in the calculation of the initiation period for carbonation-induced corrosion (Chapters II & XII)
x	x-coordinate (Chapter X)
$\boldsymbol{x}$	Spatial coordinate (Chapter III)
$\boldsymbol{X}$	Random variables (Chapters IX & XI)
$x(t)$	Reduction in rebar radius at time t (Chapters II & XII)
x_i	- Random variable (Chapter IV)
	- Measurement result (Chapter VIII)
x_k	Input parameter (Chapters VI & XII)
$\bar{x}_{lnX}$	Hyperparameter of the mean (lognormal distribution) (Chapter VII)
$\boldsymbol{y}$	Outcome of an inspection/monitoring strategy (Chapters V, IX & XI)
$\boldsymbol{y}_{add}$	Monitoring outcomes of additional monitoring strategy (Chapter XI)
y_{ijk}	k^{th} measurement made by strain gauge j on sample i (Chapter VII)
y_{RS}	Output predicted by response surface (Chapters VI & XII)
$\boldsymbol{y}_{st}$	Monitoring outcomes of a reference scenario (Chapter XI)
z	Ionic charge (Chapter VII)
Z	Limit state (Chapter IX)
z_k	Output from the finite element model (Chapters VI & XII)

Greek symbols

α	- Corrosion degree of reinforcement steel (Chapters II, IV, VI, VII, VIII & XII)
	- Gumbel parameter (Chapters II & VIII)
$\alpha_{actual,i}$	Actual corrosion degree at element i (Chapter VI)
α_{cr}	Critical value for the corrosion degree (Chapter XI)
α_i	Random effects of the different samples (Chapter VII)
$\boldsymbol{\alpha}_j$	Vector of sensitivity factors in element j (Chapter IX)
α_p	Pitting factor (Chapters II, VI, VIII, IX & XII)
β	- Reliability index (Chapters IX & XI)
	- Skew angle (Chapter XII)
β_{aj}	Reliability threshold for performing an action (Chapter IX)
β_{crit}	Critical reliability index (Chapter XII)

β_j	Random effects of the different strain gauges (Chapter VII)
β_{repair}	Reliability threshold for performing a repair (Chapter XI)
β_{up}	Reliability index to upgrade the structure to (Chapter XII)
Γ	Gamma function (Chapter III)
γ_c	Concrete density in kN/m³ (Chapter IX)
γ_r	Scaling factor for the experimental mode shape (Chapter VII)
δ_0	Thickness of the porous zone (Chapter II)
$\underline{\nabla}_\theta \underline{x}_k$	Sensitivities of the data to the model parameters (Chapter X)
δ_{ij}	Spatial distance between two degrees of freedom i and j (Chapter X)
ε	- Steel strain (Chapter II)
	- Measurement error (Chapter VII)
$\boldsymbol{\varepsilon}$	Strain vector (Chapter X)
$\boldsymbol{\varepsilon_0}$	Error on the moment of reopening of the cracks (Chapter VIII)
ε_{ijk}	Random measurement error (Chapter VII)
ε_l	Average (smeared) tensile strain in cracked concrete (Chapter II)
ε_{c0}	Strain at peak compressive stress (Chapter II)
ε_{cr}	Strain measured over a crack (Chapter VII)
$\boldsymbol{\varepsilon_{crack}}$	Error on the cracking moment (Chapter VIII)
$\boldsymbol{\varepsilon_\delta}$	Error on the load corresponding to a given displacement (Chapter VIII)
ε_{max}	Acceptable error (Chapter III)
ε_{su}	Ultimate strain of reinforcement steel (Chapter II)
ε_u	Ultimate strain of prestressing steel (Chapter II)
$\varepsilon_u{}^*$	Reduced ultimate strain of prestressing steel (Chapter II)
ε_{uncr}	Strain measured in between cracks (Chapter VII)
$\varepsilon_y{}^*$	Reduced yielding strain of prestressing steel (Chapter II)
$\boldsymbol{\zeta}$	Random vector (Chapter IV)
ζ_j	Standard normal variable in the decomposition of a random field (Chapter X)
η	- Corrosion degree of prestressing steel (Chapter VIII)
	- Random error (Chapter IX)
$\boldsymbol{\eta}_D$	Measurement error (Chapters IV & XII)

$\boldsymbol{\eta}_G$	Modelling error (Chapters IV & XII)
θ	Angle of shear cracks (Chapter XII)
θ_i	Uncertain condition or event (Chapter V)
$\boldsymbol{\theta}_M$	Variables to be updated (Chapters IV, VI, X, XI & XII)
$\widehat{\boldsymbol{\vartheta}}^{MAP}$	MAP estimate of the parameters $\boldsymbol{\vartheta}$ (Chapter XI)
λ	Length of spatial correlation (Chapter X)
$\boldsymbol{\lambda}$	Displacement field under the adjoint load (Chapter X)
Λ	Diagonal matrix with eigenvalues (Chapter X)
λ_j	Eigenvalues of the covariance matrix (Chapter III)
λ_r	Eigenvalue (Chapter X)
$\bar{\lambda}_r$	Experimental natural frequency (Chapters VI & VIII)
μ	- Gumbel parameter (Chapter II)
	- Measurement averaged over all possible strain gauges and all possible samples (Chapter VII)
$\mu''_{\alpha,i}$	Posterior mean of the corrosion degree at element i (Chapter VI)
$\boldsymbol{\mu}_{\boldsymbol{\theta}_M}$	Prior mean vector of variables to be updated (Chapter IV)
μ_S	Mean function of the random field (Chapter III)
$\boldsymbol{\mu}_S$	Mean vector of the random field (Chapters III & IX)
v	Smoothness parameter (Chapter III)
v'	Degrees of freedom of the Student's t-distribution (Chapter VIII)
v_c	Poisson's ratio of concrete (Chapter II)
$\boldsymbol{v}_{rj}$	Particular solution of the equation of Nelson (Chapter X)
v_{rs}	Ratio of volumetric expansion of oxides formed as corrosion products with respect to the virgin material (Chapter II)
ρ	Correlation coefficient (Chapters III & IX)
ρ_0	Lower bound for the correlation function (Chapter III)
ρ_c	Mass density of concrete (Chapters VIII & XI)
ρ_l	Reinforcement ratio (Chapter XII)
ρ_X	Correlation coefficient of the variable X (Chapter III)
σ	- Steel stress (Chapter II)
	- Standard deviation of the measurement error (Chapter VII)
$\sum$	Prediction error covariance matrix (Chapter X)
$\sigma_{average}$	Average standard deviation over the elements (Chapters VI & VIII)

σ_d	Standard deviation of the measurement error (Chapter VI)
$\mathbf{\Sigma}_D$	Covariance matrix of the measurement error (Chapter IV)
σ_D^2	Variance of the measurement error (Chapter XII)
σ_ε	Error on the strains (Chapter XI)
$\mathbf{\Sigma}_G$	Covariance matrix of the modelling error (Chapter IV)
$\sigma_{R\&R}$	Overall variation due to repeatability and reproducibility (Chapter VII)
$\sigma_{repeatability}$	Repeatability in the model (Chapter VII)
$\sigma_{reproducibility}$	Reproducibility of the measurements (Chapter VII)
$\mathbf{\Sigma}_{\boldsymbol{\theta}_M}$	Prior covariance matrix of the variables to be updated (Chapter IV)
σ_λ	Proportionality between the error and the experimental natural frequency (Chapters VI & XI)
$\sigma_{\lambda,r}$	Standard deviation of the error on the natural frequency of mode r (Chapter VI)
σ_{max}	Maximum standard deviation over the elements (Chapters VI & VIII)
σ_{min}	Minimum standard deviation over the elements (Chapters VI & VIII)
$\boldsymbol{\sigma_{P,i}}$	Prestress (Chapter VIII)
$\hat{\mathbf{\Sigma}}_{po}$	Approximation of the posterior covariance matrix (Chapter XI)
$\mathbf{\Sigma}_S$	Covariance matrix of the random field (Chapters III & IX)
σ_ϕ	Proportionality between the error and the experimental mode shape (Chapters VI & XI)
$\sigma_{\phi,r}$	Standard deviation of the error on the mode shape of mode r (Chapter VI)
τ_{max}	Bond strength (Chapter II)
ϕ	Reinforcement diameter (Chapter VII)
$\boldsymbol{\Phi}$	Matrix containing the eigenvectors (Chapter X)
Φ_b	Bar diameter (Chapter IX)
ϕ_j	Eigenvector of the covariance matrix (Chapter III)
Φ_m	Multivariate normal cumulative distribution function with degree m (Chapter IX)
$\boldsymbol{\phi}_r$	Eigenvector (Chapter X)
φ_r	Ratio of density of steel to density of rust (Chapter VII)
ϕ_r	Modelled mode shape (Chapter VII)
$\bar{\phi}_r$	Experimental mode shape (Chapters VI, VII & VIII)

ψ	Joint acceptance probability based on prior probability and likelihood function (Chapter IV)

Abbreviations

1D	One-dimensional
2D	Two-dimensional
3D	Three-dimensional
ANOVA	Analysis Of Variance
B-WIM	Bridge Weight-In-Motion
CC	Consequence Class
CDF	Cumulative Distribution Function
COV	Coefficient Of Variation
CSI	Combined deterministic-stochastic Subspace Identification
D	Depassivation
Det.	Deterministic
df	Degrees of freedom
Distr.	Distribution
DOF	Degree Of Freedom
FE	Finite Element
FEM	Finite Element Modelling
FORM	First Order Reliability Method
GU	Gumbel
HDI	Highest Density Interval
KL	Karhunen-Loève
LHS	Latin Hypercube Sampling
LN	Lognormal
LVDT	Linear Variable Differential Transformer
MAC	Modal Assurance Criterion
MAP	Maximum A Posteriori
MCMC	Markov Chain Monte Carlo
MLE	Maximum Likelihood Estimation
MPC	Modal Phase Collinearity
MS	Mean Square
ND	No Depassivation
NDT	Non-Destructive Testing
NoS	Number of Samples

PC	Prestressed Concrete
PDF	Probability Density Function
R&R	Repeatability and Reproducibility
RH	Relative Humidity
RC	Reinforced Concrete
RMS	Root Mean Square
SG	Strain Gauge
SHM	Structural Health Monitoring
SS	Sum of Squares
SSI-COV	Covariance-driven Stochastic Subspace Identification
SSP	Sequential Sensor Placement
Var	Variance
VoI	Value of Information

Samenvatting

In Vlaanderen is meer dan 60% van het bestaande brugpatrimonium gebouwd vóór 1981 en meer dan 25% zelfs vóór 1945, waardoor een aanzienlijk budget wordt besteed aan het onderhouden en herstellen van deze constructies. Daarom trachten ingenieurs steeds betere tools te ontwikkelen om rationeel gefundeerde beslissingen te maken met betrekking tot de besteding van de beschikbare budgetten. In het bijzonder worden daarbij nauwkeurigere berekeningsmethoden ontwikkeld die toelaten de resterende levensduur van bestaande constructies in te schatten.

De laatste decennia is er veel onderzoek uitgevoerd naar constructieve veiligheid. Desondanks blijft het moeilijk om de veiligheid van bestaande bruggen te evalueren. Er is nood aan een kader voor het evalueren van de veiligheid van verouderde en degraderende constructies waarin de resultaten van inspecties en monitoring op een correcte manier in rekening kunnen worden gebracht. Vaak is er veel data voorhanden, maar is het onduidelijk wat deze juist vertelt over de degradatietoestand van de constructie. Er is nood aan een evolutie van methodes die enkel gebaseerd zijn op de beschikbare data naar methodes die uitgaan van een onderliggend model van de beschouwde constructie en waar de data wordt gebruikt om dit model te verfijnen om zo meer accurate voorspellingen van het constructieve gedrag te bekomen.

Het beschikbare budget voor het beheer van het bestaande brugpatrimonium is beperkt en het is belangrijk om dit budget zo optimaal mogelijk te benutten. Een oplossing die hiervoor kan worden aangewend is het toepassen van een zogenaamde pre-posterior procedure die toelaat om de toegevoegde waarde van een meetcampagne te bepalen alvorens deze is uitgevoerd. In deze procedure wordt de kost over de gehele levenscyclus van de constructie bepaald in het geval geen extra maatregelen worden ondernomen enerzijds en anderzijds voor verschillende mogelijke meetcampagnes. Vervolgens worden beide verwachtte kosten vergeleken. Een meetcampagne is de investering waard indien de te verwachten kost over de gehele levenscyclus lager is dan wanneer deze meetcampagne niet wordt geïmplementeerd. Op analoge manier kunnen ook verschillende meetcampagnes met elkaar worden vergeleken en kan de meest kost-optimale meetcampagne gekozen worden. Het dient te worden opgemerkt dat in deze analyses rekening dient gehouden te worden met het tijdsafhankelijk en

ruimtelijk karakter van de degradatie waaraan de beschouwde constructie is onderworpen.

Er is veel literatuur beschikbaar over het modelleren van corrosie en de invloeden van corrosie op het gedrag van gewapende betonconstructies. Sommige van deze modellen worden in dit werk toegelicht en aangewend. Deze modellen laten toe om een voorspelling te maken van het gedrag van de bestudeerde constructie in de tijd. Dit gedrag is echter onderworpen aan onzekerheden, hetgeen kan leiden tot een grote spreiding op de geschatte degradatietoestand. Degradatie zal zich ook niet uniform manifesteren over de constructie, maar kent mogelijks een ruimtelijke spreiding die a priori moeilijk in te schatten is. Om een meer nauwkeurig beeld van de degradatietoestand te krijgen, i.e. de mate van degradatie en lokalisatie van meer gedegradeerde zones, kunnen metingen worden uitgevoerd op de constructie. De resulterende data kan dan worden gebruikt om de distributies van de degradatieparameters te updaten, wat zal leiden tot een meer nauwkeurige voorspelling van de resterende levensduur van de constructie. Verschillende types data kunnen worden gebruikt voor dit doel, elk met hun eigen voor- en nadelen. Een proefbelasting kan worden aangebracht op de constructie. Rekken en doorbuigingen kunnen dan worden opgemeten. Uit het huidige onderzoek werd geconcludeerd dat doorbuigingsmetingen over het algemeen geen lokalisatie van de schade toelaten en een beperkte reductie in onzekerheid opleveren. Rekmetingen kunnen dan weer een vrij accuraat beeld opleveren van de degradatietoestand, maar dit enkel op de locatie waar de rek wordt opgemeten. Om lokalisatie van schade mogelijk te maken zou de volledige constructie moeten worden uitgerust met reksensoren, wat praktisch vaak onmogelijk is. Anderzijds kunnen ook dynamische eigenschappen van de constructie worden afgeleid uit trillingsmetingen. Wanneer een constructie wordt uitgerust met accelerometers of optische vezels kunnen de natuurlijke frequenties en modevormen worden afgeleid uit de data verkregen ten gevolge van omgevingsexcitatie. Natuurlijke frequenties zijn gerelateerd aan de globale stijfheid (en dus globale degradatietoestand) van de constructie en laten geen lokalisatie van schade toe. Echter, lokale reducties in stijfheden kunnen een invloed hebben op de modevormen. Het combineren van de informatie uit de natuurlijke frequenties en corresponderende modevormen kan zo toelaten om schade te lokaliseren en te kwantificeren. Over het algemeen is de resterende onzekerheid groter dan deze ten gevolge van rekmetingen onder een proefbelasting. Het is aangetoond dat de combinatie van beide types data leidt tot een meer accurate voorspelling van de werkelijke degradatietoestand. Op basis van de modale data (natuurlijke frequenties en modevormen) kunnen de kritieke locaties, i.e. degene met de meeste schade, worden gelokaliseerd. Door deze vervolgens met reksensoren uit te rusten tijdens een proefbelasting en beide datasets te combineren, kan een veel betere inschatting van de degradatietoestand worden gemaakt. Het is ook aangetoond hoe het bijkomend in rekening brengen van visuele observaties een positieve invloed

heeft op de a posteriori distributie van de degradatieparameters. Wanneer bijvoorbeeld reeds visuele tekenen van corrosie zichtbaar zijn, zullen de lage corrosiegraden in de a posteriori distributie worden uitgesloten.

Ter validatie van de ontwikkelde methodologie is ook een experimentele proefcampagne uitgewerkt. Hierin werden gewapende betonbalken onderworpen aan versnelde corrosie. Op verschillende corrosiegraden werden de rekken onder een gekende belasting opgemeten en werden de natuurlijke frequenties en modevormen afgeleid uit dynamische metingen met accelerometers en optische vezels. De resultaten zijn dan vergeleken met deze voor een niet gecorrodeerde referentiebalk. De data is gebruikt om een vage a priori distributie van de corrosiegraad te updaten. Hier is ook het positieve effect aangetoond van het definiëren van een meer informatieve a priori distributie op basis van informatie van scheurmetingen. Tijdens deze proefcampagne is ook een eerste kwantificering gebeurd voor de meetfout bij statische rekmetingen op betonconstructies.

Het voorgaand onderzoek over degraderende voorgespannen betonconstructies is eerder beperkt en er is nog geen consensus met betrekking tot het modelleren en evalueren van corrosie in deze constructies. Een kort overzicht van de huidige state-of-the-art wordt in dit werk gegeven. Bijkomend wordt een eerste analyse gedaan waarbij de corrosiegraad van een eenvoudige voorgespannen en nagespannen ligger wordt geüpdatet op basis van rekmetingen onder een proefbelasting. De data resulterende uit dynamische metingen is hierin niet beschouwd omdat deze voornamelijk beïnvloed worden als de voorspanning in die mate is gereduceerd dat het beton begint te scheuren. De berekeningen tonen aan dat voor een voorgespannen ligger de corrosiegraad kan worden geüpdatet op basis van statische rekmetingen indien deze met een voldoende grote nauwkeurigheid kunnen worden uitgevoerd. Dit kan echter een probleem zijn bij betonconstructies aangezien de heterogeniteit van het beton kan leiden tot een relatief grote spreiding op de meetresultaten, zoals ook is aangetoond tijdens de experimentele proefcampagne. Voor de nagespannen ligger is het nog moeilijker om de corrosiegraad te updaten op basis van de statische rekmetingen. Indien een kabelkoker zonder grout wordt beschouwd kan wel worden achterhaald of de strengen al dan niet gefaald zijn. Het bayesiaanse raamwerk is ook toegepast op twee nagespannen dakliggers met een onbekende resterende voorspanning. Gebruik makend van experimentele data betreffende de materiaaleigenschappen en een experimentele kracht/verplaatsingscurve kan een a posteriori distributie van de resterende voorspanning worden afgeleid. Wanneer de meest waarschijnlijke waarde van deze distributie als input voor een eindige elementen model van de liggers wordt gebruikt, wordt een goede overeenkomst met de experimentele kracht/verplaatsingscurve verkregen.

Hoewel meetdata kan worden gebruikt om een meer accuraat beeld van de degradatietoestand van een constructie te krijgen, gaat het verwerven van deze

data gepaard met een bepaalde kost. Vóór het uitvoeren van een meetcampagne moet dus de vraag worden gesteld of deze de investering waard is. Een handige tool hiervoor is de zogenaamde pre-posterior analyse. Deze methodologie is in dit werk uitgebreid om rekening te houden met het tijdsafhankelijk en ruimtelijk gedrag van degradatie. Dit uitgebreide raamwerk laat toe om voor verschillende monitoringsstrategieën de waarde van de verkregen informatie (VoI, 'Value of Information') te bepalen. Deze VoI geeft het verschil weer tussen de a priori kost wanneer geen bijkomende metingen worden uitgevoerd en de a posteriori kost wanneer de voorgestelde meetcampagne zou worden geïmplementeerd. Door de VoI van verschillende meetcampagnes te vergelijken kan de meest optimale gekozen worden (i.e. deze met de hoogste VoI).

Het evalueren van de VoI kan veel rekentijd vergen. Om een monitoringsstrategie te optimaliseren moet zowel het meest optimale tijdstip om de metingen uit te voeren bepaald worden, als de meest optimale posities van de sensoren. De laatste kunnen echter al op voorhand bepaald worden zonder de (rekenintensieve) VoI te moeten berekenen. In dit werk is uitgelegd hoe aan de hand van een eindig elementenmodel van de constructie de meest optimale sensorposities kunnen worden afgeleid zodanig dat het beste beeld van de a posteriori distributie van de schade en de bijbehorende ruimtelijke spreiding verkregen wordt. Deze optimale posities van de sensoren kunnen bepaald worden zowel voor statische rekmetingen als voor dynamische metingen waar versnellingen of rekken worden opgemeten. Een aantal bijkomende hulpmiddelen zijn ontwikkeld om de rekentijd ter bepaling van de VoI verder te verminderen. Ook is aangetoond dat deze VoI in hoge mate gevoelig kan zijn aan de opgegeven input waarden. Een kritische beoordeling van de VoI is dus zeker noodzakelijk en het is aangewezen om bij twijfel de gevoeligheid van de VoI aan de betreffende input te verifiëren vooraleer beslissingen te nemen op basis van de verkregen VoI.

Tenslotte is een case study bestudeerd waar een werkelijke geometrie wordt beschouwd van een brug in Vlaanderen. De meetdata wordt gesimuleerd aan de hand van een eindig elementenmodel van de brug en een aangenomen ruimtelijke verdeling van de corrosiegraad. Opnieuw wordt aangetoond hoe op basis van de verschillende types data de a posteriori distributie van de corrosiegraad kan worden afgeleid en hoe een combinatie van data tot een meer accurate schatting van de corrosiegraad leidt. Ook wordt aangetoond dat het model van de constructie dat wordt gebruikt voor het updaten van de corrosiegraad een zo goed mogelijke benadering dient te zijn van de werkelijke constructie. Vereenvoudigingen in het model van de constructie die toegelaten zijn in het ontwerp kunnen een grote impact hebben op de a posteriori distributie van de corrosiegraad wanneer dit vereenvoudigd model ook wordt gebruikt voor het updaten van de corrosiegraad. Hierdoor kan de verkregen corrosiegraad sterk afwijken van de werkelijke in te schatten waarde. Ook het VoI raamwerk is toegepast op deze constructie en dit

voor twee situaties. In de ene situatie is de constructie onderhevig aan corrosie ten gevolge van carbonatatie. Dit proces verloopt vrij traag, waardoor geen interventies vereist zijn over de levensduur van de brug. Ook wanneer monitoring in beschouwing wordt genomen leiden de geüpdatete distributies niet tot bijkomende herstellingen. De VoI is dus negatief aangezien geen nuttige informatie uit de metingen wordt gehaald. Wanneer de constructie zich bevindt in een omgeving met veel chloriden, verloopt het corrosieproces veel sneller. De VoI is dan wel positief en het meest optimale tijdstip om de metingen uit te voeren kan bepaald worden. Ook kunnen verschillende meettechnieken met elkaar vergeleken worden en kan uiteindelijk de meest optimale techniek gekozen worden. Opnieuw is de invloed van een aantal inputparameters in de berekening van de VoI nagegaan. Het wijzigen van deze parameters kan een invloed hebben op de uitkomst van de VoI analyse. Bijgevolg wordt er aangeraden de gevoeligheidsanalyse steeds opnieuw uit te voeren indien er twijfel is over de waarden voor de inputparameters.

Summary

In Flanders, more than 60% of the existing bridge patrimony has been built before 1981, and more than 25% even before 1945. Because of their age, a considerable budget is spent on maintenance and repair of these bridges. Hence, engineers keep developing improved tools to make rationally funded decisions that allow spending the available budgets in an adequate way. In particular, accurate calculation methods are developed that allow estimating the remaining service life of existing structures on the basis of additional information.

During the last decades, a lot of research has been performed on the topic of structural safety. Despite this effort, it remains difficult to estimate the safety of existing structures. There is a need for a framework to evaluate the safety of ageing and degrading structures, where the results of inspections and monitoring can properly be accounted for. Often, many data is available, but it remains unclear what this data tells about the condition of the structure. There is a need for an evolution from methods that are only based on the available data, to methods that take basis in an underlying model of the structure, where the data is used to fine-tune this model and as such enable more accurate predictions of the structural behaviour.

The available budget for the management of the existing bridge patrimony is limited, and it is important to use this limited budget as optimal as possible. For this purpose, an extended pre-posterior framework can be applied that allows determining the benefit of a monitoring strategy. In this framework, the cost of the structure over the whole life-cycle is evaluated for the situation where no action is undertaken, and for the situation where different possible monitoring strategies are accounted for. In a next step, both costs are compared and a monitoring strategy is worth the investment if the resulting life-cycle cost is smaller than for the situation where monitoring is not accounted for. In a similar way, different monitoring strategies can be compared, and the most optimal one can be chosen. In these analyses, the time-dependent and spatial character of degradation of the structure under investigation should be accounted for.

A lot of literature is available on the modelling of corrosion and the influences of corrosion on the behaviour of reinforced concrete structures. Some of these models are highlighted in this work. These models allow predicting the behaviour of the structure under investigation over time. However, this behaviour is subjected to uncertainties, which can lead to a large spread on the estimated degradation state

of the structure. Degradation will also not be uniform along the structure, but might have some spatial variation, which is difficult to estimate a priori. To arrive at a more accurate estimate of the degradation state, i.e. the amount of deterioration and the localisation of more degraded zones, measurements can be performed on the structure. The resulting data can then be used to update the distributions of the degradation parameters, which will lead to more accurate estimates of the remaining service life of the structure. Different types of data can be used for this purpose, each with their advantages and disadvantages. A proof load can be applied to a structure, under which strains and deflections can be measured. It has been illustrated in the current work that, in general, deflection measurements do not allow localisation of damage and lead to a limited reduction in uncertainty. Strain measurements on the other hand lead to a very accurate estimate of the degradation state, but only at the measurement locations. To allow localisation of damage, the whole structure should be equipped with strain gauges, which is often practically impossible. Dynamic properties of the structure could be derived from vibrations measured under ambient excitation. When a structure is equipped with accelerometers or optic fibres, natural frequencies and mode shapes can be derived from the measurement data. Natural frequencies are related to the global stiffness of the structure, but do not allow localizing damage. On the other hand, local reductions in stiffness can influence the mode shapes, enabling localisation but no quantification of damage. As such, combining natural frequencies and mode shapes can allow for both localisation and quantification of damage. Nevertheless, in general the remaining uncertainty of the posterior distribution of the degradation parameters is larger than the one resulting from static strain data. In the current work, it has been illustrated how combining both data types (i.e. modal data and static strain data) leads to a more accurate estimate of the actual degradation state. Based on the modal data, critical locations, i.e. the ones with the highest amount of degradation, can be localised. Equipping these with strain gauges during a proof load and combining both datasets results in a more accurate estimate of the degradation state. It has also been illustrated how the introduction of visual observations has a positive influence on the posterior distribution of the degradation parameters. For example, when visual signs of corrosion are present, lower corrosion degrees will be excluded from the posterior distribution.

In order to validate the methodology, an experimental campaign has also been developed. In this experimental campaign, reinforced concrete beams have been subjected to accelerated corrosion. For specific corrosion degrees, strains have been measured under a known load, and natural frequencies and mode shapes were derived from dynamic measurements with accelerometers and optic fibres. The resulting data was then compared with the results for a non-corroded reference beam. The data has been used to update a prior distribution of the corrosion degree. Here, also the positive effect of including additional information from crack width measurements in the definition of the prior distribution has been illustrated. During

this experimental campaign, also a first step has been undertaken to quantify the measurement error for static strain measurements on concrete structures.

Research on degrading prestressed structures is rather limited and there is no consensus yet on the evaluation and modelling of corrosion in these structures. A short overview of the current state-of-the-art is provided in this work. Additionally, a first analysis is performed, where the corrosion degree of a simple prestressed and post-tensioned girder is updated based on static strain measurements. Modal data is not included herein, since modal properties are mainly influenced if the prestress is reduced to an extent that the concrete starts to crack. The calculations illustrate that for a prestressed girder the corrosion degree can be updated based on static strain measurements if these can be performed with a sufficiently accurate measuring technique. This can be a problem for concrete structures, since the heterogeneity of the concrete can lead to a relatively large spread on the measurement results, as also illustrated during the experimental campaign. For the post-tensioned girder, it is even more difficult to update the distribution of the corrosion degree based on static strain measurements. Nevertheless, for the case where an ungrouted duct has been considered, it can be determined whether the strands have failed or not. The Bayesian updating framework has also been applied to two post-tensioned roof-girders with an unknown remaining prestress. Using experimental data concerning the material properties and an experimental load-displacement curve, the posterior distribution of the remaining prestress can be determined. When the most probable value resulting from this distribution is used as input for a finite element model of the girders, a good agreement with the experimental load-displacement curve is achieved.

Hence, data can be used to arrive at a more accurate estimate of the degradation state of a structure. Nevertheless, acquisition of this data comes at a certain cost. Before implementing a monitoring strategy, the question should be posed whether it is really worth the investment. A useful tool to answer this question is the pre-posterior analysis. In the current work, this pre-posterior analysis has been extended to account for the time-dependent and spatial character of degradation. This extended framework allows determining the Value of Information (VoI) for different monitoring strategies. This VoI represents the difference between a prior cost when no additional monitoring would be performed, and the posterior cost when the suggested monitoring strategy would be implemented. By comparing the VoI of different strategies, the most optimal one can be chosen as the one with the highest VoI.

Evaluating the VoI can require a large computational cost. To optimise a monitoring strategy, the most optimal time of performing the measurements should be defined, as well as the most optimal sensor locations. However, the latter

can already be determined beforehand, without the need of evaluating the (computationally demanding) VoI. In this work, it has been explained how, based on a finite element model of the structure, the most optimal sensor positions can be derived to achieve the best representation of the posterior distribution of the degradation parameters and the corresponding spatial variation, both for static strain measurements and for dynamic measurements of accelerations or strains. Further, some additional suggestions are provided to limit the computational demand of the VoI. It has also been illustrated how the VoI can be sensitive to the given input values. A critical mind-set is hence required when evaluating the VoI, and, if there is a certain doubt on the input value to be used, it is recommended to verify the sensitivity of the VoI to this input value before making decisions based on the obtained VoI.

Finally, a case study has been discussed, where a real bridge geometry of a bridge located in Flanders is considered. Updating of the corrosion degree is performed based on simulated data, using a finite element model of the bridge and assuming different scenarios for the actual corrosion degrees. It has again been illustrated how, based on the different datatypes, the posterior distribution of the corrosion degree can be derived, and how the combination of data leads to a more accurate estimate of the latter. It has also been illustrated that the model of the bridge used in the Bayesian updating procedure should correspond to the real bridge geometry as closely as possible. Simplifications that are allowed in the design can have a large impact on the posterior distribution of the corrosion degree, due to which the latter deviates a lot from the actual value to be estimated. Also the VoI framework has been applied to this bridge, where two situations are considered. In the first situation, the bridge is subjected to carbonation-induced corrosion. This process proceeds slowly, due to which no structural interventions are required over the service life of the bridge. In addition, when monitoring is considered, the posterior distributions of the degradation parameters do not induce additional maintenance actions. The VoI is hence negative, since no additional useful information is retrieved from the monitoring data. When the bridge would be exposed to chlorides, the corrosion process will proceed at a much higher rate. The VoI becomes positive, and the most optimal time of monitoring can be determined. In addition, different monitoring strategies have been compared to each other, and the most optimal one was chosen. Again, the influence of some input parameters in the calculation of the VoI has been investigated. Changing these can have an influence on the results of the VoI analysis. However, there is no general trend between the results in this case study and previous results from another example. Hence, it is advised to perform this sensitivity study again if there is some doubt on the input parameters to be used.

General introduction

CHAPTER I

General introduction

"A true initiation never ends."
- Robert Anton Wilson

I.1 Introduction

I.1.1 Context of the research topic

All over the world, countries are facing the challenge of managing ageing infrastructure. Many concrete bridges in the bridge networks are reaching the end of their anticipated lifetime. In order to secure safe operation of these bridges, maintenance interventions might be required, and some bridges might even need replacement, since they might be subjected to structural degradation. This degradation is inherently spatially distributed and evolves over time. Although principles of modelling and assessment of existing structures are found in several standards (ISO 2394 (2015) and ISO 13822 (2010)), these remain rather general and do not provide a straightforward methodology for the assessment of existing structures.

Whereas for new structures many design guidelines are available based on semi-probabilistic methods, for existing structures, assessment of the safety is still mainly based on subjective investigations of the responsible engineers. In Belgium, visual inspections and level measurements are performed regularly, and decisions are made based on a subjective evaluation of these data. Even though Structural Health Monitoring (SHM) methods are becoming more mature, they still need to find their way into asset management for bridges. Nevertheless, SHM measurements consisting of vibration data collected in operational conditions have the advantage of easy deployment and the ability to provide information on the global behaviour of the structure. By application of system identification techniques, modal characteristics (such as natural frequencies and mode shapes) can be extracted from vibration data obtained under ambient excitation, avoiding the forced excitation of structures. Nowadays, many important structures are equipped with a permanent monitoring system, such as the Ørensund Bridge in Denmark and the Stonecutters Bridge in Hong Kong.

In the assessment of existing structures, many uncertainties are involved, especially on parameters governing the structural resistance. A well-known framework to reduce uncertainties based on available data is the Bayesian framework (Diamantidis, 2001; JCSS, 2001). By applying Bayes' theorem, prior probability distributions of the quantities of interest are updated to posterior distributions accounting for additional (measurement) information. Bayesian methods for incorporating monitoring information are for example found in (Strauss et al., 2008). The posterior distributions retrieved by applying these Bayesian methods can then be used in the probabilistic assessment of the existing structure (Bergmeister et al., 2009; Strauss et al., 2009, 2008).

In the assessment of existing structures and the planning of inspections and maintenance, the number of alternative actions such as the amount and locations

of inspections/measurements as well as strengthening and maintenance activities, can be extremely large. Hence, a framework for the systematic analysis of the corresponding consequences is expedient. A framework suitable for this purpose is Bayesian decision analysis (Raiffa and Schlaifer, 1961). In this framework, consequences are often expressed in monetary terms. A utility function should be defined together with probabilities of the different branches in the decision problem. The decision analysis is then reduced to the calculation of the expected utilities corresponding to different action alternatives. In this context, inspections and monitoring can be regarded as options for the decision-maker to 'buy' additional information before actually making his choice of action. If the cost of this information is small with respect to the obtained information on the structural state, the decision-maker should go ahead and perform the inspection/measurement. However, if different types of measurements are possible, the one yielding the overall largest utility or equivalently the smallest costs should be chosen. In this decision-making problem, the uncertain outcome of the measurements should be considered. The practical application of this pre-posterior analysis to real engineering problems such as monitoring-based bridge inspection still poses many fundamental as well as practical challenges.

I.1.2 Lacunae in current knowledge

In the management of existing structures, decisions on maintenance and repair are often based on visual observations and engineering judgement. These visual observations can be complemented by monitoring information. Nevertheless, in current practice, decisions based on monitoring information are often built on performance thresholds and data-based methods. These data-based methods make use of a pattern recognition method for detecting damage by comparison to data obtained in a reference or undamaged state. This means that monitoring results are investigated over time and action is undertaken once a predefined threshold is reached. These methods only allow detecting and localizing damage. Based on such strategies, only reactive maintenance can be performed, where action is undertaken as soon as there are anomalies detected in the monitoring data. Nevertheless, pro-active maintenance might be economically more beneficial when considering the whole service life of the structure. For the latter, damage assessment should be coupled to quantification of damage and prognosis of the remaining service life. This cannot be accomplished by data-based methods, and model-based methods (Fritzen et al., 1998; Simoen et al., 2015) are required.

Model-based methods compare the obtained data with a model of the structure. Up to now, most of these methods rely on the calibration of a linear model, and are able to quantify the damage, besides detecting and localizing it. In these linear models, quantification of damage often occurs by updating general stiffness parameters of different parts along the structure. In this way, these methods cannot assess the structural strength and do not enable prediction of the remaining service

life. Moreover, methods available up to date are often only applied to conceptual problems and need further elaboration to account for the time-dependent and spatial character of deterioration processes in real structures.

An important deterioration process in (existing) reinforced concrete structures is corrosion of the reinforcement. To improve the estimate of the remaining service life of these structures, distributions of variables in the time-dependent degradation models should be updated based on monitoring information, also accounting for the spatial character of degradation. As such, damage can be detected, localized and quantified, and prediction of the remaining service life is enabled. Nevertheless, in literature, attempts to update the variables in the time-dependent degradation models for reinforcement corrosion based on indirect and non-destructive data are scarce. Most literature up to now assumes that corrosion loss can be measured directly (Faroz et al., 2016; Ma et al., 2013; Marsh and Frangopol, 2008), which is often not the case in practice. Hence, there is a need for model-based methods that allow updating the variables in the time-dependent degradation models accounting for non-destructive data. These methods should also be able to incorporate the spatial character of the degradation processes.

To apply model-based methods to degrading structures as described above, a degradation model is required. For reinforced concrete structures subjected to corrosion, there are different models available to simulate the corrosion process and its influence on the structural resistance. These models can be used to predict the remaining service life of the investigated structure. In the past years, a lot of research interest has been devoted to the assessment of corroding reinforced concrete structures. For prestressed concrete structures on the other hand, research on this topic is rather scarce. There remains some dissension on how to model time-dependent degradation due to corrosion in pretensioned and post-tensioned concrete structures, and also for the assessment of these structures (e.g. based on non-destructive data) more thorough investigations are required.

The data to be used in the model-based methods can be collected by different monitoring strategies. Nevertheless, these monitoring strategies all come at a certain cost. Since the available budget for management of the bridge patrimony is often limited, the benefit of implementing a monitoring strategy should be investigated beforehand, and the monitoring strategy should be optimized to be as cost-efficient as possible. In section I.1.1, it has already been pointed out that Bayesian decision analysis can be used for this purpose. The value of information (VoI) of a monitoring strategy can be evaluated by application of a pre-posterior analysis (Thöns, 2018). Nevertheless, in current literature, the value of information is often evaluated for simplified models of structures, where degradation is accounted for by assigning different (discrete) condition states to the structure, e.g. ranging from a very good health to the need for immediate repair (e.g. (Nielsen

and Sørensen, 2018)). However, in reality it is important to account for the time-dependent degradation of the structure, without this need for discretization. Moreover, spatial dependencies are often not accounted for, and system effects are mostly treated for steel structures consisting of different components (Zhang et al., 2019). Especially applications to degrading reinforced concrete structures are scarce, and in the limited literature on this topic, spatial correlation of the degradation processes is often not accounted for (Zambon et al., 2020). Moreover, evaluating the value of information is often computationally challenging and there is a need for suggestions on how to reduce this computational burden (Straub et al., 2017). In general, the VoI analysis should be extended to be applicable to realistic reinforced concrete structures subjected to time-dependent and spatial degradation.

I.2 Research scope and methodology

I.2.1 Research scope

This research addresses the problem of rational decision-making in the management of ageing infrastructure to optimally exploit the limited available resources. This decision-making is based on the evaluation of the life-cycle performance of the structure under investigation (Frangopol and Liu, 2007), allowing decisions on strategies for inspection, monitoring and strengthening. In this evaluation, all relevant uncertainties, which are unavoidable in the condition assessment of existing structures as well as the life-cycle cost prediction, should be accounted for, and the potential of additional information from inspections and monitoring should be exploited. Furthermore, this research also aims at incorporating the time-dependent and spatial character of degradation processes in the assessment of existing structures. Since these methods for decision-making are often accompanied with a large computational burden, this research will also investigate different suggestions on how to reduce the required computational effort when optimizing a monitoring strategy.

The measurement information retrieved from different monitoring strategies will be used in a model-based framework in order to move beyond the state-of-the-art in damage assessment and enable prediction of the remaining lifetime of the structure. For this purpose, data from conventional tests can be supplemented by data collected from state-of-the-art vibration-assessment SHM technologies. This data will be used to calibrate a model that enables prediction of the remaining service life. The inherent time-dependent and spatially distributed character of degradation processes will also be incorporated. As such, by application of the Bayesian decision-making framework, the advantages of implementing an SHM-strategy can be investigated. The focus will be on the use of measurement information to update variables in the degradation models of reinforced concrete

structures. Nevertheless, also some first investigations will be performed on the assessment of prestressed concrete structures.

I.2.2   Research methodology

A literature survey is performed to get insights in the current state-of-the-art on (1) degradation models and the spatial character of degradation, (2) the pre-posterior framework and the calculation of the value of information, (3) measurement data and their relation to the degradation state of structures, and (4) Bayesian updating based on indirect measurement information.

In a next step, the pre-posterior framework is extended so that it can be applied to large concrete structures degrading over time, accounting for the spatial character of the degradation.

Since measurement information should be accounted for in this pre-posterior framework, an investigation is also performed on how to apply model-based methods to different types of data. A model of the structure under investigation is made, where the resistance of the structure depends on the (spatially variable) deterioration state at a certain point in time. It is investigated how the variables in the deterioration model can be updated based on different types of measurement data, and how the most accurate representation of the actual deterioration state can be found, also accounting for the spatial character of degradation.

When applying these model-based methods to update the degradation models, depending on the sensor locations applied for monitoring, a more or less accurate prediction of the actual degradation state can be found. Hence, the optimal sensor locations are derived based on a greedy search algorithm.

In a final step, all of the above is combined in the calculation of the VoI and the optimization of the monitoring strategies for the structure under consideration. Suggestions are also provided on how to limit the required computational effort in the process of optimizing a monitoring strategy. Finally, also the sensitivity of the VoI to values assumed for the input parameters in the analysis is investigated.

I.2.3   Novel contributions

The original contributions of this research to the scientific state-of-the-art can be summarized as follows:

- By application of existing methodologies for Bayesian inference, the variables in degradation models to predict a spatially variable corrosion degree are inferred based on indirect measurement information (static and dynamic). This is in contrast to existing literature where the corrosion degree itself is updated (not the

variables of the degradation models), the spatial correlation is not accounted for, and it is assumed that corrosion variables can be measured directly.

- This research has illustrated in a quantitative way the influence of the combination of different types of heterogeneous measurement data (i.e. static data, dynamic data, visual observations, etc.) when inferring degradation models for predicting the remaining service life of existing structures.
- The pre-posterior analysis is extended for application to degrading concrete structures, explicitly taking into account the time-dependent degradation models and the spatial variation of damage. A flowchart and corresponding code have been developed and are an addition to existing scientific literature.
- The (extended) VoI analysis has been applied to a 'real' reinforced concrete bridge structure, providing suggestions for limiting the computational effort and investigating the influence of initial assumptions in the analysis.
- The inclusion of random fields in the Bayesian inference and the VoI analyses has been investigated, and the benefit of including this spatial correlation has been illustrated.
- An experimental campaign is performed which provides an important contribution to the state-of-the-art on experimental tests on corroded reinforced concrete beams, since it considers both static and dynamic testing, and points out the issues related to these experiments in application to real-scale samples.
- A novel approach is provided on the assessment of time-dependent degradation parameters for evaluation of the prestressing steel section based on measurement information from static load tests.
- The remaining prestress in the girders of a roof structure has been inferred based on the results from experimental testing of only one girder. Inference has been performed by application of a novel ad-hoc procedure.

I.3   Thesis layout

This thesis consists of 13 chapters, divided into four main parts:
- **Part A** provides an overview of the state-of-the-art related to spatial and time-dependent corrosion, Bayesian updating and value of information analysis.
- **Part B** focusses on the Bayesian updating of corrosion parameters based on measurement data.
- **Part C** treats the value of information analysis.

- **Part D** represents a case study, covering all previous parts by application to a real bridge geometry.

Following the general introduction in the current **Chapter I**, an overview of the basic aspects related to time-dependent degradation due to corrosion is given in **Chapter II**.

In **Chapter III**, the spatial character of degradation due to corrosion is introduced together with different ways to model this spatial correlation.

Chapter IV introduces the main concept of Bayesian updating together with the different data types treated in this research.

In **Chapter V**, the concepts of the pre-posterior analysis and the value of information are introduced.

Chapter VI discusses how different data types can be used to update the corrosion degree in reinforced concrete structures. The results in this chapter are based on artificial data and applied to both an example of a reinforced concrete beam and a more extensive reinforced concrete girder bridge. It is also illustrated how combining different types of data can lead to a more accurate estimate of the actual corrosion degree.

Chapter VII deals with an experimental campaign on reinforced concrete beams subjected to accelerated corrosion. These beams are subjected to dynamic and static tests, and the influence of corrosion on the different gathered data sets is investigated.

In **Chapter VIII** a first investigation on updating the corrosion degree of prestressed structures is performed. This is applied to scholastic examples of a prestressed beam and a post-tensioned beam, and to a more extensive prestressed girder bridge.

In **Chapter IX**, an extended pre-posterior framework is developed that enables to include the time-dependent and spatial character of degradation. This is also applied to some simplified examples to illustrate the method.

Since optimization of a monitoring strategy based on the calculation of the value of information requires a lot of computational effort, it is suggested to determine optimal sensor positions beforehand, outside the value of information analysis. This optimal sensor placement is discussed in **Chapter X.**

In **Chapter XI**, the pre-posterior framework is applied to a reinforced concrete girder bridge. Tools to limit the computational effort are provided and the sensitivity to the choice of some input parameters is investigated and discussed.

Chapter XII deals with a case study of a reinforced concrete girder bridge in Flanders. The Bayesian updating procedure is illustrated with simulated data. In addition, the influence of a model error on the posterior distribution is investigated. The value of information is also determined under different assumptions on the exposure conditions of the bridge.

Finally, general conclusions and a summary of the research presented in this thesis are given in **Chapter XIII**.

The relation between the different chapters is also visualized in Figure I-1.
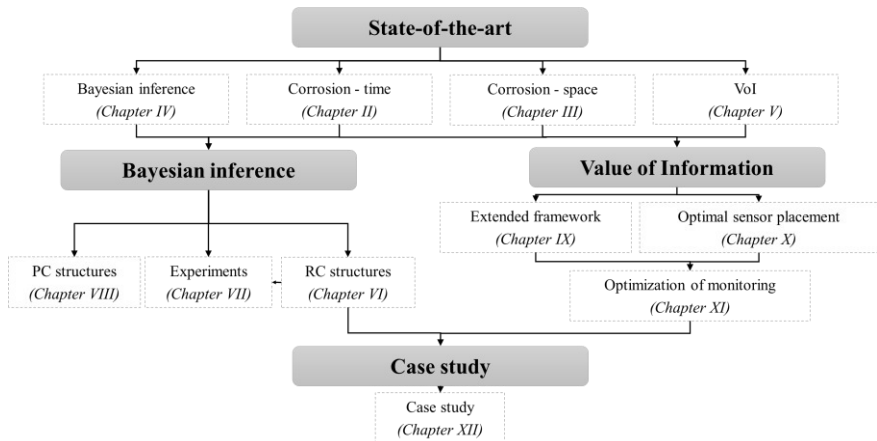
Figure I-1: Visualization of the relation between the different chapters

If the reader would like some additional background or data related to the calculations performed in this manuscript, this can be obtained from the author on request.

I.4   References

Bergmeister, K., Novak, D., Pukl, R., Červenka, V., 2009. Structural assessment and reliability analysis for existing engineering structures, theoretical background. Struct. Infrastruct. Eng. 5, 267–275.

Diamantidis, D., 2001. Probabilistic Assessment of Existing Structures, RILEM Publications SARL. France.

Faroz, S.A., Pujari, N.N., Ghosh, S., 2016. Reliability of a corroded RC beam

based on Bayesian updating of the corrosion model. Eng. Struct. 126, 457–468.

Frangopol, D.M., Liu, M., 2007. Maintenance and management of civil infrastructure based on condition, safety, optimization, and life-cycle cost. Struct. Infrastruct. Eng. 3, 29–41.

Fritzen, C.P., Jennewein, D., Kiefer, T., 1998. Damage detection based on model updating methods. Mech. Syst. Signal Process. 12, 163–186.

ISO, 2010. ISO 13822:2010: Bases for design of structures – Assessment of existing structures. Geneva, Switzerland

ISO, 2015. ISO 2394:2015: General principles on reliability for structures (4th ed). Geneva, Switzerland.

JCSS, 2001. JCSS Probabilistic Model Code.

Ma, Y., Zhang, J., Wang, L., Liu, Y., 2013. Probabilistic prediction with Bayesian updating for strength degradation of RC bridge beams. Struct. Saf. 44, 102–109.

Marsh, P.S., Frangopol, D.M., 2008. Reinforced concrete bridge deck reliability model incorporating temporal and spatial variations of probabilistic corrosion rate sensor data. Reliab. Eng. Syst. Saf. 93, 394–409.

Nielsen, J.S., Sørensen, J.D., 2018. Computational framework for risk-based planning of inspections, maintenance and condition monitoring using discrete Bayesian networks. Struct. Infrastruct. Eng. 14, 1082–1094.

Raiffa, H., Schlaifer, R., 1961. Applied statistical decision theory.

Simoen, E., De Roeck, G., Lombaert, G., 2015. Dealing with uncertainty in model updating for damage assessment: A review. Mech. Syst. Signal Process. 56, 123–149.

Straub, D., Chatzi, E., Bismut, E., Courage, W., Döhler, M., Faber, M.H., Köhler, J., Lombaert, G., Omenzetter, P., Pozzi, M., Thöns, S., Val, D., Wenzel, H., Zonta, D., 2017. Value of information: A roadmap to quantifying the benefit of structural health monitoring. 12th Int. Conf. Struct. Saf. Reliab. 3018–3029.

Strauss, A., Frangopol, D.M., Kim, S., 2008. Use of monitoring extreme data for the performance prediction of structures: Bayesian updating. Eng. Struct. 30, 3654–3666.

Strauss, A., Hoffmann, S., Wendner, R., Bergmeister, K., 2009. Structural assessment and reliability analysis for existing engineering structures, applications for real structures. Struct. Infrastruct. Eng. 5, 277–286.

Thöns, S., 2018. On the Value of Monitoring Information for the Structural Integrity and Risk Management. Comput. Civ. Infrastruct. Eng. 33, 79–94.

Zambon, I., Ariza, M.P.S., Matos, J.C., Strauss, A., 2020. Value of information (VoI) for the chloride content in reinforced concrete bridges. Appl. Sci. 10.

Zhang, W.H., Lu, D.G., Qin, J., Faber, M.H., 2019. Life cycle management of structural systems based on the optimal SHM strategy by VoI analysis. 13th Int. Conf. Appl. Stat. Probab. Civ. Eng. ICASP 2019.

Part A

State-of-the-art in
relation to spatial and
time-dependent
corrosion, Bayesian
updating and value of
information

CHAPTER II

Time-dependent degradation due to corrosion

"And the rest is rust and stardust."
- Vladimir Nabokov

II.1 Introduction

Many concrete bridges are currently reaching the end of their anticipated service life. Many of these bridges are deteriorating and corrosion of the reinforcement is one of the main concerns. This corrosion can either originate from the presence of chlorides (i.e. road salts, seawater…) or due to carbonation resulting from the exposure to CO_2. Corrosion affects reinforced concrete structures in different ways, affecting both the reinforcement steel and the surrounding concrete. This results in a decrease of structural safety, but also influences the serviceability of the structure.

The purpose of this chapter is not to give a complete overview of the existing models for each phase of the corrosion process. The most important parts of the corrosion process will be explained, and the models used in this work will be highlighted. For a more detailed review on corrosion modelling, reference is made to (Andrade and Izquierdo, 2020; Coronelli, 2020; Coronelli and Gambarova, 2004; Melchers, 2018; Qiu, 2020; Rodrigues et al., 2021).

First, the degradation models will be introduced when modelling corrosion in ordinary reinforced concrete (RC) structures. Later, also the influence of corrosion in prestressed concrete (PC) structures will be discussed. These are treated separately because of different reasons. One of these reasons is that corrosion can manifest in different ways in RC and PC structures. Moreover, there is a certain agreement on how to model corrosion in RC concrete structures, but literature and guidelines on corrosion modelling and assessment of corrosion in PC structures are more limited. Section II.2 will focus on corrosion in RC structures, whereas section II.3 will focus on corrosion in PC structures.

II.2 Modelling time-dependent degradation of RC structures

Deterioration of structures over time can be ascribed to both internal and external factors. Examples of external factors are loading and environmental conditions, whereas internal factors refer for example to material properties (Schöbi and Chatzi, 2016). Corrosion has different effects on a reinforced concrete (RC) structure (Rodriguez et al., 1997):
- reduction in steel section;
- reduction of mechanical properties of the steel;
- cracking and spalling of the concrete cover due to the expansion of corrosion products;
- reduction of the bond between steel and concrete.

Degradation models are for example provided in (Alonso et al., 1988; Andrade et al., 1993; Coronelli and Gambarova, 2004; Duracrete, 1998; El Hajj et al., 2017; Hájková et al., 2018; Lay et al., 2003; Stewart and Rosowsky, 2002; Vu and Stewart, 2000).

The evolution of corrosion takes place in different phases. First, there is an initiation period during which the aggressive agents penetrate the concrete and depassivate the protective layer on the steel. Once the steel is depassivated, the propagation period starts, i.e. corrosion products will be formed and reduce the reinforcement area. The iron oxides formed during corrosion are expansive, leading to an increased internal pressure. At a certain point in time, this pressure may become too high and the concrete starts to crack. These different phases are governed by different parameters. Mathematical models can be found in literature to describe the effects of corrosion on a RC structure (Duracrete, 1998; El Maaddawy and Soudki, 2007; Lay et al., 2003; Vu and Stewart, 2000).

In the following section, models will be provided for the initiation period, the reduction in steel section during the propagation phase, the stiffness reduction due to concrete cracking, the reduction of the ultimate strain of the reinforcing steel and the reduction in bond between steel and concrete.

II.2.1 Initiation period

The modelling of the initiation period depends on the type of corrosion considered. In this work, the focus will be mostly on chloride-induced corrosion. However, the corrosion models for carbonation-induced corrosion will also be discussed to arrive at a more comprehensive overview.

In case of chloride-induced corrosion, chlorides penetrate the concrete and change the chemical composition of the pore solution. Chloride ingress in concrete can be modelled by application of Fick's second law of diffusion. A generally accepted simplification for the initiation period is given by equation (II-1) (Duracrete, 1998; *fib*, 2006).

$$T_i = \frac{1}{4D} \frac{c^2}{\left(erf^{-1}\left(1 - \frac{C_{cr}}{C_s}\right)\right)^2} \qquad \text{(II-1)}$$

Here, D [mm²/year] is the diffusion coefficient of the concrete, C_{cr} [wt.-%/c] the critical chloride concentration, C_s [wt.-%/c] the concentration of chlorides at the surface and c [mm] the concrete cover. It should be noted that the diffusion coefficient D should be described by a time-variant model, but that a generally accepted representation of the time-dependency is at present not available. Hence, an equivalent time invariant diffusion coefficient could be chosen such that a similar initiation period is reached. However, if desirable, also the time-dependent model of D could be taken into account directly according to equation (II-2).

$$D = k_e D_{RCM} k_t A(t) \quad \text{with} \quad k_e = \exp\left(b_e\left(\frac{1}{T_{ref}} - \frac{1}{T_{real}}\right)\right)$$

$$\text{and} \quad A(t) = \left(\frac{t_0}{t}\right)^a \tag{II-2}$$

Here, b_e [K] is a regression variable, T_{ref} [K] the standard test temperature, T_{real} [K] the temperature of the structural element or the ambient air, D_{RCM} [mm²/year] is the chloride migration coefficient, k_t [-] is a transfer parameter, $A(t)$ [-] a subfunction considering ageing, a [-] an ageing exponent, and t_0 a reference point of time [years]. Distributions for all these variables can be found in (*fib*, 2006).

In case of corrosion due to carbonation, the exposure of concrete to CO_2 results in carbonation of the hydration products accompanied by a reduction in pH, which can induce corrosion of the reinforcement. The penetration of the carbonation front depends on the concentration of CO_2 in the atmosphere and the amount of hydration products able to react with CO_2. Furthermore, it is connected to other factors such as the porosity, permeability and saturation degree of the concrete, and the presence of cracks. If gas diffusion is assumed, the carbonation depth is proportional to the square root of time. When the carbonation front has reached the reinforcement, corrosion will start. Hence, the initiation period can be derived from equation (II-3) (*fib*, 2006).

$$c = \sqrt{2k_e k_c (k_t R_{ACC}^{-1} + \varepsilon_t) C_s} \sqrt{t} W(t) \tag{II-3}$$

Here, c [mm] is the concrete cover, R_{ACC}^{-1} [(mm²/years)/(kg/m³)] is the inverse effective carbonation resistance of concrete and C_s [kg/m³] the CO_2 concentration. The factor k_e [-] is an environmental function and is given by equation (II-4) (*fib*, 2006).

$$k_e = \left(\frac{1 - \left(\frac{RH_{real}}{100}\right)^{fe}}{1 - \left(\frac{RH_{ref}}{100}\right)^{fe}}\right)^{g_e} \tag{II-4}$$

Here, RH_{real} [%] is the relative humidity of the carbonated layer, RH_{ref} [%] the reference relative humidity and g_e and f_e are exponents according to (*fib*, 2006).

The factor k_c [-] in equation (II-3) is an execution transfer parameter and is given by equation (II-5) (*fib*, 2006).

$$k_c = \left(\frac{t_c}{7}\right)^{b_c} \tag{II-5}$$

Here, b_c [-] is an exponent of regression, and t_c [days] is the period of curing.

The function $W(t)$ in equation (II-3) is given by equation (II-6) (*fib*, 2006).

$$W(t) = \left(\frac{t_0}{t}\right)^w \text{ with } w = \frac{(p_{SR}ToW)^{b_w}}{2} \tag{II-6}$$

Here, ToW [-] is the time of wetness, p_{SR} [-] is the probability of driving rain, b_w [-] is an exponent of regression, and t_0 [years] is the time of reference.

Based on the above, the initiation period for carbonation-induced corrosion is given by equation (II-7).

$$T_i = \left(\frac{c}{\sqrt{2k_e k_c (k_t R_{ACC}^{-1} + \varepsilon_t) C_s t_0^w}}\right)^{\frac{1}{w+1/2}} \tag{II-7}$$

II.2.2 Propagation period

Different approaches exist for modelling the propagation phase, such as models based on electrochemical principles, empirical models, etc. In the following, only the model used in this work will be summarized. During the propagation period, corrosion products are formed and the reinforcement area reduces. This reduction is given by the corrosion degree α, which can be defined as the ratio of the reduction in reinforcement area to the initial reinforcement area. The predicted corrosion degree at time t is given by equation (II-8) (Marsh and Frangopol, 2008; Stewart and Rosowsky, 1998).

$$\alpha(t) = \frac{A_{s0} - A_s(t)}{A_{s0}} \text{ with } A_s(t) = (r_0 - x(t))^2 \cdot \pi \cdot n_r \tag{II-8}$$

In this equation, A_{s0} [mm²] is the initial reinforcement area (n_r bars with radius r_0). Note that it is assumed that all n_r bars deteriorate in the same way. When this is not the case, the equation should be adjusted accordingly. The reduction $x(t)$ in rebar radius is given by equation (II-9) (Duracrete, 2000; Lay et al., 2003; Stewart and Rosowsky, 1998).

$$x(t) = \begin{cases} 0 & t \leq T_i \\ V_{corr} \cdot \alpha_p \cdot (t - T_i) & t > T_i \end{cases} \tag{II-9}$$

Here, t is the age of the structure [years], α_p [-] is a pitting factor to take into account the non-uniform corrosion of the rebar, and V_{corr} is the corrosion rate, which can be written as $V_{corr} = V_{corr,a} \cdot ToW$, with $V_{corr,a}$ the mean corrosion rate when corrosion is active [mm/year] and ToW the time of wetness as a fraction of the year [-].

The values for the pitting factor and the corrosion rate to be used in equation (II-9) depend on the type of corrosion. In general, carbonation-induced corrosion will result in a more uniform decrease in steel section and hence a small pitting factor. For the latter, a deterministic value of 2 is assumed in case of carbonation-induced corrosion according to (Duracrete, 2000). On the other hand, chloride-induced corrosion is often accompanied with the local formation of deep pits. This results in the use of a larger pitting factor in equation (II-9). Very often, this pitting factor is sampled from an extreme value distribution, as for example explained in (Duracrete, 2000; Guo et al., 2011b; Stewart and Rosowsky, 1998; Stewart and Suo, 2009). Another difference between both types of corrosion is the speed of corrosion. Carbonation-induced corrosion is often accompanied by very low corrosion rates, with mean values for $V_{corr,a}$ ranging from 0.002 mm/year to 0.005 mm/year in sheltered and unsheltered conditions respectively. For chloride-induced corrosion, the corrosion rates $V_{corr,a}$ are much larger, ranging from 0.004 mm/year in wet-rarely dry exposures to 0.07 mm/year in tidal zones.

General principles on propagation of reinforcement corrosion together with test methods and models for the propagation phase can be found in (Andrade, 2020, 2019). Other models for the reduction in steel section can be found in (Alonso et al., 1988; Duracrete, 2000; Lay et al., 2003; Stewart and Rosowsky, 1998; Stewart and Suo, 2009; Vu and Stewart, 2000). Pitting corrosion can also be explicitly modelled instead of using the pitting factor α_p in equation (II-9) (Stewart, 2004; Val and Melchers, 1997). The frameworks and principles that will be introduced in this work can easily be adapted to incorporate these different models.

II.2.3 Concrete cracking

Corrosion does not only lead to a reduction in steel section. The corrosion products formed on the reinforcement bars are expansive and take more volume than the initial uncorroded steel section. The expansion of the corrosion products can induce an excessive pressure on the concrete, leading to cracking of the concrete cover. The combined influence of corrosion on the steel section and concrete stiffness is visualized in Figure II-2.

The time between initiation of corrosion and the onset of cover cracking can for example be calculated from equation (II-10) (Lv and Zhu, 2016), which has been derived based on the assumption of uniform corrosion of a steel reinforcement bar.

$$T_{cr} = \frac{377204.7\left(1 + k\frac{c}{D}\right)\left\{\delta_0 + 0.3\left(0.5 + 4.33\frac{c}{D}\right)f_{ctm}\frac{R_0}{E_{ef}}\left[\frac{(R_0 + c)^2 + R_0^2}{(R_0 + c)^2 - R_0^2} + v_c\right]\right\}}{\left(1 - 0.00574\exp\left(\frac{c}{4.81D}\right)\right)i_{corr}} \qquad \text{(II-10)}$$

In equation (II-10), k ranges from 0.7 to 0.8 for long-term natural corrosion and from 0.1 to 0.3 for short-term accelerated corrosion. The corrosion current density is here written as i_{corr} and should be entered in units of µA/cm² ($i_{corr} = V_{corr}/0.0116$). The concrete cover c is given in mm, D is the diameter of the steel reinforcing bar [mm], δ_0 is the thickness of the porous zone, typically in a range of 10 to 20 µm, and $R_0 = D/2 + \delta_0$. The parameter f_{ctm} is the mean value of the concrete tensile strength, v_c is the Poisson's ratio of concrete (typically 0.2 for uncracked concrete) and E_{ef} is the effective elastic modulus of the concrete [MPa]. Equation (II-10) does not account for filling of cracks with corrosion products and the fact that the corrosion products can be compressed. Furthermore, it assumes a constant corrosion rate.
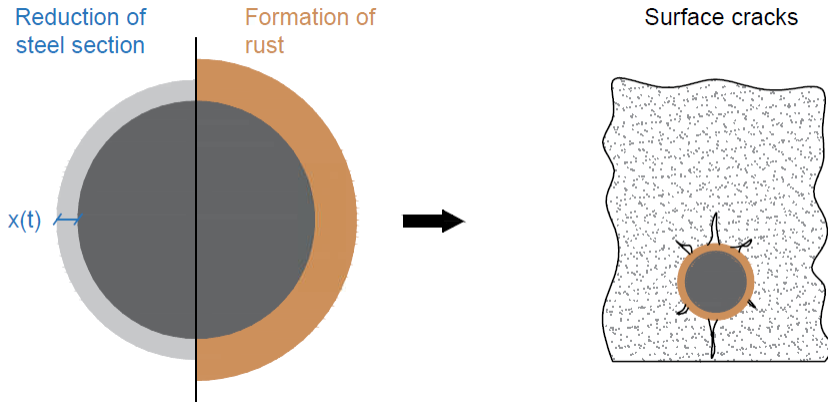
Figure II-2: Reduction of steel section and cover cracking due to corrosion

In general, the Young's modulus of concrete can be written as a function of the compression strength f_c as $E_c = 4500\sqrt{f_c}$ (Lv and Zhu, 2016), where both E_c and f_c are given in MPa. The reduced concrete strength due to cracking and spalling can be determined based on equation (II-11) (Coronelli and Gambarova, 2004), which represents the reduction of compressive strength due to tensile strains in the transverse direction that cause longitudinal microcracks. This relationship is derived from experimental research carried out by Vecchio and Collins (1986) on reinforced concrete panels under a variety of well-defined uniform biaxial stresses.

$$f_c^* = \frac{f_c}{1 + K \dfrac{\varepsilon_1}{\varepsilon_{c0}}} \tag{II-11}$$

In equation (II-11), K is a coefficient related to the bar roughness and diameter (0.1 for medium-diameter ribbed bars), ε_{c0} is the strain at the peak compressive stress f_c, and ε_1 is the average (smeared) tensile strain in the cracked concrete

perpendicular to the applied compression. This last term is given by equation (II-12) (Coronelli and Gambarova, 2004).

$$\varepsilon_1 = \frac{n_{bars}w_{cr}}{b_0} \qquad \text{(II-12)}$$

Here, b_0 is the initial concrete section width before degradation due to corrosion, n_{bars} is the number of reinforcement bars, and w_{cr} is the total crack width for a given corrosion level. This crack width can be evaluated by applying equation (II-13) (Andrade, Alonzo and Molina, 1993), which is derived from research on a numerical model based on standard finite element techniques for the simulation of cracking in concrete specimens subjected to corrosion, validated with experimental data.

$$w_{cr}(t) = 2\pi(v_{rs} - 1)x(t) \qquad \text{(II-13)}$$

In equation (II-13), $x(t)$ is the depth of the corrosion attack, and v_{rs} is the ratio of volumetric expansion of the oxides formed as corrosion products with respect to the virgin material, typically taken equal to 2 for reinforcement steel (Andrade et al., 1993).

In general, corrosion will lead to longitudinal cracks along the reinforcement and is less likely to result in a general reduction of the concrete cover stiffness. To account for this cracking more accurately, the influence of the expansive rust on the stiffness of the concrete cover can also be modelled by finite element simulations (Sánchez et al., 2010). This model can also be extended to take into account the fact that corrosion products tend to penetrate in cracks and that the oxide layer itself is also deformable (Berra et al., 2003; Zandi Hanjari et al., 2013). Also different analytical models exist to predict the time to cracking (El Maaddawy and Soudki, 2007; Liu, 1996; Teplý and Vořechovská, 2012), the reduced stiffness of the cracked concrete cover (Du et al., 2014; Li et al., 2006; Šavija et al., 2013; Teplý and Vořechovská, 2012; Zhong et al., 2009), and the crack widths (Pedrosa and Andrade, 2017). A summary of models for the onset of cracking can also be found in (Ranjith et al., 2016). The framework of this thesis can easily be adapted to incorporate these different models.

II.2.4 Other influences of corrosion

Corrosion, and the presence of pits in particular, influences the ultimate strain ε_{su} of the steel, resulting in a reduced ductility. Different models exist in literature for this reduction in ultimate strain. In this work, the (empirical) model of (Yu et al., 2015; Zhu and François, 2015, 2013) as given by equation (II-14) is used.

$$\frac{\varepsilon_{su,red}}{\varepsilon_{su}} = \begin{cases} e^{-0.1\alpha} & \alpha \geq 16\% \\ 0.2 & \alpha < 16\% \end{cases} \qquad \text{(II-14)}$$

The bond strength between concrete and steel reinforcement is also influenced by the corrosion process. Also here different models exist, but only the (empirical) model used in this work is provided. The ratio of the reduced bond strength due to corrosion relative to the initial maximal bond strength τ_{max} is given by equation (II-15) (Bhargava et al., 2007).

$$\frac{\tau_{max,red}}{\tau_{max}} = \begin{cases} 1 & \alpha \leq 1.5\% \\ 1.192e^{-0.117\alpha} & \alpha > 1.5\% \end{cases} \tag{II-15}$$

II.3 Modelling time-dependent degradation of PC structures

II.3.1 Difference between prestressed and reinforced concrete structures

Time-dependent degradation in prestressed structures differs from degradation in reinforced concrete structures. The most important difference between both types of structures is the presence of the prestress. In prestressed structures, pitting corrosion due to chlorides might induce strand failure more rapidly than general (uniform) corrosion, due to the presence of the prestress. This high prestress on stranded wires may also accelerate the pitting corrosion process (Vu et al., 2009) and lead to earlier brittle rupture than expected. Vu, Castel, and François (2009) found that stress corrosion cracking induces brittle failure of the wire when pitting corrosion has led to a 20% reduction in steel cross-section in a steel wire loaded up to 80% of its elastic limit. When the wires fail due to stress corrosion, local damage can arise in the part of the structure closest to the broken wire, with cracking in the concrete and increasing strains in the non-prestressed reinforcement (Coronelli et al., 2009). The higher stress levels in the wires can also lead to up to more than 15% more mass loss due to corrosion when compared to unstressed wires. On the other hand, the stress level does not influence the composition of corrosion products in the pits (Vu et al., 2009). Due to the high stress levels in the prestressing steel, there will also be a coupling between conventional (pitting) corrosion and steel micro-cracking, called stress corrosion (Coronelli et al., 2009). Rupture of the prestressing strands was also observed by Naito et al. (2006), who investigated the corrosion of prestressing strands in prestressed concrete box girders. For this purpose, PC box girder beams from a 46-year-old bridge were investigated. They observed pit depths greater than 20% of the wire section area.

Besides the presence of the prestress, prestressing strands generally have a much thicker concrete cover compared to reinforcement bars, leading to a more severe corrosion degree of the latter under the same exposure conditions (Guo et al., 2011a). Chloride ions take a longer time to reach the surface of the tendons or strands and hence to induce severe corrosion. Moreover, the cracking mechanism of concrete around prestressed strands might differ from the one around

reinforcement bars due to the difference in shape of cross-section of the strands and bars (Wang et al., 2019). Another important difference is that pitting corrosion of prestressing strands or tendons can form on each single wire. Hence, the failure of any wire will cause the increased load of other wires in the group due to stress redistribution. Moreover, according to (Guo et al., 2016), these pits propagate slower in prestressing steel than in reinforcing bars due to the high quality of the steel (higher quality of the passive film) and the more strict manufacturing process. The pit depth of unstressed wires is about 30% of the one of reinforcing bars under the same circumstances (Li et al., 2011). However, due to stress corrosion cracking, the mass loss of a prestressing strand can become 1.3 times as large as the one of a reinforcing bar. Li et al. (2011) observed higher corrosion rates for higher levels of prestressing and a corrosion rate decreasing over time, more rapidly in the initiation stage and slower afterwards.

Not only the differences between reinforcement bars and prestressing strands are of importance, but also their interaction. As found by Guo, Frangopol, et al. (2011), loss in the non-prestressed reinforcement bars affects the structural integrity too by influencing the stress levels of the prestressing tendons. Hence, it is necessary to account for the non-prestressed reinforcements and their loss in cross-sectional area when performing reliability assessments.

II.3.2   Reduction of steel area in prestressed concrete structures

As mentioned earlier, chloride-induced corrosion will be more important for prestressed concrete structures due to the stress corrosion cracking effect generated by the formation of pits. If carbonation-induced corrosion would occur, similar models could be used as given for the reinforced concrete structures. A summary of models for carbonation-induced corrosion applied to prestressed concrete structures is also given in (Vereecken et al., 2021). In the following, the focus will be on models for chloride-induced corrosion in prestressed structures.

The initiation period can also be modelled according to equation (II-1) for prestressed structures, as for example applied in (Nguyen et al., 2013; Tu et al., 2019), amongst others.

For the reduction of the steel cross-section in the propagation phase, different models exist. These models distinguish between uniform and pitting corrosion. For prestressed elements, the latter is the most important. For pitting corrosion, the area of a corroded bar at time *t* is given by equation (II-16) according to (Val and Melchers, 1997), assuming a hemispherical pit shape.

$$A(t) = \begin{cases} \dfrac{\pi D_0^2}{4} - A_1 - A_2, & p(t) \leq \dfrac{\sqrt{2}}{2} D_0 \\[2mm] A_1 - A_2 & \dfrac{\sqrt{2}}{2} D_0 \leq p(t) \leq D_0 \\[2mm] 0 & p(t) > D_0 \end{cases} \qquad \text{(II-16)}$$

$$\text{with } p(t) = 0.0116(t - T_i)i_{corr}R$$

Here, R [-] is the penetration ratio between maximum and average penetration (ranging from 4 to 8 for reinforcement steel embedded in concrete according to González et al. (1995)), i_{corr} the corrosion rate in $\mu A/cm^2$ and T_i [years] the initiation period.

The other parameters in equation (II-16) are given as follows (Val and Melchers, 1997), with D_0 the initial reinforcement diameter:

$$A_1 = \frac{1}{2}\left[\theta_1\left(\frac{D_0}{2}\right)^2 - a\left|\frac{D_0}{2} - \frac{p(t)^2}{D_0}\right|\right]; \quad A_2 = \frac{1}{2}\left[\theta_2 p(t)^2 - a\frac{p(t)^2}{D_0}\right] \qquad \text{(II-17)}$$

$$a = 2p(t)\sqrt{1 - \left(\frac{p(t)}{D_0}\right)^2} \qquad \text{(II-18)}$$

$$\theta_1 = 2\arcsin\left(\frac{a}{D_0}\right); \quad \theta_2 = 2\arcsin\left(\frac{a}{2p(t)}\right) \qquad \text{(II-19)}$$

Guo et al. (2011b) apply a truncated normal distribution (truncated at 1) for the penetration ratio R, with a mean value of 3 and a coefficient of variation (COV) of 0.33, which is based on the assumption that the 95% percentile corresponds to a penetration ratio $R = 4$ (Stewart and Rosowsky, 1998). These values have been derived for conventional reinforcement steel. The penetration ratio R could also be modelled by a Gumbel distribution. A model for the maximum pit depth, over a standard length L_0 of a rebar, is given by Stewart (2009). Here, the maximum pit depth over a given length L_u is expressed by means of the Gumbel parameters μ and α as given by equation (II-20).

$$\mu = 5.56 + \frac{1}{1.16}\ln\left(\frac{L_u}{L_0}\right) \text{ and } \alpha = 1.16 \qquad \text{(II-20)}$$

In this equation, the values 5.56 and 1.16 are the Gumbel parameters obtained from corrosion tests on a reinforcement bar of diameter 16 mm with standard length $L_0 = 100$ mm. The maximum pit depth should be estimated over the whole length of the reinforcement. The values 5.56 and 1.16 might change depending on the diameter of the bar, for example for a diameter of 10 mm they are respectively equal to 5.08 and 1.02, and for a diameter of 27 mm they are equal to 6.55 and

1.07 (Stewart, 2009). Nevertheless, for prestressing wires often much smaller diameters are used. For these smaller diameters, no values for the parameters of the Gumbel distribution are found in literature.

Darmawan and Stewart (2007) also developed an empirical model for the pit depth $p(t)$, further denoted as a. They applied a Gumbel distribution for the maximum pit depth based on the assumptions that the wire is exposed to a uniform corrosion rate along its length. In addition, the number of pits formed and the length of the pits are assumed constant in time after an initial period of corrosion. Only the pit depth grows in time. Finally, the model also assumes that at any location of the wire only one pit can form. The Gumbel distribution for the maximum pit depth a as a function of time t is given by equation (II-21).

$$f_a(t, i_{corr}, L) =$$

$$\frac{\alpha}{\lambda^{0.54}} \exp\left(-\alpha \left(\frac{a}{\lambda^{0.54}} - \mu\right)\right) \exp\left(-\exp\left(-\alpha \left(\frac{a}{\lambda^{0.54}} - \mu\right)\right)\right) \qquad \text{(II-21)}$$

$$\text{if } t > T_i$$

The parameters λ, μ and α are given by equations (II-22) to (II-25).

$$\lambda = \frac{\left[D_0^2 - \left(D_0 - 0.0232 i_{corr}(1)\left\{1 + \frac{\kappa}{\theta + 1}[(t - T_i)^{\theta+1} - 1]\right\}\right)^2\right]}{\left[D_0^2 - \left(D_0 - 0.0232 i_{corr}(1)\left\{1 + \frac{\kappa}{\theta + 1}[T_0^{\theta+1} - 1]\right\}\right)^2\right]} \qquad \text{(II-22)}$$

$$T_0 = \exp\left(\frac{1}{\theta + 1} \ln\left(\frac{(\theta + 1)(i_{corr-exp}T_{0-exp}) + (\kappa - \theta - 1)(i_{corr}(1))}{\kappa i_{corr}(1)}\right)\right) \qquad \text{(II-23)}$$

$$\mu = \mu_{0-exp} + \frac{1}{\alpha_{0-exp}} \ln\left(\frac{L}{L_{0-exp}}\right) \text{ and } \alpha = \alpha_{0-exp} \qquad \text{(II-24)}$$

$$i_{corr}(t - T_i) = i_{corr}(1) \cdot \kappa(t - T_i)^\theta \text{ if } t - T_i \geq 1 \text{ year} \qquad \text{(II-25)}$$

Here, D_0 [mm] is the initial diameter of the wire, $i_{corr}(1)$ [µA/cm²] is the corrosion rate at the start of corrosion propagation, T_i [years] the initiation period, and L [mm] is the wire length. κ and θ are empirical factors, with κ equal to 0.85 if the corrosion rate reduces with time and 1 if the corrosion rate is time-invariant. Accordingly, θ equals -0.29 and 0, respectively. The parameters with subscript '-exp' are the ones obtained from experimental data from (Darmawan and Stewart, 2007): i.e. $i_{corr-exp}$ = 186 µA/cm², T_{0-exp} = 0.03836 years, μ_{0-exp} = 0.84, L_{0-exp} = 650 mm and α_{0-exp} = 8.10. The distribution of the maximum pit depth given by equation (II-21) can be used to generate samples of the pit depth in a probabilistic analysis of the corrosion process and the corresponding resistance or

probability of failure. The samples of the pit depth can subsequently be inserted in equation (II-16). This model of (Darmawan and Stewart, 2007) is also applied by (Tu et al., 2019).

It is generally assumed that pitting corrosion will only occur on the exposed surface of the strands, i.e. half of the total surface of the outer six wires (Guo et al., 2016; Tu et al., 2019). This area exposed to pitting corrosion is visualized in Figure II-3. The pitting corrosion starts at these outer wires of a 7-wire strand since they are exposed to the chlorides. Hence, according to (Guo et al., 2016), the following assumptions can be made:
1. Neglect pitting corrosion of the inner wire;
2. Pitting corrosion on the outer six wires can occur at slightly different points in time;
3. The pits propagate slower than in reinforcing bars due to the high quality of the steel and the more strict manufacturing process.
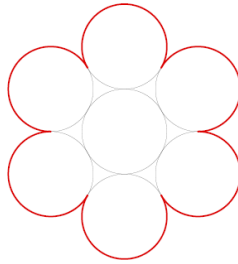
Figure II-3: Area of a prestressing strand exposed to pitting corrosion (indicated with a red bold line)

II.3.3 Influence on steel properties

To account for the high stresses due to the reduction in wire sections (which might trigger structural collapse), an adapted stress-strain curve for the corroded steel can be used. Besides the size reduction of the strands, also the degradation in mechanical properties of the steel can be modelled, including:
1. Ductility decrease;
2. Change in elastic modulus;
3. Change in ultimate strength due to the stress concentration caused by pitting and/or the asymmetric tension due to an asymmetric corrosion distribution;
4. Change in ultimate strain;
5. Loss of yielding plateau and strain hardening region if the corrosion degree is larger than a critical value.

Lu et al. (2016) performed an investigation on the mechanical behaviour of prestressing strands subjected to chloride attack. The reduced elastic modulus, ultimate strength and ultimate strain of the prestressing strands are given by equations (II-26) to (II-28), which are based on experimental results.

$$E_s^* = (1 - 1.8\alpha(t))E_s \qquad \text{(II-26)}$$

$$f_u^* = (1 - 2.8\alpha(t))f_u \qquad \text{(II-27)}$$

$$\varepsilon_u^* = (0.1 + 0.9\exp(-20\alpha(t)))\,\varepsilon_u \qquad \text{(II-28)}$$

Here, $\alpha(t)$ [-] is the corrosion degree at time t, calculated based on the strand area.

When the corrosion degree is given as a percentage, the constitutive law of the prestressing steel is given by equation (II-29) for corrosion degrees smaller than 8% (Lu et al., 2016). If the corrosion degree exceeds 8%, the hardening plateau disappears and the stress-strain curve only contains the elastic branch.

$$\sigma(\varepsilon) = \begin{cases} E_s^* \varepsilon & \varepsilon \leq \varepsilon_y^* = \dfrac{0.85 f_u^*}{E_s^*} \\ 0.85 f_u^* + \dfrac{0.15 f_u^*}{\varepsilon_u^* - \varepsilon_y^*}\left(\varepsilon - \varepsilon_y^*\right) & \varepsilon_y^* \leq \varepsilon \leq \varepsilon_u^* \end{cases} \qquad \text{(II-29)}$$

Model (II-29) is also applied by Jeon et al. (2019). However, in the latter work, the ultimate stress and strain are determined based on a fit to data extracted from prestressing steel strands in external tendons of an existing bridge. The resulting models are given by equation (II-30) and (II-31). The regression coefficients depend on the pit depth and pit shape (corresponding to three types of pit configurations based on observations on real corroded strands).

$$f_u^* = a\alpha(t) + b \qquad \text{(II-30)}$$

$$\varepsilon_u^* = \begin{cases} c\alpha(t)^2 + d\alpha(t) + e & d_p < 0.5 \\ f\alpha(t)^g & d_p \geq 0.5 \end{cases} \qquad \text{(II-31)}$$

Here, d_p is the pit depth and a to g are regression parameters dependent on the pit shape, as given in Table II-1 (Jeon et al., 2019). In expressions (II-30) and (II-31), the corrosion degree is calculated based on the wire area.

Table II-1: Regression coefficients to be used in the stress-strain model of (Jeon et al., 2019)

Pit type		Regression parameters						
		a	b	c	d	e	f	g
Type 1		-1991.8	1748.0	-5.96	-1.30	0.0754	0.0025	-0.621
Type 2		-1995.6	1801.6	-1.00	-0.69	0.0754	0.0045	-0.305
Type 3		-2302.7	1752.7	9.54	-1.77	0.0754	0.0045	-0.298

Also Tu et al. (2019) apply the same constitutive law. However, equations (II-26) to (II-28) are slightly differently formulated, according to equations (II-32) to (II-34), where $\alpha(t)$ should be given as a percentage (percentage area loss caused by corrosion). The latter equations are formulated for experimental results on prestressed tendons and not for strands; hence this might explain the difference compared to equations (II-26) to (II-28).

$$E_s^* = (1 - 0.848\alpha(t))E_s \tag{II-32}$$

$$f_u^* = \frac{\left(1 - 2.683\alpha(t)\right)}{1 - \alpha(t)} f_u \tag{II-33}$$

$$\varepsilon_u^* = (1 - 9.387\alpha(t))\varepsilon_u \tag{II-34}$$

The influence of corrosion on the yield stress at time t can for example be modelled according to equation (II-35).

$$f_y = (1 - a \cdot \alpha(t) \times 100)f_{y0} \tag{II-35}$$

Here, f_{y0} is the initial yield stress and a an empirical coefficient (0.0054 for reinforcing bars and 0.0075 for stranded wires (Du et al., 2005; Vu et al., 2009)). However, Zhang et al. (2017a) state that the effect of corrosion loss on the yield stress and Young's modulus is limited when compared to the effect on the ultimate strain of the strands. This can for example be illustrated when applying equation (II-35) for a corrosion degree of 0.08 (8%), which leads to a reduction factor on the yield stress of 0.94, which is much higher than the factors predicted by equations (II-26) to (II-28), (II-30), (II-31) and (II-32) to (II-34), and hence causes a smaller reduction.

II.3.4 Influence on concrete

In (Belletti et al., 2020), the reduction in concrete compressive strength due to corrosion is modelled according to equation (II-11) (Coronelli and Gambarova, 2004). The chemical composition of prestressing strands differs from the one of reinforcement bars. This might lead to different expansion ratios for prestressing and ordinary reinforcement steel (Li et al., 2011). Moreover, due to the different shape of, for example, 7-wire strands compared to reinforcement bars, the formed cracking pattern might deviate since the pressure generated by the corrosion products will have a different distribution. Nevertheless, the purpose of this equation is not to model the actual cracking pattern, but to provide an estimate of the influence on the concrete parameters. Whereas it seems reasonable to apply the given equation as a rough estimate of this reduction, a more detailed investigation on this topic might be required.

Considering prestressed structures, in (Dai et al., 2015) a formulation for the critical cross-section loss at the cover cracking stage is given. The disadvantages of this model are the fact that the reinforcement expansion ratio of rust is used, residual stiffness of cracked concrete is not considered and two independent theories are used for crack initiation (a mechanical model) and propagation (a geometrical model). To resolve these issues, Wang et al. (2019) investigated the cracking of concrete under combined prestress and strand corrosion. The resulting rust expansion ratios were found to be on average equal to 2.78. Since in the experiments low corrosion degrees already induced cracking and corrosion is more uniform for low corrosion degrees, uniform corrosion products are assumed in the prediction model of Wang et al. (2019). However, this does not necessarily correspond to reality. The model is based on the thick-walled cylinder theory, and accounts for filling of cracks and pores. The residual tangential stiffness in cracked concrete assuming uniformly distributed smeared cracks is calculated, and a relation between the corrosion loss of the strand and the stiffness reduction of the concrete is given. It should be pointed out that the model of Wang et al. (2019) does not account for the presence of multiple strands.

II.3.5 Assessment of post-tensioned structures

There are some important differences between pretensioned and post-tensioned structures, which influence their assessment. The most important difference between both types of structures is the presence of a duct, in which the tendons are located, which implies that they are not in direct contact with the concrete. Hence, initiation of corrosion is not determined by the same processes as for reinforced and pretensioned structures. In the following section, information is provided on how to account for corrosion in post-tensioned structures.

Despite the fact that for post-tensioned structures the strands are not in direct contact with the concrete, corrosion can still be an issue (Nguyen et al., 2013). This can for example be ascribed to the incomplete filling of the ducts with grout.

Voids created as such induce the accessibility of moisture, oxygen and chlorides (from rainwater, seawater, salt-fog or de-icing salts (Zhang et al., 2017a)). Voids in the grout also enable the transport of moisture and chlorides along the tendon and their presence can reduce the bond over parts of the tendon length. Furthermore, chlorides may be latent in the grouting (Schupack, 1994). Expansive grouting has a particularly high level of chlorides, which can induce tendon corrosion. Another possible source initiating the corrosion of the tendons can be the corrosion of the anchorage due to insufficient cover, impermeable materials or a lack of bond. This allows moisture and chlorides to enter the duct. These non-tight anchorages or construction joints (e.g. inadequate sealing of the road surface (Podroužek et al., 2014)) can form the main source of corrosive agents in ungrouted ducts (Page and Page, 2007). Another source of corrosion can be water that was already present in the ducts of post-tensioning tendons prior to injection, due to which steel might already suffer severe pitting corrosion in the ungrouted and non-prestressed condition. This might lead to a reduction in load-bearing capacity. In current practice, the chloride contents in the water used for grout and concrete mixing should be verified and limited. However, in the past, this was not always the case. Hence, in older existing structures, chlorides can still be present in the concrete or grout. According to Zhang et al. (2017a) strand corrosion in post-tensioned structures can be accelerated by galvanic coupling between the strands and the anchorage body, which might induce anchorage failure. Finally, damage of the duct, improper slices between the duct, and a non-permanent duct can lead to chlorides reaching the tendons as well. Concluding, corrosion in post-tensioned structures will mostly be induced by inappropriate construction. If tendons are well installed, corrosion should be very rare (Tu et al., 2019).

Even though corrosion should be very rare if tendons are properly installed, according to Nguyen et al. (2013), corrosion of tendons happens very often in practice since grouting is generally incomplete (Woodward, 2001). The incomplete grouting process leads to voids that contain water and oxygen along the length of the tendon, inducing depassivation of the tendon surface. The corrosion rate will depend on the type of grout and the diffusion of oxygen into the wire surface. The time to corrosion initiation can still be calculated according to equation (II-1). However, c now equals the distance between the top of the grout and the wire surface, accounting for the void size which is commonly 6 mm (Nguyen et al., 2013) (see Figure II-4). This grout void size is based on experimental experience from an NDT testing company (Fisk and Armitage, 2019), where a small bleed water void (less than 6 mm) was detected in virtually every grout classified as 'good, unvoided' after verification by drilling. The total surface concentration C_s will be a combination of the native chloride content of the grout (500 ppm for commercial grout) and the chloride in the air within the void (0.17%), or $C_s = 0.8$ kg/m³ (Nguyen et al., 2013). The diffusion coefficient D will then represent the diffusivity of the grout. Regarding the initial chloride content in the grout, different values are found in literature ranging from 80 ppm for non-commercial grout to 500 ppm in commercial grout (Wang et al., 2005). It

should also be pointed out that in the general model for reinforcement corrosion, the initial chloride concentration is not taken along in C_s but in a parameter C_0 according to (*fib*, 2006). In (Virmani and Ghasemi, 2012) a summary of codes and standards defining maximum allowable chloride limits in grout and prestressed concrete can be found.

In the case of steel ducts, these ducts can also corrode, which allows corrosive agents to reach the steel surface through the ducts. For example, Guo et al. (2016) consider tendons consisting of stranded wires inside corrugated metal ducts, modelling the time of corrosion initiation of tendons as consisting of three parts:

1) Diffusion of chloride ions from the concrete surface to the metal duct;
2) The time for a pit with a depth equal to the thickness of a duct to form in the metal duct;
3) Diffusion of the chloride ions in the grout.
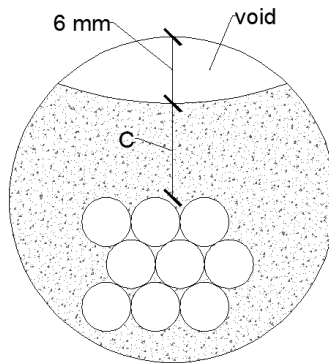
Figure II-4: Strands in grouted duct with void

The distinction between these three phases is also made by Tu et al. (2019), who state that the second phase will have the smallest contribution due to the small duct thickness. To overcome this possibility of corrosive agents reaching the steel, strong emphasis is nowadays placed on the quality, integrity and continuity of the duct as a corrosion barrier in itself, replacing steel ducts by plastic equivalents. The better performance of plastic ducts compared to steel ducts is for example illustrated in the experimental research of (Salas et al., 2008). In (Salas et al., 2004), light corrosion of steel in plastic ducts was observed, but with a much better performance compared to steel ducts. In the latter, severe duct destruction and pitting is observed. If corrosion is present in plastic ducts, it is mostly at locations where the duct is interrupted or where different pieces of the duct are connected.

Hence, there is a need for effective splicing and sealing at joints. In (McCool et al., 2011) different issues due to which plastic ducts can still lead to corrosion are listed:

- Imperfect sealing;
- Longitudinal splitting of the duct;
- Presence of grout voids;
- Improperly installed duct splices.

They also observed that strands in plastic ducts showed less corrosion than in steel ducts, and that corrosion initiated later in plastic ducts. Chlorides do not penetrate trough plastic ducts and the duct itself remains intact. However, breaches in couplers and loosening of epoxy can induce the ingress of chlorides. For new bridges, the advice is hence to use these plastic ducts. Nevertheless, in older bridges steel ducts can still be present since little attention was formerly paid to the possible role of the duct as a barrier to corrosive agents (FHWA, 2013).

The two models for corrosion in post-tensioned ducts described above are based on a completely different origin of the corrosion products and are therefore valid for specific situations. Both initiation period and corrosion rate can differ largely depending on the source of the chlorides. For the first model, assuming a grout cover of 15 mm between void and tendons, a critical chloride concentration of 0.3 kg/m³, a surface chloride concentration of 0.8 kg/m³ and a diffusion coefficient of chlorides in the grout of 10^{-11} m²/s, Nguyen et al. (2013) found an initiation period of 15 years by applying a polynomial approximation to equation (II-1). According to Nguyen et al. (2013), the corrosion rate in grout equals 6.5 µA/cm² or 0.075 mm/year. This corrosion rate would correspond to a severe outdoor environment of a tidal zone for RC structures (Lay et al., 2003). When calculating the initiation period applying the models described in (Guo et al., 2016), it would take 15 years before the chlorides would reach the duct and 8 more years before the duct is penetrated. Next, another 15 years could pass before the chlorides reach the tendons within the duct when applying the same assumptions as in (Nguyen et al., 2013). Hence, the second model leads to a much larger initiation period and may as such lead to an underestimation of the actual corrosion degree by disregarding the presence of grout voids.

Note also that for post-tensioned strands located in external ducts, i.e. outside of the concrete volume, only the first method seems reasonable. Not only is there no first stage of penetration of chlorides through the concrete, but also the choice for steel ducts will often not be made for external tendons since they are more directly exposed to the environment. If a steel duct would be used, there is still a possibility of corrosion of the duct, enabling chlorides from the environment to reach the prestressing steel.

Information on the probabilistic models for the corrosion parameters in the model for chloride ingress through grout voids is limited. To close this gap, Nguyen et al. (2013) suggest to use a Poisson distribution to model the initiation period as a stochastic variable, where the mean value is calculated based on equation (II-1). Nevertheless, other probability distributions could also be applied. For example, to model the distance between the void and the tendons, models proposed by (JCSS, 2001) for the concrete cover could be applied. The diffusion coefficients of grout and concrete are not that different according to (Guo et al., 2016), hence the distributions proposed in (*fib*, 2006) could be used for this parameter. In a similar way, the distributions from (*fib*, 2006) for the surface chloride concentration and critical chloride concentration could be adopted, using the aforementioned values as mean values for this specific example.

Regardless of the origin of the corrosion products, corrosion happens on the single wires of a tendon, where tendon failure will only occur when in all wires in the tendon the critical stress is exceeded. Concerning wire failure, the worst effects are observed for unbonded tendons in post-tensioned elements since brittle failure of these tendons leads to a prestress reduction proportional to the tendons cross-sectional loss (Coronelli et al., 2009). This is in contrast to bonded tendons, where a new anchorage on either side of the fracture can be developed after failure, due to the bond stresses between steel and concrete/grout. Hence, these failures might have a smaller structural impact.

Another important difference between pretensioned and post-tensioned structures is the discontinuous character of the concrete cover (Wang et al., 2019). In the case of post-tensioned structures, the concrete cover consists of grout, situated in the duct, which is embedded in the concrete. Hence, strand corrosion will induce first internal grout cracking before it will affect the external concrete. Concerning the influence on concrete cracking, Zhang et al. (2017b) performed experimental investigations on eight bonded post-tensioned concrete beams with different corrosion levels. These beams were tested up to flexural failure, investigating the effects of corrosion on cracking, stiffness, ultimate strength, failure mode and ductility. They found that the cracking moment almost linearly decreases with increasing strand corrosion. Corrosion of the strands has only a limited influence on the initial stiffness of the post-tensioned beam. After cracking, the influence on the stiffness was found to depend on the strand area loss. Furthermore, strand corrosion accelerates the shift of the neutral axis under self-weight and decreases the depth of the compression zone, leading to a reduced ultimate strength of the beams. Finally, with increasing corrosion loss, the failure mode was observed to change from concrete crushing to strand rupture.

II.4 Conclusions

In this chapter, degradation models for corrosion in reinforced concrete structures and prestressed concrete structures are discussed. Further chapters will mostly deal with reinforced concrete structures, and the degradation models used further in this work are summarized in this chapter. Models for both the initiation period of corrosion and the propagation phase are given. For prestressed concrete structures, literature is less clear on how to model degradation due to corrosion. Hence, a short summary on modelling degradation due to corrosion in prestressed and post-tensioned structures has also been provided. These will be used in Chapter VIII of this work.

The models in this chapter are provided without model uncertainties because these model uncertainties are not available in literature, neither the data to quantify these uncertainties. There is a need for the quantification of model uncertainties, which is a research topic of general interest for the assessment of existing structures. Nevertheless, the quantification of model uncertainties falls outside the scope of this work.

II.5 References

Alonso, C., Andrade, C., González, J.A., 1988. Relation between resistivity and corrosion rate of reinforcements in carbonated mortar made with several cement types. Cem. Concr. Res. 18, 687–698.

Andrade, C., 2020. Correction to: Propagation of reinforcement corrosion: principles, testing and modelling (Materials and Structures, (2019), 52, 1, (2), 10.1617/s11527-018-1301-1). Mater. Struct. Constr. 53, 1.

Andrade, C., 2019. Propagation of reinforcement corrosion: principles, testing and modelling. Mater. Struct. Constr. 52, 1–26.

Andrade, C., Alonso, C., Molina, F.J., 1993. Cover Cracking as a Function of Rebar Corrosion: Part II - Numerical Model. Mater. Struct. 26, 532–548.

Andrade, C., Izquierdo, D., 2020. Propagation period modeling and limit state of degradation. Struct. Concr. 21, 1720–1731.

Belletti, B., Vecchi, F., Bandini, C., Andrade, C., Montero, J.S., 2020. Numerical evaluation of the corrosion effects in prestressed concrete beams without shear reinforcement. Struct. Concr. 21, 1794–1809.

Berra, M., Castellani, A., Coronelli, D., Zanni, S., Zhang, G., 2003. Steel-concrete bond deterioration due to corrosion: Finite-element analysis for different confinement levels. Mag. Concr. Res. 55, 237–247.

Bhargava, K., Ghosh, A.K., Mori, Y., Ramanujam, S., 2007. Corrosion-induced bond strength degradation in reinforced concrete — Analytical and empirical models. Nucl. Eng. Des. 237, 1140–57.

Coronelli, D., 2020. Resistance of corroded RC beams: Extending *fib* Model Code 2010 models. Struct. Concr. 21, 1747–1762.

Coronelli, D., Castel, A., Vu, N.A., François, R., 2009. Corroded post-tensioned beams with bonded tendons and wire failure. Eng. Struct. 31, 1687–1697.

Coronelli, D., Gambarova, P., 2004. Structural Assessment of Corroded Reinforced Concrete Beams: Modeling Guidelines. J. Struct. Eng. 130, 1214–1224.

Dai, L., Wang, L., Zhang, J., Zhang, X., 2015. A global model for corrosion-induced cracking in prestressed concrete structures. Eng. Fail. Anal. 62, 263–275.

Darmawan, M.S., Stewart, M.G., 2007. Spatial time-dependent reliability analysis of corroding pretensioned prestressed concrete bridge girders. Struct. Saf. 29, 16–31.

Du, X., Jin, L., Zhang, R., 2014. Modeling the cracking of cover concrete due to non-uniform corrosion of reinforcement. Corros. Sci. 89, 189–202.

Du, Y.G., Clark, L.A., Chan, A.H.C., 2005. Residual capacity of corroded reinforcing bars. Mag. Concr. Res. 57, 135–147.

Duracrete, 2000. DuraCrete - Probabilistic Performance based Durability Design of Concrete Structures. Report No BE9521347.

Duracrete, 1998. BE95-1397. Modelling of Degradation.

El Hajj, B., Schoefs, F., Castanier, B., Yeung, T., 2017. A Condition-Based Deterioration Model for the Stochastic Dependency of Corrosion Rate and Crack Propagation in Corroded Concrete Structures. Comput. Civ. Infrastruct. Eng. 32, 18–33.

El Maaddawy, T., Soudki, K., 2007. A model for prediction of time from corrosion initiation to corrosion cracking. Cem. Concr. Compos. 29, 168–175.

FHWA, 2013. Post-Tensioning Tendon Installation and Grouting Manual 184.

fib, 2006. *fib* Bulletin 34: Model code for service life design. Lausanne.

Fisk, P., Armitage, B., 2019. Nondestructive Testing for Voided and Soft Grout in Internal Post-Tensioning Ducts. Post Tens. Inst. J. 15, 31–35.

González, J.A., Andrade, C., Alonso, C., Feliu, S., 1995. Comparison of rates of general corrosion and maximum pitting penetration on concrete embedded steel reinforcement. Cem. Concr. Res. 25, 257–264.

Guo, T., Chen, Z., Liu, T., Han, D., 2016. Time-dependent reliability of strengthened PSC box-girder bridge using phased and incremental static analyses. Eng. Struct. 117, 358–371.

Guo, T., Frangopol, D.M., Han, D., Chen, Y., 2011a. Probabilistic assessment of deteriorating prestressed concrete Box-Girder bridges under increased vehicle loads and aggressive environment. J. Perform. Constr. Facil. 25, 564–576.

Guo, T., Sause, R., Frangopol, D.M., Li, A., 2011b. Time-dependent reliability of PSC box-girder bridge considering creep, shrinkage, and corrosion. J. Bridg. Eng. 16, 29–43.

Hájková, K., Šmilauer, V., Jendele, L., Červenka, J., 2018. Prediction of reinforcement corrosion due to chloride ingress and its effects on

serviceability. Eng. Struct. 174, 768–777.

JCSS, 2001. Probabilistic Model Code.

Jeon, C.H., Lee, J.B., Lon, S., Shim, C.S., 2019. Equivalent material model of corroded prestressing steel strand. J. Mater. Res. Technol. 8, 2450–2460.

Lay, S., Schießl, P., Cairns, J., 2003. Lifecon Deliverable D3.2.

Li, C., Melchers, R.E., Zheng, J., 2006. Analytical Model for Corrosion-Induced Crack Width in Reinforced Concrete Structures. ACI Struct. J. 103, 479–487.

Li, F., Yuan, Y., Li, C.Q., 2011. Corrosion propagation of prestressing steel strands in concrete subject to chloride attack. Constr. Build. Mater. 25, 3878–3885.

Liu, Y., 1996. Modeling the Time-to-Corrosion Cracking of the Cover Concrete in Chloride Contaminated Reinforced Concrete Structures. PhD Thesis, Virginia Polytechnic Institute and State University.

Lu, Z.H., Li, F., Zhao, Y.G., 2016. An investigation of degradation of mechanical behaviour of prestressing strands subjected to chloride attacking. Int. Conf. Durab. Concr. Struct. ICDCS 2016 57–65.

Lv, Q., Zhu, R., 2016. Model for forecasting the time of corrosion-induced reinforced concrete cracking, in: Dilum Fernando, Jin-Guang Teng, J.L.T. (Ed.), Proceedings of the Second International Conference on Performance-Based and Life-Cycle Structural Engineering (PLSE 2015). School of Civil Engineering, The University of Queensland, Brisbane, QLD, Australia, pp. 902–910.

Marsh, P.S., Frangopol, D.M., 2008. Reinforced concrete bridge deck reliability model incorporating temporal and spatial variations of probabilistic corrosion rate sensor data. Reliab. Eng. Syst. Saf. 93, 394–409.

McCool, G.E., Ahern, M.E., Bree, J.E., Wood, S.L., 2011. Evaluation of Corrosion Resistance of Improved Post-tensioning Materials after Long-term Exposure Testing.

Melchers, R.E., 2018. Progress in developing realistic corrosion models. Struct. Infrastruct. Eng. 14, 843–853.

Naito, C., Sause, R., Hodgson, I., Pessiki, S., Desai, C., 2006. Forensic Evaluation of Prestressed Box Beams from the Lake View Drive over I-70 Bridge.

Nguyen, V., Jeong, M.C., Han, T.S., Kong, J.S., 2013. Reliability-based optimisation design of post-tensioned concrete box girder bridges considering pitting corrosion attack. Struct. Infrastruct. Eng. 9, 78–96.

Page, C.L., Page, M.M., 2007. Durability of concrete and cement composites. Woodhead Publishing Limited, Cambridge.

Pedrosa, F., Andrade, C., 2017. Corrosion induced cracking: Effect of different corrosion rates on crack width evolution. Constr. Build. Mater. 133, 525–533.

Podroužek, J., Strauss, A., Bergmeister, K., 2014. Robustness-based performance assessment of a prestressed concrete bridge. Struct. Concr. 15, 248–257.

Qiu, Q., 2020. A state-of-the-art review on the carbonation process in cementitious materials: Fundamentals and characterization techniques. Constr. Build. Mater. 247, 118503.

Ranjith, A., Balaji Rao, K., Manjunath, K., 2016. Evaluating the effect of corrosion on service life prediction of RC structures – A parametric study. Int. J. Sustain. Built Environ. 5, 587–603.

Rodrigues, R., Gaboreau, S., Gance, J., Ignatiadis, I., Betelu, S., 2021. Reinforced concrete structures: A review of corrosion mechanisms and advances in electrical methods for corrosion monitoring. Constr. Build. Mater. 269, 121240.

Rodriguez, J., Ortega, L.M., Casal, J., 1997. Load Carrying Capacity of Concrete Structures With Corroded Reinforcement. Constr. Build. Mater. 11, 239–248.

Salas, R.M., Schokker, A.J., West, J.S., Breen, J.E., Kreger, M.E., 2008. Corrosion risk of bonded, post-tensioned concrete elements. PCI J. 53, 89–107.

Salas, R.M., Schokker, A.J., West, J.S., Breen, J.E., Kreger, M.E., 2004. Conclusions, Recommendations and Design Guidelines for Corrosion.

Sánchez, P.J., Huespe, A.E., Oliver, J., Toro, S., 2010. Mesoscopic model to simulate the mechanical behavior of reinforced concrete members affected by corrosion. Int. J. Solids Struct. 47, 559–570.

Šavija, B., Luković, M., Pacheco, J., Schlangen, E., 2013. Cracking of the concrete cover due to reinforcement corrosion: A two-dimensional lattice model study. Constr. Build. Mater. 44, 626–638.

Schöbi, R., Chatzi, E.N., 2016. Maintenance planning using continuous-state partially observable Markov decision processes and non-linear action models. Struct. Infrastruct. Eng. 12, 977–994.

Schupack, M., 1994. Durability study of a 35-year-old post-tensioned bridge. J. Concr. Int. 16, 54–58.

Stewart, M.G., 2009. Mechanical behaviour of pitting corrosion of flexural and shear reinforcement and its effect on structural reliability of corroding RC beams. Struct. Saf. 31, 19–30.

Stewart, M.G., 2004. Spatial variability of pitting corrosion and its influence on structural fragility and reliability of RC beams in flexure. Struct. Saf. 26, 453–470.

Stewart, M.G., Rosowsky, D.V., 2002. Structural Safety and Serviceability of Concrete Bridges Subject to Corrosion. J. Infrastruct. Syst. 4, 146–155.

Stewart, M.G., Rosowsky, D.V., 1998. Time-dependent reliability of deteriorating reinforced concrete bridge decks. Struct. Saf. 20, 91–109.

Stewart, M.G., Suo, Q., 2009. Extent of spatially variable corrosion damage as an indicator of strength and time-dependent reliability of RC beams. Eng. Struct. 31, 198–207.

Teplý, B., Vořechovská, D., 2012. Reinforcement corrosion: Limit states, reliability and modelling. J. Adv. Concr. Technol. 10, 353–362.

Tu, B., Dong, Y., Fang, Z., 2019. Time-Dependent Reliability and Redundancy of Corroded Prestressed Concrete Bridges at Material, Component, and System Levels. J. Bridg. Eng. 24.

Val, D.V., Melchers, R.E., 1997. Reliability of Deteriorating RC Slab Bridges. J. Struct. Eng. 123, 1638–1644.

Vecchio, F.J., Collins, M.P., 1986. Modified Compression-Field Theory for Reinforced Concrete Elements Subjected To Shear. J. Am. Concr. Inst. 83, 219–231.

Vereecken, E., Botte, W., Lombaert, G., Caspeele, R., 2021. Assessment of corroded prestressed and post-tensioned concrete structures: A review. Struct. Concr. 22, 2556–2580.

Virmani, P.Y., Ghasemi, H., 2012. Literature Review of Chloride Threshold Values for Grouted Post-Tensioned Tendons, FHWA Publication No.: FHWA-HRT-12-067.

Vu, K.A.T., Stewart, M.G., 2000. Structural reliability of concrete bridges including improved chloride-induced corrosion models. Struct. Saf. 22, 313–333.

Vu, N.A., Castel, A., François, R., 2009. Effect of stress corrosion cracking on stress-strain response of steel wires used in prestressed concrete beams. Corros. Sci. 51, 1453–1459.

Wang, H., Sagues, A.A., Powers, R., 2005. Corrosion of the Strand-Anchorage System in Post-Tensioned Grouted Assemblies, in: Corrosion 2005. pp. 1–27.

Wang, L., Dai, L., Bian, H., Ma, Y., Zhang, J., 2019. Concrete cracking prediction under combined prestress and strand corrosion. Struct. Infrastruct. Eng. 15, 285–295.

Woodward, R., 2001. Durability of post-tensioned tendons on road bridges in the UK, in: Federation internationale du Béton (Ed.), Proceedings of Workshop on Durability of Post-Tensioning Tendons, Fédération Internationale Du Béton (*fib*). Lausanne, pp. 78–88.

Yu, L., François, R., Dang, V.H., L'Hostis, V., Gagné, R., 2015. Structural performance of RC beams damaged by natural corrosion under sustained loading in a chloride environment. Eng. Struct. 96, 30–40.

Zandi Hanjari, K., Lundgren, K., Plos, M., Coronelli, D., 2013. Three-dimensional modelling of structural effects of corroding steel reinforcement in concrete. Struct. Infrastruct. Eng. 9, 702–718.

Zhang, X., Wang, L., Zhang, J., Liu, Y., 2017a. Corrosion-induced flexural behavior degradation of locally ungrouted post-tensioned concrete beams. Constr. Build. Mater. 134, 7–17.

Zhang, X., Wang, L., Zhang, J., Ma, Y., Liu, Y., 2017b. Flexural behavior of bonded post-tensioned concrete beams under strand corrosion. Nucl. Eng. Des. 313, 414–424.

Zhong, J., Gardoni, P., Rosowsky, D., 2009. Stiffness Degradation and Time to

Cracking of Cover Concrete in Reinforced Concrete Structures Subject to Corrosion. J. Eng. Mech. 136, 209–219.

Zhu, W., François, R., 2015. Structural performance of RC beams in relation with the corroded period in chloride environment. Mater. Struct. 48, 1757–69.

Zhu, W., François, R., 2013. Effect of corrosion pattern on the ductility of tensile reinforcement extracted from a 26-year-old corroded beam. Adv. Concr. Constr. 1, 121–36.

CHAPTER III

Spatial character of degradation due to corrosion

_____

"Coincidences, in general, are great stumbling-blocks in the way of that class of thinkers who have been educated to know nothing of the theory of probabilities – that theory to which the most glorious objects of human research are endebted for the most glorious of illustration."

- Edgar Allan Poe, The Murders in the Rue Morgue

III.1 Introduction

Degradation of a structure often does not propagate in a uniform way. There can be differences between the structural parts of the structure, for example the different girders and slabs of a girder bridge. These differences can arise due to different casts of concrete, different exposure to the environment, etc. Also within these structural elements, there can be spatial variation of degradation. This can be ascribed to workmanship, the composite nature of concrete and the intrinsic spatial variability of the corrosion process (for example the existence of pitting corrosion).

A lot of research is performed about the influence of this spatial variation on, for example, reliability calculations. Taking into account spatial variations in concrete properties and the influence of degradation can have a large influence on the probability of failure. Furthermore, by accounting for possible correlation between structural elements or within an element, information gathered at one location of the structure might also provide information about non-inspected locations on the same structure. By making use of this correlation, more optimal inspection plans can be formulated.

Although it is clear that taking into account the spatial variation of concrete and its degradation is important in structural assessment, literature on how to model these correlations is scarce. There is no consensus yet on the extent of spatial correlation of different concrete properties.

In the following, available information on how to account for spatial variation of degradation will be summarized, including a discussion on hyperparameters and random fields. The focus will be mostly on the latter, since these will be used in further chapters of this work. Next, the modelling of spatial variation of the corrosion process will be discussed for reinforced concrete and prestressed concrete structures.

III.2 Modelling the spatial character of degradation

Corrosion in general is not materializing in a uniform way over a structure. Schneider et al. (2015) provide a framework that allows accounting for the spatial distribution of reinforcement corrosion for assessing and updating the reliability of concrete bridges subjected to corrosion. For this purpose, the structure is subdivided into different zones with similar exposure conditions and material characteristics. Between these different zones, there is no interdependence of the deterioration state. For example, when considering a box girder bridge, the bridge deck might be more susceptible to chloride-induced corrosion due to de-icing salts than the bottom flange. Hence, the bridge deck is considered as one zone, whereas the webs and bottom flange are grouped in another zone (Figure III-1 left).

These zones also need further discretization to model the spatial character of degradation within these zones. Hence, the zones will be further subdivided into elements. Within these elements, degradation will be considered uniform. When looking at the different elements, realizations can be independent, i.e. there is no correlation between the degradation states in the different elements, or there can be some correlation. To model this correlation, two methods are highlighted in the following: hierarchical models (i.e. using hyperparameters) and random fields.
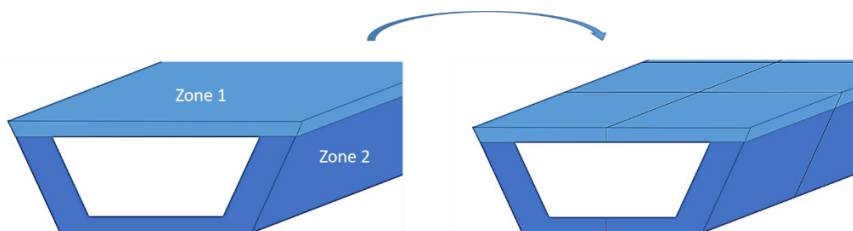
Figure III-1: Division of a box girder bridge in zones (left) and subdivision of zones in elements (right)

III.2.1 Hyperparameters

In most literature, common exposure conditions are modelled with hyperparameters. For example, if the box girder of Figure III-1 would be located in a marine environment, all elements of zone 2 would be exposed to this same environment. Similarly, the elements might consist of concrete from the same batch, due to which for example also the diffusion coefficient of the concrete can be modelled in a similar way. This statistical dependence of common (exposure) conditions is modelled by a common parent variable for all elements in zone 2, which is called a hyperparameter. In case of chloride-induced corrosion, hyperparameters can for example be used to describe the dependence between the chloride concentration or the diffusion coefficient at different elements (Schneider et al., 2015). These hyperparameters are the same for all elements within a zone, but can differ between zones.

III.2.2 Random fields

Hyperparameters model the common (exposure) conditions for all elements within a zone. However, for two elements in the same environment and hence with common exposure conditions, there might still be a spatial variation depending on the geometric location. For example, considering zone 2 of the box girder in Figure III-1, the exposure to chlorides might be similar in all elements, but the concrete cover can vary along the bridge, e.g. due to irregularities in the formwork. The concrete cover at locations close to each other will be more correlated than the concrete cover at the extremities of the structure. To model this spatial variation of the related properties, random fields are used (Luque and Straub, 2019; Sudret et al., 2007; Uribe et al., 2017).

III.2.2.1 General introduction to random fields

With a random field model, the correlation between elements is a function of the location. A Gaussian random field $S(\boldsymbol{x}, \theta)$ is defined by a mean function $\mu_S(\boldsymbol{x})$ and a covariance function $C_S(\boldsymbol{x}, \boldsymbol{x}')$, where, $\boldsymbol{x}$ and $\boldsymbol{x}'$ represent spatial coordinates. θ denotes the elementary events, part of the sample space Θ. In the covariance function, the correlation between two locations $\boldsymbol{x}$ and $\boldsymbol{x}'$ can for example be modelled by an exponential (equation (III-1)) or a squared exponential correlation function (equation (III-2)).

$$\rho_X(\boldsymbol{x}, \boldsymbol{x}') = \exp\left(-\frac{|\boldsymbol{x} - \boldsymbol{x}'|}{l_c}\right) \tag{III-1}$$

$$\rho_X(\boldsymbol{x}, \boldsymbol{x}') = \exp\left(-\left(\frac{|\boldsymbol{x} - \boldsymbol{x}'|}{l_c}\right)^2\right) \tag{III-2}$$

The correlation functions depend on the correlation length l_c and the distance between the two spatial coordinates $\boldsymbol{x}$ and $\boldsymbol{x}'$ ($|\boldsymbol{x} - \boldsymbol{x}'|$).

III.2.2.2 Discretization of random fields

In practical examples, it is necessary to represent a random field by means of a finite sum of random variables. This can be achieved by application of the Karhunen-Loève expansion (Sudret and Der Kiureghian, 2000) according to equation (III-3).

$$S(\boldsymbol{x}, \theta) = \mu_S(\boldsymbol{x}) + \sum_{j=1}^{\infty} \phi_j(\boldsymbol{x}) \sqrt{\lambda_j} \zeta_j(\theta) \tag{III-3}$$

Here, the random field $S(\boldsymbol{x}, \theta)$ is written as a weighted sum of so-called Karhunen-Loève modes $\phi_j(\boldsymbol{x})$, which are the Eigen functions of the covariance function $C_S(\boldsymbol{x}, \boldsymbol{x}')$, with λ_j the corresponding eigenvalues.

An alternative approach is to discretize the random field $S(\boldsymbol{x}, \theta)$ to a random vector $\boldsymbol{S}(\theta)$, representing the random field at given points x_j. This random vector maps the probability space to a field of real numbers. If the random field is Gaussian, the corresponding discretized random vector will also be Gaussian. The latter is defined by a mean vector of size n x 1 and a covariance matrix of size n x n, with n the number of points at which the random field is evaluated. For a random field $S(\boldsymbol{x}, \theta)$, discretized in n elements with mean vector $\boldsymbol{\mu_S}$ (size n x 1) and a covariance matrix $\boldsymbol{\Sigma_S}$ (size n x n), the random vector $\boldsymbol{S}(\theta)$ is represented by equation (III-4) (Sudret and Der Kiureghian, 2000).

$$S(\theta) = \boldsymbol{\mu_S} + \sum_{j=1}^{\infty} \phi_j \sqrt{\lambda_j} \zeta_j(\theta) \qquad \text{(III-4)}$$

Here, ϕ_j are the eigenvectors of the covariance matrix $\boldsymbol{\Sigma_S}$, with λ_j the corresponding eigenvalues. Since an infinite sum is not easy in use, the summation is taken over the first n_d modes of the covariance matrix. The number of modes n_d is chosen based on the acceptable error ε_{max} and the trace $Tr(\boldsymbol{\Sigma_S})$ of the covariance matrix according to equation (III-5) (Sudret and Der Kiureghian, 2000).

$$\varepsilon(n_d) = 1 - \frac{1}{Tr(\boldsymbol{\Sigma_S})} \sum_{j=1}^{n_d} \lambda_j \leq \varepsilon_{max} \qquad \text{(III-5)}$$

Hence, if the maximum acceptable error is 5%, the sum of the first n_d eigenvalues λ_j, ranked from high to low, should at least be equal to 95% of the trace of the covariance matrix ($Tr(\boldsymbol{\Sigma_S})$). A priori, the random field is assumed stationary over the considered domain.

When non-Gaussian fields are used, the application of a Nataf transformation allows modelling the fields by an underlying Gaussian random field. As illustrated in (Liu and Der Kiureghian, 1986), the error on the covariance matrix of the transformed discretized field compared to the underlying discretized Gaussian field is limited for the most common distribution types.

Figure III-2 shows four realizations of a random field of the corrosion degree. In this example, a uniform probability distribution function between zero and one is assumed for the corrosion degree, together with a squared exponential correlation model with correlation length 1 m.

III.2.3 Random fields vs. hyperparameters

Random fields and hyperparameters can be used for different purposes and both have their advantages and limitations. These are summarized in this section. Nevertheless, it should be pointed out that both methods serve other purposes and that parameters that should be modelled by random fields often cannot be modelled by hyperparameters, and vice versa. Hence, the two methods could not be mutually compared, but advantages and disadvantages of the methods should be kept in mind when applying them.
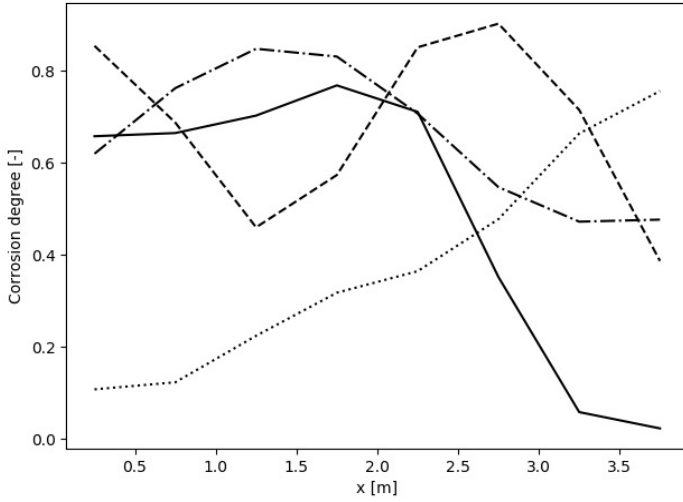
Figure III-2: Different realizations of the random field for the corrosion degree (squared exponential correlation model, $l_c = 1$ m)

Hyperparameters are used to model common realizations of the variables within a zone, and the hyperparameters itself are in most cases time-invariant. The type of correlation that can be modelled is limited to matrices of the Dunnett-Sobel class (Schneider et al., 2015), with linear constant correlation. However, it is a very transparent method to model the underlying assumption of a common source. In addition, the use of hyperparameters has less computational challenges when compared to random field models.

Random fields are used to model the spatial distribution of a parameter. A disadvantage of the use of random fields is their possibly large computational cost. Moreover, when applying a random field, the underlying correlation structure should be known. The latter might be difficult to determine since it should ideally be based on a large amount of experimental data. Hence, often correlation models are based on engineering judgement. If experiments are performed to determine the correlation model, they should be designed as such that small and large scale variability is accounted for (Malioka and Faber, 2004). In general, two methods exist to determine the correlation length and correlation model based on experimental data. The first is based on finding the model parameter that provides the best fit to the autocorrelation of the measured data (Vanmarcke, 2010). The second procedure is based on the maximum likelihood method (Schoefs et al., 2017, 2016). However, this falls outside the scope of this work and use is made of common proposals as available in existing literature and summarized in section III.3.2.

III.2.4 Structural analysis

To account for spatial variation of degradation, the structure under investigation should be discretized in zones and elements, as pointed out in section III.2. When a finite element model of the structure is generated, these elements should not necessarily correspond to the finite element discretisation. One element for the discretisation of the spatially variable degradation process can contain multiple finite elements, depending on the required discretisation lengths. The degradation state in each of these elements of the model is then adjusted accounting for the corresponding realizations of the hyperparameters and of the discretized random field. When for example a beam is subdivided into n elements, the random field will be discretized into a random vector of size n x 1. Hence, each element of the discretized beam corresponds to an element of the vector representing the discretized random field.

To properly account for the variation of variables modelled by a random field, an appropriate element size in the discretization of the structure is important. The element size is typically a fraction of the correlation length l_c. For a squared exponential correlation model, the element size should be smaller than $l_c/2$ to $l_c/3$. For an exponential correlation function, element sizes of $l_c/5$ to $l_c/10$ are generally considered adequate (DIANA FEA BV, 2017). In general, when discretizing a structure, the maximum element size should be chosen as such that convergence of the probability of failure of the structure is reached, and a sensitivity study on the influence of the element size on the model outputs should be performed.

III.3 Spatial character of degradation in RC structures

When modelling the spatial character of corrosion in RC structures, there is often assumed some correlation of the corrosion process at different locations along the structure. In the following sections, suggestions for the use of hyperparameters and random fields when modelling corrosion in RC structures are provided.

III.3.1 Hyperparameters in degrading RC structures

For chloride-induced corrosion, the initiation period is a function of environmental variables such as chloride content, but also of material parameters such as the diffusion coefficient of the concrete. Hence, when for example the bridge deck in Figure III-1 is simulated as one zone with common exposure conditions, the chloride content C_s and the diffusion coefficient D of the concrete within this zone can be modelled by hyperparameters. The bridge deck is then discretized in elements, where the random variables C_s and D of the different elements are conditionally independent, given a realization of the hyperparameters.

III.3.2 Random field modelling of degrading RC structures

In literature, different assumptions on the correlation models in RC structures can be found. Criel et al. (2014) summarize some correlation lengths commonly found in literature for corrosion variables and concrete parameters. These are given in Table III-1. The correlation models mentioned in this work are the exponential correlation model (equation (III-1)), the squared exponential model (equation (III-2)) and the Matérn model (equation (III-6)). The last one depends not only on the correlation length l_c, but also on a smoothness parameter v. In equation (III-6), $\Gamma(.)$ is the Gamma function and $K_v(.)$ the BesselK($v,.$) function.

$$\rho_X(\boldsymbol{x}, \boldsymbol{x}') = \frac{1}{\Gamma(v)2^{v-1}}\left(\frac{2\sqrt{v}|\boldsymbol{x} - \boldsymbol{x}'|}{\theta}\right)^v K_v\left(\frac{2\sqrt{v}|\boldsymbol{x} - \boldsymbol{x}'|}{\theta}\right)$$

$$\text{with } \theta = l_c \frac{\sqrt{\pi}\Gamma\left(v + \frac{1}{2}\right)}{\sqrt{v}\Gamma(v)} \tag{III-6}$$

Table III-1: Correlation lengths as summarized in (Criel et al., 2014)

Variable	Correlation lengths	References
Concrete cover c	1 m – 2 m – 3.5 m	(Li et al., 2004; Stewart and Mullard, 2007; D. Straub, 2011)
Surface chloride concentration C_s	1 m – 1.96 m – 2 m – 3.5 m	(Duprat, 2007; Engelund, 1997; Straub, 2011; Vu, 2003)
Concrete compressive strength f_c	3.5 m	(Duprat, 2007)

In (Straub, 2011), the exponential correlation model is applied, with the correlation lengths mentioned in Table III-2. In (Tran et al., 2012), a correlation length of 1.1 m is considered for the diffusion coefficient.

Table III-2: Correlation lengths as summarized in (Straub, 2011)

Variable	Correlation lengths
Concrete cover c	1 m
Surface chloride concentration C_s	2 m
Critical chloride concentration C_{cr}	2 m
Diffusion coefficient of concrete D	2 m

Vu and Stewart (2005) assume a squared exponential correlation model with correlation lengths as given in Table III-3.

Table III-3: Correlation lengths as summarized in (Vu and Stewart, 2005)

Variable	Correlation lengths
Concrete cover c	2 m
Surface chloride concentration C_s	1 m – 1.96 m – 2 m
Water/cement ratio w/c	0.5 m
Young's modulus of the concrete E_c	2 m
Poisson coefficient of concrete v	2 m
Concrete compressive strength f_c	2 m

In (Straub et al., 2009), an exponential correlation model is considered with a correlation length of 80 cm for the chloride conductivity. In (Hajializadeh et al., 2016), a squared exponential correlation model is considered with a correlation length of 1 m for the concrete cover and concrete compressive strength, and in (Stewart and Mullard, 2007) also a squared exponential correlation model is considered, but with a correlation length of 2 m for the concrete cover, concrete compressive strength and surface chloride concentration. For the surface chloride concentration and concrete cover, Ying et al. (2003) assume a squared exponential correlation model with a lower bound ρ_0 of 0.5 or 0 and a correlation length of 2 m, according to equation (III-7).

$$\rho_X(\boldsymbol{x}, \boldsymbol{x}') = \rho_0 + (1 - \rho_0) \cdot \exp\left(-\frac{|\boldsymbol{x} - \boldsymbol{x}'|^2}{l_c^2}\right) \qquad \text{(III-7)}$$

Furthermore, also (Stewart and Suo, 2009) assume a correlation length of 2 m combined with an exponential correlation function for the concrete cover, concrete compressive strength and surface chloride concentration.

III.4 Spatial character of degradation in PC structures

As explained in the previous chapter, in prestressed concrete structures the effect of pitting corrosion is even more important than in reinforced concrete structures. When pitting corrosion occurs in prestressed concrete structures, the pits will be distributed along the wires, with different pit depths on the wires, even at the same location along the strand. Due to the local character of these pits, often the pitting factor at different locations along the structure is assumed uncorrelated. To model spatial variation due to pitting corrosion in prestressed structures, Darmawan and Stewart (2007) subdivided the beams studied in their work into different elements, with element lengths equal to twice the development length of the bond between steel and concrete. This element length is based on the assumption that when

failure of the steel occurs, there will be a loss of capacity at a distance equal to this development length at either side of the fracture since the bond strength has to redevelop starting from the location of fracture. Assigning the element length equal to two times the development length of the bond is based on the assumption that failure occurs in the middle of the elements. In reality, strand failure could occur near element sides with higher or lower action effects, inducing reduced or increased reliabilities. Nevertheless, it is assumed that differences in reliabilities for non-central strand ruptures will level out, leading to similar reliabilities at the level of the structure when compared to those obtained from the proposed failure criterion.

Dias-da-Costa et al. (2019) also account for the fact that pitting can vary in space. To model the spatial variability, they divide the prestressing reinforcement into different segments, with different pit depths for each segment. For this purpose, the ratio between maximum and average pit depth R is randomly generated. A Gumbel distribution is assigned to R, with parameters $u = 5.56$ and $\alpha = 1.16$ based on (Stewart and Al-Harthy, 2008), where these values were experimentally derived for reinforced concrete beams. All segments are considered statistically independent. The resistance capacity of the strands is then governed by the tensile capacity of each segment, depending on the reduced prestressing area. In contrast to Darmawan and Stewart (2007), who define the discretization length based on the transfer length of the prestressing force to the concrete, Dias-da-Costa et al. (2019) define the discretisation length as the distance at which pitting corrosion influences the structural safety, i.e. in the range of 0.1 to 1 m. The latter means that the reliability index cannot suddenly drop at the onset of corrosion.

When comparing both models for the spatial variability, some observations can be made. For example, when an accurate estimate of the reliability index is required, the element lengths assumed by Darmawan and Stewart (2007) might be too large and can result in an underestimation or overestimation of the reliability index because of the mentioned possibiltiy of non-central strand ruptures and the assumed statistical independence of the segments. The criterion suggested by Dias-da-Costa et al. (2019) will lead to more accurate reliability estimates, but at the cost of requiring smaller element lengths leading to higher computational costs. Hence, the engineer should consider all of these aspects when making decisions on the element length.

The effect of the spatial distribution of pitting in PC beams was also studied in (Belletti et al., 2020). Here it was demonstrated that the knowledge of the actual corrosion distribution over the length of the PC beam is fundamental for a reliable prediction of the ultimate limit state. Moreover, assumptions regarding the spatial distribution of pitting corrosion might also affect the location of the section where failure takes place.

For prestressed structures, the effect of pitting has been assumed the most prominent one, and hence in the references provided above, discretization is based on this pitting process, assuming no correlation between the different elements into which the structure is subdivided. Nevertheless, if desired, concrete cover, diffusion coefficient, etc. could also still be modelled with random fields and hyperparameters, as discussed for RC structures in section III.3

In Chapter II, it was explained how corrosion in prestressed and post-tensioned structures can differ, due to multiple causes. Hence, also the spatial variation of corrosion could be simulated in different ways. When corrosion occurs through the presence of voids in the duct, a method to account for this incidental distribution of pits in post-tensioned structures is described by Nguyen et al. (2013). They subdivide the girder in n_M elements. Each of these elements has a length L_w and contains n_p pits. The number of pits in each element is predicted by a Poisson distribution with mean n_p and the number of occurrences equal to the number of elements n_M. This is based on the assumption that there is only a single pit in one wire in each element. Besides the distribution of pits in an element, the number of pits that can be present in one tendon is also considered random. Nguyen et al. (2013) use a Poisson distribution to predict the number of pits in one tendon. The mean value of this distribution is equal to one, representing the common case that at least one pit is formed in the tendon. The number of occurrences now equals the number of tendons in an element. As such, the number of pits in each tendon in each element can be calculated. This differs from the approaches by Darmawan and Stewart (2007) and Dias-da-Costa et al. (2019), who assume that each strand is exposed to pitting, while the pitting factors for the wires are considered as independent random variables. As such, a different sample for the pitting factor is generated for each wire of each strand in each element. Pitting corrosion caused by penetration of chlorides through the duct will also be characterized by a spatial variability. For the latter, the models for prestressed structures can still be used.

III.5 Conclusions

In this chapter, different ways of modelling the spatial variability of the corrosion process are described. First, a general introduction is given to the use of hyperparameters and random fields to model spatial correlation between variables. The advantages and disadvantages of both methods are also presented. Then, suggestions are provided on how random fields and hyperparameters can be used to account for spatial degradation in reinforced concrete structures. Since reinforced concrete structures and prestressed concrete structures suffer in slightly different ways from corrosion, also models to account for the spatial variability of (pitting) corrosion in prestressed concrete structures are provided.

All indications on how to model a certain variable (i.e. with hyperparameters or random fields) that are provided in this chapter are only suggestions. In the

following chapters, when the spatial correlation of corrosion is accounted for, the assumptions on which variables are modelled with random fields and which variables are modelled with hyperparameters will be discussed before introducing the calculations and results. In general, mostly random fields will be used to model spatial correlation of corrosion in reinforced concrete structures.

III.6 References

Belletti, B., Corres Peiretti, H., Andrade, C., Ghiretti, M., Franceschini, L., Vecchi, F., 2020. Evaluation of the Residual Life of Corroded Prestressed Concrete Beams, in: Proceedings of the *fib* CACRCS DAYS 2020 - Capacity Assessment of Corroded Reinforced Concrete Structures, 1-4 December 2020. pp. 429–437.

Criel, P., Caspeele, R., Taerwe, L., 2014. Bayesian updated correlation length of spatial concrete properties using limited data. Comput. Concr. 13, 659–677.

Darmawan, M.S., Stewart, M.G., 2007. Spatial time-dependent reliability analysis of corroding pretensioned prestressed concrete bridge girders. Struct. Saf. 29, 16–31.

DIANA FEA BV, 2017. Random fields for non-linear finite element analysis of reinforced concrete structures [WWW Document].

Dias-da-Costa, D., Neves, L.A.C., Gomes, S., Hadigheh, S.A., Fernandes, P., 2019. Time-dependent reliability analyses of prestressed concrete girders strengthened with CFRP laminates. Eng. Struct. 196.

Duprat, F., 2007. Reliability of RC beams under chloride-ingress. Constr. Build. Mater. 21, 1605–1616.

Engelund, S., 1997. Probabilistic Models and Computational Methods for Chloride Ingress in Concrete. PhD thesis, Aalborg University.

Hajializadeh, D., Stewart, M.G., Enright, B., OBrien, E., 2016. Spatial time-dependent reliability analysis of reinforced concrete slab bridges subject to realistic traffic loading. Struct. Infrastruct. Eng. 12, 1137–1152.

Li, Y., Vrouwenvelder, T., Wijnants, G.H., Walraven, J., 2004. Effect of Spatial Variability on Maintenance and Repair Decisions for Concrete Structures. Struct. Concr. 5, 121–129.

Liu, P.L., Der Kiureghian, A., 1986. Multivariate distribution models with prescribed marginals and covariances. Probabilistic Eng. Mech. 1, 105–112.

Luque, J., Straub, D., 2019. Risk-based optimal inspection strategies for structural systems using dynamic Bayesian networks. Struct. Saf. 76, 68–80.

Malioka, V., Faber, M.H., 2004. Modeling of the spatial variability for concrete structures, in: Proceedings of IABMAS 2004, Kyoto, Japan.

Nguyen, V., Jeong, M.C., Han, T.S., Kong, J.S., 2013. Reliability-based optimisation design of post-tensioned concrete box girder bridges considering pitting corrosion attack. Struct. Infrastruct. Eng. 9, 78–96.

Schneider, R., Fischer, J., Bügler, M., Nowak, M., Thöns, S., Borrmann, A., Straub, D., 2015. Assessing and updating the reliability of concrete bridges

subjected to spatial deterioration - Principles and software implementation. Struct. Concr. 16, 356–365.

Schoefs, F., Bastidas-Arteaga, E., Tran, T.V., 2017. Optimal embedded sensor placement for spatial variability assessment of stationary random fields. Eng. Struct. 152, 35–44.

Schoefs, F., Bastidas-Arteaga, E., Tran, T. V., Villain, G., Derobert, X., 2016. Characterization of random fields from NDT measurements: A two stages procedure. Eng. Struct. 111, 312–322.

Stewart, M.G., Al-Harthy, A., 2008. Pitting corrosion and structural reliability of corroding RC structures: Experimental data and probabilistic analysis. Reliab. Eng. Syst. Saf. 93, 373–382.

Stewart, M.G., Mullard, J.A., 2007. Spatial time-dependent reliability analysis of corrosion damage and the timing of first repair for RC structures. Eng. Struct. 29, 1457–1464.

Stewart, M.G., Suo, Q., 2009. Extent of spatially variable corrosion damage as an indicator of strength and time-dependent reliability of RC beams. Eng. Struct. 31, 198–207.

Straub, D., 2011. Reliability updating with inspection and monitoring data in deteriorating reinforced concrete slabs, in: Application of Statistics and Probability in Civil Engineering. London.

Straub, D., Malioka, V., Faber, M.H., 2009. A framework for the asset integrity management of large deteriorating concrete structures. Struct. Infrastruct. Eng. 5, 199–213.

Sudret, B., Defaux, G., Pendola, M., 2007. Stochastic evaluation of the damage length in RC beams submitted to corrosion of reinforcing steel. Civ. Eng. Environ. Syst. 24, 165–178.

Sudret, B., Der Kiureghian, A., 2000. Stochastic Finite Element Methods and Reliability: A State-of-the-Art Report, University of California Berkeley.

Tran, T.V., Bastidas-Arteaga, E., Schoefs, F., Bonnet, S., O'Connor, A.J., Lanata, F., 2012. Structural reliability analysis of deteriorating RC bridges considering spatial variability. Bridg. Maintenance, Safety, Manag. Resil. Sustain. - Proc. Sixth Int. Conf. Bridg. Maintenance, Saf. Manag. 698–705.

Uribe, F., Papaioannou, I., Betz, W., Ullmann, E., Straub, D., 2017. Random Fields in Bayesian Inference : Effects of the Random Field Discretization, in: Safety, Reliability, Risk, Resilience and Sustainability of Structures and Infrastructure, 12th Int. Conf. on Structural Safety and Reliability. pp. 799–808.

Vanmarcke, E., 2010. Random Fields Analysis and Synthesis. World Scientific.

Vu, K.A.T., Stewart, M.G., 2005. Predicting the Likelihood and Extent of Reinforced Concrete Corrosion-Induced Cracking. J. Struct. Eng. 131, 1681–1689.

Vu, K.A.T., 2003. Corrosion-induced cracking and spatial timedependent reliability analysis of reinforced concrete structures. PhD thesis, The

University of Newcastle, New South Wales, Australia.

Ying, L., Vrouwenvelder, T., Wijnants, G.H., 2003. Spatial Variability of Concrete Degradation, in: Life-Cycle Performance of Deteriorating Strucutres: Assessment, Design and Management; Third IABMAS Workshop on Life-Cycle Cost Analysis and Design of Civil Infrastructures Systems. pp. 49–58

CHAPTER IV

Updating of corrosion models using Bayesian inference

"Uncertainty isn't just a sign of human ignorance; it's what the world is made of."

- Ian Stewart, Do Dice Play God?

IV.1 Introduction

In this chapter, the principle of Bayesian inference will be introduced. Bayesian inference is a technique to incorporate information from data, taking into account uncertainties. As such, depending on the choice for the prior distribution, there might be a reduction in uncertainty, and the posterior distribution resulting from the Bayesian inference can provide more specific information on the variable under investigation. Bayesian inference has often been referred to in literature as a powerful tool to perform model updating, structural system identification and damage assessment (Beck, 2010; Beck et al., 2001; Huang et al., 2019; Vanik et al., 2002; Yuen et al., 2006). The incorporated information can consist of data resulting from measurements directly providing information on the variable of interest. However, such data is often not available since in many situations the variable of interest (i.e. the variable to be updated) cannot be measured directly. Other parameters are then measured, which depend on the variable of interest, providing indirect information on the latter. In section IV.3 of this chapter, different data types treated further in this work will be summarized. All these types of measurements will provide indirect information on the stiffness and hence the corrosion degree of a reinforced concrete structure under investigation.

IV.2 Introduction to Bayesian inference

The principle of Bayesian inference traces back to the theory of Thomas Bayes on how to assess the probability of a certain value of a non-observed quantity, making use of a set of related measurements. Bayes theorem to calculate the probability P of an event E_i given the observation A (i.e. the posterior probability of E_i) is given by equation (IV-1).

$$P[E_i|A] = \frac{P[A|E_i]P[E_i]}{P[A]} \qquad \text{(IV-1)}$$

Bayes theorem cannot only be applied to events but also to random variables or random vectors, for example X and Y, with prior probability density functions $f_X(x)$ and $f_Y(y)$. The posterior probability density function of X given Y is then given by equation (IV-2), which represents a general formulation of Bayes theorem (Gelman et al., 2014).

$$f_X"(x) = f(x|y) = \frac{f(y|x)f_X(x)}{\int f(y|x)f_X(x)\,dx} \qquad \text{(IV-2)}$$

Here, $f_X"(x)$ is the posterior probability density function of X.

In the current work, Bayesian inference will be applied for model updating purposes, i.e. updating the degradation model of a reinforced concrete structure under investigation. Hence, the random variables that are updated are the structural

model parameters $\boldsymbol{\theta}_M$. Equation (IV-2) could then be written according to equation (IV-3).

$$f''(\boldsymbol{\theta}_M) = f(\boldsymbol{\theta}_M|\overline{\boldsymbol{d}}) = cf'(\boldsymbol{\theta}_M)L(\boldsymbol{\theta}_M|\overline{\boldsymbol{d}}) \qquad \text{(IV-3)}$$

Here, $f'(\boldsymbol{\theta}_M)$ is the prior distribution of the structural model parameters $\boldsymbol{\theta}_M$, L is the likelihood function of $\boldsymbol{\theta}_M$ given the data $\overline{\boldsymbol{d}}$, and c is a constant to normalize the probability density function (PDF). To evaluate the likelihood function, the data $\overline{\boldsymbol{d}}$ will be compared with the outcomes of a (structural) model representing the relationship between the variables of interest $\boldsymbol{\theta}_M$ and the measured quantity. In the following, $\boldsymbol{G}$ is the model to simulate the measured quantity $\boldsymbol{d}$ as a function of the input variables $\boldsymbol{\theta}_M$.

The likelihood function $L(\boldsymbol{\theta}_M|\overline{\boldsymbol{d}})$ can be interpreted as a measure of how well a model succeeds in explaining the observations $\overline{\boldsymbol{d}}$. The latter will often deviate from the true system output and from the modelled output. Hence, the measurement data $\overline{\boldsymbol{d}}$ can be written according to equation (IV-4) (Simoen et al., 2015).

$$\overline{\boldsymbol{d}} = \boldsymbol{d} + \boldsymbol{\eta}_D = \boldsymbol{G}(\boldsymbol{\theta}_M) + \boldsymbol{\eta}_G + \boldsymbol{\eta}_D \qquad \text{(IV-4)}$$

Here, $\boldsymbol{\eta}_G$ is a modelling error describing the discrepancy between model predictions of the measured quantity $\boldsymbol{G}(\boldsymbol{\theta}_M)$ and the true system output $\boldsymbol{d}$, and $\boldsymbol{\eta}_D$ is the measurement error, which represents the discrepancy between the observed structural behaviour $\overline{\boldsymbol{d}}$ and the true response $\boldsymbol{d}$. Accordingly, in the present work, equation (IV-5) is used for the likelihood (Simoen et al., 2015).

$$L \sim (\det(\boldsymbol{\Sigma}_D + \boldsymbol{\Sigma}_G))^{-1/2} \exp\left(-\frac{1}{2}F_{ML}\right) \qquad \text{(IV-5)}$$

This expression is based on the assumption of a normally distributed measurement error $\boldsymbol{\eta}_D$ and modelling error $\boldsymbol{\eta}_G$, both with zero mean and covariance matrixes $\boldsymbol{\Sigma}_D$ and $\boldsymbol{\Sigma}_G$ respectively. F_{ML} is the maximum likelihood function and is given by equation (IV-6) (Simoen et al., 2015).

$$\begin{aligned} F_{ML} &= (\boldsymbol{\eta}_D + \boldsymbol{\eta}_G)^T (\boldsymbol{\Sigma}_D + \boldsymbol{\Sigma}_G)^{-1} (\boldsymbol{\eta}_D + \boldsymbol{\eta}_G) \\ &= (\boldsymbol{G}(\boldsymbol{\theta}_M) - \overline{\boldsymbol{d}})^T (\boldsymbol{\Sigma}_D + \boldsymbol{\Sigma}_G)^{-1} (\boldsymbol{G}(\boldsymbol{\theta}_M) - \overline{\boldsymbol{d}}) \end{aligned} \qquad \text{(IV-6)}$$

The assumption of normally distributed errors is generally accepted (Geyskens et al., 1998) since it is based on the principle of Maximum Entropy (Simoen et al., 2013). Also other distributions for the measurement and modelling errors can be assumed by adjusting the shape of the likelihood function. An example of including a multiplicative lognormal distribution for the modelling error will be discussed in Chapter XII.

In many cases, no closed form analytical expression can be found for the posterior distribution in equation (IV-3). To derive the posterior distribution for these

situations, sampling based methods such as Markov Chain Monte Carlo (MCMC) methods were developed. These methods obtain samples from probability distributions based on a Markov chain, which is defined as a sequence of random variables x_i for which the distribution, conditioned on past realizations, depends only on the previous sample x_{i-1} (Gelman et al., 2014). Hence, a chain of samples from the posterior distribution can be drawn in this way. The generated samples will then asymptotically behave as the PDF to be sampled. In this work, a 'cascade' Metropolis-Hastings algorithm will be used for evaluating the Markov chain. The algorithm for the transition between two estimates of the posterior distribution is based on equation (IV-7) (Gelman et al., 2014).

$$x_{i+1} = \begin{cases} \tilde{x} \propto q(\tilde{x}|x_i) & \text{with probability } \psi \\ x_i & \text{else} \end{cases} \qquad \text{(IV-7)}$$

Here, $q(\tilde{x}|x_i)$ is the transition distribution. A common choice for this is a random walk, by adding a random increment to the previous estimate, as shown by equation (IV-8).

$$\tilde{x} = x_i + \zeta \qquad \text{(IV-8)}$$

Here, ζ is a random vector that does not depend on the previous chain. These values are most often drawn from a normal distribution with zero mean and standard deviation σ_ζ. This last one determines how fast the algorithm will converge.

The probability ψ is the joint acceptance probability based on the prior probability and the likelihood function. This can be restated as the probability that a random sample u_P, drawn from a uniform distribution between zero and one, is accepted according to the prior distribution and that a random sample u_L, drawn from a uniform distribution between zero and one, is accepted according to the likelihood function.

When applying the MCMC procedure, the first part of the generated samples is not considered to avoid taking along the burn-in period in the estimate of the posterior distribution. Convergence is checked by investigation of the evolution plots of the generated chains, i.e. the generated samples as a function of the iteration number. Furthermore, convergence is also verified in terms of the mean and standard deviation of the posterior distributions.

In some cases, an analytical expression of the posterior distribution is available, and MCMC should not necessarily be applied. For example, when $G(\theta_M)$ is a linear model (i.e. $G(\theta_M) = R_G\theta_M$), and θ_M has a (multivariate) Gaussian distribution with prior mean and covariance matrix μ_{θ_M} and Σ_{θ_M}, the posterior distribution of θ_M will also be Gaussian and the posterior mean vector and covariance matrix are given by equations (IV-9) and (IV-10) respectively (Malings and Pozzi, 2018; Vanmarcke, 2010).

$$\mu_{\theta_M|\bar{d}} = \mu_{\theta_M} + \Sigma_{\theta_M} R_G^T \left(R_G \Sigma_{\theta_M} R_G^T + \Sigma_\eta \right)^{-1} \left(\bar{d} - R_G \mu_{\theta_M} \right) \qquad \text{(IV-9)}$$

$$\Sigma_{\theta_M|\bar{d}} = \Sigma_{\theta_M} - \Sigma_{\theta_M} R_G^T \left(R_G \Sigma_{\theta_M} R_G^T + \Sigma_\eta \right)^{-1} R_G \Sigma_{\theta_M}^T \qquad \text{(IV-10)}$$

Here, Σ_η is the error matrix ($\Sigma_D + \Sigma_G$) and $\bar{d}$ is the vector of the available data.

IV.3 Types of data considered in this work

When applying the Bayesian inference procedure, different types of data can be considered. This can be direct data, measuring directly the variable of interest, or indirect data related to the variables of interest in an indirect way.

When performing an inspection or measurement at time t_{insp}, in the ideal case one would directly measure the remaining reinforcement area perfectly: $A_{s,insp}$. When this is smaller than the reinforcement area initially present in the structure (A_{s0}), there is some corrosion present in the structure. Hence, one knows for sure that the initiation period T_i is smaller than t_{insp}, as indicated in Figure IV-1. Different combinations of T_i and the corrosion rate V_{corr} (e.g. (T_i^1, V_{corr}^1) and (T_i^2, V_{corr}^2)) might lead to the same reinforcement area $A_{s,insp}$ at t_{insp}. Since a variety of combinations of T_i and V_{corr} is still possible, there is no unique solution. In a Bayesian context, a distribution with a certain mean and standard deviation will be specified for the initiation period, and the same will be done for the corrosion rate. Moreover, in reality, measurements will provide indirect information on the remaining steel section and measurement and/or modelling errors will be present, leading to a more vague posterior distribution.

In the following sections, different data types used in the next chapters will be introduced. It will be illustrated how these are linked to the corrosion degree and can hence be used in the Bayesian inference procedure to find posterior distributions of the corrosion variables, such as the initiation period and corrosion rate. Here, following definitions of monitoring and inspection are considered:
-   Monitoring: The retrieval of global information from the structure. Dynamic or static tests are performed and relevant data is captured. The duration of the tests can be some days up to some weeks. The term does not necessarily refer to continuous long-term measurements.
-   Inspection: Local short-term measurements or observations, such as visual inspections and crack width measurements.
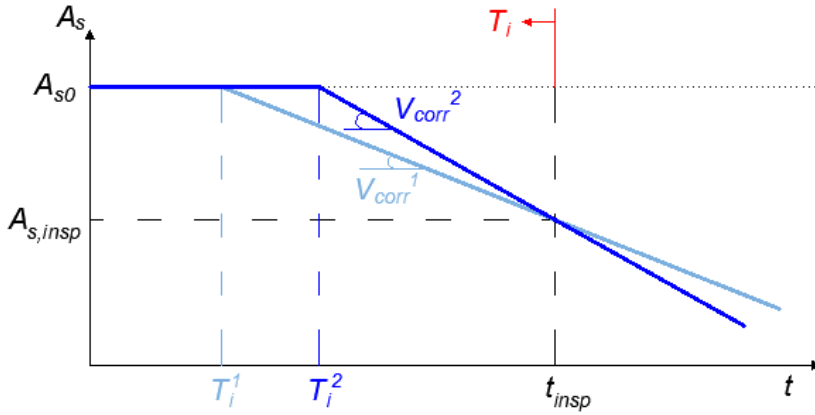
Figure IV-1: Observations on the corrosion process

IV.3.1 Visual data

Visual inspections are the most frequently occurring types of inspections. In Flanders, visual inspections for bridges occur very frequently (Vlaams Ministerie van Mobiliteit en Openbare Werken, 2012). They do not require any equipment, except from a photo camera, if available. By performing these inspections, it can be observed whether the safety of the user of the structure is in danger, or whether there are any abnormal evolutions in the behaviour of the bridge (Vlaams Ministerie van Mobiliteit en Openbare Werken, 2012).

Regarding corrosion, the most important visual observations are the presence of:
- Rust stains;
- Corrosion cracks;
- Concrete spalling.

If any of these signs are present, it can be concluded that the reinforcement of the structure has started to corrode. If spalling is present, corrosion is already in an advanced stage and measures might have to be taken to prevent any further corrosion.

In Figure IV-2 it is illustrated how visual observations can influence the distribution of the initiation period T_i. If at the time of visual inspection t_{insp} it is observed that rust stains are present, the initiation period T_i should be smaller than t_{insp}, since for higher T_i no corrosion would be present in the structure yet.
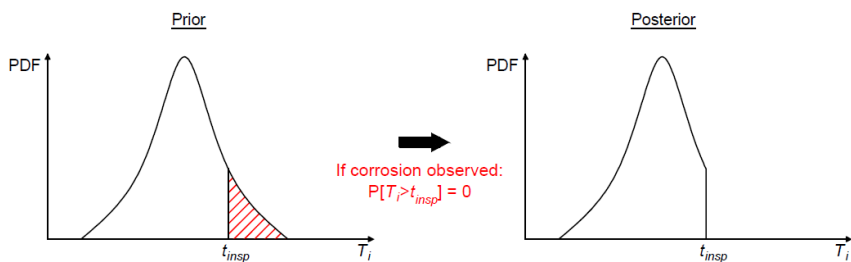
Figure IV-2: Influence of a visual observation of corrosion on the PDF of the initiation period

From visual observations, the presence of bending cracks can also be observed. This might indicate possible overloading of the structure, i.e. loads exceeding the service loads. On the other hand, this might also point to a reduced resistance of the bridge, where service loads already induced concrete cracking. The presence of these cracks should be taken into account when models of the bridge would be made.

It should be pointed out that visual inspections can suffer significantly from operator bias. If such bias is present, this bias should be accounted for when evaluating the information from the visual inspections.

IV.3.2 Data from static diagnostic load testing

According to (Transportation Research Board, 2019a), diagnostic load tests are performed with small fractions of the design live loads. A controlled and known load is applied to the structure to facilitate the comparison between the predicted bridge response (by an analytical or finite element model) and the actually measured response. In this way, the model of the bridge can be calibrated, improving the accuracy of the model-based predictions. However, it should be noted that part of the difference between the field measurements and the predicted response could be attributed to the presence of measurement and/or modelling errors. The measured responses are zeroed at the beginning of the load test and hence only include the live load effects. Influences of degradation on the capacity can be determined by estimating their effect on the structural stiffness. To identify the nature and source of the degradation, the diagnostic test results should be supplemented with other data such as visual inspections, non-destructive testing or material testing.

Diagnostic load tests can be executed in a relatively short amount of time (typically 1 day). Most activities can be carried out on a subset of the traffic lanes of a bridge while the remaining lanes remain open to traffic. Full closures are only required

during the data collection phase, which can typically be completed in 5 to 15 minutes per load path. When access to the underside of the bridge is necessary, partial closures of the roadway under the bridge may be required.

Typically measured parameters during a diagnostic load test are strains and deflections. Both give an indication on the actual stiffness of the structure. Whereas deflections depend on the global stiffness of the structure, for a statically determinate structure, strains depend on the stiffness of the cross-section where the strains are measured. If the structure is statically indeterminate, the global stiffness distribution will also influence the strain results. Measuring strains in RC bridges requires relatively large gauge lengths. When using very small gauge lengths, the heterogeneous nature of the concrete will result in significant measurement uncertainties. Moreover, for small gauge lengths the effect of local cracking can result in strain variations. The gauge length should be large enough to capture cracking effects in a smeared way. When multiple strain gauges are applied over the height of a girder, a strain profile can be developed to check if the cross-section behaves as cracked or uncracked. If the lower part of the cross-section is cracked, the neutral axis moves upwards. Environmental effects on the data should be investigated prior to any load test. If the effect on a sensor is large, experimental results should be adjusted accordingly. Typically, a very slow moving test vehicle is used (8 km/h). Due to this short load cycle, effects of temperature and humidity might be considered relatively constant during the test.

According to (Transportation Research Board, 2019b) strain sensors are widely used to capture the strain response associated with applied loads. It is stated to be probably the most (cost) effective sensor for determining how a structure reacts to its load demand, leading to determination of the structural integrity. Different types of strain sensors are listed, such as polymer-based sensors, electrical resistance based sensors, bolted-on sensors, epoxied sensors, weldable sensors, vibrating wire sensors, etc. The mentioned advantages of strain sensors are the easy-to-understand data, a well-known technology that is widely in use, and the versatility of the strain sensors. A disadvantage is the temperature effect that should also be accounted for. In (Transportation Research Board, 2019b), displacement sensors are stated to be typically used for the determination of relative linear movement of a structural element due to a loading event. The main disadvantages of displacement sensors are the limited scale and the requirement of a point of fixed reference.

IV.3.3 Ambient vibration data

For small structures, vibrations can be measured under a known impact with a hammer, where the force of the latter can also be measured. For bridge structures, this becomes more difficult. Here, vibrations are measured either under ambient conditions, or a dynamic test is performed, for example by driving a truck over the bridge. Dynamic data is often used for model updating. Common modal-based

damage detection features are reviewed in (Moughty and Casas, 2017). These include natural frequencies, modal damping, displacement mode shapes, modal curvatures, modal strain energy and modal flexibility. Frequency shifts might be attributed to damage in the structure. The principle of damage detection based on modal damping is that cracking in a cross-section will increase internal friction and hence raises the value of the section's damping. Displacement mode shapes have the advantage of being less influenced by the environment. Modal curvatures are the second derivative of the displacement mode shapes or can be derived based on the strain mode shapes. Modal strain energy is the energy stored in a structure when it deforms in its mode shape pattern, and the modal flexibility method defines the flexibility matrix as the inverse of the stiffness matrix (Catbas et al., 2008; Jaishi and Ren, 2006; Pandey and Biswas, 1994). In this work, the focus will be on natural frequencies, displacement mode shape and strain mode shapes.

The natural frequencies of a structure depend on its stiffness. The higher the stiffness, the larger the natural frequencies. However, since these natural frequencies depend on the global stiffness of the structure, it is impossible to localize damage based on natural frequency data. Localization of damage can be performed by combining the information from the natural frequencies with the corresponding displacement mode shapes. Local damage can change the displacement mode shape, as for example illustrated in Figure IV-3. Hence, by comparing the modelled with the experimental displacement mode shapes, the locations of regions with higher or lower stiffness can be identified. To estimate the absolute values of the stiffness based on modal data, the natural frequencies are also required. A same spatial distribution of the stiffness, but with other absolute values will induce the same displacement mode shapes, but the natural frequencies will differ.
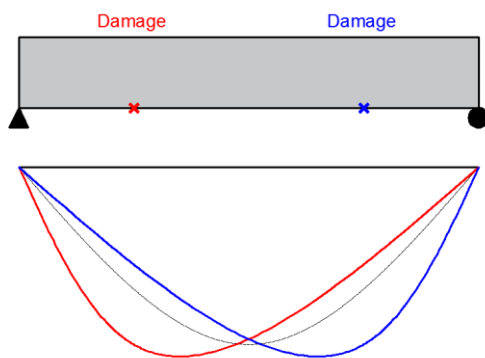

Figure IV-3: Influence of damage in a beam on the displacement mode shape of the first bending mode. Not that the damaged zone should be sufficiently large to influence the mode shape.

By making use of fibre-optic Bragg gratings, dynamic strains can be measured directly in a quasi-distributed way along the length of the fibre (Anastasopoulos, 2020). These measured dynamic strains can then be used to identify the strain mode shapes for the monitored structure by making use of advanced system identification techniques. As such, cracks can be identified and localized by identifying changes in the strain mode shapes and in the position of the neutral axis. Strain mode shapes (and the corresponding modal curvatures) will be more sensitive to local damage compared to displacement mode shapes.

When dynamic tests are performed, the obtained natural frequency will correspond to a certain stiffness. In this work, the stiffness of a reinforced concrete structure will be related to the corrosion degree of the reinforcement. Measurement errors and numerical errors in the processing of the data to obtain the experimental natural frequencies lead to uncertainties regarding the latter, which can be characterized by a probability distribution function. As illustrated in Figure IV-4, this will also lead to an uncertainty on the corrosion degree α.
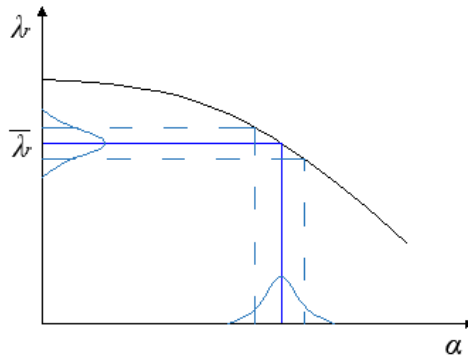
Figure IV-4: Uncertainty on the corrosion degree (α) based on the uncertainty on the experimental natural frequency ($\bar{\lambda}_r$)

In (Transportation Research Board, 2019b) accelerometers are mentioned to be used for the determination of the resonant frequency of a structure for comparison with a baseline analysis. The advantages are that accelerometers are relatively easy to install and can be reused (low costs per use). The disadvantages are the substantial amount of data that is produced which is difficult and/or expensive to process. Moreover, the resulting natural frequencies (after data processing) are global in nature and cannot pinpoint the location of concern on the structure that generated a response. For this purpose, also the displacement mode shapes should be extracted from the data. Transportation Research Board (2019b) also states that the obtained global structural modal response can be combined with subsequent responses in order to identify whether structural damage has occurred. Regarding

fibre-optic sensors, Transportation Research Board (2019b) mention as advantages the accuracy of 1 micron or less (i.e. very low strain values can be measured compared with traditional strain gauges), the low cost to install in long, linear cables with serial sensors (compared to many multiple strain gauges), and the effectiveness when used as long gauge length strain sensors on surfaces subject to strain variations, such as older concrete surfaces. The disadvantages are the fact that the sensors and data acquisition can be more expensive than standard strain measurements, and the fragility of the sensors. A critical note should be made on the accuracy, since this also depends on the equipment, environmental conditions, post-processing, etc.

IV.3.4 Combinations of data

As pointed out in the previous sections, each of the mentioned test methods and corresponding data types has its advantages and limitations. Hence, in this work the combinations of the different types of data will be investigated. Natural frequencies and displacement mode shapes will be combined, based on the arguments provided in section IV.3.3. Moreover, gathering modal data can be less expensive than measuring static strains all over the structure. Modal data will give an idea of the stiffness distribution of the structure, but the identified stiffness distribution is accompanied with relatively large uncertainties. Static strains on the other hand provide local information on the stiffness, but no information on the general stiffness distribution. Hence, it might be difficult to determine beforehand where these static strains need to be measured. A possible solution that will be investigated in this work is the combination of both types of data. The critical elements of the structure will be localized based on the modal data. If the identified stiffness is very low, diagnostic load tests can be performed after the dynamic tests, where strains will be measured at the critical locations.

In addition, visual data can be used to supplement the static and/or dynamic data. It will give an indication on the origin of the stiffness reduction. Moreover, it can limit the possible ranges of some of the uncertain parameters in the updating procedure. For example, if rust stains or corrosion cracks are observed, the time of this observation provides an upper boundary for the distribution of the initiation period. Furthermore, models to predict the crack width or time to cracking can be updated based on the observed crack locations or crack widths.

IV.4 Conclusions

In this chapter, formulations are provided for Bayesian inference, i.e. updating a prior distribution to a posterior distribution based on obtained measurement data. It is explained how sampling procedures can be used to generate the posterior distribution. Furthermore, different data types that are considered in this work are introduced. These consist of visual observations, strains or displacements

measured under a diagnostic load test, and modal data (natural frequencies, displacement mode shapes and strain mode shapes) obtained from dynamic tests. All indications on which variables should be updated with the application of Bayesian inference are only suggestions. In the following chapters, when Bayesian inference is applied, the assumptions on which variables are inferred (and which prior distributions are assigned to them) will be discussed before introducing the calculations and results.

IV.5 References

Anastasopoulos, D., 2020. Structural Health Monitoring based on operational modal analysis from long gauge dynamic strain measurements. PhD thesis, KU Leuven.

Beck, J.L., 2010. Bayesian system identification based on probability logic. Struct. Control Heal. Monit. 17, 825–847.

Beck, J.L., Siu-Kui, A., Vanik, M.W., 2001. Monitoring structural health using a probabilistic measure. Comput. Civ. Infrastruct. Eng. 16, 1–11.

Catbas, F.N., Gul, M., Burkett, J.L., 2008. Damage assessment using flexibility and flexibility-based curvature for structural health monitoring. Smart Mater. Struct. 17.

Gelman, A., Carlin, J.B., Stern, H.S., Rubin, D.B., 2014. Bayesian Data Analysis, 3rd ed, Texts in Statistical Science. CHAPMAN & HALL/CRC, Boca Raton.

Geyskens, P., Der Kiureghian, A., Monteiro, P., 1998. Bayesian Prediction of Elastic Modulus of Concrete. J. Struct. Eng. 124, 89–95.

Huang, Y., Shao, C., Wu, B., Beck, J.L., Li, H., 2019. State-of-the-art review on Bayesian inference in structural system identification and damage assessment. Adv. Struct. Eng. 22, 1329–1351.

Jaishi, B., Ren, W.X., 2006. Damage detection by finite element model updating using modal flexibility residual. J. Sound Vib. 290, 369–387.

Malings, C., Pozzi, M., 2018. Value-of-information in spatio-temporal systems: Sensor placement and scheduling. Reliab. Eng. Syst. Saf. 172, 45–57.

Moughty, J.J., Casas, J.R., 2017. A state of the art review of modal-based damage detection in bridges: Development, challenges, and solutions. Appl. Sci. 7.

Pandey, A.K., Biswas, M., 1994. Damage detection in structures using changes in flexibility. J. Sound Vib. 169, 3–17.

Simoen, E., De Roeck, G., Lombaert, G., 2015. Dealing with uncertainty in model updating for damage assessment: A review. Mech. Syst. Signal Process. 56, 123–149.

Simoen, E., Papadimitriou, C., Lombaert, G., 2013. On prediction error correlation in Bayesian model updating. J. Sound Vib. 332, 4136–4152.

Transportation Research Board, 2019a. Primer on Bridge Load Testing. Transportation Research Board, Washington DC.

Transportation Research Board, 2019b. Transportation Research Circular Number

E-C246 - Structural Monitoring. Transportation Research Board, Washington DC.

Vanik, M.W., Beck, J.L., Au, S.K., 2002. Bayesian Probabilistic Approach to Structural Health Monitoring. J. Eng. Mech. 126, 738–745.

Vanmarcke, E., 2010. Random Fields Analysis and Synthesis. World Scientific.

Vlaams Ministerie van Mobiliteit en Openbare Werken, 2012. Cursus bruginspecteur 2012 (In Dutch).

Yuen, K.V., Beck, J.L., Katafygiotis, L.S., 2006. Efficient model updating and health monitoring methodology using incomplete modal data without mode matching. Struct. Control Heal. Monit. 13, 91–107.

CHAPTER V

Pre-posterior and Value of Information analysis

"All models are wrong, but some are useful."
- Common aphorism in statistics

V.1 Bridge management – current practice

In current bridge management, routine or regular inspections are carried out periodically at intervals defined by the design service life. These routine inspections are performed to identify whether any changes in the structural conditions have occurred, and to detect indications of deterioration and the time of their first appearance. To meet these objectives, the inspections are carried out with appropriate tools and techniques (*fib*, 2013). These tools and techniques, and the frequency of the inspections, should be determined based on factors such as the likely mechanism of deterioration, environmental conditions, importance of the structure, etc.

In Flanders, routine inspections are visual inspections. They are performed very regularly and the only required material is a photo camera. Routine inspections enable to detect endangered safety for the bridge users, abnormal evolutions in the behaviour of the bridge, or certain defects. When severe defects are present, a so-called O-inspection should be performed. These O-inspections or occasional inspections happen in between the three years and six years cycles of the A and C-inspections (cfr. infra). General inspections or A-inspections are performed systematically every three years and consist of level measurements. C-inspections are control inspections, performed every six years, alternating with the A-inspections. They are similar to the A-inspections, but the inspection happens faster and with less means. C-inspections are applied to structures where little problems are expected. The B-inspection or special inspection requires extra means and special qualified staff. It is performed if further investigation is required for a specific element of a bridge (and not the entire structure, in contrast to the A and C-inspections, which are inspections for the total structure).

In (*fib*, 2013) a chapter is devoted to the conservation of structures. In this chapter, information is provided on inspections and maintenance of new and existing structures. It is stated that proactive conservation requires more than just periodic visual inspections, since changes may happen to the internal conditions of the structure, without exposure to the outer zone of the concrete and hence without visible indicators. These changes cannot be recognised based on visual inspections. Information on the progress of internal degradation is generally gathered from appropriate non-destructive tests or samples from the concrete.

There are various circumstances when a detailed investigation might be required (*fib*, 2013):
- Signs of significant deterioration or changes in performance level are observed during a routine inspection;
- A routine inspection is unable to provide the required information;
- It is suspected that the structural integrity has adversely been affected by deterioration.

According to (*fib*, 2011), a reactive strategy follows visual observations, where more in depth investigations are performed when deterioration has been observed. The results of these investigations determine the required repair. The type of repair and the optimal point in time are mainly based on the results of visual inspections only. There are some major disadvantages of this reactive strategy:
- When deterioration is visible, the degree of deterioration can already be well-advanced and expensive repair work will be required;
- The possibility to perform pro-active maintenance (which is economically more beneficial in the long term) will already have passed;
- Visual signs of deterioration reduce the attractiveness of the structure and the trust of the users.

Non-Destructive Testing (NDT) and structural monitoring can provide better knowledge on the deterioration mechanism and degradation state, and provide a basis for a proactive repair strategy. This will allow early quantification of deterioration before visual damage occurs. As such, proactive interventions can be performed, delaying further deterioration. The advantages of a proactive strategy are the possible elimination of future corrective interventions and the proactive intervention will be cheaper than the otherwise required extensive repairs. Moreover, the visual appearance of the structure will be better, providing more trust to the users. By performing the proactive repair, also the residual value of the asset is improved.

Since the costs for monitoring can become very high, it might be beneficial to determine beforehand whether a monitoring campaign is actually worth the investment. Moreover, the optimal time and/or locations of the measurements should be determined, and the number of sensors should be quantified. For example, according to (Transportation Research Board, 2019b), placing too much sensors should be avoided for the sake of collecting data, and good engineering judgment should be used when determining the number of sensors. These aspects (whether, when and where to measure) can be answered by application of the pre-posterior analysis and the Value of Information (VoI). These concepts will be explained more thoroughly in the following sections.

V.2   Pre-posterior analysis

In engineering, decisions are often made under uncertainty. This uncertainty is present due to incomplete or uncertain information on the parameters in the decision. To cope with this uncertainty, Bayesian statistical decision theory can be applied. The question to be answered is the following: 'Is it worth to collect more information before making a decision?'.

The decision process consists of choosing an action out of a set of possible actions a_j. Moreover, a number of uncertain conditions or events θ_i can occur. The

combination of such a condition and an action results in a utility u, often expressed in monetary terms. This can be visualized by a decision tree as illustrated in Figure V-1.
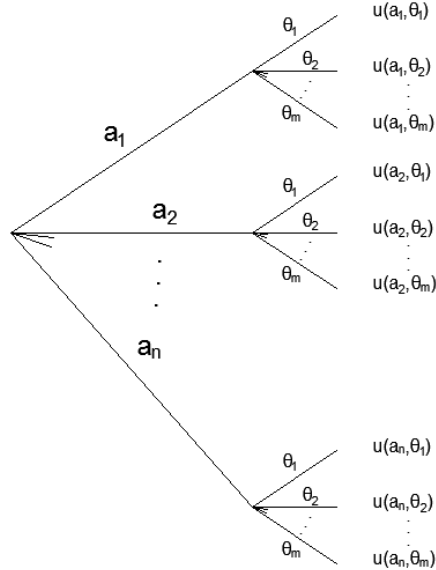

Figure V-1: Example of a decision tree

A priori, a probability is assigned to the different conditions θ_i. By multiplying the utility of θ_i and a_j ($u(a_j, \theta_i)$) with the prior probability of θ_i ($P'(\theta_i)$) and taking the sum over the different conditions, the utility corresponding to the action a_j can be determined ($u(a_j) = \sum P'(\theta_i)u(a_j, \theta_i)$). The optimal action will then be the one resulting in the highest utility. If now additional information becomes available, the prior probabilities assigned to the different conditions can be updated. Using these updated probabilities ($P''(\theta_i)$), a new (posterior) utility for each of the action alternatives is found. Based on these utilities, the posterior optimal action can be chosen, taking into account the available additional information. The question of whether or not to gather this additional information has to be answered before actually collecting it. However, when making this decision, the outcome of additional tests is not known yet. Different possible test outcomes are considered, and for each of these test outcomes, the posterior utility is calculated and multiplied with the prior probability of actually measuring that test outcome. By summing up these results, an estimate of the total utility is found, taking into account the measurements. As such, the question 'Is it worth to collect more

information before making a decision?' can be answered. This latter analysis is called the pre-posterior analysis.

The framework of pre-posterior decision analysis (Raiffa and Schlaifer, 1961) has enormous potential as a decision support tool in structural engineering, and is commonly applied in inspection and maintenance planning (e.g. (Faber et al., 1993; Sorensen et al., 1993)). Utilities are often expressed as costs, where the optimal decision will be the one resulting in the lowest costs. The costs considered in the analysis are life-cycle costs and should cover the whole (remaining) life-cycle of the structure. The objective of the pre-posterior analysis is to minimize these long-term expected costs, which should be discounted to the present value (Memarzadeh and Pozzi, 2016a, 2016b). Another important benefit of the pre-posterior analysis is the possibility to compare different maintenance strategies and select the (sub)optimal one. The application of such a methodology for the integrated life-cycle cost decision-making related to monitoring of concrete structures with time-dependent degradation phenomena has at present not yet been investigated in detail. More specifically, the basic methodology of the pre-posterior analysis must be extended to incorporate time-dependent and spatially distributed degradation processes inherent to existing concrete structures. These aspects will be investigated further in this work.

V.3 Decision-making based on VoI

V.3.1 Risk-based inspection planning

The conditions or events in the pre-posterior analysis (earlier denoted with θ_i) often consider failure or survival of the structure. Hence, calculations of life-cycle costs in the pre-posterior analysis require calculations of failure probabilities, and decisions for structures or structural systems are often tackled with a risk-based approach. Risk-based inspection planning concerns the optimisation of inspection strategies, which define when and where to inspect, and which inspection technique to be used. All these different inspection strategies might provide different information and involve different costs. The cost of an inspection strategy $\mathcal{S}$, with outcome $\boldsymbol{y}$, is given by equation (V-1), where C_T is the total cost, C_I the inspection cost, C_R the repair cost and C_F the failure cost or the lifetime risk (Luque and Straub, 2019).

$$C_T(\mathcal{S}, \boldsymbol{y}) = C_I(\mathcal{S}, \boldsymbol{y}) + C_R(\mathcal{S}, \boldsymbol{y}) + C_F(\mathcal{S}, \boldsymbol{y}) \qquad (V\text{-}1)$$

As pointed out in the previous section, the inspection outcomes are not known beforehand, and the estimated total cost will be the average over the possible inspection outcomes according to equation (V-2) (Luque and Straub, 2019).

$$E[C_T(\mathcal{S}, \mathbf{Y})] = \int_Y C_T(\mathcal{S}, \mathbf{y}) f_Y(\mathbf{y}) d\mathbf{y} \qquad \text{(V-2)}$$

Finally, the optimal inspection strategy is the one that minimizes this expected lifetime cost, mathematically described by equation (V-3) (Luque and Straub, 2019).

$$\mathcal{S}^* = argmin[E[C_T(\mathcal{S}, \mathbf{Y})]] \qquad \text{(V-3)}$$

The number of possible inspection strategies might become very extensive. To overcome this issue, heuristics can be used to limit the set of possible strategies (Bismut et al., 2017). Examples hereof are probability thresholds and fixed inspection intervals. When investigating a structure at the system level, not only the timing, but also the location of the inspections is of importance. Therefore, heuristics at the component level can be extended to the system level. The components to be inspected can be taken along in the optimization as one of the decision variables. Furthermore, a limit on the system reliability can be used as a probability threshold instead of or next to a limit on the element reliability. In a similar way, the criteria to perform repairs can also be fixed. In most works, the latter is based on damage size (Luque and Straub, 2019). The flow chart of this heuristic implementation is illustrated in Figure V-2.

When considering low-probability-high-consequence events in the optimization as given by equation (V-3), these could be accounted for by increasing the corresponding failure costs of the high-consequence events. Their occurrence could also be avoided by setting reliability thresholds, keeping the failure probability below a maximum tolerable level.

V.3.2   Value of Information

The Value of Information (VoI) is a metric to guide the decision on the implementation of an inspection strategy and the choice hereof. The optimal inspection strategy can be considered as the one that maximizes the VoI. The VoI represents the expected benefit from the implementation of an inspection strategy. It is calculated as the difference in the expected total life-cycle cost with and without the implementation of the inspection strategy, or hence the difference between posterior and prior expected costs. The VoI is quantified before any real observation is made, hence not the actual posterior cost, but a pre-posterior estimate of these costs is involved. This means that all possible inspection outcomes are considered (computed by sampling), and the posterior costs for these samples are calculated and weighted with their (prior) probability of occurrence. As such, an expected value of the pre-posterior cost is obtained. The VoI is calculated by equation (V-4) (Straub, 2014).

$$VoI = E[C_{prior}] - \left[\int_Y f_Y(\boldsymbol{y}) \min_a [C_T(\mathcal{S}, \boldsymbol{y}, a)] d\boldsymbol{y} \right] \qquad \text{(V-4)}$$

Here, $f_Y(\boldsymbol{y})$ is the joint PDF of the inspection outcomes $\boldsymbol{Y}$, $C_T(\mathcal{S}, \boldsymbol{y}, a)$ is the expected total life-cycle cost corresponding to action a, inspection strategy $\mathcal{S}$ and outcomes $\boldsymbol{y}$. This is calculated according to equation (V-2) for one specific decision on action/repair (i.e. the threshold for performing an action/repair and the corresponding type of action/repair). $E[C_{prior}]$ is the prior expected lifetime cost without inspections (or when considering a baseline inspection scenario) and is given by equation (V-5). It is calculated as the minimum of the costs over the different possible decisions or actions a.

$$E[C_{prior}] = \min_a C_T(a) \qquad \text{(V-5)}$$

Set heuristics:
- Fixed inspection intervals Δt_I
- Reliability thresholds p_{th}
- Initial number of inspection locations n_I
- Repair criterion d_R

Define system-wide inspection strategies $\mathcal{S}$,
accounting for the heuristics

Solve equation (V-3):

For every $\mathcal{S}$:

Sample inspection outcomes $\boldsymbol{y}_K$

Calculate $C_T(\mathcal{S}, \boldsymbol{y}_k)$ (equation (V-1))

Calculate $E[C_T(\mathcal{S}, \boldsymbol{y}_k)]$ (equation (V-2))

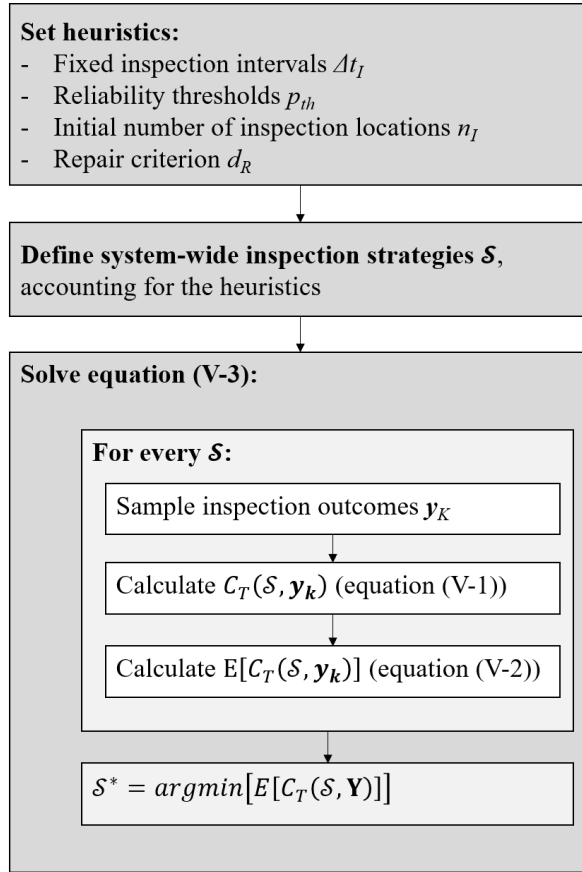$\mathcal{S}^* = argmin[E[C_T(\mathcal{S}, \mathbf{Y})]]$

Figure V-2: General flow in risk-based inspection planning

It is noteworthy to mention that an exact assignment of costs and utilities is often not necessary in the determination of the VoI. For decision-making, approximate estimates are sufficient for calculating and ranking the VoI of different monitoring/inspection strategies. The VoI can be quantified for different inspection and monitoring strategies, i.e. different inspection/monitoring methods with different accuracy, sensitivity and cost, but also different locations to perform inspections or place sensors, and different points in time at which inspections or measurements are performed.

The optimal inspection or monitoring strategy will be the one that maximizes the VoI, taking into account the costs of the inspections as well. More information regarding this optimisation of information can be found in (Diamantidis et al., 2018; Diamantidis and Sykora, 2018; Malings and Pozzi, 2017; Thöns and Stewart, 2019; Zhang et al., 2019). The optimisation is performed within the relevant constraints, such as limitations in time and on budget. Optimization of the inspection strategies by the VoI metric is also illustrated by equation (V-3): minimizing the expected pre-posterior life-cycle cost corresponds to maximizing the VoI, as also pointed out in (Diamantidis and Sykora, 2018; Thöns and Stewart, 2019; Zhang et al., 2019). In (Luque and Straub, 2019), the computational challenge of considering all possible inspection strategies, especially at system level, is addressed. Three possible solutions are provided. One of these solutions is the use of heuristics to limit the set of possible strategies to a small number of parametrized stationary strategies. This optimization method will be used in this work. It will be assumed that decisions will be made based on reliability or damage thresholds. Moreover, the inspection times and locations will be chosen based on practical constraints imposed by the operator or other heuristics like reliability thresholds, the predicted level of damage, constant inspection intervals, etc. Inspection locations can also be determined based on sensor placement strategies as for example illustrated in (Papadimitriou and Lombaert, 2012).

It should be pointed out that the VoI could be defined in two ways. In the above, the prior cost is assumed to not take into account any inspections. This is the case when the VoI is used as a metric in a decision to be made at the design stage, i.e. whether or not it would be useful to implement a more extensive inspection or monitoring strategy, next to the regular visual inspections. In this case, the cost of this extensive inspection or monitoring campaign could be compared with the cost without any inspection. Alternatively, the VoI could also be used as a metric for the optimisation of different inspection strategies. Here the prior cost could correspond to a baseline scenario of the least required inspections the operator would implement. Which of these two definitions of the VoI should be applied depends on the practical application.

The concept of the value of information is also visualized in Figure V-3. Here, the grey curves correspond to the prior situation. The prior reliability index β (where a higher reliability index represents a lower probability of failure) decreases in

time, until a certain threshold level (β_{th}) is reached. The resultant action is to perform a repair and restore the reliability index to its initial level. The corresponding expected costs gradually increase in time due to the increase in probability of failure over time. At the moment of repair, a repair cost is added. At t_{insp}, a measurement will be performed. This can give different outcomes, resulting in different reliability levels after the inspection. Two examples are visualized in Figure V-3. *'Posterior 1'*, the blue curve, corresponds to an inspection/measurement with a beneficial outcome, leading to a larger reliability index than a priori expected. The decrease in reliability is also slower, for example because the inspection revealed a slow corrosion process. Due to these beneficial effects, repair can be performed later in time, which is cheaper when also discounting effects are considered. *'Posterior 2'*, the red curve, corresponds to a negative inspection outcome, inducing a decreased reliability index compared to the a priori expected one. This can for example be the case when the corrosion degree is much larger than a priori estimated. Based on this inspection outcome, it can be decided to immediately perform the repair and for example apply a repair mortar and corrosion protection to reduce the future corrosion rate. When again considering the costs, it can be seen that the inspection cost is added at t_{insp} and that the gradual increase in cost depends on the rate of decrease in reliability. When evaluating the VoI, the prior cost is the cost at the end of the service life of the grey curve (C_{prior}). For different possible inspection outcomes, different posterior costs are found (i.e. again the costs at the end of the anticipated service life). These are indicated in Figure V-3 as $C_{SL,1}$ and $C_{SL,2}$. These costs should be weighed with the probabilities of the corresponding inspection outcomes, i.e. P_1 and P_2 respectively. Depending on the type of measurement, more than two possible inspection outcomes can or should be considered, denoted with the subscript i. The expected value of the posterior cost is then calculated as the weighted sum of the posterior costs corresponding to the different inspection outcomes, or as $\sum P_i C_{SL,i}$.

When looking at Figure V-3, it can be seen that repair actions have a twofold influence on the life-cycle cost. First, there is the cost of performing the repair itself. Second, repair leads to a reduced failure probability, and, depending on the type of repair, it can also lead to a slower increase of the probability of failure over time. As such, it also influences the contribution of the failure costs in the life-cycle cost assessment.

V.4 Conclusions

In this chapter, a brief introduction is provided to the pre-posterior analysis and the VoI framework. It is illustrated how this can be used as a decision-making tool when deciding whether or not to implement a monitoring strategy. The VoI can also be used to compare different alternative monitoring strategies and choose the most optimal one as the one with the largest VoI. In the following chapters, the pre-posterior framework and VoI analysis will be further extended in order to take into account the time-dependent and spatial character of degradation.
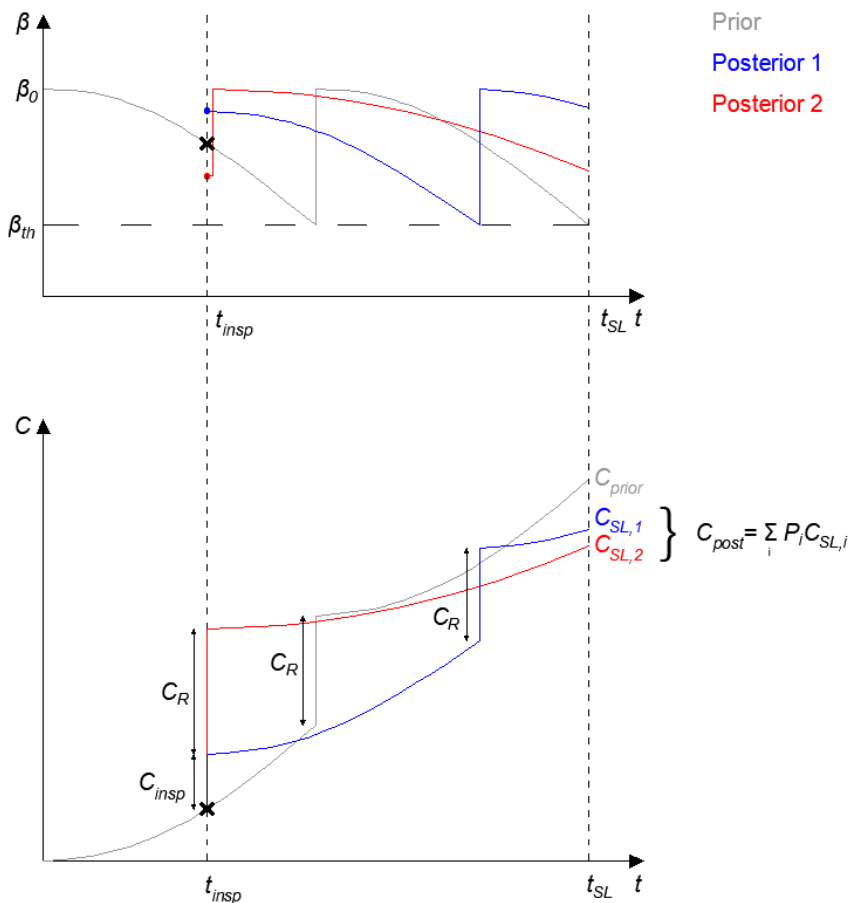
Figure V-3: Concept of VoI

V.5 References

Bismut, E., Luque, J., Straub, D., 2017. Optimal prioritization of inspections in structural systems considering component interactions and interdependence, in: 12th Int. Conf. on Structural Safety and Reliability. pp. 2260–2269.

Diamantidis, D., Sykora, M., 2018. Optimizing Monitoring – Implementation of Draft Guideline and Case Study of Roof Exposed to Snow Loads, in: IABSE Symposium Nantes, 2018 Tomorrow's Megastructures.

Diamantidis, D., Sykora, M., Lenzi, D., 2018. Optimising Monitoring: Standards, Reliability Basis and Application to Assessment of Roof Snow Load Risks. Struct. Eng. Int. 28, 269–279.

Faber, M.H., Sørensen, J.D., Kroon, I.B., 1993. Optimal Fatigue Testing: A reassessment tool, in: Proc. of IABSE Colloquium on Remaining Structural

Capacity: IABSE Report Vol. 67 Grupo Espanol de IABSE. pp. 61–68.

fib, 2013. Model Code for Concrete Structures 2010.

fib, 2011. *fib* bulletin 59 - Condition control and assesment of reinforced concrete structures.

Luque, J., Straub, D., 2019. Risk-based optimal inspection strategies for structural systems using dynamic Bayesian networks. Struct. Saf. 76, 68–80.

Malings, C., Pozzi, M., 2017. Optimal Sensor Placement and Scheduling with Value of Information for Spatio-Temporal Infrastructure System Management. ICOSSAR - 12th Int. Conf. Struct. Saf. Reliab. 3320–3330.

Memarzadeh, M., Pozzi, M., 2016a. Value of information in sequential decision making: Component inspection, permanent monitoring and system-level scheduling. Reliab. Eng. Syst. Saf. 154, 137–151.

Memarzadeh, M., Pozzi, M., 2016b. Integrated Inspection Scheduling and Maintenance Planning for Infrastructure Systems. Comput. Civ. Infrastruct. Eng. 31, 403–415.

Papadimitriou, C., Lombaert, G., 2012. The effect of prediction error correlation on optimal sensor placement in structural dynamics. Mech. Syst. Signal Process. 28, 105–127.

Raiffa, H., Schlaifer, R., 1961. Applied statistical decision theory.

Sorensen, J.D., Faber, M.H., Kroon, I.B., 1993. Reliability-Based Optimal Design of Experiment Plans for Offshore Structures, in: Reliability and Optimization of Structural Systems: Proc. of the 5th IFIP WG7.5 Working Conference on Reliability and Optimization of Structural Systems. Pergamon Press, North-Holland, pp. 253-260 (IFIP Transactions; No. B-12).

Straub, D., 2014. Value of information analysis with structural reliability methods. Struct. Saf. 49, 75–85.

Thöns, S., Stewart, M.G., 2019. On decision optimality of terrorism risk mitigation measures for iconic bridges. Reliab. Eng. Syst. Saf. 188, 574–583.

Transportation Research Board, 2019. Transportation Research Circular Number E-C246 - Structural Monitoring. Transportation Research Board, Washington DC.

Zhang, W.H., Lu, D.G., Qin, J., Faber, M.H., 2019. Life cycle management of structural systems based on the optimal SHM strategy by VoI analysis. 13th Int. Conf. Appl. Stat. Probab. Civ. Eng. ICASP 2019.

Bayesian inference of corrosion parameters

CHAPTER VI

Bayesian inference of degradation parameters in the service life model of reinforced concrete bridges

"Under Bayes' theorem, no theory is perfect. Rather, it is a work in progress, always subject to further refinement and testing."
- Nate Silver

VI.1 Introduction

Monitoring and inspection of structures are important for estimating their remaining lifetime and to support decisions on maintenance and repair. Current practice in bridge management consists of performing a limited number of tests and inspections, but the information is often not used to assess or update the deterioration state of the bridge in a quantitative way. Visual data are usually supplemented by data from proof loading where, for example, strains and deflections are measured, or modal data is extracted from ambient vibration tests, including for example acceleration measurements and strain measurements. In general, these inspections and measurements are only used to identify parts of the bridge suffering from degradation or showing unexpected deformations. This is partly due to a lack of knowledge on how to use such measurement data to update the estimation of the remaining lifetime of the structure. In (Heitner et al., 2019), a methodology is presented to update the estimated level of corrosion damage using data such as strains, deflections and rotations measured in operational conditions, supplemented by bridge weight-in-motion (B-WIM) data to estimate the corresponding service loads to which the bridge is exposed. Subsequently, the distribution characterizing the uncertainty in the loss of reinforcement area is updated. Sousa et al. (2020) also illustrate that strain measurements are a good indicator for corrosion damage resulting in a reduction in stiffness.

In addition to these inspections commonly used in practice, much focus in research has gone to vibration-based structural health monitoring (SHM), e.g. techniques based on modal analyses (Carden and Fanning, 2004; Cross et al., 2010). Up to now, these measurements are often used for data-based SHM methods (Soman et al., 2018), considering only the measured values, without translating them into adaptations in the prediction model. This means that an intervention is done when the measurements show unexpected deviations from previously identified trends (Rodrigues et al., 2010). However, when the prediction of the remaining lifetime of a structure is required, model-based SHM methods might be more appropriate (Simoen et al., 2015). In these methods, updating is most often performed on linear elastic models, where an (equivalent) stiffness is adapted in order to localize damage (Beck et al., 2001; Dilena et al., 2011; Simoen et al., 2015). Hence, these models cannot be used to quantify the remaining service life of the structure, which requires models where damage is accounted for in a more realistic way.

Whereas Bayesian theory has often been used to update bridge resistance and/or reliability based on observed and/or historical data, attempts to update the variables in the time-dependent corrosion models based on indirect and non-destructive data like strains and modal data are scarce. For example, Marsh and Frangopol (2008) use corrosion rate sensor data to improve the accuracy of reliability estimates accounting for spatial and temporal variability of the corrosion

rate. Hence, they assume that the variable of interest, i.e. the corrosion rate, is directly measured. Also Enright and Frangopol (1999) use corrosion rate inspection data to predict the deterioration of concrete bridges, referring to (Geyskens et al., 1998; Zheng and Ellingwood, 1998) where Bayesian methods are used to improve strength and structural reliability predictions. Also Ma et al. (2013) directly measure the variables of interest: they use field inspection results of concrete strength and concrete cover to update their respective distributions. The distribution of the corrosion loss is also updated, but based on destructive measurements of this corrosion loss, which is often not possible in practice. Also Faroz et al. (2016) performed Bayesian updating of the steel loss assuming that there exists a non-destructive tool that is capable of measuring steel loss in concrete. A completely different approach is found in (Strauss et al., 2008), where a prediction function is first fitted to SHM data and later updated based on monitored data. Finally, Heitner et al. (2016) update a general remaining reinforcement section based on deflection-based damage indicators. In contrast to (Heitner et al., 2016), in this work, no damage indicators will be used, but the corrosion variables will be updated based on indirect non-destructive data, including static strains and modal data extracted from vibration measurements.

The real corrosion state and/or progress of both existing and new structures might differ from the predictions made by different corrosion models. To arrive at a more accurate prediction of the remaining lifetime, a better knowledge of the real state of deterioration is required. Such information can be extracted from relevant measurement data. Measurements and inspections might (1) give an indication on whether corrosion has initiated or not, (2) enable updating of the deterioration state of the structure based on the (indirectly) measured stiffness, or (3) support the localization of damage. As such, the distributions assigned to the model parameters describing the deterioration process can be updated, inducing a more accurate estimation of the remaining lifetime of the structure.

In this chapter, the parameters of the degradation model will be updated, taking into account the spatial character of degradation. Two (non-destructive) types of tests will be considered: proof loading and ambient vibration tests. It is investigated how the uncertainty on the deterioration state of reinforced concrete structures is reduced based on the resulting data from the individual types of tests. Furthermore, it is investigated to what extent more accurate predictions are achieved by combining both types of tests. A model-based method is used, identifying damage through the calibration of a finite element model of the structure (Friswell and Mottershead, 1995; Fritzen et al., 1998; Mottershead and Friswell, 1993; Simoen et al., 2015; Teughels and De Roeck, 2005). This model calibration is performed using Bayesian methods, implying that the prior uncertainty on the model parameters is reduced to a posterior uncertainty by taking

into account the information contained in the measurement data. Environmental effects on the modal characteristics and strain measurements are considered to have been filtered out and are hence disregarded in the following investigation.

VI.2 Considered example structures

Throughout this chapter, two example structures will be used to illustrate the concepts. The first one is an illustrative example of a simply supported beam and the second one considers a more realistic RC girder bridge.

VI.2.1 Illustrative example: simply supported beam

The simply supported beam that will be considered throughout this chapter is visualized in Figure VI-1. The beam has a length of 4 m and is 500 mm high and 300 mm wide. The reinforcement area has been designed for a permanent and variable line load, both of 25 kN/m. The bottom reinforcement consists of three bars of 20 mm diameter ($A_{s0} = 942.5$ mm²).
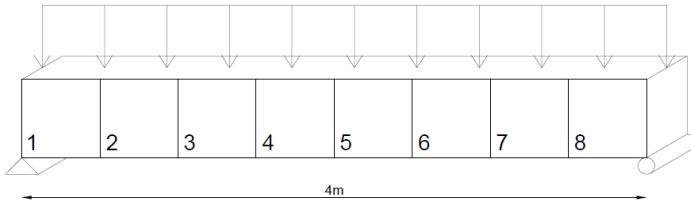

Figure VI-1: Simply supported beam for illustration of concepts

The reinforcement area of the beam A_s varies in time according to equations (II-8) and (II-9) since the beam is assumed to be subjected to chloride-induced corrosion. The prior distributions of the corrosion variables used in this example are given in Table VI-1. These are based on CEMI/42.5 with a water/cement ratio of 0.45 and a cyclic wet-dry exposure class. The distribution of the initiation period is based on the distributions of the variables appearing in equation (II-1).

Corrosion is not uniform along the structure, hence neither is A_s. To account for this spatial character of degradation, the initiation period and corrosion rate are modelled as random fields, with marginal distributions according to Table VI-1. The random fields are discretized into elements and are transformations of underlying Gaussian random fields, which are defined by a mean vector and a covariance matrix. A squared exponential correlation model is assumed, considering a correlation length of 1 m for both parameters. In general, the correlation length should be chosen proportional to the length scale of the expected

damage. For the case under consideration, and for the purpose of illustration, the correlation length is chosen relatively small. To adequately capture the random field, an element length of 0.5 m is chosen. Hence, as also visible on Figure VI-1, the beam is discretized in eight elements. Within these elements, degradation is assumed constant. However, the corrosion degree varies for the different elements. The random fields for the initiation period T_i and the corrosion rate V_{corr} are discretized in an (8 x 1) matrix. The mean vector of the underlying Gaussian random field is an (8 x 1) vector and the covariance matrix is an (8 x 8) matrix. To discretize the random fields, Karhunen-Loève decomposition of the underlying Gaussian random field is applied according to equation (III-4). For the initiation period and corrosion rate as given in Table VI-1, four modes are required in the decomposition of the random fields (equation (III-5)).

Table VI-1: Distributions of variables related to the corrosion model of the simply supported beam

Variable	Symbol [unit]	Mean	Standard deviation	Distribution	Reference
Pitting factor	α_p [-]	2	-	Deterministic	(Duracrete, 2000)
Mean corrosion rate while corrosion is active	$V_{corr,a}$ [mm/yr.]	0.03	0.04	Weibull	(Lay et al., 2003)
Time of wetness	ToW [-]	0.75	0.2	Normal	(Lay et al., 2003)
Initiation period	T_i [years]	22	10	Lognormal	-
Diffusion coefficient of concrete[*]	D [mm²/yr.]	20	10	Lognormal	(fib, 2006)
Surface chloride concentration[*]	C_s [wt.-%/c]	2	0.9	Lognormal	(fib, 2006)
Critical chloride concentration[*]	C_{cr} [wt.-%/c]	0.6	0.15	Lognormal	(fib, 2006)

[*]These distributions are used in the determination of the parameters of T_i using Taylor approximations

VI.2.2 Practical example: RC girder bridge

To illustrate the applicability of the concepts introduced in this chapter, they are also applied to a more realistic bridge structure. The bridge as discussed in (Enright and Frangopol, 1999) is considered. The investigated span has a length of 9.1 m and a width of 11.60 m. The deck is carried by five girders, each with a width of 400 mm and a height of 600 mm (Figure VI-2). The main longitudinal reinforcement of the girders consists of eight bars with diameter 35 mm, in two layers of each four bars (Figure VI-3).
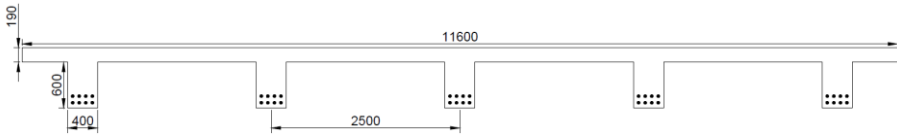

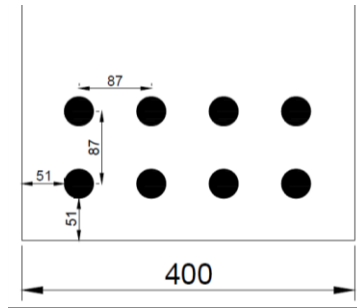Figure VI-2: Cross-section of the RC girder bridge (dimensions in mm)

Figure VI-3: Bottom reinforcement of the girders of the studied bridge (dimensions in mm)

In line with (Yang et al., 2019), this bridge is considered to be exposed to a medium level of corrosion. The reduction in steel section over time is evaluated according to equations (II-8) and (II-9). The probability distributions for the different corrosion variables in these models are based on the distributions provided by (Yang et al., 2019), and the spatial variation of the corrosion process is accounted for. Instead of a lognormal distribution for the corrosion rate V_{corr} with mean 0.0116 mm/year and a coefficient of variation of 0.2 (as adopted in (Yang et al., 2019)), a 2D lognormal random field is considered, with the same mean and standard deviation, which are a priori equal in all elements. The correlation model of the random field is a squared exponential correlation model with correlation length 2 m along the length of the bridge and correlation length

5.8 m along the width of the bridge. The bridge is therefore subdivided into 50 elements, 10 along its length and 5 along its width (i.e. exactly corresponding to the positions of the 5 girders). As such, the element length in the transverse direction equals 2.5 m and the element length in the longitudinal direction equals 0.91 m, which are both smaller than half the correlation length in the respective directions (DIANA FEA BV, 2017). Furthermore, the diffusion coefficient of the concrete D is modelled by a random field as well, with marginal lognormal distribution with mean value 129 mm²/year and a coefficient of variation of 0.10. The correlation structure is the same as for the corrosion rate, since both characteristics follow from the same physical process. Finally, the chloride concentration at the surface C_s is modelled as a scalar random variable with a lognormal distribution, assuming all elements are subjected to common exposure conditions. The distribution for C_s is a lognormal distribution with mean 0.1% and a coefficient of variation of 0.1 (Yang et al., 2019). The value of C_s is constant for the whole structure. By modelling the diffusion coefficient and the corrosion rate by random fields and taking them along in the updating procedure, correlation between the degradation in the different elements is considered. As such, the characteristics of each element will depend on the neighbouring elements as well. The joint distribution in this case concerns a distribution over all 50 elements in which the bridge is discretized. Based on the chloride concentration at the surface C_s, the diffusion coefficient D, the concrete cover c and the critical chloride concentration C_{cr} (lognormal, mean 0.04%, COV = 0.1), the initiation period can be calculated according to equation (II-1).

According to (Dey et al., 2019), assuming correlation between the different girders is reasonable since they are uniform in shape and material. Nevertheless, a reasonable assumption might also be that there is correlation within the girders, but that there is no correlation between the different girders. In such a case, a 1D random field is assigned to each of the girders. These random fields have the same correlation properties in longitudinal direction as the 2D random field mentioned above. It will be investigated how changing this assumption influences the posterior distribution of the corrosion degree along the bridge.

VI.3 Updating of corrosion variables

As already mentioned, in this chapter, a model-based method will be followed to update the corrosion model taking into account (heterogeneous) measurement data, including vibration data or static strain measurements. The corrosion models will be updated, taking into account the time-dependent and spatial character of degradation. Heterogeneous measurement data following from static load tests and ambient vibration tests will be combined to update prior distributions reflecting parametric uncertainties in the service life model. As such, this facilitates a more accurate estimate of the remaining service life. In the following, it is stepwise

explained how measurement data can be used to update the distributions of the variables in the corrosion model, and the methodology will also be illustrated by application to the simply supported beam and the RC girder bridge.

When posterior distributions are provided in the following, these are the posterior distributions of the corrosion degree at the point in time when the measurements are performed. Nevertheless, not only the distribution of the corrosion degree is inferred, but also the distributions of the variables in the models for the initiation and propagation phase (see Chapter II). By evaluating these models at the point in time at which the measurements are performed, and by accounting for the updated distributions of the corrosion variables, the posterior distribution of the corrosion degree at different points in time can be obtained. By updating the variables in the models of the initiation and propagation phase, there is also accounted for the fact that it is often unknown whether the reinforcement is already depassivated and whether the propagation phase has started or not.

VI.3.1 General framework

The general formulation for the posterior distribution is already given in section IV.2. Here, the likelihood function is provided and it is described how Bayesian updating is performed based on MCMC sampling, requiring multiple evaluations of a model. The model used in the likelihood function can be a finite element model. However, evaluating the finite element model can be computationally demanding, while many samples are required in the MCMC procedure. To avoid the evaluation of the finite element model at every iteration in the MCMC sampling, a response surface approach is used to predict the response of the finite element model for different values of the input parameters. The response surfaces are based on a least-square approximation (Bucher, 2009). Latin Hypercube Sampling (LHS) samples are generated for the input parameters, and for each set of samples, the corresponding finite element output is evaluated. A polynomial response surface is fit to the latter according to (Bucher, 2009). A smaller number of new LHS samples (verification samples) is generated for the verification of the response surface. The suitability of the response surface is verified by considering the coefficient of determination R^2. This statistical measure describes the correlation between the output predicted by the response surface y_{RS} for a set of input parameters x_k and the actual data following from the finite element model z_k, for m different evaluations of the model. This coefficient R^2 is given by equation (VI-1).

$$R^2 = 1 - \frac{\sum_{k=1}^{m}[z_k - y_{RS}(x_k)]^2}{\sum_{k=1}^{m}[z_k]^2} \qquad \text{(VI-1)}$$

When the number of data samples is low with respect to the number of parameters in the response surface, the R^2 value can tend to be too optimistic and there is a risk of overfitting of the response surface. To avoid this overfitting, it is generally accepted to adjust the coefficient of determination R^2 according to equation (VI-2) (Bucher, 2009).

$$R_{adj}^2 = R^2 - \frac{\nu - 1}{m - \nu}(1 - R^2) \qquad \text{(VI-2)}$$

Here, ν is the number of unknown parameters in the response surface.

An additional verification of the response surface is performed by changing one of the variables x_k in the model and the response surface from a low to a high value, while keeping the others constant. The outcomes are evaluated for the finite element model and for the response surface, and visualized on a graph. As such, it can be verified whether the behaviour of the response surface corresponds to the actual behaviour of the finite element model.

VI.3.2 Updating based on static data

When data is gathered under proof loading, the load is known accurately. Hence, the measured parameters can be compared with the predicted ones under the same load at the time of proof loading. Static data giving an indication of the stiffness of the structure are for example strains and deflections. Amongst others, this stiffness depends on the deterioration state, which can consequently be updated based on the static data. In practice, this data can also depend on effects of creep and shrinkage, temperature, etc. However, it is considered that these effects have already been be filtered out prior to the analysis. Only the random fields for the corrosion variables, and hence the corresponding corrosion degree, are updated.

The maximum likelihood function F_{ML} to be used in equation (IV-5) is given by equation (VI-3), which is based on equation (IV-6), assuming independent errors.

$$F_{ML} = \sum_{j=1}^{N} \frac{\left(\bar{d}_j - G(\boldsymbol{\theta}_M)\right)^2}{\sigma_d^2} \qquad \text{(VI-3)}$$

Here, N is the number of measurements available, σ_d the standard deviation of the measurement error, and $\bar{d}_j$ represents the measurement data. $\boldsymbol{\theta}_M$ are the input parameters to be updated, and $G(\boldsymbol{\theta}_M)$ are the model results obtained from a finite element model or a response surface fit to the finite element simulations. In the latter case, the model error due to the use of the response surface is also included in σ_d.

VI.3.2.1   Static strains

First, the illustrative example of the simply supported beam as described in section VI.2.1 will be considered, with a spatially variable corrosion degree. To evaluate the strains in the simply supported beam, the Finite Element (FE) software DIANA FEA (DIANA FEA BV, 2019) is used. The FE model is a 2D model, with a linear mesh with quadrilateral elements. The different elements in which the beam is discretized are modelled as different planar 'sheets' in DIANA FEA. Within one sheet, the Young's modulus of the concrete varies over the height, with lower values in the cracked regions, according to section II.2.3. The initial Young's modulus of the concrete is 33 GPa, according to a concrete type C30/37. In the uncracked region, the Poisson coefficient is 0.2. The tensile strength of the concrete is modelled by a Hordijk curve, with tensile strength f_{ct} equal to 2.9 MPa. The compressive strength f_c is initially (before the effect of degradation) equal to 38 MPa. The reinforcement is modelled as 'embedded' reinforcement (DIANA FEA BV, 2019) and is defined by the total reinforcement area in each element. The reinforcement is discretized, corresponding to the different elements in which the beam is discretized. To account for corrosion, the reinforcement area is reduced correspondingly, and varies in the different elements. A stiffness adaptation analysis is adopted since it is able to provide accurate predictions of strains and cracking behaviour (Schreppers et al., 2011). This approach is less suitable for ultimate limit state calculations, but this is not the objective of the case under consideration.

A polynomial response surface has been fit to the finite element model output. The input of the response surface are the standard normal variables appearing in the decomposition of the random fields for the initiation period and corrosion rate (see equation (III-4)). The output of the response surface is the static strain at the considered measurement location, i.e. for each measurement location a separate response surface has been generated. A polynomial response surface of degree 2 considering no interaction between the variables is found to be appropriate for the case under consideration, since this resulted in a sufficiently high value of the coefficient of determination R^2. Moreover, it has been checked that the error made by introducing the response surface is sufficiently small compared to the measurement error accounted for in the likelihood function. The prior corrosion degree in all elements has a mean of 0.12 and a standard deviation of 0.16, based on the prior distributions for the initiation period and the corrosion rate, evaluated at time $t = 35$ years (i.e. the time of performing the measurements) (see Figure VI-4). It is investigated how this distribution is updated based on the measurement results. To simulate the situation that the load is known when a bridge is subjected to proof loading, the beam is subjected to a known point load of 30 kN at 1.75 m from the left support. The measurement results are based on simulations of the underlying corrosion degree in the eight elements, which is represented by the

black dash-dotted line in Figure VI-5. They are generated by evaluating the FE model for these corrosion degrees and adding a random value of the measurement error to these results. In the first case considered, only the strain at element 4 is measured both at top and bottom fibre since this element has the highest corrosion degree. Different values for the measurement error are assumed to investigate the influence hereof. In (Heitner et al., 2019), a measurement error of 1.95 µε is used. Sousa et al. (2020) mention smaller errors based on strain measurements, with an order of magnitude of 0.2 to 0.5 µε. When other strain measuring techniques are applied, the measurement error can be even larger, e.g. 3 µε for electrical resistance strain gauges according to (Neild et al., 2005). Finally, also a measurement error of 10 µε is assumed. Literature on the measurement error to be used in these analyses is rather limited. That is why in this chapter and further chapters, different values will be considered. Nevertheless, in this research, also an effort is made to derive an appropriate value for this measurement error. For these analyses, reference is made to Chapter VII.

a) Prior distribution of the corrosion degree along the beam

b) Histogram of the prior corrosion degree at one location
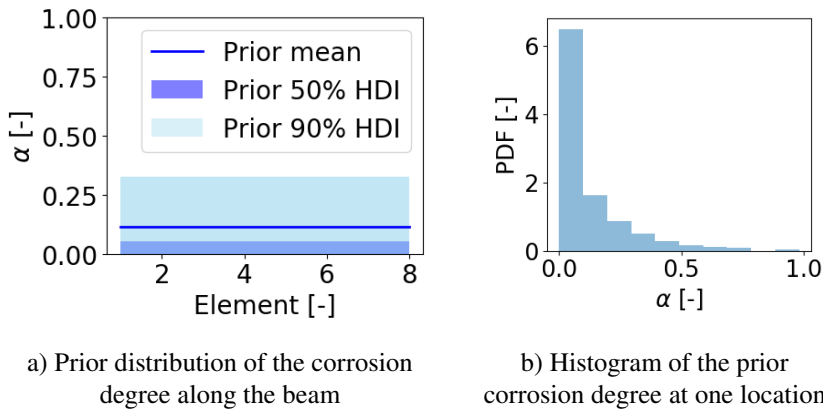
Figure VI-4: Prior distribution of the corrosion degree of the simply supported beam at $t = 35$ years

In the following, the posterior distribution of the corrosion degree is derived for the different assumptions on the measurement error. The posterior distribution of the corrosion degree is visualized in Figure VI-5 (a) for the measurement error of 0.5 µε and in Figure VI-5 (b) for the measurement error of 10 µε. The posterior uncertainty is given as the Highest Density Interval (HDI) calculated based on the samples of the corrosion degree obtained from the MCMC simulations. This HDI is the shortest interval on a posterior density for some given confidence level (Turkkan and Pham-Gia, 1993). At the inspected element, the posterior distribution of the corrosion degree has a decreased uncertainty. At the non-

inspected elements on the other hand, the posterior distribution of corrosion degree has a larger remaining uncertainty. The results of the different measurement errors are summarized in Table VI-2 where the root mean square (RMS) value of the difference between the actual corrosion degree and the posterior mean at all elements is given (Ni et al., 2020), together with the difference between the actual corrosion degree and the posterior mean at the inspected element, and the posterior uncertainty (minimum standard deviation σ_{min}, maximum standard deviation σ_{max} and average standard deviation $\sigma_{average}$). The RMS value is given by equation (VI-4).

$$RMS = \sqrt{\frac{\sum_{i=1}^{n}\left(\alpha_{actual,i} - \mu''_{\alpha,i}\right)^2}{n}} \qquad \text{(VI-4)}$$

Here, n is the number of elements in the discretization of the structure, $\alpha_{actual,i}$ is the actual corrosion degree at element i, and $\mu''_{\alpha,i}$ is the posterior mean of the corrosion degree at element i.

In Table VI-2, it can be seen that the lower the measurement error, the closer the posterior mean corrosion degree corresponds to the actual value, especially at the inspected element. Moreover, the higher the measurement error, the higher the posterior uncertainty. The fact that the RMS value is largest for the measurement error of 1.95 µε could be ascribed to an overestimation of the corrosion degree at the non-inspected elements 1, 2 and 3.

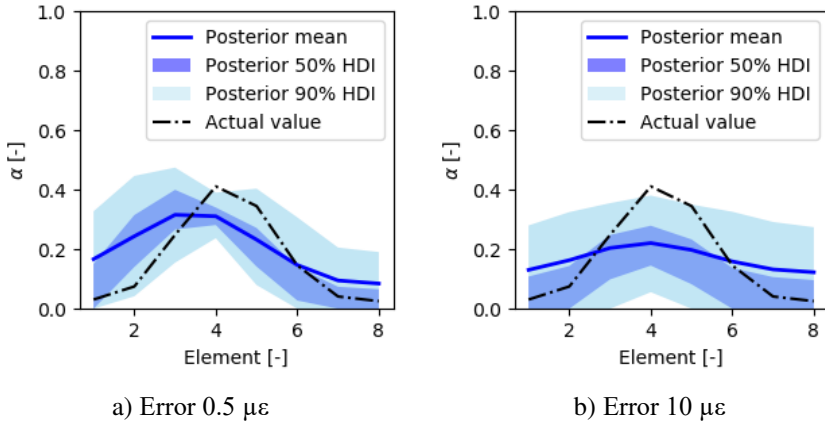a) Error 0.5 µε   b) Error 10 µε

Figure VI-5: Posterior distribution of the corrosion degree of the simply supported beam for updating based on static strain measurements at element 4 (i.e. 1.75 m from the left support) for (a) a measurement error of 0.5 µε, and (b) a measurement error of 10 µε

Table VI-2: Comparison of some posterior statistics (RMS, difference between the actual corrosion degree α_{actual} and the posterior mean μ''_α at the inspected element (element 4), minimum standard deviation σ_{min}, maximum standard deviation σ_{max} and average standard deviation $\sigma_{average}$) when changing the measurement error in the likelihood function - simply supported beam, static strains measured at element 4

Error	RMS	$(\mu''_\alpha - \alpha_{actual})_{element\ 4}$	σ_{max}	σ_{min}	$\sigma_{average}$
0.5 με	0.09	0.09	0.13	0.05	0.10
1.95 με	0.13	0.11	0.13	0.05	0.10
3 με	0.09	0.13	0.13	0.08	0.11
10 με	0.11	0.19	0.12	0.10	0.11

For the RC girder bridge, the corrosion degree is modelled as spatially variable over the bridge as discussed in section VI.2.2. Also for this case, a finite element model has been generated in DIANA FEA (DIANA FEA BV, 2019). This is a 3D model, where the girders and the slab are modelled with solid elements. The reinforcement is modelled as embedded reinforcement. The different elements in which the girders are discretized to represent the discretization of the random fields are modelled by different 'blocks'. The concrete properties are according to (Yang et al., 2019), i.e. a concrete compressive strength of 25.9 MPa, a concrete tensile strength of 2.2 MPa and a Young's modulus of the concrete of 30 GPa. The concrete model in compression is again ideal (i.e. a linear elastic behaviour until the concrete compressive strength, followed by a constant stress equal to the concrete compressive strength) and the tensile model is a Hordijk curve. The proof load applied to the bridge is simulated by a truck of 200 kN located over the middle girder. The static load test is performed at 50 years after construction considering a prior corrosion degree with mean value 0.038 and standard deviation 0.009 (see Figure VI-6). This is based on samples generated for the initiation period and the corrosion rate, and evaluating the corresponding corrosion degree according to equation (II-8) at t = 50 years. The measurement results are generated based on the corrosion degrees represented by the black dashed-dotted lines in Figure VI-7. Bayesian updating is performed assuming accurate strain measurements according to (Sousa et al., 2020), with a measurement error of 0.5 με. The results from the Bayesian updating are given in Figure VI-7 for the case where the data consists of strains measured at all 50 elements at top and bottom fibre under the proof load (Figure VI-8). The measurement locations are in the middle of the elements corresponding to the elements of the random field. However, it is considered not realistic to measure the strains at all 50 elements. Hence, Figure VI-9 gives the posterior distribution of the corrosion degree when measuring the strains at the middle two elements of all five girders. Here it is observed that the shape of the posterior distribution depends on the measurement locations, i.e. there is a smaller deviation between posterior mean and actual corrosion degree at the measurement locations. At these locations, there is also a smaller posterior uncertainty.
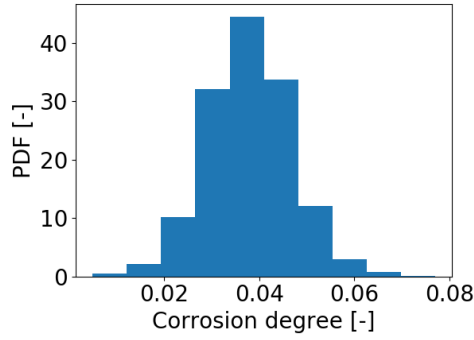
Figure VI-6: Prior distribution of the corrosion degree of the RC girder bridge (at one location)
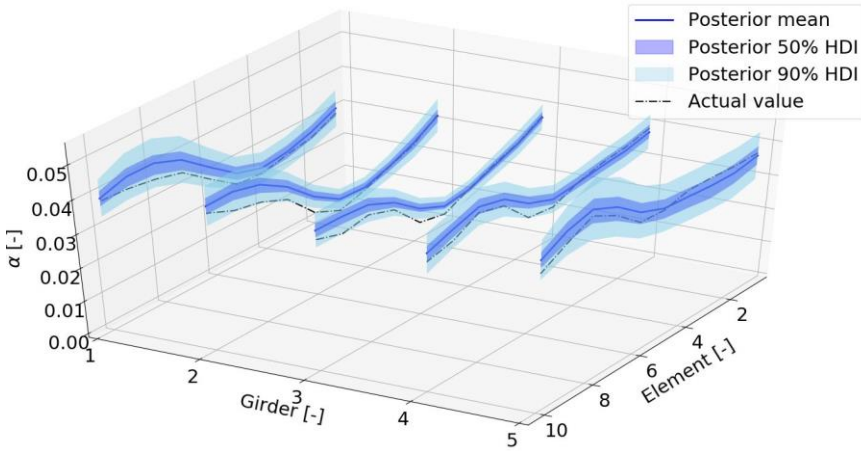

Figure VI-7: Posterior distribution of the corrosion degree of the RC girder bridge for strain data measured under proof loading at top and bottom fibre at the middle of all 50 elements in which the structure is discretized (see Figure VI-8) (measurement error 0.5 µε)

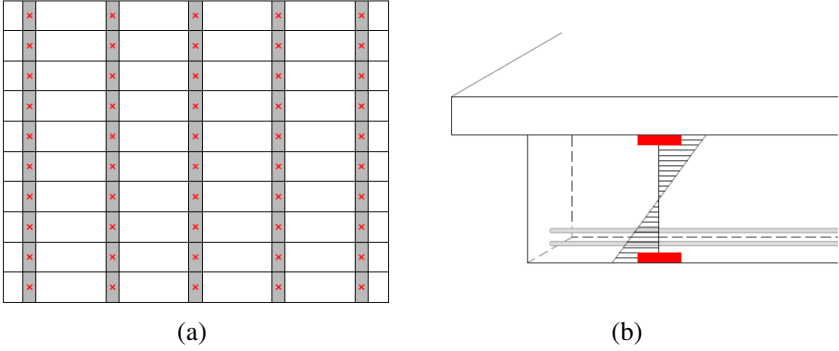<center>(a)   (b)</center>

Figure VI-8: Measurement locations to arrive at the posterior distribution visualized in
Figure VI-7 (a) bottom view, and (b) side view (part of a girder)

The effect of the measurement error on the posterior distribution is investigated,
and the results are summarized in Table VI-3. The posterior distribution has been
evaluated for different sampled values of the corrosion degree (and hence the
corresponding simulated measurement results) and for different assumptions on
the measurement error. The RMS value and maximum, minimum and average
posterior standard deviation are given for different orders of magnitude of the
actual corrosion degree and different assumptions on the measurement error. The
RMS value and the standard deviation are each time also given for the prior
distribution of the corrosion degree, in order to allow easier comparison. For all
cases, the RMS value and posterior uncertainty are smaller than the values found
a priori. The larger errors only provide accurate posterior distributions for higher
corrosion degrees, due to the larger influence of these higher corrosion degrees on
the measured strains. Hence, depending on the measurement accuracy, there is a
threshold on the corrosion degree that can be estimated.

Table VI-3: Comparison of some posterior statistics (RMS, minimum standard deviation σ_{min}, maximum standard deviation σ_{max} and average standard deviation $\sigma_{average}$) when changing the measurement error in the likelihood function for different corrosion degrees – RC girder bridge, static strains. 'Max α' refers to the maximum corrosion degree sampled along the bridge to generate the measurement result.

| Max α [-]	Error [$\mu\varepsilon$]	RMS	σ_{max}	σ_{min}	$\sigma_{average}$
0.05	Prior	0.0094	0.017	0.017	0.017
	0.2	0.0035	0.0095	0.0054	0.00070
	1	0.0078	0.010	0.0078	0.0089
	3	0.0088	0.010	0.0088	0.0096
	5	0.0090	0.010	0.0089	0.0098
	10	0.0090	0.010	0.0090	0.0099
0.15	Prior	0.029	0.040	0.040	0.040
	0.2	0.011	0.024	0.011	0.017
	1	0.017	0.031	0.018	0.024
	3	0.025	0.030	0.024	0.027
	5	0.030	0.030	0.025	0.028
	10	0.028	0.030	0.026	0.028
0.30	Prior	0.047	0.058	0.058	0.058
	0.2	0.0045	0.037	0.020	0.026
	1	0.021	0.044	0.028	0.035
	3	0.031	0.044	0.035	0.039
	5	0.037	0.044	0.037	0.041
	10	0.043	0.045	0.039	0.043
0.40	Prior	0.064	0.067	0.067	0.056
	0.2	0.009	0.044	0.024	0.032
	1	0.025	0.053	0.033	0.042
	3	0.036	0.055	0.044	0.050
	5	0.046	0.057	0.047	0.053
	10	0.056	0.059	0.051	0.056
0.50	Prior	0.078	0.081	0.081	0.081
	0.2	0.0044	0.045	0.026	0.033
	1	0.014	0.058	0.035	0.045
	3	0.031	0.065	0.047	0.056
	5	0.46	0.065	0.055	0.060
	10	0.059	0.068	0.058	0.064
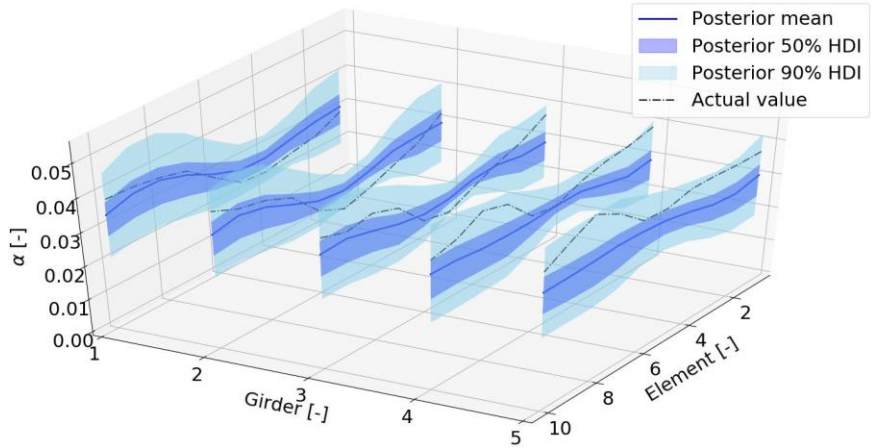
Figure VI-9: Posterior distribution of the corrosion degree of the RC girder bridge when performing strain measurements under proof loading at the two middle elements of all girders (measurement error 0.5 µε)

Similar calculations are performed for simulations where the corrosion variables are modelled with independent random fields for each girder. The results are summarized in Table VI-4. Here it can be seen that in general the RMS value and posterior uncertainty are higher compared to the results of Table VI-3. For very large corrosion degrees, posterior distributions generated accounting for measurement errors up to 5 µε provide a reasonable estimate of the actual corrosion degree, i.e. the posterior mean shows the same spatial variation as the actual corrosion degree, as visible in Figure VI-10. Nevertheless, the approximation is less good compared to the results with 2D random fields. This can be ascribed to the increased number of unknowns due to the reduced correlation. Hence, relatively less information is available.

Table VI-4: Comparison of some posterior statistics (RMS, minimum standard deviation σ_{min}, maximum standard deviation σ_{max} and average standard deviation $\sigma_{average}$) when changing the measurement error in the likelihood for different corrosion degrees – RC girder bridge, static strains, assuming independent random fields for the different girders. 'Max α' refers to the maximum corrosion degree sampled along the bridge to generate the measurement result.

| Max α [-]	Error [$\mu\varepsilon$]	RMS	σ_{max}	σ_{min}	$\sigma_{average}$
0.05	Prior	0.030	0.018	0.018	0.018
	0.2	0.0071	0.0071	0.0024	0.0047
	1	0.0054	0.0086	0.0027	0.0057
	3	0.0072	0.0097	0.0048	0.0073
	5	0.0071	0.0097	0.0053	0.0074
	10	0.016	0.010	0.0087	0.0095
0.15	Prior	0.057	0.039	0.039	0.039
	0.2	0.031	0.025	0.008	0.016
	1	0.032	0.030	0.013	0.019
	3	0.034	0.032	0.017	0.022
	5	0.034	0.032	0.018	0.023
	10	0.036	0.030	0.020	0.024
0.30	Prior	0.098	0.057	0.057	0.057
	0.2	0.017	0.035	0.010	0.021
	1	0.019	0.046	0.013	0.025
	3	0.020	0.050	0.018	0.029
	5	0.022	0.050	0.022	0.031
	10	0.028	0.044	0.025	0.033
0.40	Prior	0.10	0.070	0.070	0.070
	0.2	0.014	0.048	0.023	0.035
	1	0.056	0.055	0.026	0.038
	3	0.076	0.056	0.026	0.038
	5	0.078	0.054	0.029	0.040
	10	0.088	0.062	0.046	0.053
0.50	Prior	0.100	0.080	0.080	0.080
	0.2	0.010	0.049	0.025	0.039
	1	0.048	0.061	0.034	0.048
	3	0.067	0.065	0.040	0.055
	5	0.091	0.068	0.048	0.060
	10	0.097	0.071	0.056	0.065
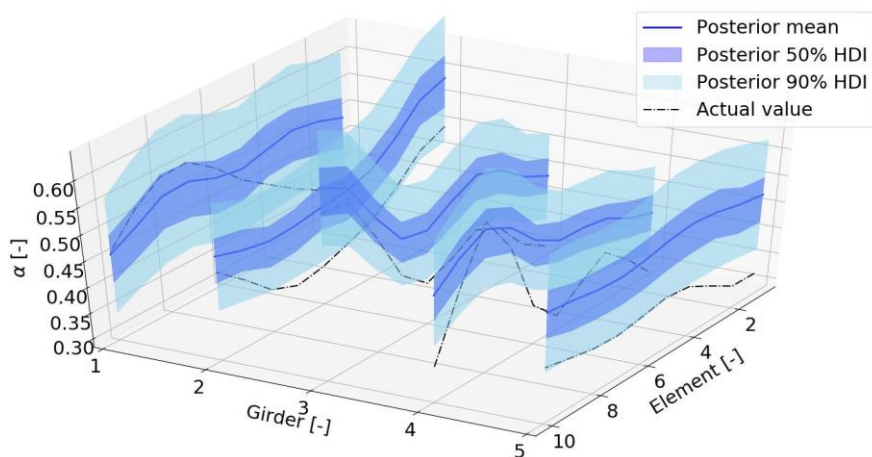
Figure VI-10: Posterior distribution of the corrosion degree of the RC girder bridge with measurement error 5 με when updating independent random fields for each girder – updating based on static strains at all elements in which the structure is discretized

VI.3.2.2   Deflections

It is also investigated how measuring deflections under a known load allows reducing the prior uncertainty on the corrosion degree. Similar as for the static strains, first the illustrative example of the simply supported beam will be considered. The finite element model used to generate the data is the same as for the static strains, and the time of performing the analysis is again $t = 35$ years. Assuming a measurement error of 0.05 mm (Heitner et al., 2019; Sousa et al., 2020) and a measured deflection at element 4, the posterior distribution of the corrosion degree of the simply supported beam is given in Figure VI-11 (a). The posterior distribution is similar to the one achieved by measuring the strains at element 4, but with a larger posterior uncertainty at element 4. In general, less information is extracted regarding the corrosion degree when measuring deflections under proof loading. The updating based on deflection measurements is also performed for a lower maximum underlying corrosion degree, with posterior distribution according to Figure VI-11 (b). Here it can be seen that the posterior mean of the corrosion degree lies close to the prior one (mean corrosion degree of 0.12 and a standard deviation of 0.16), and that there is a large difference between the posterior mean and the actual value of the corrosion degree. Moreover, the posterior uncertainty is rather large. This can be ascribed to the lower corrosion degrees and hence the smaller difference in displacements. When this difference becomes too small with respect to the measurement error, the effect of the Bayesian updating will be very limited. Hence, similar as for the static strains, there will be a threshold on the corrosion degree that can be detected depending on the measurement accuracy.

a) Higher actual corrosion degree   b) Lower actual corrosion degree
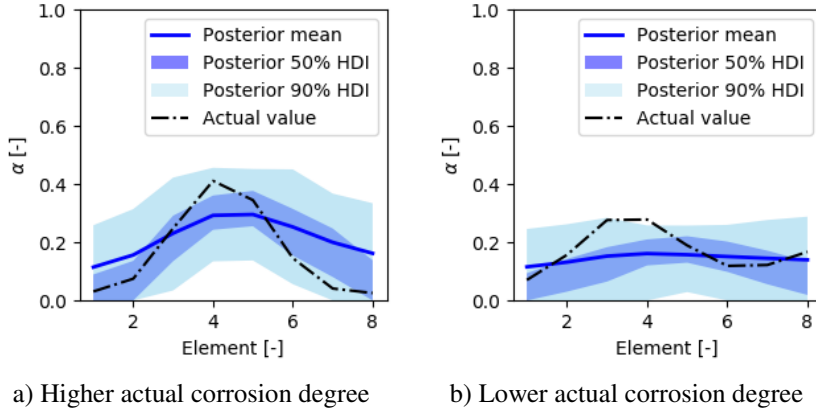
Figure VI-11: Posterior distribution of corrosion degree when measuring the deflection at element 4

Also for the girder bridge, the influence of deflection measurements is investigated. The finite element model used to generate the data is again the same as for the static strains and the time of analysis equals 50 years, inducing the same prior distribution of the corrosion degree. In Figure VI-12, the posterior distribution of the corrosion degree is given when measuring the vertical deflections under a known load at all elements in which the bridge is subdivided. Again, a measurement error of 0.05 mm is considered. A very vague posterior distribution is achieved, which is close to the prior distribution. The measurements do not provide sufficient information to represent the actual corrosion degree.
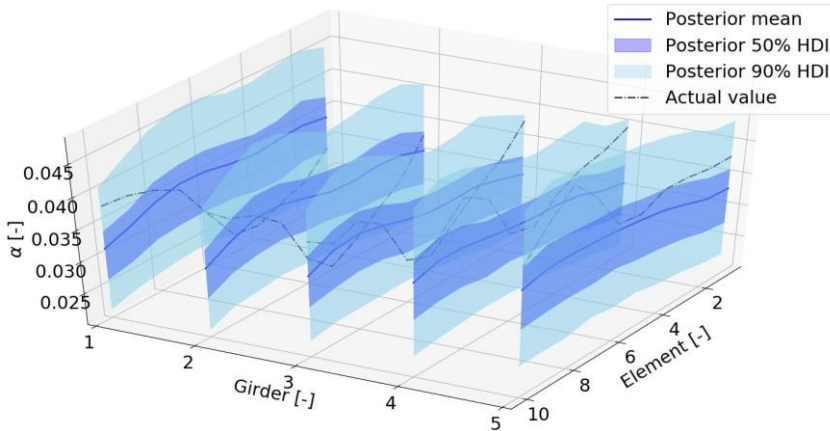

Figure VI-12: Posterior distribution of the corrosion degree of the RC girder bridge when measuring the vertical deflections at 50 locations

VI.3.3 Updating based on ambient vibration data

Model-based structural health monitoring is often done through vibration-based finite element model updating. It assumes that local structural damage results in a local reduction of stiffness. The presence of damage can be detected, located and quantified (Simoen et al., 2015). Modal characteristics can be identified from ambient data collected in an ambient vibration test, avoiding interruption of traffic.

When the measurement errors of all measurement data are assumed statistically independent, their covariance matrix $\mathbf{\Sigma}_D$ (equation (IV-6)) is a diagonal matrix. The diagonal elements consist of the variances, assumed proportional to the experimental values, according to equation (VI-5) (Simoen, 2013).

$$\sigma_{\lambda,r} = \sigma_\lambda \bar{\lambda}_r \text{ and } \sigma_{\phi,r} = \sigma_\phi \|\bar{\phi}_r\| \tag{VI-5}$$

Here, $\bar{\lambda}_r$ is the experimental frequency and $\bar{\phi}_r$ the experimental mode shape vector. σ_λ and σ_ϕ represent the proportionality between the variance of the measurement error and the experimental frequency and mode shape respectively. When considering $\mathbf{\Sigma}_G = 0$ for illustrative purposes, the maximum likelihood function (equation (IV-6)) can be rewritten according to equation (VI-6) (Simoen, 2013).

$$
\begin{aligned}
F_{ML} &= \sum_{r=1}^{N_m} \frac{\left(\bar{\lambda}_r - \lambda_r(\boldsymbol{\theta}_M)\right)^2}{\sigma_{\lambda,r}^2} + \sum_{r=1}^{N_m} \frac{\left\|\bar{\phi}_r - \phi_r(\boldsymbol{\theta}_M)\right\|^2}{\sigma_{\phi,r}^2} \\
&= \sum_{r=1}^{N_m} \frac{\left(\bar{\lambda}_r - \lambda_r(\boldsymbol{\theta}_M)\right)^2}{\sigma_\lambda^2 \bar{\lambda}_r^2} + \sum_{r=1}^{N_m} \frac{\left\|\bar{\phi}_r - \phi_r(\boldsymbol{\theta}_M)\right\|^2}{\sigma_\phi^2 \|\bar{\phi}_r\|^2}
\end{aligned}
\tag{VI-6}
$$

Here, N_m is the number of modes considered. In this equation, it is implicitly assumed that suitable mode shape scaling has been performed.

It should be pointed out that, since the error on the displacement mode shapes is proportional to the norm of the mode shape (equation (VI-5)), the error will increase if more accelerometers are used and hence the experimental displacement mode shape is available at more locations. Nevertheless, in this case also in the denominator of equation (VI-6), more data points are considered. Another note is that the error considered here is not only reflecting the experimental error, but refers to a more global prediction error, also including modelling errors. Reference can be made to (Simoen et al., 2013), where both the influence of introducing correlation in this prediction error and the influence of the number of accelerometers are investigated. If more information is available on the mode shapes and the experimental errors, other assumptions on this error could also be applied.

In the following, it is assumed that the Young's modulus in the models to simulate the modal characteristics is the same as the one applied in the models for the static load tests, i.e. the dynamic modulus E_{cd} is equal to the static modulus E_{cs}. Nevertheless, in reality the dynamic modulus will be larger than the static modulus, with a linear relationship between both, i.e. $E_{cd} = a{\cdot}E_{cs}$, with a a factor larger than or equal to 1. When working with actual data (instead of simulated data, as assumed in the current and following chapters), either the static and dynamic Young's modulus should both be tested experimentally to establish this relationship, either the factor a is also assigned a distribution and considered in the Bayesian inference. In the analyses performed further in this work, a is assumed to be equal to 1.

VI.3.3.1 Natural frequencies

In this section, updating is performed only taking along the natural frequencies in the likelihood function. First, the simply supported beam is considered. To calculate the modal properties of the simply supported beam, a 2D FE beam model is used (Dooms et al., 2014) where the stiffness is replaced by an equivalent stiffness in each element, accounting for the corroded reinforcement and the cracked concrete due to corrosion. The assumed material properties are the same as mentioned in section VI.3.2.1. The corrosion degree is assumed uniform along the structure (i.e. no spatial variability is considered) and a uniform prior distribution between 0 and 1 is assumed for the corrosion degree. The simulated measurement result is generated in the same way as explained in the previous sections, i.e. by generating a value for the corrosion degree and evaluating the finite element model to find the corresponding natural frequencies. To these values, a sample of the measurement error is then added. When updating is performed based on the natural frequencies, this uniform corrosion degree is approximated quite well, as can be seen in Figure VI-13 for two different situations corresponding to two different actual corrosion degrees. In these analyses, the error on the natural frequencies is assumed equal to 1% of the experimental value (or $\sigma_\lambda = 0.01$). For situation 1, the posterior distribution of the corrosion degree is also visualized when the error on the natural frequencies is increased by a factor 10 (or $\sigma_\lambda = 0.1$). Here it can be seen that due to the very high experimental error, the posterior distribution lies close to the prior distribution. Nevertheless, there is a slight increase in posterior probability close to the actual corrosion degree.
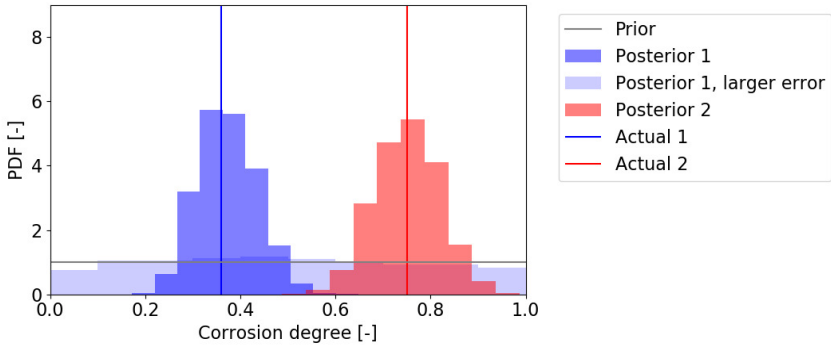
Figure VI-13: Posterior distribution of the corrosion degree for the simply supported beam where the corrosion degree is considered uniform along the beam. Updating is performed based on natural frequency data for two different actual corrosion degrees.

For the RC girder bridge, also a uniform corrosion degree along the whole structure is considered. The finite element model to generate the data is the same as in the previous sections, and the time of analysis again equals $t = 50$ years. The simulated measurement result is generated in the same way as described in the previous sections. The prior distribution is based on the marginal distributions of the initiation period and corrosion rate as given in section VI.2.2. The posterior distribution based on the natural frequency data is visualized in Figure VI-14 when assuming an error equal to 1% of the experimental value (or $\sigma_\lambda = 0.01$). When the measurement error is decreased by a factor 10 (or $\sigma_\lambda = 0.001$), the posterior distribution becomes less vague and a more accurate representation of the actual value is found. When assuming spatial variation of corrosion and an error of 0.1% of the experimental frequency, the posterior corrosion degree is visualized in Figure VI-15. Here it can be seen that no spatial variation of the corrosion degree is present in the posterior distribution, since the natural frequencies only provide global information on the stiffness.
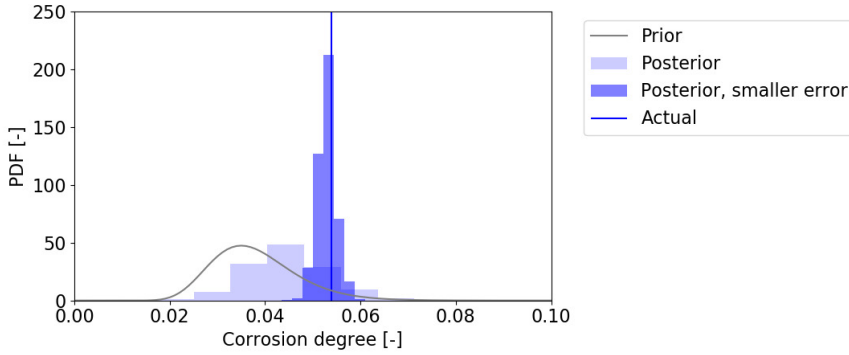
Figure VI-14: Posterior distribution of the corrosion degree of the RC girder bridge when this is modelled uniform along the bridge. Updating based on natural frequencies for two different errors in the likelihood function.
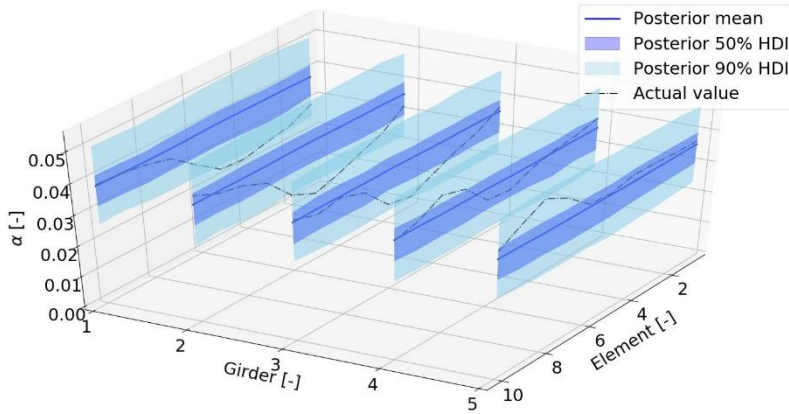

Figure VI-15: Posterior distribution of the (spatially variable) corrosion degree of the RC girder bridge when updating based on natural frequencies (prior mean of the corrosion degree equal to 0.038 and prior standard deviation equal to 0.009)

VI.3.3.2   Displacement mode shapes

In this section, the influence of also incorporating displacement mode shapes in the likelihood function is evaluated. Similar as in the previous sections, the illustrative example of the simply supported beam is considered first. The data is generated in the same way as described in the previous sections, using the same model as described in section VI.3.3.1. For the simply supported beam and a uniform corrosion degree along the length of the beam, the posterior distribution is visualized in Figure VI-16 for two different actual corrosion degrees. The

assumed errors in the likelihood function are $\sigma_\lambda = 0.01$ and $\sigma_\phi = 0.01$. In Figure VI-16, it can be seen that for the higher actual corrosion degree, the posterior uncertainty is reduced compared to Figure VI-13, even though displacement mode shapes only change if there is a change of stiffness along the structure. Nevertheless, for the very high corrosion degrees, the structure has such a low resistance that it is cracked under the service load at some locations. This might lead to changes in the displacement mode shapes. Hence, these very high corrosion degrees are not present anymore in the posterior distribution. For a lower actual corrosion degree, no additional reduction in uncertainty is found when the displacement mode shapes are considered together with the natural frequencies in the likelihood function and assuming uniform corrosion along the length of the beam.
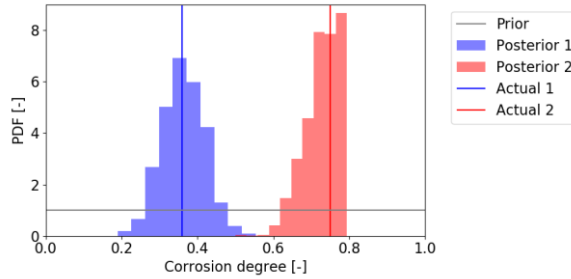

Figure VI-16: Posterior distribution of uniform corrosion degree along the beam based on natural frequencies and displacement mode shapes for two actual corrosion degrees

When the natural frequencies and displacement mode shapes of the first four bending modes (accelerations measured at 0.5 m, 1 m, 1.5 m, 2 m, 2.5 m, 3 m and 3.5 m from the left support of the beam) are used as data when the corrosion degree is modelled as spatially variable, the posterior distribution visualized in Figure VI-17 (b) is obtained. Here it can be seen that the posterior standard deviation is higher at element 4 when compared to the case where strains are measured at this element with an accurate strain measuring technique (Figure VI-5).

a) $\sigma_\lambda = 0.001, \sigma_\phi = 0.01$

b) $\sigma_\lambda = 0.01, \sigma_\phi = 0.01$

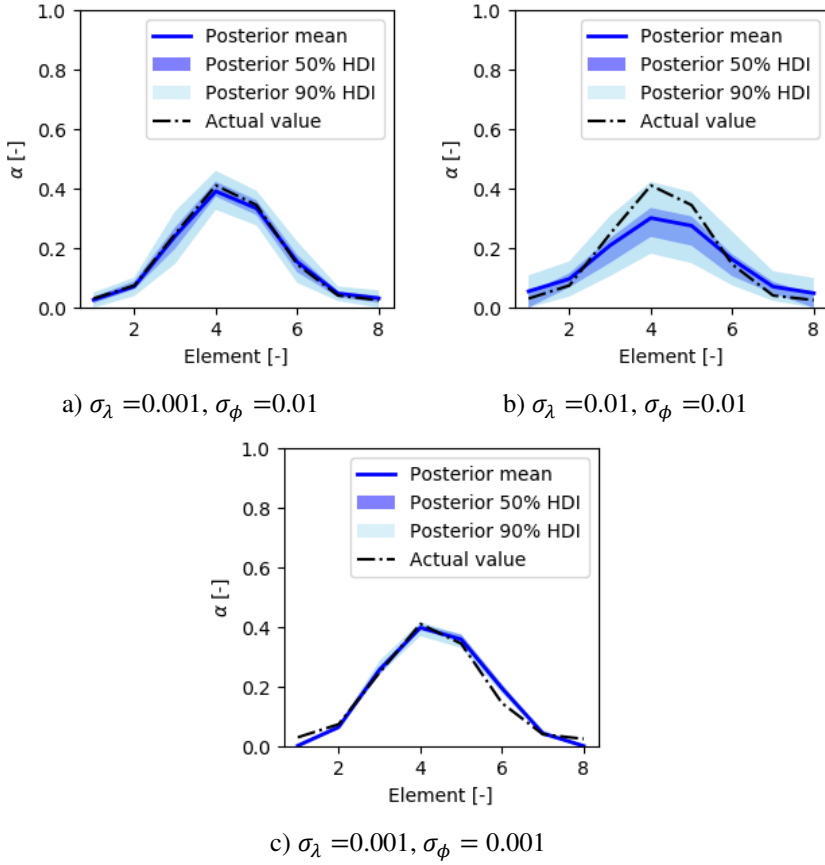c) $\sigma_\lambda = 0.001, \sigma_\phi = 0.001$

Figure VI-17: Influence of the measurement error of the dynamic data on the posterior corrosion degree of the simply supported beam (spatially variable corrosion)

Similar as for the static strain measurements, the 'measurement error' on the modal data influences the posterior distribution. The larger the error, the more uncertain the posterior distribution will be. The influence of the measurement error is visualized in Figure VI-17. The difference between figure a and b is an increased error on the natural frequencies (from 0.1% of the experimental value to 1% of the experimental value). The difference between figures a and c is a decreased error on the norm of the mode shape, i.e. from 1% of the measured value to 0.1% of the measured value. A reduction of these errors leads to a reduction of the posterior uncertainty.

Next, the RC girder bridge is considered. The finite element model is the same as in the previous sections, and the measurement results are generated in the same way as described before. The time of analysis is again $t = 50$ years. Only the first four natural frequencies and corresponding displacement mode shapes at the sensor locations are assumed to be extracted from the acceleration data. The posterior distribution of the corrosion degree based on modal data of these first four modes is given in Figure VI-18 ($\sigma_\phi = 0.01$ and $\sigma_\lambda = 0.001$). Here, the accelerations are assumed to be measured at the middle node at the bottom of all 50 elements of the discretized structure. The posterior uncertainty on the corrosion degree found by updating based on modal data is larger than the posterior uncertainty on the corrosion degree when accounting for static strain measurements. This can be attributed to two reasons: first, the relative measurement error assumed for the displacement mode shapes is larger than for the static strains. Second, displacement mode shapes and natural frequencies of the lower, global modes give a more global characterization of the stiffness. Next to these two reasons, the number of measured mode shape components is also of importance. Although the exact stiffness cannot be identified from the posterior distribution, the critical regions with the lowest stiffness and hence the largest corrosion degree can be found.

The influence of the measurement error on the posterior distribution is also investigated for the RC girder bridge. For updating based on modal data, three cases are considered, which are the same as for the simply supported beam:

1. $\sigma_\lambda = 0.001 \cdot \bar{\lambda}_r$, $\sigma_\phi = 0.01 \cdot \|\bar{\phi}_r\|$
2. $\sigma_\lambda = 0.01 \cdot \bar{\lambda}_r$, $\sigma_\phi = 0.01 \|\bar{\phi}_r\|$
3. $\sigma_\lambda = 0.001 \cdot \bar{\lambda}_r$, $\sigma_\phi = 0.001 \|\bar{\phi}_r\|$

The difference in posterior distribution can be seen when comparing the results in Table VI-5. Here it can be seen that case 3 approaches much better the actual value compared to case 2 and case 1. The posterior uncertainty is also smaller for case 1 than for case 2.

Table VI-5: Comparison of some posterior statistics (RMS, minimum standard deviation σ_{min}, maximum standard deviation σ_{max} and average standard deviation $\sigma_{average}$) when changing the measurement error in the likelihood – RC girder bridge, modal data

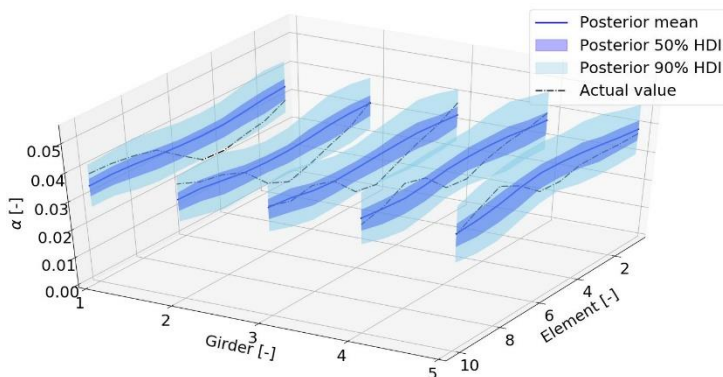| Error	RMS	σ_{max}	σ_{min}	$\sigma_{average}$
Case 1	0.004	0.009	0.006	0.008
Case 2	0.005	0.010	0.007	0.009
Case 3	0.003	0.009	0.005	0.007

Figure VI-18: Posterior distribution of the corrosion degree of the RC girder bridge when updating is performed based on the natural frequencies and displacement mode shapes of the first four modes (accelerations are measured in the middle of all 50 elements).

VI.3.3.3   Strain mode shapes

In this section, it is considered that dynamic strains are measured under ambient excitation to provide strain mode shapes. The corrosion variables are updated based on natural frequencies and strain mode shapes. The natural frequencies are accounted for according to equation (VI-6) and the strain mode shapes are accounted for according to equation (VI-3). The error on the natural frequencies is assumed equal to 0.1% of the experimental value (cfr. supra), and the error on the strains is assumed equal to 0.2 µε (cfr. supra). This error of the strains relates to the strain mode shapes as derived from the displacement mode shapes provided by the finite element model (order of magnitude of some microstrain). If actual data is available and the strain mode shapes are scaled (to the mass matrix or to those of the finite element model), other values for the error might be more appropriate and/or a relative error could be assumed.

Similar as in the previous sections, the illustrative example of the simply supported beam is considered first. The data is generated in the same was as described in the previous sections, and the same model is used. The modal strains are assumed the average strains over the elements in which the beam is discretized. The posterior corrosion degree obtained after updating based on natural frequencies and strain mode shapes at top and bottom fibre at all eight elements is given in Figure VI-19. Strains under operational conditions are often very low and hence difficult to measure. The use of optical fibres and recently developed data processing techniques can resolve this problem (Anastasopoulos et al., 2018). When the error on the natural frequencies is increased by a factor of 10, the results are visualized in Figure VI-20 (a). Here it can be seen that a larger posterior uncertainty is found and that the posterior distribution is a less good approximation of the actual

corrosion degree. When the error on the strains is increased to 1.95 µε, the influence is less significant (Figure VI-20 (b)).

Figure VI-19: Posterior distribution of the corrosion degree of the simply supported beam after measuring the modal strains at all eight elements (i.e. the average strain in each element)

a) Increased error on natural frequencies
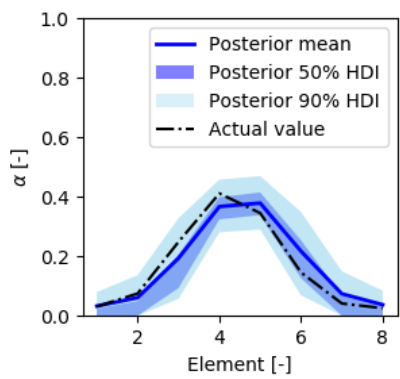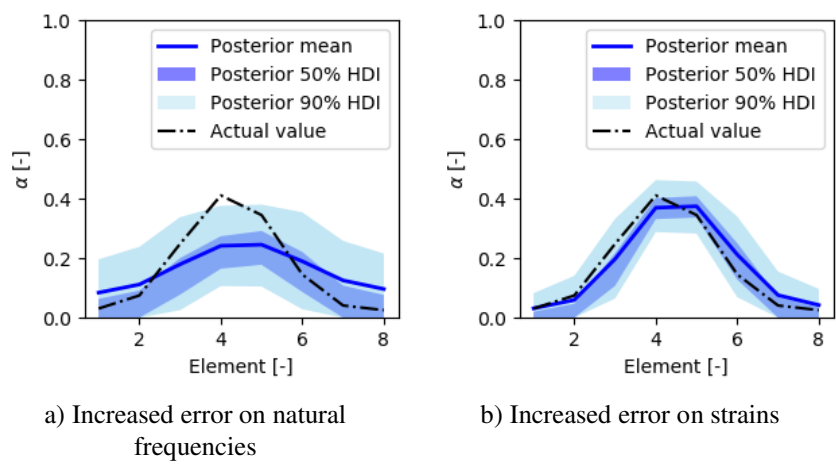
b) Increased error on strains

Figure VI-20: Posterior distribution of the corrosion degree of the simply supported beam after measuring the modal strains at all eight elements (i.e. the average strain in each element) with an increased error (a) on the natural frequencies or (b) on the strains

For the RC girder bridge, Figure VI-21 shows the posterior distribution of the corrosion degree when natural frequencies and strain mode shapes are incorporated in the likelihood function, assuming an error of 0.2 µε and 0.1% of the experimental frequency. The strains are average strains measured over a length of 100 mm. When compared to the case where displacement mode shapes have been used for updating (Figure VI-18), the posterior uncertainty is reduced. However, approximation of the actual corrosion degree is not as good as for the case where static strains are measured at all elements (Figure VI-7).

Also for the strain mode shapes, the influence of the measurement error is investigated. For the error on the natural frequencies, two cases are considered: $0.001 \cdot \bar{\lambda}_r$ and $0.01 \cdot \bar{\lambda}_r$. For the error on the strains, following values are considered: 0.2 µε, 1.95 µε and 3 µε. The results are summarized in Table VI-6. Here it can be seen that the actual corrosion degree is better represented by the posterior mean if the measurement error decreases.
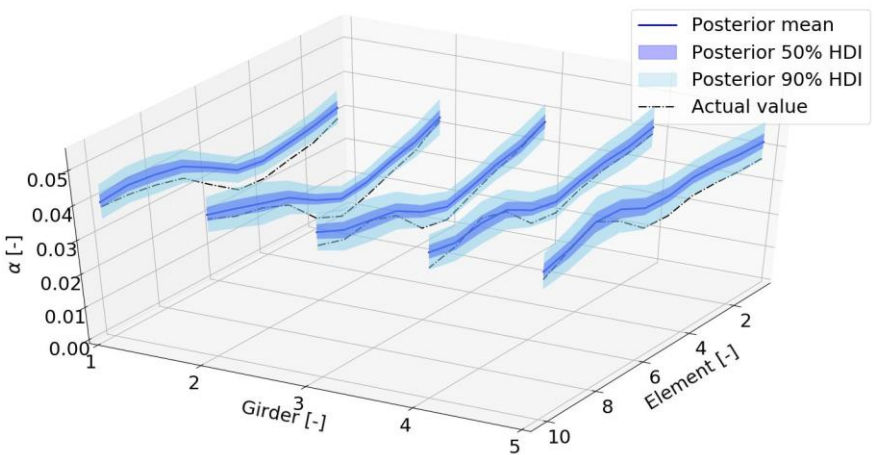

Figure VI-21: Posterior distribution of the corrosion degree of the RC girder bridge after measuring the modal strains at all 50 elements with a measurement error of 0.2 µε and 0.1% of the experimental frequency

Table VI-6: Comparison of some posterior statistics (RMS, minimum standard deviation σ_{min}, maximum standard deviation σ_{max} and average standard deviation $\sigma_{average}$) when changing the measurement error in the likelihood – RC girder bridge, strain mode shapes

Error on strain	Error on natural frequency	RMS	σ_{max}	σ_{min}	$\sigma_{average}$
0.2 µε	$0.01\bar{\lambda}_r$	0.0036	0.0070	0.0039	0.0055
0.2 µε	$0.001\bar{\lambda}_r$	0.0036	0.0070	0.0039	0.0055
1.95 µε	$0.01\bar{\lambda}_r$	0.0041	0.0078	0.0047	0.0063
1.95 µε	$0.001\bar{\lambda}_r$	0.0040	0.0079	0.0047	0.0063
3 µε	$0.01\bar{\lambda}_r$	0.0043	0.0079	0.0050	0.0075
3 µε	$0.001\bar{\lambda}_r$	0.0043	0.0081	0.0048	0.0065

VI.3.4 Updating based on visual inspection data

Visual signs of corrosion can be rust stains (i.e. rust penetrating through corrosion-induced cracks) and the presence of (severe) corrosion cracks. When rust stains are visually observed at a particular point in time, this implies not only that corrosion has initiated, but also that the first corrosion cracks are present in the concrete cover. For the time to cracking (T_{cr}), different models exist in literature. In this work, the model of (Lv and Zhu, 2016) will be used, which is given by equation (II-10).

When rust stains have been observed, T_i+T_{cr} should be lower than t_{rust}, with t_{rust} the first time at which rust stains are observed. Furthermore, Stewart and Suo (2009) also give the time to severe cracking, which corresponds to a crack width of 1 mm (w_{lim}). The time between first cracking (T_{cr}) and severe cracking (crack widths exceeding 1 mm) is given by equation (VI-7).

$$T_{ser} = k_R \frac{0.0114}{i_{corr}} \left[A \left(\frac{c}{w/c} \right)^B \right]$$

$$\text{with } k_R \approx 0.95 \left[\exp\left(-\frac{0.3 i_{corr(exp)}}{i_{corr}} \right) - \frac{i_{corr(exp)}}{2500 i_{corr}} + 0.3 \right]$$

(VI-7)

Here, w/c is the water-to-cement ratio of the concrete, A (700 or 65) and B (0.23 or 0.45) are empirical constants for limit crack widths (of 1 mm and 0.3 mm respectively), and $i_{corr(exp)}$ (100 µA/cm²) is the accelerated corrosion rate used to derive the constants A and B. When severe cracking is observed, $T_i+T_{cr}+T_{ser}$ should be lower than $t_{ser,observed}$, i.e. the first time at which this severe cracking is observed. When performing MCMC-based Bayesian updating considering these visual observations, samples of the initiation period and corrosion rate not fulfilling either of the two mentioned criteria will be rejected.

The influence of accounting for the visual observations is first illustrated for a very general example. Consider the following prior distributions: a lognormal distribution for the initiation period with mean 21 years and standard deviation 10 years, and a lognormal distribution for the corrosion rate with mean 0.03 mm/year and standard deviation 0.02 mm/year. Assume that it is visually observed that corrosion cracks and rust stains are present at $t = 15$ years. The influence on the distributions of the initiation period, corrosion rate and corrosion degree is visualized in Figure VI-22 to Figure VI-24. Here it can be seen that the influence on the distribution of the initiation period is quite large and that only initiation periods lower than 15 years are retained. For the corrosion rate, there is a shift to higher values due to the early presence of corrosion cracks. Also the corrosion degree shifts to higher values and a corrosion degree of zero is not present anymore in the posterior distribution. If also severe cracking would be observed at 15 years, the posterior distributions are visualized in the same figures. The influence on the initiation period is limited, and the corrosion rate and corrosion degree shift to slightly higher values.
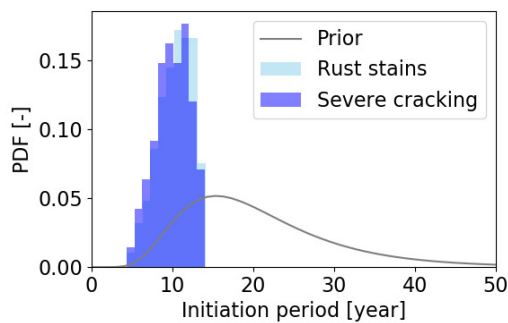

Figure VI-22: Influence of visual observations on the distribution of the initiation period
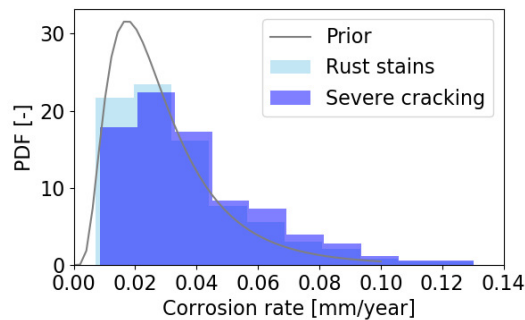

Figure VI-23: Influence of visual observations on the distribution of the corrosion rate
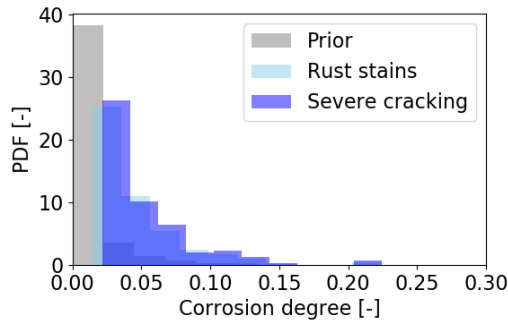
Figure VI-24: Influence of visual observations on the distribution of the corrosion degree

In the following, for each element in which the structure is discretized, the first time of observing rust stains and/or severe cracking will be accounted for in the Bayesian updating, assuming inspection intervals of 3 years. Virtual measurement data are generated based on samples of the random fields of the initiation period and corrosion rate. Based on these samples, the times for visual observations are derived. For the simply supported beam, rust stains are observed at [33, 30, 21, 15, 15, 18, 27, 30] years and severe cracking at [33, 30, 21, 15, 15 18, 27, 33] years. These different values correspond to the observations in the different 'elements' in which the beam is discretized. Note that the time instances for observing rust stains and severe cracking are mostly equal, which can be ascribed to 1) the low values of T_{ser}, and 2) the assumed fixed time of 3 years between visual observations. Because of the latter reason, cracking can have occurred shortly after an earlier inspection and once the next inspection is performed, severe cracking might already be present. For the simply supported beam, the posterior distribution is visualized in Figure VI-25 when only accounting for the visual observations of rust stains. Here it can be seen that this posterior distribution is rather vague and that the visual observations alone are not sufficient to update the corrosion degree.

Also for the RC girder bridge, information from visual inspections can be accounted for. Again, a three-year inspection interval is assumed. The times of observing rust stains or corrosion cracks, vary between 18 years and 27 years for the different elements in which the structure is discretized. When the posterior distribution is determined for the RC girder bridge only based on visual observations of rust stains and/or corrosion cracks, the posterior distribution is visualized in Figure VI-26. Here it can be seen that because visual signs of corrosion are observed, the lowest corrosion degrees are excluded from the posterior distribution. Nevertheless, the actual corrosion degree is not accurately represented by the posterior distribution.
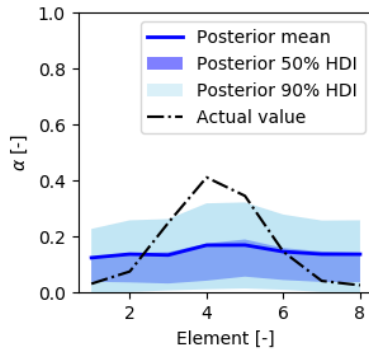
Figure VI-25: Posterior corrosion degree when only accounting for the visual inspection results up to $t = 35$ years
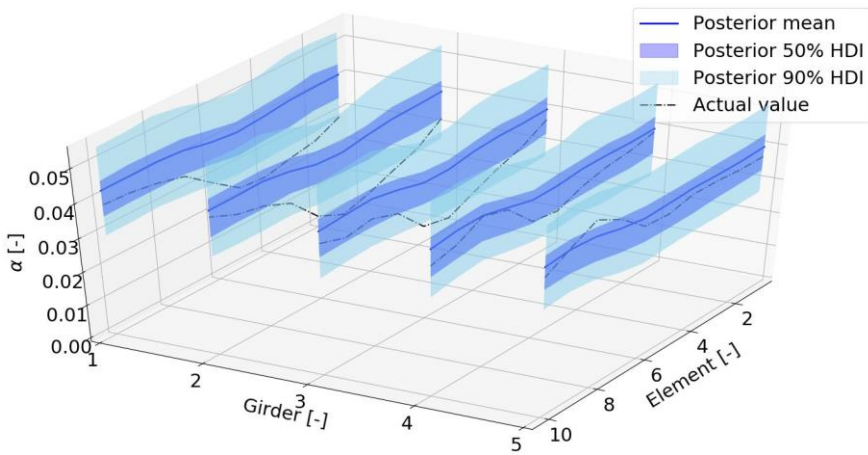

Figure VI-26: Posterior distribution of the corrosion degree of the RC girder bridge based on visual inspection data only

VI.3.5 Updating based on heterogeneous data

In the previous sections, the influence of different types of data on the posterior distribution of the corrosion degree was studied. In the following sections it is investigated how different types of data can be combined in order to arrive at a more accurate estimate of the corrosion degree.

VI.3.5.1   Modal data and static strain data

Based on the conclusions obtained in the previous sections, a first possible strategy is to determine locations where the structure is likely damaged based on modal data, and prioritize these locations when collecting strain data under proof loading. Combining the data of both measurements will lead to reduced identification uncertainties when compared to the case where the measurements are considered separately. This means that the posterior uncertainty and the deviation between the posterior mean and actual value will decrease. A conceptual illustration of the advantage of combining both sources of information is provided in Figure VI-27.

When considering the simply supported beam, the posterior distribution of the corrosion degree resulting from modal data suggests that the most damaged region of the beam is in the middle of the beam (see Figure VI-17). It is considered that, after updating based on the modal data of the first four modes (errors 1% of the experimental frequency and displacement mode shape), a proof load is applied and the strain in the middle of element 4 is measured (i.e. at 1.75 m from the left support, error 0.5 µε). The corresponding posterior distribution is given in Figure VI-28. When looking at Figure VI-28, it can be seen that the posterior uncertainty is smaller compared to the posterior distribution of the corrosion degree when only accounting for the modal data (Figure VI-17) or the static strain data (Figure VI-5), and that also at the elements where no static strains are measured a more accurate representation of the corrosion degree is found.
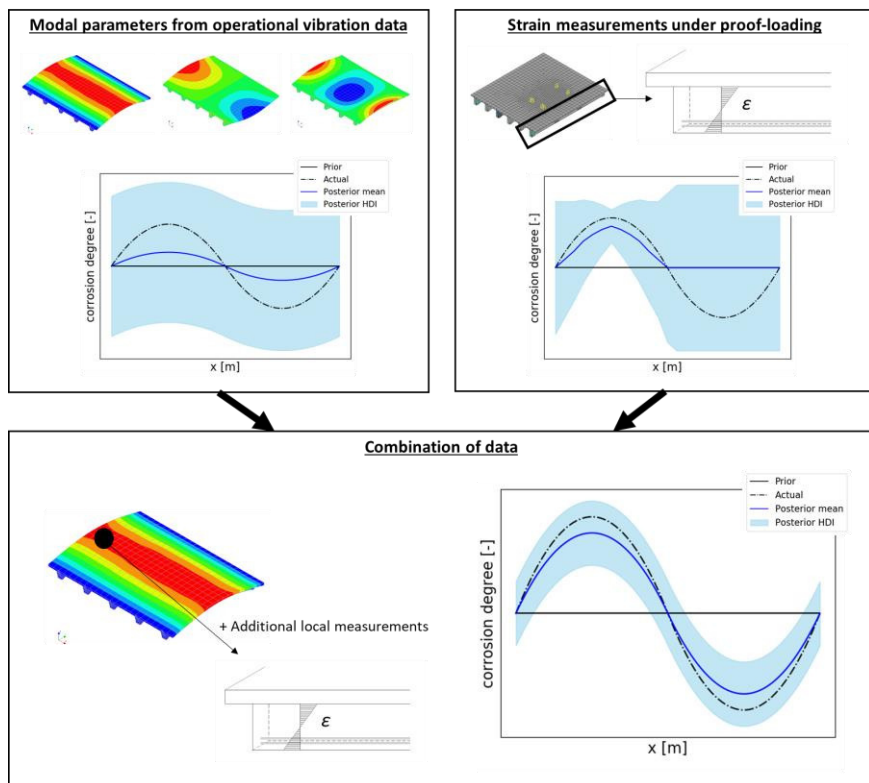
Figure VI-27: Conceptual representation of updating of the corrosion degree based on strain data from proof loading and modal data from ambient acceleration measurements, and the improved predictability when considering both sources of information

Also for the RC girder bridge, the HDI from the posterior distribution based on the modal data is very wide. The corrosion degree is not predicted very accurate and precise. However, the general pattern of the posterior distribution along the bridge points towards critical locations to perform additional static strain measurements. These locations to perform additional strain measurements under proof loading are based on an assumed critical corrosion degree of 0.042, which represents an increase of 10% compared to the prior mean. Strains are only measured at the locations were the critical corrosion degree lies in the 50% HDI of the posterior distribution as identified from the modal data. The results are given in Figure VI-29. By combining the information of modal data and static strain data, the posterior uncertainty is reduced when compared to the case where only modal data or static strain data at a limited number of sensor locations are considered.
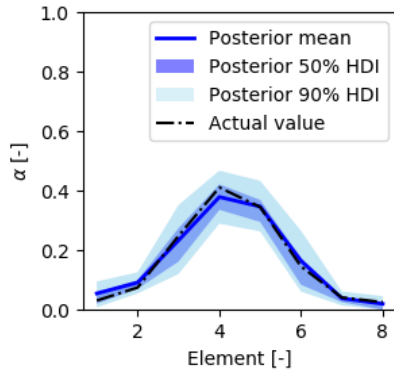
Figure VI-28: Posterior distribution of the corrosion degree of the simply supported beam after a combination of modal data and static strain data
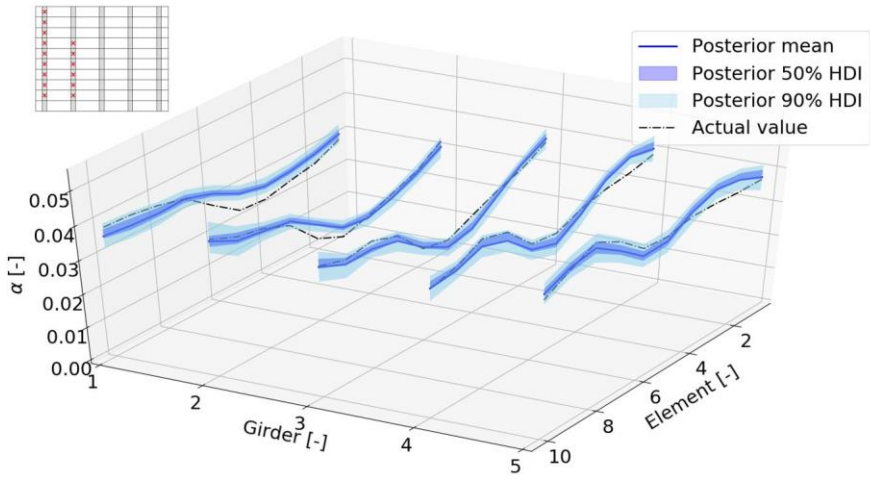

Figure VI-29: Posterior distribution of the corrosion degree of the RC girder bridge after updating based on modal data and static strain data at those locations where the critical corrosion degree (0.042) is within the 50% HDI of the posterior distribution when only accounting for modal data (as indicated in the top left corner of the figure)

In previous sections, it was found that an increased error on the static strain measurements leads to a more vague posterior distribution, not accurately describing the actual corrosion degree. When combining this strain data with natural frequencies and displacement mode shapes, the posterior distribution is a better approximation of the actual corrosion degree, which can be concluded based on the results in Table VI-7. If static strain measurements are performed at all locations and the error on the strain measurements is small enough, not much additional information is gained by adding the modal data. Nevertheless, if the strain measurements are not very accurate, adding the information obtained from the modal data provides a significant benefit.

Table VI-7: Comparison of some posterior statistics (RMS, minimum standard deviation σ_{min}, maximum standard deviation σ_{max} and average standard deviation $\sigma_{average}$) of the corrosion degree when changing the measurement error in the likelihood – RC girder bridge, modal data and static strain data. 'Max α' refers to the maximum corrosion degree sampled along the bridge to generate the measurement result.

Max α [-]	Error on strain	Data	RMS	σ_{max}	σ_{min}	$\sigma_{average}$
0.13	1 με	Modal + static strain	0.019	0.030	0.016	0.023
	1 με	Static strain	0.017	0.031	0.018	0.024
	3 με	Modal + static strain	0.027	0.034	0.022	0.026
	3 με	Static strain	0.025	0.030	0.024	0.027
	10 με	Modal + static strain	0.030	0.035	0.023	0.028
	10 με	Static strain	0.028	0.030	0.026	0.028
0.40	1 με	Modal + static strain	0.018	0.051	0.029	0.038
	1 με	Static strain	0.025	0.053	0.033	0.042
	3 με	Modal + static strain	0.030	0.058	0.035	0.044
	3 με	Static strain	0.036	0.055	0.044	0.050
	10 με	Modal + static strain	0.042	0.064	0.036	0.048
	10 με	Static strain	0.056	0.059	0.051	0.056

VI.3.5.2 Visual observations and strain or modal data

In this section, it is investigated how combining the visual observations with the different considered data types influences the posterior distribution of the corrosion degree.

When considering the simply supported beam, the posterior distribution of the corrosion degree is determined for a data set including strains measured under proof loading at element 4, accelerations at seven locations along the beam, or modal strains in all eight elements. Both the results with and without consideration of the visual observation of rust stains at [33, 30, 21, 15, 15, 18, 27, 30] years are determined. The results are summarized in Table VI-8. The posterior distribution is visualized in Figure VI-30 when considering the static strains. In Figure VI-30, it is observed that the addition of the visual observation leads to a smaller posterior uncertainty and a better characterization of the actual corrosion degree. For the natural frequencies and displacement mode shapes, the maximum standard deviation of the corrosion degree reduces from 0.10 to 0.075 when incorporating the information from the visual inspection (Table VI-8). For the natural frequencies and strain mode shapes, this maximum standard deviation reduces from 0.101 to 0.075 when accounting for the visual observations.

If the measurement error on the strains is increased to 3 $\mu\varepsilon$, the influence of adding the visual observations becomes even more pronounced, as visible in Table VI-9. Increasing the error in the likelihood function when accounting for the natural frequencies and displacement mode shapes has a less remarkable influence. For the natural frequencies and strain mode shapes, the effect of adding the visual data is again larger if the error in the likelihood function is increased.

Not only the corrosion degree itself is updated, but also the underlying initiation period and corrosion rate. The posterior distributions for these variables are given in Figure VI-31 and Figure VI-32 for updating with and without the visual observation when measuring strains under proof loading at element 4. It can be seen that the uncertainty of the initiation period is indeed decreased. Due to this additional information regarding the initiation period, the information obtained from the strain measurements can be used to update the corrosion rate. Here, the posterior distribution shows a decreased uncertainty and provides a better characterization of the actual corrosion rate. For the natural frequencies and displacement mode shapes or strain mode shapes, a similar effect can be observed. For the natural frequencies and displacement mode shapes, the maximum coefficient of variation (COV) of the initiation period is reduced from 0.45 to 0.19, and when updating based on the natural frequencies and strain mode shapes, the maximum COV of the initiation period is reduced from 0.41 to 0.24.
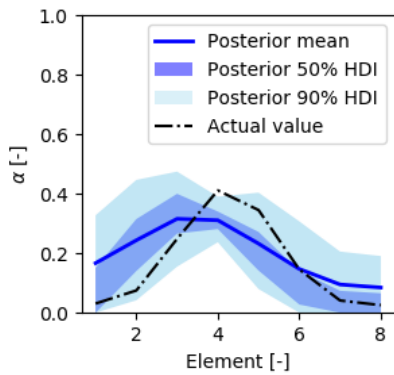
Next, both the visual observation of rust stains and the observation of severe cracking are accounted for. The posterior distribution of the corrosion degree when adding this additional visual observation is given in Figure VI-33 for the static strain data. For this case and the other cases, the posterior statistics are also summarized in Table VI-8. A first observation when looking at the provided results is that the influence of adding the visual observations is largest for the static strain data and the natural frequencies and displacement mode shapes, since these originally provide a more vague posterior distribution of the corrosion degree. A second observation is based on Figure VI-31 and Figure VI-32. Here it can be seen that the largest reduction in uncertainty is found for the initiation period. The influence on the corrosion rate is limited, even when including additional observations of severe cracking. This could be ascribed to the fact that the time to cracking and the time to severe cracking are relatively short with respect to the initiation period. Furthermore, changing the corrosion rate often does not lead to an increase or decrease of the time to (severe) cracking larger than three years (i.e. the time between consecutive visual inspections). Hence, the largest part of the reduction on the uncertainty of the corrosion rate is ascribed to the accompanying measurement data. Finally, the influence of adding the visual observation of severe cracking is rather limited compared to the initial influence of adding the visual observation of rust stains. The latter updates the initiation period to a large extent. The time to severe cracking depends on the corrosion rate, but as already pointed out, the influence is limited. Adding the time to severe cracking does not update the initiation period and only updates the corrosion rate to a very small extent. Hence, for this specific situation, including the observations of rust stains in the Bayesian procedure is worth the effort, but the observation of severe cracking should not necessarily be accounted for.

Table VI-8: Influence of visual observations on the posterior statistics (RMS, minimum standard deviation σ_{min}, maximum standard deviation σ_{max} and average standard deviation $\sigma_{average}$) for the simply supported beam

Data	RMS	σ_{max}	σ_{min}	$\sigma_{average}$
Static strain at element 4	0.093	0.132	0.053	0.102
Static strain at element 4 + rust stains	0.033	0.090	0.042	0.063
Static strain at element 4 + severe cracking	0.033	0.097	0.038	0.065
Natural frequencies and displacement mode shapes	0.023	0.101	0.079	0.090
Natural frequencies and displacement mode shapes + rust stains	0.023	0.075	0.037	0.062
Natural frequencies and displacement mode shapes + severe cracking	0.015	0.071	0.031	0.050
Natural frequencies and strain mode shapes	0.023	0.101	0.079	0.090
Natural frequencies and strain mode shapes + rust stains	0.003	0.075	0.008	0.039
Natural frequencies and strain mode shapes + severe cracking	0.003	0.071	0.008	0.038

Table VI-9: Influence of visual observations on the posterior statistics (RMS, minimum standard deviation σ_{min}, maximum standard deviation σ_{max} and average standard deviation $\sigma_{average}$) for the simply supported beam, increased measurement error

Data	RMS	σ_{max}	σ_{min}	$\sigma_{average}$
Static strain at element 4 (error 3 $\mu\varepsilon$)	0.038	0.120	0.104	0.113
Static strain at element 4 (error 3 $\mu\varepsilon$) + rust stains	0.033	0.110	0.061	0.088
Static strain at element 4 (error 10 $\mu\varepsilon$)	0.110	0.120	0.110	0.100
Static strain at element 4 (error 10 $\mu\varepsilon$) + rust stains	0.030	0.110	0.056	0.086
Natural frequencies (error $0.01\bar{\lambda}_r$,) and displacement mode shapes (error $0.01\|\bar{\phi}_r\|$)	0.003	0.100	0.078	0.089
Natural frequencies (error $0.01\bar{\lambda}_r$,) and displacement mode shapes (error $0.01\|\bar{\phi}_r\|$) + rust stains	0.023	0.082	0.037	0.063
Natural frequencies (error $0.01\bar{\lambda}_r$,) and strain mode shapes (error 0.2 $\mu\varepsilon$)	0.028	0.100	0.079	0.089
Natural frequencies (error $0.01\bar{\lambda}_r$,) and strain mode shapes (error 0.2 $\mu\varepsilon$) + rust stains	0.020	0.078	0.038	0.061

a) Without visual observation
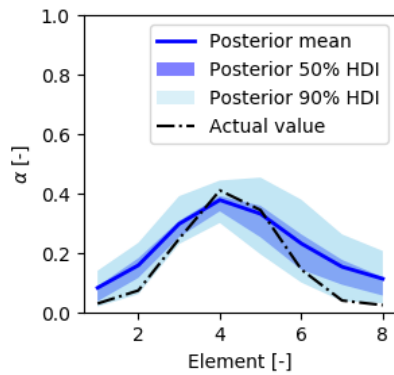
b) With visual observation of rust stains

Figure VI-30: Posterior corrosion degree of the simply supported beam when measuring the strains under proof loading at element 4 a) without visual observation, b) with visual observation of rust stains
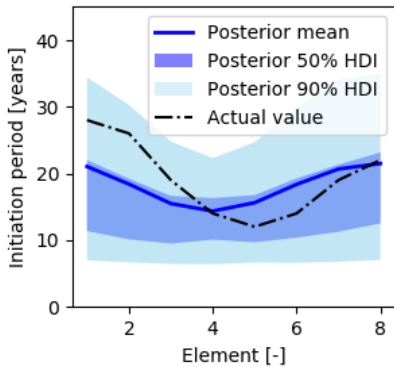
a) Without visual observation

b) With visual observation of rust stains

Figure VI-31: Posterior initiation period of the simply supported beam when measuring the strains under proof loading at element 4 a) without visual observation, b) with visual observation of rust stains

a) Without visual observation

b) With visual observation of rust stains

Figure VI-32: Posterior corrosion rate of the simply supported beam when measuring the strains under proof loading at element 4 a) without visual observation, b) with visual observation of rust stains

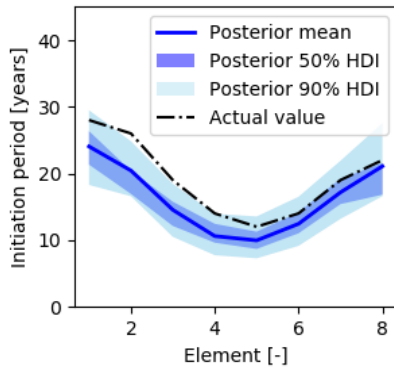a) With visual observation of rust stains

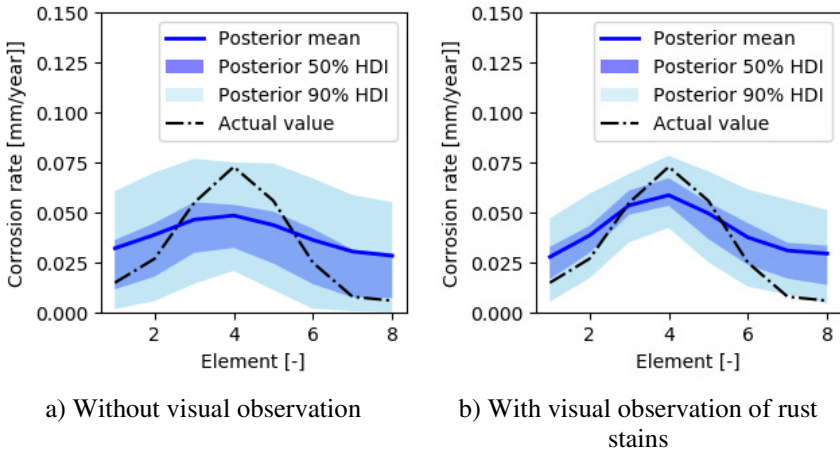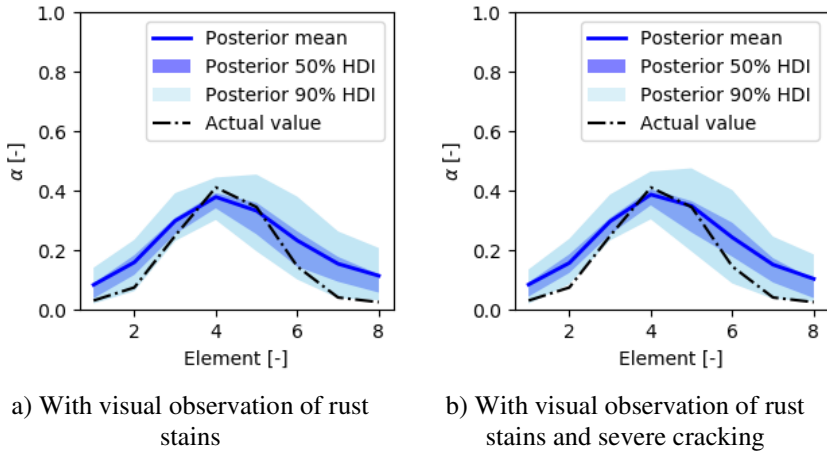b) With visual observation of rust stains and severe cracking

Figure VI-33: Posterior corrosion degree of the simply supported beam when measuring the strains under proof loading at element 4 a) with visual observation of rust stains, b) with visual observation of rust stains and severe cracking

Also for the RC girder bridge, the influence of incorporating the visual observations is investigated. The results are summarized in Table VI-10. When accounting both for the visual information and static strains measured at the two middle elements of each girder, the posterior distribution is visualized in Figure VI-34. The posterior corrosion degree shifts to higher values when including the information from the visual observations. Moreover, the posterior mean better approximates the actual corrosion degree compared to the case where only the static strain measurements are accounted for. When for the RC girder bridge the natural frequencies and strain mode shapes are combined with the visual observations, the resulting posterior distribution is visualized in Figure VI-35. Here it can be seen that the posterior uncertainty is reduced with respect to the case where no visual observations are accounted for. Moreover, the posterior distribution shifts to higher values, inducing a slight overestimation of the corrosion degree. Similar observations are found when combining the visual observations with natural frequencies and displacement mode shapes, as visualized in Figure VI-36.

Table VI-10: Influence of visual observations on the posterior statistics (RMS, minimum standard deviation σ_{min}, maximum standard deviation σ_{max} and average standard deviation $\sigma_{average}$) of the RC girder bridge

| Data	RMS	σ_{max}	σ_{min}	$\sigma_{average}$
Static strains in the middle of the girders	0.0056	0.0087	0.0030	0.0064
Static strains in the middle of the girders+ rust stains	0.0043	0.0081	0.0019	0.0058
Static strains in the middle of the girders (error 10 µε)	0.0075	0.0098	0.0090	0.0095
Static strains in the middle of the girders (error 10 µε) + rust stains	0.0090	0.0087	0.0070	0.0080
Natural frequencies and displacement mode shapes	0.0042	0.0074	0.0045	0.0059
Natural frequencies and displacement mode shapes + rust stains	0.0046	0.0070	0.0041	0.0055
Natural frequencies and strain mode shapes	0.0034	0.0044	0.0023	0.0032
Natural frequencies and strain mode shapes + rust stains	0.0043	0.0040	0.0045	0.0059
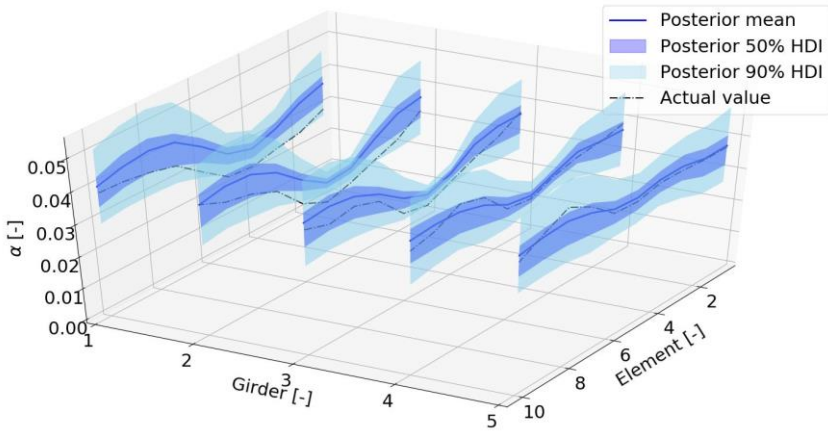
Figure VI-34: Posterior distribution of the corrosion degree of the RC girder bridge when accounting for static strains measured at the middle of the girders and visual observations
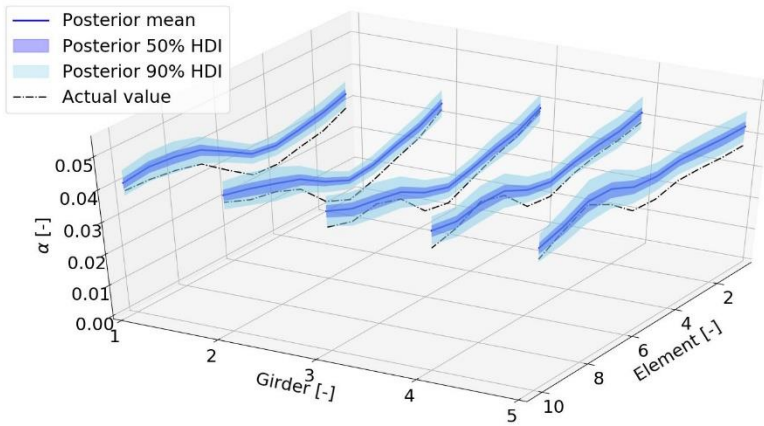

Figure VI-35: Posterior distribution of the corrosion degree of the RC girder bridge when accounting for natural frequencies, strain mode shapes and visual observations
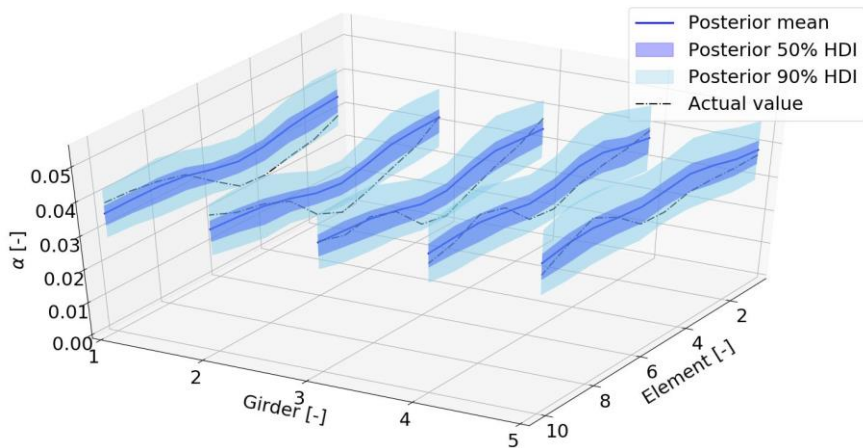
Figure VI-36: Posterior distribution of the corrosion degree of the RC girder bridge when accounting for natural frequencies, displacement mode shapes and visual observations

VI.4 Summary and conclusions

Data used for updating of a structural model is in many cases indirectly related to the degradation of the structure. This is for example the case for strains or displacements measured under proof loading and modal data, which are indirect measures of the stiffness. In this chapter, it is investigated how strain and displacement data gathered under proof loading and modal data from (ambient) vibration tests, can be (jointly) used to update the distribution of the corrosion degree, accounting for the spatial character of corrosion. Strain data under proof loading provides accurate but local information on the corrosion degree. Modal data extracted from acceleration measurements, on the other hand, provides more global information, but with a larger uncertainty. It is investigated how the combination of these different types of data leads to a more accurate representation of the actual corrosion degree. The methods are applied to a simply supported reinforced concrete beam and an RC girder bridge, where the influence of corrosion is modelled by a reduced reinforcement section and a reduced stiffness of the concrete cover due to cracking.

First, static data obtained during a proof load test are considered. When strains measured under proof loading are used to estimate the real corrosion degree, a relatively accurate estimate of the corrosion degree is found at the elements equipped with strain sensors, but not at the elements where no measurements are performed. The accuracy of the approximation also depends on the corresponding measurement error. When considering displacement data, large posterior uncertainties are found, with a posterior mean value that does not approximate the

actual corrosion degree. Damage can be detected if the corrosion degree is sufficiently large, but it cannot be estimated accurately.

A disadvantage of proof loading is that the structure should be taken out of service. Therefore, modal data from ambient vibration tests could be applied in a first step to detect the presence and location of damage, since these measurements can be performed in operational conditions. It has been illustrated that accounting for natural frequencies and displacement mode shapes in the likelihood function leads to a posterior distribution following the underlying pattern of the corrosion degree, giving an indication of reduced stiffness where corrosion damage is present. Nevertheless, the posterior uncertainty remains rather large. Next, it is investigated what information can be extracted from strain mode shapes in terms of the corrosion state of the structure. It is shown how strain mode shapes indeed provide more local information compared to displacement mode shapes because modal strains are more sensitive to local changes in stiffness. Nevertheless, under the present assumptions, less precise estimates of the corrosion degree are obtained compared to the results from strains measured under proof loading.

It is also illustrated how modal data can detect and localize damage, and for example trigger proof loading and help identifying relevant locations for strain measurements. When these measurement results are combined, a significantly more accurate and precise estimate of the actual corrosion degree is found. For the different data types, it is also illustrated how the measurement error influences the posterior distribution.

Also the influence of including visual observations about the presence of corrosion (by observing rust stains or corrosion cracks) is investigated. It should be pointed out that operator bias is assumed not to be present and hence not accounted for. If operator bias is expected, this should be included in the inference. Furthermore, in the analyses performed in this work, the visual observations are used to update the distribution of the initiation period (and of the corrosion rate). Nevertheless, an interesting addition might be to also consider information on the underlying parameters in the model for the initiation period, to improve the estimate on the latter. This information could for example be retrieved from cover measurements, measurements of chloride profiles on concrete cores, etc. The resulting data could also be included in the Bayesian inference scheme. In general, the methods described in this chapter can also be applied to other data types that are indirectly related to the stiffness of the structure and hence the underlying degradation, or directly related to variables in the degradation models.

The method developed in this chapter allows updating the corrosion degree based on heterogeneous measurement data consisting out of modal data and static strain

data, possibly combined with visual observations. The shortcomings and advantages of both types of data separately are discussed and illustrated by examples. The results of combining both types of data show how a more accurate posterior distribution of the corrosion degree can be achieved when accounting for heterogeneous measurement data. Even though for visualization purposes only the posterior distribution of the corrosion degree has been plotted, this distribution is obtained from the posterior distributions of variables such as the initiation period and corrosion rate, which can be used to model degradation at later timesteps. This will be used in later chapters of this work to evaluate the probability of failure over time. Here, the assumption will be made that the distribution of the corrosion rate is time-independent, i.e. a constant corrosion rate is assumed. Time-dependent models for the corrosion rate are also available in literature and, if required, could be taken along in the applied procedures.

The developed model-based framework can also be used to estimate which inspection technique has the highest impact on the predicted damage (and corresponding reliability), in order to assess the most optimal measurement techniques. For this purpose, different metrics exist to evaluate the performance of the posterior distribution. Examples are the Kullback-Leibler divergence (as applied in (Vereecken et al., 2022)), the information entropy (see Chapter X), the explanatory power (Sousa et al., 2020) (as applied in (Vereecken et al., 2020)), etc.

All results in this chapter depend on the assumptions made for the errors in the likelihood function (i.e. measurement and modelling errors). Other assumptions could be made, which might influence the shape and/or uncertainty of the posterior distribution. More research is required on the appropriate quantification of these measurement and/or model errors. In the current work, for the static strains, a large range of measurement errors is considered, from 0.5 to 10 µε. Even though this broad range of errors can occur in practice, for a well-designed experimental campaign with appropriate sensor locations, the measurement error can be limited, and a small measurement error can be used in the likelihood function. Nevertheless, in such a situation, also the contribution of a model error should be accounted for in the likelihood. For the natural frequencies, in the current work the experimental error is assumed relative to the natural frequency, since an absolute error would assign a relatively large weight to the higher order frequencies. Even though these can be measured more accurately due to the increasing gap between the frequencies, this effect is compensated by the decreasing excitability of these higher order modes. If more information on the difference in experimental accuracy of different modes is available, this could also be accounted for in the likelihood function. Also the models for the errors on the displacement mode shapes could be altered, which could resolve the scaling of the

error if the experimental mode shape is available at more locations (cfr. supra). For the strain mode shapes, an absolute error has been assumed, but this should be adjusted if scaling of the strain mode shapes is included. In general, lower measurement errors (if appropriate) will lead to lower posterior uncertainties and better approximations of the actual value. Nevertheless, if the measurement error is estimated too low, the posterior distribution might deviate from the actual value. The measurement error will not only depend on the measurement equipment itself, but also on environmental conditions, attachment of the sensors, possible occurrence of damage to the sensors, etc.

Since the error in the likelihood function influences the posterior distribution and hence the capability of a measurement technique to detect and quantify damage, thresholds can be defined for the required accuracy depending on the expected damage, or vice versa on the damage level that can be detected with a measuring technique with a given accuracy. Nevertheless, more research is required on this topic.

Also assumptions on the correlation models for the random fields have been made for the prior modelling of spatial correlation. In the present work, these will have limited influences on the results since the model for generating the data and the model used in the Bayesian inference are the same. When actual data is present, this prior choice for the correlation model might influence the results, even though it will also be inferred during the Bayesian updating procedure. More information on the influence of the prior correlation model can also be found in (Vereecken et al., 2021).

Even though Bayesian inference is a well-known method to account for measurement information in a probabilistic way, this chapter extends the existing state-of-the-art by updating the distributions of the variables in the degradation models based on indirect (static and dynamic) measurement information, accounting for the spatial variability and correlation of corrosion. In scientific literature, often the corrosion degree itself is inferred and not the variables in the underlying time-dependent degradation models, the spatial variation of the corrosion degree is not accounted for, and it is assumed that corrosion (variables) can be measured directly. It is hence the first time that static strains, static displacements, natural frequencies and mode shapes are used to update variables in the corrosion models, which can be modelled with random fields. Moreover, the influence of combining different data types is investigated together with the possible inclusion of information from visual observations.

VI.5 References

Anastasopoulos, D., De Smedt, M., Vandewalle, L., De Roeck, G., Reynders, E.P.B., 2018. Damage identification using modal strains identified from operational fiber-optic Bragg grating data. Struct. Heal. Monit. 17, 1441–1459.

Beck, J.L., Siu-Kui, A., Vanik, M.W., 2001. Monitoring structural health using a probabilistic measure. Comput. Civ. Infrastruct. Eng. 16, 1–11.

Bucher, C., 2009. Computational Analysis of Randomness in Structural Mechanics. CRC Press.

Carden, P.E., Fanning, P., 2004. Vibration Based Condition Monitoring: A Review. Struct. Heal. Monit. 3, 355.

Cross, E.J., Koo, K.Y., Brownjohn, J.M.W., Worden, K., 2010. Long-term monitoring and data analysis of the Tamar bridge. Proc. ISMA 2010 - Int. Conf. Noise Vib. Eng. 35, 1345–1357.

Dey, A., Miyani, G., Sil, A., 2019. Reliability assessment of reinforced concrete (RC) bridges due to service loading. Innov. Infrastruct. Solut. 4, 1–17.

DIANA FEA BV, 2019. DIANA User's Manual - Release 10.3 [WWW Document]. URL https://dianafea.com/manuals/d103/Diana.html

DIANA FEA BV, 2017. Random fields for non-linear finite element analysis of reinforced concrete structures [WWW Document].

Dilena, M., Morassi, A., Perin, M., 2011. Dynamic identification of a reinforced concrete damaged bridge. Mech. Syst. Signal Process. 25, 2990–3009.

Dooms, D., Jansen, M., De Roeck, G., Degrande, G., Lombaert, G., Schevenels, M., François, S., 2014. StaBIL : a Finite Element Toolbox for Matlab. Leuven.

Duracrete, 2000. DuraCrete - Probabilistic Performance based Durability Design of Concrete Structures. Report No BE9521347.

Enright, M.P., Frangopol, D.M., 1999. Condition Prediction of Deteriorating Concrete Bridges Using Bayesian Updating. J. Struct. Eng. 125, 1118–1125.

Enright, M.P, Frangopol, D.M., 1999. Reliability-based condition assessment of deteriorating concrete bridges considering load redistribution. Struct. Saf. 21, 159–195.

Faroz, S.A., Pujari, N.N., Ghosh, S., 2016. Reliability of a corroded RC beam based on Bayesian updating of the corrosion model. Eng. Struct. 126, 457–468.

fib, 2006. *fib* Bulletin 34: Model code for service life design. Lausanne.

Friswell, M., Mottershead, J., 1995. Finite element model updating in structural dynamics. Kluwer Academic Publishers, Dordrecht, The Netherlands.

Fritzen, C.P., Jennewein, D., Kiefer, T., 1998. Damage detection based on model updating methods. Mech. Syst. Signal Process. 12, 163–186.

Geyskens, P., Der Kiureghian, A., Monteiro, P., 1998. Bayesian Prediction of Elastic Modulus of Concrete. J. Struct. Eng. 124, 89–95.

Heitner, B., Obrien, E.J., Schoefs, F., Yalamas, T., Décatoire, R., Leahy, C., 2016. Probabilistic Modelling of Bridge Safety Based on Damage Indicators. Procedia Eng. 156, 140–147.

Heitner, B., OBrien, E.J., Yalamas, T., Schoefs, F., Leahy, C., Décatoire, R., 2019. Updating probabilities of bridge reinforcement corrosion using health monitoring data. Eng. Struct. 190, 41–51.

Lay, S., Schießl, P., Cairns, J., 2003. Lifecon Deliverable D3.2.

Lv, Q., Zhu, R., 2016. Model for forecasting the time of corrosion-induced reinforced concrete cracking, in: Dilum Fernando, Jin-Guang Teng, J.L.T. (Ed.), Proceedings of the Second International Conference on Performance-Based and Life-Cycle Structural Engineering (PLSE 2015). School of Civil Engineering, The University of Queensland, Brisbane, QLD, Australia, pp. 902–910.

Ma, Y., Zhang, J., Wang, L., Liu, Y., 2013. Probabilistic prediction with Bayesian updating for strength degradation of RC bridge beams. Struct. Saf. 44, 102–109.

Marsh, P.S., Frangopol, D.M., 2008. Reinforced concrete bridge deck reliability model incorporating temporal and spatial variations of probabilistic corrosion rate sensor data. Reliab. Eng. Syst. Saf. 93, 394–409.

Mottershead, J., Friswell, M., 1993. Model updating in structural dynamics: a survey. J. Sound Vib. 167, 347–375.

Neild, S.A., Williams, M.S., McFadden, P.D., 2005. Development of a vibrating wire strain gauge for measuring small strains in concrete beams. Strain 41, 3–9.

Ni, Y.Q., Wang, Y.W., Zhang, C., 2020. A Bayesian approach for condition assessment and damage alarm of bridge expansion joints using long-term structural health monitoring data. Eng. Struct. 212.

Rodrigues, C., Félix, C., Lage, A., Figueiras, J., 2010. Development of a long-term monitoring system based on FBG sensors applied to concrete bridges. Eng. Struct. 32, 1993–2002.

Schreppers, G.J., Frissen, C., Kang, H.J., 2011. Prediction of crack-width and crack-pattern, TNO Diana.

Simoen, E., 2013. Uncertainty Quantification in Finite Element Model Updating. PhD thesis, KU Leuven.

Simoen, E., De Roeck, G., Lombaert, G., 2015. Dealing with uncertainty in model updating for damage assessment: A review. Mech. Syst. Signal Process. 56, 123–149.

Simoen, E., Papadimitriou, C., Lombaert, G., 2013. On prediction error correlation in Bayesian model updating. J. Sound Vib. 332, 4136–4152.

Soman, R., Kyriakides, M., Onoufriou, T., Ostachowicz, W., 2018. Numerical evaluation of multi-metric data fusion based structural health monitoring of long span bridge structures. Struct. Infrastruct. Eng. 14, 673–684.

Sousa, H., Rozsas, A., Slobbe, A., Courage, W., 2020. A novel pro-active approach towards SHM-based bridge management supported by FE analysis and Bayesian methods. Struct. Infrastruct. Eng. 16, 233–246.

Stewart, M.G., Suo, Q., 2009. Extent of spatially variable corrosion damage as an indicator of strength and time-dependent reliability of RC beams. Eng. Struct. 31, 198–207.

Strauss, A., Frangopol, D.M., Kim, S., 2008. Use of monitoring extreme data for the performance prediction of structures: Bayesian updating. Eng. Struct. 30, 3654–3666.

Teughels, A., De Roeck, G., 2005. Damage detection and parameter identification by finite element model updating. Arch. Comput. Methods Eng. 12, 123–164.

Turkkan, N., Pham-Gia, T., 1993. Computation of the highest posterior density interval in Bayesian analysis. J. Stat. Comput. Simul. 44, 243–250.

Vereecken, E., Botte, W., Caspeele, R., Lombaert, G., 2020. Detecting and localizing corrosion induced damage in reinforced concrete structures based on modal data, in: Chen, A., Ruan, X., Frangopol, D.M. (Eds.), Proceedings of the 7th International Symposium on Life-Cycle Civil Engineering (IALCCE 2020). CRC Press, Shanghai, China.

Vereecken, E., Botte, W., Lombaert, G., Caspeele, R., 2021. Influence of the correlation model on the failure probability of a reinforced concrete structure considering spatial variability. Struct. Infrastruct. Eng.

Vereecken, E., Botte, W., Lombaert, G., Caspeele, R., 2022. Updating of corrosion parameters based on data from proof-loading and ambient vibration tests for the calculation of the life-cycle cost, in: Li, J., Spanos, P.D., Chen, J.B., Peng, Y.B. (Eds.), The 13th International Conference on Structural Safety and Reliability (ICOSSAR 2021). Shanghai, China.

Yang, D.Y., Frangopol, D.M., Teng, J., 2019. Probabilistic life-cycle optimization of durability-enhancing maintenance actions : Application to FRP strengthening planning. Eng. Struct. 188, 340–349.

Zheng, R., Ellingwood, B.R., 1998. Role of non-destructive evaluation in time-dependent reliability analysis. Struct. Saf. 20, 325–339.

CHAPTER VII

Experimental investigation of corroded reinforced concrete beams

"The true method of knowledge is experiment."
- William Blake

VII.1 Introduction

To validate the procedure described in the previous chapter, an experimental campaign is performed in the Magnel-Vandepitte lab. In this experimental campaign, beams are subjected to accelerated corrosion. On these corroded beams, static tests are performed, consisting of 4-point bending tests up to a load smaller than the cracking load of the beam. In addition, dynamic tests are performed, during which strains and accelerations are measured with optic fibres and accelerometers respectively. Finally, destructive tests are performed on the beams, also in a 4-point bending set-up. After the destructive tests, the reinforcement is removed from the beams, cleaned, and weighed. As such, the actual corrosion degree can be determined based on the mass loss of the reinforcement.

VII.2 Accelerated corrosion tests

To obtain sufficiently high corrosion degrees within a reasonable time, reinforced concrete specimens are in experimental research often exposed to accelerated corrosion. Accelerating corrosion can be achieved by manipulating the corrosion kinetics. To simulate the corrosion process naturally, the concentration of salts or the temperature could be increased (Zhu and François, 2014). The specimens could also be subjected to cyclic wetting and drying, as for example performed in (Altoubat et al., 2016). The wetting happens with a sodium chloride solution and is repeated until the desired corrosion degree is reached. Although the process is faster than natural corrosion, it still requires several months to depassivate the reinforcement. A more popular method is the use of anodic polarization. In this method, a DC current is applied, connecting the reinforcement (acting as the anode in the corrosion process) with a stainless steel plate (acting as the cathode) submerged in a salt solution. In literature, the concentration of the latter varies from 2% to 5% NaCl. This salt solution can be used to increase the rate of corrosion, or simulate a seawater environment. Specimens can either be immersed in the salt solution (Abosrra et al., 2011; Caré and Raharinaivo, 2007), or a bottomless basin with the salt solution can be placed on top of the specimens (Otieno et al., 2016). In some experiments, chlorides are mixed into the concrete specimens to arrive at immediate depassivation of the reinforcement and eliminate the initiation period. In this way, also a more uniform distribution of corrosion can be achieved. Regarding the electric circuit, either a constant voltage or a constant current can be applied. For the constant current, an upper limit of 100 µA/cm² is imposed in literature to have the same corrosion products as in the case of natural corrosion. However, some sources apply larger current densities, as for example (El Maaddawy and Soudki, 2007). Andisheh et al. (2019) state that the difference in corrosion products formed by applying accelerated corrosion tests is not really a problem when considering structural engineering applications and not looking into the details of the corrosion process itself. When a DC current is applied to the reinforcement bar and a stainless steel plate placed in the salt solution, the cathode

is located outside the concrete. As such, no OH- ions are formed within the concrete, which is different from the natural corrosion process, where OH- ions are produced inside the concrete. Nevertheless, from a structural point of view this is less important.

The theoretical amount of steel loss in an accelerated corrosion test can be calculated from equation (VII-1).

$$\Delta m = \frac{M \cdot I \cdot t}{z \cdot F} \tag{VII-1}$$

Here, Δm is the steel mass loss per unit surface, M is the atomic weight of iron atoms (56 g), I is the current in A, t the time in seconds, z the ionic charge, and F is the constant of Faraday (96 500 A/s).

VII.3 Description of the experimental campaign

In this experimental campaign, the procedure developed at the Building Materials and Constructions section of KU Leuven has been applied (Nasser et al., 2021; Van Steen et al., 2021, 2019a, 2019b).

VII.3.1 Layout of the beams

The tested reinforced concrete beams have a length of 5 m, a width of 300 mm and a height equal to 400 mm. The reinforcement ratio of the lower reinforcement was chosen to be equal to 1%. Hence, the tensile reinforcement consists of four bars of 20 mm diameter. The concrete cover on the longitudinal reinforcement equals 30 mm. The shear reinforcement has a diameter of 10 mm and a spacing of 270 mm. In addition, two bars of 16 mm diameter are provided as top reinforcement. A longitudinal section of the beams is given in Figure VII-1, and the cross-section of the beams is visualized in Figure VII-2. In Figure VII-1, it can be seen that the lower reinforcement extends 10 cm out of the beams in order to be able to connect the power source (cfr. infra) to the beams. At the ends of the beams, the last 5 cm of the tensile reinforcement inside the concrete and the first 5 cm of the reinforcement extending out of the concrete are coated. This coating is applied to avoid localized corrosion at the ends of the beams due to the higher presence of oxygen outside the concrete.
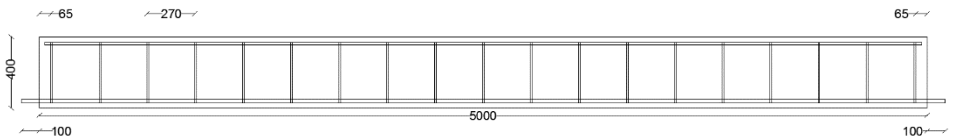
Figure VII-1: Longitudinal section of the beams (dimensions in mm)
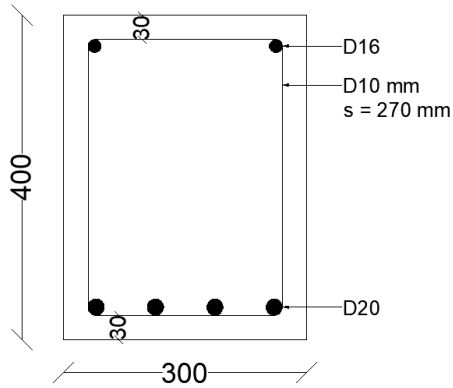
Figure VII-2: Cross-section of the beams (dimensions in mm)

In total, five beams have been casted, on three casting days. The beams are numbered according to Table VII-1 and the anticipated corrosion degrees (calculated according to equation (VII-1)) are mentioned.

Table VII-1: Specifications and names of the different beams

	Name	Anticipated corrosion degree	Remarks	Casting date
Set 1	Beam 1.1	30%		28/09/2020
	Beam 1.2	2%		
Set 2	Beam 2.1	25%		12/11/2020
	Beam 2.2	15%	No optic fibres	
Set 4	Beam 4.1	0%	Reference beam	09/12/2020

VII.3.2 Concrete composition

The concrete used for the beams corresponds to concrete code 30A4CK0S (BENOR) and has a composition according to Table VII-2. The concrete has chloride class 0.4%, environment class EI, maximum aggregate size D_{max} = 14 mm, consistency class S4 and strength class C25/30.

Table VII-2: Concrete composition

Component	Content [kg/m³]
K 6.3/14 (limestone 6.3/14 BENOR Holcim)	955
Sea sand	518
K 0/4 (washed limestone sand Holcim Gaurain BENOR)	427
CEM I 52.5 N Holcim	270
Water	174 (183 incl. absorption water)
Sky 571 (BASF)	1.9

VII.3.3 Accelerated corrosion

To accelerate the corrosion process, a current is applied to the reinforcement, together with a salt solution applied to the beam. The current and salt solution are applied for the first time when the beams have reached an age of 28 days. During the accelerated corrosion tests, the beam is turned upside down, i.e. the bottom reinforcement is located at the top of the beams. Then, a bottomless wooden tank is placed on top of the beams, which is filled with a 5% NaCl solution. Within this wooden tank, a stainless steel plate is placed, which acts as the cathode and is connected with the negative side of the power source. The 5% NaCl solution within the wooden tank works as an electrolyte. The bottom reinforcement is connected to the positive side of the power source and acts as the anode. A current density of 100 µA/cm² is applied to the reinforcement by a power source providing direct current. The top reinforcement is isolated from the stirrups and hence not subjected to the current. During the corrosion process, the set-up is placed in a climatised room with $60 \pm 10\%$ RH and temperature $21 \pm 2°C$. The set-up is illustrated in Figure VII-3.
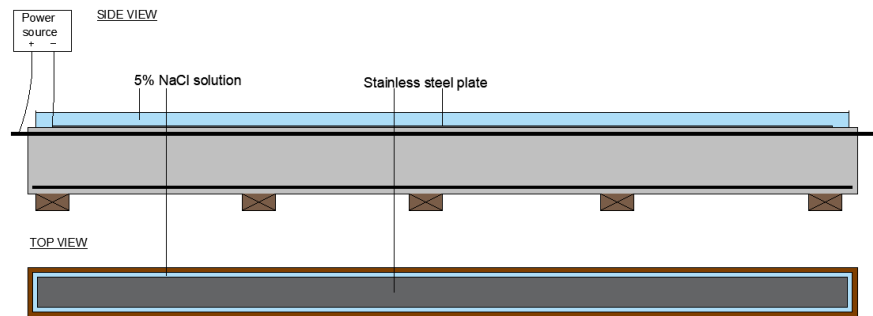
Figure VII-3: Visualization of the accelerated corrosion set-up

VII.3.4 Static and dynamic tests

The main purpose of the experimental campaign is to acquire static strain data and dynamic data on corroded reinforced concrete beams, which can then be used in a Bayesian inference procedure to estimate the corrosion degree of the beams (cfr. Chapter VI). The static tests, the destructive tests and the dynamic tests will be described in the following. The results of these tests will be discussed in more detail in section VII.6.

VII.3.4.1 Static load tests

The static tests are performed in a 4-point bending test set-up, as shown in Figure VII-4 and Figure VII-5. The locations of the loads are at one fourth of the span length. The loads are applied with hydraulic jacks. A steel plate (7.06 kg) or steel profile (12.3 kg) is placed in between the jacks and the beam in order to spread the load. When looking at the side of the beam to which the strain gauges are attached, the left support is a hinged support and the right support is a roller support (Figure VII-6). In between the jacks and the beam, also a load cell (2.592 kg (50 kN calibration), 3.960 kg (500 kN calibration)) is placed to measure the applied load (Figure VII-6).
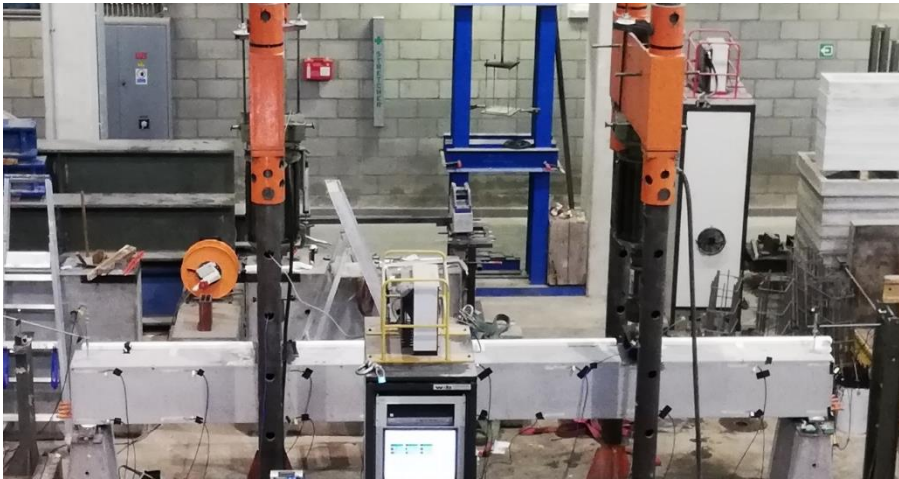
Figure VII-4: 4-point bending test set-up
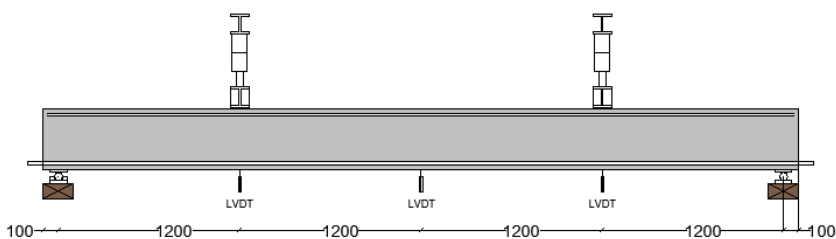
Figure VII-5: 4-point bending test set-up (schematic) (dimensions in mm)
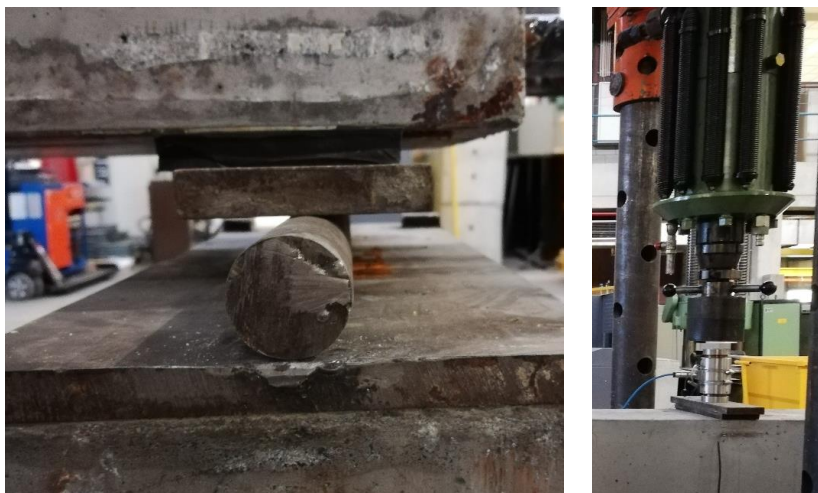
Figure VII-6: Roller support (left) and detail of jack - load cell – steel plate (right)

During the static load tests, strains are measured with strain gauges and displacements are measured with LVDT's. The locations of the LVDT's are visualized in Figure VII-5. In addition, an LVDT is present at each support. The locations of the strain gauges are visualized in Figure VII-7. The exact position of some of the strain gauges for some beams might slightly deviate from those illustrated in Figure VII-7 in order not to apply a strain gauge over existing cracks in the concrete (e.g. shrinkage cracks). The maximum applied load during the static load tests equals 15 kN in each loading point, which equals about 75% of the estimated cracking load.
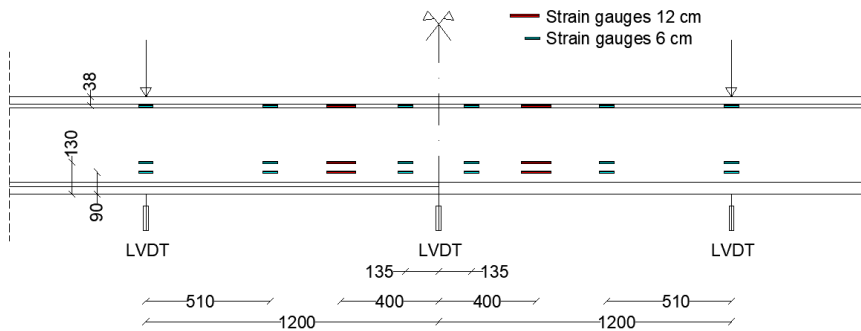
Figure VII-7: Positions of the strain gauges and LVDT's (at each support also an LVDT is present, but these are not visualized on this figure) (dimensions in mm)

VII.3.4.2 Destructive tests

The destructive tests are performed in the same set-up as the static load tests. The loading scheme is given in Table VII-3. The indicated load is the load in one of the loading points. Hence, the total load on the beam equals the given load multiplied by 2.

Table VII-3: Loading procedure for the destructive tests.

Start	Stop	Loading rate
0 kN	5 kN	50 N/s
5 kN	0 kN	50 N/s
0 kN	5 kN	50 N/s
5 kN	15 kN	50 N/s
15 kN	20 kN	50 N/s
20 kN	30 kN	50 N/s
30 kN	50 kN	50 N/s
50 kN	100 kN	50 N/s
100 kN	Failure	Displacement-controlled; +- 0.03 mm/s

After the destructive test, the tensile reinforcement is removed from the beams, cut into parts of 20 cm, and cleaned. The cleaning of the reinforcement is performed according to ASTM G1-03 (ASTM International, 2011). The specimens are submerged in a solution of 500 mL hydrochloric acid, 3.5 g hexamethylene tetramine and reagent water to make 1000 ml. Different cycles (10 minutes at room temperature) are performed, and after each cycle, the samples are weighed. The mass loss is then graphed as a function of the number of equal cleaning cycles. Two lines are obtained on this graph (AB and BC, see Figure VII-12). The second line corresponds to removal of the metal after removing the

corrosion products. The mass loss due to corrosion will hence approximately correspond to point B on the graph.
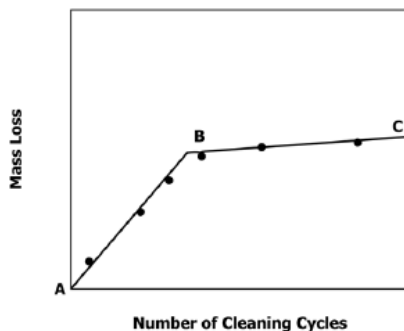
Figure VII-12: Mass loss of corroded specimens resulting from repetitive cleaning cycles (ASTM International, 2011)

VII.3.4.3 Dynamic tests

Dynamic tests are performed at an age of 28 days, i.e. before starting the corrosion process, and at the age corresponding to the anticipated corrosion degree, i.e. before performing the destructive tests. During the dynamic tests, the beams are placed on flexible supports to isolate them from the environment and solely measure the natural frequencies of the beam and not frequencies due to the interaction between the beam and the environment (free-free boundary conditions).

When performing the dynamic tests, the beams are subjected to a load inducing vibrations, and accelerations and strains are measured as a response to this load. The vibrations are induced by hitting on the beams with a small hammer. Each time, three tests are performed with thirty hammer impacts in the vertical direction and three tests with thirty hammer impacts in the lateral direction. Only for set 1 at 28 days, only two tests with lateral impacts are performed.

Accelerometers are fixed to the beam in order to measure the accelerations resulting from the hammer impacts (Figure VII-8). Twenty uniaxial accelerometers are applied to the top of the beam in order to measure the vertical accelerations and ten uniaxial accelerometers are applied to the side of the beam in order to measure the horizontal accelerations. As such, vertical bending modes, lateral bending modes and torsional modes can be extracted from the acceleration data. The positions of the accelerometers are visualized in Figure VII-9.
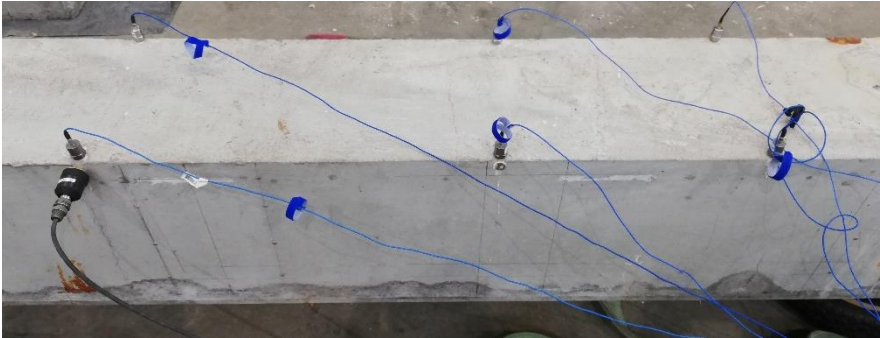
Figure VII-8: Accelerometers applied to the beam
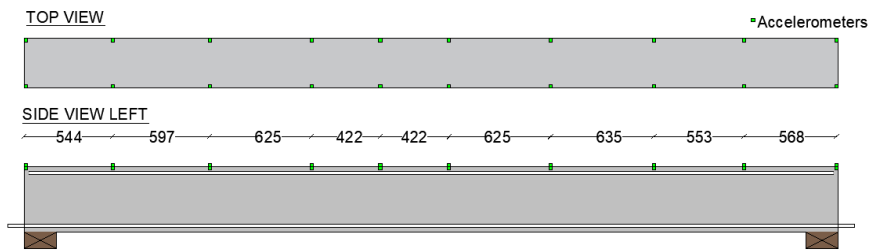
Figure VII-9: Locations of the accelerometers (dimensions in mm)

During the dynamic tests, strains are measured with optic fibres on some of the beams (cfr. Table VII-1). These strains can be used to extract strain mode shapes. The optic fibres are attached to the beams with a clamping system as visualized in Figure VII-10. The optic fibres are placed at one side of the beam. One optic fibre is applied along the top of the beam, and one at 6 cm from the bottom of the beam. The latter was chosen so that the fibres would not be in close contact with eventual corrosion products. For the reference beam, the optic fibres are respectively along the bottom of the beam and 6 cm from the top of the beam.

Figure VII-10: Optical fibre connected to the beam with clamping system

The accelerations and strains measured during the dynamic tests should be post-processed in order to obtain natural frequencies, displacement mode shapes and strain mode shapes. This post-processing is performed by a system identification with MACEC, a MATLAB toolbox for experimental and operational modal analysis developed by the Structural Mechanics Section of KU Leuven (Reynders et al., 2014). The covariance-driven stochastic subspace identification (SSI-COV) is applied, which is an output-only identification technique. Since the force is also measured, also the combined deterministic-stochastic subspace identification (CSI) can be used. Nevertheless, the signal of the hammer is not always very good, and in those situations, SSI-COV is preferred. In both techniques, the maximum system order and half number of Hankel's block rows need to be defined (Anastasopoulos, 2020; Peeters and De Roeck, 1999; Reynders and De Roeck, 2008). The latter is chosen equal to 30, and the system order is given as 2:2:100. The system identification is performed in the time domain, and during data processing, the static or direct current offset is removed from the measured signals (Anastasopoulos, 2020; Peeters and De Roeck, 1999; Reynders et al., 2014; Reynders and De Roeck, 2008). The identified frequencies are then manually selected from stabilization diagrams, as for example visualized in Figure VII-11 for beam 1.2 at 28 days and for a vertical impact.

The dynamic tests were performed in collaboration with dr. ir. Dimitrios Anastasopoulos from the Structural Mechanics section at KU Leuven, who is greatly acknowledged for his contribution in the execution of the tests. After a short introduction, processing of the data has been performed by the author herself. Hence, other than the execution of the dynamic tests, all the research mentioned in this work is original research performed by the author.
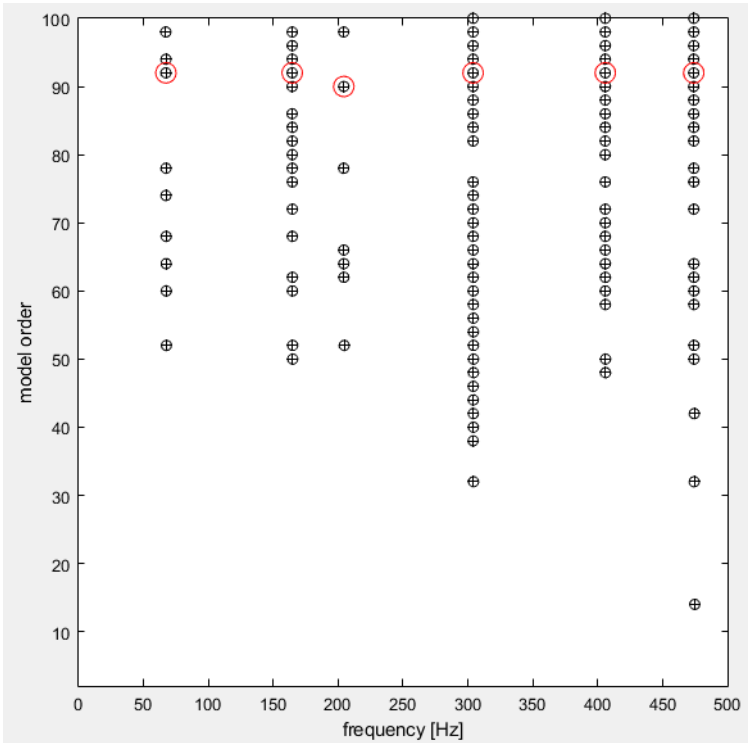
Figure VII-11: Stabilization diagram for beam 1.2 at 28 days for a vertical impact. Only the stable modes between 0 and 500 Hz are visualized. The red circles indicate the selected results.

VII.4 Test for material characterization and for the determination of the measurement error

When applying a Bayesian inference procedure, a model is required that simulates the measurement output as a function of the parameters to be updated (see section IV.2). In this research, a finite element model of the beams is used, which will be discussed in more detail in section VII.5. When creating this model, some input is required on the material properties of the concrete and the reinforcement steel. Hence, tests for material characterization have been performed. These tests and the obtained results are summarized in section VII.4.1.

When performing Bayesian inference, the obtained results depend on the measurement error (see section IV.2). Since this error is difficult to estimate for static strains measured on reinforced concrete elements, some tests on plain concrete prisms have been performed to gain insight in its order of magnitude. The test procedure and the results from these tests are discussed in section VII.4.2.

VII.4.1 Tests for material characterization

Tests to determine the strength and stiffness of the concrete have been performed. The cylinder compressive strength $f_{c,cyl}$ is tested on cylinders with height 300 mm and diameter 150 mm according to NBN EN 12390-3 (CEN, 2019a). The cube compressive strength $f_{c,cube}$ is tested on cubes with side 150 mm according to NBN EN 12390-3 (CEN, 2019a). The tensile strength is determined based on three-point bending tests on prisms with length 400 mm and sides of 100 mm. The flexural strength $f_{ct,fl}$ is determined based on NBN EN 12390-5 (CEN, 2019b). From the two parts of the sample resulting from this flexural test, the splitting strength $f_{ct,sp}$ is determined according to NBN EN 12390-6 (CEN, 2005a). Based on the splitting tensile strength, the axial tensile strength can be calculated as $f_{ct} = 0.9 \cdot f_{ct,sp}$ according to NBN EN 1992-1 (CEN, 2005b). From the bending tensile strength, the axial tensile strength can be determined according to equation (VII-2) (*fib*, 2013).

$$f_{ct} = A_{fl}f_{ct,fl} \text{ with } A_{fl} = \frac{\alpha_{fl}h_b^{0.7}}{1 + \alpha_{fl}h_b^{0.7}} \tag{VII-2}$$

Here, h_b is the beam depth (100 mm), and α_{fl} is a coefficient that accounts for the brittleness of the concrete and equals 0.06.

The fracture energy G_f is determined based on three-point bending tests on notched prisms. The prisms have a length of 400 mm and sides of 100 mm. The layout of the notch is visualized in Figure VII-13.
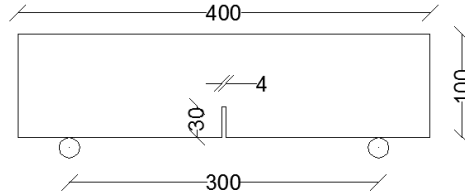
Figure VII-13: Layout of the sample for determination of the fracture energy, the rough surface is the front surface (dimensions in mm)

The chloride migration coefficient D_{RCM} is determined from non-steady-state migration experiments according to NT Build 492 (NORDTEST, 1999). These tests are performed on samples of diameter 100 mm and height 50 mm. Finally, the Young's modulus E_c is determined on cylinders of height 300 mm and diameter 150 mm according to EN 12390-13 (CEN, 2005c).

Material characterization is performed for the different sets of concrete. These test results have been determined at 28 days and at the age of the destructive tests of

the beams. For the reference beam, also intermediate results have been determined at the different testing ages. The results are summarized in Table VII-4 to Table VII-6. In these tables, only the mean value and corresponding uncertainty are provided. The reader is referred to Appendix A.2 for the individual testing results.

Table VII-4: Test results material characterization concrete set 1

	$f_{c,cyl}$ [MPa]	$f_{c,cube}$ [MPa]	f_{ct} [MPa]	G_f [N/mm]	D_{RCM} [mm²/year]	E_c [GPa]
Set 1 – 28 days						
Mean	39.0	42.9	3.3	0.10	1500	31.0
COV	0.03	0.015	0.16	/	0.07	0.02
Set 1 – 63 days (destructive test beam 1.2)						
Mean	37.8	/	2.8	0.15	/	37.6
COV	/	/	0.07	0.08	/	/
Set 1 – 330 days (destructive test beam 1.1)						
Mean	34.7	/	2.8	0.17	/	33.5
COV	/	/	0.17	/	/	/

Table VII-5: Test results material characterization concrete set 2

	$f_{c,cyl}$ [MPa]	$f_{c,cube}$ [MPa]	f_{ct} [MPa]	G_f [N/mm]	D_{RCM} [mm²/year]	E_c [GPa]
Set 2 – 28 days						
Mean	42.4	43.3	3.8	0.18	1631	32.7
COV	0.01	0.03	0.23	/	0.08	/
Set 2 – 182 days (destructive test beam 2.2)						
Mean	40.6	/	3.2	0.09	/	30.6
COV	0.04	/	0.11	/	/	0.01
Set 2 – 285 days (destructive test beam 2.1)						
Mean	40.7	/	3.7	0.12	/	33.6
COV	0.04	/	0.10	0.09	/	0.09

Table VII-6: Test results material characterization concrete set 4

	$f_{c,cyl}$ [MPa]	$f_{c,cube}$ [MPa]	f_{ct} [MPa]	G_f [N/mm]	D_{RCM} [mm²/year]	E_c [GPa]
Set 4 – 28 days						
Mean	37.6	41.0	3.2	0.13	1895	32.3
COV	0.02	0.01	0.13	0.2	0.09	0.05
Set 4 – 63 days (destructive test beam 1.2)						
Mean	40.7	/	3.3	0.12	/	/
COV	/	/	0.07	/	/	/
Set 4 – 182 days (destructive test beam 2.2)						
Mean	36.6	41.0	3.2	0.21	/	30.0
COV	/	/	0.10	/	/	/
Set 4 – 285 days (destructive test beam 2.1)						
Mean	36.3	41.0	3.5	0.14	/	35.0
COV	/	/	0.08	/	/	/
Set 4 – 330 days (destructive test beam 1.1 and beam 4.1)						
Mean	36.5	41.1	3.2	0.16	/	32.1
COV	0.04	/	0.06	/	/	0.05

Besides the concrete, also the properties of the reinforcement are characterized. Tensile tests are performed on reinforcement bars with length 1 m in a testing apparatus with a capacity of 1000 tons. The force and deformation are logged. The deformation is measured with two LVDT's with a measuring base of 200 mm. Tensile tests have been performed on the longitudinal and shear reinforcement in order to determine the stress-strain diagram. For each reinforcement type, three bars of length 1 m have been tested. The resulting stress-strain diagrams and the corresponding stress-strain diagram adopted in the finite element calculations are visualized in Figure VII-14.
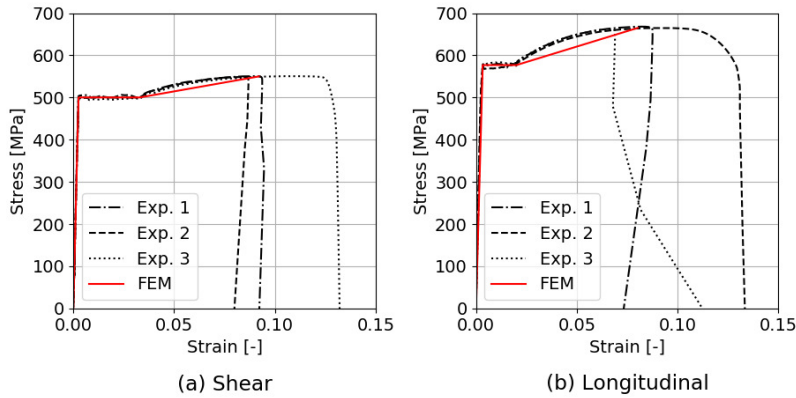
Figure VII-14: Stress-strain curve for (a) the shear reinforcement and (b) the longitudinal reinforcement

For the longitudinal reinforcement, a yield strength of 577 MPa is found and an ultimate strength of 665 MPa. The corresponding strains are 0.0033 and 0.08. For the shear reinforcement, a yield strength of 500 MPa and a tensile strength of 550 MPa are found, with corresponding strains of 0.0026 and 0.092.

VII.4.2 Determination of measurement error related to static strain measurements on (plain) concrete

Based on the results provided in Chapter VI, it could be concluded that is important to have an idea about the (order of magnitude of the) corresponding measurement error when performing Bayesian inference based on data resulting from dynamic tests or from proof loading. For static strain measurements with strain gauges, limited information on this topic is available in literature. Hence, an experimental campaign has been performed to arrive at an estimate for the measurement error corresponding to the static strain measurements. The samples used for these tests are three prisms, each with dimensions 400 mm x 100 mm x 100 mm. The prisms are subjected to 4-point bending tests with a span of 300 mm and a distance between the loading points of 150 mm. The prisms are each equipped with eight strain gauges (gauge length 6 cm), i.e. four on the front side and four on the back side, according to the configuration visualized in Figure VII-15. The names of the strain gauges are according to the same figure.

Front   **Back**
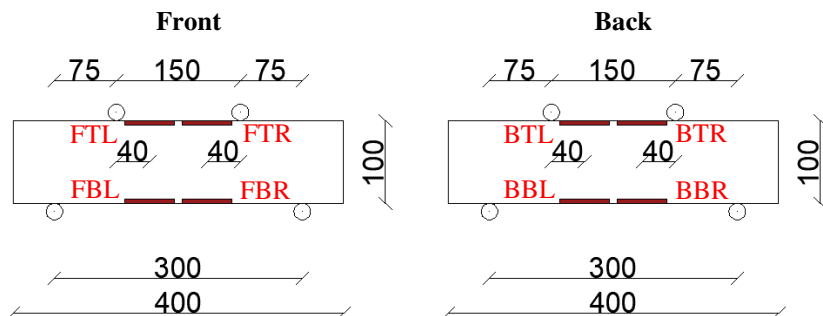
Figure VII-15: Configuration of the tests for determination of the measurement error related to static strain measurements on plain concrete (dimensions in mm)

For each sample, the load tests are performed according to the loading scheme provided in Table VII-7, where the given load represents the load in one loading point. Different load cycles are applied in order to be able to compare the strains between these different cycles. The maximum load of each cycle is 5 kN, which is lower than the cracking load. Assuming a tensile strength of 2.8 MPa, the cracking load is estimated to be 6.22 kN.

VII.4.2.1 Measurement results

In the following, the results for the different samples are summarized and discussed.

The strains at all the strain gauges of the first prism are visualized in Figure VII-16 (a). Here it can be seen that generally the differences between the results at the bottom fibre are limited. Cracking and failure occurred through strain gauges FBL and BBR. When considering the strains at the upper fibre, it can be seen that strain gauge FTR deviates from the others. This could be ascribed to the fact that this strain gauge is applied over a pit in the concrete surface. It should be pointed out that this could be prevented in practice.

Table VII-7: Loading procedure for the tests for determination of the measurement error. The load represents the load in one loading point, i.e. the total load applied to the prism equals two times this value.

Start [kN]	End [kN]	Rate [N/s]
0	1	50
1	5	50
5	0	50
0	1	50
1	5	50
5	0	50
0	1	50
1	5	50
5	0	50
0	1	50
1	5	50
5	0	50
0	1	50
1	FAILURE	50

a)   Sample 1

b)   Sample 2

c)   Sample 3

Figure VII-16: Strains in (a) sample 1, (b) sample 2 and (c) sample 3

The strains at all the strain gauges of the second prism are visualized in Figure VII-16 (b). Here a limited deviation can be observed between the results at the bottom fibre. Cracking and failure occurred through strain gauges FBL and BBR. The strains in strain gauge FBL generally deviate from the others. This could again be as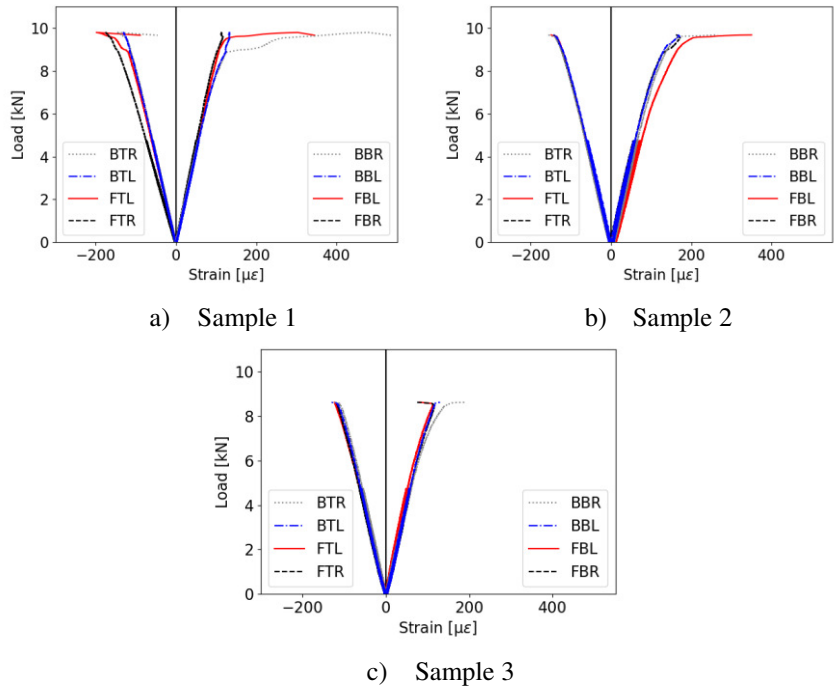cribed to the fact that strain gauge FBL is applied over a pit in the concrete surface. When considering the strains at the top fibre, it can be seen that the results of all strain gauges are close to each other.

The strains at all the strain gauges of the third prism are visualized in Figure VII-16 (c). Here it can be seen that generally the differences between the results are limited, but that the results of strain gauges FBL and BBR deviate from those of strain gauges FBR and BBL. This could again be ascribed to the presence of a pit in the concrete surface. When considering the strains at the top fibre, it can be seen that the results of all strain gauges are close to each other.

VII.4.2.2 Analysis of the measurement error

The measurement error is determined according to (Li et al., 2019). Here, a two-way ANOVA based Repeatability and Reproducibility (R&R) analysis is suggested to quantify the sources of the measurement error. This considers both the repeatability and the reproducibility. Statistical quantification of the repeatability, reproducibility, overall variability and error sources is performed. The input data for the analysis requires J different operators to measure each of I different parts a total of m times. In the current analysis, the J operators represent the eight different strain gauges on a sample ($J = 8$), the I different parts represent the three different samples ($I = 3$), and the m times the measurements are performed correspond to the five loading cycles ($m = 5$). The two-way random effects model is represented by equation (VII-3).

$$y_{ijk} = \mu + \alpha_i + \beta_j + \alpha\beta_{ij} + \varepsilon_{ijk} \qquad \text{(VII-3)}$$

Here, y_{ijk} is the kth measurement made by strain gauge j on sample i, μ is a measurement averaged over all possible strain gauges and all possible samples, α_i represents the random effects of the different samples, β_j represents the random effects of the different strain gauges, $\alpha\beta_{ij}$ represents the random joint effects to combinations of particular samples and strain gauges, and ε_{ijk} is the random measurement error.

According to the random effects model given by equation (VII-3), the only difference between different measurements for a specific combination of sample and strain gauge is the measurement error (ε), so its standard deviation (σ) is a measure of the repeatability of the model, or the repeatability error is given by equation (VII-4) (Li et al., 2019).

$$\sigma_{repeatability} = \sigma \tag{VII-4}$$

For a fixed sample i, the value $\mu + \alpha_i$ is constant for different measurements, so the measure of strain gauge bias for a fixed sample, i.e. $\sqrt{\sigma_\beta^2 + \sigma_{\alpha\beta}{}^2}$, is an appropriate measure of reproducibility:

$$\sigma_{reproducibility} = \sqrt{\sigma_\beta^2 + \sigma_{\alpha\beta}{}^2} \tag{VII-5}$$

Therefore, the overall variation due to repeatability and reproducibility ($\sigma_{R\&R}$) can be calculated based on equation (VII-6).

$$\sigma_{R\&R} = \sqrt{\sigma_{repeatability}^2 + \sigma_{reproducibility}{}^2} \tag{VII-6}$$

The two-way ANOVA analysis required to obtain the different parameters in these models is performed using the statistical software package SPSS. The resulting two-way ANOVA table will be of the shape as illustrated in Table VII-8. The samples (I) and strain gauges (J) are set as nominal variables for the two-way ANOVA analysis. The required standard deviations are calculated by application of equations (VII-7) to (VII-9) (Li et al., 2019).

$$\sigma_{repeatability} = \sigma = \sqrt{MSE} \tag{VII-7}$$

$$\sigma_{reproducibility} = \sqrt{\max\left(0, \frac{MSB}{mI} + \frac{(I-1)MSAB}{mI} - \frac{MSE}{m}\right)} \tag{VII-8}$$

$$\sigma_{R\&R} = \sqrt{\frac{MSB}{mI} + \frac{(I-1)MSAB}{mI} + \frac{(m-1)MSE}{m}} \tag{VII-9}$$

Equations (VII-7) to (VII-9) can be derived from a variance components analysis based on the ANOVA table (Table VII-8). The variance components in a two-way ANOVA analysis are given by equations (VII-10) to (VII-13).

$$\sigma^2 = MSE \tag{VII-10}$$

$$\sigma_\alpha^2 = \frac{MSA - MSAB}{mJ} \tag{VII-11}$$

$$\sigma_\beta^2 = \frac{MSB - MSAB}{mI} \qquad \text{(VII-12)}$$

$$\sigma_{\alpha\beta}^2 = \frac{MSAB - MSE}{m} \qquad \text{(VII-13)}$$

Table VII-8: Typical two-way ANOVA table for the R&R study, adapted from (Li et al., 2019)

Source	Sum of squares, SS	Degrees of freedom, df	Mean square, MS
Sample (I)	SSA	I-1	MSA=SSA/(I-1)
Strain gauge (J)	SSB	J-1	MSB=SSB/(J-1)
Sample x strain gauge (I x J)	SSAB	(I-1)(J-1)	MSAB=SSAB/(I-1)(J-1)
Error	SSE	$IJ(m$-1)	MSE=SSE/($IJ(m$-1))
Total	SSTot	IJm-1	-

The contributions of $\sigma_{repeatability}$ and $\sigma_{reproducibility}$ to $\sigma_{R\&R}$ are quantified by equations (VII-14) and (VII-15).

$$\text{Fraction of } \sigma_{R\&R} \text{ due to } \sigma_{repeatability} = \sigma_{repeatability}^2 / \sigma_{R\&R}^2 \qquad \text{(VII-14)}$$

$$\text{Fraction of } \sigma_{R\&R} \text{ due to } \sigma_{reproducibility} = \sigma_{reproducibility}^2 / \sigma_{R\&R}^2 \qquad \text{(VII-15)}$$

The abovementioned analyses are performed for the load levels ranging from 2 kN to 5 kN, based on the strain increase measured between a load of 1 kN and the considered load level. The results of the analyses are summarized in Table VII-9. Here, the COV represents the value of $\sigma_{R\&R}$ relative to the mean strain at the considered load level. When looking at the results in Table VII-9, it can be seen that the error $\sigma_{R\&R}$ increases with an increasing load level and an increasing average strain. The relative error (i.e. the COV) decreases for an increasing load level. Furthermore, the fraction due to $\sigma_{repeatability}$ decreases for an increasing load level while the fraction due to $\sigma_{reproducibility}$ increases, i.e. the contribution of the combination of sample and strain gauge decreases whereas the strain gauge bias for a fixed sample increases for an increasing load level.

Table VII-9: Results of the two-way ANOVA analysis in determination of the measurement error for load levels 2 kN to 5 kN

Load level	σ_{repeat} [με]	σ_{reprod} [με]	$\sigma_{R\&R}$ [με]	Mean strain [με]	COV [-]	Fraction σ_{repeat} [-]	Fraction σ_{reprod} [-]
2 kN	0.66	1.11	1.29	12.17	0.11	0.26	0.74
3 kN	0.72	2.12	2.24	24.19	0.09	0.10	0.90
4 kN	0.81	3.03	3.13	36.21	0.09	0.07	0.93
5 kN	1.05	4.04	4.18	48.29	0.09	0.06	0.94

The same analysis is performed for the load levels of 6 kN, 7 kN and 8 kN. For these load levels, no different loading cycles are performed, hence $m = 1$. This also means that the repeatability error cannot be determined for these load levels and only the strain gauge bias for a fixed sample can be determined ($\sigma_{reproducibility}$). The results are summarized in Table VII-10. It can be seen that the value of $\sigma_{reproducibility}$ relative to the average strain increases for an increasing load level. If the fraction of the reproducibility error to the total error would be equal to 0.94, as found for the load level of 5 kN (Table VII-9), the total error would be equal to the values given in Table VII-11.

Table VII-10: Results of the two-way ANOVA analysis in determination of the measurement error for load levels 6 kN to 8 kN

Load level	$\sigma_{reproducibility}$ [με]	Mean strain [με]	COV [-]
6 kN	4.52	60.99	0.07
7 kN	5.67	74.84	0.08
8 kN	7.37	90.70	0.08

Table VII-11: Results of the determination of the measurement error for load levels 6 kN to 8 kN, assuming Fraction due to $\sigma_{reproducibility}$ equal to 0.94

Load level	σ_{repeat} [με]	σ_{reprod} [με]	$\sigma_{R\&R}$ [με]	Mean strain [με]	COV [-]	Fraction σ_{repeat} [-]	Fraction σ_{reprod} [-]
6 kN	1.14	4.52	4.66	60.99	0.07	0.06	0.94
7 kN	1.43	5.67	5.85	74.84	0.08	0.06	0.94
8 kN	1.86	7.37	7.61	90.70	0.08	0.06	0.94

In general, repeatability and reproducibility errors are based on a one-way ANOVA analysis. Here, the repeatability variance is estimated as the error variance from the one-way ANOVA analysis and represents the variance within the considered factor. The reproducibility variance is then the sum of this repeatability variance and the between factor variance. The results of different one-way ANOVA analyses (considering different factors) are summarized in Table VII-12 for a load level of 5 kN. Three different situations are considered, i.e. in the first situation the factor is chosen to represent the different strain gauges, in the second situation the factor corresponds to the different samples, and in the last situation, the factor corresponds to the different loading cycles. From these results, it can be concluded that the total error, here represented by $\sigma^2_{reproducibility}$ indeed corresponds to $\sigma^2_{R\&R}$ found in the previous analysis (taking into account some rounding errors).

Table VII-12: Results of the measurement error for load level 5 kN based on a one-way ANOVA analysis

Factor	$\sigma^2_{repeatability}$ (within factor variance)	Between factor variance	$\sigma^2_{reproducibility}$
Strain gauge	8.106	9.086	17.192
Sample	15.774	0.519	16.293
Loading cycle	16.379	0	16.378

VII.4.2.3 Measurement error in further analysis

In the following parts of this chapter, strains will be measured on reinforced concrete beams instead of on plain concrete prisms. Due to the larger scale and the presence of the reinforcement, a larger scatter of the resulting strains and hence a larger measurement error are expected. In the following analyses, a measurement error of 0.1 or 10% of the measured value will be assumed. This is based on the COV for the error due to repeatability and reproducibility ($\sigma_{R\&R}$) provided in Table VII-9 and Table VII-10. The measurement error is given relative to the measured value, since in Table VII-9 it can be seen that the absolute value of the error depends on the load level and hence on the order of magnitude of the measured strains. However, the COV is almost the same for the different load levels, indicating that the measurement error could be expressed relative to the measured value. For strain values lower than 10 µε, the measurement error of 10% of the measured value would result in a measurement error lower than 1 µε, which equals the accuracy of the measuring equipment. Hence, for these strains, the measurement error is set equal to 1 µε. For very high measured strains, the relative

error of 10% would lead to very high measurement errors, which are not realistic. However, these situations are not covered by the current experimental set-up. An upper boundary of 100 µε is derived based on literature (Dokoupil, 2017). For the analyses similar to those in Chapter VI and those performed in the current and later chapters, the (proof)load applied to the structure remains lower than the cracking load and hence these very high strain levels are not encountered.

VII.5 Finite element model

VII.5.1 Static tests

For simulation of the static tests, a 2D finite element model is created in DIANA FEA (DIANA FEA BV, 2019). The default mesher type is Hexa/Quad and the default mesh order is quadratic. The mid-side node location is determined based on linear interpolation. All reinforcement (i.e. bottom reinforcement, top reinforcement and shear reinforcement) is modelled as embedded reinforcement. Only when modelling the behaviour up to failure, bond-slip reinforcement is considered for the bottom reinforcement. The adopted concrete properties are the mean values resulting from the tests for material characterization (section VII.4.1) for the beam under investigation at the considered age. For set 1, the tensile behaviour of the concrete is modelled with a Hordijk tensile curve. For the beams of set 2, the brittle tensile model is assumed for the concrete, with a damage based reduction model for the Poisson's ratio reduction. The brittle model has been applied to set 2 since more (shrinkage) cracks are observed for these beams. The compressive behaviour of the concrete is assumed parabolic, with the Vecchio and Collins (1993) reduction model with a lower bound of 0.6 for the reduction curve. No increase due to stress confinement is accounted for. The reinforcement is modelled with Von Mises plasticity. The stress-strain curve is the one given in Figure VII-14. For the bond-slip interface, a normal stiffness modulus of 101800 N/mm³ is assumed and a shear stiffness modulus of 10180 N/mm³, calculated based on the rule of thumb that the normal stiffness modulus equals the stiffness divided by the element size of the embedding element and multiplied by 80 to 100 (DIANA FEA BV, 2021). The hardening hypothesis is strain hardening and the hardening type is isotropic hardening. At the supports and the load application points, steel plates are modelled in order to distribute the concentrated loads. The strains are calculated by a non-linear analysis in order to account for possible cracking. The destructive tests are simulated by a displacement-controlled analysis. The element size is 25 mm.

VII.5.2 Dynamic tests

To predict the natural frequencies and mode shapes, a 3D finite element model is generated in DIANA FEA (DIANA FEA BV, 2019) with element size 50 mm. The models for the concrete and reinforcement steel are the same as for the 2D model developed for the static tests. In contrast to the 2D model, no supports and loads are applied to the 3D model (free-free boundary conditions). A structural eigenvalue analysis is applied to determine the natural frequencies and displacement mode shapes. The strain mode shapes are evaluated based on the displacement mode shapes.

VII.6 Experimental results of the static and dynamic tests

VII.6.1 Crack width measurements and corrosion degree

Before destructive testing, crack widths have been measured where possible. At the bottom surface of the beams, this was sometimes difficult due to the presence of corrosion products leaking from the cracks as well as the presence of salt in the cracks. For the different beams, the average, minimum and maximum crack widths are summarized in Table VII-13. The locations of the cracks in beams 1.1, 1.2, 2.1 and 2.2 are visualized in Figure VII-17 to Figure VII-20, respectively.

Table VII-13: Minimum, maximum and average crack widths for each beam [mm]

	Beam 1.1	Beam 1.2	Beam 2.1	Beam 2.2
Bottom				
Average	0.61	0.21	0.43	0.36
Minimum	0.04	0.15	0.08	0.20
Maximum	1.30	0.39	0.70	0.70
Side optic fibres				
Average	0.16	0.11	0.08	0.07
Minimum	0.00	0.07	0.05	0.01
Maximum	0.30	0.14	0.10	0.16
Side strain gauges				
Average	0.30	0.14	0.26	0.03
Minimum	0.10	0.12	0.05	0.02
Maximum	0.60	0.16	0.40	0.04
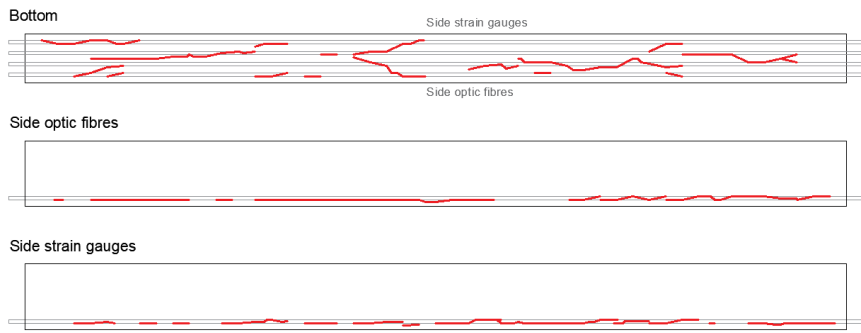
Figure VII-17: Locations of cracks on beam 1.1
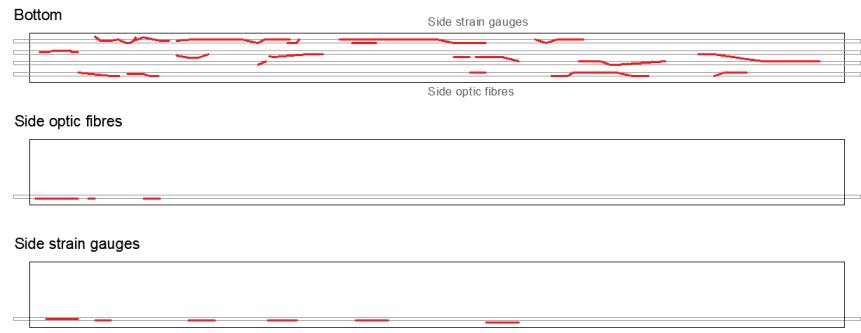
Figure VII-18: Locations of cracks on beam 1.2
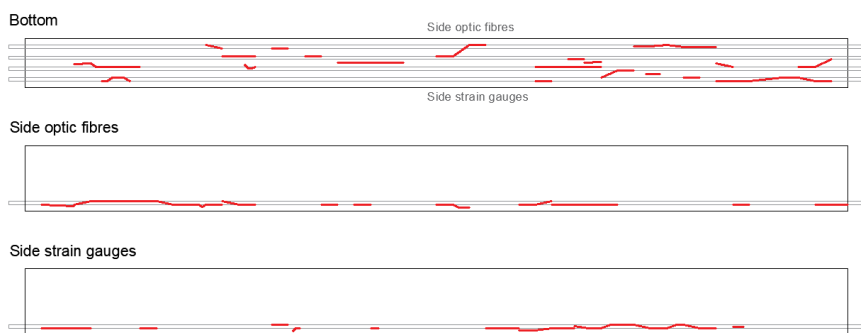
Figure VII-19: Locations of cracks on beam 2.1
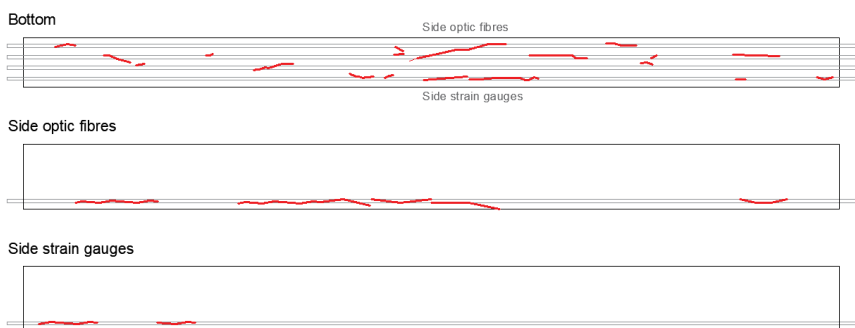
Figure VII-20: Locations of cracks on beam 2.2

The corrosion degrees of the four beams after cleaning and weighing of the reinforcement bars are visualized in Figure VII-21. These represent the total mass loss over the four bars at each location x. The x-coordinate with value 0 corresponds to the left side of the beam when looking at the side with the strain gauges. The corrosion degrees of the individual bars can be found in Appendix A.1. The average corrosion degrees over the length of the beams are the following:

- Beam 1.1: 6.2%;
- Beam 1.2: 2.7%;
- Beam 2.1: 6.6%;
- Beam 2.2: 5.2%.

These corrosion degrees only account for the longitudinal reinforcement.
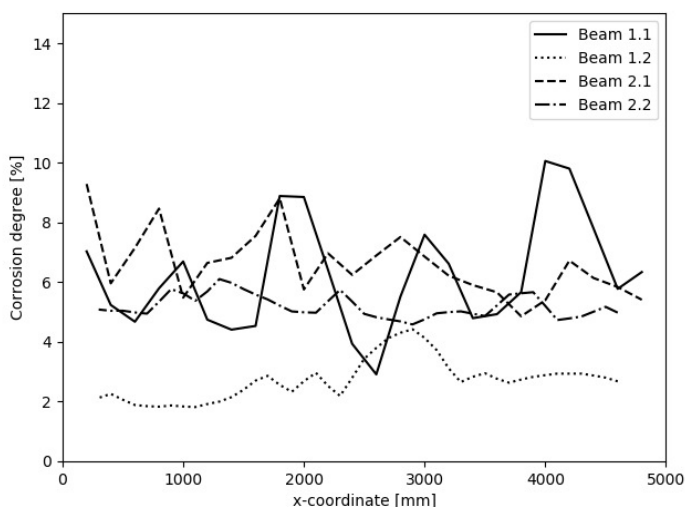
Figure VII-21: Corrosion degrees of the four corroded beams (x = 0 corresponds to the left side when looking at the side with the strain gauges)

VII.6.2 Static tests

For beam 1.1 (6.2% corrosion), beam 2.1 (6.6% corrosion) and beam 2.2 (5.2% corrosion), the differences in strains measured between the load levels of 5 kN and 15 kN (i.e. the load in one loading point) are visualized in Figure VII-22 to Figure VII-24. Here, the positive strains correspond to those measured at a height of 90 mm (upper graphs) and 130 mm. The negative strain values correspond to those measured at a height of 362 mm. For beam 1.2 (2.7% corrosion), the strain results from the static tests at 63 days are not available. In Figure VII-22 to Figure VII-24, the black lines represent the strains measured with the short strain gauges of 6 cm, whereas the black scatter plots represent the results of the long strain gauges of 12 cm. The error bars on these plots represent the 95% confidence intervals when accounting for a measurement error of 10% of the measured value (according to section VII.4.2). The red lines represent the results of the finite element model, inserting the actual spatial corrosion degrees (as visualized in Figure VII-21). The hatched red zone indicates the 95% confidence interval on the model predictions when accounting for a model uncertainty with a lognormal distribution with mean 1 and COV 0.1. The latter is based on (Allaix et al., 2015), but with an increased COV. The COV has been increased to account for the fact that different models can be used to model the influence of corrosion, since no consensus is available for this. Furthermore, there is also a minor error made by application of the analytical model for the stiffness reduction compared to a more extensive finite element model. Also, the model error in (Allaix et al., 2015) has only been derived for under-reinforced beams and has not yet been generally calibrated. Finally, only rather small beams in well-controlled environments are considered in the analysis to derive the model error, whereas in this experimental campaign larger beams are used, with many shrinkage cracks. Hence, the COV has been increased to cover for these extra uncertainties and effects possibly influencing the difference between predicted and measured strains. When looking at the results, it can be seen that in general there is a reasonable agreement between the measured and predicted strains.
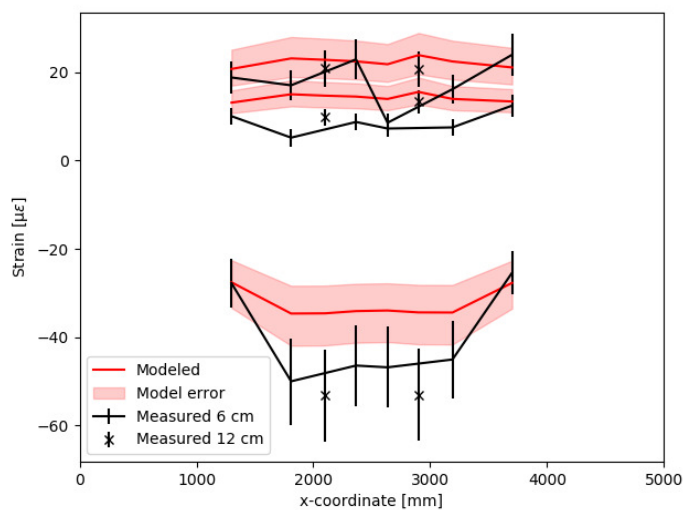
Figure VII-22: Static strains of beam 1.1 (6.2% corrosion)
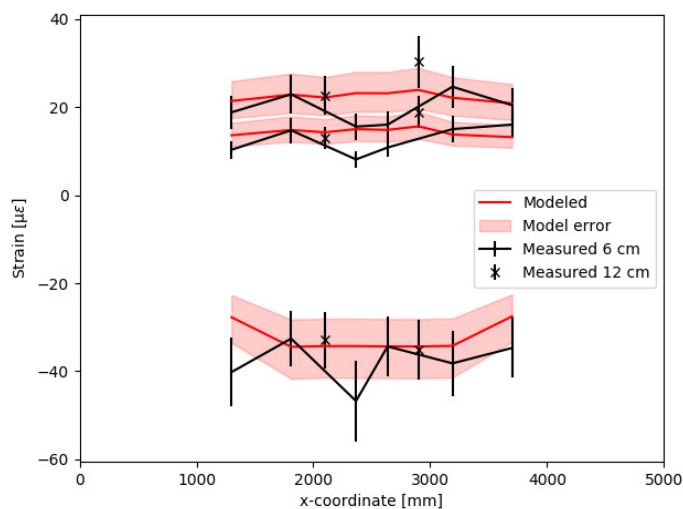
Figure VII-23: Static strains of beam 2.1 (6.6% corrosion)
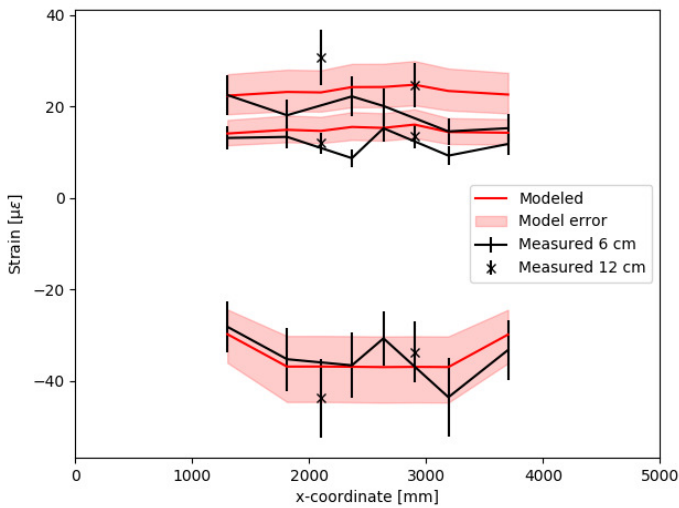
Figure VII-24: Static strains of beam 2.2 (5.2% corrosion)

When the strains of the reference beam are considered, results are available at an age of 185 days (age of destructive test on beam 2.2 (5.2% corrosion)), 285 days (age of destructive test on beam 2.1 (6.6% corrosion)) and 330 days (age of destructive test on beam 1.1 (6.2% corrosion)). These are visualized in Figure VII-25. The results obtained with the longer strain gauges around 3 m deviate significantly from the predicted strains. This could be ascribed to the fact that it was inevitable to apply these strain gauges over existing shrinkage cracks. When comparing the strain results at these different ages, the strains are very close to each other. Hence, no reduction in stiffness could be derived from these strain measurements. In addition, when comparing the results of the reference beam with those of the corroded beams, some conclusions can be made. When considering the strain results that are within the uncertainty bounds around the simulated strains (see Table VII-14), the strains at the lowest measurement level are on average higher in absolute value for the corroded beams than for the reference beam at the same age. Nevertheless, the difference in strains often does not exceed the measurement error on the strains.
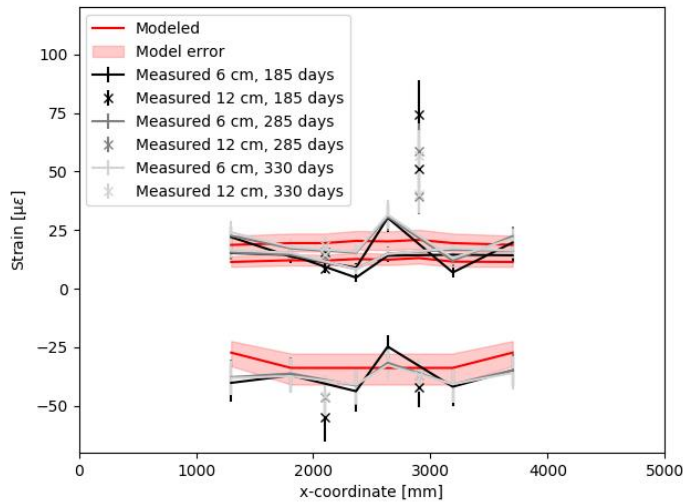
Figure VII-25: Static strains of beam 4.1 (reference)

Table VII-14: Average strains of strain results within the uncertainty bounds around the simulated strains for the different corroded beams and for the reference beam at the corresponding age

Beam (age)	Height of strain sensors		
	90 mm	130 mm	362 mm
Beam 2.2 (185 days)	22.37 με	13.39 με	-35.03 με
Beam 4.1 (185 days)	20.82 με	14.47 με	-37.03 με
Beam 2.1 (285 days)	21.68 με	14.01 με	-35.04 με
Beam 4.1 (285 days)	19.76 με	14.98 με	-33.94 με
Beam 1.1 (330 days)	21.89 με	9.40 με	-26.58 με
Beam 4.1 (330 days)	17.71 με	15.05 με	-35.00 με

VII.6.3 Destructive tests

The load-displacement curves from the destructive tests on the different beams are visualized in Figure VII-26. The displacement is the one measured at mid-span. It can be seen that the beams reached different ultimate load levels. Beam 1.1 (6.2%) failed due to crushing of the concrete in the compressive zone followed by a shear failure. A similar behaviour has been observed for beam 1.2 (2.7%). Beams 1.1 (6.2%) and 1.2 (2.7%) show a similar load-displacement behaviour. Beam 1.1 (6.2%) has a higher corrosion degree and indeed reaches a lower ultimate load than beam 1.2 (2.7%). In addition, the initial stiffness is lower for

beam 1.1 (6.2%). Beams 2.1 (6.6%) and 2.2 (5.2%) failed in shear. Beam 2.2 (5.2%) had the highest bearing capacity of all beams. Finally, beam 4.1 (reference) also failed in shear and its ultimate capacity was lower than for some corroded beams. The ultimate load for beam 4.1 (reference) and beam 2.1 (6.6%) is the same (166.5 kN). However, the behaviour of beam 4.1 (reference) is more stiff compared to the corroded beams. This can also be seen in more detail on Figure VII-27. Different failure modes are observed among the different beams. Small changes in material properties can lead to a shift in the failure mode. This also follows from analytical calculations for evaluation of a beam under bending, where, depending on the values of the material properties (within the ranges observed from the tests for material characterization), there is a shift from crushing of the concrete towards yielding and rupture of the reinforcement. Changing the material properties in the finite element model of the beams also leads to a shift in the governing failure mode or in the estimated ultimate load.
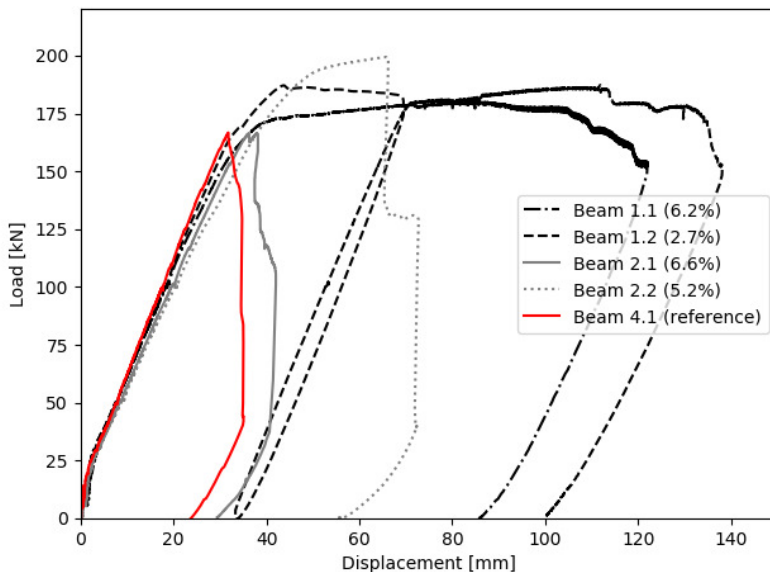
Figure VII-26: Load-displacement curves of the destructive tests on the different beams. The vertical axis represents the average of the load in the two loading points.
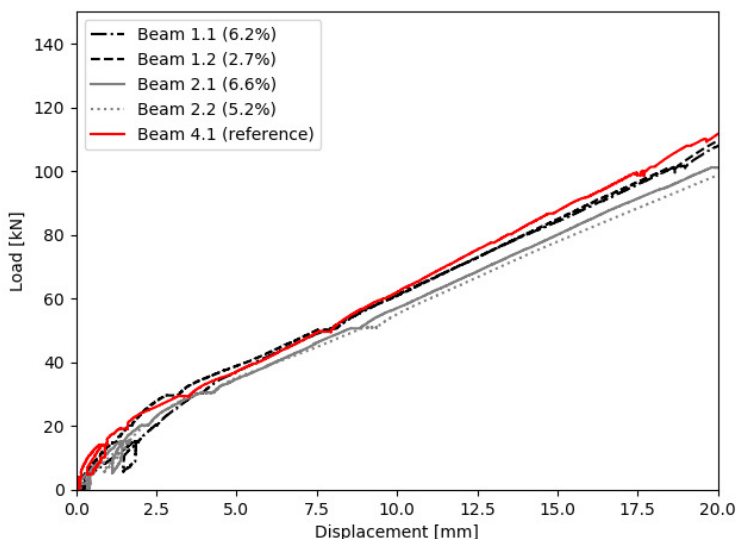
Figure VII-27: First part of the experimental load-displacement curves. The vertical axis represents the average of the load in the two loading points.

The destructive tests have also been simulated with the finite element model discussed in section VII.5.1. It has been investigated to what extent the finite element model results approximate the experimental load-displacement curve. In Figure VII-28, the load displacement curve of beam 1.1 (6.2% corrosion) is given for different finite element models and compared with the experimental curve. The different models considered are:

- **Minimum corrosion degree**. The minimum of the total corrosion degrees of beam 1.1 visualized in Figure VII-21 is assigned uniformly to the reinforcement over the total length of the beam. The steel section of the bottom reinforcement is adjusted, together with the Young's modulus of the concrete cover and the ultimate strain of the bottom reinforcement.
- **Maximum corrosion degree**. Similar as the previous model, but now the maximum of the total corrosion degrees of beam 1.1 is used instead of the minimum.
- **Average corrosion degree**. Similar to the previous models, but now assuming the average corrosion degree of 6.2% instead of the maximum or minimum corrosion degree.
- **Spatial corrosion degree**. The total corrosion degree according to Figure VII-21 is assigned to the beam, i.e. the bottom reinforcement is subdivided into different parts of 20 cm, each with a different steel section corresponding to the corrosion degree of that part. In addition, the ultimate strain of the different parts is adjusted to the corresponding

corrosion degree and the Young's modulus of the concrete cover varies
along the length of the beam.
- **Uncorroded**. The beam is modelled without assuming any corrosion.
In the finite element model, compression failure of the top reinforcement is
accounted for by altering the stress/strain relationship for the top reinforcement
according to (Akkaya et al., 2019; Maekawa et al., 2003; Massone and López,
2014; Urmson and Mander, 2012).
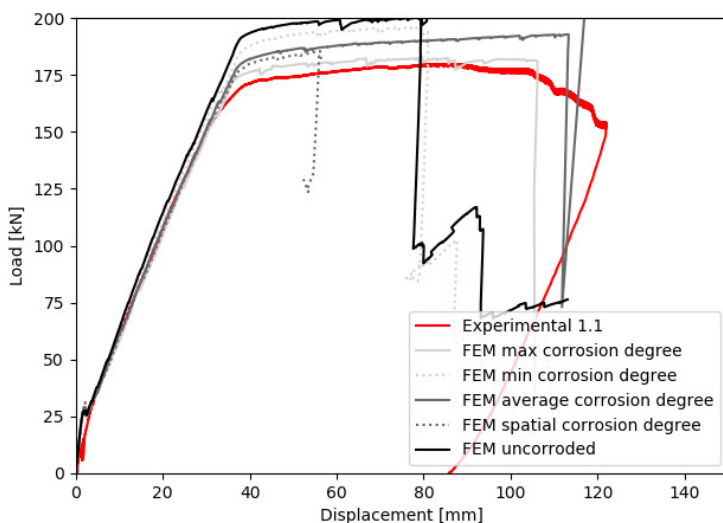
Figure VII-28: Experimental and predicted load-displacement curves of beam 1.1 (6.2%).
The vertical axis represents the average of the load in the two loading points.

When looking at the curves in Figure VII-28, it can be seen that the maximum
capacity is indeed reached for the uncorroded case. The maximum capacity
decreases when going from the minimum, over the average, to the maximum
corrosion degree. The latter curve approximates best the experimental curve.
Consequently, when in practice the corrosion degree would only be measured
locally (e.g. by locally removing the concrete cover), and this local corrosion
degree corresponds to a low value, the failure load will be overestimated. In this
specific case, the difference in estimated ultimate load based on the average
corrosion degree and the actually spatially variable corrosion degree is limited.
The fact that the load-displacement curve of the spatially variable corrosion degree
does not approximate the actual load-displacement curve could be ascribed to the
fact that this is still an average corrosion degree over a distance of 20 cm. Hence,
pit depths are averaged out over this distance. On the other hand, the finite element

model with the maximum corrosion degree gives a good approximation of the experimental failure load.

Similar analyses have been performed on the other beams.

VII.6.4 Dynamic tests

Below, the results of the dynamic tests are given for an increasing corrosion degree. When mode shapes are visualized, these are scaled to the results from the finite element model. This is required since in most cases the experimental modes are identified using output-only data, and therefore cannot be mass normalized. Hence, the experimental modes are scaled with a scaling factor γ_r, which can be obtained through a least-squares fit between experimental and predicted mode shapes according to equation (VII-16).

$$\gamma_r = \bar{\phi}_r^T \phi_r / \left\| \bar{\phi}_r \right\|_2^2 \qquad \text{(VII-16)}$$

Here, $\bar{\phi}_r$ is the experimental mode shape and ϕ_r the predicted mode shape.

VII.6.4.1 Beam 4.1 (Reference)

The reference beam is tested at 28 days and at the different testing ages of the other beams, i.e. 63 days, 182 days, 285 days and 330 days. As such, comparison can be made between the natural frequencies of a corroded beam and an uncorroded beam of the same age. This is necessary, since in young concrete there might also be other influences leading to natural frequency variations. The natural frequencies of the reference beam are summarized in Table VII-15. These are determined based on both strain measurements with optic fibres and acceleration measurements. To support the beams during the dynamic tests, three tyres were used, i.e. one at the left end, one in the middle and one at the right end of the beam. All tyres were inflated up to 1 bar. At an age of 63 days, only the measurements with the optic fibres have been performed, and at the age of 330 days, only acceleration measurements have been performed due to damage to the optic fibres. In Table VII-15, it can be seen that the natural frequencies of the reference beam decrease over time, even though the beam is not subjected to corrosion. The relative decrease is also illustrated in Figure VII-29 for the modes available at all testing ages. Here it can be seen that the natural frequencies seem to stabilize at later ages. The decrease in natural frequency over time could be ascribed to different causes. One reasoning would be to attribute the decrease to internal cracks that are present in a reinforced concrete beam. These cracks can originate from multiple causes, e.g. shrinkage. These cracks can open, even for a small load such as self-weight. Another explanation would be to ascribe the decrease in natural frequencies to the microstructure of the concrete and the composite character of reinforced concrete.

Table VII-15: Natural frequencies of beam 4.1 (reference) [Hz]

Mode	28 days	63 days	182 days	285 days	330 days
1st lateral	45.64	44.33		41.96	43.10
1st bending	61.97	60.66	58.45	58.40	55.60
2nd lateral	119.55	117.98	113.63	113.70	112.22
2nd bending	165.74	164.63	156.99	153.53	153.03
1st torsion	204.61		199.69	199.11	198.84
3rd lateral	228.89	226.25	221.30	218.41	217.51
3rd bending	305.75	301.05	292.24	288.41	286.40
4th lateral	363.71		350.62	345.68	343.85
3th torsion	409.76		403.32	402.04	400.99
4th bending	474.95		455.38	456.82	447.45
5th lateral	521.51		502.22	495.56	492.61
4th torsion	612.05		600.12	597.99	597.77
5th bending	665.19		638.55	629.76	626.69
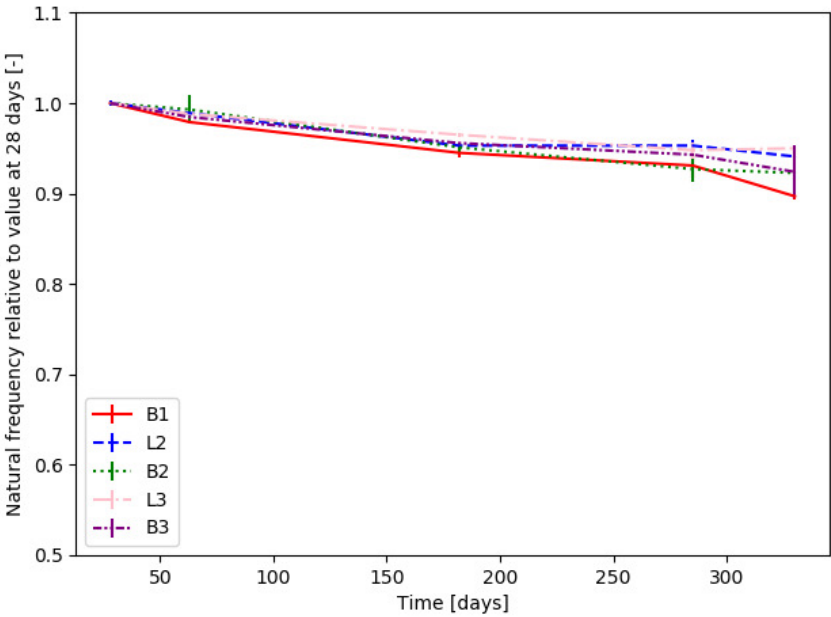
Figure VII-29: Evolution of natural frequencies of beam 4.1 (reference) as a function of time. The error bars represent the 90% confidence interval based on the standard deviation between the different dynamic tests at a specific testing age.

Besides natural frequencies, also displacement mode shapes (Figure VII-30) and strain mode shapes (Figure VII-31) are available for beam 4.1 (reference). When looking at the results at the different testing ages, there are no noticeable changes. This could be expected beforehand, since there is no damage of the beam. For the displacement mode shapes, there is a very local change in the third lateral bending mode at 285 days. However, this does not appear at the later testing age of 330 days. Hence, this could probably be ascribed to the use of damaged accelerometers in one test. Another cause for the deviation in displacement mode shapes could be damage to the glue used to attach the plate of the accelerometer, due to which the latter was not fixed tight enough to the beam.
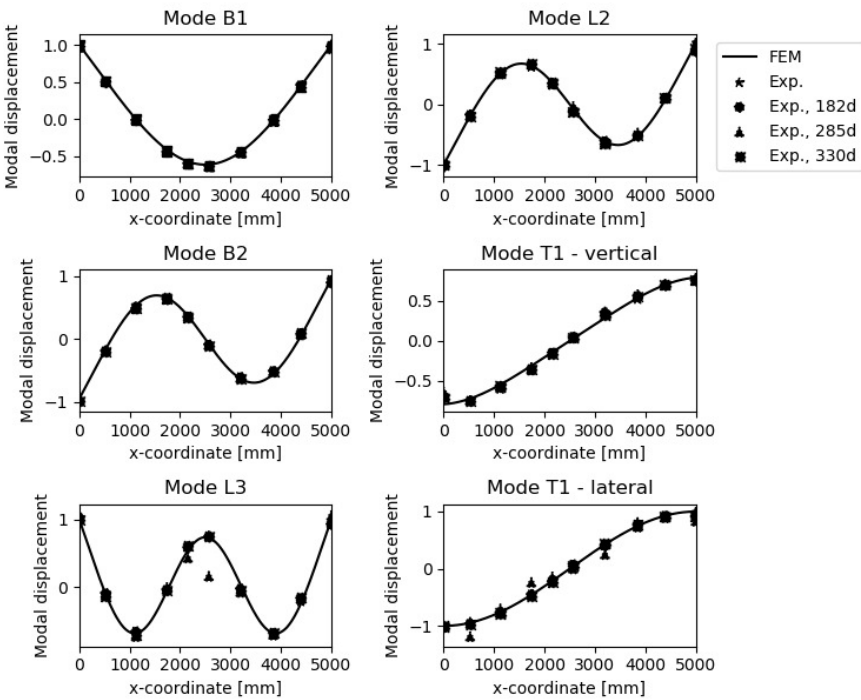
Figure VII-30: Displacement mode shapes of beam 4.1 (reference) ($x = 0$ mm corresponds to the left of the side of the beam with the optic fibres)
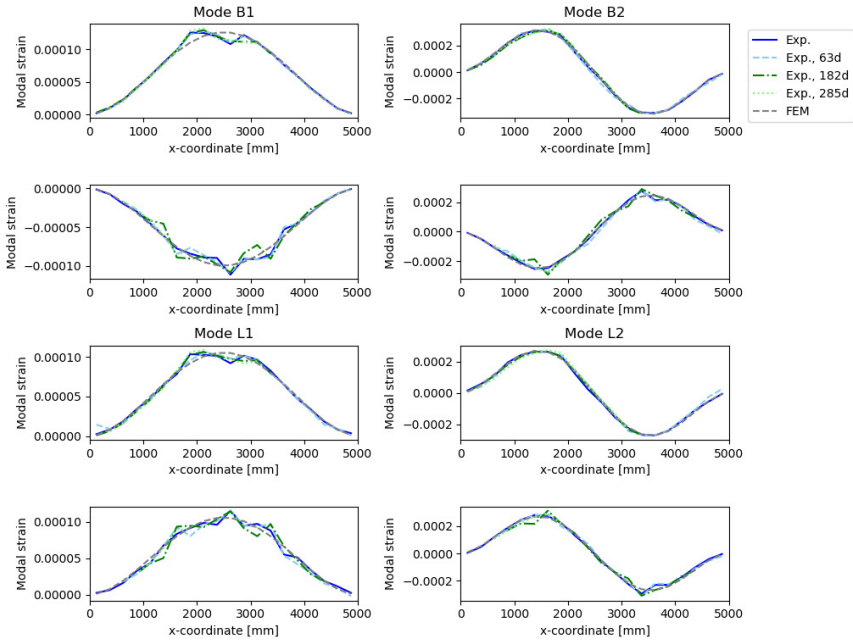
Figure VII-31: Strain mode shapes of beam 4.1 (reference) ($x = 0$ mm corresponds to the left of the side of the beam with the optic fibres)

In Figure VII-32 also the neutral axis position of the reference beam derived based on the strain mode shapes is visualized. The neutral axis is not given in regions with very low strain values, due to numerical instabilities in these zones. It can be seen that there is no shift in neutral axis position over time. This observation contradicts the reasoning of cracks causing the reduction in natural frequencies, since these would also lead to a shift in neutral axis position. Hence, the main cause of the reduction in natural frequencies will be internal effects in the concrete itself.
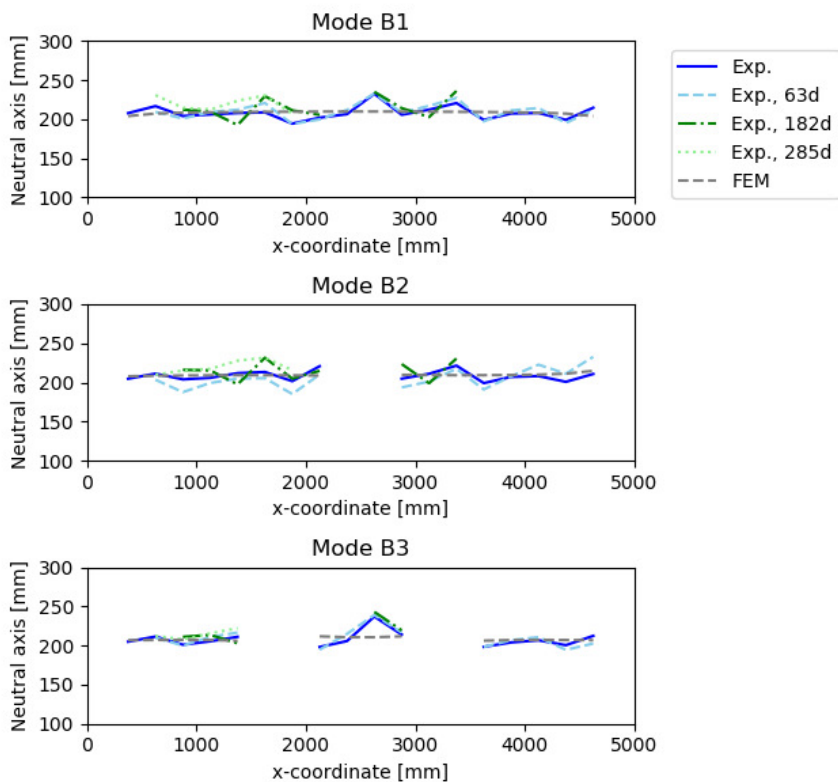
Figure VII-32: Neutral axis position of beam 4.1 (reference) based on strain mode shapes. Regions with very low strain values are neglected. ($x = 0$ mm corresponds to the left of the side of the beam with the optic fibres)

VII.6.4.2 Beam 1.2 (2.7% corrosion)

Beam 1.2 is tested at an age of 28 days (before corrosion) and at an age of 63 days (2.7% corrosion). The experimental natural frequencies for beam 1.2 are summarized in Table VII-16. The natural frequencies are each time derived both based on the acceleration measurements and based on the strain measurements with the optic fibres. Only the natural frequencies resulting from well-excited modes (high MPC (Modal Phase Collinearity) values and low damping ratios) are considered. The first vertical bending mode and the first lateral bending mode are also not taken along, since these were influenced by a difference in support conditions during the dynamic tests. For the tests at 28 days on beam 1.2, two tyres were used to support the beam during the dynamic tests, one at each end of the beam. However, two tyres proved insufficient to establish the free-free boundary conditions.

Two notes should also be made on the results with the optic fibres. As a first note, optic fibres measure axial strains. However, when a beam is subjected to torsion loading, axial strains are only present during restrained warping. For a rectangular cross-section and free-free boundary conditions, the warping is not restrained and hence theoretically, axial strains do not occur. In practice, some restraint might occur due to the presence of the tyres. That is the reason why torsion modes are not expected to be identified by the strain data, and if they do, they might not be trustworthy and are hence excluded from the data set. Accelerometers on the other hand are measuring vertical and lateral accelerations of the beam, which are not related to warping. In this case, all modes will be properly identified from acceleration data if they are properly excited, and shall hence not be excluded. As a second note, for natural frequencies larger than 250 Hz, there can be some synchronization issues for the optic fibres. The acquisition system for the optic fibres does not simultaneously scan all sensors on the optic fibres, but instead makes a high-speed sweep scan of about 0.1 pm/ns along the wavelength bandwidth. In this way, a high wavelength resolution is achieved, but a delay is introduced in the measurements. This delay leads to a phase shift between the different sensors. The results from these sensors can be synchronized by an offline synchronization technique, as explained in (Anastasopoulos et al., 2018). The phase shift between the sensors is important for the high frequency modes (> 250 Hz) and almost insignificant for the low frequency modes (0-20 Hz). Hence, the high frequency modes should be evaluated with extra care.

When looking at Table VII-16, it can be seen that most of the natural frequencies have reduced from 28 days to 63 days. However, also for the reference beam a reduction in natural frequencies was observed between 28 days and 63 days. Hence, the results at 63 days should be compared with those of the reference beam at the same age. When doing this, it can be seen that in general higher natural frequencies are found for the corroded beam. This could be ascribed to differences in concrete properties of the reference beam and beam 1.2 (2.7% corrosion) due to the different concrete batch and the small differences in natural frequencies at 28 days between both beams. Moreover, the cracks resulting from the corrosion process are longitudinal cracks, mostly affecting lateral bending modes, whereas vertical bending modes are typically influenced by transverse cracks (e.g. bending cracks). This could also be observed in Table VII-16, where the increase in frequency compared to the reference beam is smaller for the lateral bending modes than for the vertical bending modes, possibly ascribed to the larger influence of corrosion on the lateral bending modes, inducing a larger reduction in natural frequencies.

Table VII-16: Natural frequencies of beam 1.2 (2.7%) [Hz]

| Mode | 28 days | | 63 days | | Ref. | Rel. Diff. |
	Acc.	Strains	Acc.	Strains	63 days	63 days
2nd lateral	120.97	120.58		118.92	117.98	0.79%
2nd bending	164.70	164.63	167.03		164.63	1.44%
1st torsion	204.51		201.27			
3rd lateral	228.26	228.36		227.00	226.25	0.33%
3rd bending	303.97	303.94	304.43	303.89	301.05	1.02%
4th lateral	362.75		358.56			
3th torsion	405.61		403.67			
4th bending	473.79		474.54			
5th lateral	520.60		518.94			
4th torsion	604.09		601.74			
5th bending	659.18		656.35			

The displacement mode shapes of beam 1.2 (2.7% corrosion) are visualized in Appendix A.3. The displacement mode shapes are almost the same at 28 days and 63 days. Hence, based on the displacement mode shapes, no spatial variation of the corrosion degree could be derived. Furthermore, the experimental displacement mode shapes approximate quite well the results from the finite element model. Also the strain mode shapes of beam 1.2 (2.7% corrosion) are visualized in Appendix A.3. In these strain mode shapes, some irregularities can be observed. These can be ascribed to the fact that the clamps used to attach the optic fibres to the beam (Figure VII-10) were not screwed tight enough. Another explanation for the peaks in the strain mode shapes could be the inhomogeneous character of concrete. The strain mode shapes at 63 days closely correspond to the (undamaged) finite element model and there are hence no indications of local damage. Also, if the neutral axis position is evaluated based on the strain mode shapes, there is no significant change over time. Nevertheless, there is a large difference between the strain mode shapes at 28 days and 63 days, of such an extent that very large degrees of damage could be expected. The differences in strain mode shapes should here be ascribed to bad clamping of the fibres, damage in the glue used to apply the clamps and losses of prestress in the fibres. Moreover, for other beams at later ages, sagging of the fibres was observed due to which they needed to be restressed. This sagging could possibly be ascribed to shrinkage of the concrete. It might have already been present for beam 1.2 (2.7% corrosion) too, but due to the lower age of this beam the sagging might not have been visible to the unaided eye yet.

VII.6.4.3 Beam 2.2 (5.2% corrosion)

To support beam 2.2 during the dynamic tests, three tyres were used, i.e. one at the left end, one in the middle and one at the right end of the beam. All tyres were inflated up to 1 bar. The natural frequencies of beam 2.2 resulting from the dynamic tests at 28 days and at 182 days (± 5.2% corrosion) are summarized in Table VII-17. Here it can be seen that there is a reduction in natural frequencies over time. However, there was also a reduction in natural frequencies for the reference beam between 28 days and 182 days. Hence, the natural frequencies of beam 2.2 (5.2% corrosion) are compared with those of the reference beam at 182 days. Here, it can be seen that there is a general reduction in natural frequency from the reference beam to beam 2.2 (5.2% corrosion), except for the second and the fifth vertical and lateral bending mode. A possible reason for this could be the localisation of damage and/or cracks at regions with low curvature when considering these modes. Nevertheless, these differences have the same order of magnitude as those found between beam 1.2 and the reference beam, and might hence also be ascribed to an experimental error or the differences between the concrete batches.

For this beam, when looking at the frequency differences between the corroded beam and the reference beam, there could not be made a clear distinction between the vertical bending modes and the lateral bending modes, even though this could be expected beforehand (cfr. section VII.6.4.2).

Table VII-17: Natural frequencies of beam 2.2 (5.2% corrosion) [Hz]

Mode	28 days	182 days	Ref. 182 days	Rel. Diff.
1st lateral	-	41.2		
1st bending	60.66	55.9	58.45	-4.36%
2nd lateral	118.98	114.44	113.63	0.71%
2nd bending	162.76	157.06	156.99	0.04%
1st torsion	201.16	194.58	199.69	-2.56%
3rd lateral	224.95	216.82	221.30	-2.02%
3rd bending	300.54	285.58	292.24	-2.28%
4th lateral	358.84	346.72	350.62	-1.11%
3th torsion	402.98	397.53	403.32	-1.44%
4th bending	467.42	454.58	455.38	-0.18%
5th lateral	515.64	503.87	502.22	0.33%
4th torsion	604.72	590.33	600.12	-1.63%
5th bending	657.56	640.50	638.55	0.31%

The displacement mode shapes of beam 2.2 before and after corrosion are visualized in Appendix A.3. Only around 2000 mm, the displacement mode shapes of the first and third vertical bending mode are slightly different at 182 days compared to 28 days. The difference in displacement mode shapes could be ascribed to the use of damaged accelerometers, which have been replaced afterwards or due to problems with the glue used to attach the accelerometers to the beam.

VII.6.4.4 Beam 1.1 (6.2% corrosion)

The natural frequencies before (28 days) and after corrosion (330 days) of beam 1.1 are summarized in Table VII-18. The natural frequencies of the reference beam at 330 days are also provided. This enables to investigate the influence of corrosion on the natural frequencies. The natural frequencies of the corroded beam are lower than those of the reference beam at the same age. Hence, corrosion has led to a reduction in stiffness and a corresponding reduction in natural frequency. After corrosion, the optic fibres were severely damaged, so no strain measurements are available. The damage to the optic fibres originated mainly from the transportation of the beam between the different tests.

The first lateral and vertical bending mode are not considered in Table VII-18. This due to a difference in boundary conditions. At 28 days, beam 1.1 was supported by two rubber blocks, whereas at 330 days, three tyres were used, i.e. one at the left end, one in the middle and one at the right end of the beam. All tyres were inflated up to 1 bar.

Table VII-18: Natural frequencies of beam 1.1 (6.2%) [Hz]

Mode	28 days		330 days	Ref.	Rel. Diff.
	Acc.	Strains	Acc.	330 days	330 days
2nd lateral		121.50	103.60	112.22	-7.68%
2nd bending	169.16	168.65	146.33	153.03	-4.38%
1st torsion	202.01		186.57	198.84	-6.17%
3rd lateral		227.71	202.41	217.51	-6.94%
3rd bending	306.48	306.47	274.17	286.40	-4.27%
4th lateral	363.36	363.35	322.05	343.85	-6.34%
3th torsion	401.67		389.07	400.99	-2.97%
4th bending	476.21		429.16	447.45	-4.09%
5th lateral	522.36		457.57	492.61	-7.11%
4th torsion	604.17		573.83	597.77	-4.00%
5th bending	666.86		597.59	626.69	-4.64%

When investigating the difference in frequencies between the reference beam and the corroded beam, it can be observed that in general there is a larger decrease in frequencies for the lateral bending modes than for the vertical bending modes. This could again be ascribed to the longitudinal cracks originating from the corrosion process, which have a larger influence on lateral bending modes, whereas vertical bending modes are more influenced by transverse cracks.

The displacement mode shapes of beam 1.1 (6.2% corrosion) for some of the modes are visualized in Appendix A.3. The displacement mode shapes deviate from the results at 28 days and from the finite element model only at one point (around 3.2 m) and only in the lateral direction. This could possibly be ascribed to very local damage behind the plate to which the accelerometer is attached, damage of the glue used to attach the plate, or a local defect in the close neighbourhood of this accelerometer. Damage due to corrosion is expected to have a more global influence and would also be visible at other locations along the displacement mode shape.

VII.6.4.5 Beam 2.1 (6.6% corrosion)

To support beam 2.1 during the dynamic tests, three tyres were used, i.e. one at the left end, one in the middle and one at the right end of the beam. All tyres were inflated up to 1 bar. Table VII-19 summarizes the natural frequencies resulting from the dynamic tests on beam 2.1 at 28 days (before the onset of corrosion) and at 285 days (before the destructive tests). When comparing the natural frequencies at the different testing ages, it can be seen that the natural frequencies remain almost unaltered between 28 days and 285 days and that for some modes there even is a slight increase in natural frequency. In addition, when comparing the natural frequencies with those of the reference beam at 285 days, the latter are lower than the former. These results are not in line with the expectations. There is no clear cause for these observations, but some plausible reasons are the following:

- The beam was tested dynamically after first testing another beam. The pressure in the tyres could hence have been reduced due to the weight of the previous beam. It has been proven in earlier research that a lower tyre pressure and hence a higher stiffness of the supports can lead to higher natural frequencies. Nevertheless, in such a case an effect on the natural frequencies of the first modes would be expected, which reduces for the higher modes. The fact that the natural frequencies are almost the same at 28 days and 285 days for all modes does not support this hypothesis of the influence of the boundary conditions.
- It could be that the effects of creep and shrinkage are limited for this beam due to a beneficial effect of corrosion. For small levels of corrosion, the bond between reinforcement and concrete increases, compared to a non-corroded reinforcement bar. Even though on average beam 1.1 (6.2% corrosion) reached about the same corrosion level, for the latter beam, a

decrease in natural frequency could be observed. However, these average corrosion degrees are both an average over the four bars and an average over the length of the beam. Hence, this number is no exact representation of the possible internal effects in each of the individual beams.

The displacement mode shapes of beam 2.1 are visualized in Appendix A.3. For the lateral bending modes, there is a slight deviation between the different testing ages. However, this is very local and might be attributed to damage behind the plate of the accelerometer, damage to the glue, or reattachment of the plate. The strain mode shapes of beam 2.1 are also visualized in Appendix A.3. In these strain mode shapes there are again some irregularities. The irregularities at 28 days could be ascribed to improper clamping of the fibres. The irregularities at 285 days could be ascribed to rust products present on the fibres.

Table VII-19: Natural frequencies of beam 2.1 (6.6% corrosion) [Hz]

Mode	28 days		285 days		Ref. 285 days	Rel. Diff. 285 days
	Acc.	Strains	Acc.	Strains		
1st lateral		43.88		45.62	41.50	9.93%
1st bending	60.17	60.24	61.5	62.2	58.40	5.91%
2nd lateral	117.6	117.76	120.03	120.42	113.54	5.89%
2nd bending	161.85	161.86	161.74	161.51	152.32	6.11%
1st torsion	200.19		200.48		199.11	0.69%
3rd lateral	223.31	223.35	226.34	226.37	218.41	3.64%
3rd bending	298.64	298.74	299.30	299.40	288.34	3.82%
4th lateral	359.51		360.81	360.71	345.68	4.36%
3th torsion	402.72		402.90		402.04	0.21%
4th bending	468.22		468.39		456.82	2.53%
5th lateral	507.94		513.82		495.24	3.75%
4th torsion	600.56		601.18		597.99	0.53%
5th bending	650.49		649.70		629.76	3.17%

VII.6.4.6 General remarks

When investigating the results of the dynamic tests, it should be noted that longitudinal cracks (such as the cracks originating from the corrosion process) do not influence the bending stiffness directly. There is a relationship between both, but it is more indirect. When there would be a combination of corrosion and loading over the cracking moment, transverse cracks would originate due to the loading process, which would have a larger influence on the bending stiffness and

hence on the natural frequencies of the vertical bending modes. The given reasoning neglects other effects such as micro-cracking, debonding of reinforcement and concrete, etc.

Most of these beams have been subjected to many manipulations. They have been transported between the location where the accelerated corrosion process took place and the testing hall to perform the dynamic tests. The beams also had to be turned upside down for application of the salt solution, and turned back to the normal position for the tests. Only beam 4.1 (reference) did not need to be turned. This could have had an influence on the natural frequencies. The fact that all beams were subjected to turning manipulations and beam 4.1 (reference) did not, can already lead to a difference in natural frequencies between the reference beam and the other beams. However, further investigation is required on the effects of turning the beams on the natural frequencies.

Because of the problems that occurred during the analysis of the test results for the dynamic tests, these results will not be used further in this chapter for the Bayesian assessment of the corrosion degree.

VII.7 Bayesian inference

Bayesian inference will be applied to update the corrosion degree of the beams based on the static strain data. In the following sections, first the model to be used in the likelihood function will be described (section VII.7.1), followed by the assumptions on the prior distributions for the corrosion degree (section VII.7.2). Next, the posterior distributions for the corrosion degree based on the static strain data will be derived and discussed (section VII.7.3).

VII.7.1 Model used in the likelihood function

As discussed in section IV.2, for application of Bayesian inference, in the likelihood function a model is required modelling the relationship between the variables to be updated and the measurement data. In the following, the model used in the likelihood function is the finite element model as described in section VII.5.1, providing a relationship between the corrosion degree of the beams and the static strains. To account for the degradation due to reinforcement corrosion in the finite element model, the steel section of the reinforcement bars is adapted according to equation (II-8), and the Young's modulus in the concrete cover is reduced to account for cover cracking according to section II.2.3. Corrosion can also influence the ductility of the reinforcement bars and the bond between the reinforcement and the concrete cover. However, the latter two influences do not affect the strains under static loading for small load levels.

VII.7.2 Prior distribution

In contrast to Chapter VI, in this section the distribution of the corrosion degree will be updated directly and not the distributions of the variables in the corrosion models. When applying accelerated corrosion, the initiation phase will be almost completely removed and the corrosion rate will be largely influenced by the applied current. Hence, both will not correspond to results that can be obtained in natural conditions, and the choice is made to directly infer the corrosion degree.

A prior distribution is assigned to the corrosion degree of the beams. A uniform corrosion degree along the length of the beam is assumed since a salt solution was provided along the whole length of the beam. In addition, too little strain measurements along the length are performed to capture the very sudden changes in the corrosion degrees as visualized in Figure VII-21. Moreover, these very local changes in corrosion degree have a limited influence on the strains, as also visible in Figure VII-22 to Figure VII-24, especially when compared to the error on the strain measurements.

For the prior distribution of the corrosion degree, first a vague prior distribution is assumed, i.e. a uniform distribution between 0.5% and 30% corrosion (the maximum anticipated corrosion degree). The lower bound for the uniform distribution is based on the visual observation of corrosion cracks, excluding the uncorroded situations. In (Andrade and Izquierdo, 2020; Pedrosa and Andrade, 2017), it is stated that the start of the corrosion propagation phase with visible cracking occurs at a general reduction in reinforcement diameter of 50 to 100 µm. For the beams under consideration, this corresponds to a corrosion degree of 0.5%. Hence, as soon as any visual observation of cracking is present, the lower bound of the uniform distribution could be adjusted to 0.5% instead of 0%.

Besides this uniform prior distribution, also a more informative prior distribution is assumed, based on the information from crack width measurements. In (Ouzaa and Oucif, 2019) a simple model for predicting the crack width as a function of the corrosion degree is presented. This model is given by equation (VII-17).

$$\Delta w_{cr} = \gamma \Delta \phi \tag{VII-17}$$

Here, Δw_{cr} is the increase in crack width, $\Delta \phi$ the reduction in reinforcement diameter, and γ is given by equation (VII-18).

$$\gamma = \frac{(\varphi_r - 1)\pi\phi}{\left(\dfrac{\dfrac{\phi}{2}}{\dfrac{\phi}{2} + C_p} + 1\right)c} \tag{VII-18}$$

Here, φ_r is equal to the ratio of the density of steel to the density of rust (or $\varphi_r = 0.53$), ϕ is the reinforcement diameter, and c is the concrete cover.

Another model relating the crack widths to the corrosion degree is found in (Nasser et al., 2021) and is given by equation (VII-19).

$$\alpha = 13w_{cr}^{1.3} \tag{VII-19}$$

Here, α is the corrosion degree and w_{cr} the crack width.

For the same crack width, both equations result in almost the same corrosion degree. The average of the results from both equations will be used as the mean of the informative prior distribution. The corrosion degree resulting from both equations is given in Table VII-20 and Table VII-21 for each beam, evaluated based on the average crack width and the maximum crack width at the bottom side of the beam respectively. The standard deviation of the prior distribution is based on a COV of 0.5. A Beta distribution has been assumed for the prior distribution. The lower bound is again adjusted based on the presence of the cracks and equals 0.5%. The upper bound is 100%, i.e. complete loss of the steel section.

Table VII-20: Mean and standard deviation of informative prior distribution based on the average crack width

| Beam | w [mm] | Corrosion degree [%] | | μ' | σ' |
		(VII-17)	(VII-19)		
1.1 (6.2%)	0.61	6.81	6.84	6.83	3.42
1.2 (2.7%)	0.21	2.37	1.71	2.04	1.02
2.1 (6.6%)	0.43	4.83	4.34	4.59	2.30
2.2 (5.2%)	0.36	4.05	3.44	3.75	3.38

Table VII-21: Mean and standard deviation of informative prior distribution based on the maximum crack width

| Beam | w [mm] | Corrosion degree [%] | | μ' | σ' |
		(VII-17)	(VII-19)		
1.1 (6.2%)	1.30	14.23	18.28	16.26	8.13
1.2 (2.7%)	0.40	4.38	3.82	4.10	2.05
2.1 (6.6%)	0.70	7.80	8.18	7.99	4.00
2.2 (5.2%)	0.70	7.80	8.18	7.99	4.00

VII.7.3 Bayesian inference based on static strain data

The prior distributions discussed in section VII.7.2 will be updated by application of Bayesian inference by considering the model discussed in section VII.7.1 in the likelihood function. The data used in the likelihood function are the strains as visualized in Figure VII-22 to Figure VII-24, with the exception of the outliers in the strain graphs. The measurement error and model error considered in the likelihood function are according to sections VII.4.2.3 and VII.6.2. The prior distributions and resulting posterior distributions of the corrosion degrees for beams 1.1 (6.2%), 2.1 (6.6%) and 2.2 (5.2%) are visualized in Figure VII-33 to Figure VII-35.

When looking at the resulting posterior distributions, the following conclusions can be derived. For beam 1.1 (6.2% corrosion), an underestimation of the average corrosion degree is found when the uniform prior distribution is assumed. When the informative prior distribution based on the average crack width is used, the underestimation is smaller, but the best approximation is found when the prior distribution is based on the maximum crack width. This prior distribution overestimates the corrosion degree, which balances out the underestimation obtained based on the data as found with the uniform prior distribution. Moreover, the very low corrosion degrees are not accepted due to their low prior probability.

For beam 2.1 (6.6% corrosion), the posterior distribution when assuming the uniform prior distribution approximates quite well the actual corrosion degree, but an even better approximation is found when the informative prior distribution based on the maximum crack width is assumed. The informative prior distribution based on the average crack with is too informative, and the posterior distribution is almost equal to the prior distribution, since the range in strains that can be expected based on this prior distribution is sometimes smaller than the assumed measurement errors.

Finally, for beam 2.2 (5.2% corrosion) an overestimation of the corrosion degree is found when the uniform prior distribution is assumed. A better approximation of the corrosion degree is found when assuming the more informative prior distributions.

In general, the informative prior distribution based on the maximum crack width performs best. This is also in line with observations at KU Leuven, see e.g. (Nasser et al., 2019).

Figure VII-33: Posterior distribution of the average corrosion degree in beam 1.1 (6.2% corrosion) based on static strains measured between the load levels of 5 kN and 15 kN
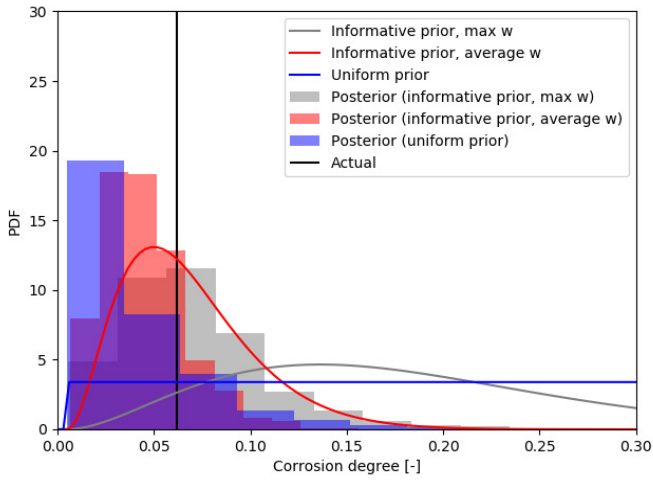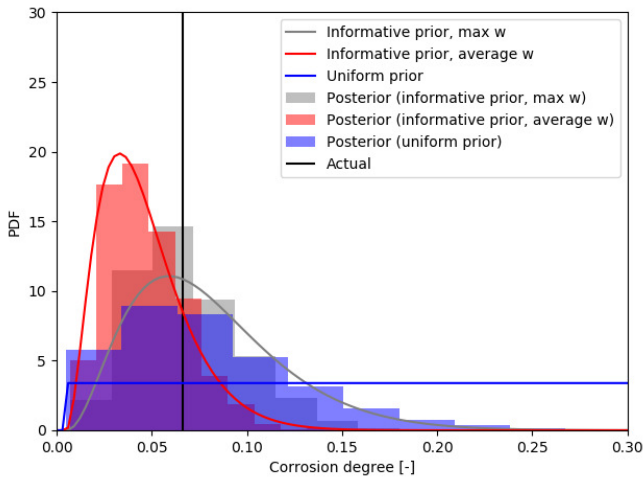

Figure VII-34: Posterior distribution of the average corrosion degree in beam 2.1 (6.6% corrosion) based on static strains measured between the load levels of 5 kN and 15 kN
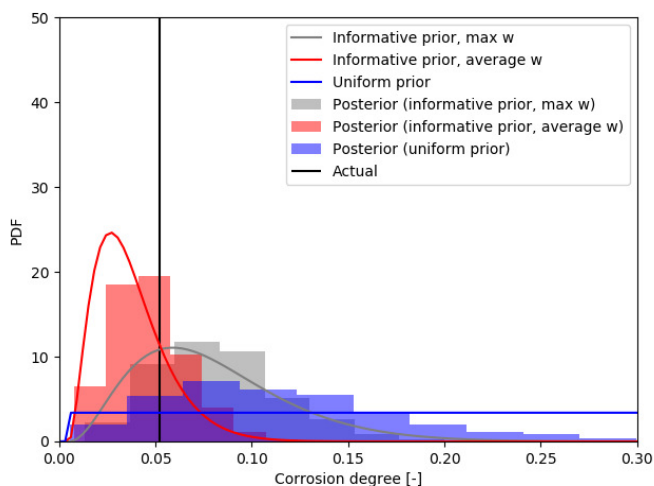
Figure VII-35: Posterior distribution of the average corrosion degree in beam 2.2 (5.2% corrosion) based on static strains measured between the load levels of 5 kN and 15 kN

In the results provided above, the difference in strain between 5 kN and 15 kN is used as data in the likelihood function. These correspond to strains under loads lower than the cracking load of the beams. This is typical for proof load testing, where stop criteria are defined as the onset of non-linear behaviour or the occurrence of damage such as cracking (Lantsoght, 2019). However, for evaluation of the stop criteria, distinction should be made between structures already cracked in bending and structures not yet cracked in bending. In both situations, the concrete strain at the bottom fibre should remain lower than a limiting value of the strains. In case of failure due to bending, for the beams under investigation this limiting value equals 2700 με (Lantsoght, 2019). In case of failure under shear, the limiting value equals 800 με (Lantsoght, 2019). When considering the latter criterion (due to the fact that failure under shear is very probable), the maximum load level that could be considered as being part of a proof load test is 30 kN for beam 1.1 (6.2%). When updating based on the strains measured between this load level and 5 kN, the posterior distributions of the corrosion degree for beam 1.1 (6.2%) are given in Figure VII-36. These posterior distributions are very similar to those obtained in Figure VII-33.

Figure VII-36: Posterior distribution of the corrosion degree of beam 1.1 (6.2% corrosion) when updating based on static strains measured between the load levels of 5 kN and 30 kN

To simulate the case where the structure is already cracked in bending, the load level of 50 kN is considered in the following. All strain gauges are used, except the strain gauges under the right loading point since here a crack appeared. In the finite element model, for the different corrosion degrees, the strain gauges are also applied in between the cracks. This could also be achieved in practice: if the structure already shows bending cracks, strain gauges could be applied in between these cracks and not over the bending cracks. When updating based on the average strain measured in the zone in between the loading points and comparing these strains with the average predicted strains in this zone, the posterior distribution is visualized in Figure VII-37. This distribution is different from the one found in Figure VII-36 and approximates the actual corrosion degree quite well for all prior distributions, i.e. the posterior uncertainty is rather small and the mean value is located close to the actual corrosion degree. This could probably be ascribed to the larger influence of the corrosion degree on the average strain at these higher load levels. This has been partly proven by performing the updating also based on the strains measured at a load level of 70 kN, showing similar posterior distributions, but with a smaller posterior uncertainty.
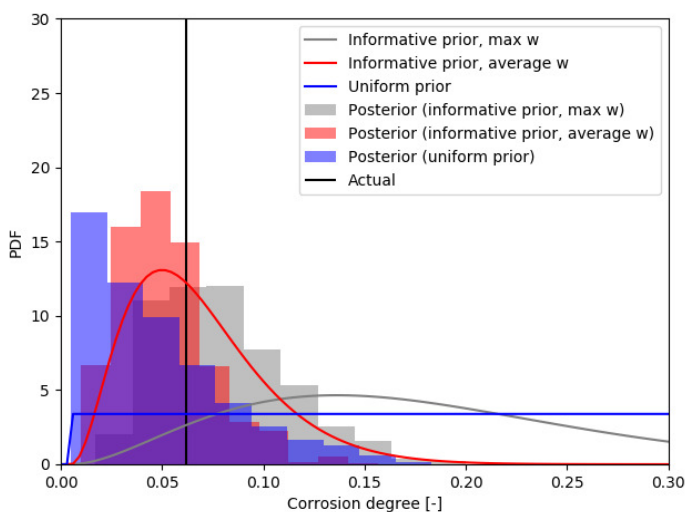
Figure VII-37: Posterior distribution of the corrosion degree of beam 1.1 (6.2% corrosion) when updating based on the average static strains in the constant moment region measured between the load levels of 5 kN and 50 kN

Another strategy could also be followed, where both the strains over a crack and the strains in between cracks are accounted for. This strategy relies on the principles of tension stiffening. When the strain over a crack is given by ε_{cr} and the strain in between cracks is given by ε_{uncr}, the average strain is given by equation (VII-20).

$$\varepsilon_m = (1 - \xi)\varepsilon_{uncr} + \xi\varepsilon_{cr} \text{ with } \xi = 1 - \left(\frac{M_{cr}}{M}\right)^2 \qquad \text{(VII-20)}$$

Here, M is the moment acting on the structure and M_{cr} equals the cracking moment. When strain gauges are applied over cracks and in between cracks, the strains ε_{cr} and ε_{uncr} can be derived from the strain readings. Similarly, in the finite element model, strains are evaluated in between cracks and over cracks. Then, the average strain ε_m based on the measured strains and the average strain ε_m based on the simulated strains are evaluated based on equation (VII-20) and compared to each other. When Bayesian inference is performed based on ε_m at a load level of 50 kN, the posterior distribution is visualized in Figure VII-38. Here it can be seen that an underestimation of the corrosion degree is found, which is reduced when assuming a more informative prior. The approximation of the corrosion degree is less good compared to the previous cases. This could be ascribed to the larger error between predicted and measured strains that might be present due to the incorporation of equation (VII-20). Only for the informative prior distribution based on the maximum crack width, the posterior distribution approximates the

actual value. This prior distribution was also found to be the best performing for the results based on the strains measured under a load lower than the cracking moment.

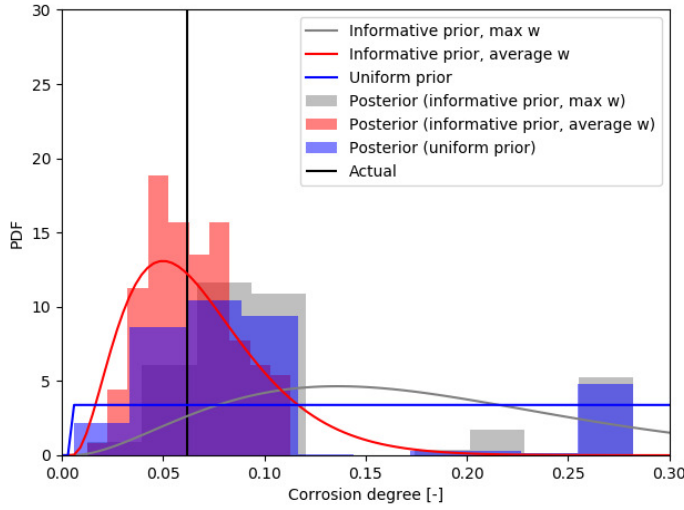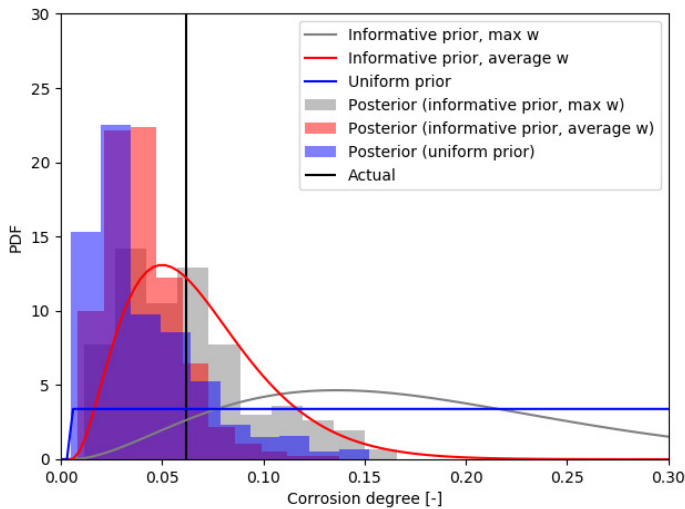

Figure VII-38: Posterior distribution of the corrosion degree of beam 1.1 (6.2%) when updating based on the average static strains calculated based on equation (VII-20) at the load level of 50 kN

In this case, a uniform distribution of the corrosion degree is updated and spatial variation is not accounted for. This could be ascribed to the fact that uniform corrosion has been generated by applying the salt solution over the whole length of the beam, where spatial variations are only arising from the pitting effect. When a spatially variable corrosion degree should be updated, the average of the strains over the constant moment region cannot be considered anymore and the measured strains should be compared with the predicted strains at the corresponding locations. In case of an uncracked structure, this can be done in the same way as earlier described. However, if the structure has been cracked previously, these bending cracks should also be simulated in the model to be able to approximate the actual strain pattern as accurate as possible.

Finally, following remark should be made. In practice, for large-scale RC bridges, LVDT's or other measuring equipment with a larger gauge length could be used to measure strains. In such cases, average strains over longer lengths are measured, averaging out the effects of cracks. For example in (Lantsoght, 2019), LVDT's measuring over a distance of 1 m are used to measure strains in an RC bridge.

VII.8 Conclusions

In this chapter, an experimental campaign on reinforced concrete beams subjected to accelerated corrosion has been described. Static loading tests and dynamic tests are performed on the beams, which each achieved a different corrosion level. It should be pointed out that for the higher corrosion levels these actual corrosion degrees were not in line with those predicted based on equation (VII-1). The influence of corrosion on the different test results has been investigated, and the results from the static tests were used to update the distribution of the corrosion degree. For this purpose, different prior distributions have been assumed, i.e. a vague uniform prior distribution and two more informative prior distributions taking into account the information from crack width measurements.

When considering the static strain data, first an estimate has been made of the measurement error when measuring strains with strain gauges on plain concrete specimens. The results of these tests give an indication of the error to be used in the likelihood function. When taking into account this measurement error and a model error for the finite element model, it has been concluded that for most of the measurements there is an overlap between the predicted values with their uncertainty bounds and the measured values with their uncertainty bounds. When these strains are used to update the corrosion degree, the posterior distribution depends largely on the assumed prior distribution. However, the mean of the posterior distribution of the corrosion degree shifts towards the actual corrosion degree and there is a reduction in uncertainty. In the model for the Bayesian inference, the influence of corrosion on the concrete stiffness has been modelled with a reduction in Young's modulus over the concrete cover, evaluated based on an analytical model. The influence of this simplification on the resulting strains has been investigated and the error was small. Also the reduction in bond between steel and concrete has been neglected, since for the considered load levels this influence is very limited. Nevertheless, models that are more detailed could also be considered, taking into account the fact that corrosion mostly results in longitudinal cracks along the reinforcement, considering the reduction in bond between steel and concrete, etc.

When looking at the data from the dynamic tests, an important conclusion is that also the reference beam, which was not subjected to any degradation, shows a reduction in natural frequencies over time. This could be ascribed to the young age of the concrete, the heterogeneous character of concrete and internal effects within the concrete. Beams 2.2 (5.2% corrosion) and 1.1 (6.2% corrosion) showed a decrease in natural frequencies due to corrosion when compared to the reference beam at the same age. For beam 1.2 (2.7% corrosion), the corrosion degree was too small for this effect to be noticeable. For beam 2.2 (6.6% corrosion), larger natural frequencies than for the reference beam were observed due to an experimental error. Due to the longitudinal cracks arising from the corrosion

process, for most beams the influence on the frequencies of the lateral bending modes was also observed to be larger than the influence on the vertical bending modes. Displacement mode shapes and strain mode shapes could also be extracted from the measured accelerations and strains. As expected, due to the generally uniform nature of corrosion, no influence on the displacement mode shapes was found. Only very local changes at consecutive testing ages were observed, which could most probably be ascribed to experimental flaws rather than corrosion. When considering the strain mode shapes, a behaviour with many unexpected peaks was observed. This could be ascribed to bad clamping of the fibres, damage of the fibres due to contact with rust stains, etc. In addition, during the experimental campaign, many fibres broke or clamps came loose, which could also induce differences in strain mode shapes. Due to the different experimental problems and issues discovered during the data processing, the results from the dynamic tests were not used in the Bayesian inference of the corrosion degree.

As could be concluded from the discussion of the results as provided in this chapter, there have been some issues with the different types of tests. These issues could be ascribed to the difficulties associated with the large scale of the beams (i.e. damage of the optic fibres during handling, the presence of shrinkage cracks influencing the strain readings, etc.). The experience of performing accelerated corrosion tests on such large-scale specimens in literature is generally scarce or not completely documented. To the knowledge of the authors, the current research is one of the first documented experimental campaigns treating accelerated corrosion of such large beams and investigating the influence of corrosion on dynamic data and static strain data. Despite the shortcomings of the current results, important lessons were learned from the performed experiments, which could be taken along in future experimental campaigns.

VII.9 References

Abosrra, L., Ashour, A.F., Youseffi, M., 2011. Corrosion of steel reinforcement in concrete of different compressive strengths. Constr. Build. Mater. 25, 3915–3925.

Akkaya, Y., Guner, S., Vecchio, F.J., 2019. Constitutive model for inelastic buckling behavior of reinforcing bars. ACI Struct. J. 116, 195–204.

Allaix, D.L., Carbone, V.I., Mancini, G., 2015. Modelling uncertainties for the loadbearing capacity of corroded simply supported RC beams. Struct. Concr. 16, 333–341.

Altoubat, S., Maalej, M., Shaikh, F.U.A., 2016. Laboratory Simulation of Corrosion Damage in Reinforced Concrete. Int. J. Concr. Struct. Mater. 10, 383–391.

Anastasopoulos, D., Maes, K., De Roeck, G., Reynders, E., 2018. A comparison of two data acquisition techniques for modal strain identification from sub-microstrain FBG data. Lect. Notes Civ. Eng. 5, 432–444.

Andisheh, K., Scott, A., Palermo, A., 2019. Experimental evaluation of the residual compression strength and ultimate strain of chloride corrosion-induced damaged concrete. Struct. Concr. 20, 296–306.

Andrade, C., Izquierdo, D., 2020. Propagation period modeling and limit state of degradation. Struct. Concr. 21, 1720–1731.

ASTM International, 2011. ASTM G1-03 Standard Practice for Preparing, Cleaning, and Evaluating Corrosion Test Specimens.

Caré, S., Raharinaivo, A., 2007. Influence of impressed current on the initiation of damage in reinforced mortar due to corrosion of embedded steel. Cem. Concr. Res. 37, 1598–1612.

CEN, 2019a. NBN EN 12390-3:2019 Testing hardened concrete - Part 3: Compressive strength of test specimens.

CEN, 2019b. Belgian Standard EN 12390-5 : 2019 NBN EN 12390-5 : 2019 Testing hardened concrete - Part 5 : Flexural strength of test specimens.

CEN, 2005a. NBN EN 12390-6 Testing hardened concrete - Part 6: Tensile splitting strength of test specimens.

CEN, 2005b. EN 1992-1-1: Eurocode 2: Design of concrete structures - Part 1-1: General rules and rules for buildings.

CEN, 2005c. NBN EN 12390-13: Testing hardened concrete – Part 13: Determinatio of secant modulus of elasticity in compression.

DIANA FEA BV, 2021. Bond-slip Models in Diana.

DIANA FEA BV, 2019. DIANA User's Manual - Release 10.3 [WWW Document]. URL https://dianafea.com/manuals/d103/Diana.html

Dokoupil, P., 2017. Determination of Measurement Uncertainty of Strain and Stress Using Strain Gages, in: Transactions of the VŠB – Technical University of Ostrava, Mechanical Series. p. 2023.

El Maaddawy, T., Soudki, K., 2007. A model for prediction of time from corrosion initiation to corrosion cracking. Cem. Concr. Compos. 29, 168–175.

fib, 2013. Model Code for Concrete Structures 2010.

Lantsoght, E.O.L., 2019. Load Testing of Bridges: Proof Load Testing and the Future of Load Testing. CRC Press, London, UK.

Li, C., Ashlock, J.C., Wang, X., 2019. Quantifying Repeatability Reproducibility Sources of Error and Capacity of a Measurement: Demonstrated Using Laboratory Soil Plasticity Tests. Adv. Civ. Eng. 2019.

Maekawa, K., Pimanmas, A., Okamura, H., 2003. Nonlinear mechanics of reinforced concrete. Spon Press, Taylor & Francis Group, London and New York.

Massone, L.M., López, E.E., 2014. Modeling of reinforcement global buckling in RC elements. Eng. Struct. 59, 484–494.

Nasser, H., Van Steen, C., Vandewalle, L., Verstrynge, E., 2021. An experimental assessment of corrosion damage and bending capacity reduction of singly reinforced concrete beams subjected to accelerated corrosion. Constr. Build. Mater. 286, 122773.

Nasser, H., Van Steen, C., Vrijdaghs, R., Torres-Acosta, A., Vandewalle, L., Verstrynge, E., 2019. Numerical modelling of corroded reinforced concrete beams based on visual inspection, in: SMAR 2019 - Fifth Conference on Smart Monitoring, Assessment and Rehabilitation of Civil Structures. pp. 1–8.

NORDTEST, 1999. NT BUILD 492 Concrete, mortar and cement-based repair materials: Chloride migration coefficient from non-steady-state migration experiments.

Otieno, M., Beushausen, H., Alexander, M., 2016. Chloride-induced corrosion of steel in cracked concrete - Part I: Experimental studies under accelerated and natural marine environments. Cem. Concr. Res. 79, 373–385.

Ouzaa, K., Oucif, C., 2019. Numerical model for prediction of corrosion of steel reinforcements in reinforced concrete structures. Undergr. Sp. 4, 72–77.

Pedrosa, F., Andrade, C., 2017. Corrosion induced cracking: Effect of different corrosion rates on crack width evolution. Constr. Build. Mater. 133, 525–533.

Peeters, B., De Roeck, G., 1999. Reference-based stochastic subspace identification for output-only modal analysis. Mech. Syst. Signal Process. 13, 855–878.

Reynders, E., De Roeck, G., 2008. Reference-based combined deterministic-stochastic subspace identification for experimental and operational modal analysis. Mech. Syst. Signal Process. 22, 617–637.

Reynders, E., Schevenels, M., De Roeck, G., 2014. MACEC 3.3: a Matlab toolbox for experimental and operational modal analysis.

Urmson, C.R., Mander, J.B., 2012. Local Buckling Analysis of Longitudinal Reinforcing Bars. J. Struct. Eng. 138, 62–71.

Van Steen, C., Nasser, H., Verstrynge, E., Wevers, M., 2021. Acoustic emission source characterisation of chloride-induced corrosion damage in reinforced concrete. Struct. Heal. Monit. 14759217211013324.

Van Steen, C., Pahlavan, L., Wevers, M., Verstrynge, E., 2019a. Localisation and characterisation of corrosion damage in reinforced concrete by means of acoustic emission and X-ray computed tomography. Constr. Build. Mater. 197, 21–29.

Van Steen, C., Verstrynge, E., Wevers, M., Vandewalle, L., 2019b. Assessing the bond behaviour of corroded smooth and ribbed rebars with acoustic emission monitoring. Cem. Concr. Res. 120, 176–186.

Zhu, W., François, R., 2014. Corrosion of the reinforcement and its influence on the residual structural performance of a 26-year-old corroded RC beam. Constr. Build. Mater. 51, 461–472.

CHAPTER VIII

Bayesian inference of remaining prestress in PC structures

"Prediction is very difficult, especially about the future."
- Niels Bohr

VIII.1 Introduction

Similarly as for reinforced concrete structures, there is a need for more clear guidelines on the assessment of the deterioration state and the corresponding strength of existing prestressed concrete structures. Studies regarding the structural response of prestressed and post-tensioned structures subjected to corrosion are rather limited. For example, Podroužek et al. (2014) model the degradation due to corrosion by applying a reduction of prestressing tendons to critical elements in a finite element model, without modelling the actual corrosion process. Nevertheless, corrosion is a major durability concern since it might result in rupture of strands and might lead to a reduction of strength and serviceability up to an unacceptable level (Dias-da-Costa et al., 2019). As such, the structure might fail at an early stage due to the occurrence of brittle fracture (Page and Page, 2007). Hence, accurate knowledge of the corrosion state and corresponding effective prestressing force is an important factor in the assessment of the structural health and corresponding performance of a prestressed concrete structure (Osborn et al., 2012). The importance of studying corrosion of prestressed structures is also shown by the study of Papé and Melchers (2011). Here, 45-year-old post-tensioned bridge girders were tested after a bridge was taken out of service. Whereas corrosion of the non-prestressed reinforcement was according to the expectations, some of the prestressing strands were severely corroded, with cross-section losses between 75% and 100%. Nevertheless, little evidence of this corrosion could visually be observed, since no rust stains were formed. Even in an apparently sound beam, severe localised corrosion of the prestressing strands was observed after demolition. Moreover, if rust stains were observed, they originated from corrosion of the non-prestressed reinforcement. Also in (Moravcik et al., 2020) a precast prestressed bridge from the early 1950's was tested. Here the failure of the superstructure of the bridge could mainly be ascribed to corrosion of the prestressing wires at the anchors, since these were installed without grouting and no proper maintenance was applied. As such, corrosion contributed to the loss of prestress and hence a reduced resistance of the bridge superstructure.

In this chapter, it is investigated whether it is possible to update the remaining steel section/prestressing force based on different (non-destructive) measurements. In a first stage, based on static strain data and modal data, a posterior distribution of the remaining prestressing steel section will be derived for a prestressed beam (section VIII.2). In a next stage, this is extended to a prestressed girder bridge (section VIII.3). In section VIII.4, a post-tensioned beam is studied, making the distinction between a grouted (section VIII.4.1) and an ungrouted (section VIII.4.2) duct. Finally, a case study of two prestressed roof girders is investigated (section VIII.5). These girders were not subjected to corrosion. However, other time-dependent phenomena can lead to a loss of prestress. A lot

of experimental data was available, and the remaining prestress of the girders is updated based on these data.

VIII.2 Updating of corrosion in a prestressed girder

A prestressed girder with length 6 m, height 730 mm and width 350 mm is considered. The girder has three layers of prestressing strands, each consisting out of three 7-wire strands of 93 mm² (Figure VIII-1). It is assumed that the girder is subjected to corrosion. The girder is modelled in finite element software DIANA FEA (DIANA FEA BV, 2019), making use of a non-linear 2D model. The non-linear calculations include the non-linear material behaviour, i.e. cracking of the concrete. For this purpose, the tensile strength of the concrete is modelled by a Hordijk curve, with concrete tensile strength f_{ct} = 3.8 MPa. A total strain based crack model is used with rotating cracks. The non-linear material behaviour of the steel is modelled by adding the ultimate tensile strength and modelling the steel behaviour as such that the stress approaches zero if the ultimate tensile strength is exceeded. The yield strength equals 1674 MPa and the ultimate tensile strength equals 1860 MPa. Pitting corrosion may cause an extreme steel section loss only at a few locations. In order to be able to model the spatial behaviour of the corrosion process, the finite element model of the girder is subdivided into six elements of 1 m, and the three layers of strands are modelled separately. This distribution in elements is based on (Darmawan and Stewart, 2007). Here, the subdivision is derived from the assumption that the largest pitting effect happens in the middle of the element and that the prestressing force is again fully transferred to the concrete by the bond between steel and concrete when reaching the next element. Hence, the corrosion degree modelled within an element is the maximum corrosion degree within that element, depending on the maximum pit depth over the element length. In reality, this maximum pit depth might not be in the middle of the element, but the error made by this assumption is limited according to (Darmawan and Stewart, 2007). In the finite element model, when a strand fails, the strand is removed from the model and the increased load on the remaining strands is calculated.
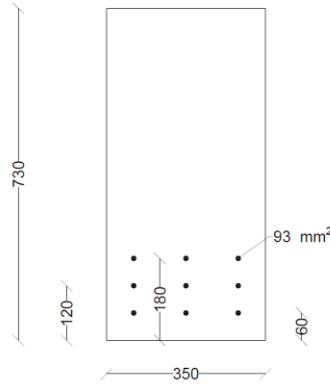
Figure VIII-1: Cross-section of the investigated prestressed girder (dimensions in mm)

In the following, a prior distribution is assigned to a variable η, representing the reduction in prestressing steel area according to $A_p = A_{p0}(1 - \eta)$, with A_p the area of the prestressing steel and A_{p0} the initial area of prestressing steel before corrosion. Since η cannot be negative, a lognormal distribution is assumed. This distribution will also be restricted to an upper limit of one, since the steel section cannot be negative. The mean value of the distribution of η is calculated based on a degradation model (cfr. infra), inserting the mean values of the corrosion variables (i.e. corrosion rate, initiation period and pitting factor). This mean value is calculated accounting for corrosion of individual wires and strands, where the total remaining steel area is evaluated as the sum of the remaining strands and their corresponding sections. In the analysis performed herein, the initiation period is higher for strands with larger concrete covers. The corrosion rate and initiation period are both modelled with a lognormal distribution: $V_{corr} \sim$ LN(0.03, 0.02) [mm/year] (Lay et al., 2003) and $T_i \sim$ LN(21, 10) [years] (for the strands with the smallest concrete cover) (Botte, 2017). The pitting factor α_p is modelled by a Gumbel distribution with location parameter 6.66 and scale parameter 1.07, i.e. mean 6 and standard deviation 3 (Darmawan, 2009; Darmawan and Stewart, 2007; Stewart, 2004). The remaining steel section of each wire is calculated based on the remaining diameter, which is given by $D(t) = D_0 - V_{corr}(t - T_i)\alpha_p$, with D_0 the initial wire diameter (4.1 mm). Based on the wire cross-sections, the remaining strand section is calculated and the corresponding increase in stress. If this increased stress exceeds the tensile strength of the strand, the strand is removed and the force is redistributed over the remaining strands. The stress in a strand is calculated based on a constant pretensioning force on the strand (based on an initial prestress of 1395 MPa per strand), accounting for the remaining wire area. By applying this procedure, the remaining steel area and the total pretensioning force are calculated for each

element of the beam. When assuming that the age of the beam is equal to $t = 50$ years, a mean value of 0.066 is found for η. The COV is assumed equal to 0.3, i.e. corresponding to a rather vague prior.

The posterior distribution of the corrosion degree η is obtained by application of MCMC sampling and assuming the likelihood function provided in equation (VI-3). A proof load is assumed to be placed on the girder, which is simulated by a uniform line load of 10 N/mm over the length of the beam. The data used in this equation consists of simulated static strains at the top and bottom fibre in each of the six elements in which the girder is subdivided. These strains are simulated by inserting the values of η as represented by the black vertical lines in Figure VIII-2 in the finite element model and adding a random sample of the measurement error to these modelled strains. In this analysis, a measurement error of 0.2 µε is assumed. The values of η in the different elements are assumed independent (to account for the local effects of pitting). The model used in the likelihood is a response surface fit to the output of the finite element model of the girder. The output of the response surface are the strains at the different measurement locations and the input are the values of η in each of the six elements in which the girder is subdivided. The response surface is a polynomial response surface of first degree.
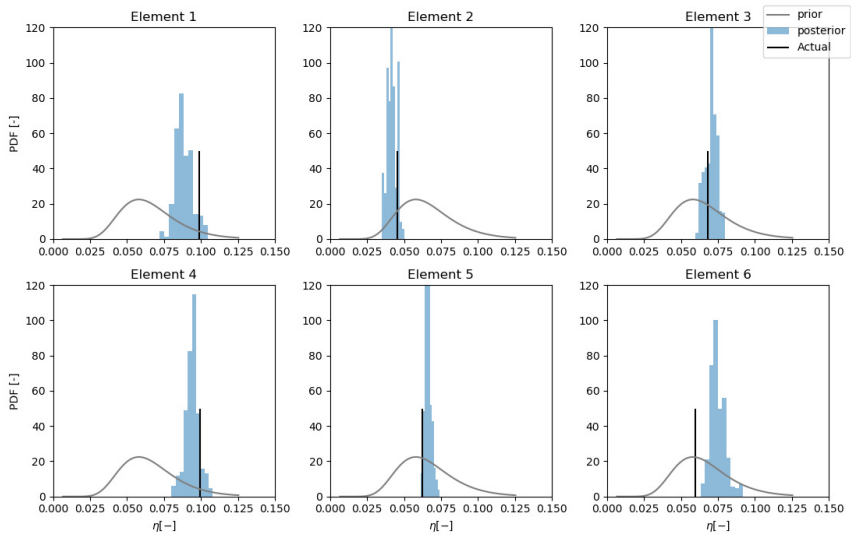

Figure VIII-2: Posterior distribution of the reduction factor η after measuring static strains at top and bottom fibre at all elements when the actual corrosion degree is spatially variable - prestressed girder

When static strains are measured at the top and bottom fibre, centrally at each of the six elements, the posterior distributions of η in all six elements are given in Figure VIII-2. When looking at Figure VIII-2, it can be seen that the actual corrosion degree is approximated well by the posterior distribution, i.e. the posterior mean lies close to the actual value and the corresponding posterior uncertainty is rather small. In Figure VIII-2, the strains are assumed to be measured at all six elements. When the strains are only measured at one element, a reduction of uncertainty is only found at the inspected element.

When the measurement error is increased to 3 µε, the statistics of the posterior distribution are summarized in Table VIII-1. Here it can be seen that, because of the larger measurement error, the posterior uncertainty increases. When the measurement error increases further to 10 µε, again an increase in posterior uncertainty is found. However, the actual corrosion degree is still approximated by the posterior distribution, which follows from the RMS value. Only at the elements closest to the supports, the posterior distribution is almost equal to the prior distribution and there is no reduction of uncertainty. This could be ascribed to the too small (difference in) strains compared to the measurement error.

Table VIII-1: Influence of the measurement error on the posterior uncertainty (minimum standard deviation σ_{min}, maximum standard deviation σ_{max} and average standard deviation $\sigma_{average}$) and the deviation between the posterior mean and the actual value of the corrosion degree (RMS) – prestressed girder

Measurement locations	Measurement error	RMS	σ_{max}	σ_{min}	$\sigma_{average}$
All elements	0.2 µε	0.004	0.006	0.002	0.005
	3 µε	0.008	0.012	0.006	0.008
	10 µε	0.018	0.018	0.014	0.016
Element 4	0.2 µε	0.024	0.023	0.007	0.018
	3 µε	0.023	0.021	0.008	0.018
	10 µε	0.023	0.024	0.015	0.020

The abovementioned calculations only provide a posterior distribution of the corrosion degree η and do not allow forecasting the remaining prestressing steel area, i.e. predicting the reduction over time. Hence, in the following investigation, the reduction in steel area is dependent on the initiation period T_i and a rate of reduction over time a, i.e. $\eta = a(t - T_i)$ if $t > T_i$, else $\eta = 0$. The mean of the rate a is calculated based on the corrosion rate and pitting factor as given earlier, by applying a Taylor approximation. The uncertainty is represented by a COV of 0.3 (also for the initiation period). Both the rate and the initiation period are modelled by a lognormal distribution. Instead of only updating the corrosion

degree η, now also the distributions of the initiation period T_i and the corrosion rate a are updated based on the (simulated) data. The posterior distribution of the reduction in reinforcement area η is now given in Figure VIII-3 for static strain measurements at all elements when the actual underlying corrosion degree is uniform along the length of the beam and depends on the initiation period and reduction rate. Here it can be seen that slightly larger posterior uncertainties are achieved since there are more unknowns. Nevertheless, the posterior distribution provides a good estimate of the actual reduction in steel area. Again, when the measurement error increases, the posterior uncertainty increases, as visible in Table VIII-2.
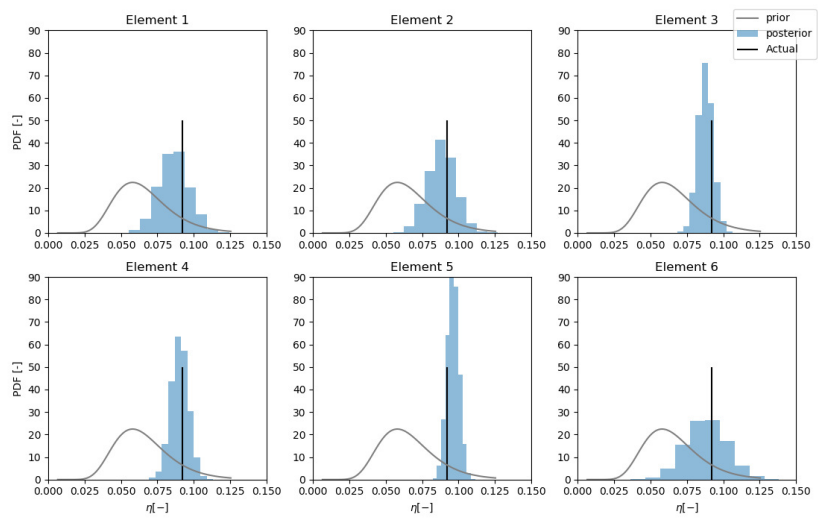
Figure VIII-3: Posterior distribution of the reduction factor η when measuring static strains at all elements when assuming a relationship between the reduction factor η and an initiation period and a reduction rate - prestressed girder

Table VIII-2: Influence of the measurement error on the posterior uncertainty (minimum standard deviation σ_{min}, maximum standard deviation σ_{max} and average standard deviation $\sigma_{average}$) and the deviation between the posterior mean and the actual value of the corrosion degree (RMS) – prestressed girder, corrosion degree as a function of initiation period and reduction rate

Measurement error	RMS	σ_{max}	σ_{min}	$\sigma_{average}$
0.2 µε	0.004	0.014	0.004	0.008
3 µε	0.005	0.016	0.007	0.010
10 µε	0.011	0.021	0.014	0.017

The aforementioned results are based on the measurement of strains under a known load. The influence of modal data extracted from ambient vibration tests is also investigated. For this purpose, the same 2D finite element model is applied, but now without the proof load and with a structural eigenvalue analysis. In Figure VIII-4, the posterior distribution of the reduction in steel section is given when updating is performed based on strain mode shapes and natural frequencies from the first four modes (strains measured at all six elements, measurement error 0.2 µε for the strains and 0.1% of the experimental frequency for the natural frequencies). The posterior distribution shifts to the actual value, but has a larger uncertainty compared to the case where static strain data is accounted for. When the measurement error increases, the posterior distribution becomes more vague, as summarized in Table VIII-3. When displacement mode shapes are accounted for instead of strain mode shapes, the posterior distribution has a quite large uncertainty, as visible in Figure VIII-5 (assumed errors in the likelihood function are 1% of the norm of the experimental mode shapes and 0.1% of the experimental natural frequency) and Table VIII-3. This increased uncertainty could be ascribed to the relative error assumed in both situations, but also to the fact that strain mode shapes are more sensitive to local changes in stiffness than displacement mode shapes.
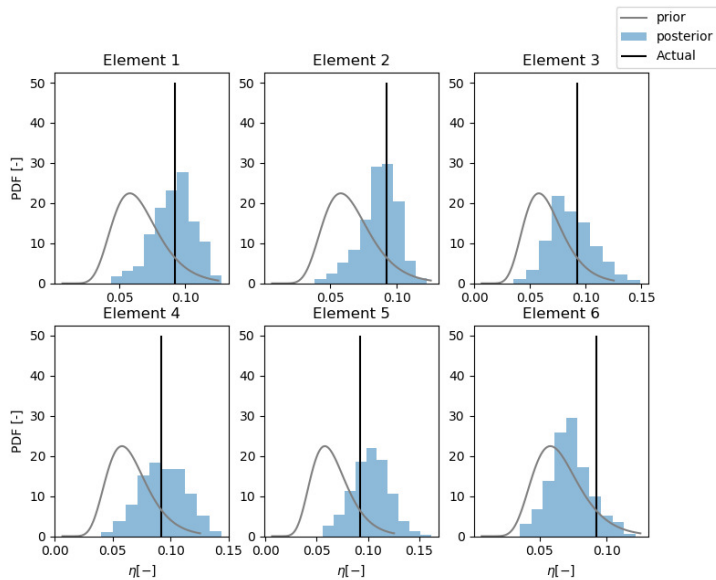
Figure VIII-4: Posterior distribution of the reduction factor η when updating based on natural frequencies and strain mode shapes at all elements at the lower fibre - assuming a relationship between the reduction factor η and an initiation period and a reduction rate - prestressed girder

Table VIII-3: Influence of the error in the likelihood function on RMS, minimum standard deviation σ_{min}, maximum standard deviation σ_{max} and average standard deviation $\sigma_{average}$ when accounting for modal data – prestressed girder

Data type	Measurement error	RMS	σ_{max}	σ_{min}	$\sigma_{average}$
Natural frequencies and strain mode shapes	$0.2\ \mu\varepsilon,\ 0.001\bar{\lambda}_r$	0.009	0.020	0.014	0.017
	$1.0\ \mu\varepsilon,\ 0.01\bar{\lambda}_r$	0.018	0.029	0.020	0.024
Natural frequencies and displacement mode shapes	$0.01\|\bar{\phi}_r\|,\ 0.001\bar{\lambda}_r$	0.005	0.029	0.022	0.026
	$0.1\|\bar{\phi}_r\|,\ 0.01\bar{\lambda}_r$	0.015	0.034	0.028	0.031
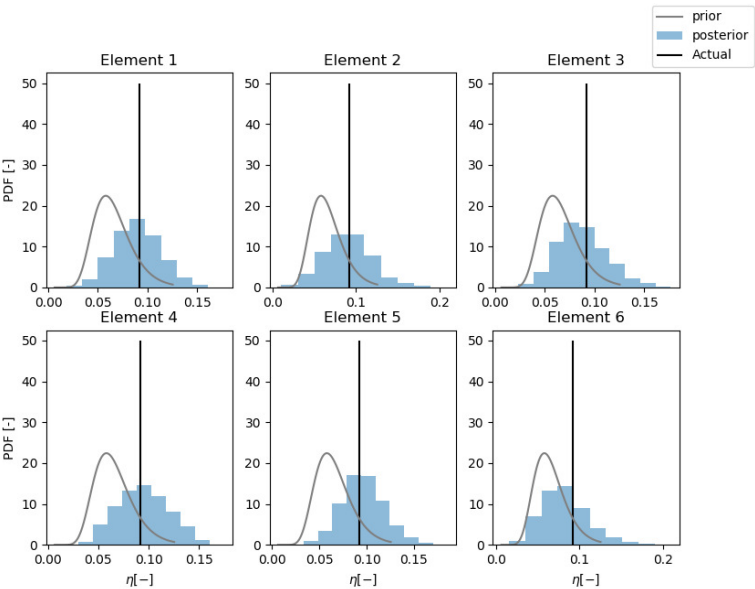
Figure VIII-5: Posterior distribution of the reduction factor η when updating based on natural frequencies and displacement mode shapes at all elements - assuming a relationship between the reduction factor η and an initiation period and a reduction rate - prestressed girder

VIII.3 Updating of corrosion variables in a prestressed bridge

The analysis is extended from the prestressed girder to a more realistic case of a prestressed concrete bridge. The bridge is described in (Lebeau and Wadia-Fascetti, 2010), has a span of 13.1 m, and consists of 6 prestressed girders spaced 2 m from each other. The slab on top of the girders has a thickness of 165 mm and a total width of 11.6 m. The dimensions of the girders themselves are given in Figure VIII-6.

A 3D finite element model of the whole bridge deck is developed in DIANA FEA (DIANA FEA BV, 2019), where strains are calculated based on non-linear analyses. In the finite element model, the Young's modulus of the concrete equals 37 GPa, the tensile strength 4.1 MPa and the concrete compressive strength 40 MPa. The tensile strength of the strands equals 1860 MPa and the initial applied prestress is equal to 1395 MPa, which corresponds to a force of 72540 N per strand. The Young's modulus of the steel equals 190 GPa.

The remaining steel section along the bridge is estimated based on simulated data. Similarly as in the previous application, this is done based on Bayesian methods and the MCMC algorithm. No correlation in the pitting factor in neighbouring strands is considered according to (Darmawan and Stewart, 2007). The initiation period and corrosion rate are assumed constant along the bridge. The mean of the initiation period is assumed 21 years and the standard deviation equals 10 years. The mean of the corrosion rate is 0.03 mm/year (airborne seawater) and the standard deviation equals 0.04 mm/year. The pitting factor for a bar of 8 mm diameter has a Gumbel distribution with mean 6 and COV 0.2 (Darmawan and Stewart, 2007; Stewart, 2009). The parameter α of the Gumbel distribution remains unaltered and equals 1.07. The parameter u is altered to account for the correct area of the strands and equals 6.66. The bridge is subdivided into elements based on the anchorage length, which equals 848 mm based on 9.5 mm diameter 7-wire strands. The element length is checked to reach a converged probability of failure, i.e. if the element length is further reduced, this does not influence the failure probability of the bridge anymore. For calculating the failure probability, bending failure of the bridge girders is considered, modelling each girder as a series system consisting of the different elements in which it is subdivided. As such, the girders are subdivided into 16 elements of 818.75 mm. To account for spatial variation of the corrosion process, the pitting factor will be different in each of the elements, assuming no correlation between the different elements.
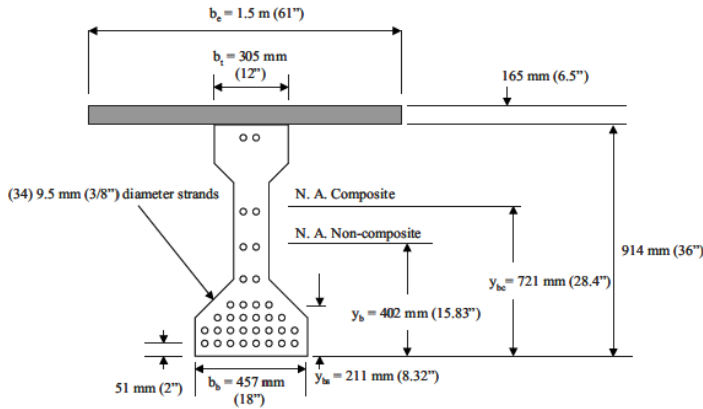
Figure VIII-6: Cross-section of a girder of a prestressed bridge (Lebeau and Wadia-Fascetti, 2010)

The bridge is assumed to be subjected to a proof load. The applied proof load is modelled by a uniform load of 9 kN/m², inspired by the highest lane loads suggested by the Eurocode. This is just an assumption to model a load that has a sufficient high influence on the structural behaviour of the bridge without exceeding the cracking moment. For a real case study, information about the applied proof load will be available and this load should be simulated in the model of the bridge. It has been assumed that the strains are measured at all the elements in which the bridge is subdivided, except for the first and last element of each girder (since these are assumed not to be accessible). First, only corrosion of the lowest layer of strands is assumed. The model in the likelihood function will consist of a polynomial response surface of first degree fit to the output of the finite element model, i.e. the strains at the different measurement locations. The input of the response surface will be the corrosion degree in each of the elements in which the structure is discretized. The posterior distribution of the remaining steel section is given in Figure VIII-7 for an error of 0.2 µε, and the posterior statistics are summarized in Table VIII-4 considering different values for the measurement error. Results are each time given for a small measurement error (0.2 µε) and a larger measurement error (3 µε and 10 µε). It has also been investigated how the posterior distribution is influenced if only half of the elements are inspected. When elements are alternately inspected and not inspected, the results are also summarized in Table VIII-4. Here it can be seen that when less elements are inspected, the uncertainty of the posterior distribution increases. This increase will especially take place at the non-inspected elements.

Table VIII-4: Influence of the measurement error on the posterior uncertainty (minimum standard deviation σ_{min}, maximum standard deviation σ_{max} and average standard deviation $\sigma_{average}$) and the deviation between the posterior mean of the corrosion degree and the actual value (RMS) – prestressed bridge, lowest layer of strands subjected to corrosion

Measurement locations	Measurement error	RMS	σ_{max}	σ_{min}	$\sigma_{average}$
All elements	0.2 µε	74.98	107.69	21.17	60.29
	3 µε	73.16	116.12	39.83	70.77
	10 µε	75.38	122.45	47.35	77.86
Half of the elements	0.2 µε	73.98	120.72	38.27	76.68
	3 µε	76.76	125.70	44.50	89.52
	10 µε	78.43	136.82	57.47	96.61

Figure VIII-7: Posterior distribution of the remaining steel section of the lowest layer of strands for the prestressed bridge at each girder

When looking at Figure VIII-7, there is still some deviation between the posterior mean and actual value, where the latter is not always located in the Highest Density Intervals (HDI) of the posterior distribution. Due to modelling the corrosion process as a function of initiation period and corrosion rate, only limited corrosion levels are considered in the abovementioned analysis, where only the lowest layer of strands is affected by corrosion. In the following analysis, the corrosion degree will not be modelled dependent on the initiation period and corrosion rate, but a uniform prior distribution will be assumed between no strands present in the lowest three layers of reinforcement and all strands present in the lowest three layers of reinforcement. The response surface is again a polynomial response surface of first degree. To calculate the response surface, LHS samples

of the remaining steel section in the lowest three layers of strands are generated, assuming a uniform distribution between zero bars present and all bars present, and this for all the elements. As such, a larger variation on the amount of prestressing reinforcement present in the girder is possible compared to the previous analysis. This larger variation in prestressing steel results in a larger variation on the resulting strains. When updating is performed based on this response surface, a posterior distribution is found with the actual value located within the highest density intervals of the posterior distribution. Hence, this posterior distribution is capable of estimating the remaining steel section at all locations where measurements are performed. When measurements are performed at all elements, except at the first and last element of each girder, the posterior distribution is visualized in Figure VIII-8 for a gradual progression of the actual remaining steel sections along the length of the girders and a measurement error of 0.2 με. For a measurement error of 3 με and for a measurement error of 10 με, results are summarized in Table VIII-5. Further, also for a more irregular behaviour of the corrosion process, the actual remaining steel section can be approximated by the posterior distribution, as illustrated in Figure VIII-9. When measurements are not performed at all locations, a larger posterior uncertainty is found, especially at the non-inspected locations. Also for this simulated measurement result, statistics of the posterior distribution are given in Table VIII-5 for different measurement errors. The better results for this situation compared to the previous situation could be ascribed to the fact that a larger variation in total remaining steel section is considered, leading to a larger variation on the resulting strains, especially when compared to the assumed measurement error. This larger spread on the possible results leads to a better identification.
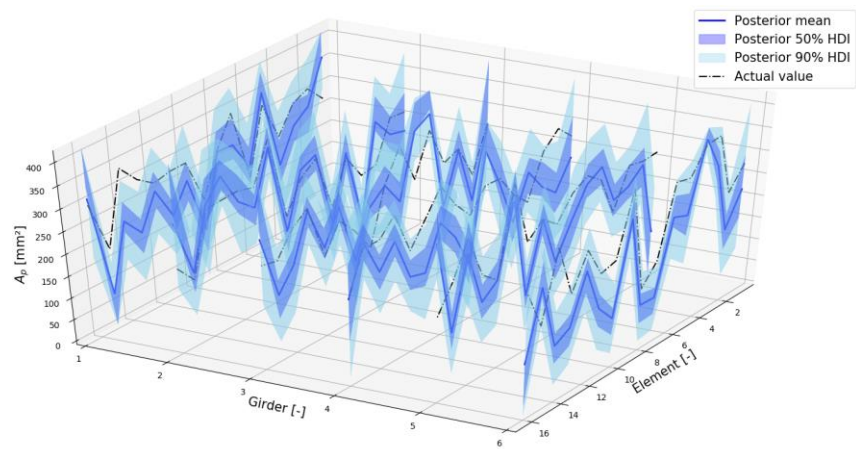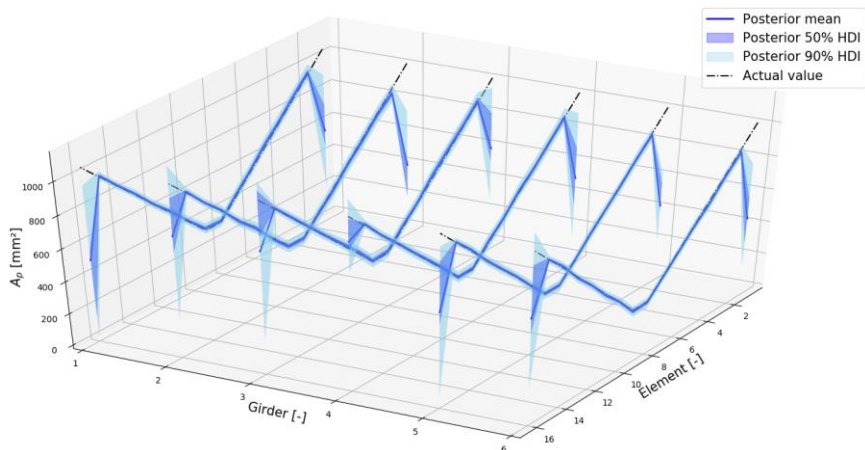

Figure VIII-8: Posterior distribution of the remaining steel section of the lowest three layers of strands for the prestressed bridge – measurement results based on gradual progression of the actual remaining steel section

Table VIII-5: Influence of the measurement error on the posterior uncertainty (minimum standard deviation σ_{min}, maximum standard deviation σ_{max} and average standard deviation $\sigma_{average}$) and the deviation between the posterior mean of the remaining steel section and the actual value (RMS) – prestressed bridge, three layers of strands subjected to corrosion

| Meas. result	Meas. location	Meas. error	RMS	σ_{max}	σ_{min}	$\sigma_{average}$
Gradual (Figure VIII-8)	All elements	0.2 με	166.05	317.62	13.31	47.57
		3 με	207.56	379.25	17.62	79.69
		10 με	185.73	366.49	34.95	95.74
Random (Figure VIII-9)	All elements	0.2 με	94.64	253.98	12.18	41.29
		3 με	155.96	338.56	16.69	56.39
		10 με	163.93	355.74	29.13	79.39
	Half of the elements	0.2 με	176.83	341.53	15.11	89.15
		3 με	214.26	343.90	21.74	143.63
		10 με	243.66	368.06	34.75	192.85
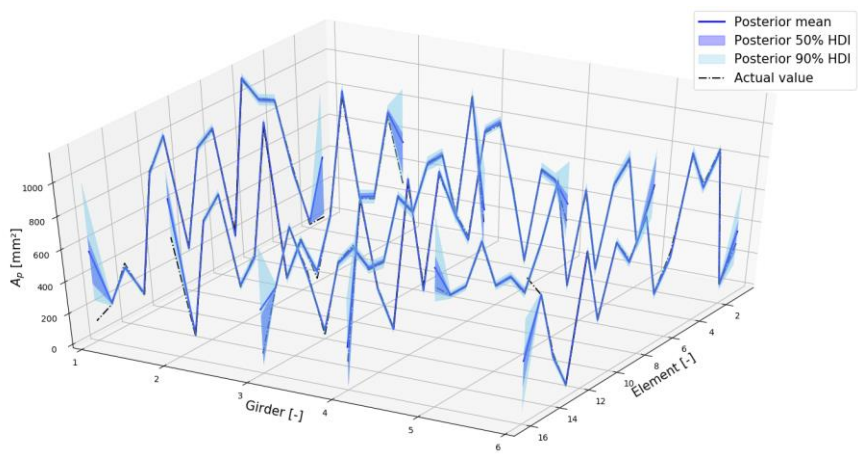
Figure VIII-9: Posterior distribution of the remaining steel section of the lowest three layers of strands for the prestressed bridge – random progression of the actual remaining steel section

VIII.4 Updating of corrosion in a post-tensioned beam

The influence of corrosion of reinforcement and strands in a post-tensioned beam is also investigated. The beam under consideration is taken from (Vu et al., 2010). This is a beam with length 3 m, height 200 mm and width 150 mm. The beam has a tendon with diameter 8 mm in a plastic duct, to which a post-tensioning force of 54 kN is applied (Figure VIII-10). The Young's modulus of the tendon is 200 GPa and the ultimate strength equals 1600 MPa. There are also three reinforcement bars of 6 mm diameter present in the section. When the beam is subjected to a corrosive environment, corrosion of these reinforcement bars will arise. Furthermore, due to the presence of voids in the grout of the duct, the post-tensioning strand can also corrode. The influence of corrosion of the tendon and of the unstressed reinforcement on the static strains and natural frequencies is investigated. For this purpose, a finite element model of the beam is created and a non-linear analysis is performed. To model the spatial variation of corrosion, the beam is subdivided into six elements of 0.5 m.
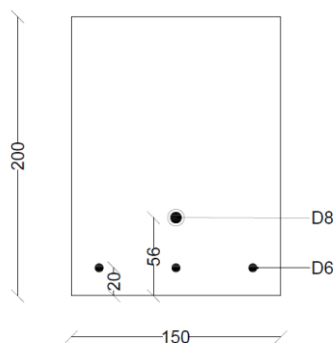
Figure VIII-10: Cross-section of the considered post-tensioned beam (dimensions in mm)

It is investigated whether the corrosion variables can be updated based on static strain measurements performed under proof loading (i.e. a known load represented by a uniform load of 3 N/mm over the length of the beam). The corrosion variables are assumed to vary over the different elements, assuming no correlation of the corrosion degree between the elements. When the reduction is ascribed to pitting corrosion, the assumption of no correlation of the corrosion degree makes sense, since the pit depths in the different elements will be independent. For the tendon, the initiation period T_i is assumed to have a mean of 15 years according to (Nguyen et al., 2013) and a COV of 0.3. The mean value of the initiation period is based on the assumption that corrosion initiates due to the presence of chlorides in grout voids in the duct. The initiation period is modelled by a lognormal distribution. The rate at which the prestressing steel section reduces (a) is also modelled by a

lognormal distribution and has a mean of 0.0036 mm/year. The area of a tendon is given by $A_p(t) = A_{p0} \cdot (1 - \eta)$ with $\eta = a \cdot (t - T_i)$. For the unstressed reinforcement, the reduction in reinforcement radius is calculated as $x(t) = 2V_{corr}ToW(t - T_i)$. Here, ToW is the time of wetness (equal to 0.75), V_{corr} the corrosion rate (lognormal distribution with mean 0.03 mm/year and standard deviation 0.02 mm/year) and T_i the initiation period (lognormal distribution with mean 21 years and standard deviation 10 years). The grout cover on the tendons can be smaller than the concrete cover on the unstressed reinforcement, leading to a smaller initiation period for the prestressing reinforcement, as is also assumed in this example.

Two situations are possible in case of a post-tensioned structure, i.e. either the duct is grouted or the duct is ungrouted. If the duct is grouted and a tendon breaks, the pretension can be retransferred to the structure at a distance equal to the transfer length from the breakage location due to the bond between the grout and the steel. On the other hand, if the duct is ungrouted, this is not possible and the complete prestress of the broken tendon will be lost.

VIII.4.1 Grouted duct

A response surface is used to model the strains and is generated based on LHS samples of the initiation period and corrosion rate of the reinforcement bars in all elements and the initiation period and corrosion rate of the tendon in all elements. As such, different samples of the corrosion degree η of the tendon elements and of the corrosion degree α of the reinforcement elements are generated. Inserting these in the finite element model results in different samples of the strains. A response surface of first degree is applied as a function of the corrosion degree α of the reinforcement bars at all elements and the corrosion degree η of the tendon elements. When the standard deviation of the strains resulting from these LHS samples is calculated for each of the elements individually, it appears to be 6 to 20 times larger than the error on the strains by replacing the finite element model by the response surface. Hence, the error of the response surface is considered sufficiently small as it is well below the expected influence of the corrosion degrees η and α on the strains. On the other hand, the standard deviation of the resulting strains is of the order of magnitude of 1.4 µε, whereas the measurement error is assumed equal to 0.2 µε (which already corresponds to very accurate measurements). Hence, this measurement error is quite large compared to the variation in strains due to corrosion.

Based on the assumed corrosion variables described above, the reduction in area of the tendons is only limited. Hence, when updating is performed based on strain measurements, the posterior distribution of the corrosion degree of the tendon is very close to its prior distribution and only the distribution of the corrosion degree α of the reinforcement bars is updated, as illustrated in Figure VIII-11 and Figure

VIII-12. In these results, only the corrosion degree α of the unstressed reinforcement is updated since for all sampled values of η, no failure of the strands has occurred and hence there is no influence of the reduced strand area on the structural behaviour of the girder. The corrosion degree of the tendon is not updated in both cases (i.e. the posterior distribution is (almost) equal to the prior distribution), which could be ascribed to the fact that it only influences the strains to a noticeable extent once the tendon has failed. When the measurement error on the strains is increased, the posterior distributions are close to the prior distributions.
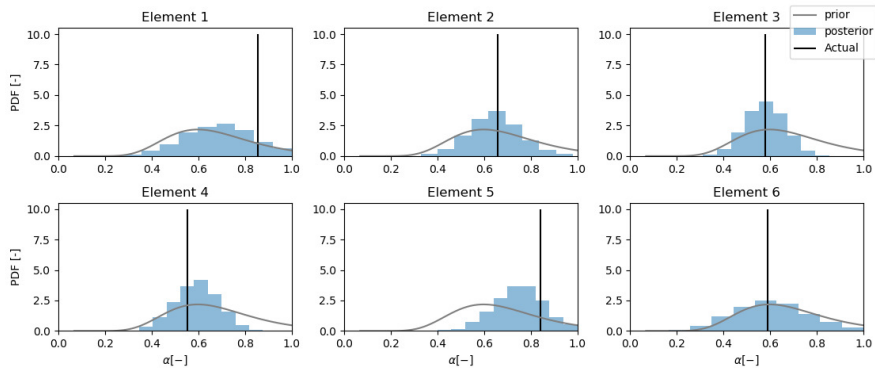
Figure VIII-11: Prior and posterior distribution of the corrosion degree α of the unstressed reinforcement for the grouted post-tensioned girder when the actual corrosion degree is spatially variable
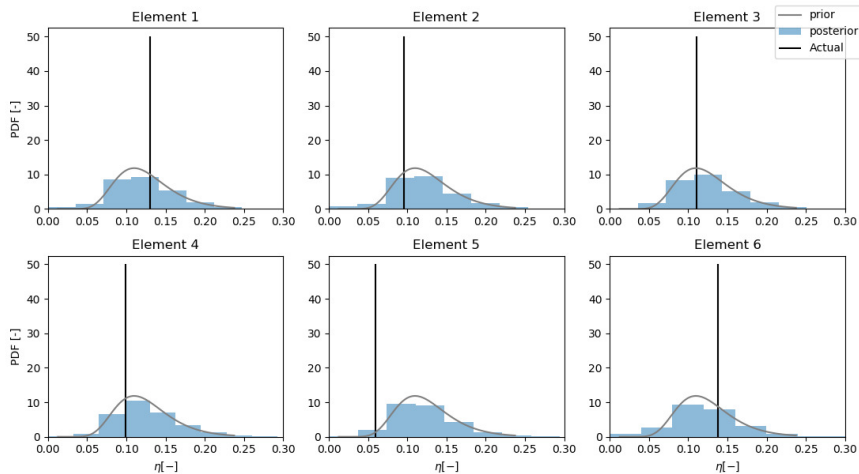
Figure VIII-12: Prior and posterior distribution of the corrosion degree η of the prestressing tendon for the grouted post-tensioned girder when the actual corrosion degree is spatially variable

VIII.4.2 Ungrouted duct

When the duct is ungrouted, the tendon has either ruptured somewhere and the complete prestress is lost, or the tendon has not ruptured and all prestress remains available. In this case, the spatial distribution of the corrosion degree η of the tendon does not need to be considered due to the aforementioned structural behaviour. On the other hand, spatial variability of the corrosion degree α of the unstressed reinforcement steel remains possible. Hence, the duct is assumed ungrouted and two response surfaces are made, i.e. one when the tendon in the duct is active and one where the tendon is ruptured. In each of the response surfaces, the corrosion degree of the unstressed reinforcement varies along the length of the girder. The applied response surfaces are polynomial response surfaces of the first degree, where the strain is given as a function of the corrosion degree in the unstressed reinforcement. The posterior distributions are given in Figure VIII-13 and Figure VIII-14 when assuming uniform prior distributions between zero and one for the different corrosion degrees. This differs from the previous section since now the focus is on the influence of the tendon rupture. Hence, for η lower than a specific threshold, the tendon would still be delivering prestress and if η exceeds this threshold, the tendon will break and no prestress will be present anymore. Here it can be seen that the posterior distributions approach the actual corrosion degree α of the unstressed reinforcement or the corrosion degree η of the prestressing steel. Nevertheless, the posterior distributions remain rather vague. When the measurement error is increased to $3\,\mu\varepsilon$, the posterior distributions are (almost) equal to the prior distributions for this case.
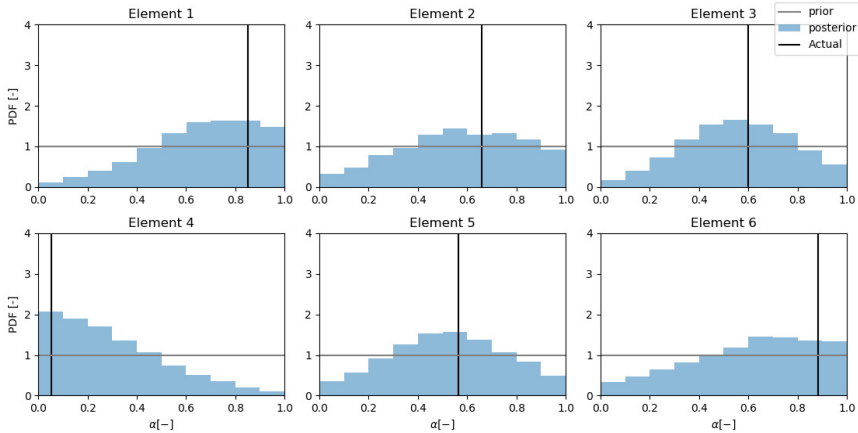
Figure VIII-13: Posterior corrosion degree α of the unstressed reinforcement for an ungrouted post-tensioned girder
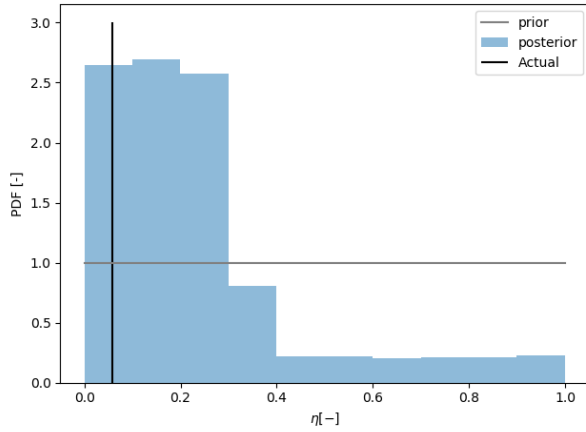
Figure VIII-14: Posterior corrosion degree η of the prestressing tendon for an ungrouted post-tensioned girder

VIII.5 UCO case study

The next section does not focus on a corrosion-related problem but on a more general problem, i.e. the assessment of the remaining prestress of a post-tensioned structure, which can also be tackled with the developed approaches. During previous investigations at the Magnel-Vandepitte Laboratory, 70-year old post-tensioned concrete beams were subjected to destructive testing, and the results of this experimental campaign are used to update the remaining prestress of the beams.

VIII.5.1 Introduction to the case study

The textile factory 'Union Cottonière' (UCO) at Ghent was constructed in 1947-1948 and hence dates from the pioneering period of prestressed concrete structures. Its roof structure consists of large post-tensioned concrete beams and was originally designed by prof. Gustave Magnel. The primary beams have a nominal span of 20.5 m and are supported by concrete corbels, which are monolithically attached to the columns of the structure. They have a height of 1.75 m with a top flange of 90 cm wide and a bottom flange of 50 cm wide (Magnel, 1948) (Figure VII-15). The prestressing tendons in these beams consist of three bundles of 48 wires with a diameter of 5 mm, with an initial prestress of 1000 MPa (Magnel, 1948). In addition, these beams do not contain any other reinforcement, except for some stirrups in the anchor blocks and the reinforcement in the corbels that carry the secondary beams. Note that no supporting reinforcement is provided to anchor the corbels. The secondary beams have a height of 1.0 m, the top flange has a width of 30 cm and the bottom flange has a width of 16 cm. The web has a thickness of only 10 cm. The prestressing tendon

consists of a single bundle of 24 wires with a diameter of 5 mm, with an initial prestress of 1000 MPa. The prestress was applied according to the Blaton-Magnel system. No other reinforcement was present, except for the prestressing reinforcement and some stirrups in the anchor blocks. According to (Magnel, 1948), the design was performed considering a maximum compressive stress of 13 MPa in the concrete, while the compressive strength of concrete at the moment of prestressing was estimated at 40 MPa.

(a) Primary beam

(b) Cross-sections of primary beam
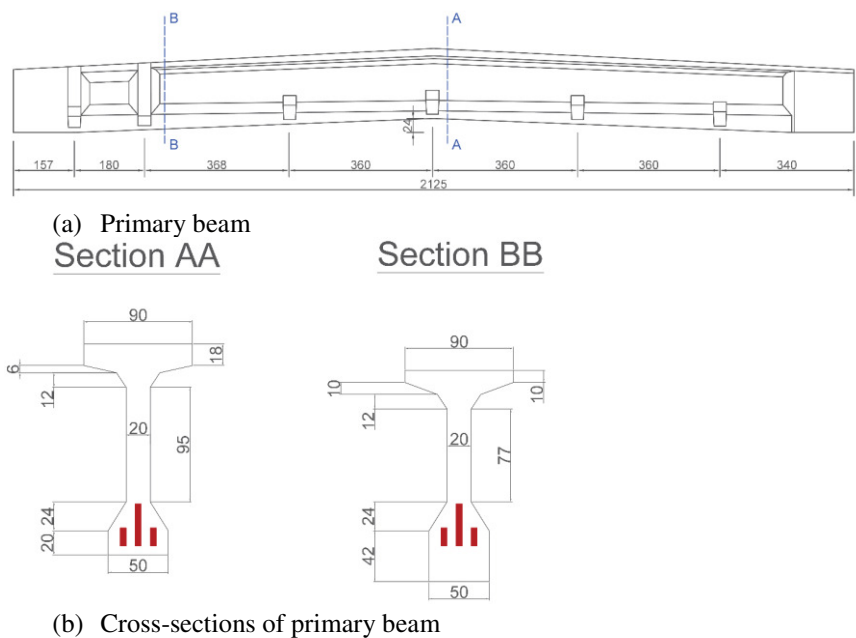
Figure VIII-15: (a) Dimensions of the primary beam; (b) dimensions of a cross-section at mid-span (AA) and close to the anchor block (BB) (Dimensions in cm) (Botte et al., 2021)

In 2016, part of the factory was demolished. Subsequently, one primary beam and one secondary beam were transported for testing to the Magnel-Vandepitte Laboratory for Structural Engineering and Building Materials of Ghent University, where they were tested up to failure. The experimental campaign included tests for material characterisation and destructive testing of the beams. Based on the available test results, a Bayesian framework is adopted to determine the distributions for the material parameters and for the remaining prestress.

VIII.5.2 Experimental program

VIII.5.2.1 Material properties

The mechanical properties of the concrete and the prestressing steel were determined based on specimens taken from another beam situated in the same building. The concrete compressive strength (according to EN 12390-3) and density were determined based on three cylindrical specimens with a height of 100 mm and a diameter of 100 mm. Furthermore, the characteristics of the prestressing steel were determined based on tensile tests performed on three wires according to EN ISO 15630-3. The results are presented in Table VIII-6. Additional cores were drilled from remaining pieces of the test on the primary beams, and a tensile splitting test has been performed on these cores, yielding an average value $f_{ct,sp} = 4.2$ MPa. According to EN1992-1-1 (paragraph 3.1.2(8)) the average tensile strength can be calculated as $f_{ctm} = 0.9 f_{ct,sp}$, i.e. $f_{ctm} = 3.7$ MPa.

Table VIII-6: Characteristics of concrete and prestressing steel

	Concrete		Prestressing steel		
	$f_{c,cyl\ 100x100}$ [MPa]	ρ_c [kg/m³]	$F_{p0.2}$ [MPa]	F_m [MPa]	E_p [GPa]
μ	52.6	2310	1478	1704	194.4
σ	5.6	30	43	24	0.8

Notations: $f_{c,cyl100x100}$: compressive strength determined on cylinders with a height and diameter of 100 mm; ρ_c: mass density of concrete; $F_{p0.2}$: 0.2% strain limit; F_m: tensile strength; E_p: Young's modulus

VIII.5.2.2 Testing of the primary beam

The primary beam was prestressed by means of three bundles of 56 Ø 5 mm, which deviates from the description provided in (Magnel, 1948) and can be attributed to the specific load configuration and geometry of this particular beam. To test the beam, the beam was simply supported using a hinged support at the left and a roller support at the right. The distance between the two supports was 20.5 m, which corresponds to the nominal span according to (Magnel, 1948). The primary beam was loaded up to failure by means of two point loads located at 7.25 m from the supports. At each loading point, two jacks with a capacity of 500 kN each were used to apply the force on a mortar embedded steel profile in order to properly distribute the two point loads on the top flange of the beam. The test set-up is visualized in Figure VIII-16.
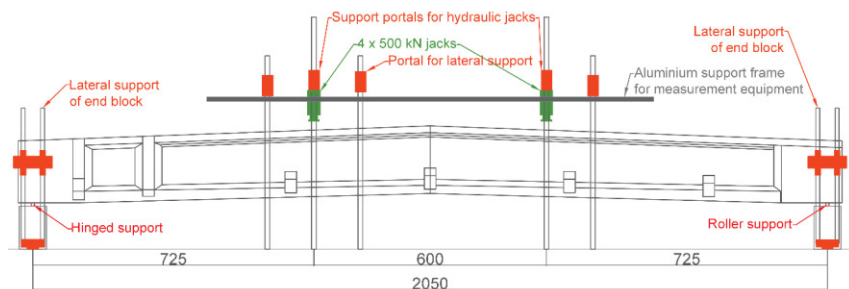
(a) Schematic test set-up primary beam

(b) Actual test set-up primary beam

Figure VIII-16: (a) Schematic overview of the test set-up for the primary beam (dimensions in cm); (b) picture of the actual test set-up for the primary beam (Botte et al., 2021)

The test on the primary beam was performed in two phases. In the first phase, the load applied at each of the two load application points was increased up to a load level higher than the cracking moment and subsequently the beam was fully unloaded. During phase 2, the load was increased up to failure of the beam. It should be noted that due to the limited stroke of the jacks (i.e. 125 mm), the jacks had to be readjusted while the loads were taken over by an auxiliary reaction system.

The load-deflection diagram is shown in Figure VIII-17. The load P represents the load applied in one load application point. The deflection is the vertical deflection at mid-span measured by means of an LVDT. Additionally, the displacements obtained by means of dial gauges at discrete load levels are also shown in Figure VIII-17. The load-deflection curve related to phase 1 shows a linear elastic behaviour up to approximately 450 kN, after which a non-linear behaviour is observed up to 580 kN. Subsequently, the load is completely removed and a residual deflection of 2.5 mm is found. The load-deflection curve of phase 2 shows a linear elastic behaviour up to a load level of approximately 400 kN after which a non-linear behaviour is observed. At a mid-span deflection of 140 mm, the take-over procedure was executed. The beam failed at a load level of approximately

800 kN per load application point (or 1600 kN in total) and a mid-span deflection of 170 mm.

Deformation gauges are applied at a bottom fibre located around mid-span. The deformation measurements related to phase 1 allow detecting the moment of cracking. The first and second crack appear at a load level of approximately 420 kN and 460 kN, respectively. The latter is reflected by a sudden increase of the opening of the deformation gauges. These load levels correspond approximately to the load level at which the load-deflection behaviour in Figure VIII-17 becomes non-linear. The deformation measurements related to phase 2 allow detecting the moment of reopening of the previously formed cracks, i.e. the moment of decompression of the bottom fibre. The first crack reopens at a load level of approximately 350 kN.

For more details and additional measurements, reference is made to (Botte et al., 2021).
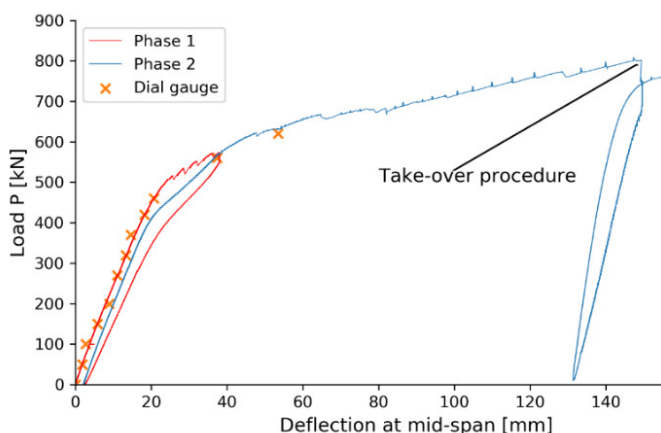
Figure VIII-17: Load applied in one load application point as a function of the deflection at mid-span for the primary UCO beam (Botte et al., 2021)

VIII.5.2.3 Testing of the secondary beam

Similar to the primary beam, also the secondary beam is simply supported: a hinged support at one side and a roller support at the other side. The supports have an intermediate distance of 13.7 m, which corresponds to the theoretical span length as indicated in (Magnel, 1948). The beam was loaded by four point loads: the outer load application points were located at 1.7 m from the supports, while the inner load application points were located at a nominal distance 5.1 m from the supports. Considering the slender geometry of the beam, it was decided to

support against lateral displacements at both end sections and near one of the load application points. The test set-up is visualized in Figure VIII-18.
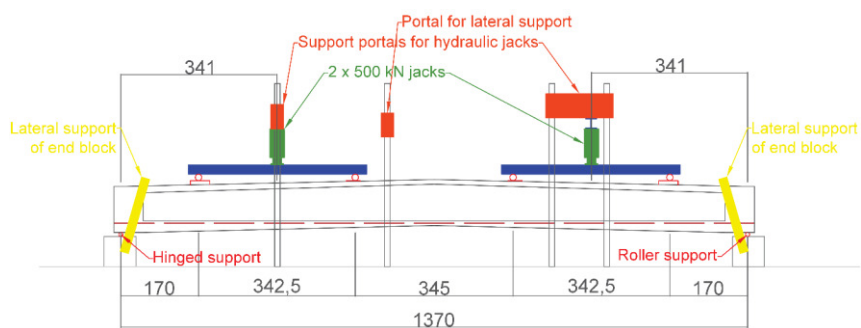
(a) Schematic test set-up secondary beam

(b) Actual test set-up secondary beam

Figure VIII-18: (a) Schematic overview of the test set-up for the secondary beam (dimensions in cm); (b) picture of the actual test set-up for the secondary beam (Botte et al., 2021)

Similar to the test on the primary beam, also the test on the secondary beam was executed in two phases. In the first phase, the load P was increased up to a load level higher than the cracking moment and subsequently the beam was partially unloaded. During phase 2, the load P was increased up to failure of the beam. Figure VIII-19 shows the load P applied by one jack as a function of the mid-span deflection. Additionally, the displacements obtained by means of a dial gauge located at mid-span at discrete load levels are also shown. The beam failed at a load level of approximately 160 kN per jack (or 320 kN in total) and a mid-span displacement of 150 mm. Deformation measurements revealed that the cracks reopen at a load level of approximately 40 kN to 50 kN.

For more details and additional measurements, reference is made to (Botte et al., 2021).
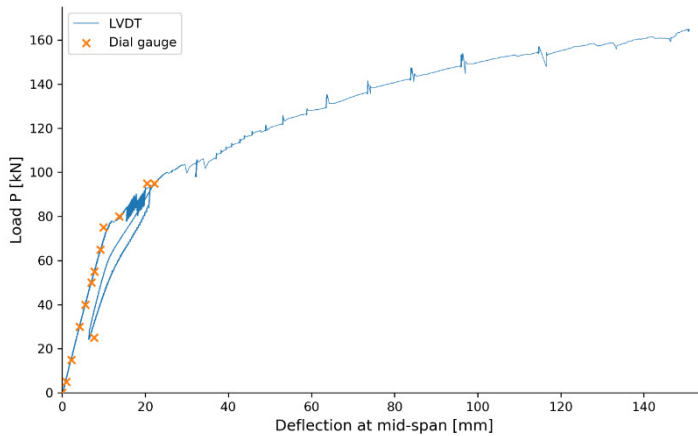

Figure VIII-19: Load applied by one jack as a function of the deflection at mid-span for the secondary UCO beam (Botte et al., 2021)

VIII.5.3 Bayesian updating based on the experimental results

The remaining prestress of the beams is determined based on a Bayesian assessment procedure. First, the assumed prior distributions of the material parameters are updated based on the available data from the material characterization. Then, these updated distributions are used to determine a probability distribution for the remaining prestress. This last step is performed for both the primary and secondary beam.

To simulate the relationship between the prestress and the load-displacement diagram, a numerical model of the beams was made in DIANA FEA (DIANA FEA BV, 2019). A 2D finite element model was developed. Eight-node quadrilateral isoparametric plane stress elements based on quadratic interpolation and Gauss integration were used to model the concrete. The average element size was 75 mm. These properties were selected based on convergence of the results of the finite element model. Non-linear material properties were assigned to the concrete elements (i.e. non-linear material behaviour in tension and compression), and a total strain based fixed crack model was used to allow for cracking. A Hordijk tension-softening model was used for concrete in tension, while for concrete in compression a parabolic stress-strain relationship based on the fracture energy was implemented. A variable shear retention model was used in which de shear stiffness gradually reduces to zero for a crack width of half the average aggregate size (which was assumed equal to 10 mm). For the reinforcement, one-

dimensional fully embedded reinforcement was applied for which perfect bond between the reinforcement and the neighbouring concrete elements is assumed. Non-linear material properties were assigned to these reinforcement elements. The strain-hardening hypothesis together with the Von Mises plasticity criterion was used.

A sensitivity study has been performed to determine the most important input parameters of the numerical model influencing the measurement results used in the Bayesian analysis, i.e. the moment of decompression of the bottom fibre, the cracking moment and the displacement at a certain (arbitrary) load level in the non-linear branch of the second phase. From this sensitivity study, it is found that the following variables need to be considered:
- The tensile strength of the concrete;
- The prestress;
- The Young's modulus of the concrete;
- The stress-strain diagram of the steel, defined by the Young's modulus and the steel yield stress;
- The concrete density.

Hence, distributions for these variables are updated in the following.

VIII.5.3.1 Updating of distributions for material characteristics

From a mathematical point of view, the use of so-called natural conjugate priors in the Bayesian updating procedure is very useful, since it allows having a posterior distribution that is of the same form as the prior distribution, after the additional information is taken into account (Gelman et al., 2014) (cfr. infra). However, they can only be used when the variable to be updated is measured directly. This is the reason why these conjugate priors could not be used in the previous analyses, since there is only an indirect relationship between the static and dynamic data that has been experimentally obtained and the corrosion variables. In the following analyses, material properties will be updated based on direct measured results of the considered property. In case one considers e.g. a material property modelled as a lognormal distribution, the lognormal-inverse-gamma distribution is a conjugate prior when the mean M and standard deviation Σ of the lognormal distribution are considered as random variables. The joint probability density function for M and Σ is a lognormal-gamma distribution. In that case, the predictive prior distribution of the lognormally distributed variable (i.e. the distribution incorporating parameter uncertainties) is given by equation (VIII-1) (Rackwitz, 1983).

$$F_X(x) = T_{\nu'}\left(\frac{\ln(x) - \bar{x}'_{lnX}}{s'_{lnX}}\sqrt{\frac{n'}{n'+1}}\right) \qquad \text{(VIII-1)}$$

Here, $T_{\nu'}(.)$ is the Student's t-distribution with ν' degrees of freedom, $\bar{x}'_{lnX}$ is the (prior) lognormal hyperparameter of the mean value, s'_{lnX} is the (prior) lognormal hyperparameter of the standard deviation, and n' is the (prior) hyperparameter for the sample size. In case $n'\nu' > 10$, the distribution in equation (VIII-1) can be approximated by a lognormal distribution with mean $\bar{x}'_{lnX}$ and standard deviation $s'_{lnX}\sqrt{\frac{n'}{n'-1}\frac{\nu'}{\nu'-2}}$ according to the JCSS Probabilistic Model Code (JCSS, 2001).

Considering conjugate prior distributions, these distributions can be easily updated based on available measurement information. The parameters of the distribution can be updated based on equations (VIII-2) to (VIII-5) (Gelman et al., 2014).

$$\bar{x}"_{lnX} = \frac{\bar{x}'_{lnX}n' + \bar{x}_{lnX}n}{n"} \qquad (VIII-2)$$

$$n" = n' + n \qquad (VIII-3)$$

$$s"_{lnX} = \frac{1}{\nu"}[(\nu's'_{lnX} + n'\bar{x}'_{lnX}{}^2) + (\nu s_{lnX}{}^2 + n\bar{x}_{lnX}{}^2) - n"\bar{x}"_{lnX}{}^2] \qquad (VIII-4)$$

$$\nu" = \nu' + \nu + 1 \qquad (VIII-5)$$

Here, $'$ refers to the prior parameters and $"$ to the posterior parameters. When n measurement results x_i are available, these are accounted for by the parameters $\bar{x}_{lnX} = \frac{1}{n}\sum_{i=1}^{n}\ln(x_i)$ and $s_{lnX} = \sqrt{\frac{1}{\nu}\sum_{i=1}^{n}(\ln(x_i) - \bar{x}_{lnX})^2}$. The abovementioned formulas are only valid under the given assumptions, i.e. for the assumed pairs of conjugate priors.

VIII.5.3.1.1   *Updating of the compressive strength of concrete*

The concrete compressive strength can be modelled as a lognormal variable and can hence be updated by the formulas given above. For the concrete compressive strength, the only available information is found in the work by Magnel (1948), where a concrete strength of 40 MPa is mentioned. Suggestions for prior distributions for the concrete strength can be found in (Rackwitz, 1983). Based on the previously mentioned information provided by Magnel (1948), a concrete type C35 for precast elements is considered to be an appropriate prior. This prior distribution is summarized in Table VIII-7 by means of the so-called hyperparameters $(\bar{x}'_{lnX}, n', s'_{lnX}, \nu')$ which describe the prior predictive distribution of a lognormally distributed variable considering parameter uncertainties (cfr. supra). Subsequently, the prior distribution is updated considering the measurement results 40.8 MPa, 42.8 MPa and 33.7 MPa using Equations (VIII-2) to (VIII-5). Accounting for these results, the posterior hyperparameters are given in Table VIII-7.

Table VIII-7: Parameters of prior and posterior distribution of concrete compressive strength. Prior information based on (Rackwitz, 1983)

Concrete type	$\bar{x}'_{lnX}$	n'	s'_{lnX}	v'	$\bar{x}''_{lnX}$	n''	s''_{lnX}	v''
C35 – Concrete for precast elements	3.95	2.5	0.08	4.5	3.79	5.5	0.097	7.5

The posterior predictive distribution of the concrete compressive strength based on the previously derived hyperparameters is subsequently used in the determination of the distributions of tensile strength and Young's modulus of the concrete, since these properties are considered to be strongly correlated to the concrete compressive strength (JCSS, 2001).

VIII.5.3.1.2   Updating of the tensile strength of concrete

The distribution for the tensile strength of the concrete is determined based on the distribution of the concrete compressive strength. Since no prior information is available in literature regarding the concrete tensile strength, a prior distribution for the latter is derived by sampling the posterior distribution of the compressive strength and assuming the following relationship between tensile and compressive strength (JCSS, 2001): $f_{ct} = 0.3 \cdot f_c^{2/3} \cdot Y_{2,j}$, where $Y_{2,j}$ has a lognormal distribution with mean 1 and coefficient of variation 0.3. This results in a prior lognormal distribution for the tensile strength with a mean value of 3.8 MPa and a standard deviation of 0.7 MPa.

This distribution can be updated based on the available test results for the tensile strength, which are derived from two splitting tests, i.e. 3.6 MPa and 4.0 MPa. This updating procedure is performed based on MCMC sampling assuming a measurement error of 0.5 MPa. This error includes both the measurement error in the tensile tests and the model error for calculating the tensile strength. The posterior mean and standard deviation are 3.8 MPa and 0.2 MPa, respectively.

VIII.5.3.1.3   Updating of the Young's modulus of concrete

The distribution of the Young's modulus of the concrete is also based on sampling of the posterior distribution for the concrete compressive strength (similar as for the concrete tensile strength). The relationship between both variables is assumed to be $E_c = 2.15 \cdot 10^4 \cdot \left(\frac{f_{cm}}{10}\right)^{1/3}$ (CEN, 2005b). The prior mean and standard deviation of the Young's modulus are 35.28 GPa and 1.48 GPa, respectively, derived based on the posterior hyperparameters for the concrete compressive strength as given in Table VIII-7. No experimental results on the Young's modulus are available. Hence, this distribution is not updated and the prior distribution is used in the subsequent analyses.

VIII.5.3.1.4   Updating of the density of concrete

The prior distribution of the concrete density is based on the JCSS Probabilistic Model Code (JCSS, 2001), which suggests a normal distribution with mean 2400 kg/m³ and coefficient of variation 0.02. The test results available are 2300 kg/m³, 2280 kg/m³ and 2340 kg/m³. Applying Bayesian updating (by using MCMC sampling), a posterior distribution with mean 2389 kg/m³ and standard deviation 45 kg/m³ is found. This is based on a likelihood with a measurement error of 200 kg/m³ of the measured value. This error includes the measurement errors in the weighing of the samples and in measuring the sample dimensions.

VIII.5.3.1.5   Updating of the Young's modulus of prestressing steel

The prior distribution for the Young's modulus of the steel is based on the JCSS Probabilistic Model Code (JCSS, 2001), which suggests a normal distribution with mean 200 GPa and a coefficient of variation of 0.02. For the Young's modulus of the steel, following test results are available: 194.8 GPa, 194.9 GPa and 193.5 GPa. Based on MCMC sampling, the posterior distribution is found to be a normal distribution with mean 199.4 GPa and standard deviation 3.86 GPa. This is based on a likelihood with an error of 20 GPa. This error includes the measurement error of the performed tests and the error made by calculating the Young's modulus based on these test results.

VIII.5.3.2   Updating of the remaining prestress

Considering the previously updated variables, the remaining prestress is consecutively updated based on the experimental results, i.e. the measurements obtained in the large-scale load tests. In particular, the cracking moment, the moment of reopening of the cracks and the behaviour in the non-linear branch of the load-displacement diagram are used, since these depend significantly on the remaining prestress level. For the behaviour in the non-linear branch of the load-displacement curve, the load corresponding to a displacement of 40 mm (i.e. in the non-linear branch) is considered as measurement result. The measurement results are accompanied by measurement errors originating from the measurement equipment. Moreover, the moment of reopening of the cracks and the moment of cracking are derived based on the experimental load-displacement curve, introducing an additional uncertainty on these values. Hence, in the procedure outlined below, an error term is added to the respective output values of the numerical model to account for these uncertainties: ε_{crack} denotes the error on the cracking moment, ε_0 denotes the error on the moment of reopening of the cracks, and ε_δ denotes the error on the load corresponding to a displacement of 40 mm. Distributions of these error terms are estimated based on engineering judgement, taking into account both the accuracy of determining measurement results from the experimental graphs and the measurement error itself. The assumptions on these error terms are summarized in Table VIII-8.

Table VIII-8: Distributions of the material parameters used in the Bayesian assessment of the remaining prestress (Botte et al., 2021)

Parameter		Unit	μ	σ	Distr.[*]	Lower bound	Upper bound
Concrete tensile strength	f_{ct}	MPa	3.8	0.2	LN		
Young's modulus of the concrete	E_c	MPa	35,283	1480	N		
Young's modulus of the steel	E_p	GPa	199.4	3.86	N		
Concrete density	ρ_c	kg/m³	2389	45	N		
0.2% strain limit	$F_{p0.2}$	MPa	1477	86	N		
Error on the cracking moment (primary beam)	ε_{crack}	kN			U	-25	25
Error on the moment of decompression (primary beam)	ε_0	kN			U	-50	50
Error on the load at 40 mm	ε_δ	kN	0	10	N		
Error on the cracking moment (secondary beam)	ε_{crack}	kN			U	-5	5
Error on the moment of decompression (secondary beam)	ε_0	kN			U	-5	5

[*]*Distribution type: N – Normal distribution; LN – Lognormal distribution; U – Uniform distribution*

The remaining prestress is not updated using standard Bayesian methods, such as the MCMC sampling used in Chapter VI and sections VIII.2 to VIII.4. The reason for this is that this would yield an unrealistically small posterior uncertainty when accounting for the different measurement results. The latter can be ascribed to not adequately taking into account the correlation between the measurement results. When the different measurement results are assumed to be independent in a standard Bayesian procedure, inherent variability of the measurement results, for example due to their different origin and inherent variability of structural properties, is not accounted for (Behmanesh et al., 2015). Moreover, standard Bayesian procedures would only update the prestress specifically valid for the tested beams and not account for the possible variations between similar beams in the same structure (which are not tested). If it would have been possible to perform multiple similar tests (on the different roof girders in the structure), these could induce varying measurement results. Hence, this uncertainty should also be accounted for when performing the Bayesian inference. In (Behmanesh et al., 2015), a hierarchical Bayesian inference procedure is applied to resolve these issues. However, in this work there will be opted for another procedure, which will be explained in more detail below.

In order to derive a posterior distribution for the remaining prestress:
1. A set of n prestress values $\sigma_{P,i}$ ($i = 1,…,n$) is considered;
2. For each prestress value $\sigma_{P,i}$ m random sets of input parameters $(f_{ct,j}; E_{c,j}; E_{p,j}; \rho_{c,j}; F_{p0.2,j}; \varepsilon_{crack,j}; \varepsilon_{0,j}; \varepsilon_{\delta,j})$ ($j = 1,…,m$) are generated based on the posterior distributions of those parameters derived before (see Table VIII-8) as input for the numerical model;
3. For each $\sigma_{P,i}$ a multivariate normal distribution $f_{P_0,P_{cr},P_\delta,i}(P_0, P_{cr}, P_\delta)$ is fit on the output of the numerical model for the load $P_{0,ij}$ corresponding to decompression of the bottom fibre, the cracking load $P_{cr,ij}$ and the load $P_{\delta,ij}$ corresponding to a displacement of 40 mm;
4. For each $\sigma_{P,i}$ the latter distribution function is evaluated in the measured load P_0^{meas} corresponding to decompression of the bottom fibre, the measured cracking load P_{cr}^{meas} and the measured load P_δ^{meas} corresponding to a displacement of 40 mm, i.e. $f_{P_0,P_{cr},P_\delta,i}(P_0^{meas}, P_{cr}^{meas}, P_\delta^{meas})$;
5. Finally, as a probability is found for each value of the prestress, the most probable value of the prestress can be determined.

By applying this procedure, a vague prior distribution where the prestress could range up to 1000 MPa (initial prestress) is updated to a posterior distribution accounting for the uncertainties on the experimental results and their mutual correlation. When relating this ad-hoc procedure to standard Bayesian inference procedures, the prior distribution for the prestress can be considered a uniform

prior distribution, where all considered prestress values $\sigma_{P,i}$ have an equal prior probability. The multivariate normal distribution $f_{P_0,P_{cr},P_\delta,i}(P_0, P_{cr}, P_\delta)$ is related to the likelihood function, providing the likelihood of P_0, P_{cr} and P_δ for the considered prestress value $\sigma_{P,i}$.

For the primary beam, the resulting distribution of the prestress is given in Figure VIII-20. The markers correspond to the probabilities found for the different considered prestress levels $\sigma_{P,i}$. The shaded area represents the 90% Highest Density Interval (HDI), which spans the interval between 755 MPa and 812 MPa. The most probable value is between 775 and 800 MPa. For the latter prestress levels and considering the mean values of the material characteristics according to Table VIII-8, the load-displacement diagram obtained from the numerical calculations is shown together with the experimental curve in Figure VIII-21. In these figures, it can be seen that the numerical results considering the most probable prestress levels correspond closely to the experimentally observed load-displacement diagram.
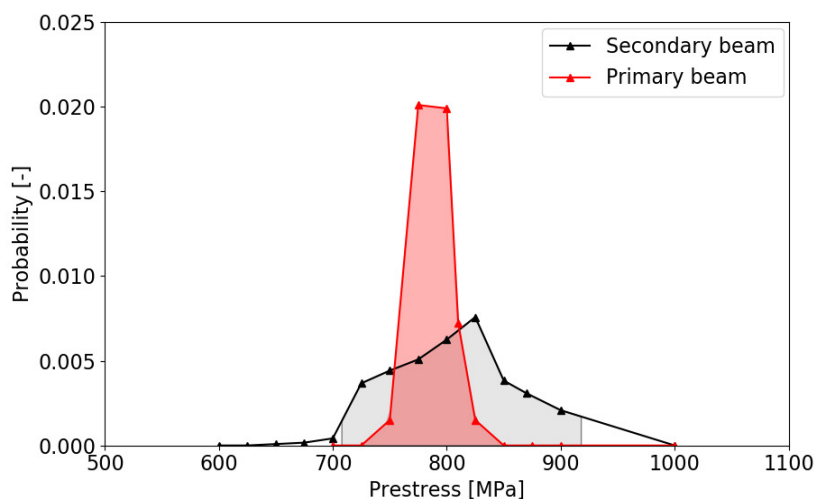
Figure VIII-20: Posterior distribution of the remaining prestress of the primary and secondary UCO beam. The different markers correspond to the probability found for the different prestress values $\sigma_{P,i}$ on the horizontal axis.

For the secondary beam, the posterior distribution of the prestress is also given in Figure VIII-20. The shaded area represents the 90% HDI. The boundaries of this interval are 708 MPa and 918 MPa. The most probable value equals 825 MPa. Hence, for this prestress and the mean values of the material characteristics according to Table VIII-8, the load-displacement diagram obtained from the

numerical calculations is shown together with the experimental curve in Figure VIII-22. It can be seen that this curve corresponds closely to the experimentally observed load-displacement diagram.

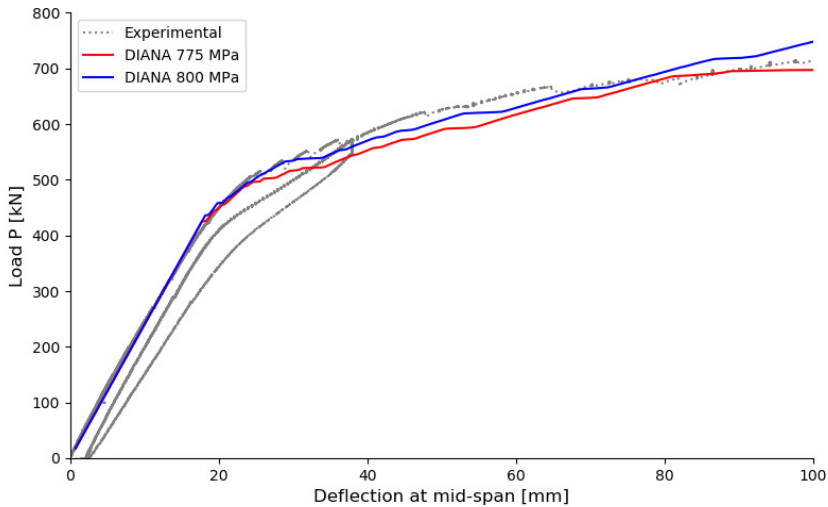Figure VIII-21: Posterior estimate of the load-displacement diagram for the primary UCO beam (Botte et al., 2021)
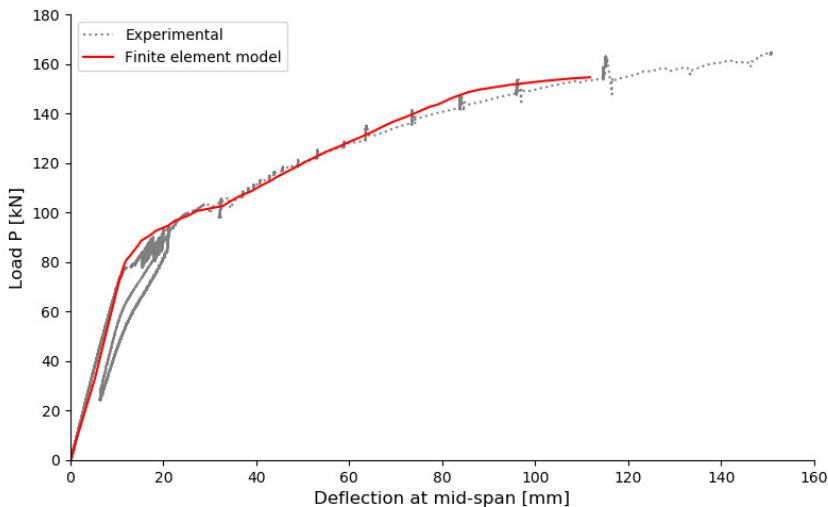

Figure VIII-22: Posterior estimate of the load-displacement diagram for the secondary UCO beam (Botte et al., 2021)

It is important to indicate that the Bayesian approach presented above not only allows deriving a most probable value of the remaining prestress, but also provides an indication related to the uncertainty on this parameter. Comparing the posterior distributions of the primary and secondary beam, it is clear that although a higher most probable value is found for the prestress in the secondary beam, also a higher uncertainty is expected for the latter. Furthermore, the latter shows that although all available information was incorporated in the updating procedure, still important uncertainties regarding the remaining prestress remain. The larger uncertainty for the secondary beam can be mainly attributed to two reasons. First, relative to the load values, the measurement errors for the cracking moment and the load at a displacement of 40 mm are larger in case of the secondary beam compared to the primary beam. Furthermore, it was found that the intrinsic uncertainty of the load-displacement response, originating from the uncertainty related to the material properties, is significantly larger in case of the secondary beam. More specifically, the coefficient of variation considering a specific prestress level is up to three times higher for the cracking moments, up to four times higher for the moment of decompression of the bottom fibre and up to two times higher for the load at a displacement of 40 mm.

VIII.6 Conclusions

In this chapter, existing scientific literature is expanded with a novel approach to update the (time-dependent) prestressing steel section based on indirect measurement data. It is first illustrated how for a prestressed structure the remaining prestressing steel area can be updated based on available data from static strain measurements. For this purpose, a Bayesian updating procedure is applied. To account for spatial variability, the structure is subdivided into different elements with a varying amount of remaining prestress. It is illustrated how the posterior distribution of the remaining steel section indeed approaches the actual value for the considered cases. In a next step, this remaining steel section is modelled by an initiation period and a rate of reduction in order to predict the remaining prestress over time. For the studied example, also these distributions could be updated, where the posterior distributions approximated the actual underlying value. Nevertheless, due to the addition of unknown variables, the posterior uncertainty has increased compared to the case where only the reduction in steel section is updated. In general, when the number of unknowns increases, it becomes more difficult to perform the identification and more data is required to arrive at a similar degree of identification.

The analysis is also extended to a prestressed girder bridge. Here, the change in steel section of a limited number of strands does not have a very large influence on the measured strains, especially when compared to the measurement error. Hence, a more vague prior distribution is required, taking into account a possible variation between all strands present in the lowest three layers and no strands

present in the lowest three layers. In this case, a more accurate posterior distribution is found, due to the larger range of possible strain outcomes. From these results, it could be concluded that, similar as in Chapter VI, it might be beneficial to define thresholds on the measurement accuracy to detect a certain damage extent, or vice versa, to define thresholds on the deterioration state that can be detected with a given monitoring technique and its accuracy.

Next, a post-tensioned beam is investigated, where the purpose is twofold, i.e. both the corrosion degree of the unstressed reinforcement steel and the corrosion degree of the prestressing steel are updated. Two situations are considered, one where the duct is grouted and one where the duct is ungrouted. In the first situation, the corrosion degree of the unstressed reinforcement bars could be updated based on the strain data, but not the corrosion degree of the prestressing steel. This could be ascribed to the fact that the latter only influences the strains to a noticeable extent once the strands have failed. When the duct is ungrouted, the remaining area of prestressing steel, and hence the remaining prestress, is considered uniform along the beam. When the Bayesian updating is performed based on static strain data, vague posterior distributions are found, but still approaching the actual underlying value. Nevertheless, increasing the measurement error leads to a posterior distribution almost equal to the prior distribution, due to the limited strain differences between the corroded case and the uncorroded case.

In general it could be concluded that the remaining steel section of prestressing steel could be updated based on static strain data, but only as soon as some strands have ruptured and hence induced a noticeable effect on the strains. Moreover, at the cost of higher posterior uncertainties, also variables in a model to predict the loss of steel section over time could be updated. It should be emphasized that the examples in this work are still largely simplified and extension to a real case study is required (i.e. a real bridge geometry with actual data). For example, for existing prestressed structures there is also expected to be some post-tension loss over their lifetime. Together with the corrosion effects, this will influence the behaviour of the structure, and both phenomena can interfere with each other. To tackle this, one can either include additional degradation models describing the time-dependent post-tensioning losses, or one can included an additional model error in the likelihood function. Furthermore, all results provided in this chapter depend on the assumptions made for the errors in the likelihood function (i.e. measurement and modelling errors). Other assumptions could be made here, which might influence the shape and/or uncertainty of the posterior distribution. Nevertheless, more research is required on the appropriate quantification of these measurement and/or model errors.

In the last section, the remaining prestress of two 70-year old post-tensioned beams tested up to failure is updated. The beams originated from a roof structure

originally designed by professor Gustave Magnel. Considering the age of the beams, significant prestress losses are expected. Hence, based on the available test results, it is investigated whether an estimate could be made of the remaining prestress of the beam. In a first step, the material properties are updated based on the tests performed for material characterization. In a second step, a posterior distribution for the prestress is generated based on the load-displacement diagram of the testing up to failure and considering the posterior distributions found for the material properties in step 1. The most likely value for the prestress is determined for both beams and verified based on the load-displacement curve of the finite element model, accounting for this prestress. These load-displacement curves closely approximated the experimentally observed curves.

The updating of the remaining prestress in the girders of a roof structure based on the experimental results of only one girder is a novel contribution to the existing state-of-the-art. Furthermore, the algorithm for treating this inference problem in an ad-hoc way has not been applied before.

VIII.7 References

Behmanesh, I., Moaveni, B., Lombaert, G., Papadimitriou, C., 2015. Hierarchical Bayesian model updating for structural identification. Mech. Syst. Signal Process. 64–65, 360–376.

Botte, W., 2017. Quantification of Structural Reliability and Robustness of New and Existing Concrete Structures Considering Membrane Action. PhD thesis, Ghent University.

Botte, W., Vereecken, E., Taerwe, L., Caspeele, R., 2021. Assessment of posttensioned concrete beams from the 1940s: Large-scale load testing, numerical analysis and Bayesian assessment of prestressing losses. Struct. Concr. 22, 1500–1522.

CEN, 2005. EN 1992-1-1: Eurocode 2: Design of concrete structures - Part 1-1: General rules and rules for buildings.

Darmawan, M.S., 2009. Pitting Corrosion Model for Partial Prestressed Concrete (PC) Structures in a Chloride Environment. IPTEK J. Technol. Sci. 20, 109–114.

Darmawan, M.S., Stewart, M.G., 2007. Spatial time-dependent reliability analysis of corroding pretensioned prestressed concrete bridge girders. Struct. Saf. 29, 16–31.

DIANA FEA BV, 2019. DIANA User's Manual - Release 10.3 [WWW Document]. URL https://dianafea.com/manuals/d103/Diana.html

Dias-da-Costa, D., Neves, L.A.C., Gomes, S., Hadigheh, S.A., Fernandes, P., 2019. Time-dependent reliability analyses of prestressed concrete girders strengthened with CFRP laminates. Eng. Struct. 196, 109297.

Gelman, A., Carlin, J.B., Stern, H.S., Rubin, D.B., 2014. Bayesian Data Analysis, 3rd ed, Texts in Statistical Science. CHAPMAN & HALL/CRC, Boca

Raton.

JCSS, 2001. Probabilistic Model Code.

Lay, S., Schießl, P., Cairns, J., 2003. Lifecon Deliverable D3.2.

Lebeau, K., Wadia-Fascetti, S., 2010. Predictive and diagnostic load rating model of a prestressed concrete bridge. J. Bridg. Eng. 15, 399–407.

Magnel, G., 1948. La nouvelle usine de l'union cotonnière a Gand - Application du béton précontraint. La Tech. des Trav. 186–194.

Moravcik, M., Bujnakova, P., Bahleda, F., 2020. Failure and damage of a first-generation precast prestressed bridge in Slovakia. Struct. Concr. 21, 2353–2362.

Nguyen, V., Jeong, M.C., Han, T.S., Kong, J.S., 2013. Reliability-based optimisation design of post-tensioned concrete box girder bridges considering pitting corrosion attack. Struct. Infrastruct. Eng. 9, 78–96.

Osborn, G.P., Barr, P.J., Petty, D.A., Halling, M.W., Brackus, T.R., 2012. Residual prestress forces and shear capacity of salvaged prestressed concrete bridge girders. J. Bridg. Eng. 17, 302–309.

Page, C.L., Page, M.M., 2007. Durability of concrete and cement composites. Woodhead Publishing Limited, Cambridge.

Papé, T.M., Melchers, R.E., 2011. The effects of corrosion on 45-year-old pre-stressed concrete bridge beams. Struct. Infrastruct. Eng. 7, 101–108.

Podroužek, J., Strauss, A., Bergmeister, K., 2014. Robustness-based performance assessment of a prestressed concrete bridge. Struct. Concr. 15, 248–257.

Rackwitz, R., 1983. Predictive distribution of strength under control. Matériaux Constr. 16, 259–267.

Stewart, M.G., 2009. Mechanical behaviour of pitting corrosion of flexural and shear reinforcement and its effect on structural reliability of corroding RC beams. Struct. Saf. 31, 19–30.

Stewart, M.G., 2004. Spatial variability of pitting corrosion and its influence on structural fragility and reliability of RC beams in flexure. Struct. Saf. 26, 453–470.

Vu, N.A., Castel, A., François, R., 2010. Response of post-tensioned concrete beams with unbonded tendons including serviceability and ultimate state. Eng. Struct. 32, 556–569.

Part C

Pre-posterior analysis

CHAPTER IX

An extended pre-posterior framework incorporating the time-dependent and spatial nature of degrading concrete structures

"Brains are decision-making machines, making guesses about the future."
- Ian Stewart, Do Dice Play God?

IX.1 Introduction

The pre-posterior framework and VoI analysis were already introduced in Chapter V. In the current chapter, the pre-posterior framework is extended in order to include the time-dependent and spatial character of degradation. The time-dependent degradation models described in Chapter II will be applied, and the hyperparameters and random fields as introduced in Chapter III will be incorporated in the framework. In the current chapter, the framework will only be applied to simplified examples in order to illustrate the concepts. In the following chapters, the Bayesian updating based on different data types as introduced in Chapter VI will be included, and it will be illustrated how the VoI can be used as a metric to optimize a monitoring strategy.

IX.2 Incorporation of the time-dependent and spatial character of corrosion in the pre-posterior framework

This section explains the extension of the pre-posterior framework that has been developed to determine the VoI based on yet unknown inspection results. Since in a pre-posterior analysis the inspection results are not known in advance, they are sampled based on the probability distributions of underlying stochastic variables. Once the inspection results are known, a posterior analysis can be performed. This pre-posterior framework extends previous formulations by taking into account the time-dependent character and spatial dependence of degradation, and is visualized in the flowchart of Figure IX-1, which is stepwise explained in the following sub-sections. The framework requires a run for the prior case without consideration of inspection results, and one for the pre-posterior case where unknown inspection results are accounted for. For this reason, the flowchart differentiates between the prior and pre-posterior case (the latter containing unknown, hence sampled, measurement results). The same procedure is followed in both cases, but without any inspections or updating procedures in the prior case. In the following, the flowchart is explained for the more extensive pre-posterior case. It should also be noted that once the measurement results are available, the posterior cost could be calculated based on the actual measurement results. In this case, the difference between prior and posterior cost can be evaluated in order to illustrate whether the obtained measurement results were really worth their costs.
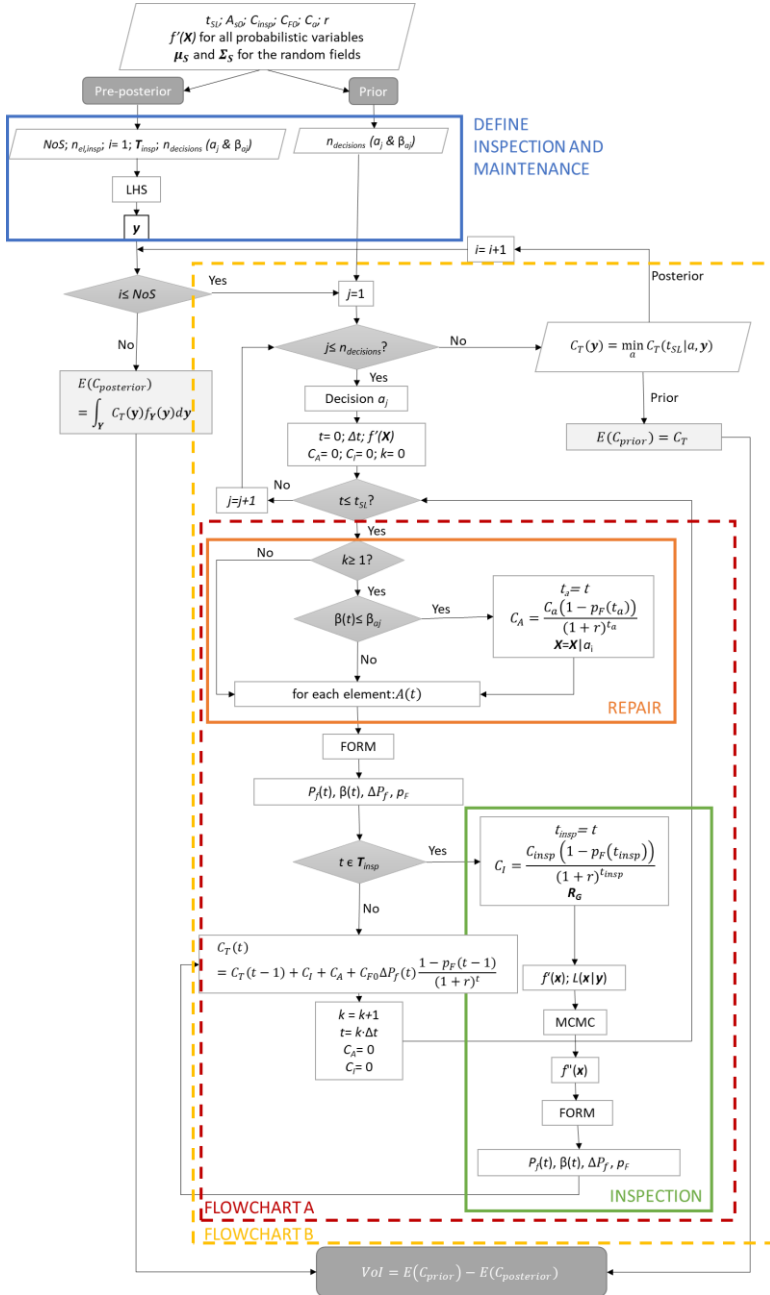
Figure IX-1: Flowchart for the determination of the VoI accounting for time-dependent and spatial discretization

An extended pre-posterior framework incorporating the time-dependent and spatial nature of degrading concrete structures

233

IX.2.1 Discretization of the structure and definition of degradation

Before starting the analysis, the considered structure should be modelled, and the relevant variables and corresponding probability distributions should be defined. Failure is considered through an appropriate limit state, and probability distributions can be assigned to the uncertain input variables. Furthermore, the relevant effects of deterioration in time and space on the failure probability need to be considered and properly taken into account. To account for the spatial dependence, variables correlated by means of hyperparameters or random fields should be defined. The structure under investigation should be subdivided into elements with the element length chosen such that correlation is strong within an element for the variables modelled by common hyperparameters and that the random field is properly represented. As such, within one element, deterioration is considered uniform. In addition, a model for simulating the degradation as a function of time is required. For reinforcement corrosion, this can be done according to the models presented in Chapter II.

IX.2.2 Definition of inspection and decision strategies

In this framework, the inspection/monitoring strategy to be evaluated is chosen in advance. The strategy is defined by the number of elements (of the discretized structure) to be inspected ($n_{el,insp}$) and the timesteps $\boldsymbol{T_{insp}}$ at which inspections/measurements will be performed. Furthermore, $n_{decisions}$ possible decision/repair strategies a_j are considered. When evaluating the flowchart for the prior case (i.e. without considering inspection/monitoring outcomes), only the prior decision strategies are used as input. In Figure IX-1, these input parameters can be found in the frame at the top of the flowchart indicated by '*Define inspection and maintenance*'.

IX.2.3 Definition of the possible inspection outcomes

In the pre-posterior case, the value of (yet) unknown inspection results/monitoring outcomes is accounted for by considering *NoS* combinations of test outcomes. As the test outcomes are not known in advance, these are sampled according to the prior information. Later in the framework, the occurrence probability of all the possible inspection/monitoring outcomes will be accounted for. It should be noted that the number of test outcomes should be chosen large enough so that convergence of the VoI is reached. Sampling of the test outcomes can be done based on Latin Hypercube Sampling (LHS). LHS is adopted since less samples are needed to approximate the distributions when compared to Monte Carlo sampling. For each of the sets of inspection/monitoring outcomes $\boldsymbol{y}$, a corresponding lifetime cost $C_T(\boldsymbol{y})$ will be determined, leading to *NoS* values of $C_T(\boldsymbol{y})$.

IX.2.4 Determine costs associated to a set of inspection/monitoring outcomes

IX.2.4.1 Accounting for inspection/monitoring outcomes

As indicated before, the inspection/monitoring outcomes are not known beforehand and are hence sampled. The inspection/monitoring outcomes (y) are random variables that are a function of other random variables (X), where the relationship is given by $G(X)$. For example, when a deflection would be measured, this depends on the stiffness of the structure and hence on the random variables included in the corrosion modelling. In this work, inspection/monitoring outcomes are modelled by sampling the input variables X with LHS and calculating the corresponding inspection/monitoring outcomes by evaluating the model G for these different samples. To these modelled values, a random error η (depending on the measured quantity and the equipment used) is added to generate the inspection/monitoring outcome, according to equation (IX-1). This error η can incorporate a measurement error η_D and/or a model error η_G.

$$y = G(X) + \eta \qquad \text{(IX-1)}$$

In this way, samples for the inspection/monitoring outcomes can be generated at different times and locations, by evaluating the model at the corresponding times and/or locations. When the inspection/monitoring outcomes are of the inequality type (e.g. indication / no indication of corrosion initiation), both inspection/monitoring outcomes are considered, and each is weighed with their corresponding probability. The inspection/monitoring outcomes in this case are binary (discrete) random variables.

Based on the sampled inspection/monitoring outcomes, the probability distributions of the model parameters are updated by applying Bayesian methods, according to Chapter IV. Through the representation of spatial correlation of corrosion variables by hyperparameters and random fields, inspections/measurements at one location of the structure also provide information on non-inspected locations. These hyperparameters and random fields are included in the variables X. To account for multiple inspection/monitoring outcomes in time, the posterior distribution of a previous timestep is used as the prior distribution at a later timestep. Furthermore, the inspection results at different timesteps are based on the same simulations of the variables governing degradation. As such, inspection/monitoring outcomes at a later timestep will be correlated to those at an earlier timestep. Moreover, the model $G(X)$ takes into account the spatial degradation, where the variables X can have a spatial correlation.

When all distributions are updated based on the inspection/monitoring outcomes, these updated distributions can be used to calculate the updated probability of failure, e.g. based on a FORM (First Order Reliability Method) analysis. To perform the FORM analysis, a distribution is fit to the samples following from MCMC, and the mean and standard deviation are calculated. FORM is then performed assuming these distributions.

IX.2.4.2 Cost corresponding to a set of inspection/monitoring outcomes and a decision strategy

In order to determine the life-cycle cost for a fixed set of inspection/monitoring outcomes, a loop over the different decision alternatives is made (counter j in Figure IX-1). At the start of every loop, the following parameters are initialized: the initial time t and the counter for the time k are set equal to zero, all probability distributions corresponding to deterioration, material properties and loads are set to their prior distributions (X), and costs for performing an action (C_A) or an inspection (C_I) are set equal to zero.

At every timestep $t = k \cdot \Delta t$ (except for the first one), it is checked whether at the previous timestep $(k\text{-}1) \cdot \Delta t$ a threshold for making an action (e.g. performing a repair) was exceeded (e.g. a reliability threshold β_{aj}, damage threshold…), in case this is imposed by the decision strategy. If this is the case, repair will be performed and the expected cost of repair C_A will be calculated according to equation (IX-2).

$$C_A = \frac{C_a\left(1 - p_F(t_a)\right)}{(1 + r)^{t_a}} \tag{IX-2}$$

Here, C_a is the cost of the action (e.g. the cost of repair), t_a equals $(k\text{-}1) \cdot \Delta t$, i.e. the time at which the threshold is exceeded, p_F is the cumulative probability of failure at this timestep (cfr. infra), and r is the discount rate. When repair is performed, this may affect some of the variables in X, which is indicated by $X|a_i$. For example, when assuming perfect repair, degradation is returned to its initial condition. When repair is assumed to stop degradation, degradation is kept constant in all following evaluations of the probability of failure. The section where repair is accounted for in the flowchart of Figure IX-1 is indicated by the orange frame labelled '*Repair*'.

Next, the reliability index should be determined, accounting for time-dependent degradation. The state of deterioration (e.g. the remaining reinforcement section) is evaluated at the timestep considered. Accounting for this reduced resistance, the failure probability P_f, reliability index β, cumulative probability of failure p_F and failure rate ΔP_f for the considered timestep are evaluated based on FORM analyses. The failure rate ΔP_f is given by equation (IX-3).

$$\Delta P_f = \frac{p_F(k \cdot \Delta t) - p_F((k-1) \cdot \Delta t)}{\Delta t\left(1 - p_F(k \cdot \Delta t)\right)} \qquad \text{(IX-3)}$$

The cumulative probability of failure p_F is calculated according to equation (IX-4) (Straub, 2004).

$$p_F(T) = 1 - \prod_{t=0}^{T} \left(1 - P_f(t)\right) \qquad \text{(IX-4)}$$

In this work, the number of variables in the FORM analysis is still limited and the problem is not high dimensional. Hence, FORM is applicable. For high-dimensional problems, the performance of FORM should be assessed. Some information on this and alternative methods to calculate the failure probability can be found in (Hadidi et al., 2017; Jiang and Li, 2017; Katafygiotis and Zuev, 2008; Lehar and Zimmermann, 2012; Schuëller et al., 2004; Wang and Grandhi, 1996; Wang and Song, 2018, 2016).

When the timestep considered belongs to one of the imposed inspection/monitoring times in the vector T_{insp}, the sampled inspection/monitoring outcomes are used to update the appropriate probability distributions, and the corresponding cost C_I for inspection/monitoring should be accounted for, as given by equation (IX-5).

$$C_I = \frac{C_{insp}\left(1 - p_F\left(t_{insp}\right)\right)}{(1 + r)^{t_{insp}}} \qquad \text{(IX-5)}$$

Here, C_{insp} is the cost of the inspection/monitoring, t_{insp} equals $k \cdot \Delta t$, i.e. the time at which the inspection/monitoring is performed, p_F is the cumulative probability of failure at this timestep, and r is the discount rate.

In this work, inspection/monitoring outcomes are used to reduce the uncertainties on the variables involved in the reliability analysis by using the updated distributions of the variables influenced by the inspection/monitoring and not to check whether certain thresholds are reached and corresponding repairs need to be performed. By updating the distributions of the hyperparameters and by updating the random fields, inspections at one element will also affect the uncertainty of other correlated elements. When all distributions are updated, FORM analyses are again performed and the updated failure probability is determined, together with the reliability index and failure rate. The section on inspections/monitoring can be found in the flowchart of Figure IX-1 within the green frame labelled '*Inspection*'.

Given the failure probability (after updating at a timestep in T_{insp}), the costs are evaluated at the end of every timestep, according to equation (IX-6). In this equation, C_{F0} is the failure cost of the construction.

$$C_T(k \cdot \Delta t) = C_T((k-1) \cdot \Delta t) + C_I + C_A$$
$$+ C_{F0} \Delta P_f(k \cdot \Delta t) \frac{1 - p_F((k-1) \cdot \Delta t)}{(1+r)^{t_i \cdot \Delta t}} \qquad \text{(IX-6)}$$

Subsequently, the next timestep can be considered, i.e. $k = k{+}1$, and C_A and C_I are set equal to zero.

Finally, the cost corresponding to the set of considered inspection outcomes $\boldsymbol{y}$ and decision a is the cost at the final timestep (the expected service life t_{SL}) and is denoted as $C_T(t_{SL}|a,\boldsymbol{y})$.

The procedure set out above is summarized in Figure IX-2, which is also indicated by the dashed frame in Figure IX-1.

IX.2.4.3 Costs associated to a set of inspection outcomes

In the decision analysis performed by this framework, the optimal repair strategy will be chosen for each possible inspection/monitoring outcome. The different possible heuristics for the repair strategy relate to possible decisions on the repair strategy. For each inspection/monitoring outcome, these will be evaluated and the repair strategy with the lowest cost will be chosen. This will lead to the total life-cycle cost associated with this particular inspection/monitoring outcome. Hence, the cost $C_T(\boldsymbol{y})$ corresponding to a set of inspection outcomes $\boldsymbol{y}$, is the minimum over all actions/decisions considered (equation (IX-7)).

$$C_T(\boldsymbol{y}) = \min_a C_T(t_{SL}|a, \boldsymbol{y}) \qquad \text{(IX-7)}$$

Here, a represents the different actions/decisions considered and $C_T(t_{SL}|a,\boldsymbol{y})$ the cost at the anticipated service life corresponding to action or decision a, accounting for the inspection outcomes $\boldsymbol{y}$. This cost $C_T(t_{SL}|a,\boldsymbol{y})$ is evaluated at the expected service life and is an accumulation of all failure costs over time, including the inspection/monitoring costs (C_I) and the action/repair costs (C_A), discounted to the year of calculation of the VoI (net present value). For a specific set of inspection/monitoring outcomes, costs need to be evaluated for all possible decision strategies a_j.
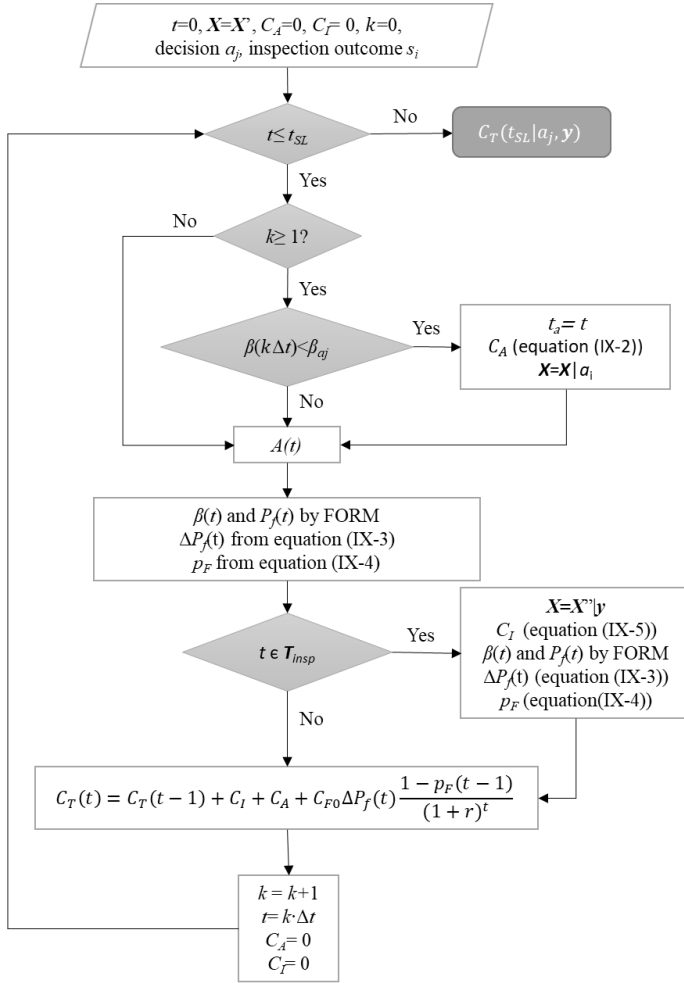
Figure IX-2: Flowchart a - Cost for a given set of inspection outcomes and a given decision strategy

When the abovementioned framework is run through for all possible decisions (according to Figure IX-3), the costs for the set of inspection/monitoring outcomes considered can be evaluated according to equation (IX-7). When no inspection/monitoring outcomes are considered, equation (IX-7) gives the prior costs.

An extended pre-posterior framework incorporating the time-dependent and spatial nature of degrading concrete structures

239
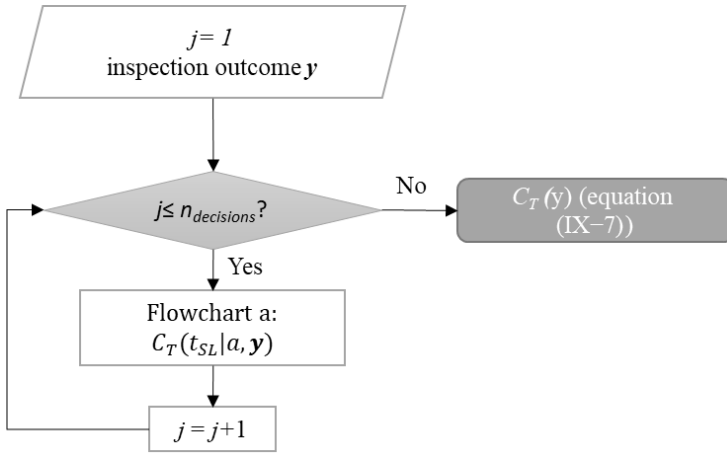
Figure IX-3: Flowchart b - Costs associated to a set of inspection/monitoring outcomes

IX.2.5 Determination of the pre-posterior costs and VoI

When the costs corresponding to each inspection/monitoring outcome are calculated, these will be weighed with the probability of occurrence of these inspection/monitoring outcomes, leading to the expected value of the pre-posterior cost. Hence, when all samples of inspection/monitoring outcomes are considered, the estimated posterior cost can be evaluated based on equation (IX-8).

$$E[C_{posterior}] = \int_Y C_T(\mathbf{y}) f_Y(\mathbf{y}) d\mathbf{y} \qquad \text{(IX-8)}$$

Here, the PDF $f_Y(\mathbf{y})$ is calculated based on the PDF's of the variables of which the inspection/monitoring outcomes are a function, evaluated at the samples used for the generation of the inspection/monitoring outcomes. The probability is then based on the samples for the different input variables, based on which the inspection/monitoring outcomes at different locations and times are calculated. As such, in equation (IX-8), the costs corresponding to a set of inspection/monitoring outcomes are weighed with the probability that these measurement results would actually be obtained. Hence, the expected pre-posterior cost is obtained by averaging over the different sampled inspection/monitoring outcomes. The final result, i.e. the VoI, is then found by subtracting the expected pre-posterior costs from the expected prior costs (equation (IX-9)).

$$VoI = E[C_{prior}] - E[C_{posterior}] \qquad \text{(IX-9)}$$

Here, $E[C_{posterior}]$ is calculated by equation (IX-8) and $E[C_{prior}]$ is calculated in a similar way. It should be pointed out that C_{prior} could be calculated according to two possible definitions of the VoI, i.e. without considering any inspection results

if the VoI is calculated in the design stage, or with consideration of some baseline inspection scenario. A positive value of the VoI implies that an inspection/monitoring strategy is economically interesting. The most optimal inspection/monitoring strategy will be the one with the largest VoI, or hence the lowest expected value of the pre-posterior cost.

IX.3 Example applications of the extended pre-posterior framework

In this section, the application of the extended pre-posterior framework will be illustrated by application to two simplified examples.

IX.3.1 Application example 1 - simply supported beam

The first illustration is by application of the framework to the simply supported beam introduced in section VI.2.1.

IX.3.1.1 Definition of the structure: limit state, degradation and decision alternatives

It is assumed that the design service life equals 50 years (hence the VoI will be evaluated at t_{SL} = 50 years). In this case, a random field is assigned to the concrete cover with a squared exponential correlation model and a correlation length of 1 m (Straub, 2011). Hence, element lengths of $l_c/2$ = 0.5 m are considered sufficient. This element length indeed leads to convergence of the failure probability of the beam. Besides the random field assigned to the concrete cover, the chloride content at the concrete surface C_s and diffusion coefficient of the concrete D are also assumed to be spatially correlated. This dependence is modelled by using a common hyperparameter for the distributions of D and C_s in these elements. The diffusion coefficient D for the different elements is equi-correlated with a correlation coefficient of 0.5. The same is assumed for the chloride concentration C_s. Hence, these are statistically independent for a given realization of the hyperparameter. The beam represents one zone and is subdivided into eight elements of 0.5 m as visualized in Figure VI-1.

The assumptions on the hyperparameters, random fields and correlation models are based on literature in the field of structural engineering, where the surface chloride concentration is often assumed constant and other properties, including the concrete cover, are modelled by random fields. Considering the material science behind corrosion, the spatial dependence of the initiation period will be mainly due to a difference in surface chloride concentration and the influence of spatial variation of the concrete cover is not that pronounced. Another note on the spatial variation is that this can be completely different for different structures. In a very large structure, there will be a certain correlation, from one anode to another, where the anodes determine the corrosion process. This can lead to

correlation lengths ranging from 1 m to a few meters. This correlation between anodes could also be used as an estimate for the correlation in the propagation phase. However, it is not the purpose of this work to model the corrosion process in detail, but to illustrate some concepts on the application of the VoI analysis to time-dependent and spatially degrading concrete structures. The framework can incorporate any kind of correlation or time-dependent degradation.

To determine the failure probability over time, the limit state function given by equation (IX-10) is adopted.

$$g(\boldsymbol{X}, t) = K_R A_s(t) f_y \left(h - c - 0.5 \frac{A_s(t) f_y}{b f_c} \right) - K_E (G + Q) \qquad \text{(IX-10)}$$

The distributions used for the variables in this equation are summarized in Table IX-1 and Table IX-2. The values provided for the load effect are the maximum bending moments, resulting from a uniformly distributed load applied to the beam. For the variable load effect, the distribution for a 5-year reference period is used (Holicky and Sykora, 2010). Since the load is considered to be constant in a reference period of 5 years, it is the same distribution as for a 1-year reference period (Honfi, 2014; JCSS, 2001; Leonardo da Vinci Pilot Project CZ/02/B/F/PP-134007, 2005). The probability of failure will be evaluated every year, and a threshold for repair will be based on a target reliability for a reference period of 1 year.

In equation (IX-10), the time-dependent character of degradation is accounted for by including $A_s(t)$, i.e. the reinforcement area at time t. This is evaluated based on equations (II-8) and (II-9), and probabilistic models are assigned to the variables in the models for the initiation and propagation phase (Table IX-1) to evaluate the probability of failure over time. The variables that will be inferred based on the measurement information are those appearing in these degradation models (similar as in Chapter VI). The posterior distributions of these variables will be used for evaluation of the probability of failure at the timesteps following inspection/monitoring.

The probability of failure is calculated considering the beam to be a series system that fails when one of its eight elements fails. The failure probability can be calculated according to equations (IX-11) and (IX-12).

$$P_{f,s}(t) = 1 - \Phi_m(\boldsymbol{\beta}(\boldsymbol{t}), \boldsymbol{\rho}) \qquad \text{(IX-11)}$$

$$\rho_{ij} = \boldsymbol{\alpha}_i^T \boldsymbol{\alpha}_j \qquad \text{(IX-12)}$$

Here, ρ_{ij} represents the correlation between the reliabilities of elements i and j, calculated based on the sensitivity factors of the input variables in elements i and

j, according to equation (IX-12). $\boldsymbol{\beta}(t)$ is the vector of element reliabilities at time t, and Φ_m represents the multivariate normal CDF of degree m (here $m = 8$). The element reliabilities are evaluated based on equation (IX-10), where the moments are recalculated towards the maximum moment in the considered element and the steel section $A_s(t)$ is evaluated for the corresponding element in the discretization of the random field.

Table IX-1: Distributions of variables related to corrosion for the simply supported beam

Variable	Symbol [unit]	Mean	Standard deviation	Distr.	Reference
Pitting factor	α_p [-]	2	-	Det.	(Duracrete, 1998)
Mean corrosion rate while corrosion is active	$V_{corr,a}$ [mm/yr.]	0.03	0.02	Weibull	(Lay et al., 2003)
Time of wetness	ToW [-]	0.75	0.2	Normal	(Lay et al., 2003)
Surface chloride concentration	C_s [wt.-%/c]	2	0.9	Lognormal	(*fib*, 2006)
Diffusion coefficient of concrete	D [mm²/year]	20	10	Lognormal	(*fib*, 2006)
Critical chloride concentration	C_{cr} [wt.-%/c]	0.6	0.15	Lognormal	(*fib*, 2006)
Concrete cover	c [mm]	30	5	Gaussian Random Field	(JCSS, 2001)

Table IX-2: Distributions of variables in the limit state under bending for the simply supported beam (JCSS, 2001)

Variable	Symbol	Units	Mean	Standard deviation	Distribution
Resistance model uncertainty	K_R	-	1	0.05	Lognormal
Reinforcement yield stress	f_y	MPa	550	11	Normal
Depth of the beam	h	mm	500	10	Normal
Width of the beam	b	mm	300	-	Deterministic
Concrete compressive strength	f_c	MPa	38.78	4.6	Lognormal
Load model uncertainty	K_E	-	1	0.10	Lognormal
Permanent load effect	G	kNm	50	2.5	Normal
Variable load effect (imposed loads, 5-year reference period)	Q	kNm	10	11	Gumbel
Initial reinforcement cross-section	A_{s0}	mm²	785.4	-	Deterministic

In this example, two decisions are considered: do nothing, or repair the elements of which the reliability index drops below the annual target reliability of 4.3, which represents an increase in failure probability by a factor 10 compared to the initial failure probability. This initial failure probability is derived based on the reliability analysis applied to the undamaged beam. Repair is assumed to stop degradation of the corresponding element. It is assumed that this repair is perfect and that the structure will not further degrade after the repair. This repair strategy is assumed for the purpose of illustration and other repair models can be incorporated in the framework.

For the results represented in the following, the costs of Table IX-3 are used, which are all relative to the cost of failure (inspired by (Straub, 2004)).

Table IX-3: Cost parameters in the example of the simply supported beam

Parameter	Value	Parameter	Value
C_{F0}	1	C_a	10^{-2}
C_{insp}	10^{-6}	r	0.01

IX.3.1.2 Determination of the value of information

According to the flowchart in Figure IX-1, the prior and pre-posterior costs are derived. When it is decided not to perform any interventions, the prior relative lifetime cost equals 0.06091. This means that, when the cost of failure of the beam is 1 million euros (accounting for structural but also human costs) and the cost of repair is 10 000 euros, the total expected lifetime cost equals 60 910 euros, when accounting for possible repairs and the probability of failure. When the threshold for repair is an element reliability of 4.3, the prior relative lifetime cost becomes 0.007692. Minimizing over the actions, the final prior cost is the minimum of both, which equals 0.007692. A priori, the decision will be made to do the repair when an element reliability drops below 4.3, since this leads to a lower total lifetime cost.

When the chloride concentration is measured at 5 years at element 4, measurement outcomes for this chloride concentration are sampled and the corresponding distributions and hyperparameters are updated. Based on these analyses, the pre-posterior relative lifetime cost is evaluated and equals 0.007660. This is smaller than the prior cost. Hence, this inspection is economical for the current assumed repair and inspection/monitoring costs. The pre-posterior cost is determined according to costs and probabilities from which some are given in Figure IX-4. For different sampled test outcomes C_{si}, the corresponding lifetime cost is shown in the lower graph (which is the minimum over the actions "repair" and "no repair") together with the corresponding probability of occurrence of this test outcome in the upper graph.

By varying the time of inspection/monitoring, the costs and corresponding VoI can change. As such, the best inspection strategy (time of inspection/monitoring) can be chosen. A simple comparison is made by varying the time of measuring the chloride content at element 4 from 5 years to 25 years. The results are shown in Figure IX-5. The VoI is expressed relative to the prior costs. If the VoI is positive, it might be beneficial to perform the measurements. Furthermore, in this example, more benefit will be gained when the measurements are performed earlier.
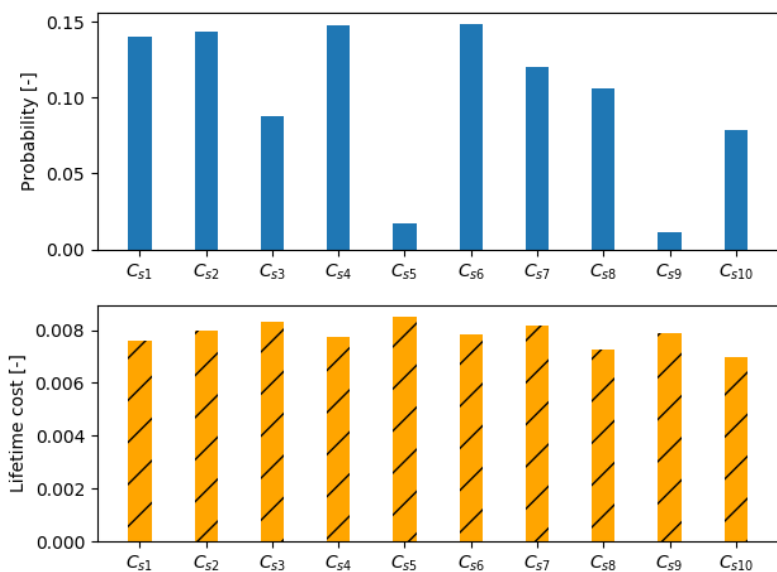
Figure IX-4: Measurement of chloride concentration at 5 years: costs and probabilities for different sampled test outcomes for the chloride concentration C_{si}
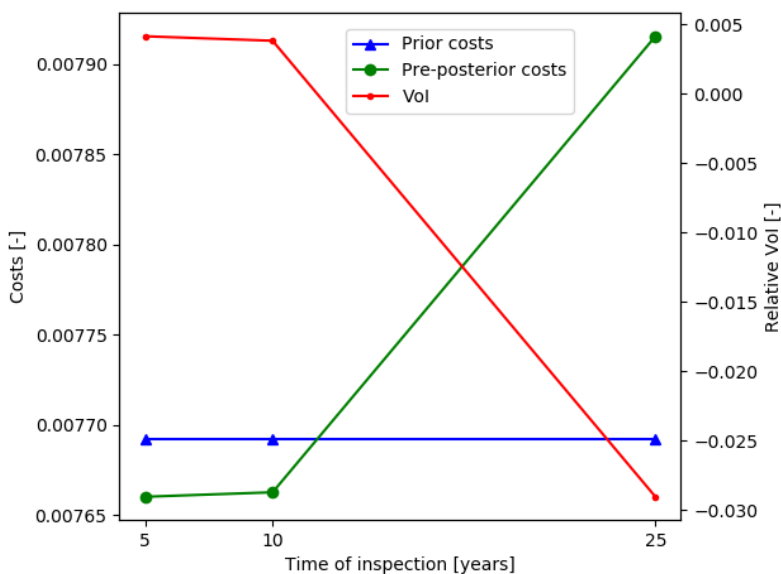

Figure IX-5: Prior and pre-posterior costs for measuring chloride content at element 4 at an age of 5, 10 and 25 years, and the corresponding relative VoI

IX.3.2 Application example 2 - bridge girder

As a second example, a simply supported highway bridge described in (Mandić Ivanković et al., 2019) is considered with a single span of 24.8 m. The superstructure is composed of five prefabricated I-type prestressed concrete girders connected with a monolithic concrete deck (Figure IX-6). The deck is modelled as a zone, and the girders are grouped in a second zone, since these are subjected to different chloride exposure. The concrete cover of each girder is modelled by a random field while the dependence of the diffusion coefficient of the concrete D and the chloride concentration C_s between elements of the girder is modelled by hyperparameters. The probability distributions of the chloride concentration and diffusion coefficient are given in Table IX-4. The value of the diffusion coefficient is based on CEMI/42.5 with a water/cement ratio of 0.45 (*fib*, 2006). The probabilistic models for the corrosion rate and time of wetness are also given in Table IX-4. This corresponds to a cyclic wet-dry exposure class. The pitting factor is assigned a normal distribution with mean value 9.28 and standard deviation 4.04 according to (Duracrete, 1998). It is assumed that the girders are pretensioned.

Considering the ultimate limit state of bending, failure of the girders is modelled analytically by limit state equation (IX-13) with resistance and load effect according to equations (IX-14) and (IX-15) respectively.

$$Z = R - E = M_{Rd}K_R - (M_G K_{E,G} + M_Q K_{E,Q}) \tag{IX-13}$$

$$R = M_{Rd}K_R = \left[\left(h - c - \frac{\Phi_b}{2}\right)n_r A_s f_y + n_g d A_p f_{ypk}\right]0.9K_R \tag{IX-14}$$

$$E = M_G K_{E,G} + M_Q K_{E,Q}$$
$$= \left[(A + h_d b_d)\gamma_C \frac{L^2}{8} + \Delta M_g\right]K_{E,G} + M_Q K_{E,Q} \tag{IX-15}$$

The parameters appearing herein and their corresponding probability distributions are summarized in Table IX-5. The additional permanent load ΔM_g describes the effect of permanent claddings or permanent loads besides the self-weight of the concrete.
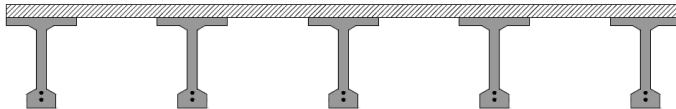
Figure IX-6: Superstructure of the investigated bridge

An extended pre-posterior framework incorporating the time-dependent and spatial nature of degrading concrete structures

247

Table IX-4: Distributions of variables related to corrosion used for the bridge girder

Variable	Symbol	Mean	Standard deviation	Distribution	Reference
Pitting factor	α_p [-]	9.28	4.04	Normal	(Duracrete, 1998)
Mean corrosion rate while corrosion is active	$V_{corr,a}$ [mm/yr.]	0.03	0.02	Weibull	(Lay et al., 2003)
Time of wetness	*ToW* [-]	0.75	0.2	Normal	(Lay et al., 2003)
Surface chloride concentration	C_s [wt.-%/c]	2	0.9	Lognormal	(*fib*, 2006)
Diffusion coefficient of concrete	D [mm²/yr.]	20	10	Lognormal	(*fib*, 2006)
Critical chloride concentration	C_{cr} [wt.-%/c]	0.6	0.15	Lognormal	(*fib*, 2006)

Table IX-5: Distributions of variables in the limit state under bending for the bridge girder (JCSS, 2001; Mandić Ivanković et al., 2019)

Variable		Distribution	Mean	Standard deviation
Girder height	h [m]	Deterministic	1.66	-
Girder cross-section area	A [cm²]	Normal	3.14	0.06
Concrete cover	c [mm]	Gaussian random field	20	5
Number of reinforcement bars	n_r [-]	Deterministic	4	-
Number of tendons	n_g [-]	Deterministic	2	-
Bar diameter (initial)	Φ_b [mm]	Deterministic	20	-
Permanent load effect uncertainty	K_{EG} [-]	Lognormal	1	0.12
Yield strength of reinforcement	f_y [MPa]	Normal	550	11
Concrete compressive strength	f_c [MPa]	Lognormal	38.8	4.65
Resistance model uncertainty	K_R [-]	Lognormal	1.2	0.15
Traffic load effect model uncertainty	K_{EQ} [-]	Lognormal	1	0.19
Concrete density	γ_c [kN/m³]	Normal	25	1
Deck height	h_d [mm]	Deterministic	240	-
Deck width	b_d [mm]	Deterministic	2800	-
Traffic load effect	Q [kNm]	Gumbel	905.4	130.3
Tensile strength of prestressing steel	f_{ypk} [N/mm²]	Normal	1515.1	75.8
Effective depth of tendons	d [mm]	Normal	1410	352.5
Area of tendon	A_p [mm²]	Normal	2200	440
Additional permanent load	ΔM_G [kNm]	Normal	403.1	20.2

For evaluation of the probability of failure of a girder, again a series system is assumed according to equations (IX-11) and (IX-12), considering the different elements in which the girder is discretized. For evaluation of the element reliabilities, the moments are recalculated towards the maximum moments in the considered element. The steel section of the girders will reduce in time due to corrosion. This reduction in steel section is evaluated based on equations (II-8) and (II-9), and probabilistic models are assigned to the variables in the models for the initiation and propagation phase (Table IX-4) to evaluate the probability of failure over time.

To reduce uncertainties, information on the bridge condition can be gathered. This information can be used to update the probability distributions of the variables. The variables that will be inferred based on the measurement information are the surface chloride concentration C_s, the diffusion coefficient of the concrete D and the concrete cover c. The posterior distributions of these variables will be used for evaluation of the probability of failure at the timesteps following inspection. Two different techniques for detection of corrosion are compared, where it is assumed that technique 2 is more accurate than technique 1. It should be pointed out that in prestressed or post-tensioned structures the most common corrosion mechanism is stress corrosion cracking. This type of corrosion cannot be detected by half-cell potential measurements. Nevertheless, the procedure applied in the following is a more general simplification, with the purpose of illustrating the concepts of the pre-posterior framework, rather than diving deep into detail with respect to corrosion mechanisms and different inspection methods. Hence, there will be assumed that corrosion can be detected or not, each with a certain probability. This is an assumption made to illustrate how the pre-posterior framework will differentiate the VoI of two techniques with different accuracy.

The assumed accuracy of both techniques is given in Table IX-6, which is also a representation of their measurement reliabilities. The probability of a true positive relates to the number of samples correctly classified as initiated. The probability of a true negative relates to the number of samples correctly classified as no initiation. The larger these values, the more accurate the measurement technique. The probability that the inspection outcome is 'no initiation of corrosion' when the steel is actually depassivated is the probability of false negatives. Finally, the probability that the inspection outcome is 'initiation of corrosion' when the steel is actually not depassivated relates to false positives, which is smaller for the more accurate technique 2. It should be pointed out that the values in Table IX-6 are just crude estimates, provided here to illustrate the application and benefit of the pre-posterior framework. In reality, Probability of Detection (PoD) curves will also correlate spatially, but no information on this topic is available in literature.

Table IX-6: Accuracy of two inspection techniques (Courage, 2018) (D stands for Depassivation and ND for No Depassivation)

	Technique 1		Technique 2	
	D	ND	D	ND
No initiation of corrosion	0.40	0.60	0.10	0.90
Initiation of corrosion	0.60	0.40	0.90	0.10

To get the probability of detecting initiation of corrosion at each timestep, the probability of indication given depassivation (D) should be multiplied by the probability of depassivation at those timesteps, hence by $F_{Ti}(t)$, which is the CDF of the initiation period T_i. The probability that the measurements at time t give no indication of corrosion initiation is found by multiplying the values related to the situation of no depassivation (ND) by $(1 - F_{Ti}(t))$. These probabilities are illustrated in Figure IX-7 for both techniques.

In this example, two possible decisions are considered: 'do not intervene and leave the structure as is' or 'repair an element (assuming perfect repair) when the failure probability increases with a factor 10 compared to the initial failure probability for the undamaged girder (cfr. supra for the simply supported beam)'. In this example, the lifetime cost of the girder is considered. Hence, the failure cost and the corresponding probability of failure relate to failure of the girder. Also system and force redistribution effects could be considered when evaluating failure. However, this falls outside the scope of this chapter. The design lifetime of the bridge is assumed 100 years, and the VoI will be calculated at $t_{SL} = 100$ years. In the calculation of the costs, the cost of inspection/monitoring is not considered. Hence, the possible difference in cost between both techniques should be accounted for when comparing the VoI of both techniques. When, at the end, the VoI of the techniques is calculated, the maximum cost of these inspections can be determined in order to be economic. The cost of repair is assumed to be 10^{-3}, which means that this cost is only 0.1% of the cost of failure, which equals 1. The discount rate equals 0.02. With the derived probabilities of indication / no indication (Figure IX-7) and based on the method described above, the relative VoI of both techniques can be defined for different inspection strategies. In order to find an optimal inspection strategy, the time of inspection and the location of the inspection are varied. The influence of inspection time and location is given in Figure IX-8 and Figure IX-9 respectively.

An extended pre-posterior framework incorporating the time-dependent and spatial nature of degrading concrete structures
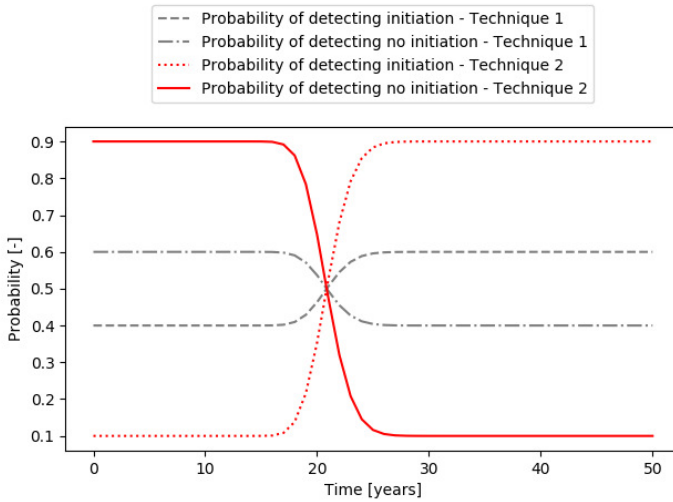
251

Figure IX-7: Probabilities of indication whether corrosion has initiated or not of both inspection techniques as a function of time

When the VoI is evaluated at different points in time, as in Figure IX-8, the best time of inspection can be found. Until 15 years, the VoI generally increases since later inspections are associated to lower costs if 'no indication of corrosion initiation' follows from the inspection. These costs are generally lower than the prior costs, but decrease further when inspection is done later. If 'indication of corrosion initiation' follows out of the inspections, the costs are larger than the prior costs. However, the pre-posterior costs also decrease when the inspection is done later. Nevertheless, after $t = 15$ years, the probability of having 'no indication of corrosion initiation' as inspection outcome largely decreases for technique 2. For technique 1, this decrease is less remarkable, as can be seen in Figure IX-7. Moreover, due to the large uncertainty associated to this inspection, the posterior distributions lie closer to the prior distributions when compared to those obtained when the more accurate technique is used. Hence, in general the lifetime costs accounting for technique 1 lie closer to the prior costs, inducing lower values of the VoI.

Figure IX-9 shows that the relative VoI obtained through different inspection locations is symmetric along the mid-span of the beam. As already observed in Figure IX-8, the more accurate technique 2 leads to a larger VoI at every inspection location. The most beneficial location of inspection, only considering the VoI and this inspection set-up, can be derived from this figure for both techniques. It seems that inspecting at mid-span is the most beneficial for this case. These results

confirm what can be intuitively expected, since the failure of the beam will mostly be defined by failure of its critical elements, which are located at mid-span where the largest load effects (i.e. bending moments) are found. When inspecting further away from mid-span, the amount of information gained on the most critical elements is limited. Inspecting at 2 m from mid-span still provides information on the concrete cover at mid-span, which is modelled by a random field (correlation length 1 m). The influence on the distribution of the chloride concentration and diffusion coefficient of the concrete at mid-span is the same for all inspection locations different from mid-span, since for these parameters the correlation is constant as the dependence is modelled by hyperparameters. Hence, the VoI is largest at mid-span, decreases when measuring further from mid-span and becomes constant when inspections are performed at locations that are at a distance much larger than the correlation length of the random field.
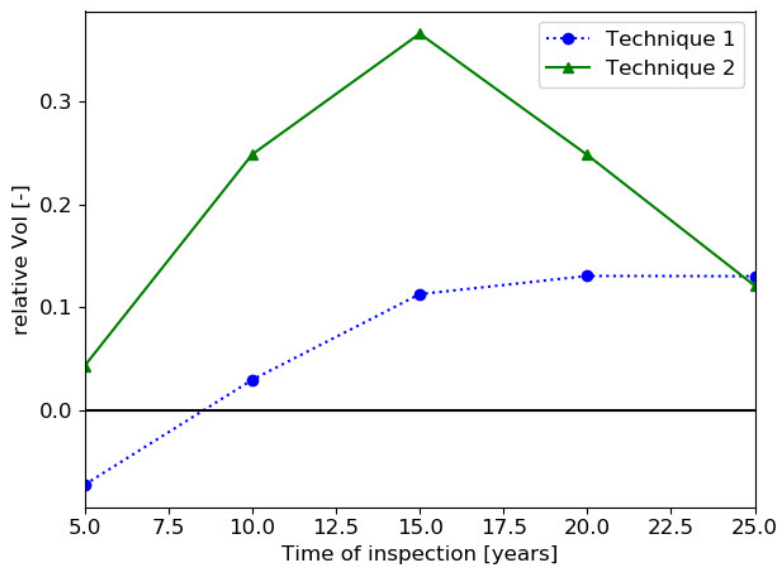

Figure IX-8: VoI as a function of the inspection time for both techniques (inspection at mid-span). The black line corresponds to a VoI of zero

An extended pre-posterior framework incorporating the time-dependent and spatial nature of degrading concrete structures
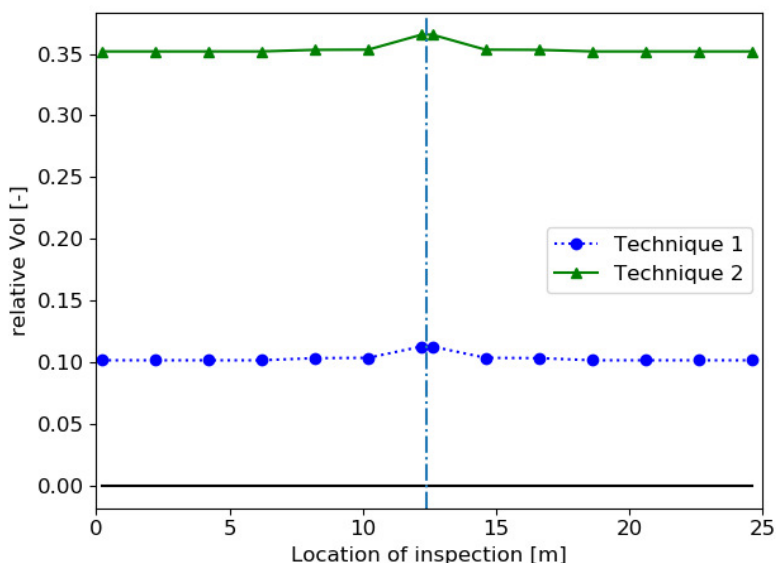
253

Figure IX-9: VoI as a function of the location of inspection for both techniques (at $t = 15$ years). The black line corresponds to a VoI of zero. The vertical dashed line represents the axis of symmetry located at mid-span.

IX.4 Summary and conclusions

In this chapter, the existing pre-posterior analysis has been extended to account for the time-dependent and spatial character of degradation. As such, the VoI of a given inspection/monitoring strategy can be defined before actually implementing it. This enables the comparison of different strategies, varying in inspection/monitoring time, location, and even the type of inspection/monitoring. For illustrative purposes, the framework is applied to a simple analytical example and to a bridge girder subjected to corrosion.

The traditional pre-posterior framework is extended to account for structural degradation. In order to account for the time-dependent character, a deterioration mechanism is modelled and the probability of failure and corresponding costs are calculated at every timestep. In this thesis, the focus is put on corrosion of reinforced concrete elements as deterioration mechanism. The time (and location) when (and where) to undertake action is determined by heuristics, e.g. the exceedance of a damage threshold. Since, in general, degradation is not uniform along the structure, the spatial character is accounted for as well, by the use of hyperparameters and random fields. Different types of inspections/monitoring can be included. The determination of the VoI with this extended framework enables

the comparison of different inspection/monitoring strategies, consisting of different types of inspections/monitoring, but also different points in time at which the inspection/monitoring is performed and varying inspection/monitoring locations.

To account for the spatial character of degradation in reinforced concrete structures, the structure is discretized in elements and the optimal inspection/monitoring locations along the structure can be determined to describe this corrosion process. Moreover, in most literature the decision-making framework is based on discrete states of the structure with respect to their degradation, i.e. no corrosion, a lot of corrosion, etc. However, here the corrosion phenomenon is not discretised and the distributions of the variables in the time-dependent model are updated based on the inspection/monitoring outcomes. This also pushes forward the current state-of-the-art, as inspection/monitoring outcomes are mostly only used to trigger repair, but now also enable to update the degradation model. Hence, a novel coupling between the traditional pre-posterior framework and structural time-dependent and spatial degradation of reinforced concrete structures has been developed, in which the variables of the degradation model can be updated based on the inspection/monitoring outcomes. As such, an optimal inspection/monitoring or maintenance strategy can be defined over the whole lifetime of the structure.

The applied methods are illustrated by application to an analytical example case considering a simply supported beam and a prestressed concrete girder. Including other monitoring strategies than those considered in the illustrative examples (such as the ones used in Chapter VI), will be done in Chapter XI.

The analyses performed in this chapter take into account the probability of failure over time. Nevertheless, decision-makers do not always have the necessary background or tools for evaluating failure probabilities. Instead of target reliabilities, other thresholds for actions could be derived, e.g. based on critical deformations. Further research is required on the definition of these thresholds. In case no failure probabilities can be evaluated, also the formulations for the (failure) costs need to be reconsidered.

The flowchart for the extended pre-posterior framework as developed in this chapter (and the corresponding code) provide an important contribution to the existing state-of-the-art. It allows evaluating the VoI for real-case corroding RC structures, as will be illustrated in Chapters XI and XII.

An extended pre-posterior framework incorporating the time-dependent and spatial nature of degrading concrete structures

255

IX.5 References

Caspeele, R., Steenbergen, R., Sykora, M., 2016. *fib* Bulletin 80: Partial factor methods for existing concrete structures.

Courage, W.M.G., 2018. TNO Case Study Concrete Bridge - COST TU1402.

Duracrete, 1998. BE95-1397. Modelling of Degradation.

fib, 2015. *fib* Bulletin 76: Benchmarking of deemed-to-satisfy provisions in standards. Lausanne.

fib, 2006. *fib* Bulletin 34: Model code for service life design. Lausanne.

Hadidi, A., Azar, B.F., Rafiee, A., 2017. Efficient response surface method for high-dimensional structural reliability analysis. Struct. Saf. 68, 15–27.

Holicky, M., Sykora, M., 2010. Stochastic models in analysis of structural reliability, in: Proceedings of the International Symposium on Stochastic Models in Reliability Engineering, Life Sciences and Operations Management. pp. 428–439

Honfi, D., 2014. Serviceability floor loads. Struct. Saf. 50, 27–38.

JCSS, 2001. Probabilistic Model Code.

Jiang, Z., Li, J., 2017. High dimensional structural reliability with dimension reduction. Struct. Saf. 69, 35–46.

Katafygiotis, L.S., Zuev, K.M., 2008. Geometric insight into the challenges of solving high-dimensional reliability problems. Probabilistic Eng. Mech. 23, 208–218.

Lay, S., Schießl, P., Cairns, J., 2003. Lifecon Deliverable D3.2.

Lehar, M., Zimmermann, M., 2012. An inexpensive estimate of failure probability for high-dimensional systems with uncertainty. Struct. Saf. 36–37, 32–38.

Leonardo da Vinci Pilot Project CZ/02/B/F/PP-134007, 2005. Implementation of Eurocodes - Handbook 2 - Reliability Backgrounds. Prague.

Mandić Ivanković, A., Skokandić, D., Žnidarič, A., Kreslin, M., 2019. Bridge performance indicators based on traffic load monitoring. Struct. Infrastruct. Eng. 15, 899–911.

Schuëller, G.I., Pradlwarter, H.J., Koutsourelakis, P.S., 2004. A critical appraisal of reliability estimation procedures for high dimensions. Probabilistic Eng. Mech. 19, 463–474.

Straub, D., 2011. Reliability updating with inspection and monitoring data in deteriorating reinforced concrete slabs, in: ICASP11 - Applications of Statistics and Probability in Civil Engineering. pp. 2309–2316.

Straub, D., 2004. Generic Approaches to Risk Based Inspection Planning for Steel Structures. PhD thesis, ETH Zürich.

Wang, L., Grandhi, R.V., 1996. Safety index calculation using intervening variables for structural reliability analysis. Comput. Struct. 59, 1139–1148.

Wang, Z., Song, J., 2018. Hyper-spherical extrapolation method (HEM) for general high dimensional reliability problems. Struct. Saf. 72, 65–73.

Wang, Z., Song, J., 2016. Cross-entropy-based adaptive importance sampling

using von Mises-Fisher mixture for high dimensional reliability analysis. Struct. Saf. 59, 42–52.

An extended pre-posterior framework incorporating the time-dependent and spatial nature of degrading concrete structures

257

CHAPTER X

Optimal sensor placement

"True optimization is the revolutionary contribution of modern research to decision processes."
- George Dantzig

X.1 Introduction

In the previous chapter, the concept of VoI analysis has been introduced. This can be used as a decision support tool when optimizing a monitoring strategy. However, for optimizing both the time and locations of measurements, many (computationally expensive) evaluations of the VoI are required. In this chapter, a solution will be provided for this issue by illustrating how the optimal sensor positions can also be optimized without running the VoI analysis. An optimal sensor configuration can be selected such that the resulting data are most informative on the actual condition of the structure (Yuen et al., 2001). This is especially important when the sensors are limited in number (Chisari et al., 2017). By optimizing the sensor placement, the cost of the monitoring campaign can be reduced without compromising the quality of the obtained data (Ostachowicz et al., 2019). A possible optimal sensor placement strategy will be highlighted in this chapter and applied to the different monitoring strategies discussed in Chapter VI. The sensor placement strategy discussed in the current chapter might be suboptimal since it is based on heuristics, but the influence on the VoI will be limited, drastically reducing the computational effort.

Optimal sensor placement has already extensively been discussed in literature. A lot of research is performed on optimal sensor placement for the extraction of modal data, both based on a deterministic model (i.e. not accounting for uncertainties of the underlying model parameters) (Beal et al., 2008; Meo and Zumpano, 2005) and based on Bayesian models accounting for uncertainties (Argyris et al., 2017; Li and Der Kiureghian, 2016; Vincenzi and Simonini, 2017). Different methods exist herein, for example sensor placement based on the modal assurance criterion (MAC) (Ostachowicz et al., 2019; Sun and Büyüköztürk, 2015), Fisher information matrix (Ostachowicz et al., 2019), energetic approaches (e.g. structural deformation energy (Banfu and Miyamoto, 1998)), etc. In most of these works, the purpose of the optimal sensor placement is to accurately detect the mode shapes with the modal analysis (i.e. distinguish well between the different modes), and to identify the parameters of interest.

Whereas a lot of research has been performed on optimal sensor placement for optimally extracting modal data out of the sensor readings, the identification of model parameters is often required in the assessment of existing structures (Chisari et al., 2017). Therefore, the number, type and location of the sensors have to be estimated such that the uncertainties on the estimated model parameters are minimized (Capellari et al., 2018). These uncertainties are related to the uncertainties of the underlying model parameters. Nevertheless, deterministic methods do not take into account these uncertainties. When uncertainty on model parameters should be accounted for in the optimal sensor placement, Bayesian theory can be used. The utility function for the optimal sensor placement in this case depends on the information entropy, which is a metric for the decrease in

uncertainty from the prior distribution of the model parameters to a posterior distribution after updating based on the obtained data (Argyris et al., 2017; Ostachowicz et al., 2019; Zhang et al., 2017). This information entropy will depend on the sensitivity of the measured variable to changes in the model parameter to be estimated. Hence, these sensitivities have an important share in the derivation of (an asymptotic approximation of) the information entropy.

For complex structures, the data is often generated by a finite element model. Moreover, analytical expressions of the utility function to be used in the optimization scheme are often not available or difficult to derive. In those case, Monte Carlo sampling of the utility function can be performed, as for example done in (Capellari et al., 2018, 2016a; Huan and Marzouk, 2013; Yuen and Kuok, 2015). Evaluating a finite element model for every sample in the Monte Carlo evaluation can be computationally very expensive. In (Capellari et al., 2018, 2016a, 2016b; Huan and Marzouk, 2013), this is resolved by applying a meta-model, which will then be used in the Monte Carlo sampling. (Chow et al., 2011) also use a finite element model to generate the responses of the structure. Their optimal sensor placement is also based on information entropy as utility function and an asymptotic approximation of the posterior distribution. However, it is not clear how they have derived the sensitivities of the measured variables to the parameters of the finite element model. Nevertheless, the computationally expensive objective function and possible unavailability of first-order derivatives of the data to the model parameters are important challenges in the derivation of the optimal sensor placement (Beal et al., 2008).

For a reinforced concrete structure subjected to corrosion, the model parameters in the corrosion model should be identified, as for example performed in Chapter VI, where distributions of the corrosion variables are updated based on monitoring data. Hence, in the calculation of the information entropy, sensitivities of the data to these corrosion variables should be derived. The relationship between these corrosion variables and the data is mostly non-linear and modelled with a finite element model. In this chapter, no Monte Carlo evaluations will be used for calculation of the objective function. The sensitivities of the data to the corrosion variables will be estimated directly based on the finite element model by the method of Nelson (Nelson, 1976). To account for the spatial character of corrosion, in contrast to existing literature, the structure will not be subdivided into independent substructures, each modelled with an independent variable for the stiffness, but the methods to account for spatial variation/correlation as summarized in Chapter III will be applied.

X.2   Optimal sensor placement based on information entropy

X.2.1   Information entropy

The optimal sensor locations for parameter estimation based on experimental data can be derived from a metric called the information entropy. This information entropy can be used as a performance measure of a specific sensor configuration. The optimal sensor configuration is found by minimizing the information entropy. To determine the optimal sensor configuration beforehand, asymptotic approximations for the information entropy are generally applied. These approximations provide insight in the dependence of the information entropy on the number and locations of sensors.

The posterior distribution of the variables of interest represents the uncertainty in these variables based on the information contained in the data. The information entropy h is hence given by equation (X-1) (Papadimitriou et al., 2000), where $f''(\boldsymbol{\theta}_M|\overline{\boldsymbol{d}})$ is the posterior distribution of the variables $\boldsymbol{\theta}_M$ given the measurement data $\overline{\boldsymbol{d}}$. The variables $\boldsymbol{\theta}_M$ are still unknown at this stage and information on them will be derived based on the measurement data. With the method that will be explained below, the optimal sensor locations can be derived to extract the best possible information on $\boldsymbol{\theta}_M$.

$$h(L; \overline{\boldsymbol{d}}) = E_{\boldsymbol{\theta}_M}[-\ln(f''(\boldsymbol{\theta}_M|\overline{\boldsymbol{d}})] \qquad \text{(X-1)}$$

The information entropy is a unique scalar measure of the uncertainty in the estimate of the structural parameters of interest $\boldsymbol{\theta}_M$, where a higher information entropy corresponds to a higher uncertainty. The information entropy depends on the available data $\overline{\boldsymbol{d}}$ and the sensor configuration L. For a large number of data points, an asymptotic approximation of this information entropy can be found according to (Papadimitriou, 2004). This asymptotic approximation is useful in the experimental stage of designing an optimal sensor configuration. The information entropy is approximated according to equation (X-2).

$$h(L; \overline{\boldsymbol{d}}) \sim H(L; \boldsymbol{\theta}_{M,0}) = \frac{1}{2} N_\theta \ln(2\pi) - \frac{1}{2} \ln\left[\det\left(Q(L; \boldsymbol{\theta}_{M,0})\right)\right] \qquad \text{(X-2)}$$

Here, N_θ is the number of variables in $\boldsymbol{\theta}_M$. For the prior estimate, nominal values $\boldsymbol{\theta}_{M,0}$ that are representative for the system can be used for $\boldsymbol{\theta}_M$. The matrix $Q(L; \boldsymbol{\theta}_{M,0})$ is an $N_\theta \times N_\theta$ semi-positive definite matrix, asymptotically approximated by equation (X-3).

$$Q(L; \boldsymbol{\theta}_{M,0}) = \sum_{k=1}^{N} \left(L\underline{\nabla}_\theta \underline{x}_k\right)^T (L\Sigma L^T)^{-1} \left(L\underline{\nabla}_\theta \underline{x}_k\right) \qquad \text{(X-3)}$$

Here, $\underline{\nabla}_\theta \underline{x}_k$ represents the sensitivities of the data to the variables $\boldsymbol{\theta}_M$. The matrix Q is known as the Fischer information matrix and contains information on the uncertainty in the values of the variables $\boldsymbol{\theta}_M$ based on the data from all measured positions in L. The prediction error covariance matrix Σ consists out of two contributions: a contribution of the measurement error and one of the model error. When assuming independence between the measurement error and the model error, the total covariance matrix of the prediction error is given by the sum of the covariance matrices of the measurement and model error. A reasonable assumption is that the measurement error is independent of the location of the sensor and hence has a diagonal covariance matrix. However, a certain degree of correlation can be expected for the model error between two neighbouring locations, arising from the underlying model dynamics. To take into account this correlation, the covariance matrix of the model error will be non-diagonal. The correlation between the model error of two degrees of freedom i and j can be given by $\Sigma_{ij} = \sqrt{\Sigma_{ii}\Sigma_{jj}} R(\delta_{ij})$. This expression accounts for the spatial distance δ_{ij} between the two degrees of freedom i and j. The function $R(\delta_{ij})$ is a correlation function that should satisfy the condition $R(0) = 1$. In theory, the covariance matrix should be consistent with the actual errors and correlations as observed from measurements. However, these are not available in an experimental design stage. Hence, a correlation function needs to be chosen based on prior engineering judgement. In the following, for illustrative purpose, an exponential correlation function is assumed according to equation (X-4).

$$R(\delta) = \exp\left(-\frac{\delta}{\lambda}\right) \qquad \text{(X-4)}$$

Here, λ represents the length of spatial correlation. In the following, based on results observed by Simoen (2013), this length of spatial correlation is taken equal to the wavelength of the measured mode shape.

The optimal sensor locations can be found by solving a discrete-valued optimization problem. The sensors should be placed such that the resulting measurement data are most informative about the variables $\boldsymbol{\theta}_M$. The information entropy gives the amount of useful information contained in the measured data, where a higher information entropy reflects a higher uncertainty in the estimate. Hence, the optimal sensor configuration L_{opt} is the one that minimizes the information entropy. This minimization is constrained over the set of N_p measurable degrees of freedom. Two heuristic sequential sensor placement (SSP) algorithms exist in literature: the forward and the backward SSP (Papadimitriou, 2004). In the forward algorithm, in each iteration the sensor that results in the highest reduction in information entropy is added. Hence, at each iteration the sensor configuration is selected with the minimum information entropy. The backward algorithm works in the reverse order, starting from sensors at all

possible locations and each time removing the sensor with the position that results in the smallest increase in information entropy.

X.2.2 Information entropy for model parameter estimation

The optimal sensor configuration is now formulated for the particular case where modal data are used for model parameter estimation. The parameter set $\boldsymbol{\theta}_M$ consists of the variables related to stiffness and mass characteristics. To calculate the sensitivity matrix $\underline{\nabla}_\theta \underline{x}_k$, which represents the sensitivity of the modal data to changes in the variables $\boldsymbol{\theta}_M$, a sensitivity analysis needs to be performed. If the Fischer Information Matrix is singular, instead of the determinant of the matrix, the product of the first non-zero eigenvalues should be considered in the calculation of the information entropy when applying equation (X-2).

X.2.2.1 Model parameters in spatially degrading concrete structures

To determine the extent of damage in concrete structures subjected to degradation, the model parameters are the variables governing degradation. For a reinforced concrete structure subjected to corrosion, the governing parameters are assumed to be the initiation period and the corrosion rate. To account for the non-uniform corrosion along the structure, the initiation period and corrosion rate are modelled as random fields. Under these modelling assumptions, the variables that need to be estimated by the modal data are the standard normal variables ζ_j appearing in the decomposition of the random field (equation (III-5)). Hence, these form the set of variables $\boldsymbol{\theta}_M$ governing the stiffness and mass characteristics of the structure. To derive the optimal sensor locations, the sensitivities of the mode shapes to these variables ζ_j are required (to find $\underline{\nabla}_\theta \underline{x}_k$ to be used in equation (X-3)).

X.2.2.2 Sensitivities of modal data to model parameters

Two methods exist to derive the sensitivities of the modal data. A first method is described by Fox and Kapoor (1968). However, in this method all eigenvalues and eigenmodes are required to calculate the sensitivities. To overcome this issue, Nelson (1976) introduced a more efficient way to calculate the sensitivities of eigenvectors. This last method will be used in this chapter.

Consider the undamped eigenvalue problem $\boldsymbol{K\Phi} = \boldsymbol{M\Phi\Lambda}$, with $\boldsymbol{\Phi}$ the matrix containing the eigenvectors $\boldsymbol{\phi}_r$ and $\boldsymbol{\Lambda}$ a diagonal matrix with the eigenvalues λ_r on the diagonal. $\boldsymbol{K}$ and $\boldsymbol{M}$ are the stiffness and mass matrix respectively. Out of this undamped eigenvalue problem, following expression can be derived:

$$(\boldsymbol{K} - \lambda_r \boldsymbol{M})\boldsymbol{\phi}_r = 0 \tag{X-5}$$

Deriving equation (X-5) to the variables θ_j (elements of the vector $\boldsymbol{\theta}_M$) gives:

$$(\boldsymbol{K} - \lambda_r \boldsymbol{M}) \frac{\partial \boldsymbol{\phi}_r}{\partial \theta_j} + \left(\frac{\partial \boldsymbol{K}}{\partial \theta_j} - \lambda_r \frac{\partial \boldsymbol{M}}{\partial \theta_j} - \frac{\partial \lambda_r}{\partial \theta_j} \boldsymbol{M} \right) \boldsymbol{\phi}_r = 0 \tag{X-6}$$

Multiplying at the left with $\boldsymbol{\phi}_r{}^T$ and considering the fact that $\boldsymbol{\phi}_r{}^T \boldsymbol{M} \boldsymbol{\phi}_r = 1$ and $\boldsymbol{\phi}_r{}^T (\boldsymbol{K} - \lambda_r \boldsymbol{M}) = (\boldsymbol{K} - \lambda_r \boldsymbol{M}) \boldsymbol{\phi}_r = 0$, leads to equation (X-7).

$$\frac{\partial \lambda_r}{\partial \theta_j} = \boldsymbol{\phi}_r{}^T \left(\frac{\partial \boldsymbol{K}}{\partial \theta_j} - \lambda_r \frac{\partial \boldsymbol{M}}{\partial \theta_j} \right) \boldsymbol{\phi}_r \tag{X-7}$$

Hence, the sensitivity of λ_r only depends on the eigenvalue λ_r itself and the corresponding eigenvector.

In order to derive the sensitivity of the eigenvectors, equation (X-7) needs to be inserted into equation (X-6):

$$\begin{aligned} (\boldsymbol{K} - \lambda_r \boldsymbol{M}) \frac{\partial \boldsymbol{\phi}_r}{\partial \theta_j} = -&\left(\frac{\partial \boldsymbol{K}}{\partial \theta_j} - \lambda_r \frac{\partial \boldsymbol{M}}{\partial \theta_j} \right. \\ &\left. - \boldsymbol{\phi}_r{}^T \left(\frac{\partial \boldsymbol{K}}{\partial \theta_j} - \lambda_r \frac{\partial \boldsymbol{M}}{\partial \theta_j} \right) \boldsymbol{\phi}_r \boldsymbol{M} \right) \boldsymbol{\phi}_r \end{aligned} \tag{X-8}$$

To simplify the notation, this expression is in the following referred to as $\boldsymbol{A}_r \frac{\partial \boldsymbol{\phi}_r}{\partial \theta_j} = \boldsymbol{b}_{rj}$. The matrix $\boldsymbol{A}_r$ has no inverse since it is not of full rank, but has rank N_d-1, with N_d the degrees of freedom. Hence, Nelson (1976) suggests to split the solution into a particular and homogeneous solution according to equation (X-9).

$$\frac{\partial \boldsymbol{\phi}_r}{\partial \theta_j} = \boldsymbol{v}_{rj} + c_{rj} \boldsymbol{\phi}_r \tag{X-9}$$

It can be demonstrated that $\boldsymbol{v}_{rj}$ can be calculated based on the system of equations $\boldsymbol{A}_r^* \boldsymbol{v}_{rj} = \boldsymbol{b}_{rj}^*$. To get this system of equations, a slight modification needs to be done to the original matrix $\boldsymbol{A}_r$ and vector $\boldsymbol{b}_{rj}$, according to equation (X-10).

$$\boldsymbol{A}_r^*: [\boldsymbol{A}_r]_{.k} = 0; \ [\boldsymbol{A}_r]_{k.} = 0; \ [\boldsymbol{A}_r]_{kk} = 1$$
$$\boldsymbol{b}_{rj}^*: [\boldsymbol{b}_{rj}]_k = 0 \tag{X-10}$$

In this way, the adapted matrix $\boldsymbol{A}_r^*$ is again of full rank and has an inverse matrix, which is necessary for the calculation of $\boldsymbol{v}_{rj}$. The index k in equation (X-10) can in principle be chosen freely, as long as $[\boldsymbol{\phi}_r]_k$ is not equal to zero. However, in most cases k is chosen as such that $|[\boldsymbol{\phi}_r]_k|$ is maximal. The coefficient c_{rj} can be found from the orthogonality condition $\boldsymbol{\phi}_r{}^T \boldsymbol{M} \boldsymbol{\phi}_r = 1$, by deriving this equation to θ_j and using equation (X-9). As such, equation (X-11) is found.

$$c_{rj} = -\boldsymbol{\phi}_r^T \boldsymbol{M} \boldsymbol{v}_{rj} - \frac{1}{2} \; \boldsymbol{\phi}_r^T \frac{\partial \boldsymbol{M}}{\partial \theta_j} \boldsymbol{\phi}_r \tag{X-11}$$

X.2.2.3 Sensitivities of modal data to corrosion variables

The expressions given in previous section will be used to derive the sensitivities of the displacement mode shapes to the random fields used to model the initiation period and corrosion rate. It is assumed that degradation due to corrosion only influences the stiffness of the structure and not its mass (i.e. the effects of spalling are neglected). In this case, equation (X-8) simplifies to equation (X-12).

$$(\boldsymbol{K} - \lambda_r \boldsymbol{M}) \frac{\partial \boldsymbol{\phi}_r}{\partial \theta_j} = -\left(\frac{\partial \boldsymbol{K}}{\partial \theta_j} - \boldsymbol{\phi}_r^{\;T} \left(\frac{\partial \boldsymbol{K}}{\partial \theta_j} \right) \boldsymbol{\phi}_r \boldsymbol{M} \right) \boldsymbol{\phi}_r \tag{X-12}$$

The derivative $\partial \boldsymbol{K} / \partial \theta_j$ is required in equation (X-12). The stiffness will indirectly depend on the corrosion variables since these will induce a reduced reinforcement section and will lead to a reduced stiffness in the regions were the concrete is cracked due to the expansive properties of the formed oxides.

In the following analysis, the simply supported beam as introduced in section VI.2.1 is considered. Due to the use of random fields, the beam is subdivided into eight beam elements.

The stiffness matrix of one beam element is given by equation (X-13).

$$\boldsymbol{K} = \begin{bmatrix} EA/l & 0 & 0 & -EA/l & 0 & 0 \\ 0 & 12EI/l^3 & 6EI/l^2 & 0 & -12EI/l^3 & 6EI/l^2 \\ 0 & 6EI/l^2 & 4EI/l & 0 & -6EI/l^2 & 2EI/l \\ -EA/l & 0 & 0 & EA/l & 0 & 0 \\ 0 & -12EI/l^3 & 0 & 0 & 12EI/l^3 & -6EI/l^2 \\ 0 & 6EI/l^3 & 2EI/l & 0 & -6EI/l^2 & 4EI/l \end{bmatrix} \tag{X-13}$$

For a beam under bending, only the terms in EI will be of importance. For a reinforced concrete beam, this bending stiffness EI depends on the reinforcement area, which reduces due to corrosion. Besides a reduction in reinforcement area, corrosion also induces cracking of the concrete cover due to the expansive character of the oxides. This cracking is modelled by a reduction of the Young's modulus of the concrete cover. This reduced Young's modulus is denoted by E_d. The stiffness EI of a beam element hence depends on A_s and E_d, which on their turn depend on the corrosion variables (i.e. the initiation period and corrosion rate). Since these are modelled with random fields, these corrosion variables on their turn depend on the standard normally distributed variables ζ_j in the

decomposition of the random fields of the initiation period and the corrosion rate, according to equation (III-4). Based on these considerations, the derivative of the stiffness matrix to the variables ζ_j is found by application of the chain rule according to equation (X-14).

$$
\begin{aligned}
\frac{\partial \boldsymbol{K}}{\partial \zeta_j} = {} & \frac{\partial \boldsymbol{K}}{\partial EI} \cdot \frac{\partial EI}{\partial E_d} \cdot \frac{\partial E_d}{\partial V_{corr}} \cdot \frac{\partial V_{corr}}{\partial \zeta_j} \\
& + \frac{\partial \boldsymbol{K}}{\partial EI} \cdot \frac{\partial EI}{\partial A_s} \cdot \frac{\partial A_s}{\partial V_{corr}} \cdot \frac{\partial V_{corr}}{\partial \zeta_j}
\end{aligned}
\tag{X-14}
$$

This equation is valid for the derivative of $\boldsymbol{K}$ to the standard normal variables ζ_j in the decomposition of the random field representing the corrosion rate. For the standard normally distributed variables ζ_j in the decomposition of the random field representing the initiation period, a similar equation is found. All the derivatives appearing in these equations and the application of the chain rule have been checked by comparing them with their estimate based on finite differences.

The sensitivities are a measure for the extent to which a change in a particular parameter will affect another parameter. If a very small sensitivity is found, changing one parameter will not affect the other. Hence, when the mode shape at a particular location has a very small sensitivity to the standard normally distributed variables ζ_j in the decomposition of the random fields for the initiation period and corrosion rate, it will not be beneficial to measure at that location, since changes in these standard normally distributed variables ζ_j do not affect the mode shape at that location.

X.2.3   Optimal sensor locations to estimate corrosion variables based on modal data

Based on the equations given in the previous sections, the information entropy can be calculated for a given number of sensors. Optimal sensor positions can be derived based on this information entropy by application of the forward sensor placement algorithm. In each iteration, the sensor that results in the highest reduction in information entropy is added. Hence, at each iteration the sensor configuration is selected with the minimum information entropy. This is illustrated in Figure X-1. In the initial stage, no sensors are selected yet. The information entropy is calculated accounting for each of the individual possible sensor locations. The sensor with the lowest resulting information entropy is chosen (i.e. sensor 4 in the example of Figure X-1). This sensor position is then fixed when starting the next iteration. In this next iteration, the information entropy is calculated accounting for the already placed sensors (i.e. sensor 4 in the example) combined with the other possible sensor positions. In the example, following

combinations should hence be considered: 1 and 4, 2 and 4, 3 and 4, 5 and 4, and 6 and 4. In this example, adding sensor 1 to the sensor set (i.e. the combination of sensor 1 and sensor 4) results in the lowest information entropy. Hence, sensor 1 will be added next. In the next stage, sensors 1 and 4 are already part of the sensor set and the process continues in a similar way, until the a priori fixed number of sensors is reached.
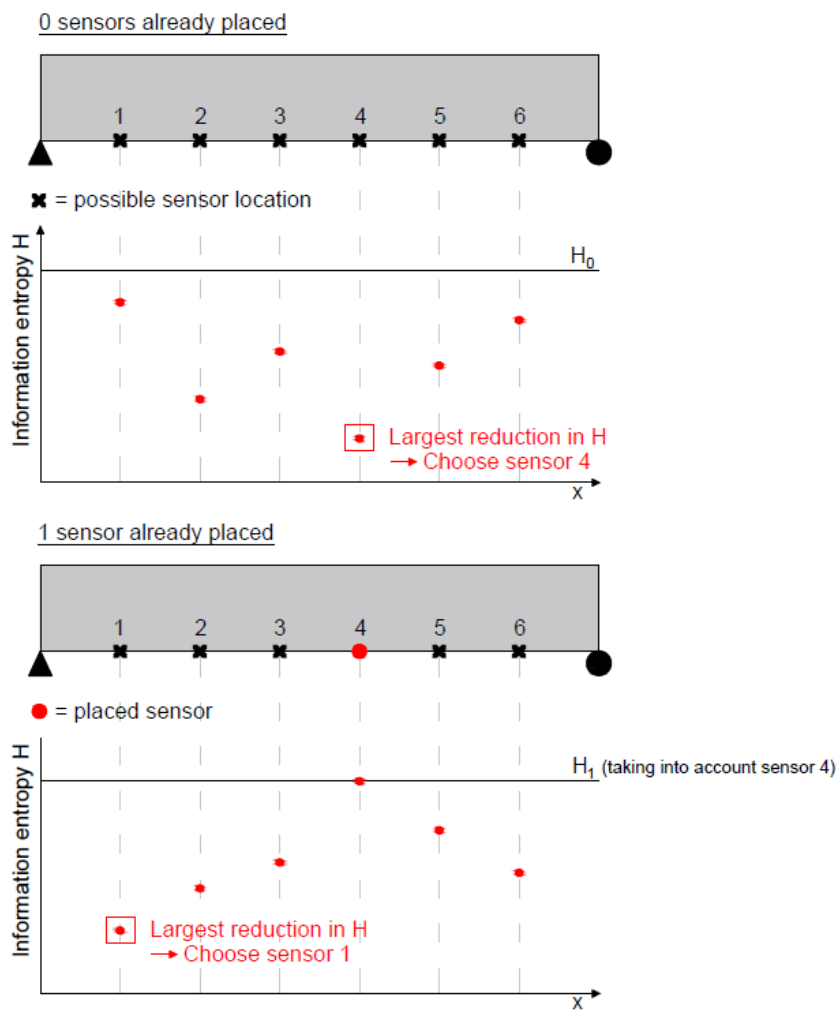

Figure X-1: Illustration of the forward sensor placement algorithm

When the sensitivities of the mode shapes to the standard normally distributed variables ζ_j in the decomposition of the random fields are calculated, these can be inserted in the expressions for the information entropy. The latter can then be used to determine the optimal sensor positions. In the analyses in this chapter, the number of sensors will be fixed beforehand. This number of sensors will be optimized by evaluating the VoI, as will be explained in the following chapter.

For the example of the simply supported beam, a first case considers possible sensor locations at 0.5 m, 1 m, 1.5 m, 2 m, 2.5 m, 3 m and 3.5 m. These sensor locations not necessarily need to correspond to the elements used in the discretization of the random fields. First, the situation is considered where only the first mode is measured, without correlation between the sensor locations. In that case, the matrix $\sum$ in Q (expression (X-3)) is a diagonal matrix. The optimal sensor configuration for this situation is given in Table X-1. For the first (bending) mode and assuming no correlation (i.e. $R(\delta_{ij}) = 0$ if $i \neq j$ and $R(\delta_{ij}) = 1$ if $i = j$), it is expected that the optimal sensor locations are in the middle of the beam, since there the largest modal displacements are found. However, the sensitivities of the second and fourth KL mode (with corresponding standard normally distributed variables ζ_2 and ζ_4) in the decompositions of the random fields are very small in the middle measurement location and even approach zero. This corresponds to the middle of the beam and to a node in the second and fourth KL mode in the decomposition in the random field. Hence, this location will provide no information on these standard normally distributed variables ζ_2 and ζ_4 in the decomposition of the random fields. That is why the optimal sensor locations are shifted away from the middle of the beam. However, due to the symmetry of the first mode shape, the sensors are also placed symmetrically with respect to the mid-span of the beam. There is no difference in information entropy of the sensors at 1 m and 3 m at the first iteration, hence one of the two is chosen. It should also be pointed out that the information entropy indeed decreases when adding sensor locations, as visible on Figure X-2. Here, the information entropy is given relative to the value when only one sensor is considered.

When assuming correlation between the sensor locations for the first mode according to equation (X-4), the correlation length λ equals $2L = 8$ m. The optimal sensor locations are also given in Table X-1. Here it can be seen that the sequence of locations is altered compared to the case considering no correlation. The first sensor is still placed at the same location. However, without assuming correlation, the sensors are chosen symmetrically, which is not the case when assuming correlation. In the latter case, the next sensor is closer to mid-span, where the largest mode shape displacement will take place. Furthermore, this measurement location corresponds to a large sensitivity of the mode shape displacement to changes in the KL modes, resulting in a lot of information. Next, the location left from mid-span is added (not the sensor at mid-span itself due to the reason

mentioned previously, this is again added last). Sensor locations at 3 m and 3.5 m are symmetrical to 1 m and 0.5 m, and are hence added later, since these will provide similar information (and have the same contribution to the information entropy).

Table X-1: Optimal sensor configuration for the simply supported beam

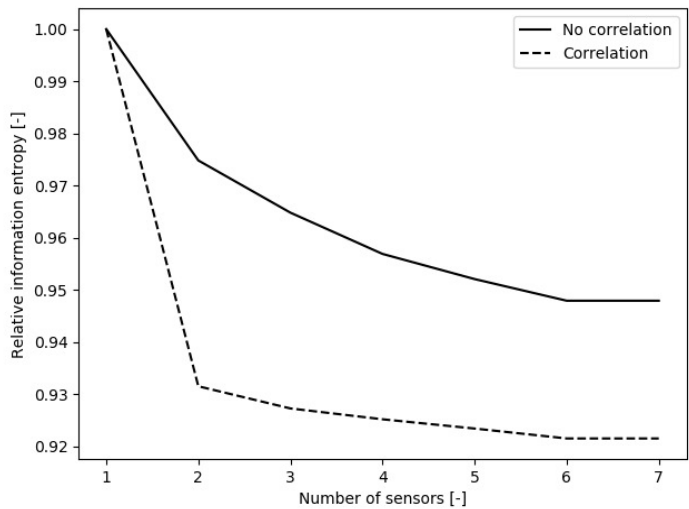| Bending mode	Correlation	Order of sensor positions						
		1	2	3	4	5	6	7
1	No	1 m	3 m	1.5 m	2.5 m	0.5 m	3.5 m	2 m
1	Yes	1 m	2.5 m	1.5 m	0.5 m	3 m	3.5 m	1 m
1-3	No	2.5 m	1.5 m	2 m	1 m	3 m	0.5 m	3.5 m
1-3	Yes	2.5 m	1.5 m	0.5 m	3.5 m	2 m	1 m	3 m

Figure X-2: Information entropy as a function of the number of sensors when assuming the data from the first mode with or without correlation between the sensor locations for the simply supported beam

Also, multiple modes can be considered. In equation (X-3), k then represents the considered mode and N the total number of modes considered. As an example, the first three bending modes are considered here. The optimal sensor placement is also given in Table X-1. This sensor order is again very different from the one when only considering one mode. When assuming correlation between the errors at different sensor locations, the correlation lengths are dependent on the measured mode shapes. The correlation lengths for the first three bending modes are

respectively equal to 8 m, 4 m and 2.7 m. Also for this situation, the optimal sensor placement is summarized in Table X-1. The optimal sensor placement has also been derived for different points in time (i.e. different corrosion degrees), but it was found that this has no influence on the optimal sensor configuration.

X.3 Application to finite element models

The derivation of the sensitivities as performed in section X.2.2 uses analytical expressions for the stiffness matrix. However, for a finite element (FE) model, this stiffness matrix is often very large. Moreover, in many cases the stiffness matrix is not given as output from the finite element software. Hence, the method of Nelson should be slightly adapted to allow for the derivation of sensitivities of the mode shape vector based on a FE model. In this work, FE model software DIANA FEA (DIANA FEA BV, 2019) is used to calculate the displacement mode shapes. However, any other FE software can be used, as long as it allows performing similar calculations. The sensitivities of the displacement mode shapes to the standard normally distributed variables ζ_i in the decomposition of the random fields for the initiation period and corrosion rate are derived. The application of the method of Nelson on a DIANA FEA model will be explained below.

As explained in section X.2.2, in the method of Nelson derivatives of the stiffness matrix K to the variables ζ_i are required according to equation (X-15) for the corrosion rate, and similar for the initiation period.

$$\frac{\partial K}{\partial \zeta_i} = \sum_z \frac{\partial K_d(z)}{\partial E_d(z)} \frac{\partial E_d(z)}{\partial V_{corr}(z)} \frac{\partial V_{corr}(z)}{\partial \zeta_i} + \frac{\partial K_{As}(z)}{\partial A_s(z)} \frac{\partial A_s(z)}{\partial V_{corr}(z)} \frac{\partial V_{corr}(z)}{\partial \zeta_i}$$

(X-15)

Here, z are the different elements in which the random fields and hence the structure are discretized. K_d is the stiffness matrix of the finite element elements in the damaged concrete, E_d is the Young's modulus of the damaged concrete, K_{As} is the stiffness matrix of the finite elements modelling the reinforcement, and A_s is the reinforcement area.

When using a FE model, $\partial K_d(z)/\partial E_d(z)$ and $\partial K_{As}(z)/\partial A_s(z)$ cannot be calculated by analytical expressions anymore. Nevertheless, the derivative of the stiffness matrix of an element to its Young's modulus equals the stiffness matrix divided by the Young's modulus, or $\partial K/\partial E = K/E$. Furthermore, the derivative of the stiffness matrix of a 2D truss element to its area also equals this stiffness matrix divided by the area of the truss element, or $\partial K/\partial A = K/A$. This is only applicable when the parameter to which the derivation should be made has only one power in the expression of the stiffness matrix. For example, in the case of

bending combined with axial forces, the length l appears in the stiffness matrix both as $1/l$ and $1/l^3$. Here, the power of l equals one or three, depending on the location in the stiffness matrix. In this case, the mentioned simplification cannot be applied to calculate the derivative of the stiffness matrix to l.

When inserting $\partial K / \partial A = K / A$ and $\partial K / \partial E = K / E$ in equation (X-15), one gets expression (X-16) for the derivative of the stiffness matrix to the standard normally distributed variables ζ_i in the decomposition of the random fields of the corrosion rate, and similar for the initiation period.

$$\frac{\partial K}{\partial \zeta_i} = \sum_z \frac{K_d(z)}{E_d(z)} \frac{\partial E_d(z)}{\partial V_{corr}(z)} \frac{\partial V_{corr}(z)}{\partial \zeta_i} + \frac{K_{As}(z)}{A_s(z)} \frac{\partial A_s(z)}{\partial V_{corr}(z)} \frac{\partial V_{corr}(z)}{\partial \zeta_i} \quad \text{(X-16)}$$

The derivatives $\partial E_d(z)/\partial V_{corr}$, $\partial V_{corr}/\partial \zeta_i$, etc. can still be derived based on analytical expressions. Equation (X-16) can shortly be written as equation (X-17).

$$\frac{\partial K}{\partial \zeta_i} = \sum_z (c_1(z)K_d + c_2(z)K_{As}) \quad \text{(X-17)}$$

Here, the matrix K_d differs from zero only for the degrees of freedom (DOF's) corresponding to the nodes located in the damaged concrete. For the other nodes, there will be no influence of corrosion and hence of the standard normally distributed variables ζ_i in the decomposition of the random fields, so the derivative equals zero. Similar, K_{As} only differs from zero in the degrees of freedom of the nodes influenced by the reinforcement.

Reconsidering equation (X-8), equation (X-18) is found.

$$(K - \lambda_r M)\frac{\partial \phi_r}{\partial \zeta_i} = -\frac{\partial K}{\partial \zeta_i}\phi_r + \phi_r^T \frac{\partial K}{\partial \zeta_i}\phi_r M\phi_r \quad \text{(X-18)}$$

Filling in equation (X-17) and accounting for the fact that $(K - \lambda_r M)\phi_r = 0$, equation (X-19) is found.

$$(K - \lambda_r M)\frac{\partial \phi_r}{\partial \zeta_i} = -\sum_z (c_1(z)K_d + c_2(z)K_{As})\,\phi_r - c_2 K_{As}\phi_r$$
$$+ \phi_r^T(\sum_z (c_1(z)K_d + c_2(z)K_{As})\,\phi_r)\frac{K\phi_r}{\lambda_r} \quad \text{(X-19)}$$

The stiffness matrix is still appearing multiple times in this expression. However, in the right hand side, it is always multiplied by the mode shape vector. A stiffness matrix times a displacement matrix represents the element forces when the

displacement is applied as a displacement load. Since these element forces are often available as output to a FE analysis, this principle will be used to derive the sensitivities of the mode shapes based on a finite element model.

To calculate the right hand side of equation (X-19), the mode shape vector will be applied as a displacement load to the FE model. The corresponding element forces will be calculated:

1) In all elements to calculate $\boldsymbol{K}\boldsymbol{\phi}_r$.
2) In the elements of the damaged concrete to calculate $\boldsymbol{K}_d\boldsymbol{\phi}_r$. These forces will be calculated for the different zones in the discretization of the random field and multiplied with the corresponding derivatives appearing in the chain rule according to equation (X-17), i.e. the factors $c_1(z)$. Finally, the forces will be combined in a vector with length equal to the number of nodes, with a value of zero in all nodes that do not belong to the damaged concrete.
3) In the elements constituting the reinforcement to calculate $\boldsymbol{K}_{As}\boldsymbol{\phi}$. These forces will be calculated for the different zones in the discretization of the random field and multiplied with the corresponding derivatives appearing in the chain rule according to equation (X-17), i.e. the factors $c_2(z)$. Finally, the forces will be inserted in a vector with length equal to the number of nodes, with a value of zero in all nodes that are not influenced by the reinforcement.

Based on these element forces, the right hand side of equation (X-19) is found, or the vector $\boldsymbol{b}_{rj}$ to calculate $\boldsymbol{v}_{rj}$ (equation (X-9)). Subsequently, $\boldsymbol{v}_{rj}$ can be calculated by performing a harmonic analysis under the frequency corresponding to the eigenvalue λ_r and force $\boldsymbol{b}_{rj}$. However, a similar adaptation as in equation (X-10) has to be made. One degree of freedom of the model will be restricted and the corresponding value of $\boldsymbol{b}_{rj}$ will be set equal to zero. Once $\boldsymbol{v}_{rj}$ is found, c_{rj} is still required to calculate the sensitivities based on equation (X-9). Reconsidering equation (X-11), c_{rj} is given by equation (X-20).

$$c_{rj} = -\boldsymbol{\phi}_r^T \boldsymbol{M} \boldsymbol{v}_{rj} \qquad \text{(X-20)}$$

The mass matrix is required to solve equation (X-20). However, it is not given as an output of the FE model. This can be circumvented by applying the harmonic analysis $(\boldsymbol{K} - \lambda_r \boldsymbol{M})\boldsymbol{v}_{rj} = \boldsymbol{F}$, with $\boldsymbol{K}$ equal to zero and $\lambda_r = 1$. The forces following from this harmonic analysis are then equal to $-\boldsymbol{M}\boldsymbol{v}_{rj}$ and enable the calculation of c_{rj} based on equation (X-20). Finally, the sensitivities can then be found by applying equation (X-9). It should be pointed out that the calculated sensitivities were checked based on finite differences and that a good agreement was found. Based on the derived sensitivities, the optimal sensor configuration can be calculated in the same way as described above.

X.4   Application to a reinforced concrete girder bridge

X.4.1   Optimal sensor placement for displacement mode shapes

Based on the method described above, the optimal sensor placement is determined for a span of a simply supported RC girder bridge, as already described in section VI.2.2. For the determination of the optimal sensor placement, the sensitivities of the mode shapes to the variables in the corrosion model should be derived, i.e. $\partial\phi/\partial C_s$, $\partial\phi/\partial\zeta_{D,i}$, $\partial\phi/\partial\zeta_{Vcorr,i}$. Here, $\zeta_{D,i}$ and $\zeta_{Vcorr,i}$ are the standard normally distributed variables in the decomposition of the random fields for the diffusion coefficient of the concrete D and the corrosion rate V_{corr} respectively. For both random fields, 13 modes are required in the decomposition in order to reach a maximum error of 5%. Hence, the sensitivities of the mode shapes are derived to these 27 variables in total, based on the method described above and verified based on finite differences. The sensitivities are derived assuming an age of the bridge equal to 50 years. Based on the sensitivities, the optimal sensor locations can be found by application of equation (X-2) and the forward SSP algorithm. The sensor locations are picked out of 40 previously selected sensor locations, in the middle of the elements in which the structure is discretized. Here, the elements at the supports are left out, for practical reasons. The optimal sensor locations for the first four modes assuming an uncorrelated model error are visualized in Figure X-3. Here, the x-axis represents the number of sensors placed on the structure. At a vertical line through this axis, there are *x* markers from the scatter plots, representing the *x* sensors placed on the structure. The different marker types correspond to the girder at which the sensor is placed, and the position on the vertical axis represents the location along the girder. When looking at Figure X-3, the sensors are first placed at the ends of the girders and only later in the middle. The girders itself are about equally chosen, without any clear preference for a girder. There is a difference in information entropy in the first iteration, but this difference is limited for the different girders (from 21.189 in girder 5 to 21.385 in girder 3 in the first iteration). The very first chosen sensor is at 1.5 m from the left support on the fifth girder.

Also, correlation between the mode shape locations can be assumed (i.e. a correlated model error). There can be correlation in two directions, namely the *x* (length of the bridge) and *y*-direction (width of the bridge). The correlation length depends on the wavelength of the mode shape. The correlation lengths of the first four modes are given in Table X-2. The correlation function is given by equation (X-4), but now with a contribution in both directions. The resulting optimal sensor placement when assuming correlation is visualized in Figure X-4. The first sensors are placed on all girders at 1.5 m from the left support. For the later sensors, there is a preference to the ends of the girders. All girders are about equally chosen.
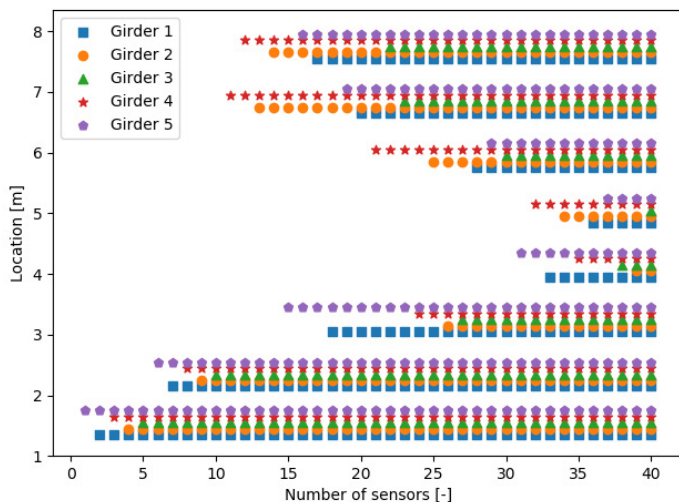
Figure X-3: Optimal sensor placement for the RC girder bridge considering the first four modes and no correlation between the sensor locations (uncorrelated model error)

Table X-2: Correlation lengths for the first four modes – case 1

Mode	$l_{c,y}$	$l_{c,x}$
1	∞	18 m
2	23.2 m	18 m
3	11.6 m	18 m
4	9.28 m	18 m

The influence on the information entropy of considering correlation in the model error or not is visualized in Figure X-5. Here the information entropy is calculated assuming an uncorrelated model error, both for the sensor configurations following from Figure X-3 and Figure X-4. It can be seen that for the first sensors both configurations would lead to a similar reduction in information entropy. Between 10 and 40 sensors, the sensor configuration derived based on a correlated model error is suboptimal if there would be no correlation in reality. Nevertheless, the relative difference in information entropy is only 2%. When more than 40 sensors are placed, the difference in information entropy is again negligible.
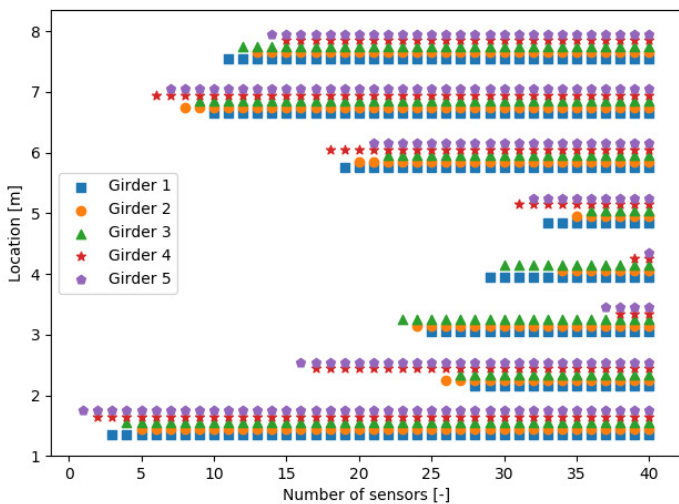
Figure X-4: Optimal sensor placement for the RC girder bridge when considering the first four modes and correlation between the sensor locations (correlated model error)
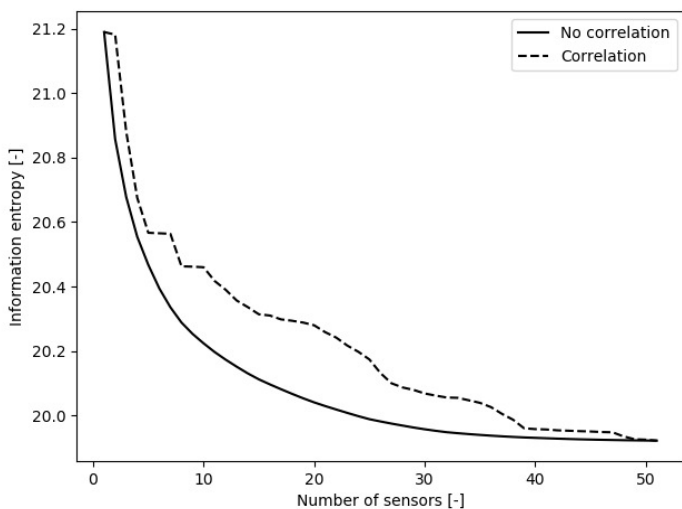

Figure X-5: Influence of the sensor configuration on the information entropy of the RC girder bridge when considering the first four modes

The influence of the time of monitoring has also been investigated. The sensor placement is determined for the first mode for measurements at $t = 100$ years. When no correlation between the sensor locations is assumed (uncorrelated model error), the optimal sensor placement remains unchanged. Also when measurements would be performed earlier in time, e.g. at $t = 20$ years, the optimal sensor placement remains unaltered. The same optimal sensor placement is found at $t = 5$ years. This is a beneficial observation, since this means that during the whole operational life of the structure, the sensors can remain at the same locations and still be optimal.

The influence of considering correlation between the sensor locations (correlated model error) was already investigated, but only for one assumption on the correlation lengths (further denoted as case 1). However, the actual correlation lengths can be different from the ones assumed above. Hence, in the following the influence of the assumed correlation lengths is investigated. In (Papadimitriou and Lombaert, 2012), the correlation length is taken as a fraction of the characteristic length, where the characteristic length is the wavelength of the highest contributing mode. In the following analyses, the correlation lengths are chosen according to two more cases, as summarized in Table X-3. The optimal sensor placement for case 2 is visualized in Figure X-6. The sensors are first placed between 1 m and 2 m on all girders. In case 1, the next sensors are placed around 7 m. However, in case 2 due to the smaller correlation length, the next sensors are placed around 3 m, which is closer to the first sensors. The optimal sensor configuration is still different from the one found without correlation between the sensor locations. For correlation case 3 (Figure X-7), the order in which the locations along the beam are chosen is more similar to that of case 2. However, at 3 m, for case 2 first only sensors are placed at girders 1, 2 and 3, whereas for case 3 all girders are chosen there, except for girder 1. Also, sensor locations around 5 m for girders 2 and 3 are chosen much earlier compared to case 2. This difference in choice of girders is attributed to the difference in correlation length, not only in the length direction of the bridge, but also along its width: the correlation length in case 3 in this width direction is for the last modes smaller than the distance between the girders.

It could be concluded that the optimal sensor configuration depends on the assumed correlation length in the model error. However, the first sensors will be placed at the same locations (between 1 m and 2 m on all girders). The chosen sensor configuration based on the assumption of one correlation model might be suboptimal for another, but it will also not correspond to the worst possible sensor configuration. The influence of the different sensor configurations on the information entropy when the model error is uncorrelated is visualized in Figure X-8. Here it can be seen that there is an error when placing the sensors assuming a specific correlation model in the model error, but that the difference between

different assumptions on the correlation length is limited. When the actual correlation model is according to case 1, the influence of using the sensor configuration following from the assumption of another correlation model is again limited, as visible in Figure X-9. Hence, the actual assumption on the correlation length has a smaller influence in this case than the difference between assuming correlation or not.

Table X-3: Correlation lengths assumed in the investigation on the influence of the correlation length assumed in the model error for the RC girder bridge

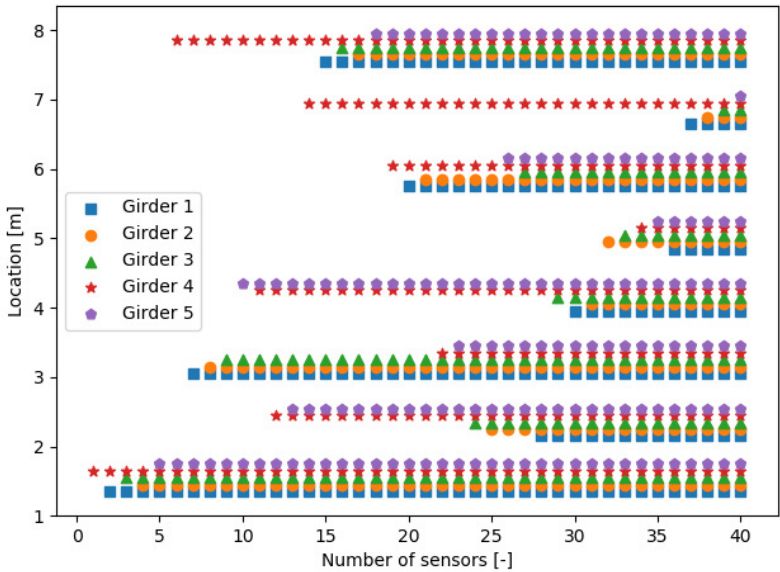| Mode	Case 2		Case 3	
	$l_{c,y}$	$l_{c,x}$	$l_{c,y}$	$l_{c,x}$
1	∞	6 m	∞	2.5 m
2	7.7 m	6 m	3.3 m	2.5 m
3	3.8 m	6 m	1.6 m	2.5 m
4	3.0 m	6 m	1.3 m	2.5 m

Figure X-6: Optimal sensor placement for the RC girder bridge when assuming correlated model error with correlation lengths according to case 2 and all four modes
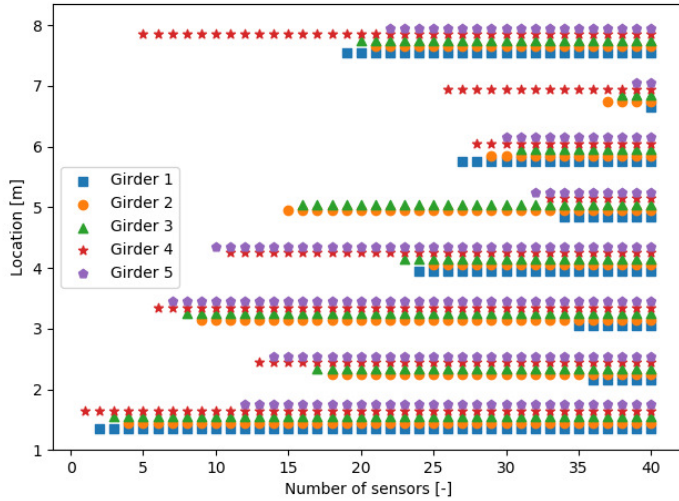
Figure X-7: Optimal sensor placement for the RC girder bridge when assuming a correlated model error with correlation lengths according to case 3 and all four modes
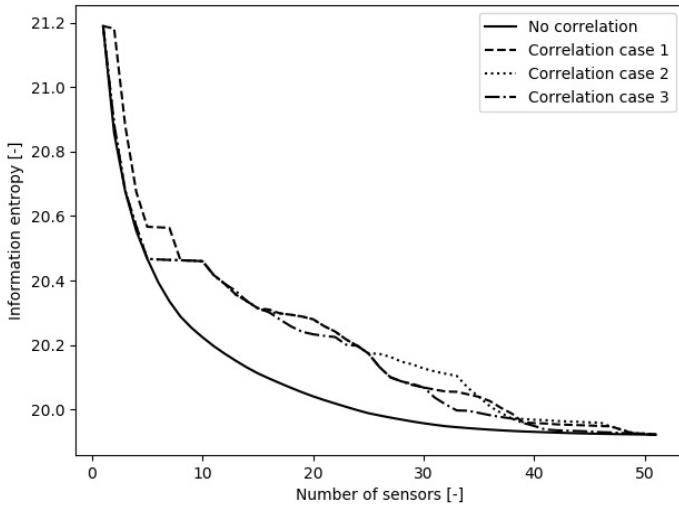

Figure X-8: Influence of sensor configuration on the information entropy of the RC girder bridge when the sensor configuration is determined based on different assumptions on the correlation lengths in the model error and in reality the model error is uncorrelated
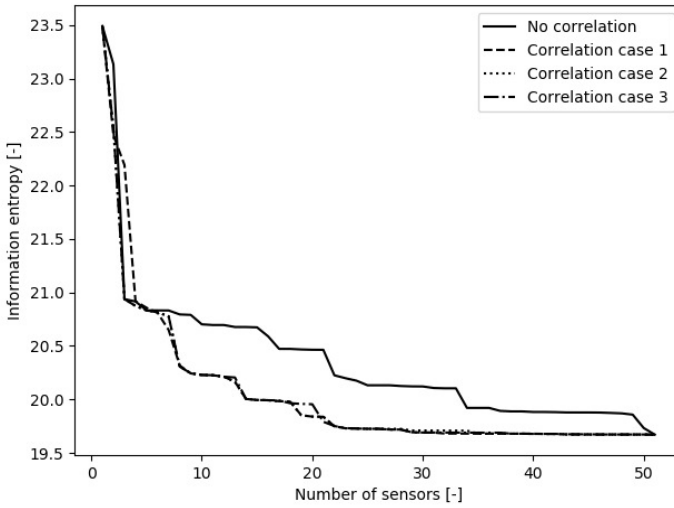
Figure X-9: Influence of sensor configuration on the information entropy of the RC girder bridge when the sensor configuration is determined based on different assumptions on the correlation lengths in the model error and in reality the model error is correlated according to case 1

The abovementioned results are based on a squared exponential correlation model for the random fields, as also described in section VI.2.2. To investigate the influence of the correlation model of the random fields, the optimal sensor configuration has also been derived for an exponential instead of a squared exponential correlation model for the random fields of the corrosion variables, both when assuming correlation and no correlation between the sensor locations (i.e. a correlated and an uncorrelated model error). In both cases, no difference in optimal sensor configuration was found for both random field models. When still considering an exponential random field but with an increased correlation length, the optimal sensor configuration also remains unaltered. Furthermore, the initial squared exponential correlation function for the random fields was again considered, but now with a lower bound on the correlation of 0.5 (equation (III-7)). The optimal sensor configuration remains again unaltered. Hence, even though the sensitivities change (because of the different number of modes in the decomposition of the random fields) the optimal sensor configuration remains unaltered and the optimal sensor configuration is to a certain extend robust for the chosen correlation model for the random fields used to model the corrosion variables.

X.4.2 Optimal sensor placement for strain mode shapes

The optimal sensor locations can also be determined when strain mode shapes are used to update the corrosion variables. In general, the strain mode shapes can be written according to equation (X-21). Here, $\boldsymbol{B}$ is a matrix giving the relationship between the strains and the displacements, and $\boldsymbol{\phi}$ are the mode shape displacements.

$$\boldsymbol{\varepsilon} = \boldsymbol{B}^T \boldsymbol{\phi} \qquad \text{(X-21)}$$

Out of equation (X-21), the sensitivities of the modal strains can be calculated as a function of the sensitivities of the mode shape displacements, which are already known. Since $\boldsymbol{B}$ is not a function of the variables of interest $\boldsymbol{\theta_M}$, the sensitivities of the modal strains are given by equation (X-22).

$$\frac{\partial \boldsymbol{\varepsilon}}{\partial \boldsymbol{\theta_M}} = \boldsymbol{B}^T \frac{\partial \boldsymbol{\phi}}{\partial \boldsymbol{\theta_M}} \qquad \text{(X-22)}$$

In the FE model of the RC bridge, CHX60 elements are used, which are twenty-node isoparametric solid brick elements (see Figure X-10) and the strains in x-direction vary linearly in this direction. The matrix $\boldsymbol{B}$ can be derived from the interpolation functions for this element type. The polynomial interpolation function for the displacement along one of the axes is a quadratic function. For example, when the function of the displacement u along the line 3-4-5 is required, this will be given by equation (X-23).

$$u = u_3 \left(\frac{2}{l^2} x^2 - \frac{3}{l} x + 1 \right) + u_4 \left(\frac{-4}{l^2} x^2 + \frac{4}{l} x \right) + u_5 \left(\frac{2}{l^2} x^2 - \frac{1}{l} x \right) \qquad \text{(X-23)}$$

Here, l is the element length and x the location along the axis 3-4-5. The strain is the derivative of the displacement and is hence given by equation (X-24).

$$\varepsilon = u_3 \left(\frac{4}{l^2} x - \frac{3}{l} \right) + u_4 \left(\frac{-8}{l^2} x + \frac{4}{l} \right) + u_5 \left(\frac{4}{l^2} x - \frac{1}{l} \right) \qquad \text{(X-24)}$$

However, the strain will be measured over a finite length, so equation (X-24) needs to be integrated over this length and divided by it, to get the average strain over the measurement length. As such, the strain will be given as a function of the mode shape displacements u_i, and the matrix $\boldsymbol{B}$ can be calculated.
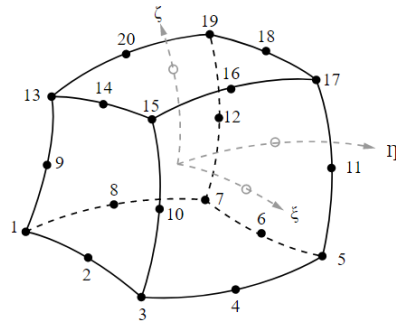
Figure X-10: CHX60 element (DIANA FEA BV, 2019)

Based on the abovementioned considerations, the sensitivities of the strain mode shapes can be derived for the same case as considered in the previous sections. When all four modes are considered, the sensor placement is given in Figure X-11. The fact that there is no clear pattern or no clear preference for one of the girders could be ascribed to the fact that the modal strains provide more local information compared to the mode shape displacements.

In practice, the strain mode shapes will be measured with optic fibres. These fibres have different sensors along their length, and hence all these sensors will be used at the same time. The influence hereof on the information entropy has been investigated. The information entropy is once evaluated for the optimal sensor positions as derived above and once assuming the placement of fibres with the same length as the girders (considered as 'suboptimal'). These are first placed along the bottom fibre of the beam, with the order of the girders equal to 2-4-3-1-5. Then they are placed along the top fibre of the beam, with the order of the girders equal to 5-4-1-3-2. These choices are based on the optimal sensor placement of Figure X-11, considering at which girders sensors are preferably located. The resulting information entropy is visualized in Figure X-12. Here it can be seen that the information entropy is higher for the suboptimal sensor configuration, with a difference of up to 3%, which is still relatively small. The decrease in information entropy when adding sensors is also less gradual, with sudden drops almost corresponding to the addition of an extra fibre. Adding fibres at the bottom of the beam provides also more information than to the top of the beam.
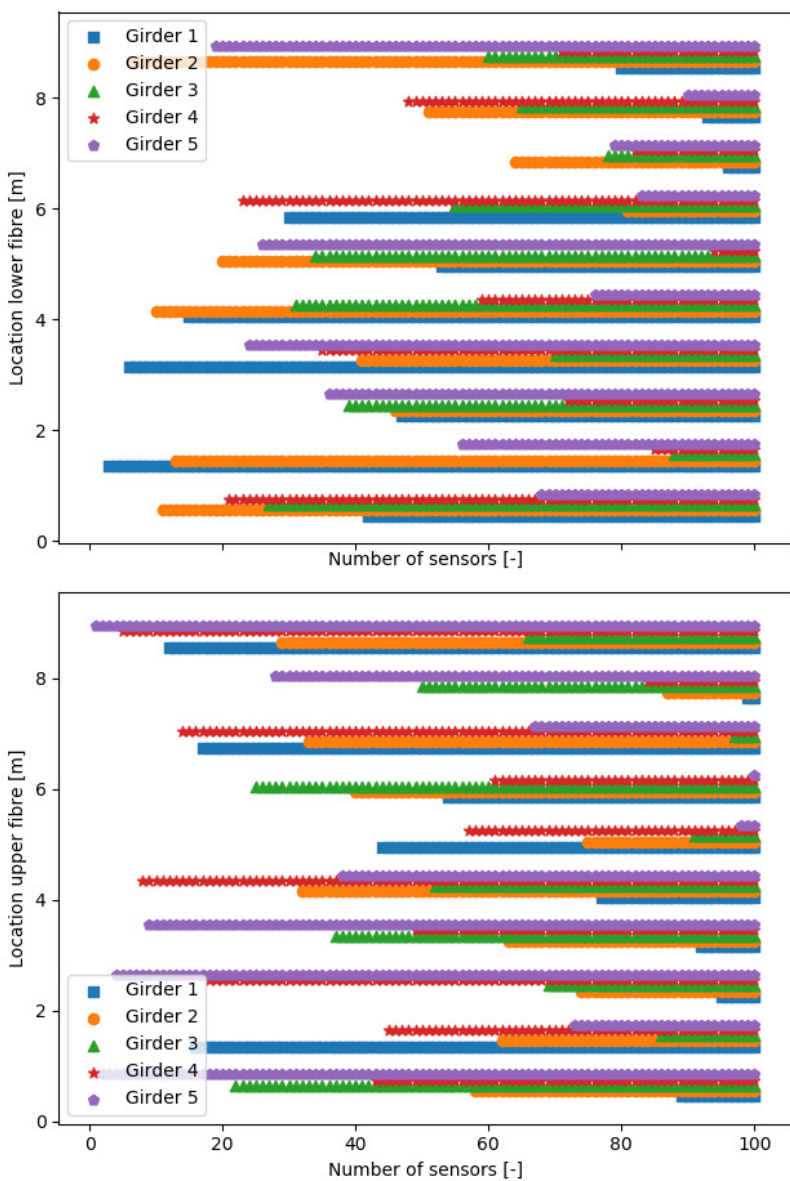
Figure X-11: Sensor locations when measuring modal strains on the RC girder bridge when considering the first four modes assuming no correlation
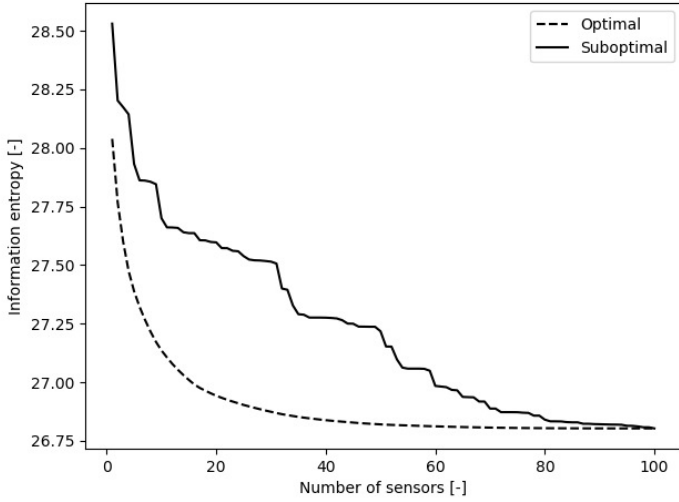
Figure X-12: Influence of using fibres to measure modal strains (suboptimal sensor configuration) on the information entropy of the RC girder bridge

X.4.3 Optimal sensor placement for static strains under proof loading

The optimal sensor placement is also derived when strains are measured under proof loading. Initially, the sensor locations could be chosen as the most critical locations following from the updating based on the natural frequencies and displacement mode shapes (see Chapter VI). These sensor locations could be supplemented by additional sensors, chosen based on the information entropy. As such, possibly a better posterior approximation of the random field will be achieved.

Similar as for the modal strains, the static strains $\boldsymbol{\varepsilon}$ are written as a function of the displacements $\boldsymbol{U}$, according to equation (X-25).

$$\boldsymbol{\varepsilon} = \boldsymbol{L}^T \boldsymbol{U} \qquad \text{(X-25)}$$

To find the derivatives of the strains to the corrosion variables, the adjoint method (Haftka and Gürdal, 2012) will be used. According to this method, an extra term equal to zero will be added to equation (X-25), which leads to equation (X-26).

$$\boldsymbol{\varepsilon} = \boldsymbol{L}^T \boldsymbol{U} + \boldsymbol{\lambda}^T (\boldsymbol{F} - \boldsymbol{K} \boldsymbol{U}) \qquad \text{(X-26)}$$

Here, $\boldsymbol{F}$ corresponds to the load vector inducing the displacements $\boldsymbol{U}$, or $\boldsymbol{F} = \boldsymbol{K}\boldsymbol{U}$. The derivatives of the strains to the corrosion variables (denoted by θ_j in the following equations) are then given by equation (X-27).

$$\frac{\partial \boldsymbol{\varepsilon}}{\partial \theta_j} = \boldsymbol{L}^T \frac{\partial \boldsymbol{U}}{\partial \theta_j} + \boldsymbol{\lambda}^T \left(-\frac{\partial \boldsymbol{K}}{\partial \theta_j} \boldsymbol{U} - \boldsymbol{K} \frac{\partial \boldsymbol{U}}{\partial \theta_j} \right)$$
$$= (\boldsymbol{L}^T - \boldsymbol{\lambda}^T \boldsymbol{K}) \frac{\partial \boldsymbol{U}}{\partial \theta_j} - \boldsymbol{\lambda}^T \frac{\partial \boldsymbol{K}}{\partial \theta_j} \boldsymbol{U} \tag{X-27}$$

In the last equation, the term $\boldsymbol{L}^T - \boldsymbol{\lambda}^T \boldsymbol{K}$ cancels out if $\boldsymbol{L}^T = \boldsymbol{\lambda}^T \boldsymbol{K}$ or $\boldsymbol{L} = \boldsymbol{K}^T \boldsymbol{\lambda}$. The latter is called the adjoint loading case and can be solved to $\boldsymbol{\lambda}$, which is the displacement field under the adjoint load $\boldsymbol{L}$. When $\boldsymbol{\lambda}$ is found, the derivatives of the strains can be calculated according to equation (X-28).

$$\frac{\partial \boldsymbol{\varepsilon}}{\partial \theta_j} = -\boldsymbol{\lambda}^T \frac{\partial \boldsymbol{K}}{\partial \theta_j} \boldsymbol{U} \tag{X-28}$$

Hence, practically for each possible sensor location, a load case $\boldsymbol{L}$ is considered and the corresponding displacements $\boldsymbol{\lambda}$ should be calculated. This corresponds to many load cases, but in finite element software, this can be done within reasonable computational time since there is only one generation of the stiffness matrix required to evaluate all these load cases. As such, the vector $\boldsymbol{\lambda}$ for each sensor location can be derived. The part $\frac{\partial \boldsymbol{K}}{\partial \theta_i} \boldsymbol{U}$ can be calculated similarly as for the mode shape displacements, i.e. based on the element forces. The only difference is that now the displacement vector does not consist of mode shape displacements, but of the displacements under the proof load.

Figure X-13 gives the optimal sensor configuration for strains measured under a proof load located over the middle girder of the beam, when no correlation between the sensor locations is assumed (i.e. an uncorrelated model error). Here it can be seen that at the upper fibre, only the sensor location at girder 5 at the beginning of the beam is chosen in an early stage. The other sensors are first placed at the lower fibre. Hence, placing sensors at the lower fibres first is more beneficial. This is logical, since there is a higher influence of corrosion on these strains at the lower fibre. In the lower fibre, there is a preference to the ends of the girders. Furthermore, girders 1, 2, 4 and 5 are preferred over girder 3, over which the proof load is applied. This could possibly be ascribed to the very local effects that can arise below the proof load. It should be pointed out that the preferred locations might correspond to lower strain values. This issue is addressed later in the text. When the proof load is located between girder 4 and girder 5, the optimal sensor configuration for the strains at upper and lower fibre is given in Figure X-14. Here it can be seen that depending on the location of the proof load, a different optimal sensor layout is found.

The optimal sensor configurations are here derived to optimally describe the corrosion variables modelled by random fields based on the measured strains. Nevertheless, the absolute values of the measured strains are not taken into account in these calculations. The strains will be largest underneath the proof load, but these sensor locations do not follow from the sensitivities as the optimal ones, even though they might still be preferable since strain measurements are also accompanied by a possibly quite large measurement error. When the measured strains are smaller than this error or equal in order of magnitude, the posterior distribution will approach the prior distribution and no updating will be performed. Hence, this aspect should also be accounted for when choosing the locations to perform strain measurements. In Chapter VI it has also been illustrated how the locations with the largest corrosion degree can already be determined based on the posterior distribution of the corrosion degree updated accounting for modal data. These locations are hence preferable for extra strain measurements under proof loading since they are more critical. Nevertheless, if extra sensors are available, these can be supplemented by sensor locations based on the optimal sensor configuration in order to optimally describe the corrosion variables modelled by random fields. Here, attention should be paid to the fact that the expected strains to be measured at these locations should be larger than the measurement error. Another way to account for the fact that the strains should be large enough to be measured is, after a first analysis, only including these points as possible measurement locations in the derivation of the optimal sensor configuration.
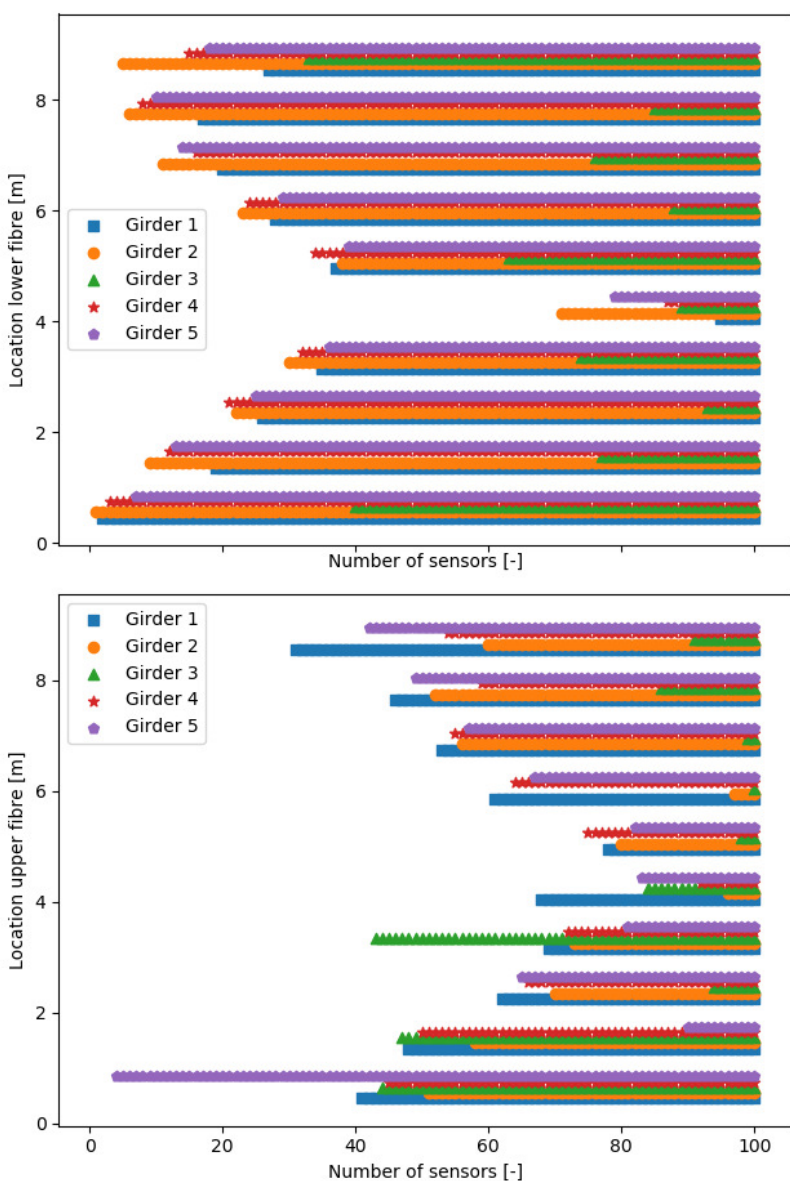
Figure X-13: Optimal sensor configuration for strains measured under proof loading over the middle girder on the RC girder bridge assuming no correlation between the sensor locations (uncorrelated model error)
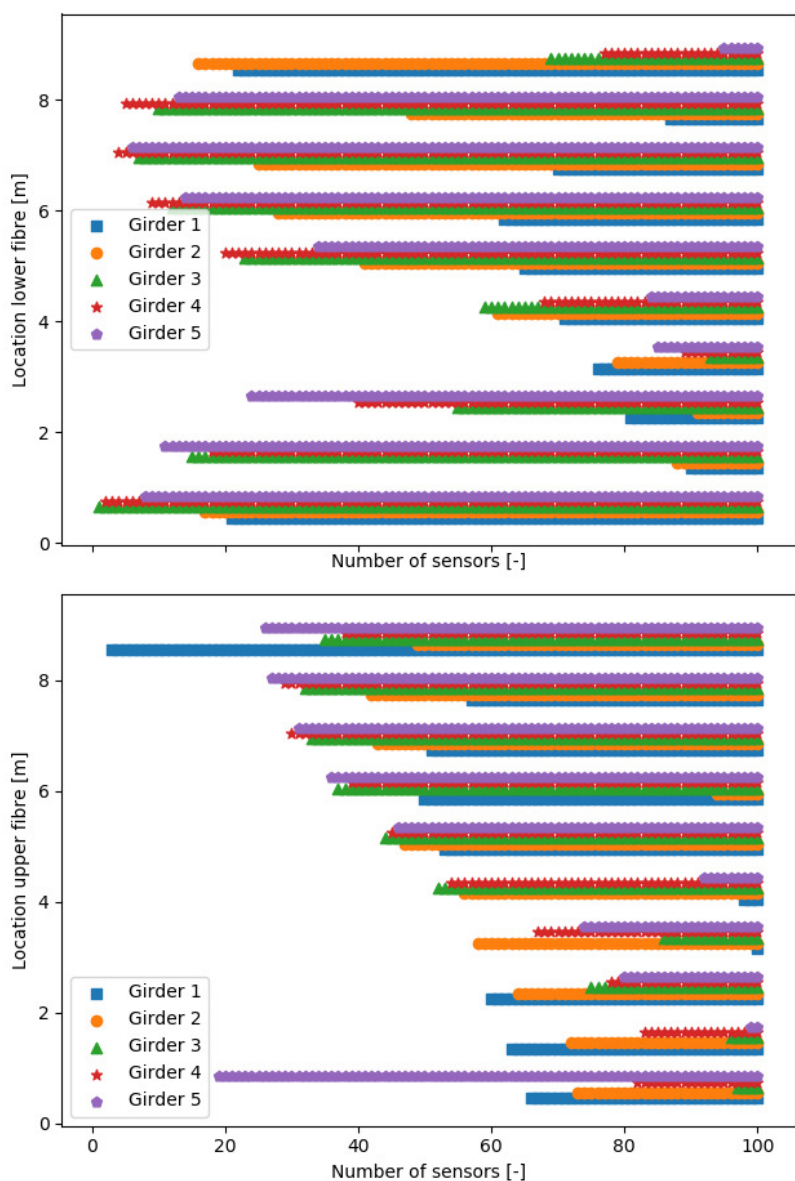
Figure X-14: Optimal sensor configuration for strains measured under proof loading between girder 4 and girder 5 of the RC girder bridge assuming no correlation between the sensor locations (uncorrelated model error)

X.5 Summary and conclusions

In this chapter, a method to determine the optimal sensor configuration for Bayesian updating of (the random fields of) the corrosion variables is introduced. For illustration of the principles, the method is first applied to an analytical model where a simply supported beam is considered. The influence of different assumptions has been investigated. Assuming correlation between the sensor locations (correlated model error) leads to a different optimal sensor configuration compared to the case where no correlation is assumed. Furthermore, the sensor configuration remains constant in time. Nevertheless, if the random field model for variables in the initiation phase would differ from those in the propagation phase, this might lead to changing sensitivities over time and hence varying optimal sensor positions.

Next, the approach is extended in order to be applicable to finite element models too. As an example, the method is applied to an RC girder bridge. Here, optimal sensor configurations are derived for displacement mode shapes, strain mode shapes and static strains measured under proof loading. The influence of the assumption of correlation between sensor locations is again investigated. Assuming a correlated model error leads to a different optimal sensor configuration compared to the case of an uncorrelated model error, but the correlation lengths itself have a smaller influence for the investigated ranges of the correlation length.

It should be pointed out that the optimal sensor placement as derived in this chapter might depend on the damage type. Another damage type might have another influence on the measured response, which can lead to other sensitivities. On the other hand, the optimal sensor placement will not depend on the measurement accuracy, since this will just scale the matrix Σ in the Fisher information matrix. However, the measurement accuracy will influence the posterior distribution (cfr. Chapter VI) and the VoI (Chapter XI).

It is important to indicate that the optimal sensor configurations are determined only for some given predefined (practical) possible sensor positions. The number of sensors is also fixed. This number of sensors will later be optimized by evaluating the value of information for different numbers of sensors (see Chapter XI). The optimal positions of these sensors can then be selected using the method described in the current chapter. In practical situations, there will be a lower bound for the number of sensors to be considered, since mode shapes need to be available at sufficient locations to be able to make a distinction between the different modes.

Even though the optimal sensor positions are derived based on some simplified relations between stiffness reduction and corrosion, they provide a helpful tool to determine optimal sensor positions before performing any measurements. If

models that are more detailed are available for the relations between stiffness reduction and corrosion, these can also be included in the analyses for determining the optimal sensor placement.

Most of the principles applied in this chapter are based on existing literature. A novel contribution is the fact that the sensitivities are based on the finite element analysis directly, without metamodels and Monte Carlo sampling. Also the derivation of the sensitivities towards the corrosion variables and not to the stiffness, and the inclusion of the random fields are an addition to the scientific state-of-the-art.

X.6   References

Argyris, C., Papadimitriou, C., Panetsos, P., 2017. Bayesian Optimal Sensor Placement for Modal Identification of Civil Infrastructures. J. Smart Cities 2, 1–24.

Banfu, Y., Miyamoto, A., 1998. Optimal Sensor Arrangement for Bridge Life Cycle Monitoring System Using Genetic Algorithms.

Beal, J.M., Shukla, A., Brezhneva, O.A., Abramson, M.A., 2008. Optimal sensor placement for enhancing sensitivity to change in stiffness for structural health monitoring. Optim. Eng. 9, 119–142.

Capellari, G., Chatzi, E., Mariani, S., 2018. Cost–benefit optimization of structural health monitoring sensor networks. Sensors (Switzerland) 18, 1–22.

Capellari, G., Chatzi, E., Mariani, S., 2016a. An optimal sensor placement method for SHM based on Bayesian experimental design and Polynomial Chaos Expansion. ECCOMAS Congr. 2016 - Proc. 7th Eur. Congr. Comput. Methods Appl. Sci. Eng. 3, 6272–6282.

Capellari, G., Chatzi, E., Mariani, S., 2016b. Sensor placement for structural health monitoring: an optimal Bayesian experimental design approach, in: Engineering Mechanics Institute Conference 2016 (EMI 2016)/Probabilistic Mechanics & Reliability Conference 2016 (PMC 2016): Book of Abstracts. Vanderbilt University, pp. 254–254.

Castro-Triguero, R., Murugan, S., Gallego, R., Friswell, M.I., 2013. Robustness of optimal sensor placement under parametric uncertainty. Mech. Syst. Signal Process. 41, 268–287.

Chisari, C., Macorini, L., Amadio, C., Izzuddin, B.A., 2017. Optimal sensor placement for structural parameter identification. Struct. Multidiscip. Optim. 55, 647–662.

Chow, H.M., Lam, H.F., Yin, T., Au, S.K., 2011. Optimal sensor configuration of a typical transmission tower for the purpose of structural model updating. Struct. Control Heal. Monit. 18, 305–320.

DIANA FEA BV, 2019. DIANA User's Manual - Release 10.3 [WWW Document]. URL https://dianafea.com/manuals/d103/Diana.html

Fox, R.L., Kapoor, M.P., 1968. Rates of change of eigenvalues and eigenvectors.

AIAA J. 6, 2426–2429.

Haftka, R.T., Gürdal, Z., 2012. Elements of structural optimization, Vol. 11. ed. Springer Science & Business Media.

Huan, X., Marzouk, Y.M., 2013. Simulation-based optimal Bayesian experimental design for nonlinear systems. J. Comput. Phys. 232, 288–317.

Li, B., Der Kiureghian, A., 2016. Robust optimal sensor placement for operational modal analysis based on maximum expected utility. Mech. Syst. Signal Process. 75, 155–175.

Li, Y., Xiang, Z., Zhou, M., Cen, Z., 2008. An integrated parameter identification method combined with sensor placement design. Commun. Numer. Methods Eng. 24, 1571–1585.

Meo, M., Zumpano, G., 2005. On the optimal sensor placement techniques for a bridge structure. Eng. Struct. 27, 1488–1497.

Mustafa, S., Debnath, N., Dutta, A., 2015. Bayesian probabilistic approach for model updating and damage detection for a large truss bridge. Int. J. Steel Struct. 15, 473–485.

Nelson, R.B., 1976. Simplified calculation of eigenvector derivatives. AIAA J. 14, 1201–1205.

Ostachowicz, W., Soman, R., Malinowski, P., 2019. Optimization of sensor placement for structural health monitoring: a review. Struct. Heal. Monit. 18, 963–988.

Papadimitriou, C., 2004. Optimal sensor placement methodology for parametric identification of structural systems. J. Sound Vib. 278, 923–947.

Papadimitriou, C., Beck, J.L., Au, S.K., 2000. Entropy-Based Optimal Sensor Location for Structural Model Updating. J. Vib. Control 6, 781–800.

Papadimitriou, C., Lombaert, G., 2012. The effect of prediction error correlation on optimal sensor placement in structural dynamics. Mech. Syst. Signal Process. 28, 105–127.

Simoen, E., 2013. Uncertainty Quantification in Finite Element Model Updating. PhD thesis, KU Leuven.

Sun, H., Büyüköztürk, O., 2015. Optimal sensor placement in structural health monitoring using discrete optimization. Smart Mater. Struct. 24, 125034.

Vincenzi, L., Simonini, L., 2017. Influence of model errors in optimal sensor placement. J. Sound Vib. 389, 119–133.

Yuen, K.-V., Kuok, S.-C., 2015. Efficient Bayesian sensor placement algorithm for structural identification: a general approach for multi-type sensory systems. Earthq. Eng. Struct. Dyn. 44, 757–774.

Yuen, K.V., Katafygiotis, L.S., Papadimitriou, C., Mickleborough, N.C., 2001. Optimal sensor placement methodology for identification with unmeasured excitation. J. Dyn. Syst. Meas. Control. Trans. ASME 123, 677–686.

Zhang, J., Maes, K., De Roeck, G., Reynders, E., Papadimitriou, C., Lombaert, G., 2017. Optimal sensor placement for multi-setup modal analysis of structures. J. Sound Vib. 401, 214–232.

CHAPTER XI

Application of the pre-posterior framework for the optimization of monitoring

_____ —

"If you cannot measure it, you cannot control it."
- Lord Kelvin

XI.1 Introduction

In Chapter V, it has been pointed out why condition-based maintenance should be preferred over predictive-based maintenance. In Chapter VI it has been illustrated how based on obtained site-specific data (from dynamic tests or diagnostic load tests), prediction models of the structure (i.e. corrosion models) can be updated by application of Bayesian methods (Val et al., 2000). Nevertheless, monitoring the condition of the bridge also comes at a certain cost. In Chapter IX it has been illustrated how the Value of Information (VoI) can be used as a metric to investigate whether this monitoring is worth its cost. In the current chapter, it will be explained how the VoI can be used as a metric to optimize the monitoring strategy, i.e., the type of measurements performed, the time at which the measurements are performed, and the locations of the sensors. Moreover, by calculating the VoI for different monitoring strategies, the best strategy can be chosen as the one with the highest VoI.

In Chapter V and Chapter IX, it has been illustrated how the costs in the calculation of the VoI correspond to the life-cycle costs, including costs for maintenance actions and repairs, costs for monitoring and inspection, and failure costs. For all these costs, relevant values should be used as input in the VoI analysis. Moreover, from Chapter V and Chapter IX it is also clear that prior distributions to be used in the pre-posterior analysis should also be defined. Assigning prior distributions to the model parameters and estimating the different costs required in the analysis can be a difficult task. Investigation is needed to determine whether the assumptions on these parameters influence the resulting VoI, and whether a robust result is obtained or not. Furthermore, the calculation of the VoI can be computationally challenging, for example because evaluation of the posterior distributions is often based on sampling based methods (as also applied in Chapter VI), where many model evaluations are required.

In general, different works on the VoI analysis have contributed greatly to the introduction of the VoI as an objective tool in decision-making (Li and Pozzi, 2019; Cappello et al., 2016; Nielsen and Sørensen, 2018; Thöns et al., 2017; Björnsson et al., 2019). However, it is not always clear how sensitive the computed VoI is to different choices for the relevant input parameters. Literature is especially lacking applications for the optimization of monitoring strategies in the case of reinforced concrete structures. Some publications can be found where the influence of assumptions on the input variables is investigated. However, this is often very limited and applied to simplified conceptual models of structures. In (Zhang et al., 2019), the effects of different system properties on the VoI are demonstrated. In addition, Konakli et al. (2016) illustrate how the decision problem is influenced by the assumed probabilistic models, i.e., the type of probability distribution, the level of uncertainty, the choice of degradation law, the quantity and quality of information, and the probabilistic dependencies between

components of systems. The influence of the measurement accuracy on the VoI is investigated in (Straub, 2014). The challenges in the selection of suitable monitoring thresholds for action alternatives are also pointed out. These concern both defining the threshold values for monitoring outcomes triggering an action and the choice among different actions. In (Thöns et al., 2015), the influence of the threshold on the annual probability of component fatigue failure is investigated, and in (Qin et al., 2015) the influence of the inspection time and monitoring plan is studied. In (Straub et al., 2017), the computational burden of the VoI is pointed out as one of the main challenges in real world applications. From this work and others, it can be concluded that computational cost is an important bottleneck in the calculation of the VoI, since calculations over the whole service life are required. In (Zambon et al., 2020), the VoI analysis is applied to a reinforced concrete structure to determine the cost effectiveness of measuring the chloride content as an alternative to visual inspections. The work provides a valuable basis for the application of VoI analysis to reinforced concrete structures affected by chloride ingress. However, some issues for future work are mentioned, such as the fact that actual costs should be known and might influence the results. No particular case study is considered in that work, discrete inspection outcomes are assumed (depassivation is detected or not detected), and it is recognized that the accuracy of the measurements might influence the results.

In this chapter, the practical use of the VoI as a tool for optimization of a monitoring strategy is investigated, particularly focusing on reinforced concrete structures. Section XI.2 provides a short recapitulation of the calculation of the VoI, and section XI.3 focuses on some issues in the practical implementation. In section XI.4, a realistic case is introduced in the form of a reinforced concrete (RC) girder bridge subjected to corrosion for which the monitoring strategy should be optimized. In section XI.5, the sensitivity of the VoI to initial assumptions on the input values is investigated.

XI.2 Calculation of the VoI

The calculation of the VoI for a spatially degrading reinforced concrete structure is explained in Chapter IX, where it is illustrated how the VoI depends on the expected prior ($E[C_{prior}]$) and posterior ($E[C_{post}]$) costs. To calculate these expected values, a series of steps are required. First, the structure needs to be defined together with all relevant input parameters. Since the evaluation of the VoI requires the calculation of service life costs, the service life t_{SL} and different costs C need to be defined. The evaluation of the VoI takes place in a Bayesian framework. Hence, probabilistic analysis is required and stochastic distributions are assigned to the relevant model parameters. By application of Bayesian analysis, these prior distributions of the model parameters f' are updated to posterior distributions f'' based on (yet unknown) monitoring data. Hence, the

prior distributions of the model parameters need to be defined at the start of the VoI analysis.

The prior cost is the life-cycle cost accounting for no monitoring, eventually taking into account a standard inspection strategy (i.e., for example regular visual inspections, indicated further with subscript 'st'). In the posterior cost, the monitoring strategy for which the VoI is calculated is taken into account. Hence, this monitoring strategy should also be defined: what type of measurements, when and where to measure, and the corresponding costs. In both the prior and posterior analysis, different decision alternatives a should be considered, which can be based on reliability thresholds or monitoring outcomes. To calculate an expected value of the costs, all possible inspection and/or monitoring outcomes should be sampled, inducing the samples y. These contain both the outcomes y_{st} from the reference scenario (prior analysis) and those of the additional monitoring strategy in the posterior analysis y_{add}. For each set of monitoring outcomes, the life-cycle cost $C_T(y)$ is calculated. This is the minimum of the life-cycle costs for the different possible action alternatives in the maintenance strategy of the structure, i.e., $min(C_T(t_{SL}|a,y))$. The costs for each of these action alternatives are evaluated by calculating failure probabilities at every timestep between the current time t_0 and the service life t_{SL}. The corresponding failure costs C_F are accounted for, depending on the cumulative probability of failure $p_F(t)$. At times where measurements are obtained, the relevant distributions are updated, i.e., at t_{insp}, prior distributions of the model parameters f' are updated to posterior distributions f''. The costs of monitoring/inspections C_I are also accounted for. When maintenance actions are performed at t_a, model parameters are changed accordingly, and the relevant costs C_R are accounted for.

This framework allows accounting for different types of data gathered from the monitoring strategy, possibly at different locations along the structure. Chapter VI illustrates how strain data obtained from proof loading and modal data obtained from dynamic tests can be used to infer the state of corrosion of the structure for a reinforced concrete bridge. These data can be incorporated into the VoI framework. This enables the optimization of a monitoring strategy itself, or choosing the most optimal strategy among different possible strategies.

As pointed out above, different (modelling) assumptions are required in the evaluation of the VoI such as costs, prior distributions, etc. Moreover, since the calculation of the VoI involves Bayesian updating and the consideration of the entire service life, calculating the VoI can be computationally expensive. Using the VoI both for optimizing a monitoring strategy itself and for choosing the most optimal strategy among a set of possible strategies requires many evaluations of the VoI. Hence, some approximations might be required to limit both the number of required evaluations of the VoI and the computational time of a single VoI

evaluation. For example, to reduce the number of evaluations of the VoI, part of the optimization of the monitoring strategy can be performed outside the VoI analysis. Optimal sensor positions can be determined beforehand based on optimal sensor placement algorithms as explained in Chapter X. In the following sections, a balance is made between accuracy and computational time, and the influence of different choices related to the input parameters is investigated.

XI.3 Practical implementation of the calculation of the VoI

XI.3.1 Approximating the posterior distribution

In section XI.2, it is mentioned that the prior distributions f' of the model parameters are updated to posterior distributions f'' based on the available monitoring data. For this purpose, Markov Chain Monte Carlo (MCMC) sampling is generally used (Chapter VI). However, the application of MCMC requires a considerable computational effort when the posterior distribution has to be derived for different possible monitoring outcomes, as is the case when calculating the VoI. To overcome this issue, approximate methods can be used to estimate the posterior distributions. Since for the calculation of the VoI, the sign of the resulting VoI and the relative difference between different monitoring alternatives are most important, an approximation that leads to an error that is small compared to this difference in VoI is justified.

According to (Beck and Katafygiotis, 1998; Papadimitriou et al., 1997), when a large amount of data is available, the posterior Probability Density Function (PDF) can be asymptotically approximated by a normal distribution, centred around the Maximum A Posteriori (MAP) point and with a covariance matrix $\widehat{\boldsymbol{\Sigma}}_{po}$. For a set of variables $\boldsymbol{\theta}_M$ to be estimated, with prior probability $f'(\boldsymbol{\theta}_M)$, the MAP estimate is given by equation (XI-1) (Beck and Katafygiotis, 1998; Papadimitriou et al., 1997).

$$\widehat{\boldsymbol{\theta}_M}^{MAP} = \underset{\boldsymbol{\theta}_M}{\mathrm{argmin}}(F_{MAP})$$

$$\text{with } F_{MAP} = -\log\left(L\left(\boldsymbol{\theta}_M\middle|\overline{\boldsymbol{d}}\right)\right) - \log(f'(\boldsymbol{\theta}_M)) = F_{ML} + F_{MAPr} \tag{XI-1}$$

Here, $L\left(\boldsymbol{\theta}_M\middle|\overline{\boldsymbol{d}}\right)$ is the likelihood function accounting for data $\overline{\boldsymbol{d}}$. When this likelihood function is Gaussian, the first term F_{ML} corresponds to a generalized least-squares objective function. The term F_{MAPr} corresponds to a regularization term based on the available prior information.

The approximate posterior covariance matrix $\widehat{\boldsymbol{\Sigma}}_{po}$ is computed as the inverse Hessian of the MAP objective function F_{MAP}, evaluated at the MAP point according to equation (XI-2).

$$\widehat{\boldsymbol{\Sigma}}_{po}^{-1} = \nabla_{\boldsymbol{\theta}_M}^2 F_{MAP}\big|_{\boldsymbol{\theta}_M = \widehat{\boldsymbol{\theta}_M}^{MAP}} \qquad\qquad (\text{XI-2})$$

In many optimization algorithms, this Hessian is computed as a by-product in the solution of the optimization problem to solve for the MAP point.

For more background on the MAP approximation, the reader is referred to (Papadimitriou, 2020). The error of the asymptotic approximation with a Gaussian distribution with mean vector $\widehat{\boldsymbol{\theta}_M}^{MAP}$ and covariance matrix $\widehat{\boldsymbol{\Sigma}}_{po}$ equals N^{-1}, with N the number of data (Papadimitriou, 2020). Furthermore, for a linear prediction model and a Gaussian prior and prediction error model, the asymptotic approximation becomes exact (Simoen, 2013).

XI.3.2 Optimization of time of monitoring

In addition to choosing the locations of the sensors (see Chapter X), the time at which monitoring is performed also needs to be defined. Very often, time bounds when monitoring is useful can already be defined beforehand. For example, when it is the aim of monitoring or inspection to collect data that allow assessing the corrosion degree of a reinforced concrete structure, these measurements are only useful when it is likely that corrosion has initiated. For this reason, the initial time range following construction is not considered in the search for optimizing the point in time at which monitoring should be performed. To optimize this time to perform the measurements, a number of steps are followed to arrive at a maximum value for the VoI. No minimization algorithm is used in this work, but a greedy search is applied in order to detect local optima, similar to the optimization of the sensor locations. In the first step, the posterior cost is calculated for different points in time at which the monitoring could be performed, and for one possible monitoring strategy. Then, the point in time leading to the lowest posterior cost is chosen. At this point in time, gradually, the number of sensors is increased or decreased, until the minimum posterior cost is obtained. For a given number of sensors, the sensor locations are chosen based on the optimal sensor placement as explained in Chapter X. As illustrated in Chapter X, these optimal sensor locations are time-independent.

XI.4 Case study: a simply supported RC girder bridge

XI.4.1 Problem description and probabilistic models

In this case study, the same reinforced-concrete (RC) girder bridge is considered as described in section VI.2.2. The bridge is subjected to chloride-induced corrosion, which leads to a reduced resistance over time. The probability of failure $P_f(t)$ and the corresponding reliability index $\beta(t)$ are quantified based on the bending limit state given by equation (XI-3). The probability of failure can be used

to evaluate the cumulative probability of failure $p_F(t)$ according to equation (IX-4). Based on this cumulative probability of failure, the cost of failure at time t ($C_F(t)$) can be calculated (see equation (IX-6)).

$$g(\boldsymbol{X}, t) = K_R \min\left(A_s(t)f_y\left(h - c - \frac{h_f}{2}\right); f_c\left(h - c - \frac{h_f}{2}\right)b_f h_f\right)$$
$$-K_E(Q + G) \tag{XI-3}$$

In equation (XI-3), $A_s(t)$ is the reinforcement area at time t, which changes over time due to corrosion (see equations (II-8) and (II-9)), and G represents the load effects due to permanent loads, which are among others a function of the concrete density ρ_c (see Table XI-1). The other variables in the limit state function and their probability distributions are summarized in Table XI-1. The characteristic values of the load effects relate to a traffic load according to the Eurocode (CEN, 2003). The reference period for the probabilistic load models and hence for the resulting probability of failure is equal to one year.

The probability of failure is evaluated based on the assumption of a parallel/series system, considering the different element reliabilities of the elements in which the structure is discretized. The load effects are recalculated towards the maximum load effect within the considered element, and the corrosion variables from the appropriate element within the random field discretization are selected.

Table XI-1: Probabilistic distributions for the evaluation of the probability of failure of the considered RC girder bridge

Var. [Unit]	Name	Distr.	Mean	Stdev.	Ref.
f_y [MPa]	Yield stress of reinforcement	LN	550	11	(JCSS, 2001)
h [mm]	Height of the beam + slab	Det.	790	/	(Yang et al., 2019)
c [mm]	Concrete cover	Det.	69	/	(Yang et al., 2019)
h_f [mm]	Height of the slab	Det.	190	/	(Yang et al., 2019)
f_c [MPa]	Concrete compressive strength	N	25.9	3.9	(Yang et al., 2019)
b_f [mm]	Slab flange width	Det.	2500	/	(Yang et al., 2019)
K_R [-]	Resistance model error	LN	1.05	0.105	(JCSS, 2001)
ρ_c [kg/m³]	Concrete density	N	2500	75	(Holicky and Sykora, 2010)
K_E [-]	Load effect model error	LN	1	0.1	(JCSS, 2001)
Q [kNm]	Variable load effect (traffic loads)	GU	$0.728Q_k$	$0.146Q_k$	(Caspeele et al., 2016)

XI.4.2 Time-dependent degradation

The bridge is subjected to chloride-induced corrosion, leading to a reduction of its resistance over time. The reduction in resistance of the RC structure due to chloride-induced corrosion depends on the reduction of the reinforcement area over time $A_s(t)$, as given by equation (II-8).

The prior distributions assumed for the corrosion variables are the same as in section VI.2.2. The corrosion rate V_{corr} is modelled by means of a 2D lognormal random field, with mean 0.0116 mm/year and a coefficient of variation of 0.2 (Yang et al., 2019), and the correlation model of the underlying Gaussian random field is a squared exponential correlation model with a correlation length of 2 m along the length of the bridge and a correlation length of 5.8 m along the width of the bridge. For the diffusion coefficient D, a similar random field is applied, with mean value 129 mm²/year and a coefficient of variation of 0.10. The chloride concentration at the surface C_s is modelled by a scalar random variable with a

lognormal distribution with mean 0.1% and a coefficient of variation of 0.1. To account for the spatial variation of the properties that are modelled by random fields, the bridge is discretized in 50 elements, i.e. each of the five girders is divided into 10 elements of equal length (similar as in section VI.2.2).

XI.4.3 Monitoring strategies

The required service life of the bridge is equal to 100 years. The standard inspection strategy consists of visual inspections every 5 years. Diagnostic load testing (e.g. measuring strains under a proof load applied to the bridge) or dynamic tests can provide information on the real deterioration state of the bridge (Chapter VI). Hence, the question arises whether performing these tests on the bridge would be worth their costs, or whether it would be better to perform only the regular maintenance schedule. The different investigated monitoring strategies are:

1. Dynamic tests using accelerometers from which natural frequencies and displacement mode shapes can be derived;
2. Dynamic tests with optic fibres from which natural frequencies and strain mode shapes can be derived;
3. Static proof loading tests during which strains are measured.

The considered strategies are referred to as strategy 1, strategy 2, and strategy 3, respectively. For strategy 1, the considered data vector contains the natural frequencies of the first four modes and the corresponding displacement mode shapes at multiple sensor locations. The number of sensor locations is varied in the following analyses. The natural frequencies and displacement mode shapes are accounted for in the Bayesian updating procedure according to the likelihood function given by equation (VI-6). The error on the natural frequencies σ_λ is initially assumed 0.001 (i.e. 0.1% of the experimental frequency), and the error on the norm of the mode shapes σ_ϕ is assumed 0.01 (i.e. 1% of the norm of the experimental mode shape).

For strategy 2, the considered data vector contains the natural frequencies of the first four modes of the bridge and the corresponding strain mode shapes at top and bottom fibre of the girders. The natural frequencies are accounted for in the likelihood in a similar way as in equation (VI-6). The strain mode shapes are accounted for in a similar way as in equation (VI-3). The error on the natural frequencies is the same as for strategy 1, and the error on the strain mode shapes is assumed 0.5 µε (measured strains have an order of magnitude of some microstrain).

For strategy 3, static strains are assumed to be measured under proof loading, and the data vector contains these strains measured at different locations along the girders, at both top and bottom fibre. The maximum likelihood function F_{ML} is given by equation (VI-3). The error on the strains σ_ε is initially assumed equal to

0.5 με. This can only be achieved for very accurate strain measuring techniques. Hence, the influence of this measurement error will also be investigated.

In the following, the measurement locations of accelerations, as well as static and dynamic strains, are assumed to be in the middle of the elements in which the structure is discretized. The abovementioned monitoring strategies can be performed at different points in time, with a varying number of sensors.

XI.4.4 Repair strategy

In the maintenance strategy, repair is assumed to be performed once a reliability threshold β_{repair} (which will be defined later) is reached. At this time of repair, the reliability index is considered to return to its initial value (i.e. a perfect repair). Repair can also be performed immediately after monitoring, before the planned repair based on the reliability index. This repair is only performed if the posterior mean of the corrosion degree following monitoring is larger than a critical value for the corrosion degree α_{cr}. Furthermore, when the posterior corrosion degree has a mean value larger than the a priori expected corrosion degree at the timestep under consideration, the planned repair is assumed to be performed in such a way that the corrosion rate of the repaired structure is reduced compared to the initial structure (for example by the use of better repair mortars).

XI.4.5 Costs

For the calculation of the life-cycle costs, different cost values are required: costs of maintenance/repair actions, costs of the monitoring strategy itself, and costs of failure. Although the importance of life-cycle cost analysis is generally acknowledged (Matos et al., 2017, 2018), data on these costs might be difficult to obtain. Even though some information on the costs can be available, some of them might still be hard to estimate.

As a first estimate for the monitoring costs, cost values for the three considered monitoring strategies are summarized in Table XI-2. The number of sensors for strategy 1 refers to the number of uniaxial accelerometers used. The corresponding costs are the costs for a modal analysis, which include the costs for instrumentation of the bridge and the data processing. The number of sensors for strategy 2 refers to the number of elements (in the discretization of the random fields) equipped with a sensor of an optic fibre, both at lower and upper fibre of the girder. The optic fibres have a length equal to the length of the girder and are applied each time to the top fibre and bottom fibre of the girder. Each of these fibres has 10 sensors along its length, measuring the strains. These 10 sensors correspond to the 10 elements in which the girders are discretized. For strategy 3, the number of sensors refers to the number of discrete strain sensors applied on the bridge.

Table XI-2: Assumed monitoring costs for the example bridge.

Type of monitoring data	Number of sensors	Costs
Natural frequencies and displacement mode shapes (strategy 1)	20	€ 9000
	35	€ 10 000
	50	€ 11 000
Natural frequencies and strain mode shapes (strategy 2)	10	€ 10 000
	20	€ 15 000
	30	€ 20 000
	40	€ 25 000
	50	€ 30 000
Static strains (strategy 3)	20	€ 20 000
	35	€ 25 000
	50	€ 30 000

To estimate the costs of failure and repair, in (Skokandić and Ivanković, 2020), it is stated that these costs could be monetized and presented as a percentage of the total bridge value C_{BV}, which is given by $C_{BV} = f_B \cdot C_0$, with C_0 the structural/construction costs defined as the initial bridge value per square meter of bridge deck, and f_B a factor for multiplication of the bridge value due to its importance in the network. The basic structural costs C_0 can be based on (SeRON, 2012), where a value of 1200 euros per square meter of bridge deck is suggested. The importance of the bridge in the road network f_B is evaluated based on:

- Road category (G_{RC});
- Average annual daily traffic (G_{AADT});
- Detour distance (G_{DD});
- Largest span (G_{LS});
- Total length of the bridge (G_{TL}).

Each of these variables have grade 1 to 5 and $f_B = 1 + 1/5 \cdot [0.25 \cdot (G_{RC} + G_{AADT} + G_{DD}) + 0.125 \cdot (G_{LS} + G_{TL})]$. Values for these variables can be found in (Ivanković et al., 2019). For the bridge under consideration, a structural/construction cost of $C_0 = €\ 126\ 672$ is estimated, and a factor f_B equal to $1/5 \cdot [0.25 \cdot (2 + 2 + 5) + 0.125 \cdot (2 + 2)] = 1.55$. This construction cost C_0 only relates to the superstructure of the bridge and is in line with global cost estimates provided by the local road authorities in Flanders (personal communication with the Ministry of Public Works Flanders (MOW)).

According to (Thöns and Stewart, 2019), a cost of failure of the bridge equal to five times the total bridge value is assumed, resulting in a cost of failure of € 981 708.

The influence of different assumptions on the repair costs is investigated in section XI.5.2.1, where the considered cost models are also summarized.

XI.4.6 Approximation of the posterior distribution by MAP estimates

As pointed out in section XI.3.1, approximate methods can be used to estimate the posterior distributions of the model parameters instead of the computationally expensive MCMC sampling. Before using these approximations of the posterior distribution of the model parameters in the VoI calculations, it should be investigated whether the approximation is accurate enough. For the considered bridge, the MAP estimate of the posterior distribution of the diffusion coefficient and the corrosion rate is compared with the posterior distribution found when applying MCMC for the three monitoring strategies. For monitoring strategy 2 implemented at 35 years, the resulting posterior distribution of the diffusion coefficient is visualized in Figure XI-1. Here, it can be seen that the approximation is quite good when considering the mean and uncertainty of the distribution. Similar results are obtained for the corrosion rate.
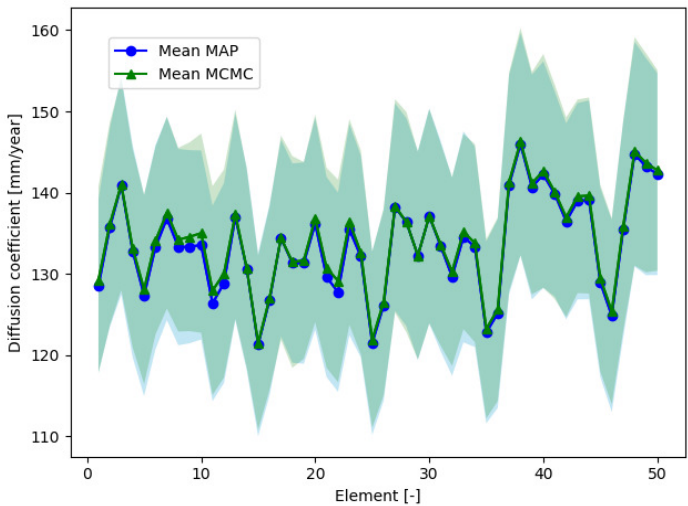

Figure XI-1: Posterior distributions of the diffusion coefficient based on strain mode shapes at all elements derived with MCMC and MAP. The shaded areas correspond to the 68% credibility intervals.

The influence of the use of approximate posterior distributions based on MAP estimates instead of MCMC sampling on the resulting VoI is also investigated. When the VoI is calculated, the difference in posterior costs found based on the MAP estimates and MCMC calculations is very small, especially compared to the total bridge value (less than 0.5%). Hence, for this specific case, the difference in VoI by applying MAP estimates instead of MCMC does not influence the decisions made based on the resulting VoI, and the MAP estimates can be used to more efficiently calculate the VoI. Whether an error on the VoI is acceptable depends on the order of magnitude of the error and the order of magnitude of differences between the VoI's of the different considered monitoring strategies. Hence, before using the approximate posterior distributions, a few checks should be made on the performance of the approximate method by evaluating the posterior distribution both with the approximate method and with MCMC simulations. In addition, the influence on the VoI should be checked at least once.

XI.4.7 Determination of optimal sensor positions

As pointed out before, the optimal sensor positions can be determined beforehand, by applying the procedures developed in Chapter X. For the bridge under investigation, the optimal sensor positions were already derived in section X.4.

The optimal sensor placement could also be determined based on the VoI analysis itself. However, this requires many evaluations of the VoI and hence a large computational effort. This is illustrated by the following example. Consider a beam of 10 m length. Assume that there are 20 possible sensor positions, spaced 0.5 m apart. When one wants to determine the optimal sensor positions based on the VoI analysis, the VoI should be evaluated for all possible combinations of sensor positions. When 10 sensors are picked out of the 20 possible locations, there are 6.7e+11 possible combinations, and many evaluations of the VoI are required. Also a greedy search algorithm could be considered such as in Chapter X. The VoI could first be evaluated based on all 20 locations. Then the VoI could be evaluated when removing one sensor and this for all 20 sensors, resulting in again 20 evaluations of the VoI, etc. Hence, also in this greedy search approach many evaluations of the VoI are required.

XI.4.8 Optimization of the point in time to perform monitoring

To determine its optimal value, the point in time at which monitoring is performed is increased in steps of five years, where only timesteps between the time at which the prior reliability index starts to decrease and the prior time of repair (also based on the reliability index) are considered. Hence, the initially considered points in time at which monitoring could be performed are 15, 20, 25, 30, 35, 40 and 45 years (counting from the time of construction). The minimum posterior costs for measuring strain mode shapes (strategy 2) are found at 35, 40, and 45 years.

Hence, the time range [34 years, 46 years] years is subsequently considered, with step sizes of 1 year. The lower and upper boundaries of the interval are taken one year apart from the previously identified optimal points in time to perform the monitoring, to verify whether there is no increase in VoI just before or after these points in time. The results are visualized in Figure XI-2 for two cases. The first case (case 1) assumes repair model 7 (cfr. infra, section XI.5.2.1) and a reliability threshold of $\beta_{repair} = 3$. The monitoring strategy is strategy 2 with strain mode shapes measured at 10 elements. The second case (case 2) gives the VoI as a function of time for repair model 1 (cfr. infra) with reliability threshold $\beta_{repair} = 3$ and monitoring strategy 2 with strain mode shapes measured at 50 elements. In both cases, the VoI generally increases if the point in time at which monitoring is performed increases. This could be ascribed to the fact that at the later timesteps, monitoring is more likely to induce repair based on the monitoring outcomes. At most timesteps, the VoI is also higher for case 1 than for case 2, due to the difference in the assumed repair criterion and cost model for repair (see also section XI.5.2.1). When looking at Figure XI-2, for case 1 the maximum VoI is reached at 35 years and at 44 years. For case 2, the maximum VoI is reached for monitoring at 35 years. The VoI is also different for the two cases and hence depends on the repair model and the considered monitoring strategy.

In the next step for case 1, the number of sensors is increased for monitoring at 35 years or 44 years since for these times of inspection the largest VoI was found (Figure XI-2). These results are given in Figure XI-3 (label 'Strategy 2'). Here, it can be seen that under these specific assumptions, applying a larger number of sensors is not worth the extra cost. Moreover, the behaviour is almost the same for the two considered points in time at which monitoring could be performed. Only when sensors are placed at all elements in which the structure is discretized, a noticeable difference in VoI is found between the two points in time.
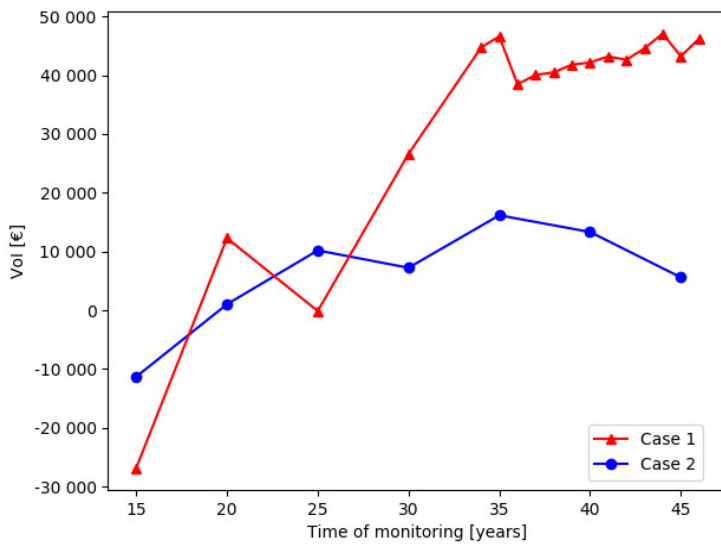
Figure XI-2: Influence of the point in time at which monitoring is performed on the VoI for the considered case study.
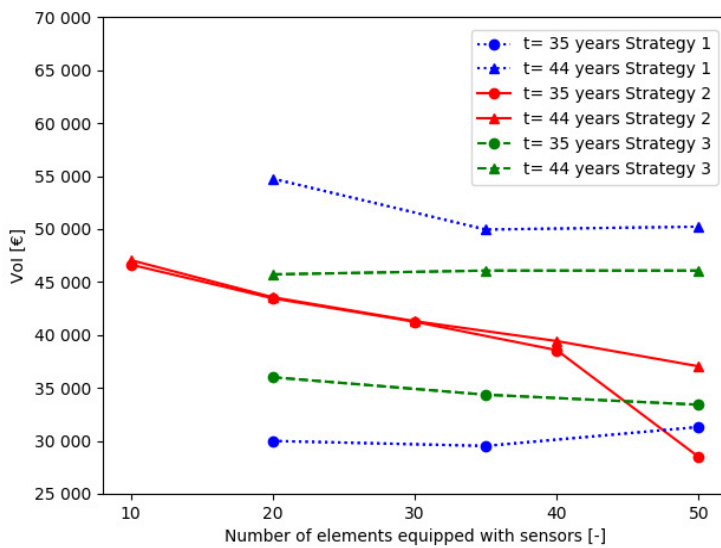

Figure XI-3: Influence of the number of elements equipped with sensors on the VoI (for the strategies, reference is made to Table XI-2).

For strategy 1, where displacement mode shapes are available as monitoring data, 20, 35 and 50 sensor locations are considered. These values are chosen based on experience from practice, where for dynamic monitoring of a bridge of this size, generally 20–50 accelerometers are used. The influence of the number of sensors on the VoI is visualized in Figure XI-3 (labelled 'Strategy 1′). Here, the largest VoI is found for the lowest number of sensors at $t = 44$ years, but the influence of the number of sensors on the VoI is very small. The VoI is also larger than for strategy 2 when monitoring is performed at 44 years, but smaller for monitoring at 35 years.

Finally, in strategy 3, static strain data is considered, respectively, at 20, 35 and 50 locations. The number of sensors is based on advice from experts. The results are given in Figure XI-3 (labelled 'Strategy 3'). Under the current assumptions, for monitoring at $t = 44$ years, the influence of the number of sensors on the VoI is limited, and the VoI is lower than for strategy 1. For monitoring at $t = 35$ years, a larger VoI is found for the lowest number of sensors, and the VoI is larger than for strategy 1.

XI.5 Sensitivity of the VoI to initial assumptions

XI.5.1 Type of monitoring technique and accuracy

The posterior distributions of the corrosion variables depend on the uncertainty of the monitoring technique applied, since this is an important parameter in the likelihood function used in the Bayesian updating. For some techniques, this might be hard to estimate accurately. For this, reference can be made to Chapter VI where different orders of magnitude are given for the measurement error on the static strains, and to Chapter VII, where a first estimate of this measurement error is provided. In this section, the influence of the measurement uncertainty on the VoI is investigated and visualized in Figure XI-4. The error on the measured static strain σ_ε is varied from 0.5 µε ("low error") to 10 µε ("high error") (Heitner et al., 2019; Neild et al., 2005; Sousa et al., 2020; Section VII.4.2), the error of the strain mode shape from 0.5 µε ("low error") to 1.95 µε ("high error") (Heitner et al., 2019; Neild et al., 2005; Sousa et al., 2020), the error on the natural frequency σ_λ from 0.001 ("low error") to 0.01 ("high error") (Reynders et al., 2016; Simoen et al., 2013), and the error on the norm of the mode shape σ_ϕ from 0.001 ("low error") to 0.01 ("high error") (Reynders et al., 2016; Simoen et al., 2013). Figure XI-4 shows that there can be a substantial effect of the measurement error. For this specific case and under the assumed cost values, the VoI increases with decreasing measurement error. The influence on the VoI is largest for the error on the static strains. The influence of the error on displacement mode shapes is the second largest, followed by the error on the natural frequencies and the error on the strain mode shapes, respectively. It is important to indicate that depending on the

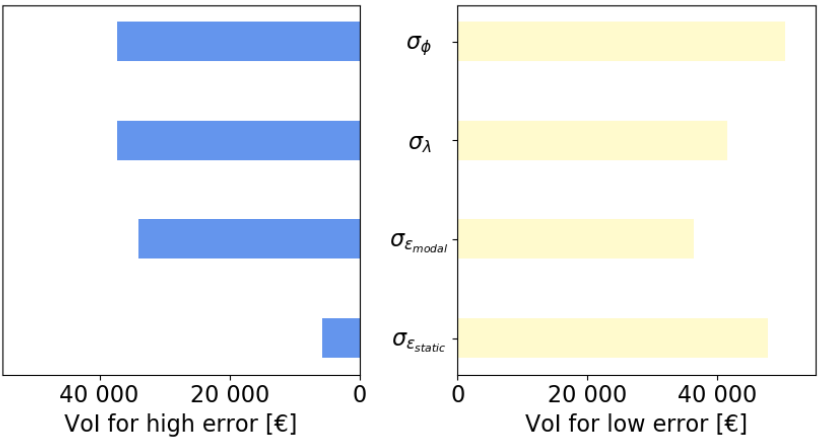adopted values for the errors, a different most optimal monitoring technique can be obtained.

Figure XI-4: Influence of the measurement error on the VoI.

XI.5.2 Costs of repair and failure

XI.5.2.1 Influence of the cost of repair

The cost of repair can be described as $f_{rep} \cdot C_{BV}$, where f_{rep}, for example, depends on the reliability index at the time of repair or on the damage extent. For the repair costs, seven different models are adopted in this work (Table XI-3 and Table XI-4). The model proposed by (Skokandić and Ivanković, 2020) is considered as cost model 1, where f_{rep} is a function of the reliability index, as provided in Table XI-3.

Table XI-3: Values for f_{rep} based on (Skokandić and Ivanković, 2020).

Damage Level (SeRON, 2012)	Minor Damage	Slight Damage	Medium Damage	High Damage	Demolition Imminent
Reliability index [-]	$\beta > 3.82$	$3.3 < \beta \leq 3.82$	$3.0 < \beta \leq 3.3$	$2.3 < \beta \leq 3.03$	$\beta \leq 2.3$
f_{rep} [%]	1.00	8.40	29.15	70.50	140

The other six models for the cost of repair are based on (Van Coile et al., 2014), where the cost of repair is given as a function of the ratio of the maximum load that can be sustained by the damaged structure to the service load requirement for the design specifications. In this work, this is slightly adapted to arrive at the cost models given in Table XI-4, by replacing the calculation of the load or resistance by the reliability index or the number of damaged elements. In Table XI-4, n_{el} is the total number of elements in which the structure is discretized, and n_d is the number of damaged elements, which are the elements with a posterior mean corrosion degree that is larger than the a priori expected corrosion degree.

The different cost models are visualized in Figure XI-5. The considered models can be subdivided into three categories. The first model (from Table XI-3) can reach values larger than 100% for f_{rep}, whereas the other models are restricted between 0 and 100%. Moreover, models 2–4 still depend on the reliability index, whereas models 5–6 depend on the number of damaged elements.

Table XI-4: Cost models based on (Van Coile et al., 2014), adapted in order to account for the reliability index or for the number of damaged elements.

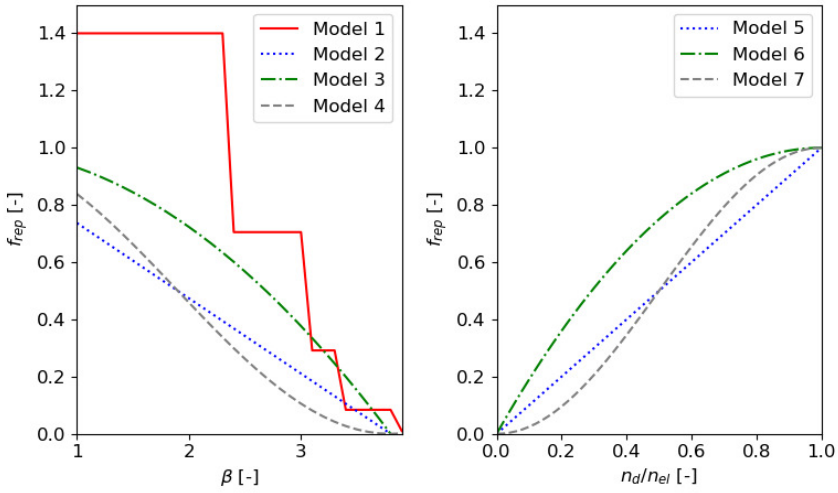| Cost model	f_{rep} [-]
2	$1 - \dfrac{\beta}{3.8}$
3	$1 - \left(\dfrac{\beta}{3.8}\right)^2$
4	$\dfrac{1 + \cos\left(\dfrac{\beta}{3.8}\pi\right)}{2}$
5	$1 - \dfrac{n_{el} - n_d}{n_{el}}$
6	$1 - \left(\dfrac{n_{el} - n_d}{n_{el}}\right)^2$
7	$\dfrac{1 + \cos\left(\dfrac{n_{el} - n_d}{n_{el}}\pi\right)}{2}$

Figure XI-5: Different assumed cost models.

The influence of each of these cost models on the VoI is investigated. The VoI is calculated for a critical reliability of $\beta_{repair} = 3$ and for accelerations measured at 20 locations (strategy 1), strain mode shapes measured at 10 elements (strategy 2) or static strains measured at 20 locations (strategy 3). The models for the cost of repair are numbered 1–7, and the VoI for the different cost models is visualized in Figure XI-6 for the three mentioned monitoring strategies. Here, it can be seen that the model used for the cost of repair has a large influence on the VoI. The absolute difference can reach up to more than € 20 000, which is 10% of the total bridge value. Hence, inaccurate estimates of the costs of repair might lead to a large over- or under-estimation of the VoI. The monitoring strategy with the highest VoI is in all cases related to the extraction of modal data from acceleration measurements.

When considering the three categories of models, it can be seen that the third category (models 5–7) provides a larger VoI. This can be ascribed to the fact that a low number of damaged elements can be present, resulting in a low repair cost. However, when these damaged elements become critical, a few damaged elements can already result in a large influence on the reliability index, leading to a larger f_{rep} according to the first four models. When comparing model 1 with models 2–4, it can be seen that the difference is relatively small since the low reliability levels for which f_{rep} becomes larger than 1 (i.e., larger than 100%) in model 1 are not reached.
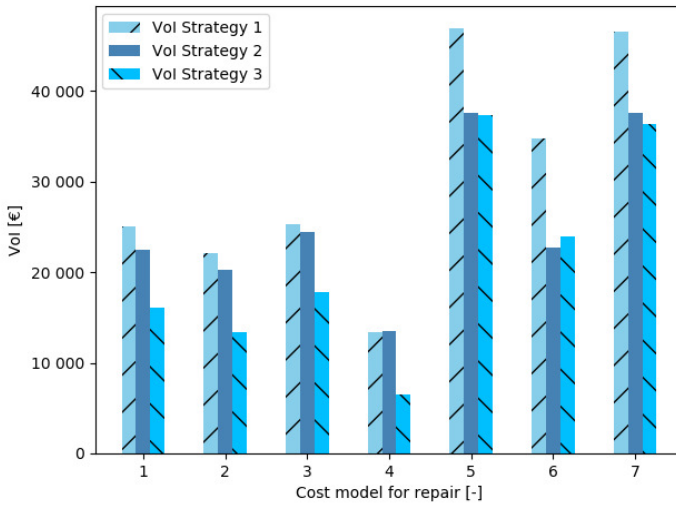
Figure XI-6: Influence of the cost model for repair on the VoI for the three considered monitoring strategies (for the strategies, reference is made to Table XI-2).

XI.5.2.2 Influence of the cost of failure

Three different values are assumed for the cost of failure: $2 \cdot C_{BV}$, $5 \cdot C_{BV}$, and $10 \cdot C_{BV}$. The results are given in Figure XI-7 for three different monitoring strategies: measuring accelerations at 50 locations (Strategy 1), measuring strain mode shapes at all 50 elements (Strategy 2) and measuring static strains at 50 locations (Strategy 3). If the cost of failure increases, the prior cost increases together with the posterior cost, but still results in a larger VoI.

XI.5.3 Prior distribution of the corrosion variables

The diffusion coefficient can be difficult to estimate when one is not sure about the properties of the concrete in the existing structure and when no monitoring data are available. Furthermore, the diffusion coefficient varies in time, and hence the prior estimate at a certain point in time might differ from the actual value. When changing the prior mean of the diffusion coefficient from 64.5 to 258 mm²/year, the VoI can vary with an amount of € 34 000, as illustrated in Table XI-5. While the monitoring strategy with the highest VoI remains the same, the difference in VoI between two techniques is not always of the same order of magnitude. When the COV of the diffusion coefficient is varied, the influence of the VoI is also given in Table XI-5. Here, the influence of the VoI is of the order of magnitude of € 35 000, which is 18% of the total bridge value for a change in COV of the diffusion coefficient from 0.05 to 0.2. Moreover, the influence differs depending on the monitoring technique considered. The VoI remains the largest when displacement mode shapes are available (strategy 1), but for the smallest

COV the difference with the static strains (strategy 3) is limited. Furthermore, when comparing the strain mode shapes (strategy 2) with the static strains, another technique might be chosen depending on the assumed COV for the diffusion coefficient.
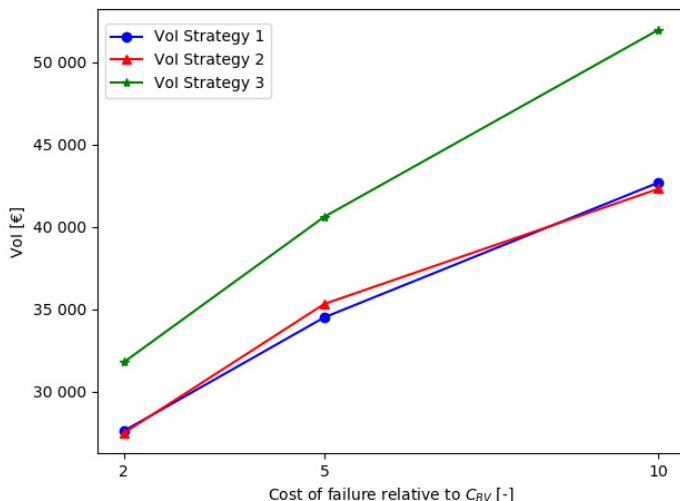

Figure XI-7: Influence of the cost of failure on the VoI for the three considered monitoring strategies (for the strategies, reference is made to Table XI-2).

For the corrosion rate, different parameters are available in literature for different exposure classes. A selection of prior models is given in Table XI-6. When there is doubt on which model to use, the impact on the VoI can be large, ranging from a large positive to a large negative VoI, as can be seen in Table XI-5. Moreover, the optimal monitoring strategy might change, with large differences in VoI between the different strategies.

The surface chloride concentration is also a difficult variable to estimate a priori. The initial value assumed for the mean surface chloride concentration and the COV is once taken half and once double the value originally considered. It is found that the influence on the VoI is very large and can range from a negative VoI to a large positive VoI, as can be seen in Table XI-5. Moreover, depending on the value of mean of the surface chloride concentration (μ_{Cs}), the difference in VoI between two techniques might change. When changing the COV of the surface chloride concentration, the optimal monitoring strategy might change depending on the prior assumptions.

Table XI-5: VoI for different monitoring strategies as a function of the prior parameters of the distributions of the corrosion variables (for the strategies, reference is made to Table XI-2).

	VoI Strategy 1	VoI Strategy 2	VoI Strategy 3
μ_D			
64.5	4524	3483	−3309
129	46 538	37 620	36 306
258	33 276	32 789	28 497
COV_D			
0.05	37 391	31 551	36 853
0.1	46 538	37 620	36 306
0.2	69 726	66 850	63 571
V_{corr}			
Model 1	98	36 049	70 780
Model 2	4633	5173	1427
Model 3	−25 940	−38 187	−15 587
Model 4	81 156	65 126	53 845
μ_{Cs}			
0.05	−3821	−4265	−8793
0.1	46 538	37 620	36 306
0.2	35 813	35 472	31 155
COV_{Cs}			
0.05	43 967	34 010	40 857
0.1	46 538	37 620	36 306
0.2	31 631	39 037	30 337

Table XI-6: Different parameters for the prior distribution of the corrosion rate based on (Lay et al., 2003).

Model	Exposure Class	μ_{Vcorr} [mm/year]	σ_{Vvorr} [mm/year]
1	Wet—rarely dry	0.004	0.006
2	Cyclic wet–dry	0.030	0.020
3	Airborne seawater	0.030	0.040
4	Tidal zone	0.070	0.070

XI.6 Conclusions

This chapter provides one of the first applications of the VoI analysis to a real-case RC structure subjected to degradation. In the scientific state-of-the-art, the VoI is presented as an important tool for the optimization of monitoring strategies of structures, but mostly applied to simplified examples. Application of the VoI analysis to real-case RC structures comes with some computational challenges. In this chapter, solutions are proposed to reduce the computational effort. One of these solutions is the use of approximate posterior distributions based on MAP estimates instead of the computationally expensive MCMC sampling to evaluate the posterior distributions. Another solution is performing part of the optimization of the monitoring strategy outside the VoI calculations. As an example, the locations of the sensors can be determined beforehand by applying an optimal sensor placement algorithm. As such, given the number of sensors, the optimal locations of these sensors are fixed. This leads to a reduced number of evaluations of the VoI. This heuristic solution method can lead to a suboptimal solution, but the influence on the resulting VoI will be limited when compared to the large reduction in computational effort.

In the scientific state-of-the-art, the influence of the assumed input parameters for the VoI analysis is often not investigated. Nevertheless, in a practical case, it might be difficult to decide on the values of the required input parameters, especially for complex structures. From the investigations performed in this chapter, it is concluded that the choice of these input parameters can have a significant impact on the VoI and the optimal monitoring strategy. Hence, caution is required when interpreting results of a VoI analysis and the results of a VoI analysis should always be evaluated with a critical mind-set. In practice, it might be beneficial to calculate the VoI for different scenarios to validate the final conclusion (for example with respect to the choice of the monitoring strategy).

Even though the VoI approach has a rather high computational cost, these costs are generally very small compared to the costs of the actual monitoring system or the costs of failure of critical infrastructure. The VoI approach seems particularly useful for the management of large and critical bridges (in terms of traffic flow). For such bridges, large costs can be involved in the closure and/or failure of the bridge, and it can be beneficial to investigate beforehand whether investing in a monitoring strategy is beneficial or whether one can better stick to an a priori determined maintenance schedule.

In the analyses provided in this chapter, the VoI is evaluated based on the expected values of the costs. Nevertheless, also the corresponding uncertainty on these estimates can be evaluated. Here, a more accurate monitoring strategy will lead to a lower uncertainty, and the uncertainty on the posterior costs will be lower than the uncertainty on the prior costs. These uncertainties can also be taken along in

the definition of the VoI. For more background and corresponding results, the reader is referred to (Vereecken et al., 2021).

It should be pointed out that all results in this chapter depend on the assumptions made for the errors in the likelihood function (i.e. measurement and modelling errors). Other assumptions could be made here, which might influence the results. Nevertheless, more research is required on the appropriate quantification of these measurement and/or model errors.

The proposed steps for finding the most optimal monitoring strategy, based on the results in this chapter, are the following:
1. The model of the structure, limit state equations, degradation models, probabilistic distributions, costs, etc. should be defined.
2. The prior life-cycle cost should be evaluated.
3. Boundaries for the appropriate point in time at which monitoring could be performed should be selected.
4. Values for the degradation parameters should be sampled from the prior distributions.
5. A monitoring technique should be selected.
6. Optimal sensor positions should be derived (Chapter X).
7. Between the boundaries selected in step 3, different timesteps should be selected for the maximum number of sensors. The corresponding monitoring outcomes should be evaluated based on the samples for the degradation parameters generated in step 4.
8. The posterior costs and value of information should be estimated.
9. Around the points in time leading to the highest VoI, extra timesteps can be selected and steps 7 to 8 can be repeated. As such, the optimal point in time to perform monitoring can be found.
10. For this point in time, the number of sensors can be decreased. The optimal number of sensors can be determined in the same way as the optimal point in time to perform monitoring.
11. For the given monitoring technique, the optimal point in time to perform monitoring and the optimal number of sensors and corresponding locations are known, together with the corresponding VoI.
12. Steps 5 to 11 can be repeated for another monitoring technique.
13. The monitoring strategy resulting in the lowest VoI should be selected.

If required, the sensitivity to some assumptions made in the first step should be checked.

XI.7 References

Beck, J.L., Katafygiotis, L.S., 1998. Updating Models and Their Uncertainties. I: Bayesian Statistical Framework. ASCE J. Eng. Mech. 124, 455–461.

Björnsson, I., Larsson Ivanov, O., Honfi, D., Leander, J., 2019. Decision support

framework for bridge condition assessments. Struct. Saf. 81, 101874.

Cappello, C., Zonta, D., Glisic, B., 2016. Expected utility theory for monitoring-based decision-making. Proc. IEEE 104, 1647–1661.

Caspeele, R., Steenbergen, R., Sykora, M., 2016. *fib* Bulletin 80: Partial factor methods for existing concrete structures.

CEN, 2003. EN 1991-3: Eurocode 1: Actions on structures - Part 2: Traffic loads on bridges.

Heitner, B., OBrien, E.J., Yalamas, T., Schoefs, F., Leahy, C., Décatoire, R., 2019. Updating probabilities of bridge reinforcement corrosion using health monitoring data. Eng. Struct. 190, 41–51.

Holicky, M., Sykora, M., 2010. Stochastic models in analysis of structural reliability, in: Proceedings of the International Symposium on Stochastic Models in Reliability Engineering, Life Sciences and Operations Management. pp. 428–439.

Ivanković, A.M., Marić, M.K., Skokandić, D., Njirić, E., Šiljeg, J., 2019. Finding the link between visual inspection and key performance indicators for road bridges. IABSE Symp. Guimaraes 2019 Towards. a Resilient Built Environ. Risk Asset Manag. - Rep. 1, 737–744.

JCSS, 2001. JCSS Probabilistic Model Code.

Konakli, K., Sudret, B., Faber, M.H., 2016. Numerical Investigations into the Value of Information in Lifecycle Analysis of Structural Systems. ASCE-ASME J. Risk Uncertain. Eng. Syst. Part A Civ. Eng. 2, 1–13.

Lay, S., Schießl, P., Cairns, J., 2003. Lifecon Deliverable D3.2.

Li, S., Pozzi, M., 2019. What makes long-term monitoring convenient? A parametric analysis of value of information in infrastructure maintenance. Struct. Control Heal. Monit. 26, 1–18.

Matos, J., Solgaard, A., Linneberg, P., Silva, M.S., Strauss, A., Stipanovic, I., Casas, J., Masovic, S., Caprani, C., Novak, D., Akiyama, M., 2018. Life cycle cost management of concrete structures, in: IABSE Conference, Copenhagen 2018: Engineering the Past, to Meet the Needs of the Future - Report. pp. 130–136.

Matos, J., Solgaard, A., Santos, C., Sanchez-Silva, M., 2017. Life Cycle Cost, As a Tool for Decision Making on Concrete Infrastructures, in: High Tech Concrete: Where Technology and Engineering Meet - Proceedings of the 2017 *fib* Symposium. pp. 1832–1839.

Neild, S.A., Williams, M.S., McFadden, P.D., 2005. Development of a vibrating wire strain gauge for measuring small strains in concrete beams. Strain 41, 3–9.

Nielsen, J.S., Sørensen, J.D., 2018. Computational framework for risk-based planning of inspections, maintenance and condition monitoring using discrete Bayesian networks. Struct. Infrastruct. Eng. 14, 1082–1094.

Papadimitriou, C., 2020. UQ and Data Analysis in Applied Sciences - Bayesian Inference & Uncertainty Propagation - Lecture CS1b: Introduction to

Bayesian Inference.

Papadimitriou, C., Beck, J., Katafygiotis, L., 1997. Asymptotic expansions for reliability and moments of uncertain systems. ASCE J. Eng. Mech. 123, 1219–1229.

Qin, J., Thöns, S., Faber, M.H., 2015. On the value of SHM in the context of service life integrity management, in: 12th International Conference on Applications of Statistics and Probability in Civil Engineering, ICASP 2015. pp. 1–8.

Reynders, E., Maes, K., Lombaert, G., De Roeck, G., 2016. Uncertainty quantification in operational modal analysis with stochastic subspace identification: Validation and applications. Mech. Syst. Signal Process. 66–67, 13–30.

SeRON, 2012. Security of Road Networks: Final Report.

Simoen, E., 2013. Uncertainty Quantification in Finite Element Model Updating. PhD thesis, KU Leuven.

Simoen, E., Moaveni, B., Conte, J.P., Lombaert, G., 2013. Uncertainty quantification in the assessment of progressive damage in a 7-story full-scale building slice. J. Eng. Mech. 139, 1818–1830.

Skokandić, D., Mandić Ivanković, A., 2020. Value of additional traffic data in the context of bridge service-life management. Struct. Infrastruct. Eng.

Sousa, H., Rozsas, A., Slobbe, A., Courage, W., 2020. A novel pro-active approach towards SHM-based bridge management supported by FE analysis and Bayesian methods. Struct. Infrastruct. Eng. 16, 233–246.

Straub, D., 2014. Value of information analysis with structural reliability methods. Struct. Saf. 49, 75–85.

Straub, D., Chatzi, E., Bismut, E., Courage, W., Döhler, M., Faber, M.H., Köhler, J., Lombaert, G., Omenzetter, P., Pozzi, M., Thöns, S., Val, D., Wenzel, H., Zonta, D., 2017. Value of information: A roadmap to quantifying the benefit of structural health monitoring. 12th Int. Conf. Struct. Saf. Reliab. 3018–3029.

Thöns, S., Faber, M.H., Val, D.V., 2017. On the value of structural health monitoring information for the operation of wind parks. Safety, Reliab. Risk, Resil. Sustain. Struct. Infrastructure, 12th Int. Conf. Struct. Saf. Reliab. 3008–3017.

Thöns, S., Schneider, R., Faber, M.H., 2015. Quantification of the value of structural health monitoring information for fatigue deteriorating structural systems. 12th Int. Conf. Appl. Stat. Probab. Civ. Eng. 1–8.

Thöns, S., Stewart, M.G., 2019. On decision optimality of terrorism risk mitigation measures for iconic bridges. Reliab. Eng. Syst. Saf. 188, 574–583.

Van Coile, R., Caspeele, R., Taerwe, L., 2014. Cost-Optimization of Concrete Slabs Exposed to Natural Fires, Taking into Account Post-Fire Behavior, in: Second International Conference on Vulnerability and Risk Analysis and Management(ICVRAM) and the Sixth International Symposium on

Uncertainty Modeling, and Analysis (ISUMA). pp. 1–10.

Vereecken, E., Botte, W., Lombaert, G., Caspeele, R., 2021. VoI-based optimization of structural assessment for spatially degrading RC structures. Appl. Sci. 11

Yang, D.Y., Frangopol, D.M., Teng, J., 2019. Probabilistic life-cycle optimization of durability-enhancing maintenance actions : Application to FRP strengthening planning. Eng. Struct. 188, 340–349.

Zambon, I., Ariza, M.P.S., Matos, J.C., Strauss, A., 2020. Value of information (VoI) for the chloride content in reinforced concrete bridges. Appl. Sci. 10, 567.

Zhang, W.H., Lu, D.G., Qin, J., Faber, M.H., 2019. Life cycle management of structural systems based on the optimal SHM strategy by VoI analysis, in: 13th International Conference on Applications of Statistics and Probability in Civil Engineering, ICASP 2019. pp. 1–8

.

Part D

Case study

CHAPTER XII

Case study

XII.1 Introduction

In this chapter, a case study is considered, applying the methods developed in the earlier chapters to a real bridge geometry. The Bayesian inference procedure will be used to update the corrosion degree (and corresponding corrosion variables) of the bridge. Levelling data is available for this bridge and will be used for the updating procedure. Since no other detailed measurement data is available for this bridge, additional data will be generated based on a finite element model of the bridge in order to illustrate the potential and feasibility of the methodology developed in the previous chapters. Different monitoring techniques will be considered together with different assumptions on the input used for generating the data. In addition, the influence of a model error or model bias will be investigated.

The VoI analysis will also be applied to the bridge (section XII.4). Costs and actions will be defined and the VoI will be evaluated for two cases: one with limited exposure (corrosion due to carbonation) and one with high exposure (corrosion due to chlorides).

The focus of this chapter is on the application of the developed procedures on an actual geometry, making use of simulated data. For Bayesian inference of the corrosion degree based on real data, reference is made to Chapter VII, where the corrosion experiments are discussed.

XII.2 Description of the case

The bridge under investigation has been built in 1948 and is at the moment of analysis (2020) 72 years old. It is an RC girder bridge with a constant height, i.e. the bridge consists of a reinforced concrete slab supported by 14 reinforced concrete girders. The bridge is located on the Belgian national road N177 and passes over the Kolonel Silvertopstraat in Reet (Flanders, Belgium). On this bridge, the last available inspection has been performed in 2019. According to the inspectors, the bridge is in an acceptable condition and no important defects are present. The driving lanes on top of the bridge, which carry intense heavy traffic, have been recently refurbished and renewed.

The bridge consists of two parts divided by a joint, which are symmetrical with respect to each other. The longitudinal girders of the first part are visualized in Figure XII-1 and Figure XII-2. The reinforcement of the longitudinal girders is given in Figure XII-3. The shear reinforcement has a spacing of 200 mm. The reinforcement of the slab consists of bars of 14 mm with a spacing of 200 mm. The numbering of the girders, as will be referred to later in this chapter, is visualized in Figure XII-4. Here it can be seen that the two smaller girders next to the joint are considered as one (i.e. girder 7). The influence of these girders on the

resistance and structural behaviour of the bridge is limited. The bridge has a length of 13 m and a skew angle of 7°.
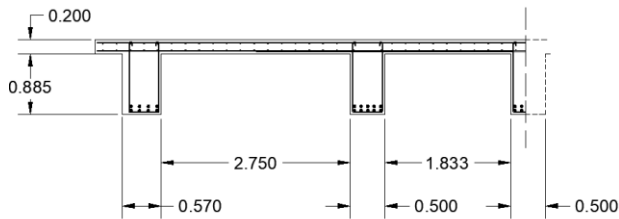

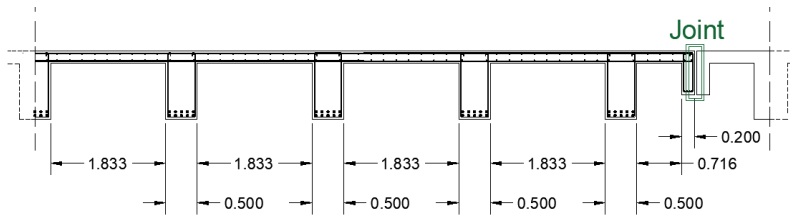Figure XII-1: Cross-section of the outer part of the bridge (dimensions in m)

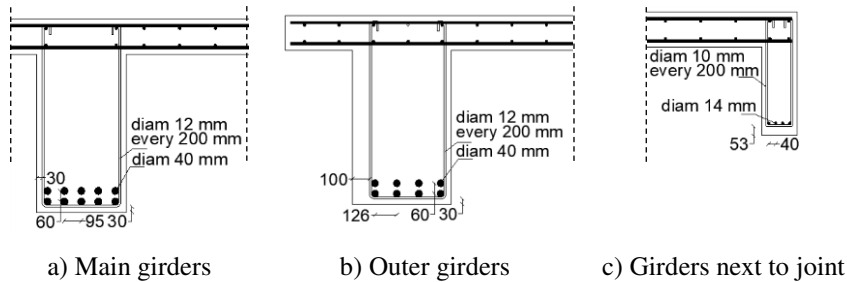Figure XII-2: Cross-section of the part close to the joint (dimensions in m)

a) Main girders   b) Outer girders   c) Girders next to joint

Figure XII-3: Reinforcement layout of the longitudinal girders (dimensions in mm)
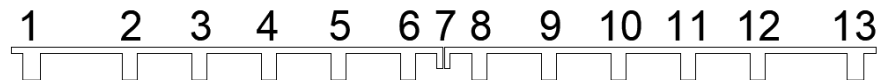
Figure XII-4: Numbering of the girders

XII.3 Bayesian inference of the corrosion degree

In the following sections, the corrosion degree of the bridge will be updated based on different types of data. Moreover, different situations will be considered for generating the measurement data. Finally, also the influence of a model error will be investigated.

XII.3.1 Prior distributions

The bridge is assumed to be subjected to degradation due to corrosion. The assumed corrosion model is the same as described in Chapter II, and no prior assumption on carbonation-induced or chloride-induced corrosion is made. The corrosion degree is assumed dependent on the initiation period and the corrosion rate, which are modelled as stochastic variables. Corrosion is assumed spatially variable along the structural elements and the corrosion variables are modelled with random fields. The prior marginal distribution of the corrosion rate is a lognormal distribution with a mean of 0.05 mm/year and a standard deviation of 0.02 mm/year. The marginal distribution of the initiation period is a lognormal distribution with a mean of 50 years and a standard deviation of 15 years. This distribution is valid for the bars with a concrete cover of 40 mm. For the other bars, the value of the initiation period is adjusted according to the change in concrete cover. When considering equation (II-1), the initiation period is proportional to the square of the concrete cover. Hence, if initiation period T_{i1} is defined for concrete cover c_1, the initiation period T_{i2} for concrete cover c_2 is given by $T_{i2} = c_2{}^2 \cdot T_{i1}/c_1{}^2$. For each longitudinal girder, independent random fields are assumed to model the spatial correlation of the initiation period and corrosion rate, each with a correlation length of 5 m. A similar assumption holds for the transverse girders. For the slab, a 2D random field is assumed with a correlation length of 5 m in both directions. The random fields of the longitudinal girders, the transverse girders and the slab are considered independent. The assumed correlation model is a squared exponential correlation model for all random fields. Since the random fields for the different girders are independent, there can be accounted for scenarios where only one of the girders is subjected to corrosion or to more severe corrosion than the others (see section XII.3.7). An example of such a situation is when the girders next to the joint are subjected to corrosion due to penetration of road salts through the joint.

Based on the initiation period and corrosion rate, both corrosion of the shear reinforcement and longitudinal reinforcement are evaluated. Nevertheless, in the following, only the corrosion degree of the longitudinal reinforcement will be visualized, since this is linked to the general behaviour of the structure. Even though only graphs are provided for the posterior distribution of the corrosion degree, the distributions that are inferred are the random fields for the initiation period and corrosion rate. The distribution of the corrosion degree at different

timesteps can then be evaluated based on the degradation models provided by equations (II-8) and (II-9) and the (posterior) distributions of the initiation period and corrosion rate.

XII.3.2 Monitoring strategies

In the following, different monitoring strategies will be considered. These are summarized in Table XII-1. In addition, the influence of the assumed measurement error for each of the strategies will be investigated. How the different data types are accounted for in the Bayesian inference procedure has been described in Chapter VI. Strains, displacements and accelerations are assumed to be measured at different locations along the bridge. For the acceleration measurements, the optimal sensor positions will be derived in section XII.3.4. For the strains measured with optic fibres, fibres are assumed to be attached along the bottom fibres of the girders, with sensors at each of the elements in which the girders are discretized (cfr. infra). The static strains are measured at the same locations as the dynamic strains.

Table XII-1: Monitoring strategies considered in this case study

Strategy	Measurement scenario	Data obtained
1	Strains measured under a proof load	Static strains
2	Deflections measured under a proof load	Static deflections
3	Accelerations measured under ambient conditions	Natural frequencies and displacement mode shapes
4	Strains measured with optic fibres under ambient conditions	Natural frequencies and strain mode shapes

To generate the measurement data, samples of the initiation period and corrosion rate for the different elements in which the structure is discretized (cfr. infra) are generated. Based on these samples, the actual corrosion degrees are calculated as well as the corresponding remaining reinforcement area and the Young's modulus of the concrete cover. Then, strains or deflections under a proof load and modal data are generated by the finite element model (cfr. infra). To these generated results, a measurement error is added. Different values for the measurement error are assumed in this chapter. For very accurate measurements, a measurement error of 0.5 µε is assumed for the static strain data, 0.1% of the experimental natural frequency for the natural frequencies, and 1% of the norm of the experimental mode shape for the displacement mode shapes. These errors are also increased to simulate less accurate measurements, i.e. errors of 3 µε and 10 µε for the static strain measurements, and 1% or 5% of the experimental natural frequencies for

the natural frequency data. For the deflection measurements, a measurement uncertainty of 0.5 mm is assumed (e.g. camera-based deflection measurements (Heitner et al., 2019; Sousa et al., 2020)). In the likelihood function, these measurement errors are combined with the error of the response surface (cfr. infra).

XII.3.3 Model of the bridge

A finite model of the bridge is made in DIANA FEA (DIANA FEA BV, 2019). For the reinforcement steel, a characteristic yield strength of 400 MPa and a characteristic ultimate tensile strength of 420 MPa are assumed, based on the steel quality known for this bridge. The concrete strength class is C25/30, with all properties according to EN 1992-1-1:2004. In the finite element model used to simulate the proof load test, a uniform load of 1.2 kN/m² is applied to represent the permanent loads of the sidewalk. This is applied over the outer 4.5 m of the bridge deck (Figure XII-5). The permanent load of the road equals 3.9 kN/m² and is applied to the part where the actual driveway for the cars is present. For the modal analysis, these permanent loads representing the self-weight should be added as mass, influencing the resulting natural frequencies and mode shapes of the bridge.
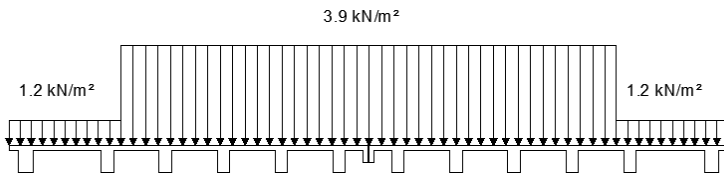

Figure XII-5: Permanent loads on the bridge deck

For a given corrosion degree, the main reinforcement of the longitudinal and transverse girders is adjusted according to equations (II-8) to (II-9). Accordingly, the shear reinforcement of those girders exposed to corrosion is also adjusted, and also the bottom reinforcement of the slabs is assumed to be subjected to corrosion. As mentioned in section XII.3.1, the initiation period is adjusted according to the concrete cover of the considered reinforcement bars. The reinforcement area is modelled to vary according to the subdivision originating from the design of the bridge. By making use of the grid of both longitudinal and transverse girders, the girders are subdivided automatically in parts between the crossing points of both types of girders. It is assumed that in between these crossing points, the structure/structural elements are subjected to common exposure conditions. This means that all longitudinal girders are subdivided into four elements (i.e. in between the transversal girders, see Figure XII-6), the transversal girders are

subdivided into 11 elements (see Figure XII-6, note that the two parts to the left and right from the middle transversal girder are taken as one (i.e. element 6 of the first transversal girder)) and the slab is subdivided into 44 elements (see Figure XII-6, note that similar as for the transversal girders the parts to the left and to the right of the middle longitudinal girders are combined). For the girders, also the Young's modulus of the concrete cover is adapted to model the cracking of the concrete according to equations (II-10) to (II-13).
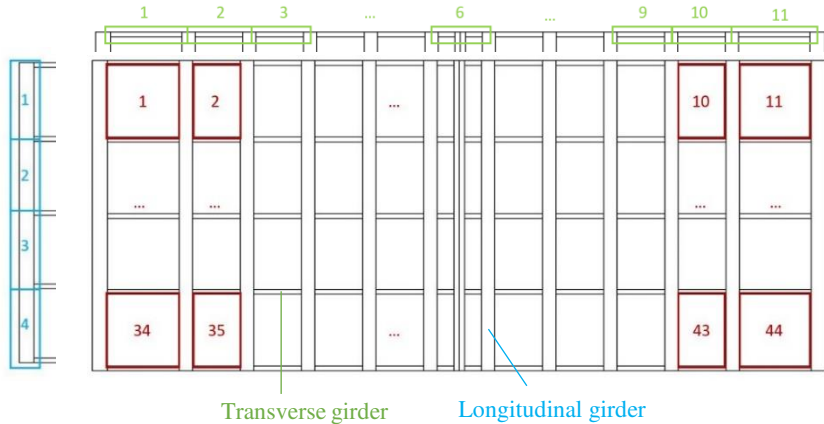
Figure XII-6: Subdivision in elements of the longitudinal girders, transvers stiffeners and slab

The different measurement scenarios of Table XII-1 are simulated by the finite element model, i.e. a modal analysis and a simulation of a proof load are modelled in DIANA FEA (DIANA FEA BV, 2016). The applied load for the proof load is based on models retrieved from the Ministry of Public Works Flanders (MOW) (2020), and consists of loaded surfaces of 2.33 m by 0.5 m with a load of 84.35 kN/m², representing trucks driving over the bridge. A number of trucks are placed on the different lanes of the bridge resulting in a large enough proof load, which does not exceed the cracking load. Linear calculations are assumed since no bending cracks are observed yet and the proof load will be applied as such that no cracking will be induced in the structure.

XII.3.4 Sensor placement

The accelerometers are point-like sensors and could be installed anywhere on the bridge. A priori, it might be difficult to decide which sensor positions will provide the most information regarding the displacement mode shapes. Hence, the optimal sensor configuration for the accelerometers is derived according to the method described in Chapter X. The possible sensor locations from which a selection is made consist of the nodes at the bottom of the finite element model. It is assumed

that the first four modes should be extracted from the dynamic data and will be used to update the corrosion degree along the bridge. The preferred sensor locations for the first forty sensors are visualized in Figure XII-7. This figure provides a bottom view of the bridge, with the width along the horizontal axis (y-coordinate) and the length of the bridge along the vertical axis (x-coordinate).The ten most preferable sensor locations are indicated with the blue dots. If ten more sensors can be applied to the bridge, they are preferably placed at the locations indicated by the green crosses. The next ten sensors are indicated by the red triangles, and if in total forty sensors are available, the last ten sensors should be positioned at the locations of the black triangles.

The strains under ambient conditions are measured with optic fibres. These are attached along the whole length of the bridge, with strains measured in between the clamping blocks (assumed measurement locations at each of the elements in which the girders are discretized). The static strains are assumed to be measured at the same locations as the dynamic strains.
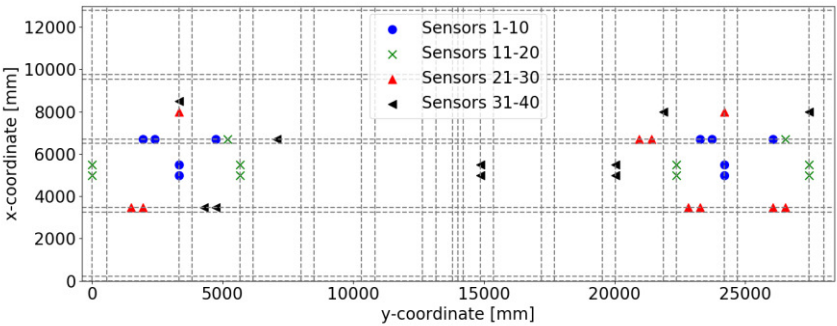

Figure XII-7: Optimal sensor placement for acceleration measurements when determining the first four modes. The dashed grey lines indicate the girder positions (longitudinal and transverse girders).

XII.3.5 Response surface fit to the finite element model

In order to avoid evaluations of the finite element model at every iteration of the MCMC sampling procedure to perform the Bayesian inference, response surfaces are used. The response surfaces have as output the data given in Table XII-1. Displacement mode shapes, strain mode shapes, static strains and static deflections are evaluated at different locations along the bridge. The input of the response surface is given by the corrosion degrees in the different elements in which the bridge is subdivided. The response surfaces are based on a set of Latin Hypercube samples (LHS). 500 sets of LHS samples are generated, i.e. for each of the

different input parameters 500 samples are generated, resulting in the model results to which the response surface is fitted.

Response surfaces of different orders are generated, and the fit of the response surface is evaluated by calculating the coefficient of determination R^2, with a correction for the number of unknowns in the response surface (see equations (VI-1) and (VI-2)). The risk of overfitting the response surface is addressed in the same way as discussed in section VI.3.1. For the natural frequencies, the values of R^2 are larger than 0.99999. For the mode shapes, the R^2 values are larger than 0.999, and for the strains, the R^2 values are larger than 0.9999. In addition, the error of the response surfaces is quantified and this is later taken along in the likelihood function. For each verification sample $\boldsymbol{x}_k$, the value z_k-$y_{RS}(\boldsymbol{x}_k)$ is evaluated, with z_k the result of the finite element model and $y_{RS}(\boldsymbol{x}_k)$ the result of the response surface. The variance of these values is calculated and added to the variance of the measurement error considered in the likelihood function (i.e. a zero mean white noise error is assumed with a normal distribution, and the error of the response surface is assumed independent from the measurement error).

XII.3.6 Posterior distribution of the corrosion degree based on levelling

When bridges are inspected in Flanders, during these inspections often level measurements are performed. During levelling, the height of one level relative to another level is determined, i.e. the elevation of a point relative to a datum. Data from levelling is available from the inspections performed every 4 years. It is investigated whether this data can provide some information on the corrosion degree of the bridge under investigation. The last available level measurements (2019) are represented in Figure XII-8 and Table XII-2. The posterior distribution of the corrosion degrees taking into account the data from these level measurements is given in Figure XII-9 for the left part of the bridge. When the posterior distribution of the corrosion degree is visualized further in this chapter, only the left part of the bridge is shown. To arrive at the posterior distribution visualized in Figure XII-9, a measurement error of 1 mm is assumed in the likelihood function, and a similar likelihood function is adopted as in section VI.3.2.2. The measurement error assumed for the level measurements is larger than the one mentioned in section XII.3.2 due to the inaccuracy of the level measurements. It can be seen that vague posterior distributions of the corrosion degree are found due to the limited amount of available data and the relatively large measurement error accompanied with these measurements. Hence, in the following it will be investigated whether other monitoring strategies will provide more accurate information on the corrosion degree. The considered monitoring strategies were already introduced in section XII.3.2. The different considered situations are summarized in the next section.
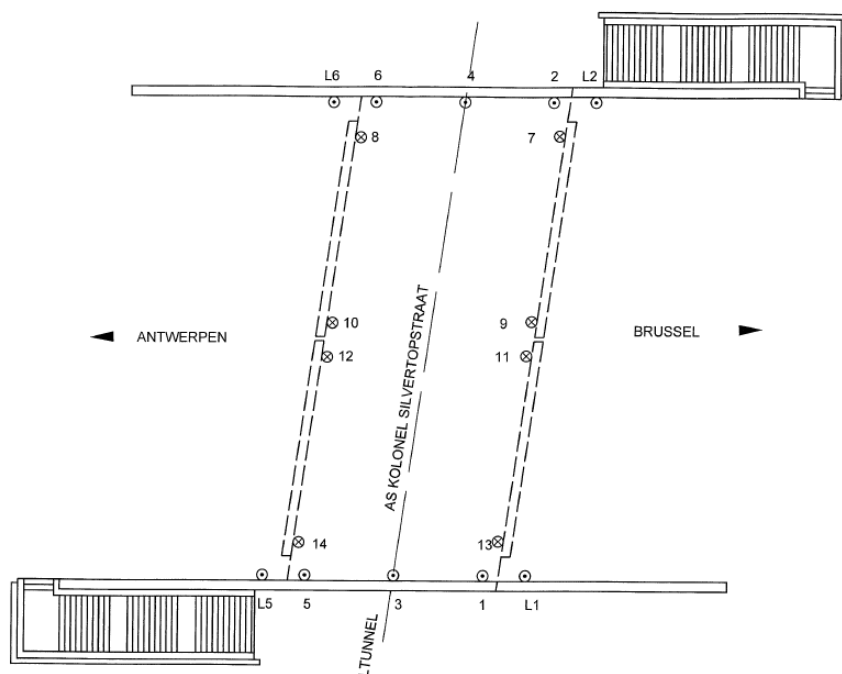
Figure XII-8: Locations of the level measurements for the case study bridge. The locations of the measuring points are indicated by the circles and a number.

Table XII-2: Difference between latest level measurement (2019) and reference level measurement (basic levelling) for the measuring locations indicated in Figure XII-8.

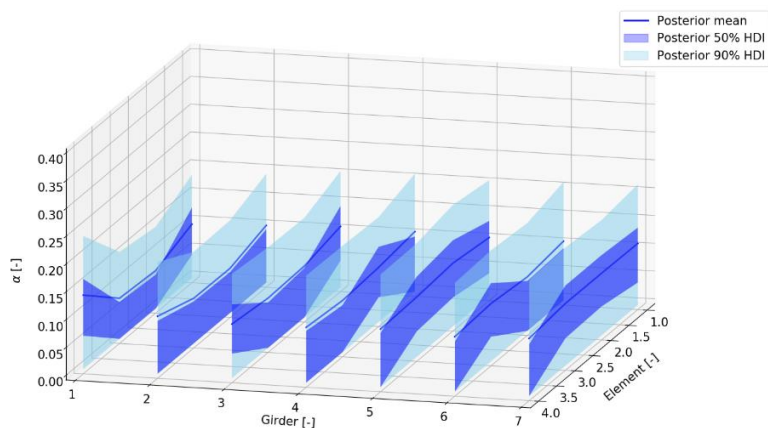| Measuring point	Difference with basic levelling [mm]	Measuring point	Difference with basic levelling [mm]
L1	0	6	0
L2	0	7	2
L5	1	8	3
L6	-1	9	1
1	-1	10	2
2	1	11	1
3	3	12	1
4	0	13	0
5	2	14	1

Figure XII-9: Posterior distribution of the corrosion degree in the longitudinal girders based on level measurements.

XII.3.7 Investigated situations

Different simulated situations for the state of corrosion of the bridge are considered as given in Table XII-3. For each situation, the different data types as provided in Table XII-1 are considered. The results for each of these situations are summarized in the following sections. In all these situations, the errors on the individual data components are assumed independent, since they solely represent measurement errors. For model errors, a certain degree of correlation is expected. A short discussion on a case with a (correlated) model error is provided in section XII.3.9.

Table XII-3 Considered cases in the analysis, i.e. the corrosion layout for generation of the measurement results

Model for data generation	Section
Spatially variable corrosion	XII.3.8.1
Corrosion only in girder next to joint (girder 7 in Figure XII-4)	XII.3.8.2
Corrosion only in outer girder (girders 1 and 13 in Figure XII-4)	XII.3.8.2

XII.3.8 Results of the Bayesian inference procedure

The posterior distribution of the corrosion degree of the longitudinal girders is generated by Markov Chain Monte Carlo (MCMC) simulations, in which the abovementioned response surfaces are used for the model evaluations.

In the following, posterior distributions will only be visualized for the longitudinal girders (and for the left part of the bridge). The posterior distributions of the transverse stiffeners and of the slabs are very close to the prior distributions and hence not updated. This could be expected beforehand since the influence of corrosion in these structural element types on strains and natural frequencies is limited. When increasing the corrosion degree in the longitudinal girders from 0% to 20%, a difference in strains of the longitudinal girders of maximum 28% is found, and a difference in natural frequencies of maximum 9%. When increasing the corrosion degree of the transverse stiffeners from 0% to 20%, the maximum increase of the strain equals only 1%, and there is almost no influence on the natural frequencies. Finally, when increasing the corrosion degree in the slab from 0% to 20%, a maximum increase in strains of 5% is found, and the largest influence on the natural frequencies equals 2.9%.

XII.3.8.1 Spatially variable corrosion

In this section, the different types of measurements are used to update a spatially variable corrosion degree.

The posterior distributions of the corrosion degree of the longitudinal girders for the different types of measurements are given in Figure XII-10 to Figure XII-12. Here it can be seen that the overall pattern of the spatial distribution of the corrosion degree in each girder is present in the posterior distribution derived based on the displacement mode shapes and corresponding natural frequencies. The posterior distribution of the corrosion degree approaches better the actual value when the updating is performed based on the strain mode shapes. Figure XII-13 gives the posterior distribution of the corrosion degree of the longitudinal girders when static strains are measured at the locations where the posterior mean of the corrosion degree μ_a'' based on the displacement mode shapes and natural frequencies of the first four modes exceeds 0.2. When the data of different tests are combined, i.e. natural frequencies, displacement mode shapes and static strains, a more informative posterior distribution of the corrosion degree is found (i.e. a posterior mean closer to the actual value and a smaller posterior standard deviation) compared to the situation where only the modal data is accounted for. It could indeed be expected beforehand that, when more data is incorporated in the likelihood function, the uncertainty reduces. However, the quantitative combination of the different types of data is unique compared to existing literature.
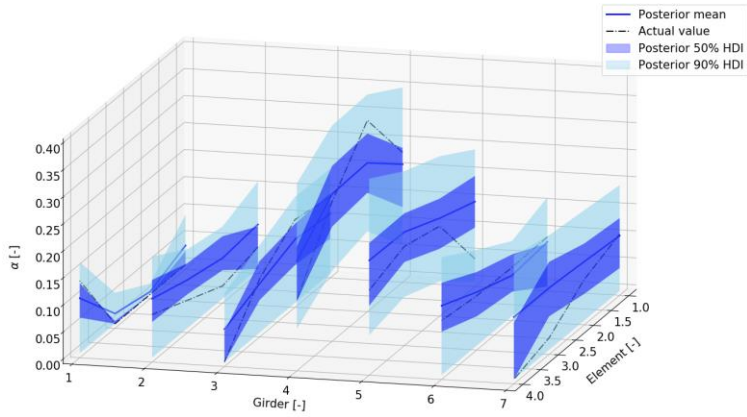
Figure XII-10: Posterior distribution of the corrosion degree of the longitudinal girders based on the natural frequencies ($\sigma_{\lambda,r} = 0.001\bar{\lambda}_r$) and displacement mode shapes ($\sigma_{\phi,r} = 0.01\|\bar{\phi}_r\|$) of the first 10 modes extracted from accelerations measured at the 26 most optimal sensor positions.
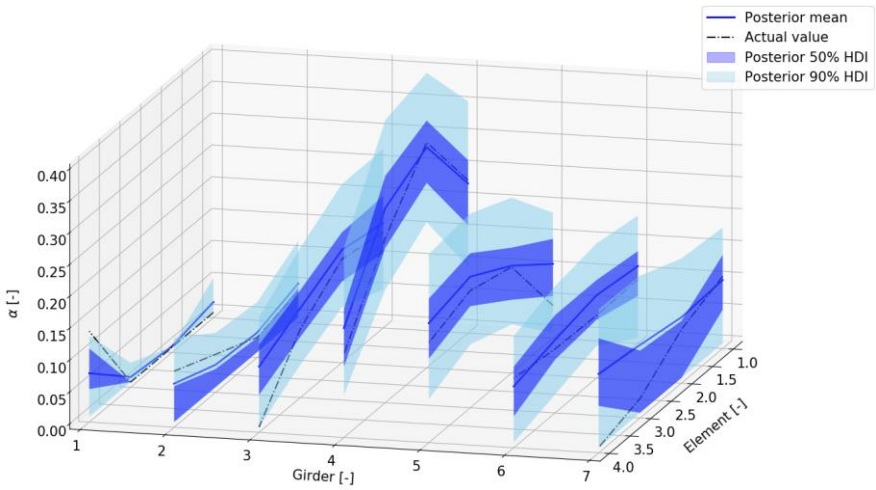

Figure XII-11: Posterior distribution of the corrosion degree of the longitudinal girders based on the natural frequencies ($\sigma_{\lambda,r} = 0.001\bar{\lambda}_r$) and strain mode shapes (error 0.5 µε, measured strains order of magnitude some microstrain) of the first four modes.
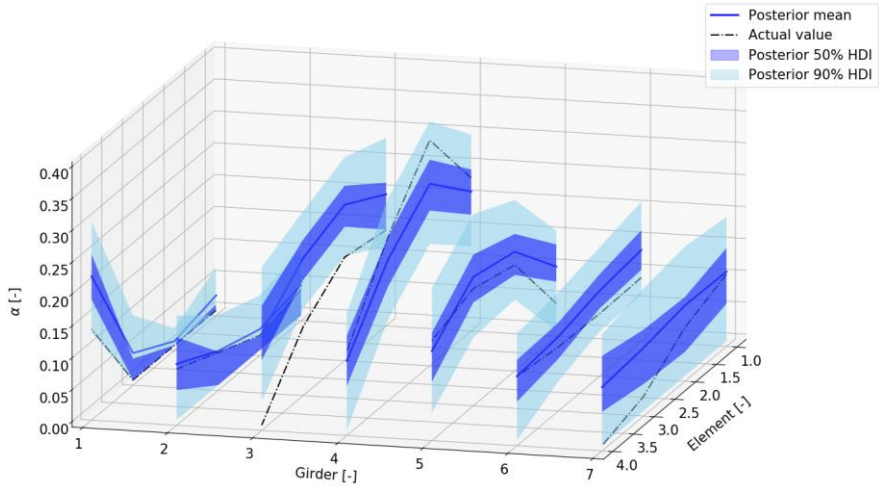
Figure XII-12: Posterior distribution of the corrosion degree of the longitudinal girders based on strains measured under proof loading (error 0.5 με).
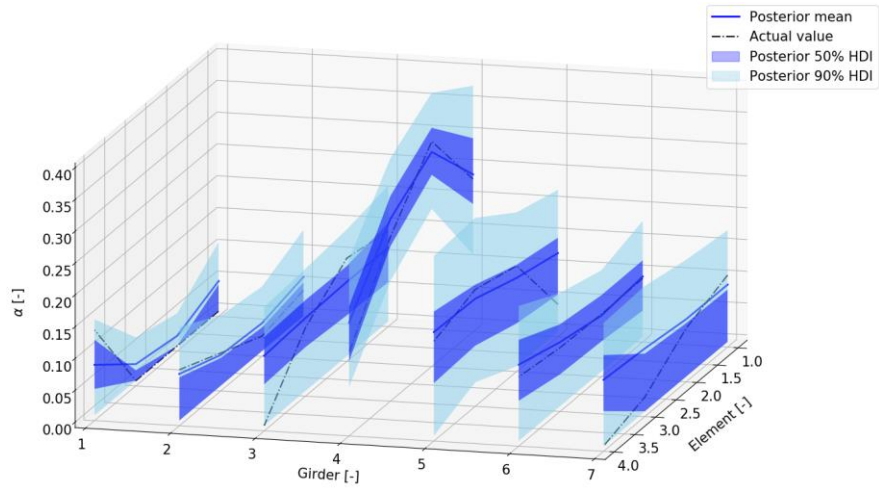

Figure XII-13: Posterior distribution of the corrosion degree of the longitudinal girders based on the natural frequencies ($\sigma_{\lambda,r} = 0.001\bar{\lambda}_r$) and displacement mode shapes ($\sigma_{\phi,r} = 0.01\|\bar{\phi}_r\|$) of the first 4 modes and static strains (error 0.5 με) measured at the locations where μ_{α}" based on the modal data is larger than 0.2.
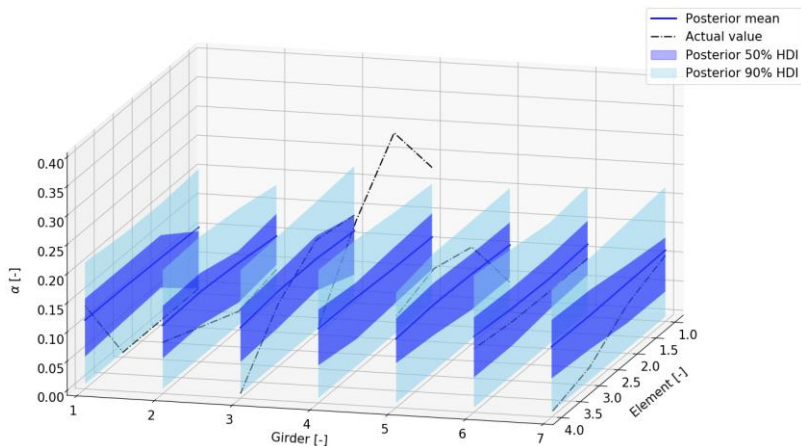
Figure XII-14: Posterior distribution of the corrosion degree of the longitudinal girders based on deflections measured under proof loading (error 0.5 mm).

In Figure XII-14, it can be seen that if the data only consists of the static deflections, the posterior distribution of the corrosion degree is almost equal to the prior distribution. When looking at the samples of the deflections generated to fit the response surface, the maximum difference in deflection is estimated to be 0.61 mm. This is a quite small value, indicating that the influence of corrosion on the deflection results of the proof load test is limited. Moreover, deflections are more dependent on the global stiffness of the structure and not to local changes in stiffness. The influence of local corrosion on the global stiffness can be rather limited. Even though a small measurement error of 0.5 mm is assumed (accurate measurements), it is relatively large with respect to the influence of corrosion on the measured deflections. Due to this large relative uncertainty, deflection measurements under proof loading lead to a vague posterior distribution of the corrosion degree, not approximating the actual corrosion degree.

All results are also summarized in Table XII-4, with different assumptions on the errors adopted in the likelihood function. Different conclusions can be made when looking at Table XII-4. When considering the deflections, the RMS value between the actual corrosion degree and the posterior mean and the posterior standard deviations are very close to the ones found when considering the prior distribution. For the natural frequencies and displacement mode shapes, incorporating more modes already leads to a more informative posterior distribution of the corrosion degree, with a reduction in RMS value and average posterior standard deviation $\sigma_{average}$. In addition, when increasing the error on the natural frequencies, the RMS value and average posterior standard deviation increase. When increasing the error on the norm of the displacement mode shapes, the RMS value and posterior uncertainty also increase. For the static strains, the same observations are found

when increasing the measurement error on the strains. Furthermore, the accurate strain measurements lead to a smaller RMS value and a smaller posterior standard deviation compared to the modal data with 10 modes and a small error on the natural frequencies. For the modal strains, the RMS value is smaller than for the static strains, but the average posterior uncertainty is higher. If the error on the natural frequencies increases, the RMS value and posterior average standard deviation increase. This increase is most remarkable when increasing the error on the natural frequencies from 0.1% to 1% of the experimental value, and is more limited when increasing from 1% to 5% of the experimental value. When the error on the modal strains increases, the RMS value and posterior uncertainty also increase, and this for different assumptions for the error on the natural frequencies. Finally, when considering the combination of modal data and static strain data, for an error on the natural frequencies of 0.1% of the experimental frequency and an error on the static strains of 0.5 µε, the RMS value and average posterior standard deviation decrease compared to only including the modal data. They are higher than for the static strains, but the number of strain sensors is not the same in both situations. When the error on the static strains increases to 3 µε, the RMS value and the average posterior standard deviation increase. When also the error on the natural frequencies is increased to 5% of the experimental frequency, the RMS value and posterior uncertainty again increase. However, the RMS value and average posterior uncertainty are still smaller than the situation where only the modal data is accounted for.

XII.3.8.2 Corrosion in one of the girders

In this section, when generating the measurement data, corrosion is assumed to occur in only one of the girders. First, corrosion is assumed to be only present in the girders next to the joint (i.e. girders 7 in Figure XII-4). All data, except for the static deflection data, enabled to localize the girder with corrosion. Nevertheless, the actual corrosion degree is not accurately represented by the posterior distribution of the corrosion degree. The results are summarized in Table XII-5 assuming different data types.

If there is already a visual proof of corrosion (e.g. rust stains), this can be taken along in the updating procedure. As also pointed out in section VII.7.2, in (Andrade and Izquierdo, 2020) a proposal is made for the reduction in rebar diameter corresponding to the cracking stage which is required for corrosion products to leak from cracks in the concrete cover. Based on this reduction of diameter, for the structure under consideration a corrosion degree of 2% is found. Hence, in the updating procedure, this is assumed as a lower bound for the sampled corrosion degrees. The posterior distribution of the corrosion degree is visualized in Figure XII-15 for the static strain data. The influence of adding the visual observations is also represented by a reduction in RMS value, as can be seen in Table XII-6.

Table XII-5: Comparison of the posterior distribution of the corrosion degree for the different data types and varying experimental errors (RMS, maximum standard deviation σ_{max} and average standard deviation $\sigma_{average}$)

Data	RMS	σ_{max}	$\sigma_{average}$
Prior	0.0724	0.0846	0.0846
Static deflections	0.0715	0.0833	0.0745
Displacement mode shapes (4 modes) and natural frequencies ($\sigma_{\lambda,r} = 0.001\bar{\lambda}_r, \sigma_{\phi,r} = 0.01\|\bar{\phi}_r\|$)	0.0568	0.0951	0.0650
Displacement mode shapes (4 modes) and natural frequencies ($\sigma_{\lambda,r} = 0.05\bar{\lambda}_r, \sigma_{\phi,r} = 0.01\|\bar{\phi}_r\|$)	0.0678	0.0860	0.0720
Displacement mode shapes (4 modes) and natural frequencies ($\sigma_{\lambda,r} = 0.001\bar{\lambda}_r, \sigma_{\phi,r} = 0.1\|\bar{\phi}_r\|$)	0.0650	0.1123	0.0668
Displacement mode shapes (10 modes) and natural frequencies ($\sigma_{\lambda,r} = 0.001\bar{\lambda}_r$)	0.0529	0.0937	0.0611
Displacement mode shapes (10 modes) and natural frequencies ($\sigma_{\lambda,r} = 0.01\bar{\lambda}_r$)	0.0546	0.0871	0.0609
Displacement mode shapes (10 modes) and natural frequencies ($\sigma_{\lambda,r} = 0.05\bar{\lambda}_r$)	0.0553	0.0943	0.0630
Static strains ($\sigma_\varepsilon = 0.5$ µε)	0.0496	0.0868	0.0505
Static strains ($\sigma_\varepsilon = 3$ µε)	0.0478	0.0768	0.0583
Static strains ($\sigma_\varepsilon = 5$ µε)	0.0471	0.0812	0.0634
Static strains ($\sigma_\varepsilon = 10$ µε)	0.0579	0.0877	0.0708
Strain mode shapes (4 modes) and natural frequencies ($\sigma_{\lambda,r} = 0.001\bar{\lambda}_r, \ \sigma_\varepsilon = 0.5$ µε)	0.0464	0.0820	0.0540
Strain mode shapes (4 modes) and natural frequencies ($\sigma_{\lambda,r} = 0.01\bar{\lambda}_r, \sigma_\varepsilon = 0.5$ µε)	0.0491	0.0832	0.0577
Strain mode shapes (4 modes) and natural frequencies ($\sigma_{\lambda,r} = 0.05\bar{\lambda}_r, \sigma_\varepsilon = 0.5$ µε)	0.0490	0.0842	0.0581
Strain mode shapes (4 modes) and natural frequencies ($\sigma_{\lambda,r} = 0.01\bar{\lambda}_r, \sigma_\varepsilon = 3$ µε)	0.0624	0.0872	0.0706
Strain mode shapes (4 modes) and natural frequencies ($\sigma_{\lambda,r} = 0.05\bar{\lambda}_r, \sigma_\varepsilon = 3$ µε)	0.0674	0.0908	0.0710
Displacement mode shapes (4 modes) and natural frequencies + static strains ($\sigma_{\lambda,r} = 0.001\bar{\lambda}_r, \sigma_\varepsilon = 0.5$ µε, $\sigma_{\phi,r} = 0.01\|\bar{\phi}_r\|$)	0.0503	0.0975	0.0621
Displacement mode shapes (4 modes) and natural frequencies + static strains ($\sigma_{\lambda,r} = 0.001\bar{\lambda}_r, \sigma_\varepsilon = 3$ µε, $\sigma_{\phi,r} = 0.01\|\bar{\phi}_r\|$)	0.0550	0.0910	0.0676
Displacement mode shapes (4 modes) and natural frequencies + static strains ($\sigma_{\lambda,r} = 0.05\bar{\lambda}_r, \sigma_\varepsilon = 3$ µε, $\sigma_{\phi,r} = 0.01\|\bar{\phi}_r\|$)	0.0616	0.0934	0.0701

Table XII-6: Characteristics of the posterior distributions of the corrosion degree (RMS, maximum standard deviation σ_{max} and average standard deviation $\sigma_{average}$) if there is only corrosion in the girders next to the joint

| Data	RMS	σ_{max}	$\sigma_{average}$
Prior	0.1031	0.0713	0.0713
Static strains ($\sigma_\varepsilon = 0.5\ \mu\varepsilon$)	0.0178	0.0552	0.0145
Static strains ($\sigma_\varepsilon = 0.5\ \mu\varepsilon$) + visual	0.0115	0.0375	0.0142
Natural frequencies and displacement mode shapes ($\sigma_{\lambda,r} = 0.001\bar{\lambda}_r, \sigma_{\phi,r} = 0.01\lVert\bar{\phi}_r\rVert$)	0.0217	0.0464	0.0067
Natural frequencies and displacement mode shapes ($\sigma_{\lambda,r} = 0.001\bar{\lambda}_r, \sigma_{\phi,r} = 0.01\lVert\bar{\phi}_r\rVert$) + visual	0.0105	0.0444	0.0074
Natural frequencies and strain mode shapes ($\sigma_{\lambda,r} = 0.001\bar{\lambda}_r,\ \sigma_\varepsilon = 0.5\ \mu\varepsilon$)	0.0177	0.0511	0.0114
Natural frequencies and strain mode shapes ($\sigma_{\lambda,r} = 0.001\bar{\lambda}_r,\ \sigma_\varepsilon = 0.5\ \mu\varepsilon$) + visual	0.0091	0.0449	0.0105
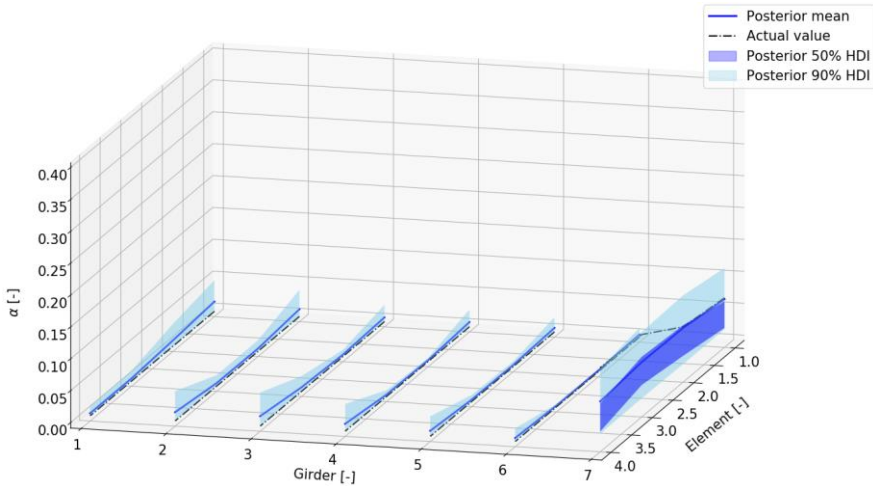
Figure XII-15: Posterior distribution of the corrosion degree in the longitudinal girders based on static strain data (error 0.5 µε) and visual observations considering corrosion only in the girders next to the joint.

When there is local corrosion at one of the outer girders, the posterior distribution of the corrosion degree for the left part of the bridge is visualized in Figure XII-16 when Bayesian updating is performed based on static strain data. This corrosion degree is better represented than the one in the girders close to the joint, since the strains in these outer girders are more influenced by corrosion. The relatively smaller strains in the girders next to the joint and the larger relative error of the response surface also result in a larger uncertainty at these girders and a less accurate posterior distribution of the corrosion degree. A similar posterior distribution of the corrosion degree as the one obtained based on static strain data is found based on the modal data. The resulting RMS values and posterior uncertainties are summarized in Table XII-7.
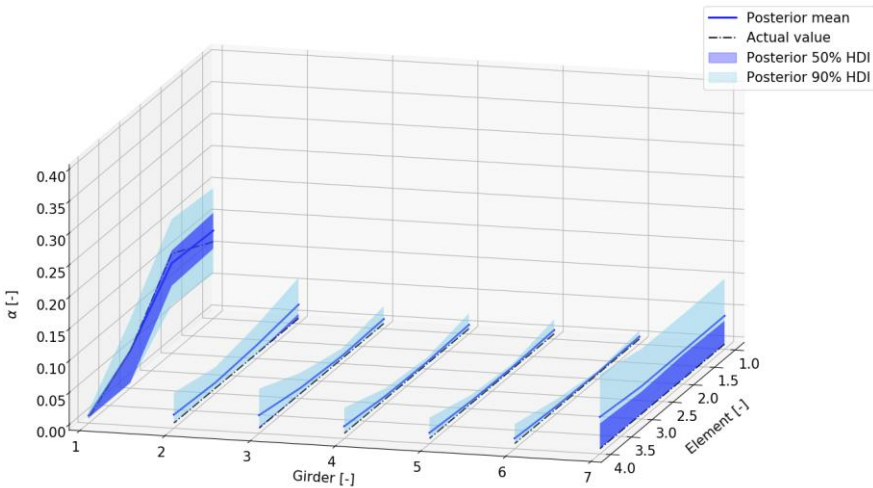

Figure XII-16: Local corrosion in outer girders: posterior distribution of the corrosion degree based on static strain data (error 0.5 µε).

Table XII-7: Characteristics of the posterior distributions of the corrosion degree (RMS, maximum standard deviation σ_{max} and average standard deviation $\sigma_{average}$) if there is corrosion in the outer girders

Data	RMS	σ_{max}	$\sigma_{average}$
Prior	0.1017	0.0692	0.0692
Static strains ($\sigma_\varepsilon = 0.5$ µε)	0.0277	0.0482	0.0202
Natural frequencies and displacement mode shapes (10 modes) ($\sigma_{\lambda,r} = 0.001\bar{\lambda}_r, \sigma_{\phi,r} = 0.01\|\bar{\phi}_r\|$)	0.0341	0.0594	0.01514
Natural frequencies and strain mode shapes (4 modes) ($\sigma_{\lambda,r} = 0.001\bar{\lambda}_r, \ \sigma_\varepsilon = 0.5$ µε)	0.0314	0.0636	0.0206

XII.3.9 Influence of a model error and prior distributions

In reality, the bridge is skewed with a skew angle of 7°. Nevertheless, in bridge design, for limited skew angles, it is common to model the bridge as straight. When bridges are skewed, they have a smaller maximum live load bending moment compared to straight bridges. Hence, modelling them as straight bridges is conservative. Furthermore, the maximum live load deflections decrease, the shear forces increase for the exterior beams and decrease for the interior beams and torsion effects increase, together with the support reactions (Bucur et al., 2008). Nevertheless, AASHTO standard specifications recommend that bridges with skew angles smaller than 20° are designed as straight (Harba, 2011). Moreover, (Nguyen et al., 2019) found that vertical accelerations are hardly affected by skewness, and that the effect is even less noticeable for small skew angles, as is the case for the structure under consideration.

The influence on bending moments in slabs and beams is investigated based on some preliminary calculations. The moments in the slab are evaluated based on equations (XII-1) to (XII-3), and the moments in the girder based on equation (XII-4). In equations (XII-1) to (XII-3), p is the load per m². In equation (XII-4), p is the load per m. G is the shear modulus, E the Young's modulus, C the torsion constant and I the second moment of area. L is the span length of the bridge and β is the skew angle. Equations (XII-1) to (XII-4) are based on (Van Bogaert, 2003).

$$m_x = \frac{pL^2}{12} \frac{\frac{GC}{EI}\tan^2(\beta)}{1 + \frac{GC}{EI}\tan^2(\beta)} \tag{XII-1}$$

$$m_y = \frac{pL^2}{12}\left(\frac{9}{8}\frac{b^2}{L^2} + \frac{\frac{GC}{EI}\left(2 - \tan^2(\beta)\right)\tan(\beta)}{1 + \frac{GC}{EI}\tan^2(\beta)}\right) \tag{XII-2}$$

$$m_{xy} = \frac{pL^2}{12} \frac{\frac{GC}{EI}\tan(\beta)}{1 + \frac{GC}{EI}\tan^2(\beta)} \tag{XII-3}$$

$$M = \frac{pL^2}{12} \frac{GC}{GC + EI\tan^2(90° - \beta)} \tag{XII-4}$$

When applying equations (XII-1) to (XII-4) to the bridge under consideration, the error on m_x is 0.9%, the error on m_y is almost zero and the error on m_{xy} is 7%. The latter is the largest since this is the contribution of the torsion moments. The error on the bending moments M in the girder is again equal to 0.9%. Hence, it is found

that the influence of accounting for the skewness of the bridge is very limited due to the small angle of skewness.

To investigate the influence on the dynamic behaviour, a simple model of the bridge is generated, without reinforcement and transverse stiffeners. The natural frequencies and mode shapes of the skewed bridge and the straight bridge are compared, and the error on the natural frequencies is given in Table XII-8 for the first 10 modes of the bridge.

Table XII-8: Error on the natural frequencies when not accounting for the skew angle of the bridge

Mode	Error on the natural frequency [Hz]	Error on the natural frequency [%]
1	0.229	3.8%
2	0.291	3.6%
3	0.054	0.5%
4	0.097	0.9%
5	0.013	0.11%
6	0.055	0.45%
7	0.127	0.89%
8	0.236	1.6%
9	0.674	3.8%
10	0.003	0.02%

In the following, the influence of the model error by modelling the bridge as straight instead of skewed is investigated. The finite element model based on which the measurement data is generated is a skewed model of the bridge. The finite element model for which the response surface is generated to be used in the Bayesian inference is a straight model of the bridge. This corresponds to a practical case, where measurements are obtained from an (actual) skewed bridge, whereas the modelling is performed using a simplified straight model of the bridge.

Static strains obtained from proof loading are generated for different values of the corrosion degree, both for the straight and for the skewed model. The strains of the skewed model are approximately 30% larger than the strains of the straight model for the investigated situation. The observation that the strains in the skewed bridge are higher than in the non-skewed bridge could be expected based on the analysis performed above. Hence, a multiplicative model error could be accounted for in the Bayesian inference procedure. In this situation, the measurement results

$\overline{d}$ are given by equation (XII-5). Here, η_M is the model error, $G(\boldsymbol{\theta}_M)$ the model with input variables $\boldsymbol{\theta}_M$, and η_D the measurement error.

$$\overline{d} = \eta_M G(\boldsymbol{\theta}_M) + \eta_D \qquad \text{(XII-5)}$$

When accounting for this model error, the maximum likelihood function is adjusted to equation (XII-6). Here, N is the number of data points, and σ_D^2 the variance of the measurement error.

$$F_{ML} = \sum_{j=1}^{N} \frac{\left(\overline{d} - \eta_M G(\boldsymbol{\theta}_M)\right)^2}{\sigma_D^2} \qquad \text{(XII-6)}$$

The analytical analysis above gives a difference in strain of +- 10%, with higher strains expected for the skewed bridge. This error can be even larger for the difference between the actual structure and the model. Hence, a priori, for the model error on the strains, a uniform distribution between 1 and 1.5 is assumed. A multiplicative model error is assumed in the analysis.

For the uniform corrosion degrees, the natural frequencies of the skewed bridge equal 0.96 to 1.01 times the natural frequencies of the non-skewed bridge. Furthermore, deviations from 0.5 to 15% between model and reality are found in literature (Bautista-De Castro et al., 2018; Brownjohn et al., 2001; Liu et al., 2017; Mankar et al., 2019; Zapico et al., 2003). Hence, a multiplicative model error with a uniform distribution between 0.85 and 1.15 is assumed.

When performing the Bayesian inference, in a first analysis uniform corrosion over all the longitudinal girders is assumed. A uniform prior distribution between 0% and 30% is assigned to the corrosion degree. Later, also spatial variation of the corrosion degree will be accounted for. The considered situations are summarized in Table XII-9.

Table XII-9: Considered situations with a model error.

| Measurement result based on	Data included in updating	Section
Uniform corrosion	Natural frequencies Static strains Natural frequencies and static strains	XII.3.9.1
Spatially distributed corrosion – corrosion in one girder	Natural frequencies and displacement mode shapes Static strains Natural frequencies and displacement mode shapes + static strains	XII.3.9.2

XII.3.9.1 Uniform corrosion

When updating is performed based on the natural frequencies, an experimental error of 1% of the experimental frequency ($\bar{\lambda}_r$) has been assumed, i.e. $\sigma_\lambda = 0.01$ in equation (VI-6). The resulting posterior distributions of the corrosion degree, considering different actual underlying corrosion degrees, are represented in Figure XII-17. Here, it can be seen that for the lowest corrosion degrees the posterior distribution is close to the prior distribution. This could be ascribed to the limited influence of small corrosion degrees on the natural frequencies, especially compared to the model error. When the actual corrosion degree increases, there is indeed a shift of the posterior distribution of the corrosion degree to higher values, with small to zero probability for the very low corrosion degrees. When comparing the results from the straight and skewed model, a difference in natural frequencies of 10%-15% is found. This is high compared to the influence of corrosion on the natural frequencies: for very large corrosion degrees, the difference in natural frequency is only 3.5 to 11% compared to the uncorroded case. This might explain why the posterior distribution of the corrosion degree has a large remaining uncertainty and that the actual corrosion degree is not located in the high probability regions of the posterior distribution.

The bounds of the prior distribution could also be adjusted taking into account some visual observations. According to (Ouzaa and Oucif, 2019), spalling will occur at a crack width of 1 mm, which corresponds to a corrosion degree of 8% according to equation (VII-18). Assuming a margin of 4% corrosion, the upper bound of the prior distribution is set equal to 12% if no spalling has been observed and the lower bound has been set equal to 4% if spalling has been observed. When comparing the posterior distributions, it can be seen that those based on a more informative prior give a better representation of the actual corrosion degree.

When for the strains the multiplicative model error with the uniform distribution between 1 and 1.5 is assumed, the posterior distributions of the corrosion degree are visualized in Figure XII-18. Here, a measurement error of 10 µε has been assumed. If the actual corrosion degree increases, the posterior distribution of the corrosion degree is also located around higher corrosion degrees. Nevertheless, the actual corrosion degree is smaller than the posterior mean corrosion degree and lies not in the high probability region of the posterior distribution. Similar as for the natural frequencies, the fact that the actual corrosion degree is not located in the high probability regions of the posterior distribution could already be expected beforehand. The difference between the strains for the skewed and the non-skewed bridge is on average 30%. When comparing the modelled strains between the uncorroded bridge and a bridge with a uniform corrosion degree of 30%, there can be a difference in strains up to 23% to 37%. This is of the same order of magnitude as the model error. For the strain data, the influence of changing the prior distribution to a more informative prior is much more limited compared to the case where updating is performed based on the natural frequencies, and there is still a large overestimation of the corrosion degree.

It is also investigated how the posterior distribution of the corrosion degree approximates the actual value when both the natural frequencies and static strains are accounted for in the likelihood function. These results are visualized in Figure XII-19. Here it can be seen that the distributions more closely resemble those obtained when the data only consists of the strain measurements. Furthermore, still an overestimation of the corrosion degree is found. The first aspect could be ascribed to the larger amount of static strain data incorporated, compared to only 10 natural frequencies. In Figure XII-19, it can be seen that the influence of choosing a more informative prior is rather limited. All these results are also summarized in Table XII-10 and Table XII-11.
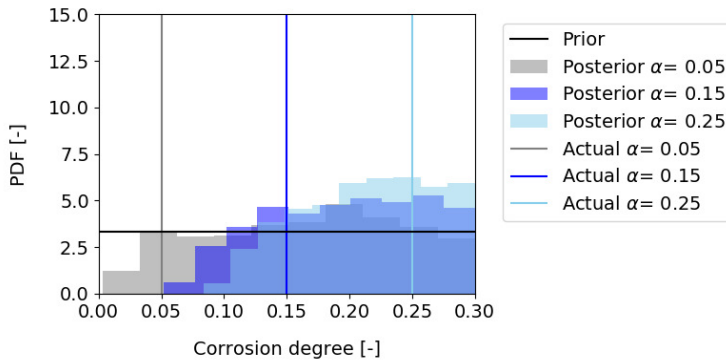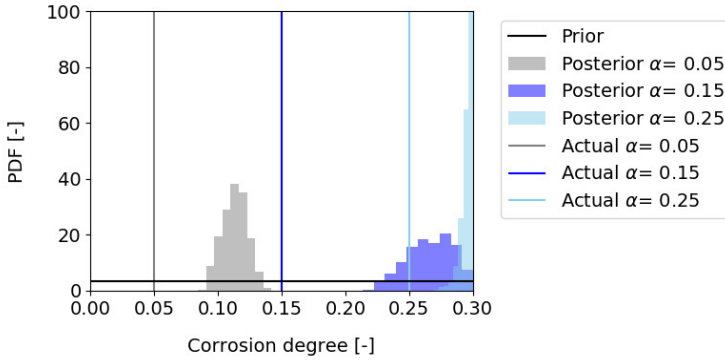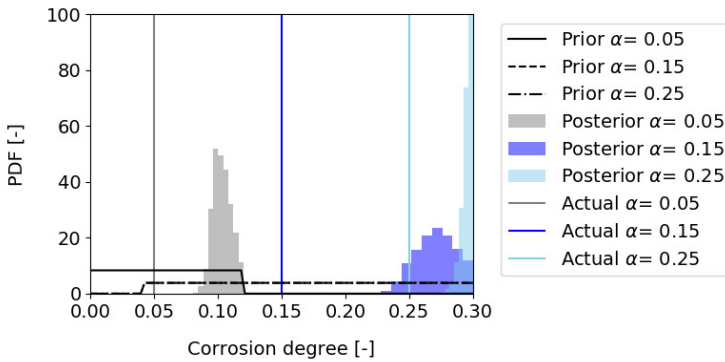
(a) Vague prior
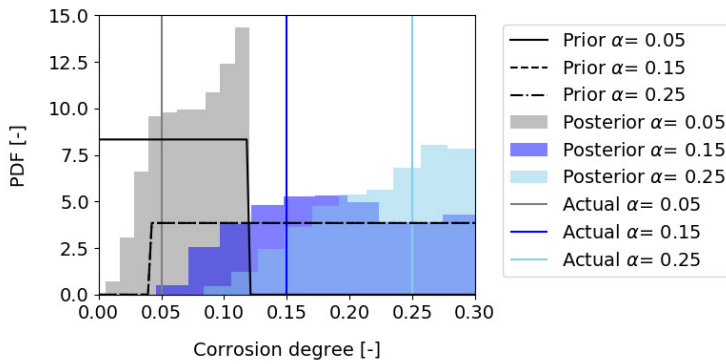
(b) More informative prior

Figure XII-17: Posterior distribution of the uniform corrosion degree based on natural frequencies (error 1% of the experimental value) when the actual bridge is skewed and the model for the bridge used in the likelihood function is straight – influence of different priors and different actual corrosion degrees. In figure (b), the prior distributions for $\alpha = 0.15$ and $\alpha = 0.25$ coincide.
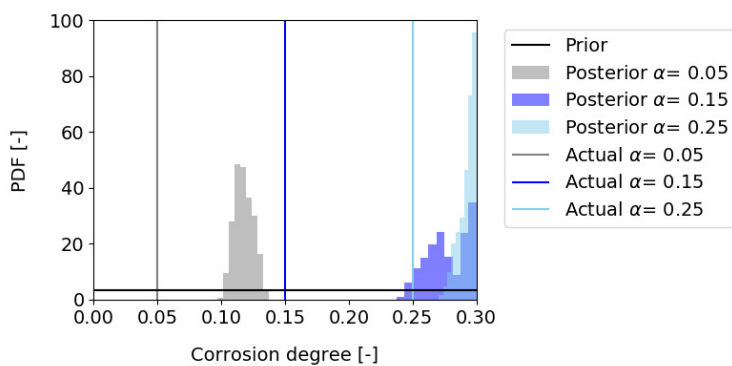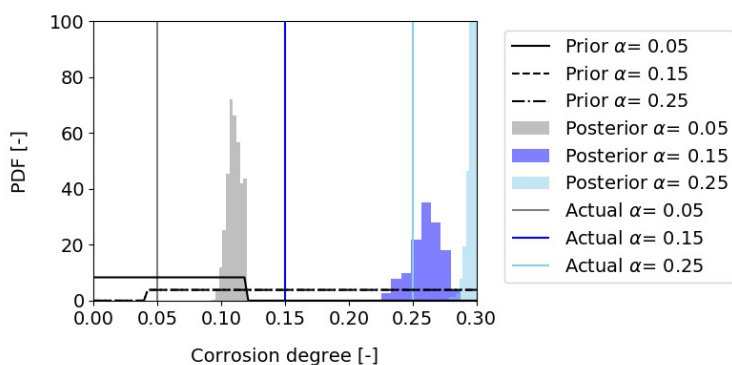
(a) Vague prior

(b) More informative prior

Figure XII-18: Posterior distribution of the uniform corrosion degree based on static strains (error 10 µε) when the actual bridge is skewed and the model for the bridge used in the likelihood function is straight – influence of different priors and different actual corrosion degrees. In figure (b), the prior distributions for $\alpha = 0.15$ and $\alpha = 0.25$ coincide.

(a) Vague prior

(b) More informative prior

Figure XII-19: Posterior distribution of the uniform corrosion degree based on static strains (error 10 με) and natural frequencies (error 1% of the experimental frequency) – influence of different priors and different actual corrosion degrees

Table XII-10: Difference between posterior mean corrosion degree and actual value, and posterior standard deviation for the different data types. Each time a value is given for different considered actual corrosion degrees [0.05, 0.15 and 0.25] – vague prior distribution

Data	Difference between posterior mean corrosion degree and actual value			Posterior standard deviation		
	0.05	0.15	0.25	0.05	0.15	0.25
Natural frequencies	0.114	0.046	-0.037	0.077	0.062	0.053
Static strains	0.063	0.116	0.046	0.010	0.018	0.004
Natural frequencies and static strains	0.068	0.127	0.042	0.007	0.016	0.006

Table XII-11: Difference between posterior mean corrosion degree and actual value, and posterior standard deviation for the different data types. Each time a value is given for different considered actual corrosion degrees [0.05, 0.15 and 0.25] – more informative prior distribution

Data	Difference between posterior mean corrosion degree and actual value			Posterior standard deviation		
	0.05	0.15	0.25	0.05	0.15	0.25
Natural frequencies	0.027	0.038	-0.024	0.028	0.062	0.050
Static strains	0.053	0.121	0.046	0.007	0.015	0.004
Natural frequencies and static strains	0.060	0.111	0.046	0.005	0.012	0.003

XII.3.9.2 Spatially distributed corrosion

Next, it is investigated how the presence of modelling errors affects localisation of damage. Measurement results are generated with the model of the skewed bridge, assuming there is 10% corrosion in the outer girders at the left and right side of the bridge (girders 1 and 13 in Figure XII-4). When the posterior distributions are generated, there is no localisation of damage possible based on static strains (see Figure XII-20) or displacement mode shapes (see Figure XII-21), and the posterior distribution deviates significantly from the actual corrosion degree. When the data consists of both the static strains and the displacement mode shapes, the posterior distribution of the corrosion degree along the whole bridge is

close to zero, and hence here the damage is not detected from this distribution (see Figure XII-22). At the outer girder at the right part of the bridge, there is a shift towards higher corrosion degrees, and hence damage could be detected in this girder (see Figure XII-23). However, the exact corrosion degree is not located in the high probability regions of the posterior distribution.
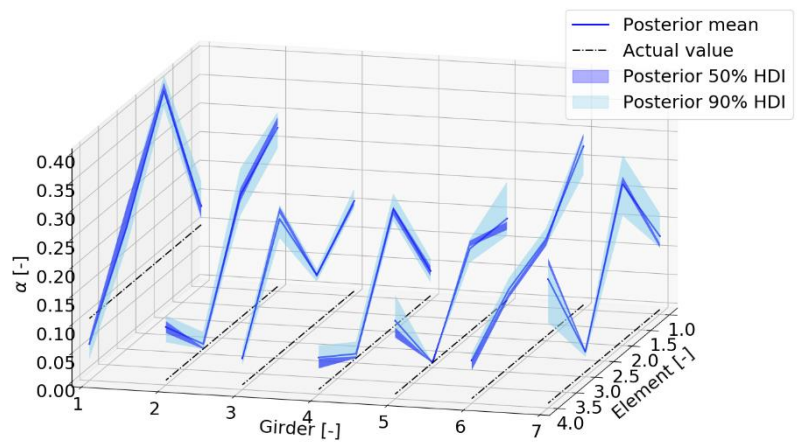

Figure XII-20: Posterior distribution of the corrosion degree based on static strains (error 10 µε) when the model used to generate the data is skewed and the model used in the identification is straight.
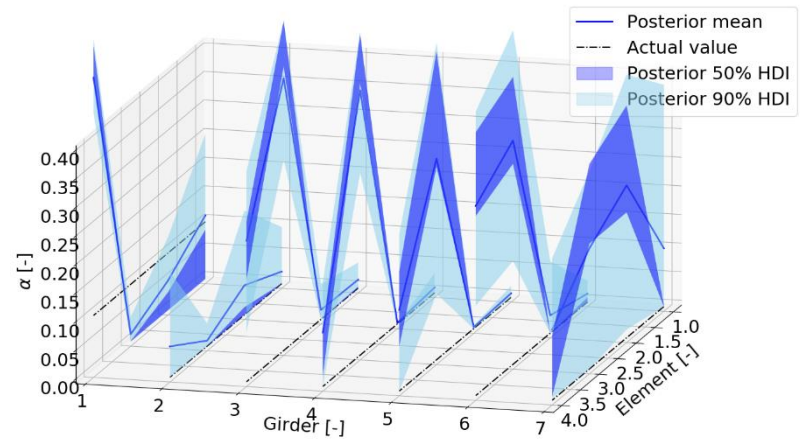

Figure XII-21: Posterior distribution of the corrosion degree based on natural frequencies (error 1% of the experimental frequency) and displacement mode shapes when the model used to generate the data is skewed and the model used in the identification is straight.
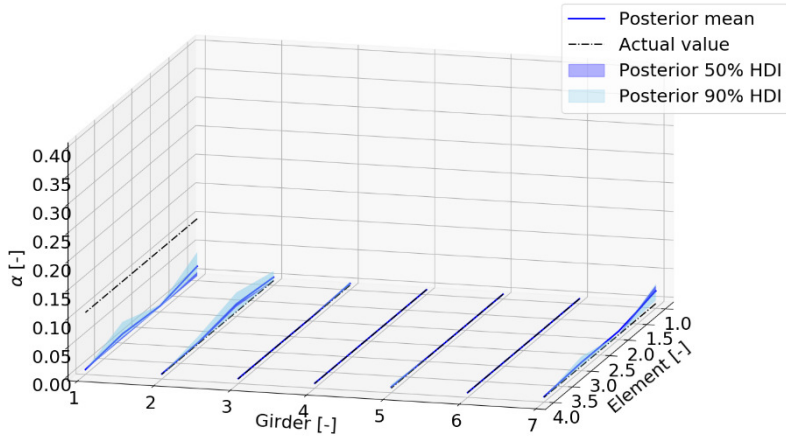
Figure XII-22: Posterior distribution of the corrosion degree based on natural frequencies (error 1% of the experimental frequency) and displacement mode shapes and static strains (error 10 µε) when the model used to generate the data is skewed and the model used in the identification is straight. (left half of the bridge)
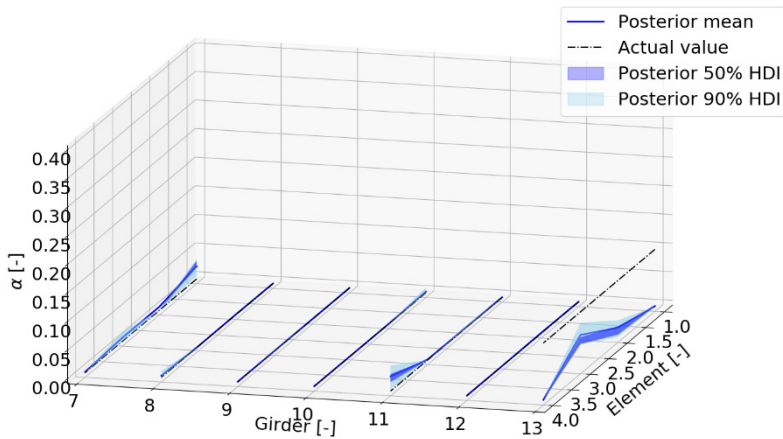

Figure XII-23: Posterior distribution of the corrosion degree based on natural frequencies (error 1% of the experimental frequency) and displacement mode shapes and static strains (error 10 µε) when the model used to generate the data is skewed and the model used in the identification is straight. (right half of the bridge)

Again, the influence of changing the prior distribution has been investigated. The bounds are adjusted in a similar way as described above. For the static strain data and modal data, the posterior distributions are visualized in Figure XII-24 and Figure XII-25 respectively. These posterior distributions approximate better the actual values compared to the results with the more vague prior distribution. When considering a combination of modal data and static strain data, it can be seen in Figure XII-26 that a better approximation of the actual corrosion degree is found, especially at the girders without corrosion. Hence, once again the beneficial effect of combining different types of data is illustrated.
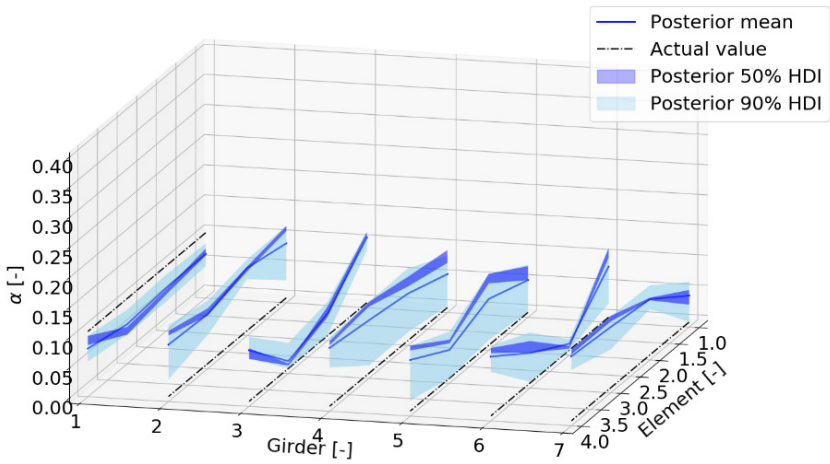

Figure XII-24: Posterior distribution of the corrosion degree based on static strains (error 10 µε) when the model used to generate the data is skewed and the model used in the identification is straight, accounting for adjusted bounds in the prior distribution of the corrosion degree.

Figure XII-25: Posterior distribution of the corrosion degree based on natural frequencies (error 1% of the experimental frequency) and displacement mode shapes when the model used to generate the data is skewed and the model used in the identification is straight, accounting for adjusted bounds in the prior distribution of the corrosion degree.
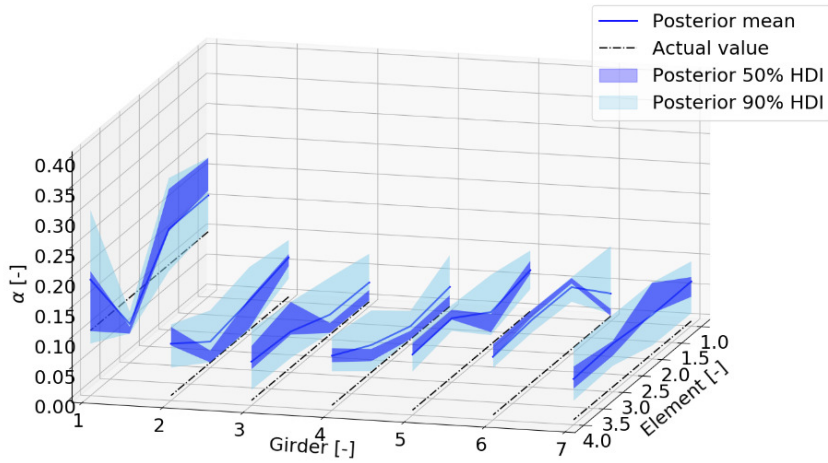

Figure XII-26: Posterior distribution of the corrosion degree based on natural frequencies (error 1% of the experimental frequency) and displacement mode shapes and static strains (error 10 με) when the model used to generate the data is skewed and the model used in the identification is straight accounting for adjusted bounds fo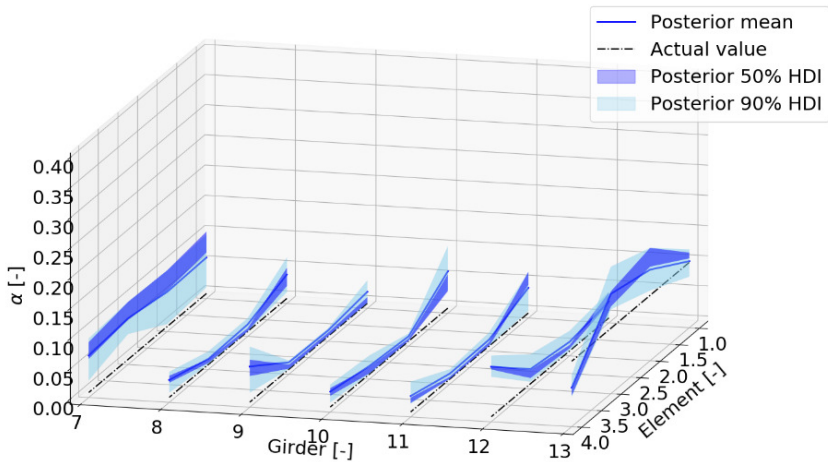r the prior distribution of the corrosion degree. Only the results related to the right half of the bridge are represented here.

Based on the results given in this section, it can be concluded that modelling errors may strongly affect the inverse identification of corrosion damage. Modelling assumptions that are reasonable in design may lead to misleading estimations of the corrosion degree. The impact of modelling errors is largest if localization of damage is required, because the ratio of measurement values at multiple locations should more closely correspond to reality, whereas for uniform corrosion it might be sufficient to only observe an increase or decrease in measurement output. If the model deviates significantly from the actual structure, more data and/or information is required to have a posterior distribution that approximates the actual corrosion degree. For example, by including visual observations the posterior approximation of the actual corrosion degree can be improved. However, this might not be generally valid, since the inclusion of more data might also push the posterior distribution further away from the actual value. Nevertheless, the inclusion of visual observations might always result in a posterior distribution better approximating reality, since these lead to the exclusion of corrosion degrees that are not in line with these visual observations. In general, it can be concluded that, to obtain a posterior distribution that corresponds to the actual value as closely as possible, the model error should be kept as small as possible, with a model that corresponds to the actual structure as good as possible.

XII.3.10 Discussion

When considering the results in section XII.3.8, the static deflections lead to very vague posterior distributions of the corrosion degree, close to the prior distributions, because of the limited influence of corrosion on the deflections. The measurement uncertainty is relatively large compared to the difference in deflection that can be expected due to corrosion. The inclusion of natural frequencies and displacement mode shapes in the likelihood enabled localisation of damage, but generally led to larger posterior uncertainties and RMS values compared to the static strain data. However, caution should be taken when comparing measurement techniques, since the RMS value and the posterior uncertainty also strongly depend on the amount of information considered in the likelihood function and the accompanying experimental error. These aspects depend on de data type, the number of data points and the uncertainty on the data.

Considering localisation of corrosion, it could be concluded that corrosion of one girder can be localized if it has a large enough influence on the measured quantity. The influence of corrosion in the girders next to the joint on the static strains and modal data is smaller than the influence of corrosion in the outer girders on these properties, especially when compared to the error assumed in the likelihood function. Hence, localisation of damage in the outer girders is better than in the girders next to the joint.

Finally, the influence of a model error has also been investigated. The measurement results are generated based on a skewed model of the bridge and the model used in the likelihood function is based on a straight bridge. The latter was chosen since in design this simplification is often justified. However, it is found that this simplification has a large influence on the inverse estimation of the corrosion degrees. Since only the corrosion degree is updated based on the measurement data, all differences in modelled and measured output are ascribed to the corrosion degree and a model error. For uniform corrosion, this generally leads to an overestimation of the corrosion degree. When corrosion is spatially variable, localisation of corrosion becomes very difficult, but can be improved by also including the information from visual observations in the definition of the prior distribution. From all these results, it can be concluded that it is important that the model resembles the actual structure as good as possible. This means that all information that is available prior to the analysis should be considered when designing the finite element model and/or the prior distributions. Examples are the proper modelling of the geometry of the structure (based on plans, but also measurements on site), the proper inclusion of permanent loads and their effects on the stiffness, modelling of the support conditions, etc. The less accurate the model, the higher the model error that should be accounted for.

It should be pointed out that all results depend on the assumptions for the errors in the likelihood function (i.e. measurement and modelling errors). Other assumptions could be made, which might influence the shape and/or uncertainty of the posterior distribution. Nevertheless, more research is required on the appropriate quantification of these measurement and/or model errors.

XII.4 Value of Information

In the following, the VoI framework as introduced in Chapters IX and XI will be applied to the case study under consideration in this chapter. The limit states considered for evaluating the probability of failure will be given, the costs to be considered in the VoI analysis, as well as the different decision alternatives. The VoI will be evaluated for three monitoring strategies, and the influence of some of the input parameters will be investigated. Two situations will be considered, i.e. one with limited exposure to chlorides, where carbonation-induced corrosion will be more important, and one with high exposure to chlorides, where the bridge will be subjected to chloride-induced corrosion. It should be pointed out that the first situation corresponds to the actual exposure conditions of the bridge. Nevertheless, the two situations are considered in order to show the possible influence of the environment on the VoI. In the following analyses, the effect of a model error is not considered.

The VoI will be evaluated as explained in Chapter IX. Different input and assumptions are required for the evaluation of the VoI. The limit states to evaluate

the probability of failure are summarized in section XII.4.2. The different considered costs are given in section XII.4.3, and the different actions or decision alternatives are given in section XII.4.4. The variables that are updated based on the monitoring data are the initiation period and corrosion rate of the corrosion process. The prior models used for these degradation variables are summarized in section XII.4.1. The different considered monitoring strategies and data types are the same as applied in the previous sections:

- Static strains measured under proof loading measured at 20 or 52 locations with a measurement error of 3 µε;
- Natural frequencies and displacement mode shapes extracted from ambient vibration tests with accelerations measured at 36 locations and assumed errors in the likelihood function of 0.1% of the experimental frequency and 1% of the norm of the experimental mode shape;
- Natural frequencies and strain mode shapes extracted from ambient vibration tests with strains measured at 52 locations and assumed errors in the likelihood of 0.1% of the experimental frequency and 0.5 µε for the strains.

The results of the VoI analysis are given in section XII.4.5.

XII.4.1 Degradation of the bridge

The bridge is assumed to be subjected to degradation due to corrosion. Depending on the situation, chloride-induced corrosion or carbonation-induced corrosion is considered. The models for the initiation period and corrosion rate are already given in Chapter II. The assumed distributions are given in the following and are all based on (*fib*, 2006).

XII.4.1.1 Carbonation-induced corrosion

For carbonation-induced corrosion, the initiation period can be derived based on equation (II-7). Here, the concrete cover c is modelled by a truncated lognormal distribution with mean equal to the nominal value and a standard deviation of 8 mm. The upper limit is $5 \cdot c$, and a lognormal distribution is chosen since the concrete cover cannot be negative. When calculating the factor k_e (according to equation (II-4)), the reference value for the relative humidity RH_{ref} equals 65%, g_e equals 2.5, and f_e equals 5. For calculation of the factor k_c, b_c is modelled by a normal distribution with mean value -0.567 and standard deviation 0.024, and t_c equals 28 days. For R_{ACC}^{-1}, a value between 0.3e-11 and 80e-11 (mm²/years)/(kg/m³) is assumed. C_s is modelled by a normal distribution with mean 0.00082 and a standard deviation of 0.0001 kg/m³. In the function $W(t)$ (equation (II-6)), according to (Lay et al., 2003), ToW equals 0.75. The factor p_{SR} equals 1, and b_w is modelled by a normal distribution with mean 0.446 and standard deviation 0.163. Finally, t_0 equals 0.0767 years. Hence, following

distributions are found for different concrete covers (corresponding to the different concrete covers of the different reinforcement bars in the bridge):

- $c = 40$ mm → $T_i = $ LN(51 years; 21 years);
- $c = 35$ mm → $T_i = $ LN(47 years; 20 years);
- $c = 30$ mm → $T_i = $ LN(41 years; 21 years).

The corrosion rate depends on $V_{corr,a}$ ($\mu = 0.005$ mm/year, $\sigma = 0.003$ mm/year), ToW ($\mu = 0.75$, $\sigma = 0.2$) and α_p ($= 2$) (Duracrete, 2000; Lay et al., 2003). Based on a Taylor approximation and accounting for the fact that the corrosion rate cannot be negative, following distribution is assumed for the rate of reduction of the reinforcement radius: LN(0.0075, 0.005) [mm/year].

XII.4.1.2 Chloride-induced corrosion

For chloride-induced corrosion, the initiation period can be derived based on equation (II-1). Here, the concrete cover c has the same distribution as mentioned in the previous section. For calculation of the diffusion coefficient D according to equation (II-2), for D_{RCM} a value between 1.4e-12 and 25e-12 m²/s is assumed, or [44, 788] mm²/year. For a, a uniform distribution between 0.3 and 0.6 is assumed, $k_t = 1$ and $t_0 = 0.0767$ years. $T_{ref} = 293$ K, $b_e \sim N(4800, 700)$. $C_{cr} \sim N(0.6, 0.15)$, but with a lower boundary of 0.2 and an upper boundary of 2. For different concrete covers, following distributions are found:

- $c = 40$ mm → $T_i = $ LN(33 years; 26 years)
- $c = 35$ mm → $T_i = $ LN(29 years; 25 years)
- $c = 30$ mm → $T_i = $ LN(26 years; 23 years)

The corrosion rate depends on $V_{corr,a}$ ($\mu = 0.03$ mm/year, $\sigma = 0.02$ mm/year), ToW ($\mu = 0.75$, $\sigma = 0.2$) and α_p ($\mu = 9.28$, $\sigma = 4.04$). Based on a Taylor approximation applied to equation (II-1) and accounting for the fact that the corrosion rate cannot be negative, following distribution is assumed for the rate of reduction in reinforcement radius: LN(0.21, 0.18) [mm/year].

XII.4.2 Limit states to evaluate probability of failure

The most important failure mechanisms are retrieved from an analysis in DIANA FEA and appeared to be bending and shear failure of the longitudinal girders. The limit state equations are given by equations (XII-7) and (XII-8). The probability distributions used herein are given in Table XII-12.

$$g(\boldsymbol{X}, t) = K_{R,M} A_s(t) f_y \left(h - c - 0.5 \frac{A_s(t) f_y}{b f_c} \right) - K_{E,M}(M_G + M_Q) \qquad \text{(XII-7)}$$

$$g(\boldsymbol{X}, t) = K_{R,V} \left[\frac{A_{sw}(t)}{s} z f_y \cot(\theta) \right] - K_{E,V}(V_G + V_Q) \qquad \text{(XII-8)}$$

For the considered reinforcement scheme (with a double pair of stirrups close to the supports), in most situations bending failure will be the governing limit state.

In equations (XII-7) and (XII-8), $A_s(t)$ and $A_{sw}(t)$ represent the remaining area at time t of the longitudinal an shear reinforcement respectively. These can be evaluated based on equations (II-8) and (II-9). When evaluating the probability of failure, the distributions assigned to the variables in these degradation models are considered. When evaluating the probability of failure at timesteps before the measurements are performed, the prior distributions of the initiation period and corrosion rate will be assumed to evaluate the probability of failure. At timesteps after the measurements, the posterior distributions of the initiation period and corrosion rate are considered. Here, a constant corrosion rate over time is assumed. If a time-dependent model for the corrosion rate is desirable, this could also be incorporated in the analysis.

XII.4.3 Costs in the VoI analysis

XII.4.3.1 Cost of failure

The cost of failure can be calculated as a function of the cost of the bridge itself (i.e. the total bridge value). For the bridge under investigation, the cost of the bridge itself (bridge deck, abutments, finishing) and removal of the old bridge mounts up to € 1 700 000.

The costs of failure also include indirect costs such as property damage, traffic closure, traffic jams on alternate routes, loss of reputation, etc. Besides these economic costs, bridge failures can also cause fatalities. Estimating all these costs for an individual bridge is very hard. Because of this reason, authors often estimate the failure costs as a percentage of the total bridge value, such as in the SERON project (SeRON, 2012), where the total cost rises to 700% of the bridge value. Thöns and Stewart (2019) estimate the total costs up to 5 times the bridge value in case of bridge closure prior to collapse, and up to 25 times the bridge value for iconic bridge failure. In this work, based on the mentioned sources, a failure cost of 10 million euros will be assumed.

XII.4.3.2 Cost of repair

Repairs of the bridge are based on the desire to keep the risk of falling concrete debris as small as possible, even for bridges in the worst condition. Costs for required sudden repairs to maintain this condition are in the range of € 10 000 to € 100 000 (Ministry of Public Works Flanders (MOW), 2020, personal communcation). However, in some cases, the total costs of these repairs can even exceed the costs of a new bridge. Examples of advanced repairs performed are

scraping off the road surface, cathodic protection on the bridge pylons, new joints in the bridge deck, steel reinforcement at the sides of the bridge deck, etc.

When repairs/maintenance are planned, they can often be performed in the weekends or during the night, when less traffic is present on the roads. As such, the costs of blocking the roads will be much smaller than in the cost of failure. The cost of building a new bridge (without failure), is estimated as € 1 700 000. The cost of just upgrading the structure to an increased reliability (see further) equals € 340 000. This cost includes the costs corresponding to economic damage resulting from roadblock during the upgrading works and the costs of the repairs itself. These costs are based on (Skokandić and Mandić Ivanković, 2021) and (Kong and Frangopol, 2004) respectively.

XII.4.3.3 Cost of monitoring

For the dynamic measurements, following costs are assumed:
- € 10 000 for triaxial acceleration measurements on 36 locations;
- € 10 000 for modal strain measurements with optic fibres;
- € 20 000 for a combination of acceleration and strain measurements in ambient conditions.

For the static strain measurements, following costs are assumed:
- € 20 000 for 20 strain sensors;
- € 28 000 for 52 strain sensors.

These costs are based on estimations by research groups involved at KU Leuven and Ghent University.

To install the sensors, the bridge itself and/or the road underneath the bridge might need to be closed for traffic. To account for the economic damage due to roadblock, a cost of € 30 000 is added to the abovementioned costs of monitoring.

Table XII-12: Probability distributions used in the evaluation of the limit states

Symbol [Unit]	Definition	Dist.	Mean	Std.	Ref.
$K_{R,M}$ [-]	Resistance model uncertainty bending	LN	1.2	0.18	(JCSS, 2001)
A_s [mm²]	Reinforcement steel section	-	5026	-	-
f_y [MPa]	Yield strength of steel	LN	560	30	(Holicky and Sykora, 2010)
f_c [MPa]	Concrete compressive strength	LN	39.1	7.03	(Holicky and Sykora, 2010)
h [mm]	Beam height	-	885	-	-
c [mm]	Concrete cover	-	40	-	-
b [mm]	Beam width	-	500	-	-
$K_{E,M}$ [-]	Load model uncertainty for bending	LN	1	0.1	(JCSS, 2001)
M_G [Nmm]	Bending moment due to permanent loads	N	G_k	$0.1G_k$	(Holicky and Sykora, 2010)
M_Q [Nmm]	Bending moment due to variable loads	GU	$0.728Q_k$	$0.146Q_k$	(Caspeele et al., 2016)
$K_{R,V}$ [-]	Resistance model uncertainty for shear	LN	1.4	0.35	(JCSS, 2001)
ρ_l [-]	Reinforcement ratio	-	0.02	-	-
d [mm]	Effective depth of reinforcement	-	845	-	-
$K_{E,V}$ [-]	Load model uncertainty for shear	LN	1	0.1	(JCSS, 2001)
V_G [N]	Shear load effect due to permanent loads	N	G_k	$0.1G_k$	(Holicky and Sykora, 2010)
V_Q [N]	Shear load effect due to variable loads	GU	$0.728Q_k$	$0.146Q_k$	(Caspeele et al., 2016)
A_{sw} [mm²]	Shear reinforcement section	-	452	-	-
s [mm]	Spacing between stirrups	-	200	-	-
$cot(\theta)$ [-]	Cotangent of angle of shear cracks	-	1.19	-	(Ministry of Public Works Flanders (MOW), 2020)

XII.4.4 Decision alternatives

Decisions can be made based on reliability thresholds. For these reliability thresholds, values can be found in *fib* bulletin 80 (Caspeele et al., 2016), the draft of *fib* Model Code 2020 (TG 3.1 *fib* MC 2020, 2020) and (ISO, 2015). These sources provide different values for the critical reliability indices, which will be summarized in the following.

When considering the draft of *fib* Model Code 2020 (TG 3.1 *fib* MC 2020, 2020), the bridge under consideration is of consequence class 2 (CC2), and for existing structures a large relative cost of safety measures might be assumed. This leads to a reliability index of 3.3 based on economic optimization only. When there are multiple equally important failure modes, a value of 0.5 should be added to this reliability threshold. Regarding the human safety requirements, a critical reliability index of 3.57 is proposed. When upgrading the structure, compliance with design levels is required, and hence the structure should be upgraded at least to a reliability level of 4.2. All these reliability levels are given for a reference period of one year.

When looking at *fib* bulletin 80 (Caspeele et al., 2016), a reliability index of 2.3 is proposed for the economic criterion and a reference period of 50 years. For the human safety criterion, *fib* bulletin 80 gives equation (XII-9).

$$\beta_{Human\ safety} = -\Phi^{-1}\left(\frac{2.75 \cdot 10^{-5}(0.09 \cdot L)^{-2}t_{ref}}{0.055}\right) \qquad \text{(XII-9)}$$

In this equation, L is the span length of the bridge, which equals 13 m. According to *fib* bulletin 80, the reference period t_{ref} is taken equal to the remaining service life and at maximum equal to 50 years. This leads to a reliability index of 2.1. Hence, the economic criterion is the governing criterion, and the critical reliability index equals 2.3. When inserting a reference period of 1 year in equation (XII-9), a reliability index of 3.4 is found. The latter is in line with the reliability index provided by the draft version of *fib* Model Code 2020. *fib* bulletin 80 also provides a reliability index for upgrading of the structure, which equals 3.3 for consequence class 2 and a reference period of 50 years. For a reference period of one year, a corresponding reliability index of 3.5 is found when based on imposed loads and a reliability index of 4.3 when based on climatic loads. This calculation of the reliability index is performed based on equation (XII-10), with $k = 1$ and $n = 50$ for climatic loads, and $k = 5$ and $n = 10$ for imposed loads.

$$\Phi(\beta_{50}) = \Phi(\beta_1)^{\frac{n}{k}} \qquad \text{(XII-10)}$$

In the following, a reference period of 1 year will be assumed and the reliability thresholds provided in the draft of *fib* Model Code 2020 will be applied.

Following action alternatives will be considered:
1) Do nothing;
2) Upgrade the structure to β_{up} (4.2) if $\beta < \beta_{crit}$ (3.57);
3) Replace the structure by a new one if $\beta < \beta_{crit}$ (3.57).

These action alternatives are based on the reliability index only, and are also applied in the prior situation, i.e. without measurements. In the pre-posterior situation, the measurements are additionally assumed to trigger an action (i.e. cathodic protection) if the following criterion is met:

$$P[x(t) > x_{crit}] \geq P_{crit} \qquad \text{(XII-11)}$$

The critical reduction in rebar radius x_{crit} is determined based on (Andrade and Izquierdo, 2020), where for pitting corrosion a critical reduction in rebar radius of 0.1 to 0.5 mm is proposed, and for general corrosion a reduction of 0.01 to 0.05 mm. For the probability P_{crit}, different values will be assumed, i.e. 25%, 50% and 75%. For each element in which the structure is discretized the probability that the reduction in reinforcement radius is larger than x_{crit} is evaluated, and if the probability exceeds P_{crit}, cathodic protection is applied to the considered element. The corresponding costs for cathodic protection are also taken into account. In this work, these costs are based on (Polder et al., 2016) and assumed equal to € 125/m² for application of the cathodic protection itself, and € 100/year for checking the equipment. These costs correspond to those of an active cathodic protection and are also in line with those mentioned in (Wyatt, 1993).

Another possible trigger for an action after monitoring is based on the following criterion:

$$P[\alpha > \alpha_{crit}] \geq P_{crit} \qquad \text{(XII-12)}$$

Here, the critical corrosion degree α_{crit} is the one corresponding to the critical reliability index as provided above. The value of P_{crit} will be assumed the same as in criterion (XII-11). For each element in which the structure is discretized $P[\alpha > \alpha_{crit}]$ is evaluated, and if it exceeds P_{crit}, cathodic protection is applied, but also additional strengthening is provided at the considered location. The corresponding costs of strengthening and cathodic protection are also taken into account.

XII.4.5 Results of the VoI analysis

In this section, the results of the VoI analysis based on the input provided above are summarized. This is done for the two considered situations:
1. Carbonation-induced corrosion;
2. Chloride-induced corrosion.

The whole service life of the structure is considered, i.e. between the time of construction ($t = 0$ years) and the anticipated service life ($t = 100$ years). Different

points in time to perform monitoring are considered. The investigated points in time lie in between the time at which the reliability index starts to decrease in the prior analysis (which depends on the investigated situation) and the anticipated service life of 100 years.

XII.4.5.1 Situation 1 – Carbonation-induced corrosion

In the first situation, the bridge is considered to be located in an environment where carbonation will be the most important phenomenon inducing corrosion. For the three considered monitoring strategies, the VoI is visualized in Figure XII-27 for different points in time to perform the monitoring, ranging between 50 years and 90 years, in steps of 10 years. The lower bound is chosen based on the mean of the initiation period and the point in time at which the reliability index starts to decrease in the prior analysis. The upper bound is chosen to cover the whole service life (100 years) but not the final value of 100 years, since no monitoring will be performed in the last year. The resulting VoI is always negative, since the corrosion process proceeds rather slow (because of the assumed corrosion due to carbonation), and the results from the measurements would only reveal very small corrosion degrees without triggering any intervention. For all sampled monitoring outcomes, the optimal action remains the same as the prior optimal action, i.e. upgrade the structure to β_{up} if $\beta < \beta_{crit}$. Hence, the quantitative measurements are found not worth their costs. This is also why the static strain measurements at 52 locations result in the most negative VoI, since they are most expensive.

As mentioned above, the influence of the assumption on P_{crit} has also been investigated, by changing the value of 50% to 25% and 75%. However, for the case under investigation, the influence on the VoI is limited. In addition, the influence of changing the cost of failure has been investigated. For this purpose, C_{F0} is once multiplied by 10 and once divided by 2. For this specific case, the influence on the VoI is limited.
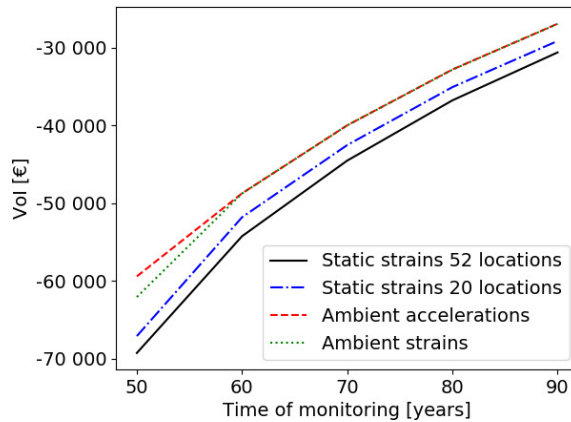
Figure XII-27: VoI as a function of the point in time at which monitoring is performed for the different types of measurements – situation 1: carbonation-induced corrosion

XII.4.5.2 Situation 2 – Chloride-induced corrosion

For the second situation, the bridge is assumed to be placed in an environment susceptible to chlorides, and the corrosion process is modelled with the initiation period and corrosion rate for chloride-induced corrosion. Critical values for the reliability index will be reached much earlier, and hence the considered times of monitoring are between $t = 25$ years and 90 years. These bounds are determined based on the same criteria as for situation 1.

First, the VoI for the different inspection strategies is evaluated and visualized in Figure XII-28. Here it can be seen that the VoI differs significantly from the case with exposure to carbonation-induced corrosion (situation 1). The largest values for the VoI are found at 40 years. The VoI is largest for the situations where updating is performed based on natural frequencies either combined with strain mode shapes or displacement mode shapes. This can be ascribed to the fact that after monitoring, a larger part of the structure is repaired/maintained based on criterion (XII-11) compared to updating based on the static strains, as can be seen in Figure XII-29, where the number of repaired elements is provided as the mean over the different sampled monitoring outcomes. Also, for updating based on these modal data types, more often another action than the prior optimal one (i.e. upgrade the structure) is chosen, as can be seen in Figure XII-30. It should also be pointed out that the cost of the dynamic monitoring techniques is estimated smaller than those of the static strain measurements.
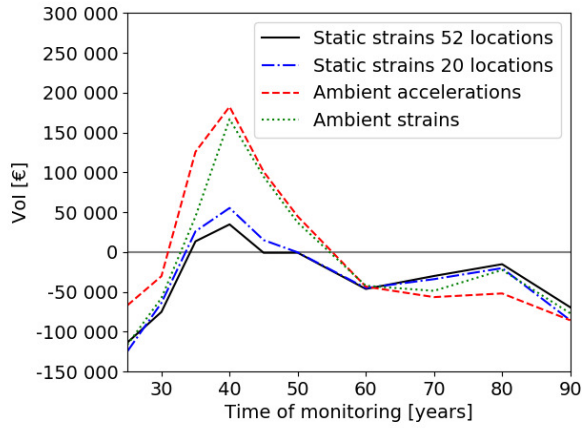
Figure XII-28: Influence of the point in time at which monitoring is performed on the VoI for different monitoring techniques – situation 2: chloride-induced corrosion
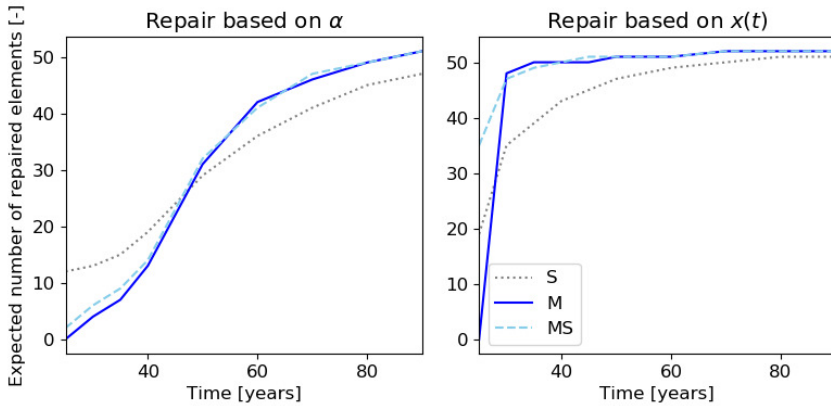

Figure XII-29: Influence of monitoring data (S = static strains, M = natural frequencies + displacement mode shapes, and MS = natural frequencies + strain mode shapes) on the number of repaired elements after inspection. The number of repaired elements is provided as the mean over the different sampled monitoring outcomes.
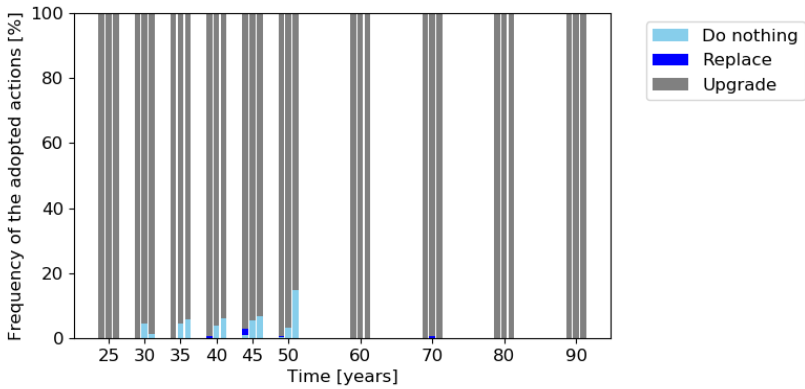
Figure XII-30: Influence of monitoring data on the chosen action as a function of time. The left bar at each timestep corresponds to static strain measurements, the middle bar to updating based on natural frequencies and displacement mode shapes, and the right bar to updating based on natural frequencies and strain mode shapes.

Also for this case, the influence of the choice for P_{crit} is investigated, and these results are visualized in Figure XII-31 for the static strain measurements. Here it can be seen that for P_{crit} equal to 25% a higher VoI is found at the earlier timesteps. This can be explained by looking at Figure XII-32, where for $P_{crit} = 25\%$, the optimal action changes to 'Do nothing' for some of the sampled inspection outcomes, where this is not the case for the higher values of P_{crit}. When P_{crit} is increased to 75%, less elements will be repaired or maintained after the inspection (as visible in Figure XII-33), and a smaller VoI is found compared to $P_{crit} = 50\%$.
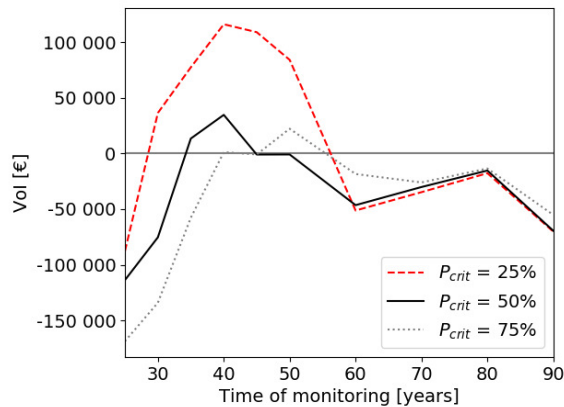

Figure XII-31: Influence of P_{crit} on the VoI for static strain measurements as a function of the point in time at which monitoring is performed – situation 2: chloride-induced corrosion
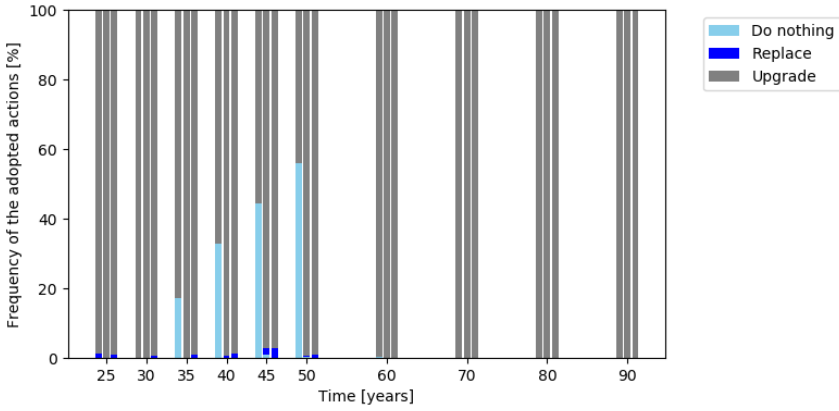
Figure XII-32: Influence of P_{crit} on the chosen action as a function of time when static strain measurements are performed (situation 2). The left bar at each timestep corresponds to $P_{crit} = 25\%$, the middle bar to $P_{crit} = 50\%$, and the right bar to $P_{crit} = 75\%$.
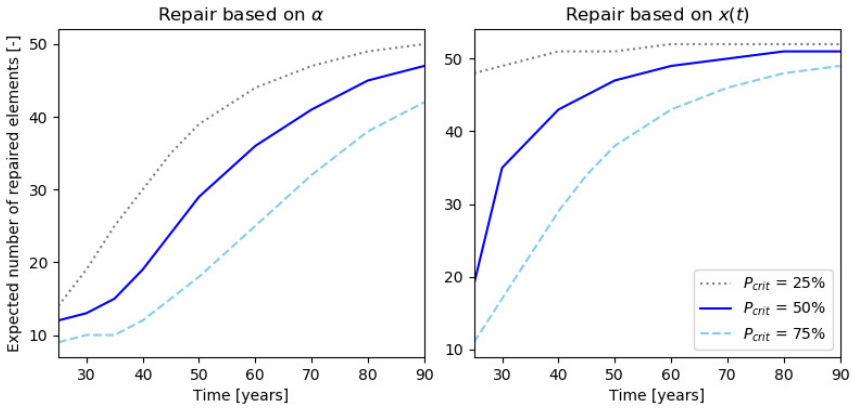
Figure XII-33: Influence of P_{crit} on the number of repaired elements after monitoring based on static strains measured at different points in time (situation 2). The number of repaired elements is provided as the mean over the different sampled monitoring outcomes.

In addition, the influence of the cost of failure has been investigated. For this purpose, the cost of failure is once divided by 2, once divided by 5, once multiplied with 5, and once multiplied with 10. The influence on the VoI is given in Figure XII-34 for static strain measurements. Here it can be seen that the influence of overestimating the failure cost by a factor 5 or 10 is relatively small. An underestimation of the failure cost by a factor 2 also does not largely influence the resulting VoI. When underestimating the failure cost by a factor 5, the VoI

drastically increases. This could be ascribed to the fact that for a failure cost reduced by a factor 5, the posterior most optimal action is to do nothing in all cases and the prior most optimal action is to upgrade the structure to β_{up} if $\beta < \beta_{crit}$. The general behaviour of the VoI remains the same in all cases: starting at a negative VoI and then increasing over time until a maximum is reached, after which the VoI starts to decrease again.

The influence of increasing the cost of failure with a factor 10 has also been investigated for the case where modal data is collected. The influence hereof is visualized in Figure XII-35. Similar as for the static strain data, the influence of increasing the cost of failure is limited until $t = 40$ years. At later timesteps, the VoI is larger for the higher failure costs. It can also be seen that when the failure cost is increased, the optimal inspection strategy remains unaltered compared to Figure XII-28.
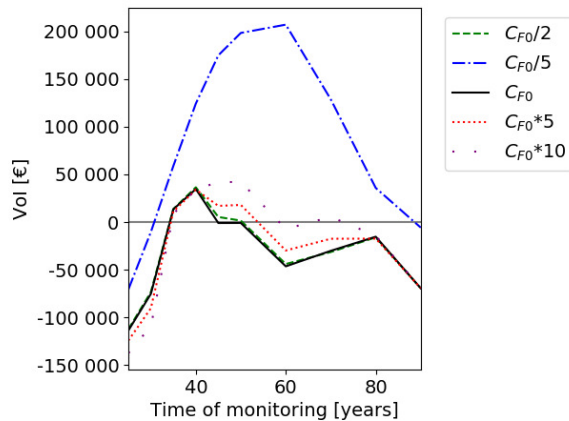

Figure XII-34: Influence of the cost of failure on the VoI for static strain measurements as a function of the point in time at which monitoring is performed – situation 2: chloride-induced corrosion
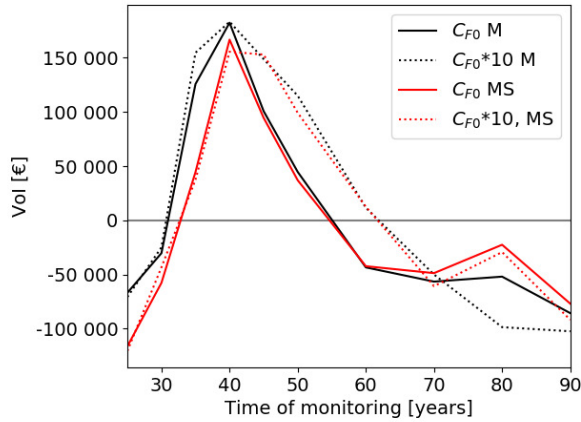
Figure XII-35: Influence of increasing the failure cost when considering natural frequencies combined either with displacement mode shapes (M) or with strain mode shapes (MS) – situation 2: chloride-induced corrosion

XII.4.6 Discussion

In this section, the VoI has been evaluated for the bridge under investigation. Different monitoring strategies are considered and different points in time at which monitoring can be performed are evaluated. The influence of some parameters, such as the failure cost and the threshold for performing an action based on the monitoring results (P_{crit}) has been evaluated. Two cases are considered: carbonation-induced corrosion and chloride-induced corrosion. In the first case, the degradation rate is very small and no repairs are required. Monitoring does not induce an intervention and hence will lead to a negative VoI. This is also the reason why changing some of the parameters in the analysis has a limited effect on the VoI. In the case of chloride-induced corrosion, a positive VoI is found for some timesteps, and the VoI reaches a maximum. This could be ascribed to the fact that monitoring triggers an intervention for this situation.

In the analysis in Chapter XI, it was found that changing the repair model could have a large influence on the VoI and on the most optimal monitoring strategy. In the current analysis, it was also found that in the case of chloride-induced corrosion the value assigned to P_{crit} influences the VoI. Furthermore, in Chapter XI it was found that if the cost of failure increases the VoI increases. However, this does not seem a general trend when considering the results in the current chapter. Hence, it could be concluded that for many of these influences, it is difficult to find a general pattern. The results might significantly depend on the considered structure, costs, decisions, prior models, etc., and preferably, for each situation a sensitivity analysis to the most important input variables should be performed.

All results provided in this chapter depend on the assumptions made for the errors in the likelihood function (i.e. measurement and modelling errors). Other assumptions could be made here, which might influence the shape and/or uncertainty of the posterior distribution and the resulting VoI. Nevertheless, more research is required on the appropriate quantification of these measurement and/or model errors.

XII.5 References

Andrade, C., Izquierdo, D., 2020. Propagation period modeling and limit state of degradation. Struct. Concr. 21, 1720–1731.

Bautista-De Castro, Á., Sánchez-Aparicio, L.J., Ramos, L.F., Sena-Cruz, J., González-Aguilera, D., 2018. Integrating geomatic approaches, Operational Modal Analysis, advanced numerical and updating methods to evaluate the current safety conditions of the historical Bôco Bridge. Constr. Build. Mater. 158, 961–984.

Brownjohn, J.M.W., Xia, P.Q., Hao, H., Xia, Y., 2001. Civil structure condition assessment by FE model updating: Methodology and case studies. Finite Elem. Anal. Des. 37, 761–775.

Bucur, C., Bucur, V.M., Moise, I., 2008. The Influence of the Bridge Skewness on the Dynamic Response To the Action of Mobile Loadings, in: ANNALS of the ORADEA UNIVERSITY Fascicle of Management and Technological Engineering, Volume VII (XVII), 2008. pp. 132–139.

Caspeele, R., Steenbergen, R., Sykora, M., 2016. *fib* Bulletin 80: Partial factor methods for existing concrete structures.

DIANA FEA BV, 2019. DIANA User's Manual - Release 10.3 [WWW Document]. URL https://dianafea.com/manuals/d103/Diana.html

Duracrete, 2000. DuraCrete - Probabilistic Performance based Durability Design of Concrete Structures. Report No BE9521347.

fib, 2006. *fib* Bulletin 34: Model code for service life design. Lausanne.

Harba, I.S.I., 2011. Effect of skew angle on behavior of simply supported R. C. T-beam bridge decks. J. Eng. Appl. Sci. 6, 1–14.

Heitner, B., OBrien, E.J., Yalamas, T., Schoefs, F., Leahy, C., Décatoire, R., 2019. Updating probabilities of bridge reinforcement corrosion using health monitoring data. Eng. Struct. 190, 41–51.

Holicky, M., Sykora, M., 2010. Stochastic models in analysis of structural reliability, in: Proceedings of the International Symposium on Stochastic Models in Reliability Engineering, Life Sciences and Operations Management. pp. 428–439.

ISO, 2015. ISO 2394:2015: General principles on reliability for structures (4th ed). Geneva, Switzerland.

JCSS, 2001. Probabilistic Model Code.

Kong, J.S., Frangopol, D.M., 2004. Cost–Reliability Interaction in Life-Cycle Cost Optimization of Deteriorating Structures. J. Struct. Eng. 130, 1704–

1712.

Lay, S., Schießl, P., Cairns, J., 2003. Lifecon Deliverable D3.2.

Liu, H., Wang, H., Tan, G., Liu, Z., Cheng, Y., 2017. Vibration Analysis of Reinforced Concrete Simply Supported Beam versus Variation Temperature. Shock Vib. 2017, 4931749.

Mankar, A., Bayane, I., Sørensen, J.D., Brühwiler, E., 2019. Probabilistic reliability framework for assessment of concrete fatigue of existing RC bridge deck slabs using data from monitoring. Eng. Struct. 201, 109788.

Nguyen, K., Velarde, C., Goicolea, J.M., 2019. Analytical and simplified models for dynamic analysis of short skew bridges under moving loads. Adv. Struct. Eng. 22, 2076–2088.

Ouzaa, K., Oucif, C., 2019. Numerical model for prediction of corrosion of steel reinforcements in reinforced concrete structures. Undergr. Sp. 4, 72–77.

Polder, R., Pan, Y., Courage, W., Peelen, W., 2016. Preliminary study of life cycle cost of preventive measures and repair options for corrosion in concrete infrastructure. Heron 61, 1–13.

SeRON, 2012. Security of Road Networks: Final Report.

Skokandić, D., Mandić Ivanković, A., 2021. Value of additional traffic data in the context of service-life management. Struct. Infrastruct. Eng.

Sousa, H., Rozsas, A., Slobbe, A., Courage, W., 2020. A novel pro-active approach towards SHM-based bridge management supported by FE analysis and Bayesian methods. Struct. Infrastruct. Eng. 16, 233–246.

TG 3.1 *fib* MC 2020, 2020. Model Code 2020 - Section 5.2 - draft Oct 2020.

Thöns, S., Stewart, M.G., 2019. On decision optimality of terrorism risk mitigation measures for iconic bridges. Reliab. Eng. Syst. Saf. 188, 574–583.

Van Bogaert, P., 2003. Bruggenbouw - vol I - Inleiding Bruggenbouw. Ghent University, Ghent, Belgium. (In Dutch)

Wyatt, B.S., 1993. Cathodic protection of steel in concrete. Corros. Sci. 35, 1601–1615.

Zapico, J.L., González, M.P., Friswell, M.I., Taylor, C.A., Crewe, A.J., 2003. Finite element model updating of a small scale bridge. J. Sound Vib. 268, 993–1012.

General conclusions and further research

CHAPTER XIII

General conclusions and further research

"We must accept the end of something in order to begin to build something new."
- Rushil Ravi

XIII.1 General conclusions

As a first part of this final chapter, some major findings and conclusions of this PhD research are highlighted. In section XIII.2, also some general recommendations for further research are provided.

XIII.1.1 Bayesian updating based on monitoring data

To gain information on the structural behaviour of an existing structure, measurements can be performed. These often lead to a lot of data, for which it remains unclear how to use this data in asset management strategies for the planning of maintenance activities. In current practice, mostly data-based methods are applied, triggering actions once the measurement data cross a predefined threshold. However, this procedure does not allow to predict the future behaviour of the structure and to evaluate its time-dependent reliability and corresponding remaining service life. For the latter, model-based methods are more appropriate. Here, data is used to improve a model of the investigated structure, which can then be used to make predictions about the structural behaviour. If a time-dependent deterioration model is also included, a more accurate prediction of the remaining service life can also be achieved. In this work, it has been illustrated how different types of data can be used to update the probabilistic distributions appearing in the (time-dependent) model of a degrading structure based on a Bayesian procedure. Prior probabilistic distributions for the variables in the degradation models are updated to posterior distributions by properly accounting for the monitoring data and the associated uncertainties. Based on the resulting posterior distributions of the variables in the degradation models, the remaining service life can be predicted more accurately. Both reinforced concrete structures and prestressed concrete structures have been studied, including different types of data and combinations of data types. Moreover, the spatial correlation of the degradation process is also accounted for by modelling (some of) the variables in the degradation models by random fields. Due to the correlation modelled by these random fields, inspections or measurements at one location might also provide information on another non-inspected location, if the correlation between both locations is sufficiently high.

In this thesis, it has been illustrated how different data types can be used to update the initiation period and corrosion rate, and hence the corresponding corrosion degree, of a corroding reinforced concrete structure. To account for the spatial correlation of the corrosion degree along the structure, the initiation period and corrosion rate are modelled with random fields. Hence, these random fields of the initiation period and corrosion rate are updated based on the different data types, resulting in a posterior distribution of the corrosion degree at the considered timestep. It was shown how static displacement data generally leads to a rather vague posterior distribution of the corrosion degree, due to the limited dependence on local stiffness changes. Static strain data on the other hand can provide a locally

more accurate estimate of the actual corrosion degree, with a posterior mean corrosion degree close to the actual value and a small posterior uncertainty. However, the disadvantage is that for statically determinate structures the static strains only depend on the local stiffness and do not provide any information on locations not equipped with strain gauges. Only for locations not equipped with strain gauges that lie close to the measurement locations, limited information on the stiffness can be retrieved due to the random field modelling and the assumed correlation. Hence, the critical locations where static strain measurements should be performed are preferably determined beforehand. A possible solution is to derive these locations based on the posterior distributions derived from modal data retrieved from acceleration measurements or strain measurements with optic fibres. Natural frequencies depend on the general stiffness of the structure, and local changes in stiffness might result in changes in the displacement mode shapes or strain mode shapes. As such, localization of damage is enabled. Nevertheless, it was found that updating based on these modal data generally leads to a more vague posterior distribution compared to a posterior distribution derived based on static strain measurements. There is a larger deviation between the posterior mean corrosion degree and the actual value, and the posterior uncertainty is still relatively large. It has been illustrated in this work how combining information from both data types leads to a more accurate posterior distribution compared to considering each of them separately.

Besides combining dynamic and static data, also visual observations can be included when determining the posterior distribution of the corrosion degree. When investigating a structure, visual signs of corrosion (rust stains, corrosion cracks, etc.) can be present. Generally, these have a filtering effect on the initiation period (lower initiation periods are excluded) and lead to larger posterior corrosion degrees. It has been illustrated by several examples how combining the visual observations with the static or modal data leads to an improved posterior distribution compared to the one found when the visual observations are not considered. The benefit of including the visual observations is largest in the case where only including the static or dynamic data leads to a relatively vague posterior distribution, or if the model used in the likelihood function deviates significantly from the actual structure under investigation. The latter has been illustrated by the case study bridge considered in Chapter XII, where the influence of a model error by neglecting the skewness of the bridge has been investigated (cfr. infra). Also in Chapter VII, it has been illustrated that using more informative prior distributions, defined based on information from visual observations, leads to a posterior distribution better approximating the actual value.

The Bayesian updating procedure has also been applied to some simplified prestressed structures. Here, only static strain data has been used due to the limited influence of corrosion of prestressed structures on the modal data. For the

investigated prestressed beam, the corrosion degree of the prestressing reinforcement could be updated based on the static strain data, together with an underlying distribution for the initiation period and degradation rate. For the investigated post-tensioned girder, the corrosion degree of both the prestressing reinforcement and the unstressed reinforcement bars has been updated based on the static strain data. Here, a grouted as well as an ungrouted duct have been considered. In the first situation, the corrosion degree of the unstressed reinforcement bars could be updated based on the strain data, but not the corrosion degree of the prestressing steel. This could be ascribed to the fact that the latter only influences the strains to a noticeable extent once the strands have failed. When the duct is ungrouted, vague posterior distributions are found for the corrosion degree of both the unstressed reinforcement and the prestressing steel, but still approaching the actual underlying value. However, this only holds for very accurate strain measurements and an accurate inverse model, resulting in a small error to be considered in the likelihood function. If the error in the likelihood function increases, e.g. due to the use of less accurate measuring techniques or less accurate inverse models, the posterior distribution is almost equal to the prior distribution, due to the limited strain differences between the corroded case and the uncorroded case. In addition, the remaining prestress of two 70-year old post-tensioned beams tested up to failure has been estimated by a Bayesian procedure. The most likely value for the prestress has determined for both beams based on three points in an experimental load-displacement curve, i.e. the cracking moment, the moment of reopening of the cracks and the load corresponding to a displacement of 40 mm (i.e. in the non-linear branch). The obtained results have been verified based on the load-displacement curve of the finite element model, accounting for the a posteriori most probable prestress. The obtained load-displacement curve closely approximated the experimentally observed curve. An important advantage of the applied procedure is that besides the most probable value of the remaining prestress, also the uncertainty on this value can be estimated.

As already pointed out, in the case study in Chapter XII, it has been illustrated that it is important that the model used in the Bayesian updating procedure resembles the actual structure as good as possible. Simplifications that are allowed in the design can have large consequences when also applied in the inverse model used for the Bayesian analysis. It can lead to posterior distributions largely deviating from the actual situation because all differences between the actual structure and the model are ascribed to the variables to be updated, in this case the corrosion variables. The error can be limited to some extent by application of more informative priors, e.g. also accounting for visual signs of corrosion cracking (cfr. supra).

In most examples, the posterior distribution that was visualized was the distribution of the corrosion degree of the longitudinal reinforcement. Nevertheless, due to the smaller concrete cover, the shear reinforcement might be more susceptible to corrosion. Since not directly the corrosion degree is inferred, but the distributions of the variables describing the initiation phase and propagation phase, these can also be used to evaluate the posterior distribution of the corrosion degree of the shear reinforcement by applying the models provided in Chapter II and accounting for the reduced concrete cover of this shear reinforcement.

All results from Bayesian inference in this work depend on the assumptions made for the errors in the likelihood function (i.e. measurement and modelling errors). In the different chapters, these assumptions and their influence on the results have been discussed. Other assumptions could be made for the measurement and modelling errors, which might influence the shape and/ uncertainty of the posterior distribution. Nevertheless, more research is required on the appropriate quantification of these measurement and/or model errors.

In the Bayesian analyses performed in this work, a near-perfect relation (with some model and measurement error) is considered between the corrosion level and the monitoring responses. This relation was validated with finite element models in Chapter XII, yet the experiments in Chapter VII showed a different view. On this aspect, some critical notes could be made. First of all, the influence of the cracking direction could be considered, where corrosion mostly induces longitudinal cracks. As a consequence, corrosion will have a lager influence on lateral bending modes than on vertical bending modes. Moreover, as stated in Chapter II, corrosion also influences the bond between steel and concrete, which can also influence the stiffness and the behaviour of the structure. Furthermore, corrosion is not the only factor influencing the structural responses. There might also be influences from the environment, effects from creep and shrinkage, etc. When performing Bayesian inference based on the measured responses, these effects should either be filtered out from the data, also considered in the model, or accounted for by introducing an additional model uncertainty. This model uncertainty can be rather large, as also has become apparent from the different analyses considered in this work, especially when looking at the results from the experimental investigations in Chapter VII. Also the choice for the type of sensors and the history of the structure (e.g. handling of the beams in the case of the experiments) influence the measurement output. Furthermore, the response for a certain corrosion degree will also depend on the layout of the reinforcement. How a given corrosion degree influences the structural behaviour will be different for different structures with different reinforcement layouts. Important influences here are the position of the longitudinal reinforcement, the presence/absence of stirrups, etc. There are two possible ways to cope with these issues: either the model is

refined, taking into account all these possible influences, either a model error is included. Very often, a combination of both will be required, and there will be some kind of trade-off, where a more accurate model will lead to a lower model error and vice versa.

XIII.1.2 Experimental investigations

In Chapter VII, the results of an experimental campaign have been discussed. In this experimental campaign, reinforced concrete beams have been subjected to accelerated corrosion by application of a salt solution and a direct current.

Static strains have been measured on the corroded beams, under a load not exceeding the cracking load. These static strains have been considered in a Bayesian inference procedure applied to update the distribution of the corrosion degree of the beams (uniform along the beam). When updating the distribution of the corrosion degree based on the static strains and assuming both a vague and a more informative prior distribution for the corrosion degree, quite good results were found for the posterior distribution. Furthermore, using a more informative prior distribution showed to be beneficial in the identification of the corrosion degrees.

The beams have also been tested until failure. When looking at the resulting load-displacement curves and the corresponding finite element simulations, the effects of spatial variation of the corrosion process become very clear. When the corrosion degree would be determined very locally by removing the cover concrete, and this would be done at a location with a limited corrosion degree, a large overestimation of the failure load might be achieved.

Dynamic tests have also been performed on the beams. Considering the resulting modal data, natural frequencies decreased for a reinforced concrete beam subjected to corrosion. Nevertheless, also the uncorroded reference beam showed a decrease in natural frequencies, due to the young age of the concrete. This effect should be accounted for when estimating the corrosion degree based on the natural frequencies. When considering strain mode shapes and displacement mode shapes, no effects of the corrosion process were present, due to the application of the salt solution along the whole length of the beam.

Further, this experimental campaign provides some important lessons for future experiments to be performed. Amongst others, when looking at the displacement mode shapes, there are very local changes observed which could not be ascribed to the corrosion process. Hence, caution should be paid to attachment of the accelerometers and the plates. Similarly, for the strain mode shapes proper clamping of the fibres should be assured, and contact with the corrosion products

should be avoided. Moreover, the optic fibres are very sensitive to breakage and should be properly protected.

XIII.1.3 Optimization of monitoring strategies

Monitoring strategies can be optimized by evaluation of the Value of Information (VoI) for different strategies, and choosing the strategy with the largest VoI as the most optimal one. It has been shown how the pre-posterior framework for the evaluation of this VoI can be extended in order to account for the time-dependent and spatial character of degradation in RC structures. To account for the time-dependent character, calculations of the service life cost are required over the anticipated service life of the structure under investigation, and time-dependent models should be applied, from which the variables could be updated based on the monitoring data. To account for the spatial behaviour, the use of random fields and/or hyperparameters is suggested to model spatial correlation of the variables of interest. As such, inspections or measurements at one location might also provide information about other, non-inspected but correlated locations.

Evaluating the VoI requires a high computational effort since calculations over the whole service life are required, and updating based on monitoring data is often performed based on MCMC sampling, which requires a lot of iterations. Moreover, for optimizing a monitoring strategy, many evaluations of the VoI are required, which can result in a large computational demand. In Chapter XI, suggestions are made to reduce the computational cost of the VoI calculation and of the optimization of monitoring strategies.

One of the suggestions to reduce the computational effort when optimizing a monitoring strategy is to determine the optimal sensor locations beforehand based on a greedy search procedure and the information entropy (as explained in Chapter X). As such, the VoI should only be evaluated for different numbers of sensors and not for different sensor locations, drastically reducing the required number of (computationally expensive) evaluations of the VoI. The procedure developed in this work differs from existing literature since it is derived for optimisation of the sensor positions when the purpose is to update random fields of the corrosion variables instead of general stiffness distributions that are not correlated (i.e. no random fields are used to model correlation between the stiffness at different locations along the structure). Furthermore, the procedure is based on a finite element model, without the need of fitting a meta-model to it. Consequently, optimal sensor positions can be derived for the extraction of displacement mode shapes, strain mode shapes and static strains.

Another way to limit the computational effort is to use approximations of the posterior distribution instead of sampling based methods. It has been illustrated that the error made by this approximation both on the posterior distribution and on

the estimate of the VoI is negligible. However, it is suggested to always check this for the case under investigation.

Also, the influence of varying some of the input parameters in the VoI analysis has been investigated, such as the cost of failure, the cost of repair, the assumed prior distributions for the corrosion variables, etc. It has been illustrated that the effect can be rather large and caution should be made when selecting the values for the input parameters. In case of doubt, it is advised to perform a sensitivity analysis.

Even though the VoI approach developed in this work requires a rather high computational cost, this cost is generally very small compared to the cost of the actual monitoring system or the cost of failure of critical infrastructure. The VoI approach seems particularly useful for the management of large and critical bridges, e.g. in terms of traffic flow. For such bridges, large costs can be involved in the closure and/or failure of the bridge, and it can be beneficial to investigate beforehand whether investing in a monitoring strategy is beneficial or whether one can better stick to an a priori determined maintenance schedule.

Finally, the VoI approach has also been applied to the case study bridge discussed in Chapter XII. Here it was found that, when the degradation rate is very small and no repairs are a priori required, the VoI is negative, as could be expected beforehand since monitoring does not induce an intervention. In such a case, the output of the VoI analysis is also less sensitive to changes in the input parameters. In the case of higher degradation rates, a positive VoI can be found for some timesteps, and the VoI will reach a maximum. This could be ascribed to the fact that monitoring triggers a repair based on the monitoring outcomes instead of only the planned repairs based on the reliability index. This repair based on the monitoring outcomes could happen before the a priori planned repair based on the reliability index. Also, when comparing the results of Chapter XII with those of Chapter XI, it could be concluded that for many input parameters, it is difficult to find a general pattern when considering the influence on the VoI. The results might significantly depend on the considered structure, costs, decisions, prior models, etc., and preferably, for each situation a sensitivity analysis to the most important input variables should be performed.

All results from the VoI analyses in this work depend on the assumptions made for the errors in the likelihood function (i.e. measurement and modelling errors). Other assumptions could be made here, which might influence the results. Nevertheless, more research is required on the appropriate quantification of these measurement and/or model errors.

In the considered examples, the optimization has been carried out for statically determinate RC girder bridges subjected to corrosion. Nevertheless, the framework could also be applied to other bridge types, such as statically indeterminate bridges. Influences of degradation on monitoring outcomes might differ, but could be accounted for by appropriate models of the structures. For prestressed and post-tensioned bridges, additional research will be required on the monitoring strategies to be applied. Other damage scenarios can also be included by altering the degradation models.

XIII.2 Recommendations for further research

In this section, recommendations for further research complementing the current work are provided.

XIII.2.1 Bayesian updating based on monitoring data

In this work, specific data types have been considered for updating the distributions of the corrosion variables, i.e. static strains and deflections, and modal data such as natural frequencies, displacement mode shapes and strain mode shapes. These different types have also been combined, and the influence of including visual observations has been investigated. However, also other data types providing information on the stiffness or directly on the corrosion degree could be included. Examples are results from acoustic emission monitoring, cover measurements, chloride penetration depths, etc. Incorporation of these data types in the methodology can be investigated. Moreover, in the present work, inference is performed based on a direct relation between the measurement output and the model parameters. Nevertheless, if probability of detection (PoD) curves would be available for the considered measurement technique, these could also be incorporated. These PoD curves give the probability of damage detection as a function of the damage extent (e.g. a defect size such as a crack width). As explained in (Straub, 2004), a PoD curve can be interpreted as a likelihood function. For example, if the measurement outcome would be an indication of damage, in the MCMC sampling, the likelihood of a sample corresponding to a certain damage extent will be the probability of detection of damage for this damage extent. A more optimal strategy will have a higher probability of detection (and a lower probability of false alarm). Different strategies can be combined by combining the different likelihood functions. Multiple measurement techniques could be considered when defining the PoD, which will lead to an increased PoD and a reduced probability of false alarm. Nevertheless, more research is required on the definition of this PoD curve for different measurement techniques.

In the current work, it has also been illustrated how a mismatch between the model and the actual structure can influence the resulting posterior distribution. Hence, effects of corrosion could be investigated in more detail. Whereas the application

of simplified corrosion models is often justified, the framework could also be applied to more complex corrosion models or even other degradation phenomena. For example, to simulate the influence of corrosion on the modal data, the cracks resulting from the corrosion process could be explicitly modelled instead of applying a stiffness reduction to the cracked concrete. As such, the influence of longitudinal cracks on lateral bending modes and the influence of transverse cracks on vertical bending modes will be accounted for in a more appropriate way.

In the Bayesian analyses performed in this work, values for the measurement errors have been assumed based on literature, and the influence of changing these measurement errors has been investigated. In the experimental program, a first quantification of the measurement error for static strain measurements was performed using measured strains on plain concrete prisms. However, this might still differ from the error when measuring strains on reinforced concrete structures. More detailed investigations on this measurement error might be required. Further, additional investigations on the quantification of the error of modal data could be performed, together with further research on deriving the model error. The latter includes the error of the finite element model (and the response surface fitted to it), but also the error of the corrosion model.

Measurement (and model) errors have also been assumed to be uncorrelated, because an uncorrelated measurement error is in correspondence with maximum data entropy in the prior estimate. However, introducing correlation can lead to a recombination of data and alter the weighing of the prior information. It also does not necessarily lead to an increase in posterior uncertainty compared to the uncorrelated case (Simoen et al., 2013). Hence, if correlation is present, neglecting this correlation is not always conservative. When considering different correlation models for the measurement and/or model error and also inferring the corresponding correlation parameters, the true correlation structure can be accurately estimated in the Bayesian inference procedure, provided sufficient data are available. As such, a more realistic joint structural-probabilistic model and corresponding Bayesian model updating results can be assured. Besides correlation, bias could also be present in the measurements. There are different options to account for this bias. The mean value of the measurement error could be assumed different from 0, an additional term in the relation between the measured and modelled output could be introduced, a multiplicative model error with mean value different from 1 could be inserted, etc. The bias from different sources could also be reduced by the consideration of redundancy in the measurement information.

The main focus of this research was on reinforced concrete structures. Nevertheless, preliminary investigations have been performed on prestressed concrete structures. Further research on this topic is advised. Information on the

state-of-the-art on the assessment of prestressed structures can be found in (Vereecken et al., 2021), which can serve as a starting point for further research.

The examples discussed in this work were often illustrative or based on literature. In the case study in Chapter XII, a real bridge geometry is considered, but simulated data is still used. In Chapter VII, real data is available for the beams subjected to accelerated corrosion, but these are tests in a rather controlled environment and on beams of limited scale when compared to a real bridge geometry. Hence, it would be very interesting to be able to perform measurements on a corroded bridge, and apply the methodology to a real bridge geometry and a rather complete data set.

XIII.2.2 Experimental investigations

With respect to the experimental investigations, additional configurations of beams could be tested. A first interesting option would consist of beams with higher corrosion degrees, to investigate whether the influence on natural frequencies and static strains would be more distinguishable for these higher corrosion degrees. Moreover, instead of applying the salt solution along the whole length of the beam, local corrosion might be induced by applying the salt solution over a smaller surface. As such, the influence of local corrosion on the displacement mode shapes and strain mode shapes can be investigated. Besides changing the corrosion process variables, other cross-sections of the concrete beam might be investigated, with different concrete covers, etc. It would also be interesting to apply the accelerated corrosion process to a reinforced concrete slab to investigate the spatial distribution of corrosion in more detail, and enable the derivation of appropriate correlation lengths. Finally, a similar experimental campaign could also be applied to prestressed concrete elements. This would provide a valuable addition to the current state-of-the-art, and can lead to relevant knowledge on the influence of corrosion on the behaviour of such structures. Moreover, this might deliver better insights in how to assess the corrosion degree and resistance of prestressed concrete structures. An important consideration in this experimental campaign should be the relation between prestress losses and the dynamic parameters.

The experimental campaign performed in this work can be used as a starting point for further experimental research. The lessons learned from the current experiments should be taken along in these future tests.

XIII.2.3 Optimization of monitoring strategies

Similar as for the Bayesian updating procedure, also the extended pre-posterior framework allows the incorporation of other monitoring techniques, more accurate

degradation models, etc. Furthermore, for the evaluation of the failure probabilities, other techniques than a FORM analysis could be relied on.

When optimizing a monitoring strategy, some suggestions are made to limit the computational effort, i.e. by optimizing sensor positions beforehand and by using approximate methods for the derivation of the posterior distribution. Nevertheless, it has also been illustrated that the resulting VoI still largely depends on different values of the input parameters, such as the costs and prior distributions. Further research might be conducted on this topic to provide general guidelines on which cost models and prior distributions should be used when evaluating an existing structure.

In the VoI analyses in the present work, the effects of repair are modelled in a simplified way. Further research could focus on which repairs are to be considered for different types of RC structures subjected to different types of degradation, their influence on the variables of interest, and the corresponding influence on the probability of failure. As such, repairs could be included in a more detailed manner in the VoI framework.

XIII.2.4 Further recommendations

Currently, research is also ongoing within the research group on a definition of appropriate and practical threshold levels related to damage. Such threshold levels could be derived based on an adjusted partial factor approach, where for example a critical value for the remaining steel section can be derived based on a target reliability index. When evaluating a (finite element) model of the structure with this adjusted steel section, corresponding displacements, strains etc. can be evaluated, which can then be used as damage thresholds. These damage thresholds can serve two purposes, i.e. in the definition of PoD curves for defining the accuracy of a monitoring/inspection strategy (cfr. supra), and in the VoI analysis as thresholds for performing a repair or maintenance action.

Generally, the aspects discussed in this work could be included in an all-encompassing framework for the assessment, evaluation and decision-making of existing reinforced concrete structures. Whereas in the current work different models are used and combined, a global workflow incorporating all aspects discussed (and which is easy to use and interpret by decision-makers) might be of very high value. This might for example be combined in a software tool that is easy to use, without requiring a full background knowledge on all the underlying calculations. This tool could enable the performance prediction, optimization of inspection and monitoring, and assessment of interventions for existing structures. For sure, this framework would still incorporate the time-dependent and spatial character of degradation and a Bayesian updating procedure to account for information from monitoring and inspections. It could also include an inspection-

based condition assessment tool, linking mechanical effects to damage parameters in a practical way. The tool could also include a framework for multi-objective performance-based optimization of maintenance strategies and repair or strengthening interventions. Extra focus could be given to modelling of the repair strategies. Choices of repair technologies and materials could then be made by explicitly considering their lifetime performance. Finally, for such a framework, suitable target performance levels for existing structures need to be derived. The whole developed methodology could then be integrated within an information management system enabling continuous life-cycle supervision based on linked data and a digital twin approach.

XIII.3 References

Simoen, E., Papadimitriou, C., Lombaert, G., 2013. On prediction error correlation in Bayesian model updating. J. Sound Vib. 332, 4136–4152.

Straub, D., 2004. Generic Approaches to Risk Based Inspection Planning for Steel Structures. PhD thesis, ETH Zürich.

Vereecken, E., Botte, W., Lombaert, G., Caspeele, R., 2021. Assessment of corroded prestressed and posttensioned concrete structures: A review. Struct. Concr. 22, 2556–2580

Appendices

APPENDIX

Corrosion experiments

A.1 Corrosion degree

Below, the results of the corrosion degree for the individual bars in each beam are presented.
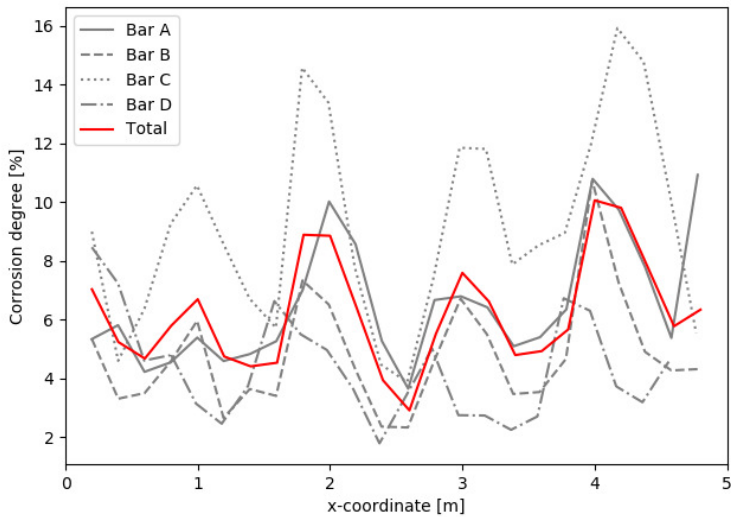

Figure A-1: Corrosion degree of beam 1.1 (6.2%) ($x = 0$ corresponds to the left when looking at the side with the strain gauges)
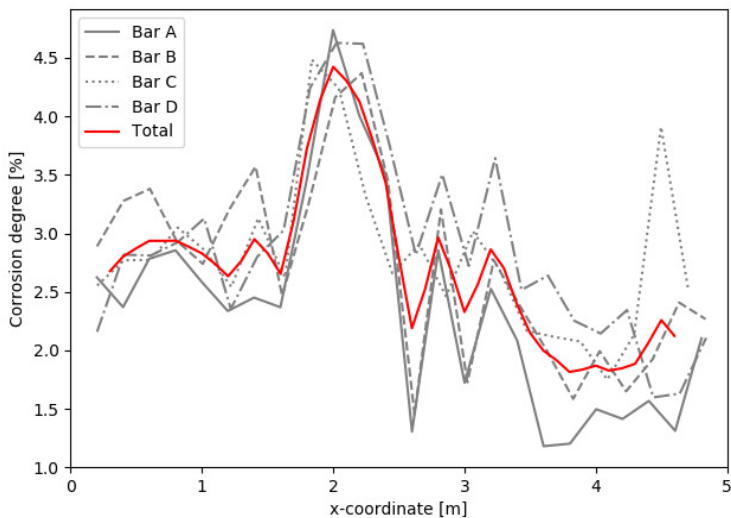

Figure A-2: Corrosion degree of beam 1.2 (2.7%) ($x = 0$ corresponds to the left when looking at the side with the optic fibres)
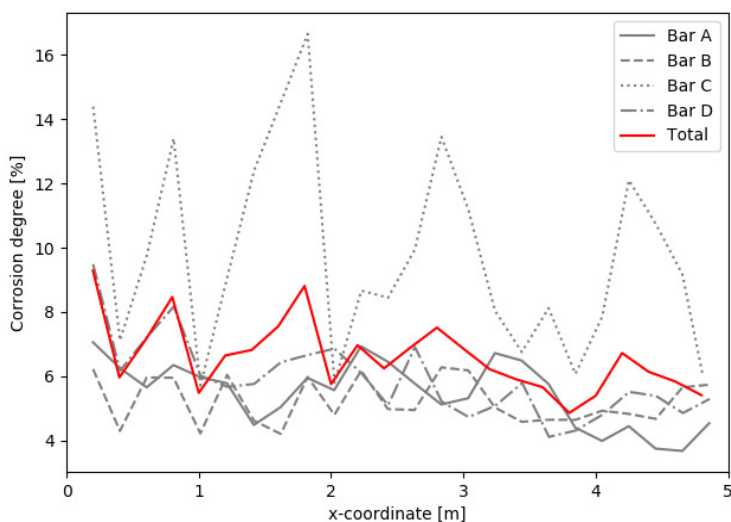
Figure A-3: Corrosion degree of beam 2.1 (6.6%) ($x = 0$ corresponds to the left when looking at the side with the strain gauges)
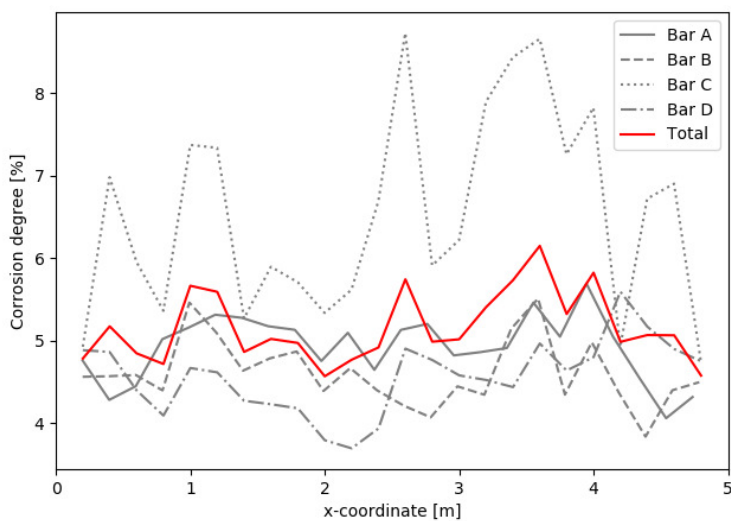

Figure A-4: Corrosion degree beam 2.2 (5.2%) ($x = 0$ corresponds to the left when looking at the side with the optic fibres)

A.2 Concrete properties

Below the experimental values for the concrete properties at the different testing ages are provided for the different concrete casts.

Table A-12: Test results material characterization set 1

	$f_{c,cyl}$ [MPa]	$f_{c,cube}$ [MPa]	f_{ct} [MPa]			G_f [N/mm]	D_{RCM} [mm²/year]	E_c [GPa]
			Set 1 – 28 days					
	38.5	42.5	3.5	4.0	2.7	0.11	1432	31.4
	38.3	43.8	3.5	3.6	3.1	0.10	1443	31.3
	40.4	42.4	3.3	3.8	2.2	/	1627	30.4
Mean	39.0	42.9	3.3			/	1500	31.0
COV	0.03	0.02	0.16			/	0.07	0.02
			Set 1 – 63 days					
	37.8	/	3.0	2.8	2.7	0.16	/	37.6
	/	/	3.0	2.6	2.6	0.16	/	/
	/	/	2.6	2.6	3.0	0.14	/	/
Mean	37.8	/	2.8			0.15	/	37.6
COV	/	/	0.07			0.08	/	/
			Set 1 – 330 days					
	36.0	/	2.1	2.5	2.3	0.20	/	33.5
	33.3	/	2.5	2.4	2.4	0.14	/	/
	/	/	3.1	2.9	3.2	/	/	/
	/	/	3.6	3.2	3.3	/	/	/
Mean	34.7	/	2.8			0.17	/	33.5
COV	/	/	0.17			/	/	/

Table A-13: Test results material characterization set 2

	$f_{c,cyl}$ [MPa]	$f_{c,cube}$ [MPa]	f_{ct} [MPa]			G_f [N/mm]	D_{RCM} [mm²/year]	E_c [GPa]
			Set 2 – 28 days					
	42.6	42.9	4.8	4.9	3.2	0.16	1496	34.3
	42.9	44.6	4.5	4.2	2.7	0.20	1645	31.1
	41.8	42.3	3.2	3.9	2.6	/	1752	/
Mean	42.4	43.3	3.8			0.18	1631	32.7
COV	0.01	0.03	0.23			/	0.08	/
			Set 2 – 182 days					
	39.8	/	3.0	3.5		0.09	/	30.2
	39.7	/	3.5	3.0		/	/	30.8
	42.3	/	2.9	3.6		/	/	30.7
Mean	40.6	/	3.2			/	/	30.6
COV	0.04	/	0.11			/	/	0.01
			Set 2 – 285 days					
	38.9	/	4.0	3.5		0.13	/	36.8
	42.1	/	3.9	3.1		0.11	/	33.4
	41.9	/	3.9	4.1		0.13	/	30.5
	40.0	/	/	/		/	/	/
Mean	40.7	/	3.7			0.12	/	33.6
COV	0.04	/	0.10			0.09	/	0.09

Table A-14: Test results material characterization set 4

	$f_{c,cyl}$ [MPa]	$f_{c,cube}$ [MPa]	f_{ct} [MPa]			G_f [N/mm]	D_{RCM} [mm²/year]	E_c [GPa]
			Set 4 – 28 days					
	37.8	41.6	3.3	3.6	2.8	0.11	1824	33.9
	38.2	41.1	3.8	3.2	2.9	0.12	1764	32.2
	36.7	40.4	3.6	2.7	2.9	0.16	2097	30.7
Mean	37.6	41.0		3.2		0.13	1895	32.3
COV	0.02	0.01		0.13		0.20	0.09	0.05
			Set 4 – 63 days					
	40.7	/		3.6		0.12	/	/
	/	/		3.1		/	/	/
	/	/		3.1		/	/	/
Mean	40.7	/		3.3		0.12	/	/
COV	/	/		0.07		/	/	/
			Set 4 – 182 days					
	36.6	41.7	3.0	3.1		0.25	/	30.0
	/	40.3	3.0	3.4		0.17	/	/
	/	/	3.0	3.8		/	/	/
Mean	36.6	41.0		3.2		0.21	/	30.0
COV	/	/		0.10		/	/	/
			Set 4 – 285 days					
	36.3	40.9	3.2	3.8		0.14	/	35.0
	/	41.0	3.3	3.8		0.13	/	/
	/	/	3.4	3.3		/	/	/
Mean	36.3	41.0		3.5		0.14	/	35.0
COV	/	/		0.08		/	/	/
			Set 4 – 330 days					
	35.2	41.9	2.9	3.2	3.2	0.17	/	33.8
	37.4	40.3	3.0	3.2	3.0	0.15	/	31.0
	35.5	/	3.0	3.3	3.1	/	/	31.6
	37.7	/	3.3	3.2	2.9	/	/	/
	/	/	3.1	3.4	3.2	/	/	/
	/	/	3.5	3.4	2.9	/	/	/
Mean	36.5	41.1		3.2		0.16	/	32.1
COV	0.04	/		0.06		/	/	0.05

A.3 Displacement mode shapes and strain mode shapes

Below the displacement mode shapes and strain mode shapes of the different corroded beams are provided.
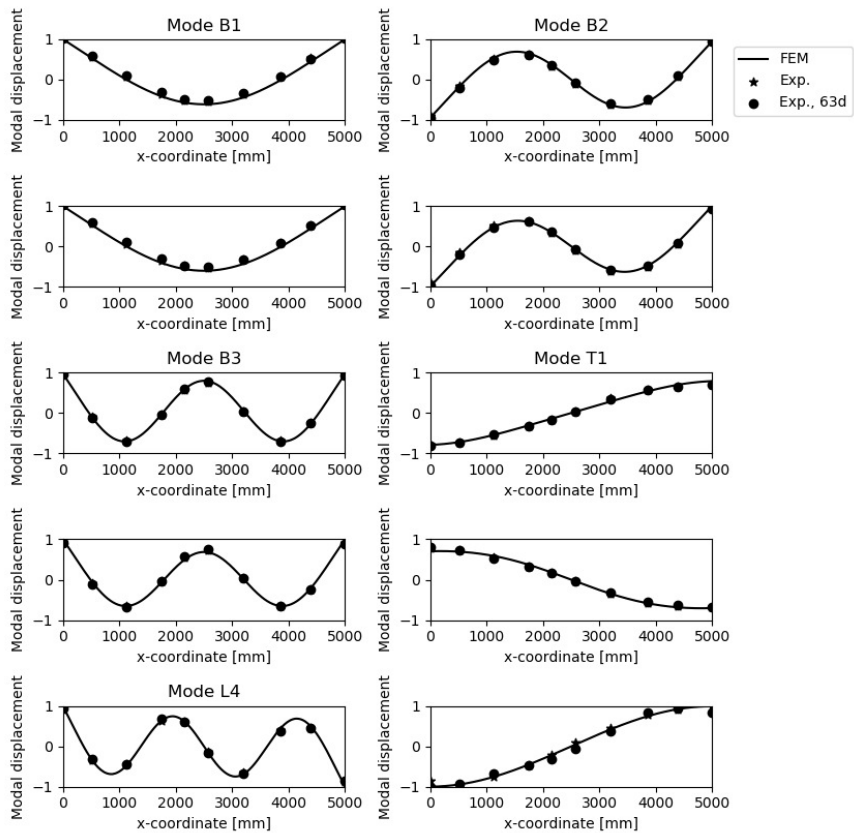

Figure A-5: Displacement mode shapes beam 1.2 (2.7% corrosion) ($x = 0$ mm corresponds to the left of the side of the beam with the optic fibres)
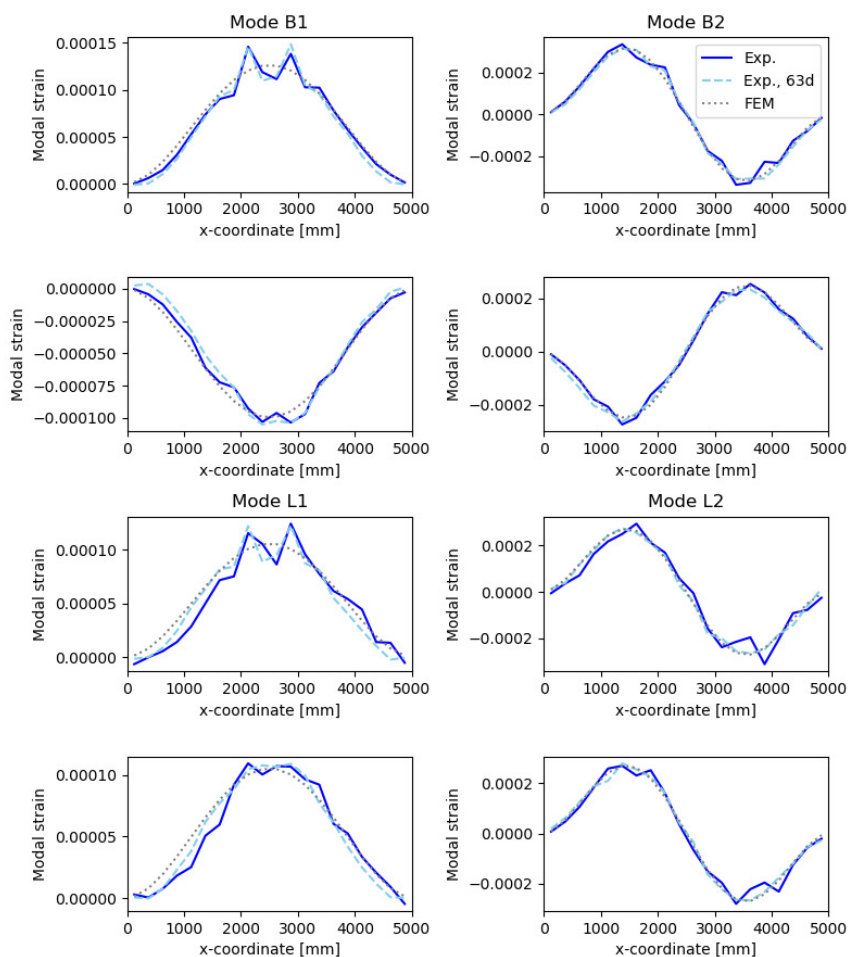
Figure A-6: Strain mode shapes beam 1.2 (2.7% corrosion) ($x = 0$ mm corresponds to the left of the side of the beam with the optic fibres)
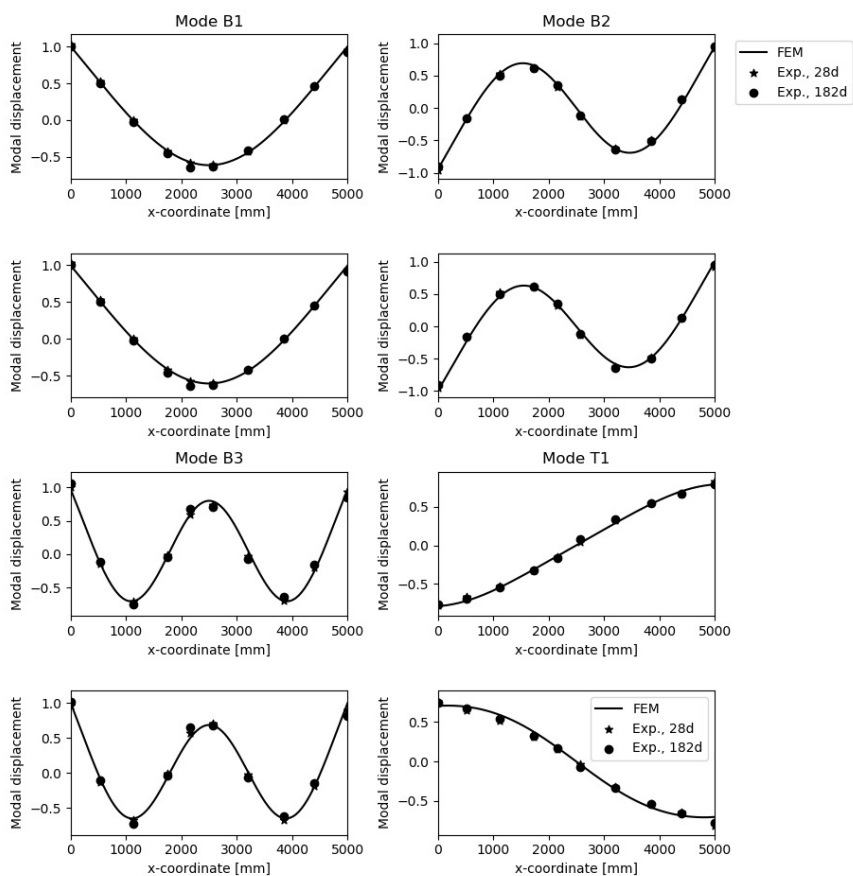
Figure A-7: Displacement mode shapes beam 2.2 (5.2% corrosion) ($x = 0$ mm corresponds to the left of the side without measuring equipment (side with optic fibres for the other beams))
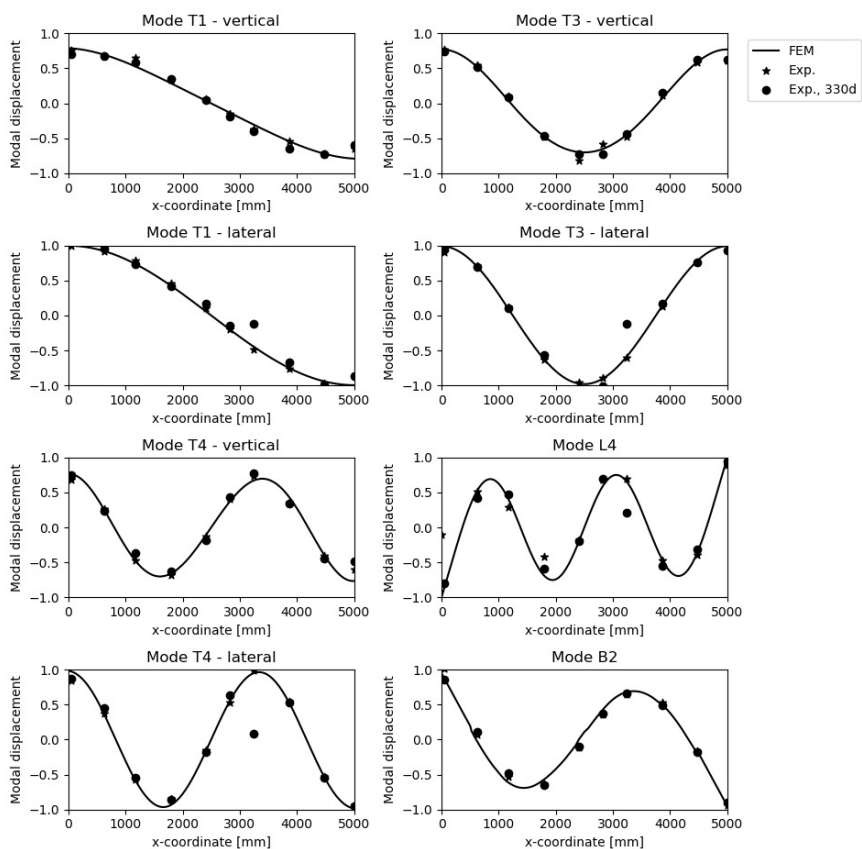
Figure A-8: Displacement mode shapes of beam 1.1 (6.2% corrosion) ($x = 0$ mm corresponds to the left of the side with the optic fibres)
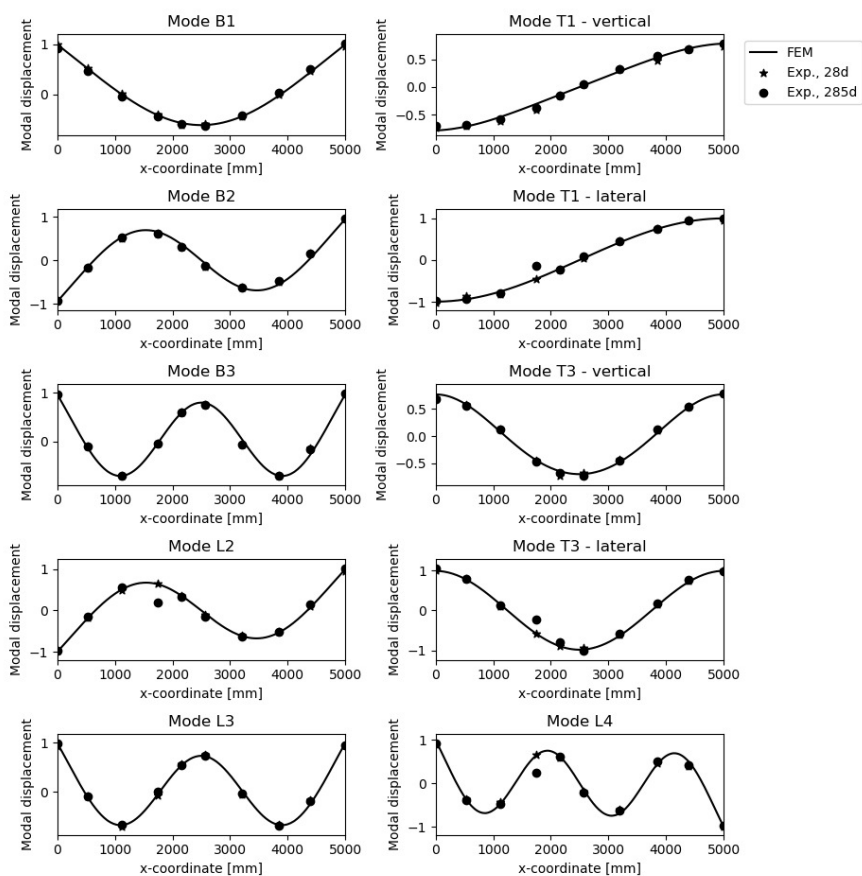
Figure A-9: Displacement mode shapes of beam 2.1 (6.6% corrosion) ($x = 0$ mm corresponds to the left of the side with the optic fibres)
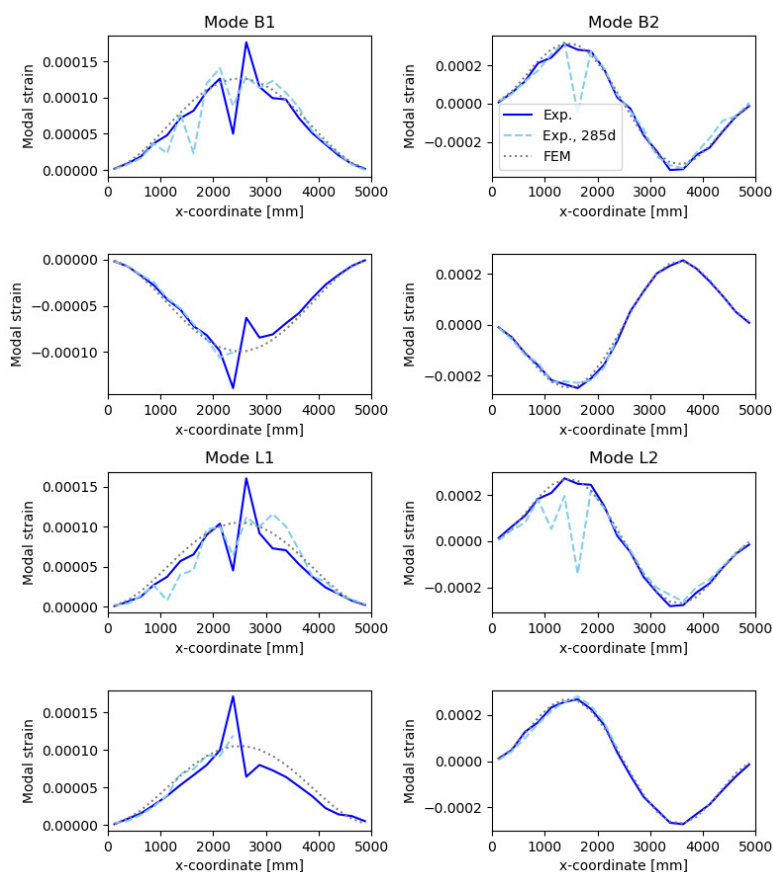
Figure A-10: Strain mode shapes beam 2.1 (6.6% corrosion) ($x = 0$ mm corresponds to the left of the side with the optic fibres)

Curriculum vitae

Eline Vereecken
°30 December 1995, Sint-Niklaas, Belgium

Education

PhD in Engineering
Department of Structural Engineering and Building Materials, Ghent University
Department of Civil Engineering, KU Leuven
September 2018 – present

M.Sc. Civil Engineering (construction design),
Ghent University
September 2016 – July 2018

B.Sc. Civil Engineering,
Ghent University
September 2013 – July 2016

Professional experience

PhD student, Department of Structural Engineering and Building Materials, Ghent University
September 2018 - present

Teaching assignments
Department of Structural Engineering and Building Materials, Ghent University
BSc Civil Engineering: Exercises *Berekening van bouwkundige constructies II*
BSc Architectural Engineering: Exercises *Draagsystemen in het architecturaal ontwerp*
Thesis advisor for one MSc student
Department of Civil Engineering, KU Leuven
BSc Engineering: Exercises: *Sterkteleer 1*
September 2018 - Present

Publications

International journal articles

[1]   Eline Vereecken, Wouter Botte, Didier Droogné & Robby Caspeele, (2020): Reliability-based calibration of partial factors for the design of temporary scaffold structures, Structure and Infrastructure Engineering, Volume 16 – Issue 4, DOI: 10.1080/15732479.2019.1670214

[2]   Eline Vereecken, Wouter Botte, Geert Lombaert & Robby Caspeele, (2020): Bayesian decision analysis for the optimization of inspection and repair of spatially degrading concrete structures, Engineering Structures, Volume 2020, 111028, DOI: 10.1016/j.engstruct.2020.111028

[3]   Eline Vereecken, Wouter Botte, Geert Lombaert & Robby Caspeele, (2021): A Bayesian inference approach for the updating of spatially distributed corrosion model parameters based on heterogeneous measurement data, Structure and Infrastructure Engineering, DOI: 10.1080/15732479.2020.1833046

[4]   Wouter Botte, Eline Vereecken, Luc Taerwe & Robby Caspeele, (2021): Assessment of post-tensioned concrete beams from the 1940s: Large-scale load testing, numerical analysis and Bayesian assessment of prestressing losses, Structural Concrete, Volume 22, Issue 3, p. 1500-1522, DOI: 10.1002/suco.202000774

[5]   Eline Vereecken, Wouter Botte, Geert Lombaert & Robby Caspeele, (2021): VoI-Based Optimization of Structural Assessment for Spatially Degrading RC Structures, Applied Sciences, 11, 4994, DOI: 10.3390/app11114994

[6]   Eline Vereecken, Wouter Botte, Geert Lombaert & Robby Caspeele, (2021): Assessment of corroded prestressed and posttensioned concrete structures: A review, Structural Concrete, DOI: 10.1002/suco.202100050

[7]   Eline Vereecken, Wouter Botte, Geert Lombaert & Robby Caspeele, (2021): Influence of the correlation model on the failure probability of a reinforced concrete structure considering spatial variability, Structure and Infrastructure Engineering, DOI: 10.1080/15732479.2021.1953082

[8]   Eline Vereecken & Robby Caspeele (2021), Conformity control of concrete durability parameters and its filtering effect on the design service life, Structural Concrete 2021, DOI: 10.1002/suco.202100459

Conference papers

[1]   Eline Vereecken, Wouter Botte & Robby Caspeele, (2019): Reliability based design of temporary structures, 6th International Symposium on Life-Cycle Civil Engineering (IALCCE) Life Cycle Analysis and Assessment in Civil Engineering: Towards an Integrated Vision, October 28-31, 2018, Ghent, Belgium

[2]   Eline Vereecken, Wouter Botte & Robby Caspeele, (2019): Calibration of Partial Factors for Temporary Structures, 13th International Conference on Applications of Statistics and Probability in Civil Engineering, ICASP13, May 26-30, 2019, Seoul, South Korea

[3]   Eline Vereecken, Wouter Botte, Geert Lombaert & Robby Caspeele, (2019): Pre-posterior analysis of inspections incorporating degradation of concrete structures, IABSE Congress The Evolving Metropolis, September 4-6, 2019, New York, United States

[4]   Eline Vereecken, Wouter Botte, Geert Lombaert & Robby Caspeele, (2020): Detecting and localizing corrosion induced damage in reinforced concrete structures based on modal data, 7th International Symposium of Life-Cycle Civil Engineering (IALCCE 2020), October 27-30, 2020, Shanghai, China

[5]   Wouter Botte, Eline Vereecken & Robby Caspeele, (2020): Large scale load testing on a 70-year old post-tensioned concrete beam, *fib* Symposium Concrete Structures for Resilient Society, November 22-24, 2020, Shanghai, China

[6]   Eline Vereecken, Wouter Botte, Geert Lombaert & Robby Caspeele, (2021): Bayesian updating of corrosion parameters based on strain measurements of a beam subjected to bending, *fib* Symposium Concrete Structures for Resilient Society, November 22-24, 2020, Shanghai, China

[7]   Eline Vereecken, Wouter Botte, Geert Lombaert & Robby Caspeele, (2021): Using heterogeneous measurement data to update the corrosion degree in bridge girders, IABSE Congress Resilient Technologies for Sustainable Infrastructures, February 3-5, 2021, Christchurch, New Zealand

[8]   Eline Vereecken, Wouter Botte, Geert Lombaert & Robby Caspeele, (2021): Bayesian assessment of the remaining prestressing reinforcement in existing concrete bridges, *fib* Symposium Concrete Structures: New

Trends for Eco-Efficiency and Performance, June 14-16, 2021, Lisbon, Portugal

[9] Eline Vereecken, Wouter Botte, Geert Lombaert & Robby Caspeele, (2022): Optimal sensor placement for updating the spatial distribution of the corrosion degree in reinforced concrete bridges, 10th International Conference on Structural Health Monitoring of Intelligent Infrastructure, SHMII 10, June 30 – July 2, 2021, Porto, Portugal

[10] Eline Vereecken, Wouter Botte, Geert Lombaert & Robby Caspeele, (2021): Updating of the corrosion degree based on visual data combined with strain or modal data, IABSE Congress Structural Engineering for Future Societal Needs, September 22-24, 2021, Ghent, Belgium

[11] Eline Vereecken, Wouter Botte & Robby Caspeele, (2021): Development of conformity criteria for diffusion coefficients of concrete and their influence on the service life of reinforced concrete structures, EuroStruct 2021 – 1st Conference of the European Association on Quality Control of Bridges and Structures, August 29 – September 1, 2021, Padova, Italy

[12] Eline Vandecruys, Charlotte Van Steen, Eline Vereecken, Geert Lombaert & Els Verstrynge, (2021): Acoustic emission monitoring of the chloride-induced corrosion process in reinforced concrete, EuroStruct 2021 – 1st Conference of the European Association on Quality Control of Bridges and Structures, August 29 – September 1, 2021, Padova, Italy

Other publications

[1] Incorporation of time-dependent and spatially distributed degradation in a pre-posterior decision making framework, Presentation at IALCCE Workshop on Life Cycle Management, October 27-29, 2019, Rotterdam, The Netherlands

[2] Beoordelen van bestaande constructies op basis van statistische updating, article in Dutch, special edition of Bouwkroniek 'Concrete Day 2021', 08/10/2021, pages 40-42, Bouwkroniek, Jette, Belgium

Reinforcement corrosion in an existing concrete structure.